BRNO UNIVERSITY OF TECHNOLOGY

FACULTY OF ELECTRICAL ENGINEERING AND COMMUNICATION

HABILITATION THESIS

Field of Research
ELECTRONICS AND COMMUNICATION

Wireless channels and physical layer algorithms

Proceedings of Original Scientific and Research Papers
from Years (2010 – 2018)

Jiří Blumenstein

BRNO 2018

Acknowledgment

I would like to thank my colleagues and friends Roman Maršálek and Aleš Prokeš. My thanks must also go to Christoph Mecklenbräuker, Thomas Zemen, Andreas Springer and Markus Rupp who provided me with a great deal of advice, constructive criticism and help significantly influencing my research career.

I am also thankful to Liu Peng and Nemanja Stefan Perović for many discussions and shared ideas. I would like to thank all the members of the Department of Radio Electronics, Faculty of Electrical Engineering, Brno University of Technology which I have had the pleasure to work with.

I am very grateful to my partner Romana Chalupová for her love, support and inspiration. A special gratitude goes to my dearest parents Jitka Blumensteinová and Jiří Blumenstein for providing me with continuous encouragement and unfailing support.

Contents

1. Preface

Today's society got used to the danger of individual transportation while tragic driving accidents are displayed on TV on a daily basis. As showed in [1], where more than 13×10^4 car accidents are studied, over 10^3 of the car crashes are with fatalities, while almost 10^4 people suffered with serious injuries. Road traffic crashes are responsible for a substantial fraction of morbidity and mortality and are responsible for more years of lost life than most of human disease [2]. In [3], [4], statistics of more than 2×10^6 car accidents are evaluated with the outcome that 94% of the accidents are caused by drivers and only 6% are caused by vehicles, environment or by unknown reasons.

Removing the human factor and an introduction of autonomous traffic could significantly reduce those numbers. Nowadays, the field of autonomous traffic is a challenging conglomerate of divergent research areas such as radar detection, signal processing, artificial intelligence, data fusion or positioning. Additionally, a recognized enabler of the large-scale autonomous traffic deployment is a dependable vehicular communication.

According to [1], a significant fraction (34.5%) of the car crashes is described as "a collision with another vehicle that is turning into or crossing a road at an intersection" [1]. Sure enough, if the vehicles on the intersections could exchange their movement vectors and positions reliably and in a timely manner, precautions could be made to avoid the collision.

Unfortunately, the current stat-of-the art of the automated driving, unsupported by ubiquitous intra- and inter-vehicular communication, is rather an error-prone process. Although strict regulations apply while operating the autonomous vehicles in a real-world traffic, serious accidents and deaths are reported [4]. Thus, the focus of this proceedings is to collects original scientific and research papers aimed at:

- vehicular wireless channel characterization [5]–[13], sounding [14] and modeling [15], namely at perspective band around 60 GHz center frequency (so called mm-wave band).

- algorithms operating at a physical layer of wireless communication systems such as algorithms for synchronization [16], channel estimation [17], signal spreading [18], [19] and perspective modulation techniques [20]–[23].

- effects of radio frequency hardware (HW) imperfections on the wireless communication systems and methods for the imperfection mitigation, i.e. I/Q imbalance compensation in systems with perspective modulation techniques such as filter bank multicarrier modulation (FBMC) [24], power amplifier linearizion [25] or effects of HW imperfections on the channel capacity [26].

Deeper understanding of the listed research fields could potentially lead to improvements in robustness and dependability of the wireless communication systems.

Part I

Introduction

2. Stochastic wireless channel parameters

The wireless communication requires the knowledge of channel characteristics in order to reach its optimal performance. With the utilization of the 60 GHz millimeter-wave (mmWave) band and with novel use cases such as the vehicle-2-vehicle communication, the channel characterization is an open research topic. This section briefly summarizes the stochastic wireless channel parameters in order to provide the reader with a fundamental theoretical background needed for the further reading [5]–[15] attached in Part II.

2.1 System functions

The time-variant channel is fully described either by its system functions or by its correlation functions. As for the system functions, we distinguish:

- channel impulse response $h(t, \tau)$,

- channel transfer function $T(t, f)$,

- Doppler-resolved impulse response $s(\nu, t)$ and

- Doppler-resolved transfer function $H(\nu, f)$.

where the functions are variables of time t, time in the delay domain τ, frequency f and Doppler frequency ν. The transition between the individual system functions is possible via the Fourier transform $\mathcal{F}$ according to [27]:

$$h(t, \tau) = \mathcal{F}_f\{T(t, f)\}, \tag{2.1}$$
$$T(t, f) = \mathcal{F}_t\{H(\nu, f)\}, \tag{2.2}$$
$$H(\nu, f) = \mathcal{F}_f\{s(\nu, \tau)\}, \tag{2.3}$$
$$s(\nu, \tau) = \mathcal{F}_t\{h(t, \tau)\}. \tag{2.4}$$

The drawback of the full channel description (i.e. $\forall[t, f]$) via the system functions is that this approach leads to a necessity to utilize multidimensional probability density function (pdf). In other words, this approach would require joint pdf of the complex amplitudes at all possible values of time and delay [28].

2.2 Correlation functions

The autocorrelation function (ACF) of channel impulse response is given as:

$$R_h(t, t', \tau, \tau') = \mathbb{E}\{h^*(t, \tau)h(t', \tau')\}. \tag{2.5}$$

where $*$ denotes the complex conjugation and $\mathbb{E}$ stands for expectation.

Obviously, R_h is a function of four variables; however, in a special case of wide sense stationary (WSS) and uncorrelated scattering (US) condition (more details in Section 2.2.1), the system functions can be transfered to the correlation functions exploiting that $t - t' = \Delta t$ and $f - f' = \Delta f$, leading to:

$$R_h(t, t', \tau, \tau') = \mathbb{E}\{h^*(t, \tau)h(t', \tau')\} = P_h(\Delta t, \tau). \tag{2.6}$$

Utilizing the Dirac function notation δ and taking into account the WSSUS condition, the correlation functions could be written as [28]:

$$R_h(t, t + \Delta t, \tau, \tau') = P_h(\Delta t, \tau)\delta(\tau, \tau'), \tag{2.7}$$
$$R_H(t, t + \Delta t, f, f + \Delta f) = P_H(\Delta t, \Delta f), \tag{2.8}$$
$$R_s(\nu, \nu', \tau, \tau') = P_s(\nu, \tau)\delta(\nu - \nu')\delta(\tau - \tau') \tag{2.9}$$
$$R_B(\nu, \nu', f, f + \Delta f) = P_B(\nu, \Delta f)\delta(\nu - \nu') \tag{2.10}$$

Now, thanks to the Wiener-Khinchin theorem stating that the power spectral density and the autocorrelation of a WSS random process are Fourier transform pairs as [29]:

$$S(f) = \sum_{k=-\infty}^{\infty} R_x \exp(-i(2\pi f)k), \text{ where } R_x = \mathbb{E}\{x[n]x^*[n - k]\}, \tag{2.11}$$

ACF of the channel impulse response can be transformed via the Fourier transform into:

$$P_h(\Delta t, \tau) = \mathcal{F}_{\Delta f}\{R_T(\Delta t, \Delta f)\}, \tag{2.12}$$
$$R_T(\Delta t, \Delta f) = \mathcal{F}_{\Delta t}\{P_H(\nu, \Delta f)\}, \tag{2.13}$$
$$P_H(\nu, \Delta f) = \mathcal{F}_{\Delta f}\{P_s(\nu, \tau)\}, \tag{2.14}$$
$$P_s(\nu, \tau) = \mathcal{F}_{\Delta t}\{P_h(\Delta t, \tau)\}, \tag{2.15}$$

where the complementary ACF functions have been given distinct names [30]:

- $P_h(\Delta t, \tau)$ is referred to as delay cross power spectral density,

- $R_T(\Delta t, \Delta f)$ is referred to as time frequency correlation function,

- $P_s(\nu, \tau)$ is referred to as scattering function,

- $P_H(\nu, \Delta f)$ is referred to as Doppler cross power spectral density.

The reason for the introduction of the correlation function is that the Fourier transform of certain random signals may not exist; however, the psd, obtained from the autocorrelation function, does exist. Moreover, the autocorrelation is directly measurable [29]. On top of that, as will be shown in the following section, marginalized correlation functions and subsequently derived condensed parameters have important implications to the design of wireless communication systems.

2.2.1 Wide-sense stationary, uncorrelated scattering (WSSUS)

The WSS condition is defined as a state when the ACF is not dependent on the variables t, t' independently, but is dependent only on their difference $t - t' = \Delta t$ (see Equation 2.6). In practice, this means that the statistics properties remain static. The US condition could be described as a situation where multipath components with different delays are uncorrelated [28]. On a first look, the WSSUS conditions does not hold for any practical mobile channel. For example, as the mobile device moves, the path loss (PL) certainly changes. Therefore, concepts like the local scattering function has been introduced in [31]. In less rigorous way it is stated that usually the wireless channel parameters are quasi static in an area of about 10λ diameter [28].

2.3 Marginalized correlation functions

It might be sometimes useful to observe only the averaged evolution of the scattering function in the delay or in the Doppler domain. Such marginalized views on the scattering function are referred to as the *Power-delay* and *Doppler-power profiles.* In this cases, the scattering function $P_s(\nu, \tau)$ can be marginalized into the Power-delay profile being given as:

$$p_d(\tau) \triangleq \int_{-\infty}^{\infty} P_s(\nu, \tau) \, \mathrm{d}\nu \ \text{ or } \ p_d(\tau) = \mathbb{E}\{|h(t, \tau)|^2\}, \tag{2.16}$$

while integration of the scattering function $P_s(\nu, \tau)$ by the time in the delay domain τ, the Doppler-power is obtained as:

$$D_p(\nu) \triangleq \int_{-\infty}^{\infty} P_s(\nu, \tau) \, \mathrm{d}\tau \tag{2.17}$$

2.4 Condensed parameters

The condensed parameters, again derived from the scattering function $P_s(\nu, \tau)$, are directly translated to the design of the wireless communication systems. The parameters and its implications are stated below, but first we remind some basics of statistical terminology.

Note on statistical terminology

For the further reading and understanding of the Delay and Doppler spreads, we remind a known notation of a k-th moment of variable X being written as:

$$\mu_{\mathrm{R}k} = \sum_{i=1}^{n} x_i^k p_i \tag{2.18}$$

where p_i is the probability of X being equal to x_i and k is the order. The variable $\mu_{\mathrm{R}k}$ is referred to as the raw moment. When adjusted by subtracting the expected value, the central moments are defined as:

$$\mu_{\mathrm{C}k} = \sum_{i=1}^{n} (x_i - E\{X\})^k p_i \tag{2.19}$$

Now, the common notation is that the first (raw) moment is called *mean*, and the second (central) moment is called *variance*.

Going back to the condensed parameters of the propagation channel, the most known and useful parameters calculated from the scattering function $P_s(\nu, \tau)$ are listed below:

- Average power attenuation, i.e. PL:

$$P_L = -10\log_{10}(\rho^2) \tag{2.20}$$

  where

$$\rho^2 = \int_{-\infty}^{\infty} \int_{-\infty}^{\infty} P_s(\nu, \tau) \, d\tau \, d\nu. \tag{2.21}$$

  The PL is needed for link budget calculation.

- The delay spread and the Doppler spread are root mean square (RMS) *widths* of power-delay profile $p_d(\tau)$ and Doppler power profile $D_p(\nu)$, respectively. First, we need to define *mean* delay and *mean* Doppler shift (first order moments) $\bar{\tau}, \bar{\nu}$ and then we calculate the second order central moments, i.e. the RMS delay spread and Doppler spread according to [32]:

$$\bar{\tau} \triangleq \frac{1}{\rho^2} \int_{-\infty}^{\infty} \int_{-\infty}^{\infty} \tau P_s(\tau, \nu) \, d\tau \, d\nu, \tag{2.22}$$

$$\sigma_\tau \triangleq \frac{1}{\rho} \sqrt{\int_{-\infty}^{\infty} \int_{-\infty}^{\infty} (\tau - \bar{\tau})^2 P_s(\tau, \nu) \, d\tau \, d\nu} \tag{2.23}$$

$$\bar{\nu} \triangleq \frac{1}{\rho^2} \int_{-\infty}^{\infty} \int_{-\infty}^{\infty} \nu P_s(\tau, \nu) \, d\tau \, d\nu, \tag{2.24}$$

$$\sigma_\nu \triangleq \frac{1}{\rho} \sqrt{\int_{-\infty}^{\infty} \int_{-\infty}^{\infty} (\nu - \bar{\nu})^2 P_s(\tau, \nu) \, d\tau \, d\nu} \tag{2.25}$$

- Coherence bandwidth and time:

  - Coherence bandwidth $B_c = 1/\sigma_\tau \propto$ number of multipath components.
  - Coherence time $T_c = 1/\sigma_\nu \propto$ the speed of the mutual movement or movement of the scatters [32].

The importance of coherence time is given by its implications to a channel estimation and equalization algorithms. Suppose that the received signal is given as $y(t) = h \, x(t)$, where h represents complex channel attenuation and $x(t)$ is the transmitted signal. Now, the estimated transmitted signal at the receiver side is written as $\hat{x}(x) = \frac{1}{h} y(t) = x(t)$ meaning that the channel needs to be estimated once the coherence time T_c.

3. Physical layer algorithms

This chapter provides brief introduction to the contributions [16]–[23], whose full reprints are available in Part II.

3.1 Two-dimensional spreading and channel estimation

Precise yet robust channel estimation is one of the key enablers of the vast data throughput increases we had experienced in last two decades. Considering a state-of-the-art example of multicarrier communication system, the channel-state information (CSI) is usually obtained by comparison of the received training sequences with the transmitted ones which are known at the receiver side [33].

This training sequence has to be two-dimensional in order to tackle the channel transfer function fluctuations in both the time and frequency domains [34]. Therefore, the training sequence, or more commonly the pilot symbols, occupies certain time and frequency resources which are then unable to carry any data payload. Between those time-frequency resources occupied by the pilot symbols, the CSI stays unknown and can only be estimated by interpolation [35].

Obviously, the more pilot symbols and the denser the time-frequency estimation grid we apply, the more reliable CSI. However, the higher overhead and the lower data throughput. Nowadays, the effort is focused mainly to determine the most effective way of processing the channel state information samples. High effort is also given into a research of a pilot density [36], or optimal pilot power allocation [37]. Moreover, second order statistic data about the noise distribution are exploited in order to improve the CSI reliability [38], thus throughput performance.

The idea of two-dimensional signal spreading in systems employing the Orthogonal Frequency Division Multiplex (OFDM) is presented in [39], [40], where the authors exploit a possibility of one-cell frequency reuse which led to significant throughput increase compared with three-cell frequency reuse. This had been possible due to the utilization of an orthogonal signal spreading, thus profiting by a code domain as well known from Code Division Multiple Access (CDMA) systems.

However, one-cell reuse is supposed for LTE [41], so we could not benefit from obtaining any additional frequency bands. Conversely, to keep the comparison of newly presented method with the state-of-the-art fair, the bandwidth widening is not acceptable.

In the following text, the fundamentals of the 2D spreading [17], [42], [43] are explained and subsequently utilized for enhanced channel estimation, mainly in difficult conditions of low signal-to-noise ratio (SNR) or impulse noise jamming. The following text also provides the reader with basic techniques of channel estimation.

3.1.1 System model

In order to illustrate the principle of the 2D spreading based channel estimation method proposed in [17], [43], we consider the implementation to the LTE physical layer system model. The aim of this section is to describe the Long Term Evolution (LTE) features related to the proposed method. The LTE utilizes a frequency bandwidth BW, where BW $\in (1.4, 3, 5, 10, 15, 20)$ MHz. This corresponds to the number of resource block $N_{rb} \in (6, 15, 25, 50, 75, 100)$, where so called resource block is a grouping of 12 subcarriers with 15 kHz spacing.

In time domain, as visible in Figure 3.1, the resources are described as frames, which lasts for 10 ms, those are divided into two slots and further, the slots consists of ten equal subframes with duration of 0.5 ms. One subframe then consists of 14 OFDM symbols. An intersection of one OFDM symbol and one subcarrier forms a resource element.

As depicted in Figure 3.2, LTE time-frequency grid contains pilot symbols that occupy certain resource elements. The placing of those pilot-symbols is standardized [44], nevertheless LTE does not mandate any specific channel estimation technique so there is a complete freedom in implementation assuming that the performance requirements are met and the complexity is affordable [41].

Since we benefit from utilization of the LTE downlink simulator [45], [46], an implementation of our novel method is straightforward. The signal processing chain of the LTE simulator is visible in Figure 3.3 with white-marked blocks according to standard [44], [47], [48]. The dark gray blocks represent the additional non-LTE standard compliant blocks for 2D spreading, despreading, modified frame builder and channel estimation.

The received signal vector $\mathbf{y} \in \mathbb{C}^{1 \times n}$ is written as:

$$\mathbf{y} = \mathbf{Zh} + \mathbf{v}, \tag{3.1}$$

so that the $\mathbf{h} \in \mathbb{C}^{1 \times n}$ is a vector of channel coefficients, n is a number of transmitted symbols and corresponds to the bandwidth BW. The $\mathbf{v} \in \mathbb{C}^{1 \times n}$ is an additive white Gaussian noise vector. One element of $\mathbf{v}$ is defined according to:

$$v = \sqrt{\frac{N_{\text{fft}}}{N_{\text{tot}}}} 10^{-\frac{SNR}{20}} \left(N(0,1) + jN(0,1) \right), \tag{3.2}$$
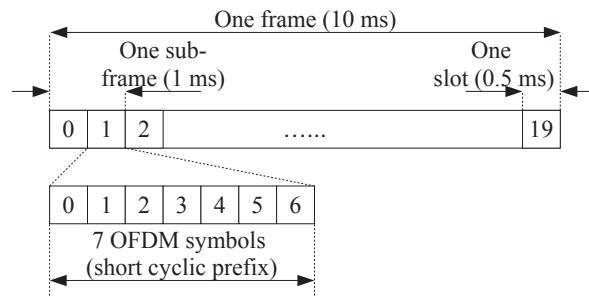
Figure 3.1: The description of LTE resources in time domain. In case of 'normal' cyclic prefix we utilize 7 OFDM symbols in one subframe.
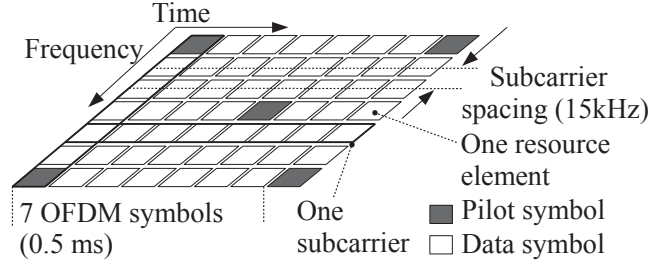
Figure 3.2: The pilot symbols (gray) are placed in a 3GPP standard compliant time-frequency pattern. The CSI between the pilot symbols should be estimated via interpolation.

where $N(0,1)$ denotes zero-mean, normally distributed pseudo-random number with variance one. The j stands for basic imaginary unit. Other symbols are described in Table 3.1. The fraction $\sqrt{\frac{N_{\text{fft}}}{N_{\text{tot}}}}$ compensates the fact that LTE utilizes so-called zero subcarriers and is given in Table 3.2.

3.1.2 Least Squares estimation

The $\mathbf{Z} \in \mathbb{C}^{n \times n}$ from Equation 3.1 is a diagonal matrix written as:

$$\mathbf{Z} = \text{diag}(\mathbf{z}), \tag{3.3}$$

where the $\mathbf{z}$ is a permuted data and pilot composite vector $\tilde{\mathbf{z}} = [\mathbf{z_p}^{\text{T}}, \mathbf{z_d}^{\text{T}}]^{\text{T}}$, permuted according $\mathbf{z} = \mathbf{P}\tilde{\mathbf{z}}$ where the matrix $\mathbf{P} \in \mathbb{N}_{0 \leq 1}^{n \times n}$ is a standardized permutation matrix given by [44]. The LS estimation is then performed according:

$$\hat{\mathbf{h}}_{\text{p}}^{LS} = \mathbf{Z}_{\text{p}}^{\text{H}} \mathbf{y}_{\text{p}}. \tag{3.4}$$

The vector $\mathbf{y}_{\text{p}} \in \mathbb{C}^{1 \times p}$ represents the received pilot signal of length p and the $\mathbf{Z}_{\text{p}}^{\text{H}}$ is the Hermitian transpose of the transmitted signal matrix $\mathbf{Z}$ at specific pilot positions. The channel coefficients between the pilot symbols have to be obtained by interpolation. In the experiments, we apply linear interpolation.

Table 3.1: LTE system parameters of the presented simulations

$\mathbb{N}, \mathbb{R}, \mathbb{C}$, and $\mathbb{N}_{0 \leq 1}$	Natural, Real, Complex and Natural non-negative number system respectively.
$N(0,1)$	zero-mean, normally distributed pseudorandom number with variance one.
j	basic imaginary unit
$\otimes$	Kronecker product
$\odot$	Hadamard product
$\mathbf{Z}^{\text{H}}$	Hermitian transpose of $\mathbf{Z}$
$\mathbf{X}_{\mathbf{d}(i,*)}$	i-th row of the matrix $\mathbf{X_d}$
Ξ	Orthogonal Walsh-Hadamard matrix

Figure 3.3: The LTE signal processing chain. The dark gray blocks represents the additional non-LTE standard compliant blocks for 2D spreading, despreading and channel estimation. Other parts remain the same in both versions, 2D spreading based LTE and standard LTE. White blocks are according to [44], [47], [48].

3.1.3 LMMSE estimation

The linear minimum mean square error (LMMSE) estimation requires knowledge of the second-order statistic of the noise and radio channel. It is visible in [49] that the LMMSE estimator represents the filtered least square (LS):

$$\hat{\mathbf{h}}_{\text{LMMSE}} = \mathbf{A}_{\text{LMMSE}} \hat{\mathbf{h}}_{\text{p}}^{LS}, \tag{3.5}$$

by minimizing MSE, we obtain the filtering matrix $\mathbf{A}_{\text{LMMSE}}$:

$$\mathbf{A}_{\text{LMMSE}} = \mathbf{R}_{\mathbf{h},\mathbf{h_p}} \left(\mathbf{R}_{\mathbf{h_p},\mathbf{h_p}} + \sigma^2 \mathbf{I} \right)^{-1}, \tag{3.6}$$

where $\mathbf{R}_{\mathbf{h},\mathbf{h_p}}$ is the channel cross-covariance matrix and $\mathbf{R}_{\mathbf{h_p},\mathbf{h_p}}$ is the channel covariance matrix. $\mathbf{I}$ is the identity matrix and σ^2 is the noise variance. Those variables are assumed to be either exactly known, which represents ideal case, or they needs to be estimated using training sequence. Both those cases are evaluated it the section Experiment and results.

3.1.4   2D spreading channel estimation method

Transmitter

In this subsection, the system model of the modified 2D spreading based LTE downlink will be described in detail. The signal from the Layer Mapping block represented by vector $\mathbf{x} \in \mathbb{C}^{1 \times n}$, as seen in Figure 3.3, is written as:

$$\mathbf{x} = [\mathbf{x_d}^{\mathrm{T}}, \mathbf{x_p}^{\mathrm{T}}]^{\mathrm{T}}, \tag{3.7}$$

The vector $\mathbf{x_d}^{\mathrm{T}} \in \mathbb{C}^{1 \times (n-p)}$ is a vector of data symbols and $\mathbf{x_p}^{\mathrm{T}} \in \mathbb{C}^{1 \times p}$ is a vector of pilot symbols (here we assume vector of ones). Again, the n corresponds with the system bandwidth and p is number of subcarriers. The received signal $\mathbf{y}$ is then, similarly as in the LS case, given by:

$$\mathbf{y} = \mathbf{X_s}\mathbf{h} + \mathbf{v}, \tag{3.8}$$

where the $\mathbf{h}$ and the $\mathbf{v}$ vectors represent the same variables as in Equation 3.1. The $\mathbf{X_s} \in \mathbb{C}^{n \times n}$ is also a diagonal matrix describing the spreading operation of the pilots and data. The matrix $\mathbf{X_s}$ is composed as:

$$\mathbf{X_s} = \mathrm{diag}\left(\underbrace{w_{SF}\left(\mathbf{x_p} \otimes \mathbf{\Xi}_{(SF,*)}\right)}_{\text{pilot sequence}} + \underbrace{\sum_{i=1}^{SF-1} w_i \left(\mathbf{X_{d}}_{(i,*)} \otimes \mathbf{\Xi}_{(i,*)}\right)}_{\text{data}} \right), \tag{3.9}$$

where

$$\mathbf{X_d} = \begin{bmatrix} x_1 & \cdots & x_{n/SF} \\ x_{n/SF+1} & \ddots & \vdots \\ \vdots & \cdots & x_n \end{bmatrix}, \tag{3.10}$$

and

$$\mathbf{\Xi} = \begin{bmatrix} \xi_{1,1} & \cdots & \xi_{1,SF} \\ \vdots & \ddots & \vdots \\ \xi_{SF,1} & \cdots & \xi_{SF,SF} \end{bmatrix}. \tag{3.11}$$

The SF is the spreading factor, the $\mathbf{\Xi} \in \mathbb{N}_{0 \leq 1}^{SF \times SF}$ is the SF-th order Hadamard matrix, the $\otimes$ represents the Kronecker product [50] and the $\mathbf{X_{d}}_{(i,*)}$ denote i-th row of the matrices $\mathbf{X_d}$. For simplicity, the $\mathbf{x_p} = \mathbf{1}_{1,n/SF}$, i.e. vector of ones of the length $\frac{n}{SF}$. The $\mathbf{x_p}$ is known at the transmitter as well as the receiver side so this is the pilot sequence, later referred to as a pilot layer.

The w_i is an element of a vector $\mathbf{w} \in \mathbb{R}_{>0}^{1 \times SF}$ representing a constant weight factors for adjusting the per-layer SNR. Here we assume the weights 1.5 for the whole pilot layer and 0.99 for all data layers. At the transmitter side, we ensure the same signal power level as in the case of standard LTE downlink signal exploiting RMS power normalization as shown in Figure 3.4.

The novel 2D spreading based channel estimation method for channel estimation results in simplification of the frame builder block so that the spread data symbols will be stacked one after another. Since the data symbols are spread with spreading factor SF,
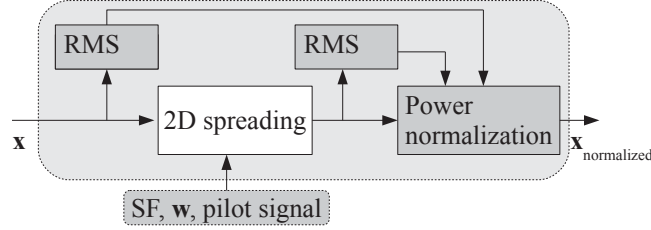
Figure 3.4: In order to keep the same transmit power levels for both, the standard compliant LTE and the novel 2D spreading method, the RMS based power normalization is employed.

Table 3.2: LTE system parameters of the presented simulations:

System bandwidth BW	1.4 MHz
Carrier frequency	2.1 GHz
Number of symbols contained in one subframe	$n \in (816, 960)$
Subcarrier spacing	15 kHz
Subframe duration	1 ms
N_{fft}	128
N_{tot}	72
Number of UE	1
Number of eNodeBs	1
Transmission Scheme	SISO
Number of subframes	1 000
CQI	1-5
SF	48
CP length	'normal' [44]
Channel estimation method	LS and 2D spreading based estimation
Channel model	VehA, VehB, ETU, RA, PedA, PedB, HT [51], [52]
User Terminal (UE) velocity	10km/h

the amount of transmitted chips (spread data symbols) is SF times the number of symbols, it equals to eSF. The chips are summed in a code domain as depicted in Figure 3.5. In the receiver side, thanks to the orthogonality of Hadamard sequences, code layers can be separated. Due to the addition of the spread signal in the code domain, the resulting signal is of length n, i.e. the same length as in a case of standard LTE, thus the bandwidth of the spread signal remains the same as in the case of standard LTE downlink.

As seen in Figure 3.5, the first $SF - 1$ code layers are devoted to data transmission, whereas the SF-th code layer carries the pilot signal - in Equation 3.9 noted as the variable $\mathbf{x_p}$.
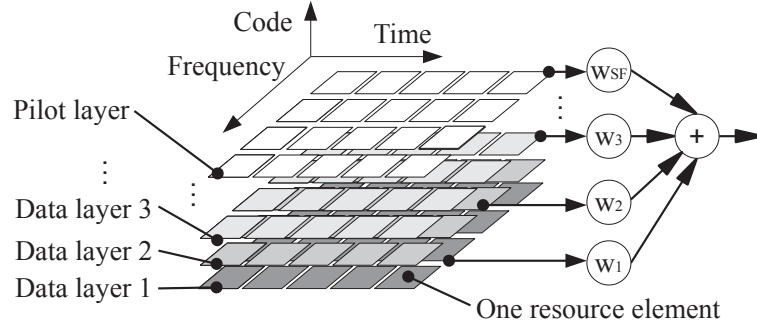
Figure 3.5: Proposed novel 2D spreading based time-frequency-code grid. The first $SF-1$ code layers are devoted to data transmission, whereas the SF-th code layer carries the pilot signal. The $\mathbf{w}$ is a vector of constant weight factors for adjusting the per-layer SNR.

Receiver

The received signal $\mathbf{y} \in \mathbb{C}^{1 \times n}$ can be written as:

$$\mathbf{y} = (y_1, y_2, \ldots, y_n). \tag{3.12}$$

Similarly to a conventional CDMA receiver, the signal is despread by correlating with the spreading matrix $\mathbf{\Theta} \in \mathbb{N}_{0 \leq 1}^{SF \times n}$. First step is the Hadamard multiplication with the despreading matrix:

$$\mathbf{Y} = \begin{pmatrix} \mathbf{y}_1 \\ \mathbf{y}_2 \\ \vdots \\ \mathbf{y}_{SF} \end{pmatrix}, \text{ where } \mathbf{y}_v = \frac{1}{SF} \left(\mathbf{y} \odot \mathbf{\Theta}_{(v,*)} \right), \tag{3.13}$$

where the $\odot$ represents the Hadamard product [50] and the despreading matrix $\mathbf{\Theta}$ is the $\frac{n}{SF}$ times replicated $\mathbf{\Xi}$ matrix. This is written as:

$$\mathbf{\Theta} = \left[\mathbf{\Xi}_1, \mathbf{\Xi}_2, \ldots, \mathbf{\Xi}_{\frac{n}{SF}} \right] \text{ such that } \mathbf{\Xi}_m = \mathbf{\Xi}, \forall m \in \left(1, 2, \ldots, \frac{n}{SF} \right). \tag{3.14}$$

The resulting matrix $\mathbf{Y_d} \in \mathbb{C}^{\frac{n}{SF} \times SF}$ is constructed by partial summation of elements y from the matrix $\mathbf{Y} \in \mathbb{C}^{n \times SF}$ defined in Equation 3.13:

$$\mathbf{Y_d} = \begin{pmatrix} \mathbf{y_{d1}} \\ \mathbf{y_{d2}} \\ \vdots \\ \mathbf{y_{d\frac{n}{SF}}} \end{pmatrix}, \text{ where } \mathbf{y_{di}} = \left(\sum_{k=1}^{SF} \{ y_{(k,SF(i-1)+1)} \}, \right.$$

$$\left. \sum_{k=1}^{SF} \{ y_{(k,SF(i-1)+2)} \}, \ldots, \sum_{k=1}^{SF} \{ y_{(k,iSF)} \} \right), \forall i = (1, 2, \ldots, \frac{n}{SF}). \tag{3.15}$$

Considering the pilot vector as vector of ones, the channel estimate is expressed as SF-th code layer of the $\mathbf{Y_d}$ matrix. Since the pilot layer is transmitted in the spread form,

15

it needs to be spread again in order to achieve complete CSI estimate over all assigned time-frequency recourses. Therefore, no interpolation is needed. Therefore it is straightforward to write:

$$\hat{\mathbf{h}}^{\mathbf{2D}} = \mathbf{y}_{\mathbf{d}\frac{n}{SF}} \otimes \mathbf{\Xi}_{(SF,*)}. \tag{3.16}$$

The computational complexity is approximately the same as in the case of the LS method. There is also no need for any kind of a priori information.

3.1.5 Experiment and results

The simulations were performed in the modified Vienna LTE downlink simulator with the setting summarized in Table 3.2 for various channel models (VehA, VehB, ETU, RA, PedA, PedB, HT [51], [52]).

Common metric for comparing channel estimators is a Mean Square Error (MSE) of the channel estimate when compared with a perfect channel knowledge. We test the following estimators:

- LMMSE estimator with ideal covariance matrix

- LMMSE estimator with covariance matrix estimated from a training sequence

- LS estimation

- 2D spreading estimation method
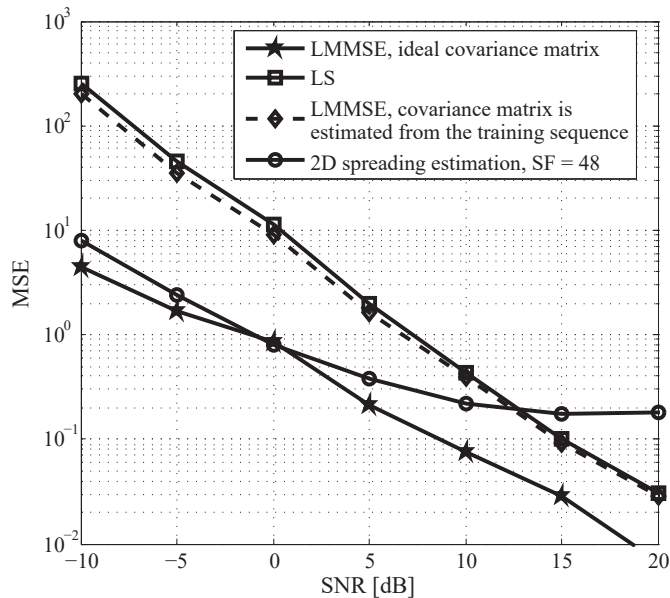
Figure 3.6: The dependency of MSE on SNR. Results are plotted for PedA channel model while the channel state is assumed to change during one symbol interval.

In Figure 3.6 we can observe MSE performance of all these estimators. The LMMSE estimator with ideal covariance matrix produces the lowest MSEs, however the method

exploits a perfect knowledge of the second order statistic of the radio channel, namely the Channel Covariance Information (CCI) [53].

The CCI is not always available, thus it needs to be estimated from the training sequence. Performance of the LMMSE estimator with estimated channel covariance matrix is notably worse and it is close to the LS estimator which does not need the CCI. Our novel method exploits an averaging principle when estimating the CSI, thus it provides superior performance in low SNRs, however at higher SNRs the channel estimate is not as detailed as in the case of LMMSE and LS estimators. This phenomenon is represented by the MSE floor of the 2D spreading based estimation method shown in Figure 3.6.

3.2 Generalized spatial modulation

The operating principle of spatial modulation (SM) or generalized spatial modulation (GSM) MIMO systems[54]–[57] is radically different from that of conventional spatial multiplexing (SMX) MIMO systems, e.g., D-BLAST (Diagonal-Bell Laboratories Layered Space-Time)[58] and V-BLAST (Vertical BLAST)[59]. In SMX MIMO, the SMX gain is achieved by simultaneous transmission of multiple in-phase and quadrature (IQ) streams at the same frequency. Typically, the same number of transmitter (TX) chains (from baseband to RF) as the number of data streams are needed in SMX multiple-input multiple-output (MIMO) thus introducing significant hardware and data processing complexities. However, in SM/GSM MIMO (see Figure 3.7), data streams are transmitted not only in the conventional IQ domain but also in a so-called spatial domain.

SM was originally proposed to activate only a single TX antenna and transmit a single stream in the IQ domain, but was later generalized to GSM which supports multiple antenna activation and even multiple IQ stream transmission[60]–[62]. Compared to SMX, SM/GSM can not only reduce hardware and signal processing complexities[63], but also show significantly improved TX energy efficiency [64], [65]. The spatial domain transmission is achieved by selecting a sub-group of TX antennas for transmission of the IQ stream and modulating the spatial stream in the antenna indicies.

In the attached papers [20], [21], for the sake of practical relevance to mmWave communications, we consider the case of GSM with only a single IQ stream. Moreover, we

---
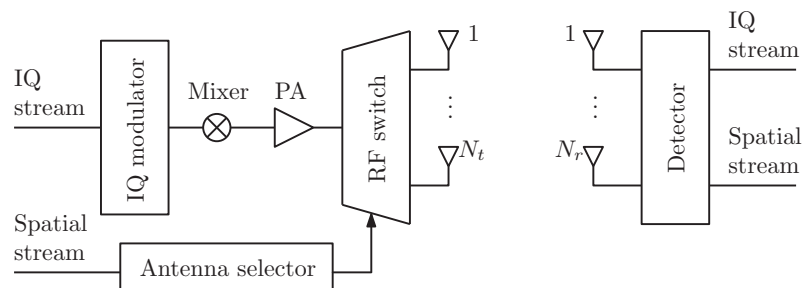
Figure 3.7: Conceptual architecture for SM/GSM MIMO.

test the novel modulation method on measured wireless channel realizations, we derive the mutual information and the cut-off rate, which is shown to be capable to practically replace the Shannon capacity as its calculation is rather cumbersome for the GSM systems .

3.3   Synchronization

Even though being an integral and crucial part of wireless communication systems for decades, time synchronization still represents an open research question. For coarse time synchronization, among other sequences, the Zadoff-Chus (Z-Chs) [66] are especially used due to their favorable autocorrelation properties. Moreover, Z-Ch belongs to the family of constant amplitude zero autocorrelation (CAZAC) waveforms implying a good peak-to-average power ratio (PAPR) and beneficial channel estimating capabilities. On the other hand, the symbols of the Z-Ch sequence are not selected from a common quadrature amplitude modulation (QAM) symbol alphabet, which may be a drawback in certain situations.

In order to evaluate the synchronization algorithm proposed in [16], we have considered a single carrier system (SC) with frequency domain equalization (FDE) similarly as in the case of LTE uplink [48]. As opposed to LTE, where a cyclic prefix (CP) is used, we utilize the concept of Unique word (UW), proposed in [67], [68] and originally intended for orthogonal frequency-division multiplexing (OFDM). The synchronization performance of the UW-SC-FDE approach is compared with other methods in [69]. In CP-OFDM, the cyclic prefix is filled with a random sequence, whereas UW is designed as deterministic. Therefore, UW can be selected optimally for appropriate tasks like synchronization and/or channel estimation [67]. The concept of UW is similar to the approach presented in [70] and [71], where cyclic prefixes together with suffixes and postfixes, respectively, are elaborated.

In the paper [16], the well-known coarse time synchronization methods by Schmidl and Cox [72] and derived methods [73]–[75] are further researched while a novel correlative metric is shown. This novel metric utilizes the time-domain symmetry of the Z-Ch sequence and therefore achieves higher correlation gain compared to the state-of-the art methods. Another approach to the coarse synchronization problem, which produces a timing metric without notable sidelobes, is presented in [76]. In essence, it is a differential cross-correlation with Z-Ch weighted by pseudo noise (PN) sequences.

The time-domain symmetry of the Z-Ch sequence is exploited in [77], where symmetric samples are added prior to multiplication with its replica, thus the multiplication complexity is reduced. In [78] a signature format based on symmetric Z-Ch sequences is proposed to deal with the frequency offset being a multiple of subcarrier bandwidth. On the other hand, in [16] the mentioned symmetry is utilized for synchronization purposes. The contribution of [16] is following:

- Demonstration of the novel correlative metric for coarse time synchronization.

- Comparison with well-known methods by Bhargava et al. [73] and Serpedin et al. [74] showing superior performance in the AWGN channel and partly also in the intersymbol interference (ISI) channel.

- The novel method is not sensitive to a carrier frequency offset (CFO) and provides better in-phase and quadrature sampling resolution, thus improving FDE capabilities.

- We evaluate the influence of the Z-Ch root index influence on the timing accuracy.

3.3.1 System model

Synchronization sequences

Each time instant n of the complex valued Z-Ch sequences $z(n) \in C^{1 \times N_{ZC}}$ is described by:

$$z(n) = \begin{cases} \exp\left(-\mathrm{j}\frac{\pi u n (n+1)}{N_{ZC}}\right) \text{ for odd } u, \\ \\ \exp\left(-\mathrm{j}\frac{\pi u n^2}{N_{ZC}}\right) \text{ for even } u, \end{cases} \tag{3.17}$$

where u is the root index and it holds that $0 < u < N_{ZC}$.

Synchronization frame designs

As a benchmark, we utilize the methods proposed in [73], [74] which we refer to as Bhargava et al. and Serpedin et al. The synchronization frame design of the proposed method is different compared to the benchmark methods. The conventional approach is depicted in Fig. 3.8a. In particular, the difference to the proposed method is that in [73], [74] authors use frame schemes [+B+B-B-B] or [+B+B-B+B], respectively, where B stands for the Z-Ch sequence of the length $L = N_S/2$. This means that within one synchronization frame we need to subsequently transmit four Z-Ch replicas with different polarity.

In Fig. 3.8b, we propose the novel synchronization frame such that the scheme is [+A-A]. Now, A represents a Z-Ch sequence with length $L' = N'_S/2$, i.e., we transmit only two Z-Chs, however, each sequence is double the length of the sequence used in the conventional schemes $L' = 2L$. Therefore, the in-phase and quadrature sampling space is improved and, as Z-Ch sequences of synchronization frames are often used for channel estimation, this capability is potentially enhanced.

Unique word guard interval

In order to maintain the possibility to perform cyclical convolution and to transform Z-Chs into the frequency domain via fast Fourier transform (FFT), we utilize the concept of UW. The common approach with CP could be also used, however, in our case, given that CP would be composed from the partial replica of the synchronization sequence, the correlation metrics may select a timing instant corresponding to CP instead of the intended synchronization sequence. Therefore, in the simulations, we utilize a vector of zeros with a length of twelve samples as the UWs.

(a)

(b)
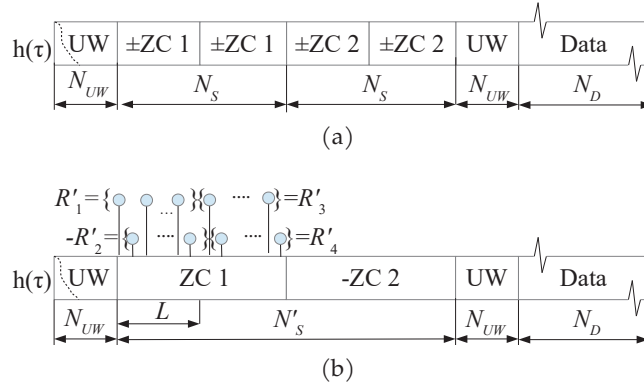
Figure 3.8: Schemes of the synchronization frame designs, (a) the methods [73] or [74] (the frames differ in the polarity of the third Z-Ch sequence), (b) The proposed method. The total length of the synchronization frames is equal. The depicted polarity of the $\mathbf{R}'_i$ segments corresponds to the case of odd u.

3.3.2 Timing metrics

State-of-the art

The received signal, in the case of the benchmark methods, is written as:

$$\mathbf{R}_i = \{r(k+(i-1)L),...,r(k+iL-1)\},\ i=[1,2,3,4], \tag{3.18}$$

where $L = \frac{N_S}{2}$ is the length of the received signal segment $\mathbf{R}_i$, and i indexes signal sections used for the correlation metric according to:

$$\mathbf{M}_{\mathrm{B}} = \frac{|\mathbf{R}_1^{\mathrm{H}}\mathbf{R}_2 + \mathbf{R}_3^{\mathrm{H}}\mathbf{R}_4|}{|\mathbf{R}_2|^2 + |\mathbf{R}_4|^2}, \tag{3.19}$$

for the [73] method. Here, $()^{\mathrm{H}}$ is the Hermitian transpose. Please note that four $\mathbf{R}_i$ segments are utilized to determine $\mathbf{M}_{\mathrm{B}}$. Now, in [74] the authors proposed utilizes a more complex timing metric written as:

$$\mathbf{M}_{\mathrm{S}} = \frac{|\mathbf{R}_1^{\mathrm{H}}\mathbf{R}_2 + \mathbf{R}_3^{\mathrm{H}}\mathbf{R}_4 - \mathbf{R}_2^{\mathrm{H}}\mathbf{R}_3|}{3(|\mathbf{R}_3|^2 + |\mathbf{R}_4|^2)} + \frac{|\mathbf{R}_1^{\mathrm{H}}\mathbf{R}_3 + \mathbf{R}_2^{\mathrm{H}}\mathbf{R}_4| + |\mathbf{R}_1^{\mathrm{H}}\mathbf{R}_4|}{3(|\mathbf{R}_3|^2 + |\mathbf{R}_4|^2)}, \tag{3.20}$$

which means that twelve $\mathbf{R}_i$ segments are used.

More detailed information regarding the novel synchronization method proposed in [16] is available in Part II.

4. Radio frequency hardware imperfections and mitigation

The capacity of the radio link is affected not only by the channel itself, but also by the imperfections of radio frequency transceivers, such as nonlinear effects of the amplifiers [25] or IQ up/down converters. In [79], the theoretical influence of the IQ imbalances on the ergodic and outage capacity of generic OFDM-based link has been investigated. The aim of this section is to join our previous results of channel sounding done in [13], [20] and RF transceiver characterization to estimate the capacity of real mm-wave RF link with impairments.

4.1 IQ mismatch measurements

Although the measurement of the RF channel was taken in 10 GHz bandwidth (BW), many of the currently available RF transceivers are limited to 1 GHz BW, such as Infineon BGT60 [80] we used as the RF up/down converter. The baseband part of the setup was created based on high speed A/D and D/A converters with FPGA interface board from Texas Instruments, complemented with an in-house designed front-end module. With this setup, we measured the frequency-dependent amplitude and phase imbalances. In order to cover the 10 GHz BW to characterize the device completely, the center frequency has been swept. Based on the imbalances, the Image Leakage Ratio (ILR) at OFDM sub-carriers n (with corresponding image at carrier $-n$) can be computed [79]. Hereinafter, a frequency spacing of 10MHz has been considered.

4.2 Capacity analysis

An expression for capacity at OFDM subcarrier n as a function of ILR_n and instantaneous values of normalized channel amplitude coefficients ψ_n, ψ_{-n} at $n-$th and its mirror subcarrier $-n$ was derived [79]:

$$C_n = \log_2\left(1 + \frac{\psi_n^2 \text{SNR}}{1 + \text{ILR}_n(\psi_{-n}^2 \text{SNR} + 1)}\right),\tag{4.1}$$

with SNR being the average signal to noise ratio. The ergodic channel capacity can then be obtained by averaging over the joint pdf $p(\psi_n, \psi_{-n})$ of channel amplitude coefficients:

$$\overline{C}_n = \int_0^\infty \int_0^\infty C_n p(\psi_n, \psi_{-n}) d\psi_n d\psi_{-n}.\tag{4.2}$$
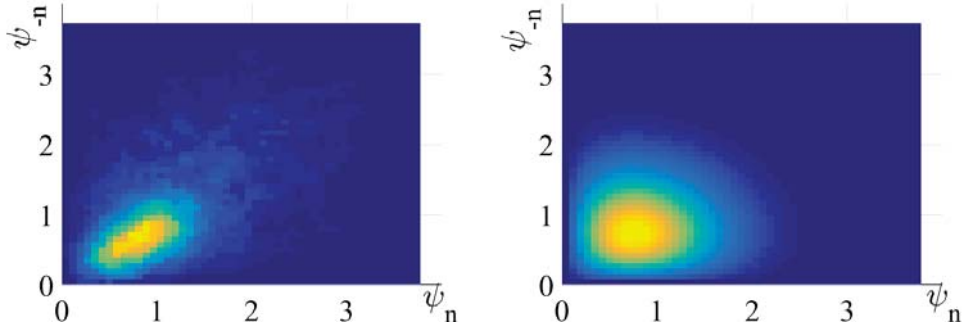
Figure 4.1: Estimated $p(\psi_n, \psi_{-n})$ (left), joint Rayleigh pdf [79] (right)

Utilizing our channel sounding campaign described in [13], [20], we estimated the sampled version of the joint PDF $p(\psi_n, \psi_{-n})$ as shown in Fig. 4.1. The pdf was smoothed with a 2D median filter. Note that as the instantaneous bandwidth of BGT60 is limited to 1 GHz, we used hereinafter only the 1 GHz portion of RF spectrum around 60 GHz center frequency to estimate the pdf.

Based on $p(\psi_n, \psi_{-n})$, the ergodic capacity at n-th subcarrier has been estimated as a function of average SNR. We considered several cases of ILRs - the case of perfectly compensated IQ transceiver corresponding to ILR=-50 dB, the case of uncompensated IQ transceiver with nominal value [80] of ILR=-20 dB and the case of measured average ILR=-27 dB. Fig. 4.2 shows the ergodic capacity, together with the Shannon limit case and the case of Rayleigh channel expected in [79].
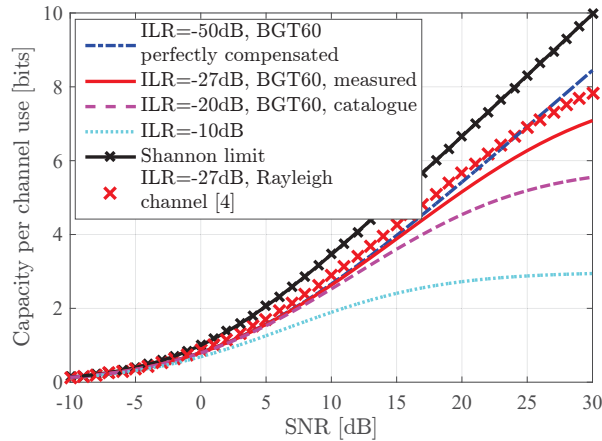
Figure 4.2: Capacity of the measured channel under IQ imperfections

The attached Figure 4.2 show how the ergodic capacity of a real millimeter-wave channel is affected by the IQ mismatch of real RF transceiver. More information regarding this matter and similar research on power amplifier (PA) nonlinearity compensation is available in Part II and in [24]–[26].

5. Conclusions

This proceedings has provided an overview of the research activities I have been involved in for about 8 years. During this period, I have contributed to the development of the Vienna LTE-A Uplink Link Level Simulator. Being used both by academia and industry (e.g. see [22]), the simulator exhibits thousands of downloads and the first paper presenting the uplink functionalities [81] gained more than 50 citations. The simulator served as a platform for testing physical layer algorithms such as the time-frequency signal spreading [18], [19] and the channel estimation [17].

The parameters and algorithms of the physical layer are directly bounded and derived from the relevant wireless channel parameters. Therefore, papers [5]–[15], represent a product of common efforts of mine and my colleagues in the field of channel sounding, characterization and modeling. Gathered knowledge served for design, evaluation and validation of novel modulation schemes [20], [21], for showing the capacity of real-world mmWave communication system [26] and for evaluation of novel modulation schemes such as FBMC in a presence of HW nonidealities [24].

Apart from the electrical engineering related topics mentioned above, we show signal processing methods of time-frequency analysis and their application to economic indicators in [82], [83].

Bibliography

[1]   T. Hummel, M. Kühn, J. Bende, and A. Lang, "Advanced driver assistance systems: An investigation of their potential safety benefits based on an analysis of insurance claims in Germany," *German Insurance Association Insurers Accident Research, Research Report FS*, vol. 3, 2011.

[2]   E. Petridou and M. Moustaki, "Human factors in the causation of road traffic crashes," *European journal of epidemiology*, vol. 16, no. 9, pp. 819–826, 2000.

[3]   S. Singh, "Critical reasons for crashes investigated in the national motor vehicle crash causation survey," National Highway Traffic Safety Administration, Tech. Rep., 2015.

[4]   F. M. Favarò, N. Nader, S. O. Eurich, M. Tripp, and N. Varadaraju, "Examining accident reports involving autonomous vehicles in California," *PLoS one*, vol. 12, no. 9, e0184952, 2017.

[5]   J. Blumenstein, A. Prokes, A. Chandra, T. Mikulasek, R. Marsalek, T. Zemen, and C. Mecklenbräuker, "In-vehicle channel measurement, characterization, and spatial consistency comparison of 3 GHz-11 GHz and 55 GHz-65 GHz frequency bands," *IEEE Transactions on Vehicular Technology*, vol. 66, no. 5, pp. 3526–3537, 2017.

[6]   A. Chandra, J. Blumenstein, T. Mikulášek, J. Vychodil, R. Maršálek, A. Prokeš, T. Zemen, and C. F. Mecklenbräuker, "Serial subtractive deconvolution algorithms for time-domain ultra wide band in-vehicle channel sounding," *IET Intelligent Transport Systems*, vol. 9, no. 9, pp. 870–880, 2015.

[7]   J. Blumenstein, J. Vychodil, M. Pospisil, T. Mikulasek, and A. Prokes, "Effects of vehicle vibrations on mm-wave channel: Doppler spread and correlative channel sounding," in *Personal, Indoor, and Mobile Radio Communications (PIMRC), 2016 IEEE 27th Annual International Symposium on*, IEEE, 2016, pp. 1–5.

[8]   E. Zochmann, C. F. Mecklenbrauker, M. Lerch, S. Pratschner, M. Hofer, D. Loschenbrand, J. Blumenstein, S. Sangodoyin, G. Artner, S. Caban, *et al.*, "Measured delay and Doppler profiles of overtaking vehicles at 60 GHz," in *Proc. of the 12th European Conference on Antennas and Propagation (EuCAP)*, pp. 1–5.

[9]   J. Blumenstein, A. Prokes, J. Vychodil, M. Pospisil, and T. Mikulasek, "Time-varying K factor of the mm-wave vehicular channel: Velocity, vibrations and the road quality influence," in *Personal, Indoor, and Mobile Radio Communications (PIMRC), 2017 IEEE 28th Annual International Symposium on*, IEEE, 2017, pp. 1–5.

[10] J. Blumenstein, A. Prokes, J. Vychodil, T. Mikulasek, J. Milos, E. Zochmann, H. Groll, C. Mecklenbrauker, M. Hofer, D. Loschenbrand, L. Bernado, T. Zemen, S. Sangodoyin, and A. Molisch, "Measured high-resolution power-delay profiles of nonstationary vehicular millimeter wave channels," in *Personal, Indoor, and Mobile Radio Communications (PIMRC), 2018 IEEE 29th Annual International Symposium on*, IEEE, 2018, pp. 1–5.

[11] J. Blumenstein, T. Mikulasek, T. Zemen, C. Mecklenbrauker, R. Marsalek, and A. Prokes, "In-vehicle mm-wave channel model and measurement," in *Vehicular Technology Conference (VTC Fall), 2014 IEEE 80th*, IEEE, 2014, pp. 1–5.

[12] J. Blumenstein, T. Mikulasek, A. Prokes, T. Zemen, and C. Mecklenbrauker, "Intra-vehicular path loss comparison of UWB channel for 3-11 GHz and 55-65 GHz," in *Ubiquitous Wireless Broadband (ICUWB), 2015 IEEE International Conference on*, IEEE, 2015, pp. 1–4.

[13] J. Blumenstein, R. Marsalek, T. Gotthans, R. Nissel, and M. Rupp, "On mutual information of measured 60 GHz wideband indoor MIMO channels: Time domain singular values," in *Personal, Indoor, and Mobile Radio Communications (PIMRC), 2017 IEEE 28th Annual International Symposium on*, IEEE, 2017, pp. 1–5.

[14] J. Blumenstein, A. Prokes, T. Mikulasek, R. Marsalek, T. Zemen, and C. Mecklenbrauker, "Measurements of ultra wide band in-vehicle channel-statistical description and TOA positioning feasibility study," *EURASIP Journal on Wireless Communications and Networking*, vol. 2015, no. 1, p. 104, 2015.

[15] A. Chandra, A. Prokeš, T. Mikulášek, J. Blumenstein, P. Kukolev, T. Zemen, and C. F. Mecklenbräuker, "Frequency-domain in-vehicle UWB channel modeling," *IEEE Transactions on Vehicular Technology*, vol. 65, no. 6, pp. 3929–3940, 2016.

[16] J. Blumenstein and M. Bobula, "Coarse time synchronization utilizing symmetric properties of zadoff–chu sequences," *IEEE Communications Letters*, vol. 22, no. 5, pp. 1006–1009, 2018.

[17] J. Blumenstein, R. Maršálek, Z. Fedra, A. Prokeš, and C. Mecklenbräuker, "Channel estimation method for OFDM in low SNR based on two-dimensional spreading," *Wireless personal communications*, vol. 78, no. 1, pp. 715–728, 2014.

[18] J. Blumenstein, M. Šimko, R. Marsalek, Z. Fedra, J. Prokopec, and M. Rupp, "Two dimensional signal spreading in UMTS LTE: Exploiting time-frequency diversity to increase throughput," *Wireless Personal Communications*, vol. 71, no. 2, pp. 1109–1119, 2013.

[19] R. Nissel, J. Blumenstein, and M. Rupp, "Block frequency spreading: A method for low-complexity MIMO in FBMC-OQAM," in *Signal Processing Advances in Wireless Communications (SPAWC), 2017 IEEE 18th International Workshop on*, IEEE, 2017, pp. 1–5.

[20] P. Liu, J. Blumenstein, N. S. Perović, M. Di Renzo, and A. Springer, "Performance of generalized spatial modulation MIMO over measured 60 GHz indoor channels," *IEEE Transactions on Communications*, vol. 66, no. 1, pp. 133–148, 2018.

[21] N. S. Perović, P. Liu, J. Blumenstein, M. Di Renzo, and A. Springer, "Optimization of the cut-off rate of generalized spatial modulation with transmit precoding," *IEEE Transactions on Communications*, 2018.

[22] R. Alieiev, J. Blumenstein, R. Maršalek, T. Hehn, A. Kwoczek, and T. Kürner, "Sensor-based predictive communication for highly dynamic multi-hop vehicular networks," in *Signal Processing Conference (EUSIPCO), 2017 25th European*, IEEE, 2017, pp. 633–637.

[23] T. Gotthans, R. Maršálek, J. Blumenstein, and G. Baudoin, "Experimental evaluation of digital predistortion with FBMC and OFDM signals," in *Wireless and Microwave Technology Conference (WAMICON), 2015 IEEE 16th Annual*, IEEE, 2015, pp. 1–3.

[24] T. Gotthans, R. Maršálek, M. Pospıšil, T. Urbanec, J. Král, and J. Blumenstein, "On the lower I/Q imbalance sensitivity using real-valued feedback of digital predistortion," in *RF/Microwave Power Amplifiers for Radio and Wireless Applications (PAWR), 2018 IEEE Topical Conference on*, IEEE, 2018, pp. 79–82.

[25] J. Dvorak, R. Marsalek, and J. Blumenstein, "Adaptive-order polynomial methods for power amplifier model estimation," in *Radioelektronika (RADIOELEKTRONIKA), 2013 23rd International Conference*, IEEE, 2013, pp. 389–392.

[26] R. Marsalek, J. Blumenstein, M. Pospisil, and M. Rupp, "Measured capacity of mm-wave radio link under IQ imbalance," in *Personal, Indoor, and Mobile Radio Communications (PIMRC), 2018 IEEE 29th Annual International Symposium on*, IEEE, 2018, pp. 1–5.

[27] P. Bello, "Characterization of randomly time-variant linear channels," *IEEE Transactions on Communications Systems*, vol. 11, no. 4, pp. 360–393, Dec. 1963.

[28] A. F. Molisch, *Wireless communications*. John Wiley & Sons, 2012, vol. 34.

[29] L. Cohen, "Generalization of the Wiener-Khinchin theorem," *IEEE Signal Processing Letters*, vol. 5, no. 11, pp. 292–294, Nov. 1998.

[30] R. Kattenbach, "Statistical modeling of small-scale fading in directional radio channels," *IEEE Journal on Selected Areas in Communications*, vol. 20, no. 3, pp. 584–592, Apr. 2002.

[31] G. Matz, "On non-WSSUS wireless fading channels," *IEEE Transactions on Wireless Communications*, vol. 4, no. 5, pp. 2465–2478, 2005.

[32] F. Hlawatsch and G. Matz, *Wireless communications over rapidly time-varying channels*. Academic Press, 2011.

[33] Y. Li, "Pilot-symbol-aided channel estimation for OFDM in wireless systems," *Vehicular Technology, IEEE Transactions on*, vol. 49, no. 4, pp. 1207–1215, 2000.

[34] P. Hoeher, S. Kaiser, and P. Robertson, "Pilot-symbol-aided channel estimation in time and frequency," in *Multi-carrier spread-spectrum*, Springer, 1997, pp. 169–178.

[35] X. Dong, W.-S. Lu, and A. Soong, "Linear interpolation in pilot symbol assisted channel estimation for ofdm," *Wireless Communications, IEEE Transactions on*, vol. 6, no. 5, pp. 1910–1920, 2007.

[36] S. Lee, K. Kwak, J. Kim, and D. Hong, "Channel estimation approach with variable pilot density to mitigate interference over time-selective cellular OFDM systems," *Wireless Communications, IEEE Transactions on*, vol. 7, no. 7, pp. 2694–2704, 2008.

[37] M. Simko, S. Pendl, S. Schwarz, Q. Wang, J. C. Ikuno, and M. Rupp, "Optimal pilot symbol power allocation in LTE," in *Vehicular Technology Conference (VTC Fall), 2011 IEEE*, IEEE, 2011, pp. 1–5.

[38] O. Edfors, M. Sandell, J.-J. Van de Beek, S. K. Wilson, and P. O. Borjesson, "OFDM channel estimation by singular value decomposition," *Communications, IEEE Transactions on*, vol. 46, no. 7, pp. 931–939, 1998.

[39] H. Atarashi, S. Abeta, and M. Sawahashi, "Variable spreading factor-orthogonal frequency and code division multiplexing (VSF-OFCDM) for broadband packet wireless access," *IEICE transactions on communications*, vol. 86, no. 1, pp. 291–299, 2003.

[40] K. Fazel and S. Kaiser, *Multi-carrier and spread spectrum systems: from OFDM and MC-CDMA to LTE and WiMAX*. Wiley, 2008.

[41] S. Sesia, I. Toufik, and M. Baker, *LTE–The UMTS long term evolution: From theory to practice, 2009 john wiley & sons, ltd*.

[42] J. Blumenstein, M. Simko, R. Marsalek, Z. Fedra, J. Prokopec, and M. Rupp, "Two dimensional signal spreading in UMTS LTE: Exploiting time-frequency diversity to increase throughput," English, *Wireless Personal Communications*, pp. 1–11, 2012.

[43] J. Blumenstein, R. Marsalek, A. Prokes, and C. Mecklenbräuker, "Impulse noise mitigation for ofdm by time-frequency spreading," in *International Workshop on Multiple Access Communications*, Springer, 2013, pp. 8–20.

[44] 3GPP Technical Specification Group RAN, "E-UTRA; physical channels and modulation," 3GPP, Tech. Rep. TS 36.211 Version 8.7.0, May 2009.

[45] C. Mehlführer, J. C. Ikuno, M. Šimko, S. Schwarz, M. Wrulich, and M. Rupp, "The vienna LTE simulators - enabling reproducibility in wireless communications research," *EURASIP Journal on Advances in Signal Processing*, vol. Vol. 2011, pp. 1–13, 2011.

[46] C. Mehlführer, M. Wrulich, J. C. Ikuno, D. Bosanska, and M. Rupp, "Simulating the long term evolution physical layer," in *Proc. of the 17th European Signal Processing Conference (EUSIPCO 2009)*, Glasgow, Scotland, Aug. 2009.

[47] 3GPP Technical Specification Group RAN, "E-UTRA; multiplexing and channel coding," 3GPP, Tech. Rep. TS 36.212, Mar. 2009.

[48] ——, "E-UTRA; physical layer procedures," 3GPP, Tech. Rep. TS 36.213, Mar. 2009.

[49] S. Omar, A. Ancora, and D. T. M. Slock, "Performance analysis of general pilot-aided linear channel estimation in LTE OFDMA systems with application to simplified MMSE schemes," in *Personal, Indoor and Mobile Radio Communications, 2008. PIMRC 2008. IEEE 19th International Symposium on*, 2008, pp. 1–6.

[50] S. Liu and G. Trenkler, "Hadamard, Khatri-Rao, Kronecker and other matrix products," *Int. J. Inform. Syst. Sci*, vol. 4, no. 1, pp. 160–177, 2008.

[51] "Recommendation itu-r m.1225: Guidelines for evaluation of radio transmission technologies for imt-2000," Tech. Rep., Tech. Rep., 1997.

[52] 3GPP, "Technical specification group radio access network; deployment aspects (release 7)," 3GPP, Tech. Rep. 25.943 V7.0.0, Jan. 2007.

[53] A. Assalini, E. Dall'Anese, and S. Pupolin, "Linear MMSE MIMO channel estimation with imperfect channel covariance information," in *Communications, 2009. ICC '09. IEEE International Conference on*, 2009, pp. 1–5.

[54] A. Younis, W. Thompson, M. Di Renzo, C.-X. Wang, M. Beach, H. Haas, and P. Grant, "Performance of spatial modulation using measured real-world channels," in *2013 IEEE 78th Veh. Technol. Conf. (VTC Fall)*, Sep. 2013, pp. 1–5.

[55] N. Serafimovski, A. Younis, R. Mesleh, P. Chambers, M. Di Renzo, C.-X. Wang, P. Grant, M. Beach, and H. Haas, "Practical implementation of spatial modulation," vol. 62, no. 9, pp. 4511–4523, Nov. 2013.

[56] J. Zhang, Y. Wang, L. Ding, and N. Zhang, "Bit error probability of spatial modulation over measured indoor channels," vol. 13, no. 3, pp. 1380–1387, Mar. 2014.

[57] K. M. Humadi, A. I. Sulyman, and A. Alsanie, "Experimental results for generalized spatial modulation scheme with variable active transmit antennas," in *Cognitive Radio Oriented Wireless Networks*, ser. Lecture Notes of the Inst. for Comput. Sci., Social Informatics and Telecommun. Eng. 156, Springer Int. Publishing, Apr. 2015, pp. 260–270.

[58] G. J. Foschini, "Layered space-time architecture for wireless communication in a fading environment when using multi-element antennas," *Bell Labs Tech. J.*, vol. 1, no. 2, pp. 41–59, 1996.

[59] P. Wolniansky, G. Foschini, G. Golden, and R. Valenzuela, "V-BLAST: An architecture for realizing very high data rates over the rich-scattering wireless channel," in *URSI Int. Symp. on Signals, Systems, and Electronics*, Sep. 1998, pp. 295–300.

[60] J. Wang, S. Jia, and J. Song, "Generalised spatial modulation system with multiple active transmit antennas and low complexity detection scheme," vol. 11, no. 4, pp. 1605–1615, Apr. 2012. (visited on 06/19/2014).

[61] A. Younis, "Spatial modulation: Theory to practice," PhD thesis, University of Edinburgh, 2014.

[62] O. Osman, "Variable active antenna spatial modulation," *IET Microwaves, Antennas & Propagation*, vol. 9, no. 15, pp. 1816–1824, Dec. 2015.

[63] M. Di Renzo, H. Haas, A. Ghrayeb, S. Sugiura, and L. Hanzo, "Spatial modulation for generalized MIMO: Challenges, opportunities, and implementation," vol. 102, no. 1, pp. 56–103, Jan. 2014.

[64] A. Stavridis, S. Sinanovic, M. Di Renzo, and H. Haas, "Energy evaluation of spatial modulation at a multi-antenna base station," in *IEEE 78th Veh. Technol. Conf. (VTC Fall)*, Sep. 2013, pp. 1–5.

[65] P. Patcharamaneepakorn, S. Wu, C. X. Wang, e. H. M. Aggoune, M. M. Alwakeel, X. Ge, and M. D. Renzo, "Spectral, energy, and economic efficiency of 5G multi-cell massive MIMO systems with generalized spatial modulation," vol. 65, no. 12, pp. 9715–9731, Dec. 2016.

[66] D. Chu, "Polyphase codes with good periodic correlation properties (corresp.)," *IEEE Trans. Inf. Theory*, vol. 18, no. 4, pp. 531–532, 1972.

[67]   M. Huemer, C. Hofbauer, and J. B. Huber, "Non-systematic complex number rs coded OFDM by unique word prefix," *IEEE Trans. Signal Process.*, vol. 60, no. 1, pp. 285–299, 2012.

[68]   H. Steendam, "Theoretical performance evaluation and optimization of UW-OFDM," *IEEE Trans. Comm.*, vol. 64, no. 4, pp. 1739–1750, 2016.

[69]   S. Reinhardt *et al.*, "Pilot aided timing synchronization for SC-FDE and OFDM: A comparison," in *ISCIT 2004.*, vol. 1, 2004, pp. 628–633.

[70]   M. M. U. Gul, X. Ma, and S. Lee, "Timing and Frequency Synchronization for OFDM Downlink Transmissions Using Zadoff-Chu Sequences," *IEEE Trans. Wireless Commun.*, vol. 14, no. 3, pp. 1716–1729, 2015.

[71]   C. L. Wang and H. C. Wang, "On joint fine time adjustment and channel estimation for OFDM systems," *IEEE Trans. Wireless Commun.*, vol. 8, no. 10, pp. 4940–4944, Oct. 2009.

[72]   T. M. Schmidl *et al.*, "Robust frequency and timing synchronization for OFDM," *IEEE Trans. Commun.*, vol. 45, no. 12, pp. 1613–1621, 1997.

[73]   H. Minn, M. Zeng, *et al.*, "On timing offset estimation for OFDM systems," *IEEE Commun. Lett.*, vol. 4, no. 7, pp. 242–244, 2000.

[74]   K. Shi and E. Serpedin, "Coarse frame and carrier synchronization of OFDM systems: A new metric and comparison," *IEEE Trans. Wireless Commun.*, vol. 3, no. 4, pp. 1271–1284, Jul. 2004.

[75]   H. Abdzadeh-Ziabari, W. P. Zhu, and M. N. S. Swamy, "Improved coarse timing estimation in OFDM systems using high-order statistics," *IEEE Trans. Commun.*, vol. 64, no. 12, pp. 5239–5253, Dec. 2016.

[76]   G. Ren, Y. Chang, *et al.*, "Synchronization method based on a new constant envelop preamble for OFDM systems," *IEEE Trans. Broadcast.*, vol. 51, no. 1, pp. 139–143, Mar. 2005.

[77]   B. M. Popovic and F. Berggren, "Primary synchronization signal in E-UTRA," in *2008 IEEE 10th International Symposium on Spread Spectrum Techniques and Applications*, Aug. 2008, pp. 426–430.

[78]   G. Cui, Y. He, P. Li, and W. Wang, "Enhanced timing advanced estimation with symmetric Zadoff-Chu sequences for satellite systems," *IEEE Commun. Lett.*, vol. 19, no. 5, pp. 747–750, 2015.

[79]   S. Krone and G. Fettweis, "Capacity analysis for OFDM systems with transceiver I/Q imbalance," in *IEEE GLOBECOM 2008- 2008 IEEE Global Telecommunications Conference*, Nov. 2008, pp. 1–6.

[80]   "Single Chip SiGe Transceiver Chipset for V-band Backhaul Applications from 57 to 64 GHz - Application Note AN376," Infineon Technologies AG, Tech. Rep., Jun. 2014.

[81]   J. Blumenstein, J. C. Ikuno, J. Prokopec, and M. Rupp, "Simulating the long term evolution uplink physical layer," in *Proceedings ELMAR-2011*, Sep. 2011, pp. 141–144.

[82] J. Blumenstein, J. Pomenková, and R. Marsalek, "Comparative study of time-frequency analysis approaches with application to economic indicators.," in *ECMS*, 2012, pp. 291–297.

[83] E. Klejmová, J. Poměnková, J. Blumenstein, and J. Pomenková, "Combination of time-frequency representations for background noise suppression.," in *ECMS*, 2017, pp. 1–6.

Part II

Appendices

Full reprints of authored and co-authored publications on topics (1) Vehicular channels, (2) Physical layer algorithms and (3) Mitigation of radio frequency hardware imperfections are listed below in a respective order.

References

[1] J. Blumenstein, A. Prokes, A. Chandra, T. Mikulasek, R. Marsalek, T. Zemen, and C. Mecklenbräuker, "In-vehicle channel measurement, characterization, and spatial consistency comparison of 3 GHz-11 GHz and 55 GHz-65 GHz frequency bands," *IEEE Transactions on Vehicular Technology*, vol. 66, no. 5, pp. 3526–3537, 2017.

[2] A. Chandra, A. Prokeš, T. Mikulášek, J. Blumenstein, P. Kukolev, T. Zemen, and C. F. Mecklenbräuker, "Frequency-domain in-vehicle UWB channel modeling," *IEEE Transactions on Vehicular Technology*, vol. 65, no. 6, pp. 3929–3940, 2016.

[3] J. Blumenstein, A. Prokes, T. Mikulasek, R. Marsalek, T. Zemen, and C. Mecklenbrauker, "Measurements of ultra wide band in-vehicle channel-statistical description and TOA positioning feasibility study," *EURASIP Journal on Wireless Communications and Networking*, vol. 2015, no. 1, p. 104, 2015.

[4] A. Chandra, J. Blumenstein, T. Mikulášek, J. Vychodil, R. Maršálek, A. Prokeš, T. Zemen, and C. F. Mecklenbräuker, "Serial subtractive deconvolution algorithms for time-domain ultra wide band in-vehicle channel sounding," *IET Intelligent Transport Systems*, vol. 9, no. 9, pp. 870–880, 2015.

[5] J. Blumenstein, J. Vychodil, M. Pospisil, T. Mikulasek, and A. Prokes, "Effects of vehicle vibrations on mm-wave channel: Doppler spread and correlative channel sounding," in *Personal, Indoor, and Mobile Radio Communications (PIMRC), 2016 IEEE 27th Annual International Symposium on*, IEEE, 2016, pp. 1–5.

[6] J. Blumenstein, A. Prokes, J. Vychodil, M. Pospisil, and T. Mikulasek, "Time-varying K factor of the mm-wave vehicular channel: Velocity, vibrations and the road quality influence," in *Personal, Indoor, and Mobile Radio Communications (PIMRC), 2017 IEEE 28th Annual International Symposium on*, IEEE, 2017, pp. 1–5.

[7] J. Blumenstein, A. Prokes, J. Vychodil, T. Mikulasek, J. Milos, E. Zochmann, H. Groll, C. Mecklenbrauker, M. Hofer, D. Loschenbrand, L. Bernado, T. Zemen, S. Sangodoyin, and A. Molisch, "Measured high-resolution power-delay profiles of nonstationary vehicular millimeter wave channels," in *Personal, Indoor, and Mobile Radio Communications (PIMRC), 2018 IEEE 29th Annual International Symposium on*, IEEE, 2018, pp. 1–5.

[8] E. Zochmann, C. F. Mecklenbrauker, M. Lerch, S. Pratschner, M. Hofer, D. Loschenbrand, J. Blumenstein, S. Sangodoyin, G. Artner, S. Caban, *et al.*, "Measured delay and Doppler profiles of overtaking vehicles at 60 GHz," in *Proc. of the 12th European Conference on Antennas and Propagation (EuCAP)*, pp. 1–5.

[9] J. Blumenstein, T. Mikulasek, T. Zemen, C. Mecklenbrauker, R. Marsalek, and A. Prokes, "In-vehicle mm-wave channel model and measurement," in *Vehicular Technology Conference (VTC Fall), 2014 IEEE 80th*, IEEE, 2014, pp. 1–5.

[10] J. Blumenstein, T. Mikulasek, A. Prokes, T. Zemen, and C. Mecklenbrauker, "Intra-vehicular path loss comparison of UWB channel for 3-11 GHz and 55-65 GHz," in *Ubiquitous Wireless Broadband (ICUWB), 2015 IEEE International Conference on*, IEEE, 2015, pp. 1–4.

[11] J. Blumenstein, R. Marsalek, T. Gotthans, R. Nissel, and M. Rupp, "On mutual information of measured 60 GHz wideband indoor MIMO channels: Time domain singular values," in *Personal, Indoor, and Mobile Radio Communications (PIMRC), 2017 IEEE 28th Annual International Symposium on*, IEEE, 2017, pp. 1–5.

[12] P. Liu, J. Blumenstein, N. S. Perović, M. Di Renzo, and A. Springer, "Performance of generalized spatial modulation MIMO over measured 60 GHz indoor channels," *IEEE Transactions on Communications*, vol. 66, no. 1, pp. 133–148, 2018.

[13] N. S. Perović, P. Liu, J. Blumenstein, M. Di Renzo, and A. Springer, "Optimization of the cut-off rate of generalized spatial modulation with transmit precoding," *IEEE Transactions on Communications*, 2018.

[14] J. Blumenstein, M. Šimko, R. Marsalek, Z. Fedra, J. Prokopec, and M. Rupp, "Two dimensional signal spreading in UMTS LTE: Exploiting time-frequency diversity to increase throughput," *Wireless Personal Communications*, vol. 71, no. 2, pp. 1109–1119, 2013.

[15] J. Blumenstein, R. Maršálek, Z. Fedra, A. Prokeš, and C. Mecklenbräuker, "Channel estimation method for OFDM in low SNR based on two-dimensional spreading," *Wireless personal communications*, vol. 78, no. 1, pp. 715–728, 2014.

[16] J. Blumenstein and M. Bobula, "Coarse time synchronization utilizing symmetric properties of zadoff–chu sequences," *IEEE Communications Letters*, vol. 22, no. 5, pp. 1006–1009, 2018.

[17] R. Nissel, J. Blumenstein, and M. Rupp, "Block frequency spreading: A method for low-complexity MIMO in FBMC-OQAM," in *Signal Processing Advances in Wireless Communications (SPAWC), 2017 IEEE 18th International Workshop on*, IEEE, 2017, pp. 1–5.

[18] R. Alieiev, J. Blumenstein, R. Maršalek, T. Hehn, A. Kwoczek, and T. Kürner, "Sensor-based predictive communication for highly dynamic multi-hop vehicular networks," in *Signal Processing Conference (EUSIPCO), 2017 25th European*, IEEE, 2017, pp. 633–637.

[19] J. Dvorak, R. Marsalek, and J. Blumenstein, "Adaptive-order polynomial methods for power amplifier model estimation," in *Radioelektronika (RADIOELEKTRONIKA), 2013 23rd International Conference*, IEEE, 2013, pp. 389–392.

[20] T. Gotthans, R. Maršálek, M. Pospíšil, T. Urbanec, J. Král, and J. Blumenstein, "On the lower I/Q imbalance sensitivity using real-valued feedback of digital pre-distortion," in *RF/Microwave Power Amplifiers for Radio and Wireless Applications (PAWR), 2018 IEEE Topical Conference on*, IEEE, 2018, pp. 79–82.

[21] T. Gotthans, R. Maršálek, J. Blumenstein, and G. Baudoin, "Experimental evaluation of digital predistortion with FBMC and OFDM signals," in *Wireless and Microwave Technology Conference (WAMICON), 2015 IEEE 16th Annual*, IEEE, 2015, pp. 1–3.

[22] R. Marsalek, J. Blumenstein, M. Pospisil, and M. Rupp, "Measured capacity of mm-wave radio link under IQ imbalance," in *Personal, Indoor, and Mobile Radio Communications (PIMRC)*, *2018 IEEE 29th Annual International Symposium on*, IEEE, 2018, pp. 1–5.

6. Vehicular channels, full reprints

In-Vehicle Channel Measurement, Characterization and Spatial Consistency Comparison of 3-11 GHz and 55-65 GHz Frequency Bands

Jiri Blumenstein, Ales Prokes, Aniruddha Chandra, Tomas Mikulasek, Roman Marsalek, Thomas Zemen, Christoph Mecklenbraeuker

In-Vehicle Channel Measurement, Characterization and Spatial Consistency Comparison of 3-11 GHz and 55-65 GHz Frequency Bands

Jiri Blumenstein, Ales Prokes, Aniruddha Chandra, Tomas Mikulasek, Roman Marsalek, Thomas Zemen, and Christoph Mecklenbräuker

Abstract—The paper provides real-word wireless measurement data of the intra-vehicular channel for both the 3-11 GHz and the 55-65 GHz frequency band under similar conditions.

By spatially averaging channel impulse response (CIR) realizations within a 10×10 grid, we obtain the power-delay profile (PDP). The data measured at 3-11 GHz and 55-65 GHz exhibit significant differences in terms of root mean square (RMS) delay spread, number of resolvable clusters and variance of the maximal excess delay. Moreover, we evaluate the spatial stationarity via the Pearson correlation coefficient and via the PDP collinearity depending on the distance in the grid. The measured and calculated results indicate that a strong reverberation inside the vehicle produces similar PDPs within the range of approximately 10 wavelengths.

We also provide a linear piecewise model of the PDP in logarithmic scale and a generalized extreme value (GEV) model of small-scale signal fading. Our channel model is validated utilizing the Kolmogorov-Smirnov (K-S) test.

Index Terms—In-vehicle channel model, UWB, mm-wave, PDP, frequency domain channel sounding, channel stationarity.

I. INTRODUCTION

INTRA-and inter-vehicular wireless connectivity is the key enabler for enhancing traffic safety, reliability, fluidity and efficiency of future transportation systems [1], [2].

A modern vehicle contains a cable harness weighting several tens of kilograms [3]. Since weight savings are crucial in the car industry in terms of fuel and power consumption, future vehicles will substitute at least part of the metallic cables with wireless connections. Thus, an in-vehicle wireless communication system is beneficial not only when connecting moving parts such as wheels or seats [4]. Moreover, the design of the cable harness is often platform specific and its manufacture and installation are a time consuming and technically demanding process. Also, assuring the reliability of the cable harnesses is not easy in the presence of moisture

or bending. Another application of the intra-vehicular wireless backbone could be seen in the possibility of retrofitting state-of-the-art driver assistance features also into older vehicles. Thus, the in-vehicle wireless connection could bring together functionalities such as being the wireless backbone for the vehicle's operational data, providing local Internet connection for the passengers, enabling the connection of vehicle parts that are otherwise difficult to connect or supporting an on-board infotainment system.

To contribute to the research into the in-vehicle wireless connectivity, we compare in detail wireless channels in the range of the 3-11 GHz and the 55-65 GHz frequency bands in the in-vehicle environment under very close conditions (differences will be clarified later in the paper and are given only by inevitably different channel sounders). We also parametrize our measured data in order to provide a specialized and detailed channel model for the typical in-vehicle environment of a mid-sized passenger car. Our findings could help to design an optimized physical layer for the broadband in-vehicle wireless communication system.

While both bands provide around 10 GHz of unlicensed bandwidth (depending on the local spectrum management authorities), the differences between the 3-11 GHz and the 55-65 GHz frequency band are significant and presented by this paper.

In order to enhance the credibility and the reproducibility of our research, the measured data are freely available on the link: http://www.radio.feec.vutbr.cz/GACR-13-38735S/

A. 3-11 GHz frequency band

In the 3-11 GHz frequency range, authors in [5], [6] deduce that the beneficial radio environment characteristics for indoor areas (such as robustness against multipath fading and low transmit power) could be extrapolated to the vehicle passenger compartment. Intra-vehicle channel measurements are performed in [7]–[13] and channel modeling in [6], [14]. The spatial stationarity and collinearity have, however, not been studied and compared with the millimeter wave band. In [15] the channel stationarity has been shown for 3-11 GHz, but the 55-65 GHz band is not mentioned.

Obstructed by seats and passengers, the in-vehicle environment will hardly offer a line of sight (LOS) component. This might be of significant importance when compared with indoor environment in [5], [6]. On the other hand, please note that

J. Blumenstein, A. Prokes, A. Chandra, T. Mikulasek and R. Marsalek are with the Department of Radio Electronics, Brno University of Technology, Czech Republic. T. Zemen is with AIT, Austrian Institute of Technology, Vienna, Austria, and Ch. Mecklenbräuker is with Institute of Telecommunications, Christian Doppler Lab, Vienna University of Technology, Vienna, Austria. e-mail: blumenstein@feec.vutbr.cz.

the 1.99 - 10.6 GHz band is deregulated for communication and wall penetrating radars in the U.S [16]–[18]. Thus, one of the research objectives for the lower band is to find out whether the multipath components could sufficiently support the intended wireless application.

B. 55-65 GHz frequency band

In [19]–[21] the ultra-wide bandwidth (UWB) and the mm-wave in-vehicle channels are compared. The comparison includes the Rician K-factor, the root mean square (RMS) delay spread and the path-loss, but no spatial stationarity evaluation is given. No specific channel model parametrization for the in-vehicle environment is offered in [20].

The 55-65 GHz band enables the usage of high-gain steerable antennas in a small physical form allowing for a beamforming, a beamsteering and a spatial multiplexing [19], [22]. By contrast, the 60 GHz band suffers from high penetration loss and insignificant diffraction contribution. Thus, shadowing effects are expected to be more significant compared to the 3-11 GHz band [23]. Also, considering the millimeter wavelength, the vibrations usually occurring in the transportation may cause difficulties in terms of increased Doppler spread [24].

However, expecting a lower delay spread of the power-delay profile (PDP), the 55-65 GHz frequency range implies a lower complexity channel estimation [25] compared to the 3-11 GHz band. Our results also show higher spatial correlation of the 55-65 GHz band for a distance of around 5 wavelengths, indicating a lower achievable transmit diversity gain for appropriate Multiple-Input Multiple-Output (MIMO) schemes. A channel model for 55-65 GHz of the in-vehicle environment is presented in [26]; however, a comparison with other bands is lacking.

C. Contribution of the paper

- Under similar conditions we compare the 3-11 GHz with the 55-65 GHz frequency band in terms of RMS delay spread, maximal excess delay, number of resolvable clusters in the PDP, and the cluster decay rate [27].
- We show a linear piecewise model of the PDP in logarithmic scale and a generalized extreme value (GEV) model of small-scale signal fading.
- The spatial stationarity of the measured channel parameters is analyzed. We evaluate:
  1) the Pearson correlation coefficient of the channel impulse responses (CIRs) in order to see the potential diversity gains.
  2) the collinearity of the PDP in order to evaluate the number of realizations of the CIR needed for calculating the PDP.
- We validate our statistical channel model utilizing the Kolmogorov-Smirnov (K-S) test.

D. Organization of the paper

The organization of the paper is as follows. First we state Introduction section, and then we present the section Measurement Setup. Next sections are Channel Description, Spatial Stationarity of Measured Channel Impulse Responses and Channel Model Validation. Conclusion section sums up the paper.
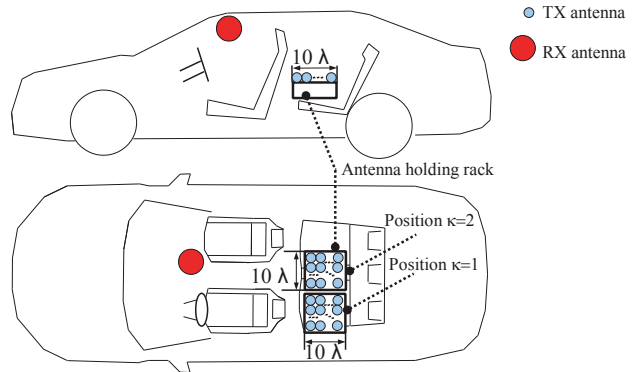
Fig. 1: Antennas layout, receiving antenna [**red**], transmitting antenna [**blue**]. We utilize one transmitting antenna, which has been manually moved over the grid depicted in Figure 2, ensuring defined antenna positions. We employed two specific measurement grid positions, the seat behind the driver ($\kappa = 1$) and the middle seat ($\kappa = 2$). The grid measurements also allow averaging out the effect of small-scale signal fading. The grid distance in both directions is 3 cm for 3-11 GHz and 4 mm for 55-65 GHz. The grid allows measuring 10×10 positions.

II. MEASUREMENT SETUP

Measurements are performed in a mid-sized Skoda Octavia III car using transmit and receive antennas marked with blue and red colors in Figure 1, respectively. The receiving (RX) antenna is placed next to the rear-view mirror on the front windshield according to Figures 1, 5a and 5b. The transmitting antenna is placed at 10×10 spatial points, using a polystyrene rack in the case of the 3-11 GHz band and a metallic X-Y table covered with absorbers in the case of the 55-65 GHz band.

Given the absorbers and the fact that the relative polystyrene permittivity is close to the relative air permittivity, we ensure that the locations of the receive antennas are well-defined, while introducing as few artificial reflections from the measurement device as possible. Between neighboring measurement locations, the polystyrene rack utilizes a 3 cm grid distance while the X-Y table step was 4 mm. Moreover, the measurement grids (for both examined bands) ware placed at two different positions on the rear bench. As seen in Figure 1, the positions of the measurement grid are denoted with index κ.

As will be discussed later, apart from the different antennas utilized for the two frequency bands examined, the different antenna holding racks are one of the inevitable dissimilarities introduced into our measurement. Without considering the antenna manipulation overhead, the measurement of one channel transfer function (CTF) took approximately 15 seconds. In total, 200 CTFs were captured for both examined frequency bands and one grid position κ.
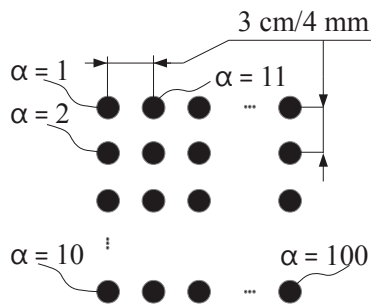
Fig. 2: 10 × 10 measurement grid. The distance between grid positions is 3 cm for 3-11 GHz and 4 mm for 55-65 GHz.

A. 3-11 GHz measurement apparatus

The Agilent Technologies E5071C four-port vector network analyzer (VNA) is used for measuring the transmission co-efficient between two antennas in the 3-11 GHz frequency band. The omni-directional conical monopole antennas having a radiation pattern as depicted in Figure 3a are used as transmitting and receiving antennas. To achieve the highest possible VNA dynamic range, we chose a maximum available output power of 5 dBm at the test port of the VNA and the intermediate frequency (IF) bandwidth of 100 Hz. The choice of the IF bandwidth value is motivated by keeping the high system dynamic range (>90 dB) while maintaining reasonable time (≈15 s for one CTF) of one measurement runtime. The measurement is performed in the frequency domain with 10 MHz frequency steps (as in [28]).

After temperature stabilization of VNA, the coaxial cables (antennas disassembled) were connected to the electronic calibration module and full four port calibration was performed.

B. 55-65 GHz measurement apparatus

The R&S ZVA67 four-port VNA is utilized for measuring the transmission coefficient between two antennas in the 55-65 GHz frequency band. The system dynamic range of the measurement setup was extended utilizing a broadband power amplifier (QuinStar QPW-50662330, measured gain of 35 dB in the band of interest) on the transmitting side. The WR15 open waveguide having a radiation pattern as depicted in Figure 3b was used as a transmitting and receiving antenna (similarly as in [29]). The system's dynamic range of this measurement setup is ≈50 dB. The VNA output power of 5 dBm and IF bandwidth of 100 Hz was chosen in the same way as in the case of the measurement apparatus for 3-11 GHz.

Note that the measurement is performed in the frequency domain with 10 MHz frequency step. We transform the channel frequency response into the time domain, utilizing the inverse Fourier transform with Blackman windowing (as in [30]). More about the influence of the windowing is elaborated in [31].

In order to avoid a degradation of the measured phase accuracy due to movements of the TX antenna, phase-stable coaxial cables were used. The full four port calibration process was performed including the power amplifier. The flanges of
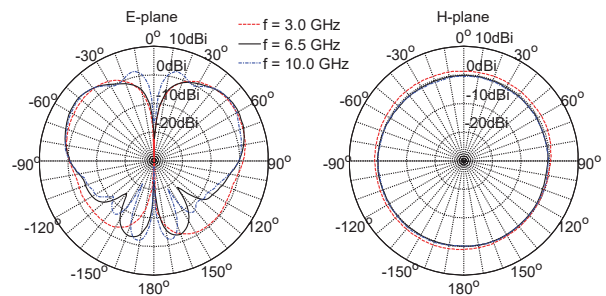
(a) Measured gain pattern of the conical monopole antennas for a frequency range of 3-11 GHz.
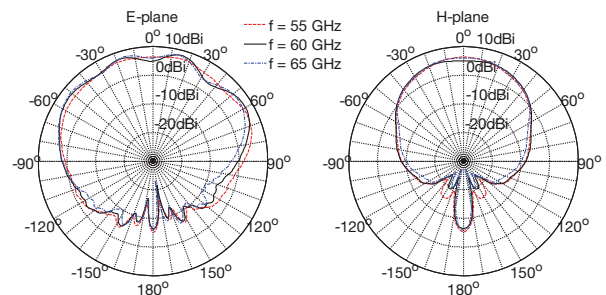
(b) Measured gain pattern of the open-ended waveguide in the E–plane and the H–plane for open-ended waveguide antenna at 55-65 GHz.

Fig. 3: Measured radiation patterns of the antennas used.

the TX and RX antennas were connected together and the VNA transmission was normalized in the forward direction.

Complete list of used components is available online: http://www.radio.feec.vutbr.cz/GACR-13-38735S/mmw-measurement-in-frequency-domain-with-rotagrip/.

C. Antenna pattern influence

The conical monopole antenna used for the channel sounding at 3-11 GHz is omnidirectional in the H-plane and 120° wide in the E-plane, while the open-ended waveguide used for the measurement at 55-65 GHz has a 120° wide radiation pattern in the E-plane and 60° wide radiation pattern in the H-plane (for 3 dB decay). This makes the comparison of the two bands seemingly problematic. On the other hand, however, there is no of-the-shelf omnidirectional antenna for the millimeter waves with 10 GHz bandwidth.

D. Comparability of the measurements with omnidirectional and directional antennas

To provide a further insight on the antenna pattern influence, the open-ended waveguide transmitting antenna has been rotated clockwise with a 60° step from 0° to 180°.

The results of this measurement are visible in Figure 4. The 60° curve, apart from being 8 dB weaker compared to the 0° heading direction, shows no significant difference. The 120° and 180° data exhibit a different behavior. The first arrival (LOS) components are 20-30 dB weaker or simply not visible (again, compared with 0°). This is predominant namely in the range of $\tau \in \{3 - 8\}$ ns.

To summarize, no additional resolvable clusters of the multipath components (MPCs) are visible in the data measured with the angular misalignment to LOS. Thus, the measurements with the open-ended waveguide antennas in the frequency range of 55-65 GHz are comparable with the measurements performed with the omnidirectional monoconical antenna for 3-11 GHz.
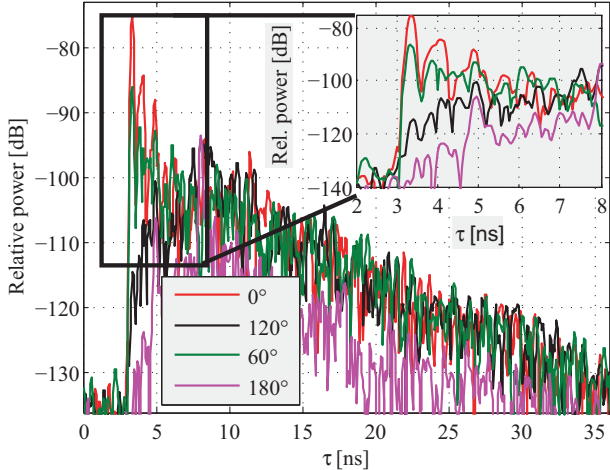
Fig. 4: The measured PDPs for following heading directions (relative to the LOS): 0°, 60°, 120° and 180°.

Symbol	Description
$^\kappa H^\alpha(k)$	channel transfer function for α-th in the measurement grid and κ-th position of the grid within the vehicle
$^\kappa h^\alpha(n)$	channel impulse response for α-th in the measurement grid κ-th position of the grid within the vehicle
ρ	Pearson correlation coefficient
$s_{21}^\alpha(k)$	scattering parameter, the forward transmission coefficient
α	index denoting the spatial position within the measurement grid
n	time in delay domain
k	frequency index
κ	index denoting the position of the measurement grid within the vehicle
$P_{\mathrm{dB}}^*(n)$	PDP model in logarithmic scale
$(.)^*$	model variable
$\mathrm{E}\{.\}$	expected value
$\|\cdot\|_F$	Frobenius norm
$(.)^H$	complex conjugate transpose
$\mathrm{tr}(.)$	trace (the sum of the elements on the main diagonal)

TABLE II: Tabulated average delay and RMS delay spread. The mean and variance values for both 3-11 GHz and 55-65 GHz. (The calculation is done for 100 measurements in each examined band.)

	position	average delay [ns]		RMS delay spread [ns]	
		mean	variance	mean	variance
3-11 GHz	$\kappa = 1$	48.07	4.50	23.34	< 0.01
	$\kappa = 2$	47.41	4.2	23.27	< 0.01
55-65 GHz	$\kappa = 1$	13.75	0.01	5.02	< 0.01
	$\kappa = 2$	12.47	0.01	5.03	< 0.01

III. CHANNEL DESCRIPTION

The measured in-vehicle radio channel is considered as time invariant. Thus, to fully describe the radio channel, we write the CTF as:

$$^\kappa H^\alpha(k) = {}^\kappa s_{21}^\alpha(k), \tag{1}$$

where k stands for the measurement index identifiable with certain frequency and where α denotes the position of the receiving antenna within the measurement grid, as visible in Figure 2 and κ stands for the location index of the whole measurement grid within the vehicle. Utilizing an inverse Fourier transform we convert the CTF into a CIR according to:

$$^\kappa h^\alpha(n) = \sum_{k=0}^{N-1} {}^\kappa H^\alpha(k) e^{jkn2\pi/N}, \tag{2}$$

where n is discrete time in the delay domain.

The PDP is then calculated as spatial average of $|^\kappa h^\alpha(n)|^2$ according to:

$$^\kappa P(n) = \mathrm{E}_\alpha\{|^\kappa h^\alpha(n)|^2\}. \tag{3}$$

The spatial measurement grid is of square layout with dimensions of approximately 10×10 wavelengths.

Please note that it holds that:

$$\tau = n\frac{1}{B}, \tag{4}$$

where τ is the time in the delay domain, B is the bandwidth and $1/B$ is the time resolution. Please note that the symbols and notations used are listed in Table I.

A. Moments of PDP

For practical reasons, the preferred parameters evaluating the wireless channel are the first and the second moment of the PDP, i.e., the average delay is given as:

$$D = \frac{\sum_n^{n_{\max}} P(n)n}{\sum_n^{n_{\max}} P(n)}, \tag{5}$$

where the maximal delay of $P(n)$, $n_{\max}$ is detected as a time in the delay domain where the PDP crosses the noise floor. Please note that the noise floor is estimated as the RMS value of the PDP before the rising edge of the first arriving MPC. For the case of 3-11 GHz band, the noise floor is -109 dBm and for the 55-65 GHz band the noise floor is -134 dBm. The RMS delay spread is defined according to:

$$S_n = \sqrt{\frac{\sum_n^{n_{\max}} P(n)n^2}{\sum_n^{n_{\max}} P(n)} - D^2}. \tag{6}$$

Our measured data are stated in Table II. The 3-11 GHz band is affected by an approximately 5 times higher delay spread than the 55-65 GHz band in a system with a peak signal-to-noise ratio of around 50 dB for both bands. We utilized 100 CIRs for the calculation of one examined frequency band and one position κ.

One reason why the 55-65 GHz channels have lower delay spread is because of the generally higher path-loss that attenuates MPCs with a large delay. Also, the non-omnidirectional antenna (open-ended waveguide) does not radiate in angles from -80° to 80°, which means that it produces a lower number of highly delayed MPCs, thus the resulting PDP might be shortened.

(a) 3-11 GHz monoconical antenna mounted on the front windshield next to the rear-view mirror.

(b) 55-65 GHz open-ended waveguide antenna fastened using a suction cap.

(c) X-Y table for precise movement of the open-ended waveguide antenna within the measurement grid. The metallic X-Y table, the antenna with power amplifier and heat sink are covered with absorbers in order to reduce the unwanted reflections and thus the influence of the measurement. The grid position corresponds to $\kappa = 1$.

(d) Polystyrene 10×10 antenna holder and 3-11 GHz monoconical antenna. The grid position corresponds to $\kappa = 1$.

Fig. 5: Photographs taken during the measurement campaign.

B. Comparison with other in-vehicle measurement campaigns

To give a perspective on the data presented in Table II, we provide a brief overview on findings of different authors. The other measurement campaigns have usually been performed under notably different conditions. We present the most similar ones.

For the much more confined area of the engine bay, the authors in [7] report RMS delay spread values of around 5 ns for the 3.1-10.6 GHz band. For the same band, the author in [9] reports around 10 ns of the RMS delay spread for the passenger compartment. In [14], the reported values of RMS delay spread are around 15 ns while the frequency range is not exactly given, but 802.15.3a is claimed as the target application. The authors in [20] compare the 5-8.5 GHz bands and the 67-70.5 GHz bands, but they report significantly lower RMS delay spread values, which range from 1 ns to 5 ns while the lower band exhibits higher RMS delay spread values. Such a notable difference might probably arise due to the different dynamic range of the channel sounder used.

C. Channel approximation

The small dimensions and metallic surroundings of the in-vehicle environment create conditions which are best described by a dense scattering model. Thus, with the model validated via the K-S test, we parametrize the well-known linear piecewise PDP model [25]. The specular components which form the leading edge of the clusters and, hence, the breakpoints of the linear piecewise characteristics, are estimated by a peak finder. The peak finder is adjusted based on visual inspection.

According to the observations and with the aim to provide a reproducible channel model, we operate with the hypothesis that the CIR is composed of PDP and small scale fading (SSF) according to:

$$|h_{\text{dB}}(n)|^2 = P_{\text{dB}}(n) + \xi(n), \tag{7}$$

where $P_{\mathrm{dB}}(n)$ and $\xi(n)$ stand for the PDP and SSF, respectively. As proposed below, SSF is modeled by an appropriate random process while the PDP is described by a piecewise linear approximation. Note that the PDP is interchangeable with a large scale fading (LSF). Since recent measurements presented in [13], [20], [21] report a very low path-loss coefficient, thus a low dependency of the path-loss on the actual antenna separation within the vehicle, we decided to introduce LSF as a function of time in the delay domain instead of the more traditional function of antenna separation.

Figure 6 presents the measured $|^{1,2}h_{\mathrm{dB}}^{\alpha}(n)|^2 \ \forall \alpha$, each aligned according to the first arrival MPC. It also presents the averaged PDP $^{1,2}P_{\mathrm{dB}}(n)$ and the piecewise linear approximation $^{1,2}P_{\mathrm{dB}}^{*}(n)$.

1) Power-delay profile: Our measured data are presented in logarithmic scale. Thus, the generally accepted one-sided exponential PDP model [25] is reduced to a linear function according to:

$$P_{\mathrm{dB},c}^{*}(n) = \begin{cases} -nP_{\mathrm{DR},c}/T_{\mathrm{m},c} & T_{\mathrm{m},c-1} < n < T_{\mathrm{m},c} \\ 0 & \text{otherwise,} \end{cases} \quad (8)$$

where c indexes the clusters, and $P_{\mathrm{DR},c}$ and $T_{\mathrm{m},c}$ stand for the the dynamic range and maximal excess delay of the relevant cth cluster. The multiple cluster PDP model is written as:

$$P_{\mathrm{dB}}^{*}(n) = \sum_{c} \left(P_{\mathrm{dB},c}(n) + C_c \right), \quad (9)$$

where C_c represents the cluster decay ratio in decibels. The quantities from (8) and (9) are visualized in Figure 7. Note that the upper index * denotes the artificial model variable derived from a measured variable. The corresponding parameters of the channel, as derived from our data, are presented in Table III.

In the case of the position $\kappa = 1$, the origin of the three MPC clusters in the 55-65 GHz band is as follows: the first cluster represents the direct/dominant component, the second cluster stands for a strong reflection and the third cluster is a reverberation diffused tail. As for the position $\kappa = 2$, three recognizable reflections are present. Please note that the term reverberation diffused tail is discussed and defined in [32]. Now, a notable difference from the 3-11 GHz band is the lack of higher number of MPC clusters on one hand, but on the other hand it features a significantly longer PDP in the delay domain.

2) Small scale fading: Exploiting the maximum likelihood estimate (MLE), we parametrize the superimposed SSF signal $\xi(n)$, using the generalized extreme value (GEV) distribution [33]. The probability density function (PDF) of the GEV is given by:

$$f(x \mid K, \Upsilon, \Gamma) = \frac{1}{\Gamma}\exp\left[-\beta^{-\frac{1}{K}}\right]\beta^{-1-\frac{1}{K}}, \forall \beta = 1 + K\frac{x-\Upsilon}{\Gamma}. \quad (10)$$

The estimated parameters of the spatially universal small-scale fading model are presented in Table IV.

Due to the high flexibility of the SSF model $\xi^{*}(n)$, which is given by three input parameters as opposed to the usual two

parameters, the MLE metric recommends GEV distribution. On the other hand, the authors in [34] claim that there is no theoretical explanation for encountering this distribution type. It is, however, worth noting, that the GEV contains the accepted Weibull distribution as a special case for $K < 0$. Please note that in [12] the authors report the Weibull distribution for their measurement results for the 2.4 GHz intra-vehicle channel. Similar results are presented in [13]. Note that there is practically a very small difference between the data for position $\kappa = 1$ and $\kappa = 2$.

D. Physical meaning of SSF parameters

The parameters K, Υ, Γ of the GEV process are commonly known as *location*, *scale* and *shape* respectively. It holds that $K \in \mathbb{R}, \Upsilon > 0$ and $\Gamma \in \mathbb{R}$.

The physical meaning of these parameters might not be exactly clear from this notation, therefore we provide the following insight into the effect of these parameters. The parameter Γ drives the tail behavior while the scale parameter Υ determines the spread of the distribution. Next, the parameter K prescribes the impulsiveness of the signal. The higher $|K|$, the higher rate of occurrence and power of an impulsive noise superimposed on the random GEV signal with parameters Υ and Γ. The polarity of these impulses is the same as the polarity of the parameter K.

It is worth noting that for the 3-11 GHz band the parameter K is almost zero (agrees with [13], [34], see Table IV), but for the 55-65 GHz frequency band the parameter K is significantly lower, implying that clusters of MPCs are more resolvable in the delay domain. Moreover, this fact also supports the finding that for the higher frequency band the popular assumption of uncorrelated scattering is not exactly valid (as presented for a vehicle-to-vehicle example in [35]).

IV. SPATIAL STATIONARITY OF MEASURED CHANNEL IMPULSE RESPONSE

The spatial stationarity of the measured wireless channel is studied via an evaluation of the Pearson correlation coefficient $|\rho^{\alpha}|$ of the measured CIR $h_{\mathrm{dB}}^{\alpha}(n)$ similarly as in [36] and via an evaluation of the collinearity of the PDP $P_{\mathrm{dB}}(n)$.

A. Pearson correlation coefficient evaluation of the 3-11 GHz and 55-65 GHz bands

In this subsection we evaluate the spatial stationarity of the whole measured bandwidths. This means that we compare the 8 GHz bandwidth of the 3-11 GHz band (later designated with uwb) with the 10 GHz bandwidth of the 55-65 GHz band (later designated with mmw). As will be shown in a following section, we also provide a comparison of spatial stationarity of sub-bands with equal relative bandwidths.

The Pearson correlation coefficient is given as:

$$\rho^{\alpha} = \frac{\mathrm{E}[(h^{\alpha}(n) - \mu^{\alpha})(h^{45}(n) - \mu^{45})]}{\sigma^{\alpha}\sigma^{45}}, \quad (11)$$

where σ^{α} denotes the standard deviation and μ^{α} the mean of $h^{\alpha}(n)$. The correlations are calculated between the spatial

(a) 3-11 GHz, $\kappa = 1$.

(b) 55-65 GHz, $\kappa = 1$.

(c) 55-65 GHz, $\kappa = 2$.
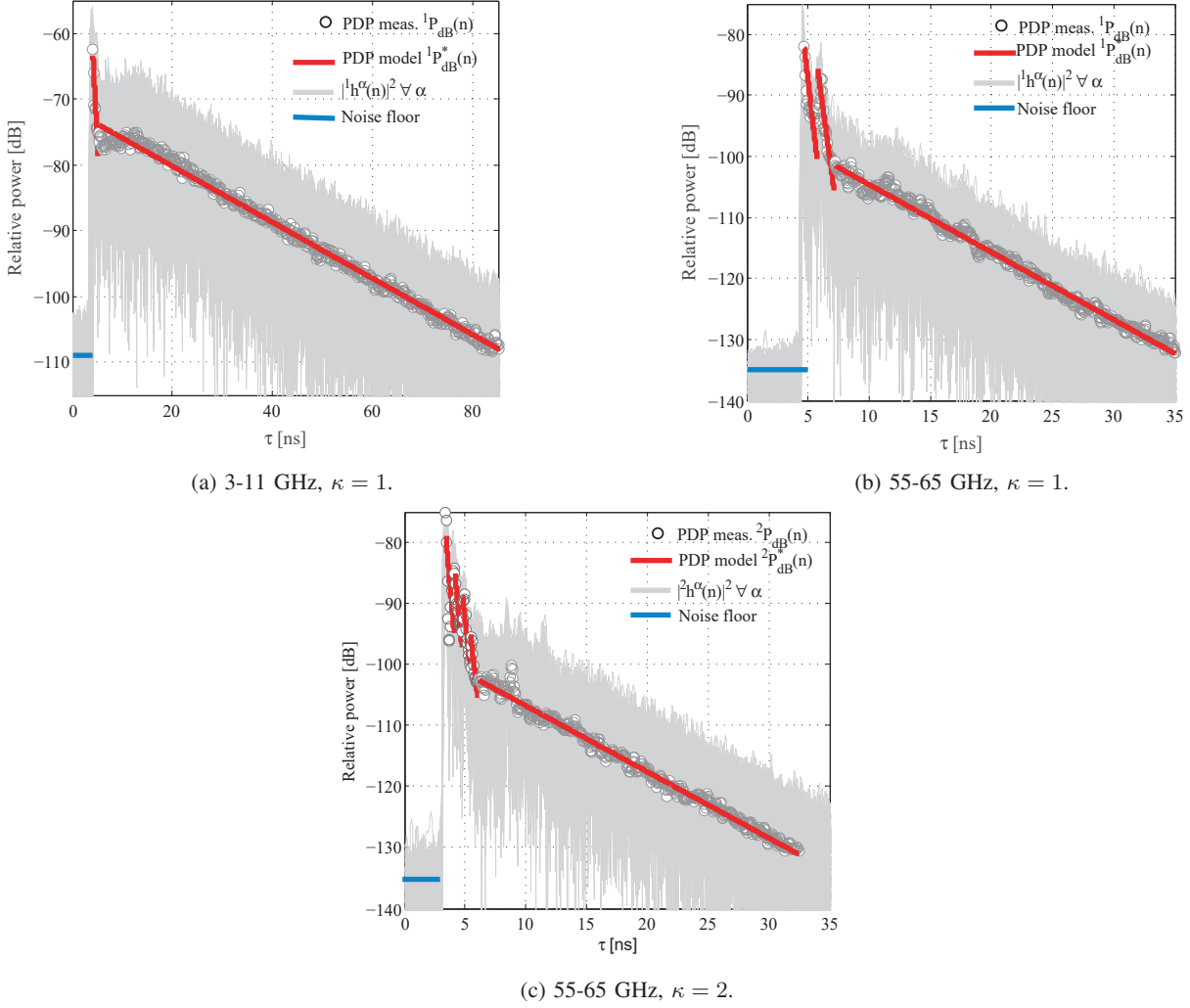
Fig. 6: Measured and calculated channel parameters in the delay domain for both investigated frequency bands, i.e., measured absolute value of squared CIR $|^1h_{\mathrm{dB}}^{\alpha}(n)|^2$, 100 realizations; Spatially averaged power-delay profile $^1P_{\mathrm{dB}}(n)$; Piecewise linear approximation $^1P_{\mathrm{dB}}^*(n)$ and estimated noise floors. The data for the 3-11 GHz band and the grid position $\kappa = 2$ exhibit no visual difference compared to $\kappa = 1$ plotted in Figure 6a.

TABLE III: Table of the PDPs measured. The values of dynamic range $P_{\mathrm{DR},c}$, maximal excess delay $T_{\mathrm{m},c}$ and cluster decay rate C_c are given. (The PDP model for the 3-11 GHz band and for position $\kappa = 2$ match the model for $\kappa = 1$.)

		3-11 GHz		55-65 GHz		
position	cluster number	1	2	1	2	3
$\kappa = 1$	$P_{\mathrm{DR},c}$ [dB]	11.56±0.30	33.2 ±0.31	18.31 ±0.32	19.92 ±0.22	30.83 ±0.25
	$T_{\mathrm{m},c}$ [ns]	1.00	80.23	1.03	1.33	27.76
	C_c,[dB]	0	9.63 ±0.34	0	3.63 ±0.30	15.68 ±0.26
		55-65 GHz				
position	cluster number	1	2	3	4	5
$\kappa = 2$	$P_{\mathrm{DR},c}$ [dB]	16.21±0.20	9.1 ±0.24	11.11 ±0.21	6.54 ±0.32	29.44 ±0.35
	$T_{\mathrm{m},c}$ [ns]	1.40	1.20	1.20	1.20	31.20
	C_c,[dB]	0	9.36 ±0.33	3.02 ± 0.31	8.06 ±0.20	6.00 ±0.36

positions $\alpha \in \{1 \ldots 100\}$ and $\alpha = 45$, which is located approximately in the middle of the measurement grid.

Reflecting the square geometry of our antenna holding rack, the maps of the correlation coefficient ρ^{α} are plotted in Figure 8.

1) 3-11 GHz: Figure 8a shows that $^1h^{\alpha}(n)$ is spatially stationary with a mean value of $|^1\rho^{\alpha}| \approx 0.17$. For the position $\kappa = 2$, the data are $|^2\rho^{\alpha}| \approx 0.15$. The coefficients $|^{1,2}\rho^{\alpha}|$ slightly decrease with the distance form the reference point $\alpha = 45$.

TABLE IV: Estimated parameters with confidence intervals of the superimposed SSF random process. We also present a best fit for each parameter ensuring the highest score in the K-S test.

	position	K	best fit of K	Υ	best fit of Υ	Γ	best fit of Γ
3-11 GHz	$\kappa = 1$	-0.0239 $\pm$0.0062	-0.0282	4.541 $\pm$0.0451	4.5682	-2.236 $\pm$0.1070	-2.7938
	$\kappa = 2$	-0.0178 $\pm$0.0055	-0.0279	4.476 $\pm$0.0554	4.0169	-2.465 $\pm$0.1102	-2.6296
55-65 GHz	$\kappa = 1$	-0.4657 $\pm$0.0081	-0.5279	6.016 $\pm$0.0488	6.2783	-2.532 $\pm$0.0809	-2.6514
	$\kappa = 2$	-0.4878 $\pm$0.0052	-0.4672	6.840 $\pm$0.0514	6.4625	-2.734 $\pm$0.0721	-2.4264

2) 55-65 GHz: Figure 8b depicts the significantly higher spatial stationarity of $^1h^\alpha(n)$ with a mean value of $|^1\rho^\alpha| \approx$ 0.30. Also, the variance of $|^1\rho^\alpha|$ is notably higher. As for the position $\kappa = 2$, the data are $|^2\rho^\alpha| \approx 0.38$. The coefficients $|^{1,2}\rho^\alpha|$ do not decrease significantly with distance from the reference point $\alpha = 45$.

B. Pearson correlation coefficient comparison of the 3-11 GHz sub-bands with equal relative bandwidth

Here we evaluate and depict the absolute value of the Pearson correlation coefficient $|^1\rho^\alpha|$ for selected sub-bands
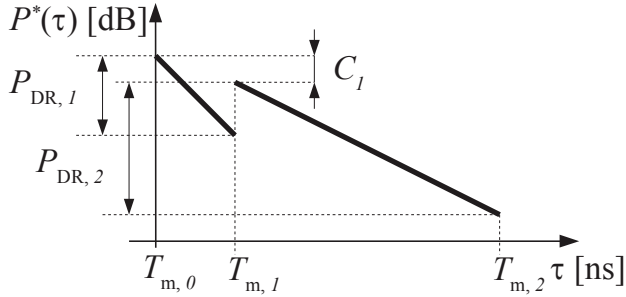
Fig. 7: An example of the piecewise linear approximation having two dominant clusters of PDP in logarithmic scale.

(a) 3-11 GHz.

(b) 55-65 GHz.
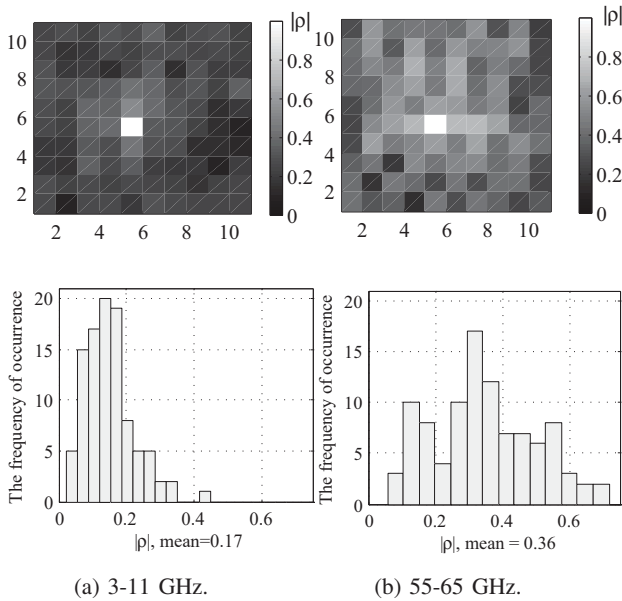
Fig. 8: Spatial maps and histograms of the calculated Pearson correlation coefficient $|^1\rho^\alpha| \, \forall\alpha$.

of the lower band from 3 GHz to 11 GHz. The sub-bands are identified such that their relative bandwidth to theirs center frequency is kept equal to the case of the relative bandwidth of the upper band from 55 GHz to 65 GHz. The relative bandwidth is given as:

$$B_\mathrm{r} = \frac{f_2^\mathrm{mmw} - f_1^\mathrm{mmw}}{f_\mathrm{c}^\mathrm{mmw}}, \qquad (12)$$

where $f_1^\mathrm{mmw} = 55$ GHz, $f_2^\mathrm{mmw} = 65$ GHz and $f_\mathrm{c}^\mathrm{mmw} = 60$ GHz is the center frequency. Now, the calculation of the sub-bands of the 3-11 GHz band is as follows:

$$f_{i+1}^\mathrm{uwb} = \frac{f_i^\mathrm{uwb}(-B_\mathrm{r} - 2)}{B_\mathrm{r} - 2}, \qquad (13)$$

where $f_1^\mathrm{uwb} = 3$ GHz and $f_{max(i)}^\mathrm{uwb} = 11$ GHz. The calculated values $f_i^\mathrm{uwb} \, \forall \, i$ are stated in Figure 9 together with maps of the Pearson correlation coefficients and theirs histograms. It is notable that the correlation coefficients are higher than in the previous case, where we compare the entire 3-11 GHz band and also, according to the histograms, theirs distributions are similar to the case of the correlation of the 55-65 GHz band (by visual inspection, the span of $|\rho^\alpha|$ is approximately from 0.1 to 0.6). It is also visible that the correlation slightly decreases with increasing center frequency f_c.

Please note that the last uwb sub-band from 8.19 GHz to 11 GHz exhibits a slightly narrower relative bandwidth B_r compared to other examined sub-bands. For the equal relative bandwidth among all sub-bands, an upper frequency of 11.41 GHz is required, but the measurement is limited to 11 GHz. Data for $^2h^\alpha(n)$ do not deviate from the presented $^1h^\alpha(n)$.

C. Collinearity of PDP

As opposed to the previously exploited definitions of PDP in (3), the PDPs are now calculated from a specified subset of measurement grid points. The subset is defined by an averaging window w_g, where g denotes the spatial location of the window w_g respective to the measurement grid. The window w_g slides over the measurement grid with a step of one measurement grid point. The graphical representation of the sliding window w_g and its movement within the measurement grid is in Figure 10. Please note that the window w_g is of square shape and of variable size ranging from 2 to 9.

Now, taking into account only the measured data covered by the averaging window w_g, the PDP is calculated as defined in (3). Then, in order to determine a sufficient size of the averaging window w_g, we evaluate the collinearity of the PDPs
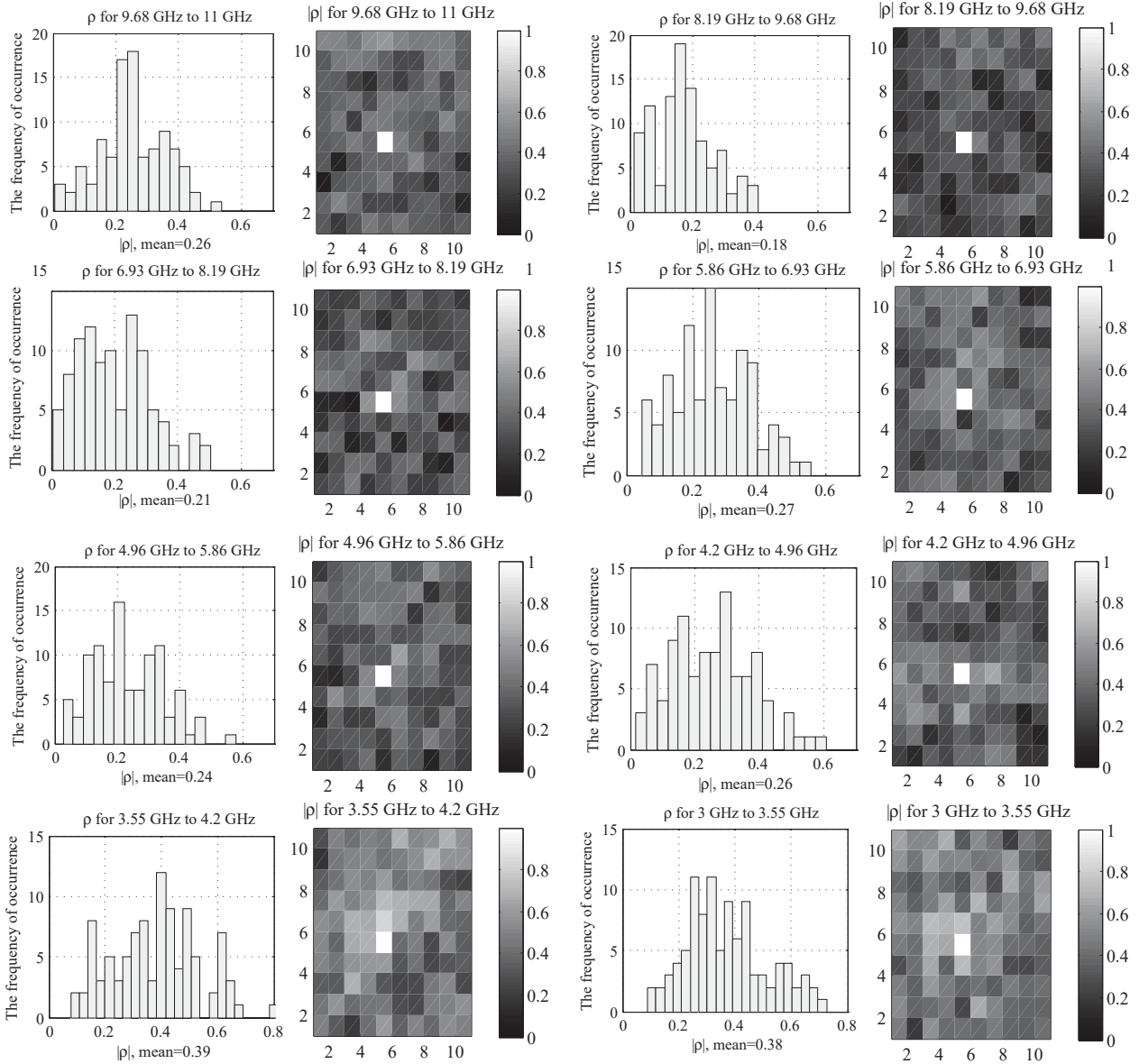
Fig. 9: Spatial maps and histograms for position $\kappa = 1$ of the sub-bands (selected from the 3-11 GHz band) having equal relative bandwidth to the relative bandwidth of the 55-65 GHz band.

for all available window sizes. The collinearity of PDP [35] is defined as:

$$c_g(P_{\mathrm{dB,ref}}, P_{\mathrm{dB},g}) = \frac{|\mathrm{tr}(P_{\mathrm{dB,ref}} P_{\mathrm{dB},g}^H)|}{||P_{\mathrm{dB,ref}}||_F ||P_{\mathrm{dB},g}||_F}, \forall g, \qquad (14)$$

where $P_{\mathrm{dB,ref}}$ is the selected reference PDP for $g = 1$ and $P_{\mathrm{dB},g}$ are the PDPs calculated from the respective spatial windows w_g. Next, $||.||_F$ denotes the Frobenius norm, $(.)^H$ represents the complex conjugate transpose and $\mathrm{tr}(.)$ is the matrix trace.

For both the frequency bands examined, the PDP collinearity results are plotted in Figure 11. In addition, the PDP collinearity has also been evaluated for different averaging window sizes with practically the same results. The mean and standard deviations of the PDP collinearity are shown in Figure
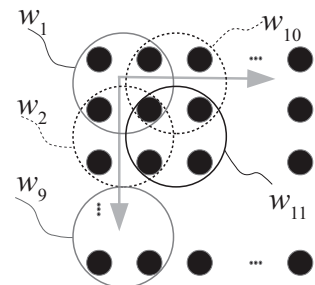
Fig. 10: 10×10 measurement grid with marked averaging windows w_g for PDP calculation. The averaging window size ranges from 2 to 9.

12. As can be seen, the collinearity difference for various window sizes is negligible, thus we claim that for the examined environment a 2×2 window is sufficient for averaging out the effect of small scale variations.

For all cases, the collinearity slightly decreases with the distance between examined PDPs in both directions of the measurement grid. This phenomenon is caused by a strong reverberation producing very similar PDPs within up to 10 wavelengths. Here, please keep in mind that the term wavelength is not rigorous as the wavelength is, of course, variable within the frequency bands examined.
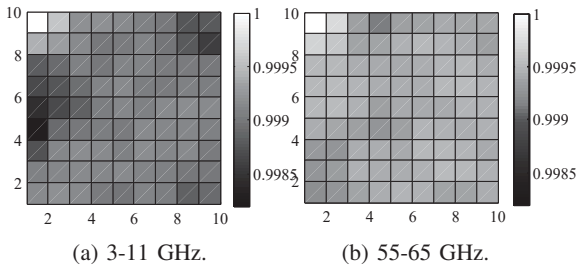
(a) 3-11 GHz. (b) 55-65 GHz.

Fig. 11: The PDP collinearity evaluation for the 3-11 GHz and 55-65 GHz bands. In this case, the size of the averaging window w_g is 2. Figures are plotted for $\kappa = 1$.

V. CHANNEL MODEL VALIDATION

In order to validate the presented in-vehicle channel model, we have visualized the two-sample K-S test in Figure 13. The comparison is performed for all the measured squared channel impulse responses $|^{1,2}h_{\mathrm{dB}}^{\alpha}(n)|^2$ with its corresponding piecewise linear model of PDP $^{1,2}P_{\mathrm{dB}}^*(n) + \xi$. We have evaluated the two-sample K-S test [37] according to:

$$^{\kappa}D_{\max} = \sup_{\alpha}\{\sup_{n}\left[F(|^{\kappa}h_{\mathrm{dB}}^{\alpha}(n)|^2) - F(|^{\kappa}h_{\mathrm{dB}}^*(n)|^2)\right], \forall\alpha\},\tag{15}$$
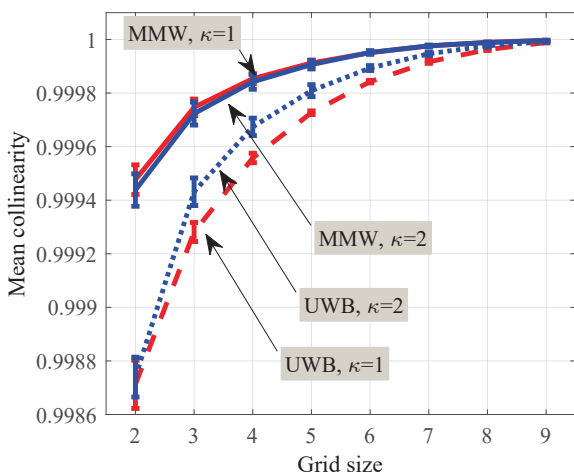
Fig. 12: Comparison of the mean PDP collinearity for both the frequency bands examined and for the averaging window size w_g showing a negligible difference between the listed window sizes. Note: the error bars are negligible for larger widow sizes due to growing averaging effect.

where F is the cumulative distribution function and the sup operator stands for *supremum* . Another useful metric is a mean square error (MSE) between the cumulative distributions of measured $|^{\kappa}h_{\mathrm{dB}}^{\alpha}(n)|^2$ and modeled $|^{\kappa}h_{\mathrm{dB}}^*(n)|^2$:

$$^{\kappa}MSE = \mathrm{E}\{\mathrm{E}\left[\left(F(|^{\kappa}h_{\mathrm{dB}}^{\alpha}(n)|^2) - F(|^{\kappa}h_{\mathrm{dB}}^*(n)|^2)\right)^2\right], \forall\alpha\}.\tag{16}$$

Finally, Table V evaluates the goodness-of-fit metrics calculated according to (15) and (16). The maximal deviation of the data measured compared to the model $D_{\max}$ is highest for the 55-65 GHz band $\kappa = 2$ probably due to the highest number of resolvable clusters. Visual inspection of the presented metrics could be performed via Figure 13. Considering the position $\kappa = 1$, the value of $D_{\max}$ is higher for the 3-11 GHz band since the maximal deviation of the model is higher, compared to the 55-65 GHz band. On the other hand, the MSE is higher for the 55-65 GHz as the model shows slightly wider range mismatch (see Fig. 13).

TABLE V: Table of goodness-of-fit metrics evaluation

	position	$D_{\max}$	MSE
3-11 GHz	$\kappa = 1$	39.41	4.83
	$\kappa = 2$	31.46	5.31
55-65 GHz	$\kappa = 1$	30.37	11.93
	$\kappa = 2$	41.65	15.56
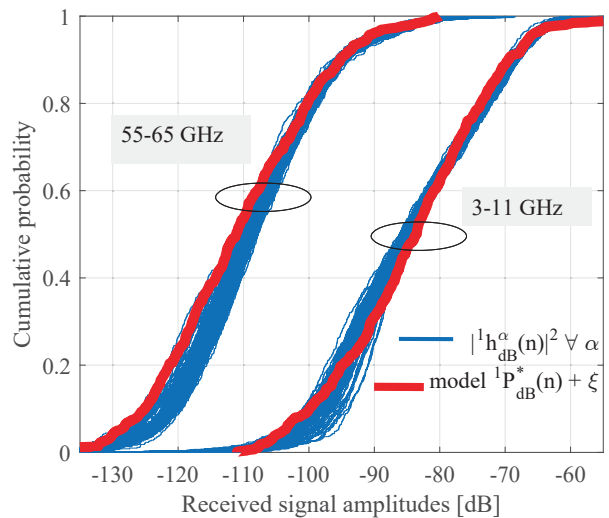
Fig. 13: **[red]** Amplitudes of the piecewise model of PDP $|^1h_{\mathrm{dB}}^*(n)|^2 = {}^1P_{\mathrm{dB}}^*(n) + \xi$ and **[blue]** the measured absolute values of the CIRs $|^1h_{\mathrm{dB}}^{\alpha}(n)|$ for both examined frequency bands.

VI. CONCLUSION

In the environment under investigation, the frequency band of 3-11 GHz is without the appearance of a high number of resolvable clusters (agrees with [38]). The two visible clusters are considered as direct/dominant component and reverberant diffuse tail. Hence, the number of clusters is 2, with a cluster decay rate of around 10 dB. On the other hand, the 55-65 GHz

frequency band exhibits a more evident clustering behavior. The number of resolvable clusters ranges from 3 to 5, with a cluster decay rates of 3.02 dB and 15.6 dB.

The RMS delay spread parameter is, due to the strong reverberation of the environment, rather high. For the 3-11 GHz band the RMS delay spread is 23 ns, whereas for the 55-65 GHz band the RMS delay spread is almost 5-times smaller, around 5 ns. The average delay is for both cases more than twice the RMS delay spread.

Regarding the spatial stationarity of the measured CIRs for the two frequency bands examined, we have observed a significantly lower achievable diversity in the 55 - 65 GHz band. If we compare the overall bandwidths, the lower achievable diversity with a mean value of the Pearson correlation of around 0.36, in the 55-65 GHz band might be problematic in terms of the exploitation of transmit diversity MIMO schemes. On the other hand, the 3-11 GHz band exhibits lower correlations in the range of 0.18. Now, if the comparison is done such that the 3-11 GHz band is divided into sub-bands exhibiting equal relative bandwidth as the 55-65 GHz band, the achievable diversity is approximately the same. The collinearity slightly decreases with the distance between examined PDPs in both directions of the measurement grid. This phenomenon is common to both the 3-11 GHz and 55-65 GHz bands and is probably caused by a strong reverberation producing very similar PDPs within up to approximately 10 wavelengths. We also show that increasing the size of the averaging window w_g produces higher collinearity values; however, the increase is very small, it is in the order of 10^{-4}. The 55-65 GHz band exhibits higher PDP collinearity than the 3-11 GHz band.

In this paper we propose a linear piecewise model of PDPs for both frequency bands. To authentically simulate the in-vehicle radio environment, we also provide parameters of the GEV random process in order to model small-scale signal fading in the delay domain. The resulting composition of the linear piecewise model of PDP and the superimposed model of SSF is validated by a comparison of cumulative probabilities as in the case of the Kolmogorov-Smirnov test. Our models show a very good match of the model with real-world measured data.

Although the 55-65 GHz band shows a higher atmospheric attenuation and is generally presumed to suffer by high shadowing losses, this paper shows the possibility to exploit this band for short-range communication even for non-line of sight (NLOS) cases in a tight and reflections-rich environment. The findings of this measurement campaign are exactly valid only for one particular vehicle type. On the other hand, authors expect similar results in all examined parameters also for vehicles sharing similar characteristics as the geometry or interior paneling. To enhance the reproducibility of our research, measured data are publicly available at: http://www.radio.feec.vutbr.cz/GACR-13-38735S/

REFERENCES

[1] C. Sommer and F. Dressler, *Vehicular Networking*. Cambridge University Press, 2014.

[2] N. Lu, N. Cheng, N. Zhang, X. Shen, and J. Mark, "Connected vehicles: Solutions and challenges," *IEEE Journal Internet of Things*, vol. 1, no. 4, pp. 289–299, Aug 2014.

[3] G. Leen and D. Heffernan, "Expanding automotive electronic systems," *Computer*, vol. 35, no. 1, pp. 88–93, 2002.

[4] G. Lasser and C. Mecklenbrauker, "Channel model for tyre pressure monitoring systems (TPMS)," in *Proceedings of the Fourth European Conference on Antennas and Propagation (EuCAP)*. IEEE, 2010.

[5] M. Win and R. Scholtz, "Characterization of ultra-wide bandwidth wireless indoor channels: a communication-theoretic view," *IEEE Journal on Selected Areas in Communications*, vol. 20, no. 9, pp. 1613–1627, 2002.

[6] R.-M. Cramer, R. Scholtz, and M. Win, "Evaluation of an ultra-wide-band propagation channel," *IEEE Transactions on Antennas and Propagation*, vol. 50, no. 5, pp. 561–570, 2002.

[7] U. Demir, C. Bas, and S. Ergen, "Engine compartment UWB channel model for intravehicular wireless sensor networks," *IEEE Transactions on Vehicular Technology*, vol. 63, no. 6, pp. 2497–2505, July 2014.

[8] M. Schack, J. Jemai, R. Piesiewicz, R. Geise, I. Schmidt, and T. Kurner, "Measurements and analysis of an in-car UWB channel," in *Vehicular Technology Conference, 2008. VTC Spring 2008. IEEE*, 2008, pp. 459–463.

[9] T. Kobayashi, "Measurements and characterization of ultra wideband propagation channels in a passenger-car compartment," in *2006 IEEE Ninth International Symposium on Spread Spectrum Techniques and Applications*, 2006, pp. 228–232.

[10] T. Tsuboi, J. Yamada, and N. Yamauchi, "UWB radio propagation inside vehicle environments," in *7th International Conference on ITS Telecommunications, 2007. ITST '07.*, 2007, pp. 1–5.

[11] M. Schack, R. Geise, I. Schmidt, R. Piesiewiczk, and T. Kurner, "UWB channel measurements inside different car types," in *3rd European Conference on Antennas and Propagation, 2009. EuCAP 2009.*, 2009, pp. 640–644.

[12] A. Moghimi, H.-M. Tsai, C. Saraydar, and O. Tonguz, "Characterizing intra-car wireless channels," *IEEE Transactions on Vehicular Technology*, vol. 58, no. 9, pp. 5299–5305, 2009.

[13] J. Blumenstein, T. Mikulasek, R. Marsalek, A. Prokes, T. Zemen, and C. Mecklenbruker, "Measurements of ultra wide band in-vehicle channel - statistical description and TOA positioning feasibility study," *EURASIP Journal on Wireless Communications and Networking*, p. 15, 2015.

[14] P. C. Richardson, W. Xiang, and W. Stark, "Modeling of ultra-wideband channels within vehicles," *IEEE Journal on Selected Areas in Communications*, vol. 24, no. 4, pp. 906–912, 2006.

[15] J. Blumenstein, T. Mikulasek, R. Marsalek, A. Chandra, A. Prokes, T. Zemen, and C. Mecklenbrauker, "In-vehicle UWB channel measurement, model and spatial stationarity," in *Vehicular Networking Conference (VNC), 2014 IEEE*. IEEE, 2014, pp. 77–80.

[16] Federal Communications Commission and others, "Revision of part 15 of the commission's rules regarding ultra-wideband transmission systems,first report and order, FCC 02," *V48, April*, 2002.

[17] R. Thoma, O. Hirsch, J. Sachs, and R. Zetik, "UWB sensor networks for position location and imaging of objects and environments," in *The Second European Conference on Antennas and Propagation, 2007. EuCAP 2007.*, 2007, pp. 1–9.

[18] R.-R. Lao, J.-H. Tarng, and C. Hsiao, "Transmission coefficients measurement of building materials for UWB systems in 3-10 GHz," in *Vehicular Technology Conference, 2003. VTC 2003-Spring. The 57th IEEE Semiannual*, vol. 1. IEEE, 2003, pp. 11–14.

[19] E. Ben-Dor, T. Rappaport, Y. Qiao, and S. Lauffenburger, "Millimeter-wave 60 GHz outdoor and vehicle AOA propagation measurements using a broadband channel sounder," in *Global Telecommunications Conference (GLOBECOM 2011), 2011 IEEE*, Dec 2011, pp. 1–6.

[20] M. Schack, M. Jacob, and T. Kurner, "Comparison of in-car UWB and 60 GHz channel measurements," in *2010 Proceedings of the Fourth European Conference on Antennas and Propagation (EuCAP)*. IEEE, 2010, pp. 1–5.

[21] J. Blumenstein, T. Mikulasek, A. Prokes, T. Zemen, and C. Mecklenbrauker, "Intra-vehicular path loss comparison of UWB channel for 3-11 GHz and 55-65 GHz," in *15th IEEE International Conference on Ubiquitous Wireless Broadband (ICUWB)*. IEEE, Sep 2015.

[22] T. Rappaport, J. Murdock, and F. Gutierrez, "State of the art in 60-GHz integrated circuits and systems for wireless communications," *Proceedings of the IEEE*, vol. 99, no. 8, pp. 1390–1436, Aug 2011.

[23] C. Gustafson, K. Haneda, S. Wyne, and F. Tufvesson, "On mm-wave multipath clustering and channel modeling," *IEEE Transactions on Antennas and Propagation*, vol. 62, no. 3, pp. 1445–1455, March 2014.

[24] J. Blumenstein, J. Vychodil, M. Pospisil, T. Mikulasek, and A. Prokes, "Effects of vehicle vibrations on mm-wave channel: Doppler spread and correlative channel sounding," in *IEEE PIMRC 2016 - accepted for publication*.

[25] A. F. Molisch, *Wireless communications*. John Wiley & Sons, 2010, vol. 15.

[26] J. Blumenstein, T. Mikulasek, R. Marsalek, A. Prokes, T. Zemen, and C. Mecklenbrauker, "In-vehicle mm-wave channel model and measurement," in *Vehicular Technology Conference (VTC Fall), 2014 IEEE 80th*. IEEE, 2014, pp. 1–5.

[27] A. A. M. Saleh and R. Valenzuela, "A statistical model for indoor multipath propagation," *Selected Areas in Communications, IEEE Journal on*, vol. 5, no. 2, pp. 128–137, 1987.

[28] A. Chandra, A. Prokes, T. Mikulasek, J. Blumenstein, P. Kukolev, T. Zemen, and C. F. Mecklenbrauker, "Frequency-domain in-vehicle UWB channel modeling," *IEEE Transactions on Vehicular Technology*, vol. 65, no. 6, pp. 3929–3940, June 2016.

[29] H. Xu, V. Kukshya, and T. Rappaport, "Spatial and temporal characteristics of 60-GHz indoor channels," *IEEE Journal on Selected Areas in Communications,*, vol. 20, no. 3, pp. 620–630, Apr 2002.

[30] H. Hashemi, "Impulse response modeling of indoor radio propagation channels," *IEEE Journal on Selected Areas in Communications*, vol. 11, no. 7, pp. 967–978, 1993.

[31] F. J. Harris, "On the use of windows for harmonic analysis with the discrete Fourier transform," *Proceedings of the IEEE*, vol. 66, no. 1, pp. 51–83, 1978.

[32] T. Pedersen, G. Steinbock, and B. Fleury, "Modeling of reverberant radio channels using propagation graphs," *IEEE Transactions on Antennas and Propagation*, vol. 60, no. 12, pp. 5978–5988, Dec 2012.

[33] S. Kotz and S. Nadarajah, *Extreme value distributions*. World Scientific, 2000.

[34] H. Hashemi, "The indoor radio propagation channel," *Proceedings of the IEEE*, vol. 81, no. 7, pp. 943–968, 1993.

[35] A. Paier, T. Zemen, L. Bernado, G. Matz, J. Karedal, N. Czink, C. Dumard, F. Tufvesson, A. Molisch, and C. Mecklenbrauker, "Non-WSSUS vehicular channel characterization in highway and urban scenarios at 5.2 GHz using the local scattering function," in *International ITG Workshop on Smart Antennas, 2008. WSA 2008*, Feb 2008, pp. 9–15.

[36] R. He, O. Renaudin, V. M. Kolmonen, K. Haneda, Z. Zhong, B. Ai, and C. Oestges, "Characterization of quasi-stationarity regions for vehicle-to-vehicle radio channels," *IEEE Transactions on Antennas and Propagation*, vol. 63, no. 5, pp. 2237–2251, May 2015.

[37] F. J. Massey Jr, "The Kolmogorov-Smirnov test for goodness of fit," *Journal of the American statistical Association*, vol. 46, no. 253, pp. 68–78, 1951.

[38] A. Ott, U. Siart, T. Eibert, O. Klemp, and R. Steffen, "Enhanced investigations of 433 MHz - 10 GHz time invariant wireless in-car communication channels," in *Microwave Conference (GeMIC), 2011 German*, March 2011, pp. 1–4.

Frequency-Domain In-Vehicle UWB Channel Modeling

Aniruddha Chandra, Ales Prokes, Tomas Mikulasek, **Jiri Blumenstein**, Pavel Kukolev, Thomas Zemen, Christoph F Mecklenbrauker

Frequency-Domain In-Vehicle UWB Channel Modeling

Aniruddha Chandra,*Member,IEEE,* Aleš Prokeš, Tomáš Mikulášek, Jiri Blumenstein, Pavel Kukolev,
Thomas Zemen,*Senior Member,IEEE,* and Christoph F. Mecklenbräuker,*Senior Member,IEEE*

Abstract—The aim of this article is to present a simple but robust model characterizing the frequency dependent transfer function of an in-vehicle ultra-wide-band channel. A large number of transfer functions spanning the ultra-wide-band (3 GHz to 11 GHz) are recorded inside the passenger compartment of a four seated sedan car. It is found that the complex transfer function can be decomposed into two terms, the first one being a real valued long term trend that characterizes frequency dependency with a power law, and the second term forms a complex correlative discrete series which may be represented via an autoregressive model. An exhaustive simulation framework is laid out based on empirical equations characterizing trend parameters and autoregressive process coefficients. The simulation of the transfer function is straightforward as it involves only a handful of variables, yet it is in good agreement with the actual measured data. The proposed model is further validated by comparing different channel parameters, such as coherence bandwidth, power delay profile, and root mean square delay spread, obtained from the raw and the synthetic data sets. It is also shown how the model can be compared with existing time-domain Saleh-Valenzuela influenced models and the related IEEE standards.

Index Terms—Ultra wide band, autoregressive model, transfer function, frequency dependency, intra-vehicle.

I. INTRODUCTION

CONNECTED-VEHICLES represents one of the key features of an intelligent transportation system (ITS) [1], [2] and such vehicles are expected to play a vital role in information and communication technology (ICT) infrastructure in urbanized regions [3]. So far, the related research has been dominantly focused towards design and development of wireless links for vehicle-to-vehicle and vehicle-to-infrastructure scenarios [4]. An IEEE standard, 802.11p [5], has also been devised for the purpose and communication devices conforming to the standard is being implemented in personal [6] and public transport [7] vehicles. For an comprehensive realization of the connected-vehicles vision, it is also important to consider the links inside a vehicle. It is well known that intra-vehicular wireless communication helps in increasing fuel efficiency by reducing the overall wiring harness and simplify manufacturing and maintenance of vehicles [8]. A typical modern day car houses hundreds of sensors [9] connected to an on-board unit (OBU) for monitoring safety, diagnostics, and convenience. The OBU can also provide last-hop wireless connectivity to personal electronic gadgets (smartphone, tablet, laptop etc.) opening up a plethora of new possibilities. On one hand, it will be possible to obtain user-defined real-time multimedia streaming for navigational or recreational purposes [10]. On the other hand, locating people and device would trigger new applications such as smart airbag control [11] or profile restriction of handheld devices [12]. However, these demands can only be met if the wireless technology provides a high bandwidth and assists in precise localization.

Ultra wide band (UWB) has established itself as a preferred technology for high-data-rate, short-range, low-power communication with centimeter-level localization accuracy. Extensive UWB measurement campaigns resulted in a series of channel models [13], [14]. Nevertheless, location specific information is a prerequisite for formulating realistic and reproducible channel models, especially in vehicular environments [15]. In order to determine the feasibility of UWB implementation in small personalized vehicles a number of UWB link measurements in passenger cars have been carried out [16]–[21]. Due to its large dynamic range, a vector network analyzer (VNA), is often preferred for such measurements. The two requirements for VNA based setups: transmitter (Tx) and the receiver (Rx) antennas should be within cable length, and the channel should be static, are satisfied for in-car sounding experiments.

Although the raw data obtained from a VNA is available in the frequency domain, most of the intra vehicular channel modeling efforts [17] are concentrated towards the time do-
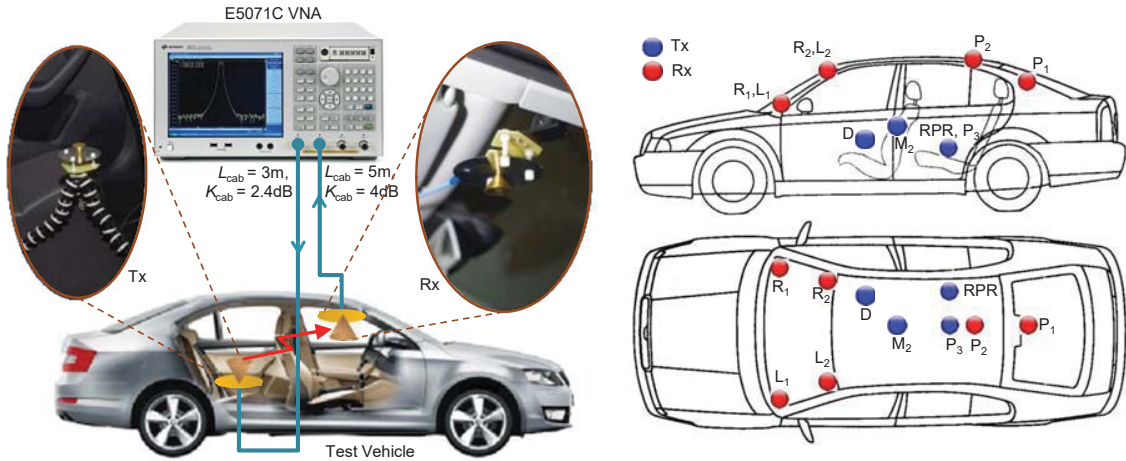
Fig. 1. Measurement setup (left) and antenna placement inside car (right).
Tx legends - D: driver, RPR: rear passenger on right, P_3: middle of backseat, M_2: midpoint between two front seats.
Rx legends - L_1: left dashboard, R_1: right dashboard, L_2: left windshield, R_2: right windshield, P_1 and P_2: positions at rear part of the ceiling.

main, with the most popular method being utilization of the Saleh-Valenzuela (S-V) model [14], [22]. The process involves inverse fast Fourier transform (IFFT) followed by certain kind of windowing (Hamming, Hanning, Blackman etc.). A series of S-V model parameters (decay and arrival rate of clusters and rays within each cluster) are found next. The method involves cluster identification which is ambiguous, requires a lot of parameters, and introduce distortion due to IFFT and windowing. If a model can be developed directly from the frequency domain data that requires only a handful of parameters for characterization, simulation of the intra-vehicle channels would be simpler and more reliable helping designers of various in-vehicle communication and localization systems.

This paper aims at analyzing the channel transfer function (CTF) of in-car UWB channels in the frequency domain. Our model is simple to implement as it is not computationally intensive like models using ray tracing based simulation [23] or propagation graphs [24]. In spite of that, the proposed model achieves a good degree of accuracy. Specifically our contributions are the following:

- We propose an autoregressive (AR) process for channel frequency transfer function modeling of UWB links in a *car*. To the best of our knowledge, this has not been attempted so far. Undoubtedly, AR models are a very mature topic that has been used since many decades but it has been applied to UWB propagation in large passenger vehicles like planes [25]. More importantly, we demonstrate that the AR process should be applied *after removing the long term frequency trend* from the transfer function. The method is also different from earlier work on characterizing the frequency dependency of intra-vehicular wireless channels, such as [26], where only simple models of large scale frequency variation were reported.
- Appropriate long term trend equations, in the form of power law, are proposed. Next, assuming that passenger occupancy affects only the long term trend parameters, we find empirical relations to predict the change in such

parameters when the number of passengers are changed. Results from an extensive measurement campaign on UWB propagation inside passenger compartment of a car is used for the purpose.
- For the short term trend modeled with a AR process, we propose a simple set of equations to predict the process coefficients. The method is simpler than those presented in [27], [28] which requires the characterization of initial conditions.
- A simple step by step process is demonstrated for simulating the overall CTF. Simulated outputs are validated against the real life measurements.

The rest of the paper is organized as follows. The next section provides description of the experimental setup. The detailed modeling for long term and short term frequency variations are presented in Section III and Section IV, respectively. The overall simulation framework is presented in Section V. This section also includes output of the model and subsequent validation through different quantities of interest. Finally, Section VI concludes the paper.

II. EXPERIMENTAL SETUP

A set of intra-vehicular channel transfer functions (CTFs) were measured with a four port VNA (model: Agilent E5071C). The vehicle under test is a four seater Skoda sedan (model: Octavia III 1.8 TSI), with dimensions: 4.659 m (length) $\times$ 1.814 m (width) $\times$ 1.462 m (height), parked at the sixth basement floor in an underground garage. The experimental setup is detailed in Fig. 1. Port 1 and port 2 of the VNA were connected to the transmitter (Tx) and the receiver (Rx) antennas, respectively, and the scattering parameter, s_{21}, which signifies the forward voltage gain approximates the CTF, $H(f)$. Tx and Rx antennas are connected to the VNA via phase stable coaxial cables. The cable length (L_{cab}) and cable attenuations (K_{cab}) were measured, and are indicated in Fig. 1.

The Tx and Rx antenna positions inside the passenger compartment are also shown in Fig. 1. The different configurations

ensure both line-of-sight (LoS) and non-line-of-sight (nLoS) propagation conditions. In order to test the effect of passenger occupancy, we varied the number of passengers (n_P) from zero to two at each location. The shadowing in nLoS cases is caused by the seats and the persons sitting inside the vehicle.
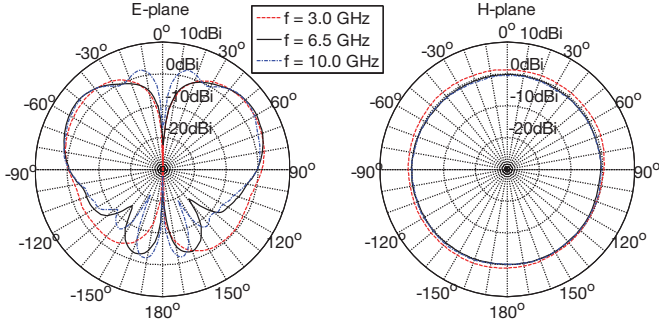
Fig. 2. Measured gain pattern of the conical monopole antennas in E-plane (left-hand side) and H-plane (right-hand side).

A pair of identical conical monopole antennas were used as Tx and Rx and it can be observed from the corresponding measured radiation pattern shown in Fig. 2 that the azimuth plane radiation is circular and invariant within the desired frequency band (3-10 GHz). Variations in the elevation plane do not pose serious concerns because in most of the measurements the Tx-Rx line is contained in the main lobe. In general, the monopole conical antennas have a low radar cross-section and provide a low voltage standing wave ratio [29]. Further, the gain of a conical monopole antenna in the frequency range 3-11 GHz is almost constant [30]. Thus it is possible to analyze the measured wideband CTF without considering the effect of frequency on antennas.

TABLE I
VNA PARAMETERS FOR UWB MEASUREMENT

Parameter	Description	Value
P_{VNA}	Transmit power	5 dBm
$\mathrm{BW}_{\mathrm{IF}}$	IF filter bandwidth	100 Hz
f_L	Start frequency	3 GHz
f_H	Stop frequency	11 GHz
BW	Bandwidth	8 GHz
N_{VNA}	Number of points	801
f_s	Frequency step size	10 MHz
t_{res}	Time resolution	125 ps
$L_{\mathrm{CIR}(t)}$	Maximum CIR length (time)	100 ns
d_{res}	Distance resolution	3.75 cm
$L_{\mathrm{CIR}(d)}$	Maximum CIR length (distance)	30 m
$H_{\mathrm{fil}}(f)$	Windowing for IFFT	Blackman

The frequency-domain measurement parameters are summarized in Table I. The maximum value of the output transmit power of the VNA (P_{VNA}) and the minimum measurable power (or noise floor) together define the system's dynamic range. A trade-off between noise floor and sweep speed may be attained by controlling the intermediate frequency filter bandwidth $(\mathrm{BW}_{\mathrm{IF}})$ and/or averaging. In our experiment, the frequency range between the start frequency, $f_L = 3$ GHz, and the stop frequency, $f_H = 11$ GHz, is swept. The number of discrete frequency tones generated by the VNA in the range, $N_{\mathrm{VNA}} = 801$, and the bandwidth, BW $= f_H - f_L = 8$

GHz, determine the frequency resolution as per the relation, $f_s = (f_H - f_L)/(N_{\mathrm{VNA}} - 1) = \mathrm{BW}/(N_{\mathrm{VNA}} - 1)$. Further, the sweeping bandwidth sets the time resolution, $t_{\mathrm{res}} = 1/\mathrm{BW}$, i.e. the minimum time between samples in the time-domain channel impulse response (CIR) function obtained after inverse fast Fourier transform (IFFT), whereas the frequency step size (f_s) characterizes the maximum observable delay spread, $L_{\mathrm{CIR}(t)} = 1/f_s$, i.e. the maximum time delay until the multipath components (MPCs) are observed. The distance resolution, $d_{\mathrm{res}} = c \cdot t_{\mathrm{res}} = c/\mathrm{BW}$, refers to the length an electromagnetic wave can propagate in free space $(c = 3 \times 10^8 \mathrm{m/s})$ during time t_{res} and the corresponding distance range is $L_{\mathrm{CIR}(d)} = c/f_s$.

The CIR obtained with VNA through the IFFT operation can be expressed as, $h_{\mathrm{VNA}}(t) = h(t) * h_{\mathrm{fil}}(t)$, where $H_{\mathrm{fil}}(f) = \mathcal{F}\{h_{\mathrm{fil}}(\tau)\}$ is the transfer function of the windowing operation. We used the Blackman window which ensures minimum spectral distortion, i.e. high side lobe suppression and reasonable main lobe width [31]. High side lobe suppression is preferred to a narrower main lobe width, because it decreases the probability of unwanted detection of a side lobe as the first arriving ray [32]. However, this feature is crucial for ranging applications and filtering considerations are not important for the basic CTF simulation.

III. LONG TERM VARIATIONS

Let us investigate a typical measured CTF as depicted in Fig. 3. The magnitude of CTF has a overall downward slope with respect to frequency and the first step of our modeling involves separating this long term variation or trend, i.e. we express the complex CTF as

$$H(f) = \tilde{H}(f) \cdot |H(f)|_{\mathrm{trend}} \tag{1}$$

where $\tilde{H}(f)$ denotes the complex short-term variations of the CTF.
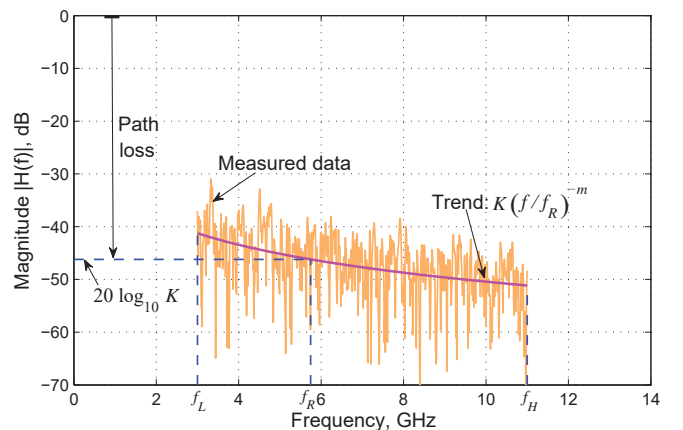
Fig. 3. CTF and estimated trend (Tx position: P_3, Rx position: L_2, and $n_P = 0$).

The well known free space path loss formula suggests that the CTF amplitude is inversely proportional to frequency [33]–[36] and the long term variations can be modeled with a simple

power law

$$|H(f)|_{\text{trend}} = K \left(\frac{f}{f_R} \right)^{-m} \qquad (2)$$

as devised in [37]. In (2), the parameter K is a proportionality constant and m is a power law exponent. The reference frequency, $f_R = \sqrt{f_L f_H}$, depends on the lower (f_L) and upper (f_H) bound of the frequency band and is equal to the geometric mean of the bounds. For the current UWB experiment ($f_L = 3$ GHz, $f_H = 11$ GHz), $f_R = 5.74$ GHz.

There also exists another exponential model for frequency dependence in ultrawide band [38]

$$20 \cdot \log_{10} |H(f)|_{\text{trend}} = K' \cdot \exp(-m' f) \qquad (3)$$

In [39], it was shown that the root mean square error for both the trends given by (2) and (3) are comparable for the whole set of experimental data. However, we considered the power law over the exponential one due to three factors; first, the power law has a sound mathematical basis, second, the majority of the authors recommended the former over the later, and third, the power equation is currently adopted in IEEE 802.15.4a UWB standard documentation [40].

In Fig. 3 the estimated trend with least mean square error fitting for a particular data set is shown. The parameter values in an empty car ($n_P = 0$) for all different antenna locations are listed in Table II.

TABLE II
PARAMETER VALUES OF THE FREQUENCY TREND FOR DIFFERENT TX AND RX ANTENNA POSITIONS (MARKINGS ARE AS PER FIGURE 1)

Tx	Rx	Tx-Rx distance in m	Path loss in dB $(-20 \log_{10} K)$	Power law exponent (m)	Remark (LoS / nLoS)
D	R_2	0.56	40.4402	0.6988	LoS
P_3	P_2	0.60	41.9495	0.7583	LoS
RPR	P_2	0.70	41.0768	1.2355	LoS
M_2	L_2	0.73	39.9511	0.4913	LoS
M_2	R_2	0.76	39.2481	0.6145	LoS
P_3	P_1	0.76	39.6790	1.1910	LoS
RPR	P_1	0.84	41.3834	0.8015	LoS
D	R_1	0.85	44.9526	0.9257	LoS
M_2	P_2	0.87	40.0627	0.9788	LoS
D	L_2	0.97	38.9088	1.2165	LoS
D	L_1	1.16	45.5443	1.1257	LoS
D	P_2	1.23	43.8985	0.9498	nLoS
P_3	L_2	1.23	46.1980	0.8776	nLoS
RPR	R_2	1.25	45.3958	0.9250	nLoS
P_3	R_2	1.28	45.4769	1.1457	nLoS
RPR	L_2	1.44	46.7050	1.2859	nLoS
D	P_1	1.48	46.4266	0.5556	nLoS
RPR	R_1	1.57	47.9343	1.0283	nLoS
P_3	L_1	1.62	48.1986	1.0062	nLoS
P_3	R_1	1.65	48.3114	1.0030	nLoS
RPR	L_1	1.74	49.7412	1.0637	nLoS

A. Characterization of K

A physical interpretation of the parameter K can be derived as hereunder. The path loss (α) of a channel is defined as the ratio of the transmit power to the receiver power (P_t/P_r), and in dB scale it may be written as

$$\alpha = 10 \log_{10} \left(\frac{P_t}{P_r} \right) = -20 \log_{10} |H(f)| \qquad (4)$$

which is obtained by noting that the CTF is the ratio of the channel output to the channel input in the frequency domain, i.e. $P_t/P_r = 1/|H(f)|^2$.

Next, substituting the CTF magnitude trend (instead of the overall CTF magnitude) from (2) in (4), we have

$$\alpha = -20 \log_{10} K + 20 m \cdot \log_{10} (f/f_R) \qquad (5)$$

From (5), it is easy to verify that $\alpha_{f_R} = -20 \log_{10} K$. In other words, the path loss at the reference frequency, $\alpha_{f_R} = \alpha(f = f_R)$, is equal to the parameter K in dB scale with a negative sign (PL is a positive quantity). The concept is graphically explained in Fig. 3 and we have listed α_{f_R} (rather than K) in Table II as it is more intuitive to deal with the path loss data.

To avoid any confusion, we would like to state that in majority of literature [41] the path loss data is computed from VNA data by averaging the inverse of squared CTF over the whole frequency range

$$\alpha = 10 \log_{10} \left(\frac{1}{N_{\text{VNA}}} \sum_{n=1}^{N_{\text{VNA}}} \frac{1}{|H(f_n)|^2} \right) \qquad (6)$$

whereas, in our case, we have computed the long term frequency trend parameters (K and m) for each measurement through finding the best-fitting curve that minimizes the sum of the squares of the residuals. This is followed by calculation of the path loss at the reference frequency (α_{f_R}) from K.

After establishing the relation of K with path loss, we investigate the effect of propagation distance on K (or to be more specific, on α_{f_R}). It is possible to relate the path loss data with the Tx-Rx separation through the following equation [42]

$$\alpha_{f_R} = \alpha_{f_R}(d_0) + 10\gamma \log_{10} \left(\frac{d}{d_0} \right) + \chi \qquad (7)$$

where $\alpha_{f_R}(d_0)$ is the path loss at $d_0 = 1$ m [1], γ is the path loss exponent and $\chi \sim \mathcal{N}(0, \sigma_\chi^2)$ is a normal distributed random variable which accounts for the log-normal shadowing. A least square linear regression fitting between computed α_{f_R} values across all the measurements and the corresponding distances (d) gives us the parameters in (7), for both LoS and nLoS conditions, which are mentioned in Table III. From the residuals of the regression analysis the log-normality of the shadowing was also verified via normal probability plots. However, the regression lines and probability plots are omitted here (as well as in all the following regression analyses in this paper) for brevity.

B. Characterization of m

For indoor UWB propagation, a value range of $0.8 < m < 1.4$ was reported earlier [43]. The m values in Table II roughly follows the limits. Our results are also consistent with

[1]Although it is a common practice to consider the smallest possible Tx-Rx separation, which is 0.56 m, as the reference distance, here we followed a general recommendation to consider $d_0 = 1$ m for indoor environments. It is highly likely that path loss values for such a common reference distance is available for other environments, and comparison with values in Table III would be more straightforward.

TABLE III
PATH LOSS PARAMETERS FOR THE LoS AND THE nLOS CASES

Scenario	Path loss intercept, dB $(\alpha_{f_R}(d_0))$	Path loss exponent (γ)	Shadowing variance, dB (σ_χ^2)
LoS	42.1737	0.9198	2.0387
nLoS	42.4952	2.7559	0.6262

previous measurements inside car compartment [44] where a $1/f^2$ decay was observed in the power spectra which translates to the $1/f$ decay in the amplitude domain. The experiments conducted at other parts (e.g. under the chasis [45]) of the vehicle with less favourable propagation modes results in a higher m.

It is interesting to note that the values of m for the current experiments are uniformly distributed and do not depend on the Tx-Rx gap. A simple averaging is thus sufficient to model the power law exponent. The average values obtained for LoS and nLoS cases are as follows

$$< m >= \begin{cases} 0.9125 & : \text{LoS} \\ 0.9841 & : \text{nLoS} \end{cases} \tag{8}$$

C. Effect of passenger occupancy

As mentioned in Section II, we have repeated our measurements for each antenna combination by varying the passenger occupancy. Although the maximum capacity of the car is four, one location was always occupied by the Tx antenna and the tripod on which it was fixed, and the other location was not accessible due to connecting cables. Thus we could test each location with minimum zero and maximum two passengers.
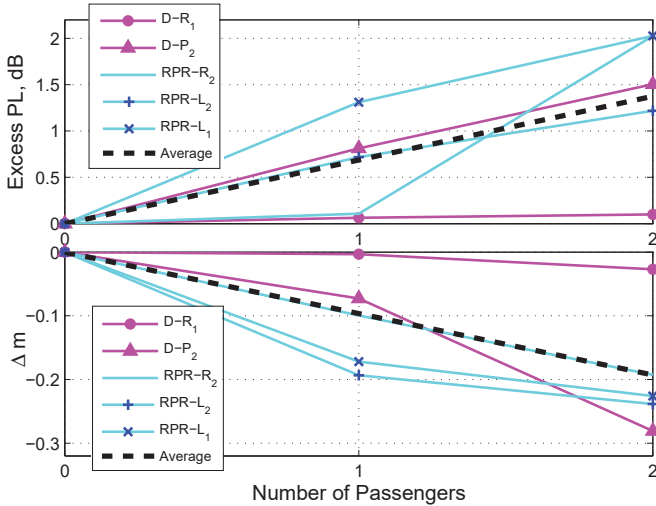
Fig. 4. Effect of passenger on PL at reference frequency and on the PL trend exponent.

The effect of number of passengers on PL and exponent value are shown in Fig. 4. For both the figures we have only plotted the change in parameter values, i.e. excess PL $= \alpha_{f_R}(n_P) - \alpha_{f_R}$ and $\Delta m = m(n_P) - m$, with respect to number of passengers (n_P). While the PL increases due to additional shadowing, the power law exponent lowers with

more passengers making the CTF flatter. This phenomena was earlier observed in [26, (2)] for in-car experiments where the exponent is quantified with a large negative slope with respect to frequency and was demonstrated for indoor office environments [46, Fig. 5(b)] where the PL coefficient decreases with more number of people in the room when the receiver is placed close to occupants. Although the human tissue exhibits a constant decrease in permittivity with frequency [47], the flattening of CTF is perhaps accounted to the absence of rich scattering multipath components.

Plots in Fig. 4 for different Tx locations are depicted with separate colours (magenta for Tx at D and cyan for Tx at RPR), but it was hard to find any specific correlation of the trends with the antenna positions.

A simple averaging of the upward trends (shown with black dotted line in Fig. 4) across different locations enables us to express the PL with passengers in the following manner

$$\alpha_{f_R}(n_P) = \alpha_{f_R} + 0.6876 \times n_P \quad ; \ n_P = 0, 1, 2 \tag{9}$$

whereas for the exponent, which is monotonically decreasing, the following average equation is found to be valid

$$m(n_P) = m - 0.0965 \times n_P \quad ; \ n_P = 0, 1, 2 \tag{10}$$

IV. SHORT TERM VARIATIONS

After finding out the long term trends, we proceed with the characterization of the normalized CTF, namely, $\tilde{H}(f)$. Autoregressive or AR modeling belongs to the class of parametric spectral estimation and as the variations of $\tilde{H}(f)$ resembles a correlated series with low peaks and deep fades, an AR model is preferred [48] over moving average (MA) or hybrid ARMA models. An AR model for wideband indoor radio propagation was first presented in [49], and later applied to UWB channel modeling in [41] for indoor scenarios and in [50] for underground mines.

The normalized CTF under a q order AR process assumption may be mathematically expressed as

$$\tilde{H}(f_n) = \sum_{k=1}^{q} a_k \tilde{H}(f_{n-k}) + \xi_n \tag{11}$$

where, f_n; $n = 1, 2, \cdots N_{\text{VNA}}$, is the nth discrete frequency in the CTF vector, a_k; $k = 1, 2, \cdots q$, are the complex AR process coefficients, and ξ_n is the nth sample of a complex Gaussian process with variance σ_ξ^2. A z-transform, $\tilde{H}(z) = \sum_n \tilde{H}(f_n) z^{-n}$, allows us to view the CTF as the output of a all pole linear infinite impulse response (IIR) filter with transfer function, $\mathcal{G}(z) = \tilde{H}(z)/\xi(z)$, excited by white Gaussian noise [49], i.e.

$$\mathcal{G}(z) = \frac{1}{1 - \sum_{k=1}^{q} a_k z^{-k}} = \prod_{k=1}^{q} \frac{1}{1 - p_k z^{-k}} \tag{12}$$

The equivalent filter structure is presented in Fig. 5.

The poles (p_k) and the noise variance (σ_ξ^2) are found by solving the Yule-Walker equations [51] which obtains the least
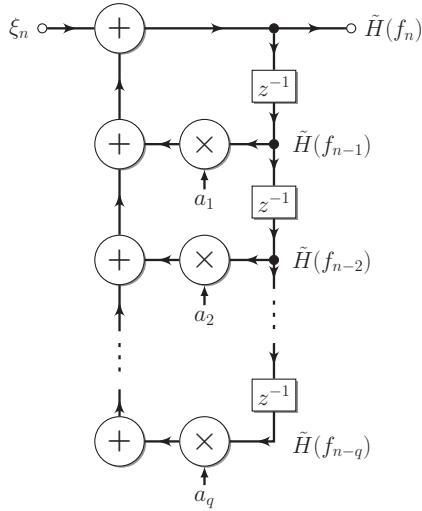
Fig. 5. Direct form filter implementation of the AR process for short term variations.

Fig. 6. Measured and estimated PDPs with two different order AR processes. Tx position: P_3, Rx position: P_1, and $n_P = 0$.

square error. The solution involves converting (11) to the autocorrelation domain

$$
\begin{aligned}
R_{\tilde{H}\tilde{H}}(j) &= \mathcal{E}\left\{\tilde{H}(f_n)\tilde{H}(f_{n-j})\right\} \\
&= \sum_{k=1}^{q} a_k R_{\tilde{H}\tilde{H}}(j-k) + \sigma_\xi^2 \delta(j)
\end{aligned}
\tag{13}
$$

with $\mathcal{E}\{\cdot\}$ denoting the expectation operator and $\delta(\cdot)$ is delta function, and then solving for the process coefficients

$$
R_{\tilde{H}\tilde{H}}(-j) - \sum_{k=1}^{q} a_k R_{\tilde{H}\tilde{H}}(k-j) = 0 \; ; \; j > 0
\tag{14}
$$

as well as the noise variance

$$
\sigma_\xi^2 = R_{\tilde{H}\tilde{H}}(0) - \sum_{k=1}^{q} a_k R_{\tilde{H}\tilde{H}}(k)
\tag{15}
$$

It should be noted here that our model does not require initial conditions of the IIR filter and thereby reduces the complexity of the models compared to those presented in [27], [28].

A. AR process order selection

In general, higher order AR process provides better estimation but with diminishing returns as q increases, and there exists a tradeoff between accuracy and complexity. Although a second order ($q = 2$) AR process was sufficient for indoor [41] and underground mines [50], we propose a fifth order ($q = 5$) process as the car compartment exhibits multiple overlapped clusters. The following figure, Fig. 6, shows the result of power delay profile (PDP) estimations with a 2nd order and with a 5th order AR process (refer to Section V for more details on PDP). One may notice that even for a direct LoS path (Tx: P_3, Rx: P_1), the estimation with 2nd order process results in incorrect delay calculation for the first arriving path or the peak. The problem is more prominent for the nLoS situations.

The pole amplitudes, pole angles, and input noise variances for the entire measurement set is listed in Table IV considering a fifth order AR process estimation of the CTF short term variations.

In [49], the AR process order estimation was carried out by comparing the cumulative distribution function (CDF) of the 3 dB width of the frequency correlation function and CDF of the root mean square delay spread (for definitions, refer to Section V). A mathematically rigorous method is, however, to choose the process order through Akaikes information criterion (AIC) [41], [52] or minimum description length (MDL) [53], [54]. We have refrained from such analysis as it is out of scope of the present paper.

B. Characterization of input noise

The AR process is driven by, $\xi_n \sim \mathcal{CN}(0, \sigma_\xi^2)$, a complex zero mean Gaussian noise, and looking at the entries in Table IV, one can find that its variance increases with Tx-Rx separation. A linear regression fitting yields the following empirical relation for the data set obtained

$$
\sigma_\xi^2 = 0.0024 + 0.107 \times d
\tag{16}
$$

where d is the propagation distance in meters. It may be noted that (16) is obtained through fitting across all the values in Table IV without attempting to differentiate between LoS and nLoS cases. This also holds true for the pole parameters which are derived next. Our general assumption is that the LoS/ nLoS conditions affect only the parameters that are associated with the long term variations. This enables us to realize a simulation model with minimum inputs.

C. Characterization of poles

Fig. 7 plots the estimated pole locations for all the different sets of experiments as listed in Table IV. When the poles are sorted in the descending order of their amplitudes, they form distinguished clusters in the complex plane.

Let us analyze the amplitude of the poles first. The pole clusters represent multipath clusters and the amplitudes of the higher order pole clusters shifts away from the unit circle as they contribute lesser power in the overall power delay profile [49]. Fortunately, the amplitudes inside a cluster is fairly constant, and it is possible to approximate the pole

Tx	Rx	Tx-Rx distance in m	Pole amplitudes					Pole angles in radians					Noise variance (σ_ξ^2)	Remark (LoS / nLoS)
			$\|p_1\|$	$\|p_2\|$	$\|p_3\|$	$\|p_4\|$	$\|p_5\|$	$\angle p_1$	$\angle p_2$	$\angle p_3$	$\angle p_4$	$\angle p_5$		
D	R₂	0.56	0.9844	0.8416	0.7801	0.6773	0.6357	−0.2578	−0.7162	−1.6014	−2.6323	2.4051	0.0577	LoS
P₃	P₂	0.60	0.9702	0.7738	0.7328	0.7038	0.6145	−0.2121	−0.7477	−1.4538	−2.6015	2.3436	0.1355	LoS
RPR	P₂	0.70	0.9775	0.8328	0.7492	0.6855	0.6211	−0.2378	−0.7358	−1.5814	−2.6406	2.4533	0.0915	LoS
M₂	L₂	0.73	0.9852	0.8352	0.6449	0.6433	0.5530	−0.1959	−0.8360	−1.6695	−2.6379	2.1722	0.0798	LoS
M₂	R₂	0.76	0.9906	0.8641	0.7322	0.6626	0.6188	−0.1874	−0.7961	−1.6229	−2.6254	2.3512	0.0555	LoS
P₃	P₁	0.76	0.9933	0.8116	0.7581	0.6821	0.6174	−0.1956	−0.8318	−1.5776	−2.7156	2.3671	0.0471	LoS
RPR	P₁	0.84	0.9890	0.8290	0.7018	0.6220	0.6133	−0.2179	−0.8231	−1.6998	−2.6755	2.3329	0.0645	LoS
D	R₁	0.85	0.9657	0.8265	0.6984	0.6131	0.6121	−0.3594	−0.8177	−1.7186	−2.6795	2.3108	0.1006	LoS
M₂	P₂	0.87	0.9859	0.8311	0.7548	0.6567	0.5884	−0.2251	−0.8518	−1.6629	−2.7682	2.2132	0.0874	LoS
D	L₂	0.97	0.9894	0.8428	0.7287	0.6151	0.5870	−0.1831	−0.7303	−1.5664	−2.5906	2.4461	0.0519	LoS
D	L₁	1.16	0.9773	0.8230	0.6759	0.5951	0.5223	−0.2676	−0.9072	−1.6699	−2.7820	2.3486	0.1285	LoS
D	P₂	1.23	0.9726	0.8503	0.7354	0.6556	0.6327	−0.3472	−0.8706	−1.7034	−2.7761	2.3318	0.1113	nLoS
P₃	L₂	1.23	0.9503	0.8463	0.7783	0.7037	0.6254	−0.3492	−0.8984	−1.7449	−2.8202	2.1729	0.1919	nLoS
RPR	R₂	1.25	0.9651	0.8026	0.7511	0.6185	0.6168	−0.3666	−0.9281	−1.7241	−2.7201	2.2717	0.1494	nLoS
P₃	R₂	1.28	0.9451	0.8495	0.7673	0.6761	0.5672	−0.3677	−0.9495	−1.7593	−2.8333	2.2411	0.1746	nLoS
RPR	L₂	1.44	0.9587	0.8560	0.7513	0.6569	0.6002	−0.3628	−0.9603	−1.8069	−2.9035	2.2118	0.2095	nLoS
D	P₁	1.48	0.9824	0.8587	0.7287	0.6682	0.6208	−0.3863	−1.0215	−1.8785	−2.8058	2.1533	0.1278	nLoS
RPR	R₁	1.57	0.9512	0.8189	0.7168	0.5949	0.5210	−0.4826	−1.0101	−1.8694	−2.9434	2.0831	0.1535	nLoS
P₃	L₁	1.62	0.9647	0.8424	0.7477	0.6882	0.6629	−0.4598	−1.0232	−1.8182	−2.8841	2.1109	0.1599	nLoS
P₃	R₁	1.65	0.9617	0.8279	0.7153	0.6775	0.6108	−0.4628	−0.9899	−1.9311	−2.8438	2.0392	0.1691	nLoS
RPR	L₁	1.74	0.9555	0.8632	0.7709	0.7080	0.6344	−0.4284	−0.9892	−1.8201	−2.8985	2.0561	0.1946	nLoS
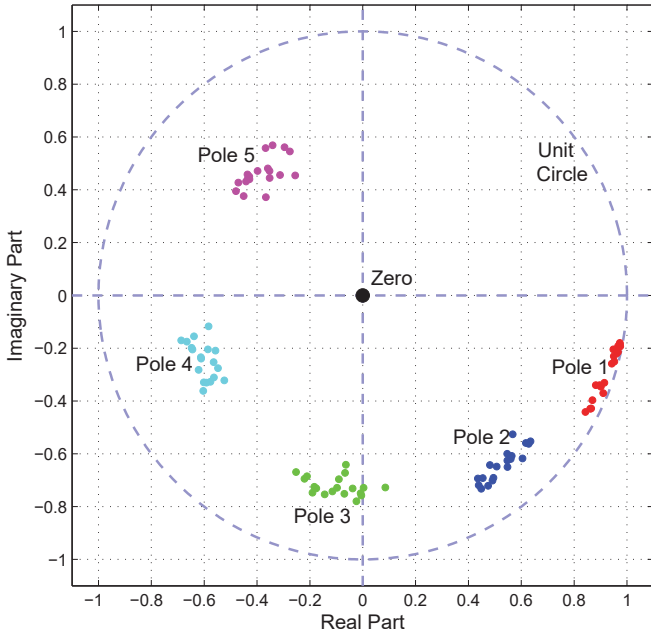
Fig. 7. Complex plane scatter plot of poles for all different experiments.

amplitudes ($|p_k|; k = 1, 2, \cdots, 5$) with the mean amplitude value of the cluster

$$< |p_k| > = \begin{cases} 0.9722 & ; k = 1 \\ 0.8346 & ; k = 2 \\ 0.7343 & ; k = 3 \\ 0.6573 & ; k = 4 \\ 0.6036 & ; k = 5 \end{cases} \quad (17)$$

It was suggested in [50], [55] that the pole angles are related to the clusters in the following manner

$$\tau_k = -\frac{\theta_k}{2\pi f_s}; \ k = 1, 2, \cdots, 5 \quad (18)$$

where τ_k and θ_k are the delay of the kth multipath cluster and angle of the kth pole respectively, while f_s is the frequency step size. During our analysis we found that all the pole angles are linearly dependent on the Tx-Rx gap and (18) overestimates the delays. Therefore we propose the following set of equations to model the pole angles

$$\begin{aligned} \angle p_1 &= -0.05 - 0.2365 \times d \\ \angle p_2 &= \angle p_1 - 0.5534 - 0.0112 \times d \\ \angle p_3 &= \angle p_2 - 0.7952 - 0.0321 \times d \\ \angle p_4 &= \angle p_3 - 1.0641 + 0.0193 \times d \\ \angle p_5 &= -\angle p_4 + 0.0878 - 0.5246 \times d \end{aligned} \quad (19)$$

In (19), we have modelled the angles in a successive manner, i.e. the angle of pole 2 depends on pole 1 and so on. The linear regression fitting was operated on the difference of the pole angles to avoid local measurement deviations.

V. SIMULATION AND MODEL VALIDATION

A. Simulation steps

Our proposed simulation model only involves three variables: the Tx-Rx separation (d), number of passengers (n_P), and the propagation condition (LoS/ nLoS). The step-by-step guide to estimate the in-vehicle channel transfer function is as follows:

I   Estimate long term variation, $|H(f)|_{\text{trend}}$

    (a)   Determine K: Find α_{f_R} from (7) and Table III. The parameter K is related to the path loss as $K = 10^{-\alpha_{f_R}/20}$.

    (b)   Determine m: Select m from (8) according to the propagation scenario (LoS/nLoS).

    (c)   Passenger effect: Modify K and m value according to the number of passengers following (9) and (10).

    (d)   Find trend from (2).

II   Estimate short term variation, $\tilde{H}(f)$

    (a)   Generate ξ: Find the input noise variance from (16) and generate a complex Gaussian random variable of length N_{VNA} with zero mean and variance σ_ξ^2.

    (b)   Estimate poles: Approximate the pole amplitudes following (17), and find the phase of each pole in a successive manner as demonstrated in (19).

    (c)   Filtering: With the poles, construct an all-pole IIR filter as mentioned in (12). Pass ξ through it to get $\tilde{H}(f)$ at output.

III   Estimate the CTF, $H(f) = \tilde{H}(f) \cdot |H(f)|_{\text{trend}}$

B. Frequency domain validation

The CTF, $H(f)$, is obtained by combining the long term frequency dependence with the simulated short term AR model based variations. The measured and simulated transfer functions for one particular Tx-Rx pair is shown in Fig. 8.
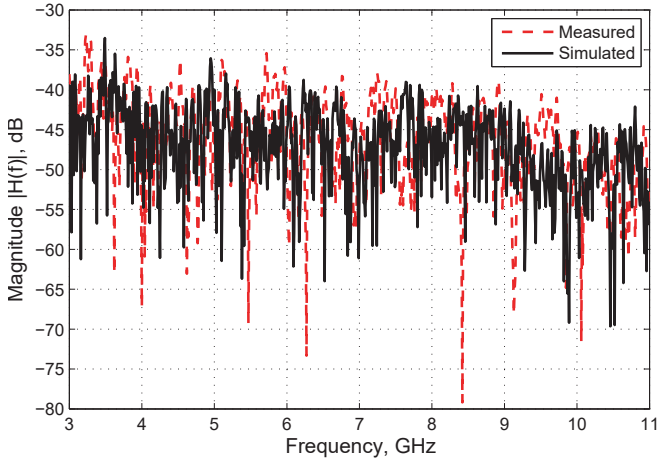
Fig. 8.   Measured and simulated CTFs. Tx position: D, Rx position: P_2, and $n_P = 2$ (two passengers on rear seat).

The frequency autocorrelation function (ACF), $R(\Delta f)$, may be found from the channel transfer function as [56]

$$R(\Delta f) = \int_{-\infty}^{\infty} H(f) H^*(f + \Delta f) \, df \qquad (20)$$

which provides a measure of the frequency selectivity. The range between DC or zero frequency, where normalized ACF attains its peak value of unity, and the frequency where ACF falls to 50% of or 3 dB lower than its peak value, is defined as the coherence bandwidth (BW), B_C. From Fig. 9, it can be seen that the measured and simulated transfer functions manifest almost similar B_C values.

A channel is considered *flat* in the coherence BW interval, i.e. if two different frequencies are separated by more than B_C, the channel exhibits uncorrelated fading at these two frequencies. There is a more direct method available for calculation of coherence BW [57], [58]. However, we computed B_C via the classical approach as the BW spans over only few samples for the current frequency step size (10 MHz), and there might be large approximation errors involved in the direct method.
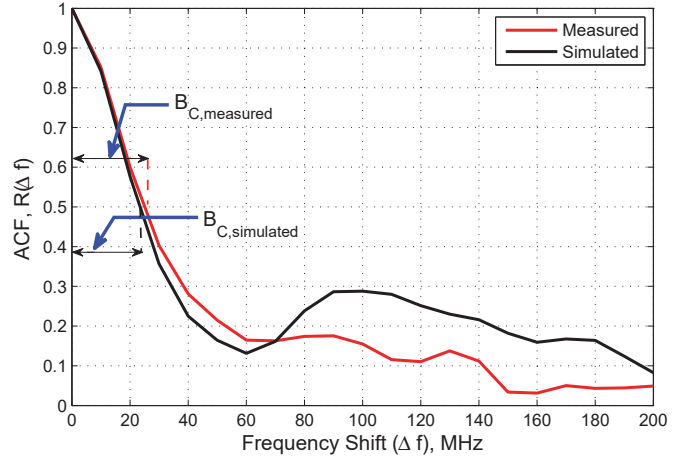
Fig. 9.   Comparison of frequency ACF for the CTFs shown in Fig. 8.

C. Time domain validation

The complex channel impulse response $h_{\text{VNA}}(t)$ extracted after IFFT operation and windowing is utilized to obtain the PDP, $\text{PDP}(t) = \mathcal{E}\{|h_{\text{VNA}}(t)|^2\}$. Fig. 10 shows the comparison of the measured PDP with the simulated PDP, and one can find that there is a close match. A matter of concern is, due to the random inputs, the difference of peaks between consecutive simulation runs can be as high as 10 dB. Fortunately, in most of the cases, the peak locations can still be detected correctly with the simulation. Another concern is the noisy rising edge of the simulated PDP before the first peak which can be suppressed with proper windowing [39], [59] during the IFFT post-processing.
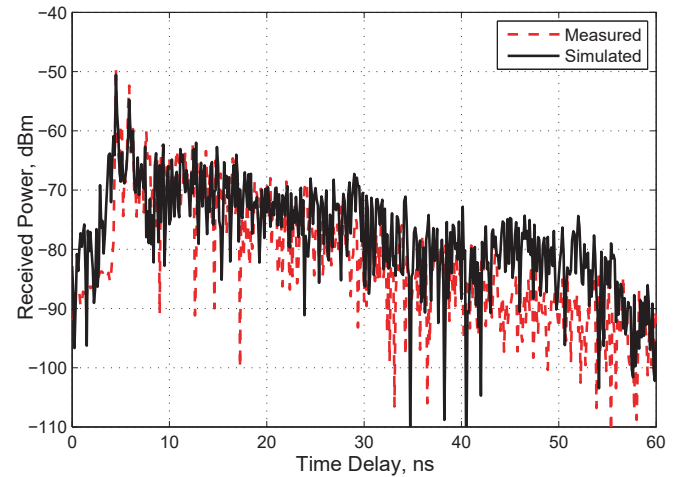
Fig. 10.   Measured and simulated PDPs. Tx position: D, Rx position: P_2, and $n_P = 2$ (two passengers on rear seat).

A quantitative comparison between the measured PDP and the simulated PDP can be performed by noting the similarity of the root mean square (RMS) delay spreads obtained for both the delay profiles. RMS delay spread is the second central

moment of the PDP

$$\tau_{\rm rms} = \sqrt{\int_0^{\tau_{\max}} (t-\bar{\tau})^2 \cdot {\rm P}_n(t)\,{\rm d}t} \qquad (21)$$

where $\tau_{\max}$ denotes the maximum excess delay, ${\rm P}_n(t) = |h_{\rm VNA}(t)|^2/\int_0^{\tau_{\max}} |h_{\rm VNA}(t)|^2 {\rm d}t$ is normalized magnitude square function, and $\bar{\tau} = \int_0^{\tau_{\max}} t \cdot {\rm P}_n(t){\rm d}t$ is the mean excess delay.

For calculating the RMS delays, the rising edge of the PDP is cut off and the time origin is shifted to the time index that corresponds to the peak. This time shifting helps in rendering the delays as excess delays relative to the peak or first arriving path which has a zero delay. Further, only those MPCs having a delay less than $\tau_{\max} = 60$ ns are considered. This step ensures that the truncated PDP does not hit the noise floor. According to the Agilent E5071C VNA data sheet, the noise floor is -120 dBm/Hz. Hence, for a 100Hz IF bandwidth, it is good enough to consider MPCs upto -100 dBm. Finally, the PDPs are normalized so that the peak occurs at 0 dB. The measured RMS delay values are between 5 to 10 ns, and are consistent with time domain measurements of intra-vehicle UWB links [60].
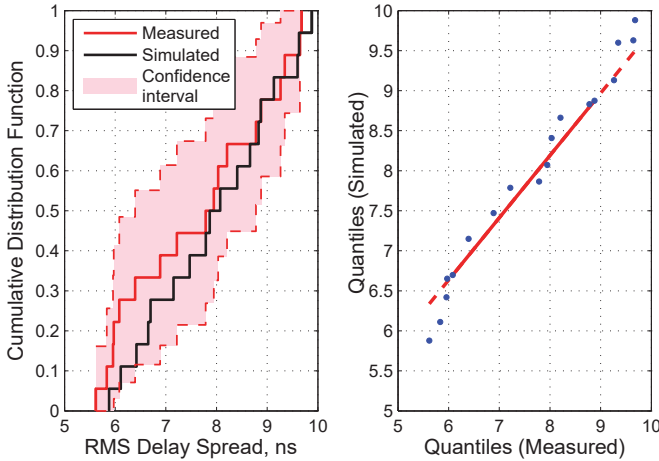
Fig. 11. Measured and simulated RMS delay spreads for empty car - comparison of empirical CDFs (left) and quantile-quantile plot (right).

The simulated PDP matches closely with the measured PDP as the percentage of error

$$\%\ {\rm error} = \frac{\tau_{\rm rms,simulated} - \tau_{\rm rms,measured}}{\tau_{\rm rms,measured}} \times 100 \qquad (22)$$

is typically 10%, with values ranging between 2% to 30%. The statistical similarity is validated in Fig. 11 which compares the empirical CDFs and it can be clearly seen that the CDF of simulated delay spread is contained within the 95% confidence interval bounds of the CDF of measured delay spread. The degree of similarity between the measured and simulated delay spreads are tested via a two sample Kolmogorov-Smirnov (K-S) test which showed a sufficiently high value, $p = 0.7088$. Linearity of the quantile-quantile plot in Fig. 11 also supports the claim.

The CDF comparison also reveals that probability of smaller delay spread values are more frequent in the measured data

compared to the simulated set. This is in line with our observation regarding percentage error which is mostly positive, i.e. the simulated PDP slightly overestimates $\tau_{\rm rms}$, especially for the LoS scenarios with small Tx-Rx separation where the delay spread is low. This is because the simulation model relies on averaging over the entire data set and the local variations for very small d values are not well represented.

D. Comparison with S-V model

Finally, in this sub-section, we show how different Saleh-Valenzuela (S-V) model parameters can be extracted from the proposed frequency-domain model. The S-V model is of considerable interest as the existing time-domain in-vehicle channel models [17]–[21] heavily rely on it. Further, it is also suggested in [18] and [19] to use the IEEE 802.15.3a and IEEE 802.15.4a models, respectively, for simulating in-vehicle UWB propagation. Both these IEEE standards recommend a time-domain model that is based on the basic S-V model.

According to the S-V model, the discrete impulse response of an UWB channel may be expressed as [13]

$$h_{\rm VNA}(t) = \sum_{n=1}^{N_c} \sum_{m=1}^{N_{r,n}} \beta_{m,n} \exp(j\theta_{m,n})\delta(t-T_n-\tau_{m,n}) \qquad (23)$$

where N_c is the number of clusters, $N_{r,n}$ is the number of rays in the nth cluster, and T_n is the arrival time of the nth cluster. The magnitude, phase, and additional delay of the mth ray within the nth cluster are given by $\beta_{m,n}$, $\theta_{m,n}$, and $\tau_{m,n}$, respectively. The inter- and intra-cluster exponential decay rates, namely Γ and γ, define the magnitude of individual rays according to

$$\beta_{m,n}^2 = \beta_{1,1}^2 \exp[-(T_n - T_1)/\Gamma] \exp(-\tau_{m,n}/\gamma) \qquad (24)$$

If we assume that both the arrival of clusters and rays within clusters follow independent Poisson processes, the inter-arrival times are exponentially distributed, i.e.

$$\Pr(T_n|T_{n-1}) = \Lambda \exp[-\Lambda(T_n - T_{n-1})] \qquad (25a)$$

$$\Pr(\tau_{m,n}|\tau_{m-1,n}) = \lambda \exp[-\lambda(\tau_{m,n} - \tau_{m-1,n})] \qquad (25b)$$

where $\Pr(\cdot)$ denotes probability. The parameters $1/\Lambda$ and $1/\lambda$ represent the average duration between two consecutive clusters and two consecutive rays within a cluster, respectively.

The first step for extracting the S-V parameters is detection of clusters which is achieved by grouping the MPCs in the discrete PDP. Unfortunately the method is ambiguous and the available algorithms (see [19] and references therein) yield results that are very different from each other. This occurs due to manual setting of various thresholds. Our aim, however, is not to resolve this ambiguity; rather we consider a simple algorithm [61] for cluster detection and show (see Fig. 12) that the algorithm provide similar cluster profiles for the measured and simulated data sets.

Fig. 12 also exhibits the extraction of inter- and intra-cluster exponential decay rates. In the dB scale, the exponential decays appear as linear decrement. The cluster decay rate is calculated through the formula, $\Gamma = -10 \times \log_{10}(e)/\Delta_{\rm PDP}$, where $\Delta_{\rm PDP}$ is the slope of the linear least squares fitting line
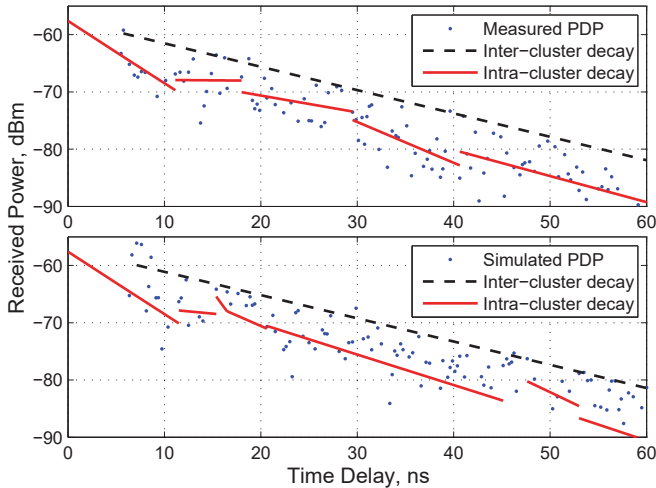
Fig. 12. Cluster identification and S-V model parameter estimation for a typical nLoS scenario. Tx position: RPR, Rx position: L_1, and $n_P = 0$.

passing through the maximum MPC of each cluster. The lines are indicated with black dashes. For deriving the ray decay rate (γ), such a linear fitting is applied to rays within each individual cluster, and are marked with red solid lines. The overall decay rate is computed by averaging the values over all identified clusters. In comparison, retrieving cluster arrival rate (Λ) and ray arrival rate (λ) are straightforward and involve only simple averaging of cluster duration and inter-MPC time, respectively.

TABLE V
COMPARISON OF AVERAGE S-V MODEL PARAMETERS FOR LoS SCENARIO

Parameter (ns)	Measured	Simulated	Liu [20]	CM 1 802.15.3a	CM 7 802.15.4a
Γ	10.74	11.15	7.20	7.1	13.47
γ	5.69	6.60	2.05	4.3	NA
$1/\Lambda$	8.27	8.87	3.80	42.92	14.10
$1/\lambda$	0.54	0.48	0.92	0.4	NA

In Table V we enlist all the four S-V parameter values averaged over the different LoS measurements performed in an empty car. The most important observation is that the measured values are in good agreement with the simulated values. The values obtained for a similar in-vehicle LoS scenario [20] cannot be directly compared due to the ambiguity in cluster identification. We also exclude values from [17], [21] as the authors conducted measurements in engine compartment and under the chasis instead of the passenger cabin. Parameter values for channel model 1 (CM 1) corresponds to indoor UWB propagation in the range 0-4 m as specified in IEEE standard 802.15.3a. On the other hand, CM 7 is specified in IEEE standard 802.15.4a for characterizing indoor industrial environment in the range 2-8 m.

VI. CONCLUSIONS

The key finding of the paper is, the transfer function of an intra-vehicle UWB channel can be modelled with an AR process after removing the frequency dependent trend. We

have developed a comprehensive simulation framework for estimating both long term and short term frequency transfer function variations. Simulated transfer functions exhibit close match with the measured values. The similarity of coherence BWs, PDPs, RMS delay spreads, and S-V model parameters further validates the model.

REFERENCES

[1] G. Karagiannis, O. Altintas, E. Ekici, G. Heijenk, B. Jarupan, K. Lin, and T. Weil, "Vehicular networking: A survey and tutorial on requirements, architectures, challenges, standards and solutions," *IEEE Commun. Surveys Tuts.*, vol. 13, no. 4, pp. 584–616, Nov. 2011.

[2] J. Rybicki, B. Scheuermann, M. Koegel, and M. Mauve, "PeerTIS: A peer-to-peer traffic information system," in *Proc. ACM VANET*, Sep. 2009, pp. 23–32.

[3] O. Altintas, F. Dressler, F. Hagenauer, M. Matsumoto, M. Sepulcre, and C. Sommer, "Making cars a main ICT resource in smart cities," in *Proc. IEEE INFOCOM*, Apr. 2015, pp. 582–587.

[4] L. Delgrossi and T. Zhang, *Vehicle Safety Communications: Protocols, Security, and Privacy*. New Jersey, USA: John Wiley & Sons, Nov. 2012.

[5] IEEE Computer Society, "IEEE Standard for Information Technology - Telecommunications and information exchange between systems - Local and metropolitan area networks - Specific Requirements, Part 11: Wireless LAN Medium Access Control (MAC) and Physical Layer (PHY) Specifications, Amendment 6: Wireless Access in Vehicular Environments," IEEE Standard 802.11p, Jul. 2010.

[6] P. Kukolev, A. Chandra, T. Mikulásek, A. Prokeš, T. Zemen, and C. Mecklenbräuker, "In-vehicle channel sounding in the 5.8 GHz band," *EURASIP J. Wireless Commun. Netw.*, vol. 2015, no. 57, pp. 1–9, Mar. 2015.

[7] L. Zhu, F. R. Yu, B. Ning, and T. Tang, "Cross-layer design for video transmissions in metro passenger information systems," *IEEE Trans. Veh. Technol.*, vol. 60, no. 3, pp. 1171–1181, Mar. 2011.

[8] A. Chandra, J. Blumenstein, T. Mikulásek, J. Vychodil, R. Maršálek, A. Prokeš, T. Zemen, and C. Mecklenbräuker, "Serial subtractive deconvolution algorithms for time-domain ultra wide band in-vehicle channel sounding," *IET Intell. Transp. Syst.*, vol. 9, no. 9, pp. 870–880, Nov. 2015.

[9] S. Abdelhamid, H. Hassanein, and G. Takahara, "Vehicle as a resource (VaaR)," *IEEE Netw.*, vol. 29, no. 1, pp. 12–17, Jan. 2015.

[10] E. Costa-Montenegro, F. Quiñoy-García, and F. González-Castaño, F. J. Gil-Castiñeira, "Vehicular entertainment systems: Mobile application enhancement in networked infrastructures," *IEEE Veh. Technol. Mag.*, vol. 7, no. 3, pp. 73–79, Sep. 2012.

[11] P. Galdia, C. Koch, and A. Georgiadis, "Localization of passengers inside intelligent vehicles by the use of ultra wideband radars," in *Proc. SIP*, Dec. 2011, pp. 92–102.

[12] N. Nguyen, S. Dhakal, and J. Womack, "Localization of handheld devices inside vehicles using audio masking," in *Proc. ICCVE*, Dec. 2013, pp. 38–42.

[13] P. Pagani, F. T. Talom, P. Pajusco, and B. Uguen, *Ultra Wide Band Radio Propagation Channel*. Hoboken, NJ, USA: John Wiley & Sons, Mar. 2013.

[14] A. F. Molisch, R. F. Jeffrey, and P. Marcus, "Channel models for ultrawideband personal area networks," *IEEE Wireless Commun.*, vol. 10, no. 6, pp. 14–21, Dec. 2003.

[15] X. Wang, E. Anderson, P. Steenkiste, and F. Bai, "Improving the accuracy of environment-specific channel modeling," *IEEE Trans. Mobile Comput.*, pp. 1–15, 2016, In press. DOI: 10.1109/TMC.2015.2424426.

[16] I. G. Zuazola, J. M. Elmirghani, and J. C. Batchelor, "High-speed ultra-wide band in-car wireless channel measurements," *IET Commun.*, vol. 3, no. 7, pp. 1115–1123, Jul. 2009.

[17] W. Niu, J. Li, and T. Talty, "Ultra-wideband channel modeling for intravehicle environment," *EURASIP J. Wireless Commun. Netw.*, vol. 2009, no. 806209, pp. 1–12, Feb. 2009.

[18] P. C. Richardson, W. Xiang, and W. Stark, "Modeling of ultra-wideband channels within vehicles," *IEEE J. Sel. Areas Commun.*, vol. 24, no. 4, pp. 906–912, Apr. 2006.

[19] B. Li, C. Zhao, H. Zhang, X. Sun, and Z. Zhou, "Characterization on clustered propagations of UWB sensors in vehicle cabin: measurement, modeling and evaluation," *IEEE Sensors J.*, vol. 13, no. 4, pp. 1288–1300, Apr. 2013.

[20] L. Liu, Y. Wang, and Y. Zhang, "Ultrawideband channel measurement and modeling for the future intra-vehicle communications," *Microw. Opt. Technol. Lett.*, vol. 54, no. 2, pp. 322–326, Feb. 2012.

[21] W. Niu, J. Li, and T. Talty, "Intra-vehicle UWB channel measurements and statistical analysis," in *Proc. IEEE GLOBECOM*, Nov. 2008, pp. 1–5.

[22] A. A. Saleh and R. Valenzuela, "A statistical model for indoor multipath propagation," *IEEE J. Sel. Areas Commun.*, vol. 5, no. 2, pp. 128–137, Feb. 1987.

[23] O. Fernandez, L. Valle, M. Domingo, and R. P. Torres, "Flexible rays," *IEEE Veh. Technol. Mag.*, vol. 3, no. 1, pp. 18–27, Mar. 2008.

[24] T. Pedersen, G. Steinböck, and B. H. Fleury, "Modeling of reverberant radio channels using propagation graphs," *IEEE Trans. Antennas Propag.*, vol. 60, no. 12, pp. 5978–5988, Dec. 2012.

[25] J. Chuang, N. Xin, H. Huang, S. Chiu, and D. G. Michelson, "UWB radiowave propagation within the passenger cabin of a Boeing 737-200 aircraft," in *Proc. IEEE VTC*, Apr. 2007, pp. 496–500.

[26] M. Schack, J. Jemai, R. Piesiewicz, R. Geise, I. Schmidt, and T. Kürner, "Measurements and analysis of an in-car UWB channel," in *Proc. IEEE VTC*, May 2008, pp. 459–463.

[27] E. R. Bastidas-Puga, F. Ramírez-Mireles, and D. Muñoz-Rodríguez, "On fading margin in ultrawideband communications over multipath channels," *IEEE Trans. Broadcast.*, vol. 51, no. 3, pp. 366–370, Sep. 2005.

[28] W. Turin, *Performance Analysis and Modeling of Digital Transmission Systems*. New York, USA: Springer Science & Business Media, 2012.

[29] T. Taniguchi, A. Maeda, and T. Kobayashi, "Development of an omnidirectional and low-VSWR ultra wideband antenna," *Int. J. Wireless Opt. Commun.*, vol. 3, no. 2, pp. 145–157, Aug. 2006.

[30] J. S. McLean, R. Sutton, A. Medina, H. Foltz, and J. Li, "The experimental characterization of uwb antennas via frequency-domain measurements," *IEEE Antennas Propag. Mag.*, vol. 49, no. 6, pp. 192–202, Dec. 2007.

[31] J. Blumenstein, A. Prokes, T. Mikulasek, R. Marsalek, T. Zemen, and C. Mecklenbrauker, "Measurements of ultra wide band in-vehicle channel - statistical description and TOA positioning feasibility study," *EURASIP J. Wireless Commun. Netw.*, vol. 2015, no. 104, pp. 1–9, Apr. 2015.

[32] A. Prokeš, T. Mikulásek, J. Blumenstein, C. Mecklenbräuker, and T. Zemen, "Intra-vehicle ranging in ultra-wide and millimeter wave bands," in *Proc. IEEE APWiMob*, Aug. 2015, pp. 246–250.

[33] A. F. Molisch, K. Balakrishnan, D. Cassioli, C. C. Chong, S. Emami, A. Fort, J. Karedal, J. Kunisch, H. Schantz, and K. Siwiak, "A comprehensive model for ultrawideband propagation channels," in *Proc. IEEE GLOBECOM*, vol. 6, Nov. 2005, pp. 3648–3653.

[34] R. C. Qiu and I. T. Lu, "Wideband wireless multipath channel modeling with path frequency dependence," in *Proc. IEEE ICC*, vol. 1, Jun. 1996, pp. 277–281.

[35] ——, "Multipath resolving with frequency dependence for broadband wireless channel modeling," *IEEE Trans. Veh. Technol.*, vol. 48, no. 1, pp. 273–285, Jan. 1999.

[36] W. Q. Malik, D. J. Edwards, and C. J. Stevens, "Frequency-dependent pathloss in the ultrawideband indoor channel," in *Proc. IEEE ICC*, vol. 12, Jun. 2006, pp. 5546–5551.

[37] J. Kunisch and J. Pamp, "Measurement results and modeling aspects for the UWB radio channel," in *Proc. IEEE UWBST*, vol. 1, May 2002, pp. 19–23.

[38] A. Álvarez, G. Valera, M. Lobeira, R. P. Torres, and J. L. C. García, "New channel impulse response model for UWB indoor system simulations," in *Proc. IEEE VTC*, vol. 1, Apr. 2003, pp. 1–5.

[39] A. Chandra, P. Kukolev, T. Mikulásek, and A. Prokeš, "Autoregressive model of channel transfer function for UWB link inside a passenger car," in *Proc. CSCC*, Jul. 2015, pp. 238–241.

[40] A. F. Molisch, K. Balakrishnan, D. Cassioli, C. C. Chong, S. Emami, A. Fort, J. Karedal, J. Kunisch, H. Schantz, U. Schuster, and K. Siwiak, "IEEE 802.15.4a channel model - final report," Technical Report Document IEEE 802.15-04-0662-02-004a, 2005.

[41] S. S. Ghassemzadeh, R. Jana, C. W. Rice, W. Turin, and V. Tarokh, "Measurement and modeling of an ultra-wide bandwidth indoor channel," *IEEE Trans. Commun.*, vol. 52, no. 10, pp. 1786–1796, Oct. 2004.

[42] N. Alsindi, B. Alavi, and K. Pahlavan, "Empirical pathloss model for indoor geolocation using UWB measurements," *Electron. Lett.*, vol. 43, no. 7, pp. 370–372, Mar. 2007.

[43] C. C. Chong, Y. E. Kim, S. K. Yong, and S. S. Lee, "Statistical characterization of the UWB propagation channel in indoor residential environment," *Wireless Commun. Mobile Comput.*, vol. 5, no. 5, pp. 503–512, Aug. 2005.

[44] T. Kobayashi, "Measurements and characterization of ultra wideband propagation channels in a passenger-car compartment," in *Proc. IEEE ISSSTA*, Aug. 2006, pp. 228–232.

[45] C. U. Bas and S. C. Ergen, "Ultra-wideband channel model for intra-vehicular wireless sensor networks beneath the chassis: from statistical model to simulations," *IEEE Trans. Veh. Technol.*, vol. 62, no. 1, pp. 14–25, Jan. 2013.

[46] Y. H. Kim and S. C. Kim, "The effect of human bodies on path loss model in an indoor LOS environment," in *Proc. ICWMC*, Jul. 2013, pp. 152–156.

[47] M. Pecoraro, J. Venkataraman, G. Tsouri, and S. Dianat, "Characterization of the effects of the human head on communication with implanted antennas," in *Proc. IEEE APSURSI*, Jul. 2010, pp. 1–4.

[48] W. A. Woodward, H. L. Gray, and A. C. Elliott, *Applied Time Series Analysis*. Boca Raton, FL, USA: CRC Press, 2012.

[49] S. J. Howard and K. Pahlavan, "Autoregressive modeling of wide-band indoor radio propagation," *IEEE Trans. Commun.*, vol. 40, no. 9, pp. 1540–1552, Sep. 1992.

[50] A. Chehri and P. Fortier, "Frequency domain analysis of UWB channel propagation in underground mines," in *Proc. IEEE VTC*, Sep. 2006, pp. 1–5.

[51] F. Castanié, *Spectral Analysis: Parametric and Non-parametric Digital Methods*. NJ, USA: John Wiley & Sons, 2013.

[52] H. Akaike, "Use of statistical models for time series analysis," in *Proc. IEEE ICASSP*, vol. 11, Apr. 1986, pp. 3147–3155.

[53] B. Aksasse and L. Radouane, "Two-dimensional autoregressive (2-D AR) model order estimation," *IEEE Trans. Signal Process.*, vol. 47, no. 7, pp. 2072–2077, Jul. 1999.

[54] A. Taparugssanagorn, L. Hentilä, and S. Karhu, "Time-varying autoregressive process for ultra-wideband indoor channel model," in *Proc. IST Mobile Wireless Commun. Summit*, Jun. 2005, pp. 1–5.

[55] G. Morrison, M. Fattouche, and H. Zaghloul, "Statistical analysis and autoregressive modeling of the indoor radio propagation channel," in *Proc. IEEE ICUPC*, Sep. 1992, pp. 97–101.

[56] I. Cuiñas and M. G. Sánchez, "Measuring, modeling, and characterizing of indoor radio channel at 5.8 GHz," *IEEE Trans. Veh. Technol.*, vol. 50, no. 2, pp. 526–535, Mar. 2001.

[57] D. Scammell, A. Hammoudeh, and M. G. Sánchez, "Estimating channel performance for time invariant channels," *Electron. Lett.*, vol. 40, no. 12, pp. 746–747, Jun. 2004.

[58] M. Ghaddar, L. Talbi, and G. Y. Delisle, "Coherence bandwidth measurement in indoor broadband propagation channel at unlicensed 60 GHz band," *Electron. Lett.*, vol. 48, no. 13, pp. 795–797, Jun. 2012.

[59] A. Chandra, P. Kukolev, T. Mikulásek, and A. Prokeš, "Frequency-domain in-vehicle channel modelling in mmW band," in *Proc. IEEE RTSI*, Sep. 2015, pp. 106–110.

[60] A. Chandra, J. Blumenstein, T. Mikulásek, J. Vychodil, M. Pospísil, R. Maršálek, A. Prokeš, T. Zemen, and C. Mecklenbräuker, "CLEAN algorithms for intra-vehicular time-domain UWB channel sounding," in *Proc. PECCS*, Feb. 2015, pp. 224–229.

[61] M. Corrigan, A. Walton, W. Niu, J. Li, and T. Talty, "Automatic UWB clusters identification," in *Proc. IEEE RWS*, Jan. 2009, pp. 376–379.

Measurements of ultra wide band in-vehicle channel-statistical description and TOA positioning feasibility study

Jiri Blumenstein, Ales Prokes, Tomas Mikulasek, Roman Marsalek, Thomas Zemen, Christoph Mecklenbräuker

IF=2.407

RESEARCH   **Open Access**

Measurements of ultra wide band in-vehicle channel - statistical description and TOA positioning feasibility study

Jiri Blumenstein[1*], Ales Prokes[1], Tomas Mikulasek[1], Roman Marsalek[1], Thomas Zemen[2] and Christoph Mecklenbräuker[1,3]

Abstract

This paper reports on a real-world wireless channel measurement campaign for in-vehicle scenarios in the UWB frequency range of 3 to 11 GHz. The effects of antenna placement in the vehicle's passenger compartment as well as the effects due to the presence of passengers are studied. The measurements have been carried out in the frequency domain, and the corresponding channel impulse responses (CIRs) have been estimated by inverse Fourier transform. The influence of a specific band group selection within the whole UWB range is also given. Statistical analysis of the measured channel transfer functions gives a description of the wireless channel statistics in the form of a generalized extreme value process. The corresponding parameter sets are estimated and documented for all permutations of antenna placement and occupancy patterns inside the vehicle's passenger compartment. Further, we have carried out a feasibility study of an in-vehicle UWB-based localization system based on the TOA. The positioning performance is evaluated in terms of average error and standard deviation.

Keywords: UWB; In-vehicle environment; Channel model; Positioning; TOA

1 Introduction

The onboard electrical power distribution, communication, and networking functionalities are realized by cable bundles in today's vehicles. We observe a trend towards increasing numbers of sensors, actuators, control units, and infotainment systems in cars and trucks. As a direct result, the weight of the wiring in all types of vehicles increases. Moreover, their flexible installation and reliability represent a challenging and costly task [1]. The weight of the wiring becomes even more serious when the vehicles are powered fully electrically.

In [2,3], the authors conclude that ultra wide band-with (UWB) technology with its favorable radio environment characteristics for indoor areas such as low transmit power and robustness against multipath fading could be extrapolated even for the vehicular passenger compartment. Naturally, attempts to replace cable bundle start

up with in-vehicle radio channel measurements were performed by authors in [4-9] and by channel modeling in [3,10], and a clustering approach for intra-bus channel modeling is studied in [11,12]. Attempts to build a prototype of an UWB-based wireless sensor network within a vehicle, both in the passenger and the engine compartments, are published in [13,14]. In [15], the topic of wireless in-vehicle communication links based on LTE is discussed while reckoning with specific in-vehicle impulse noise. In [16], the UWB channel inside a vehicle is studied from a spatial stationarity point of view. The necessity of detailed knowledge of the channel characteristics is of highest importance for the proper physical layer design of any wireless communication system.

Together with this motivation to substitute at least part of the vehicle's cable bundles by wireless links, a wireless localization service within the vehicle is desirable. Future applications of such a localization service include remote keyless entry and ignition systems, advanced child passenger safety, and beamsteering for in-vehicle high-speed Internet access.

*Correspondence: blumenstein@feec.vutbr.cz
[1] Department of Radio Electronics, Brno University of Technology, Technicka 12, 612 00, Brno, Czech Republic
Full list of author information is available at the end of the article

Blumenstein *et al. EURASIP Journal on Wireless Communications and Networking* (2015) 2015:104

Page 2 of 10

In [14,17], a localization service utilizing UWB is studied and it is concluded that in general, thanks to the high time resolution of UWB impulses, the time of arrival (TOA) technique is capable of providing sufficient spatial resolution for a variety of applications. Although the TOA works reliably in environments with LOS, it can be used with some restriction also in NLOS scenarios. In the multipath environment, the important component for ranging based on the TOA technique is the direct ray, which propagates from the transmitter towards the receiver. When the beam penetrates some obstacles whose attenuation does not avoid the beam detection, the TOA technique is applicable. Note that, for example, in the US, the frequency range of 1.99 to 10.6 GHz is deregulated for communications and wall-penetrating radars, enabling looking into or through non-metallic materials [14,18]. Thus, the presumption is that even the harsh in-vehicle ambiance with OLOS propagation may provide sufficient positioning accuracy.

In [4,6,7,19], the path-loss, seat material, and occupancy influences are presented for the frequency range of 3 to 8 GHz. Since the positioning service deployment is not seen as the aim of [4,6,7,19], the placement of transmit antennas is inappropriate from that point of view. Thus, resulting parameters could differ from parameters obtained by measurement campaigns which take the positioning into account in the first place.

1.1 Contribution of the paper
While taking into account the influence of the occupancy, antenna placement, and the influence of a specific frequency band group selection, in this paper, we address the following:

- Intra-vehicle channel measurement and statistical evaluation via GEV. This allows a reproducibility of the measured results for 90 selected wireless links within a passenger car compartment.
- Statistical analysis and the in-vehicle positioning in the UWB range of 3 to 11 GHz. The aim of the article is to give a general overview of the achievable accuracy of ranging regardless of LOS and NLOS scenarios.

The paper is organized as follows. In Section 2, we provide an overview of our measurement site including a hardware description. In Section 3, we present our channel measurement tools including our conical monopole antenna design [20] and we define the sought channel parameters. In Section 4, the feasibility of the positioning service deployment within a vehicle compartment is assessed, while the conclusion in Section 5 sums up the paper.

2 Measurement setup
2.1 Measurement bandwidth and dynamic range
The scheme of the measurement setup is shown in Figure 1. The complex CIRs (below introduced by (1)) corresponds to the s_{41}, s_{42}, and s_{43} scattering parameters which are measured in the frequency domain for two different frequency bands, 3 to 11 GHz (entire UWB band with a bandwidth of $B = 8$ GHz) and 3.3168 to 4.752 GHz (first band group with a bandwidth of $B = 1.58$ GHz), utilizing a four-port vector network analyzer Agilent Technologies E5071C (VNA; Agilent Technologies Inc., Santa Clara, CA, USA) (Figure 2). The spatial placement of the receiving (RX) and transmitting (TX) antennas inside the vehicle is depicted in Figure 3.

The dynamic range of the measurement setup is higher than 90 dB ($P_{\text{outVNA}} = 5$ dBm, IF bandwidth = 100 Hz). The chosen frequency step of 10 MHz results in 801 frequency points in the case of the entire UWB band and 159 frequency points in the case of the first band group.

In order to avoid a degradation of the measured phase accuracy due to movements of the RX antenna, phase-stable coaxial cables were used and included in the calibration process. The measurement is carried out in the Skoda Octavia 1.8 TSI car.

2.2 Antenna placement
As depicted in Figure 3, the RX antenna is placed at various locations inside the car compartment (on all seats and in the boot) and the TX antennas are placed on the left and right sides of the dashboard, top corners of the windshield, and at the rear part of the ceiling.

The channel measurements are carried out for both LOS and NLOS scenarios. NLOS is caused by the backrest of the seats, the dashboard, and/or persons sitting inside the vehicle.

Figure 1 Measurement setup containing the vector network analyzer Agilent Technologies E5071C and the car Skoda Octavia 1.8 TSI.

Blumenstein *et al. EURASIP Journal on Wireless Communications and Networking* (2015) 2015:104

Page 3 of 10
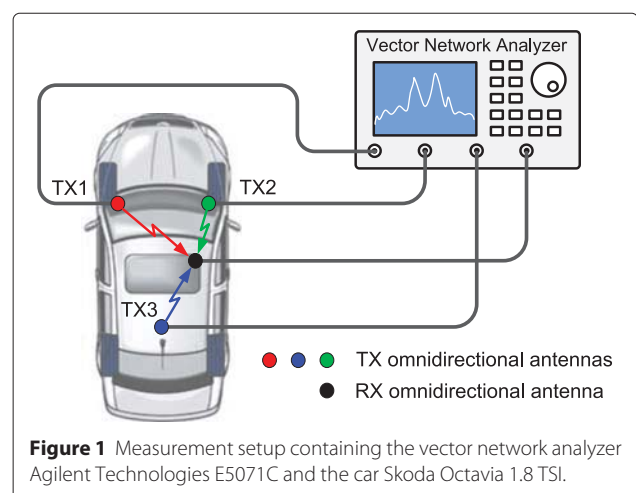
Figure 2 Images of the conical monopole antenna, measurement position, and four-port VNA. [left] Detail of the conical monopole antenna mounted on the front windshield. [middle] One measurement position inside the vehicle. [right] Four-port VNA connected with antennas inside the measured vehicle.

Since the radiation pattern of the conical monopole antenna [20] is very close to the omnidirectional radiation pattern, we were able to capture a maximal number of multipath components (reflected waves).

In Figure 4, the conical monopole has an omnidirectional H-plane radiation pattern which is invariant in the frequency band of interest. Due to a variable gain in the lower half E-plane radiation pattern (elevation angle from 90° to −90°), the antennas were placed in the car compartment so that the upper half E-plane radiation pattern (almost constant) was used. It means that when the antenna was placed at the cabin ceiling, it was situated bottom up. Thus, the LOS and NLOS are minimally affected by the radiation pattern; however, with the reflected waves arriving from the TX antenna or incident on the RX antenna, the lower elevation angle might be affected by the non-ideal radiation pattern of the antennas.

3 Channel parameters

The CIR describes the wireless channel. We utilize an inverse discrete Fourier transform of the windowed scattering parameter series, expressed as:

$$h^\alpha(n) = \sum_{k=0}^{N-1} w(k) s_\zeta^\alpha(k) e^{jkn2\pi/N}, \tag{1}$$

where $s_\zeta^\alpha(k)$ corresponds to the kth measured scattering parameter (as described in Section 2) and $w(k)$ represents the Blackman window. Parameter α denotes the spatial positions of the transmit and the receive antenna in the measured vehicle and $\zeta \in \{41, 42, 43\}$. For practicality in the following statistical processing, we arbitrarily merge indices α and ζ into one measurement number $\alpha \in \{1, \ldots, 90\}$. Hence, in the following, it is not possible to assign the specific measured data to the actual spatial positions.
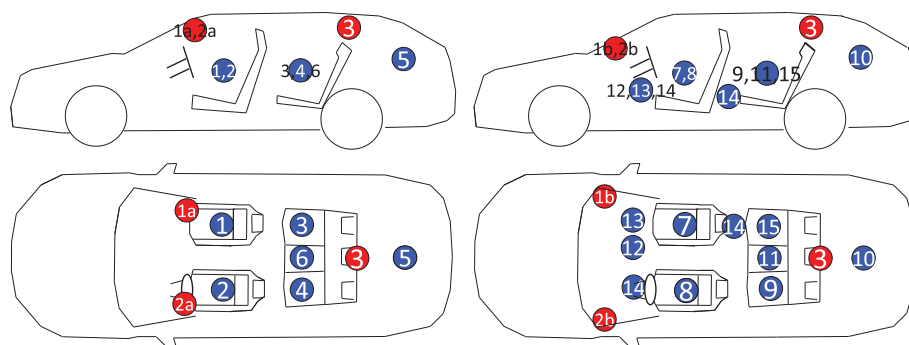
Figure 3 The positions of transmitting (red) and receiving (blue) antennas. We employ two possible receive antenna placement patterns. As seen on the left part, the antennas 1a and 2a occupy the left and right top corners of the windshield, while on the right part, the antennas 1b and 2b are positioned in the lower corners. Please note that all measurements have been measured for various passenger layouts. We have considered (1) empty vehicle and (2) driver and two to three passengers.

Blumenstein *et al. EURASIP Journal on Wireless Communications and Networking* (2015) 2015:104

Page 4 of 10
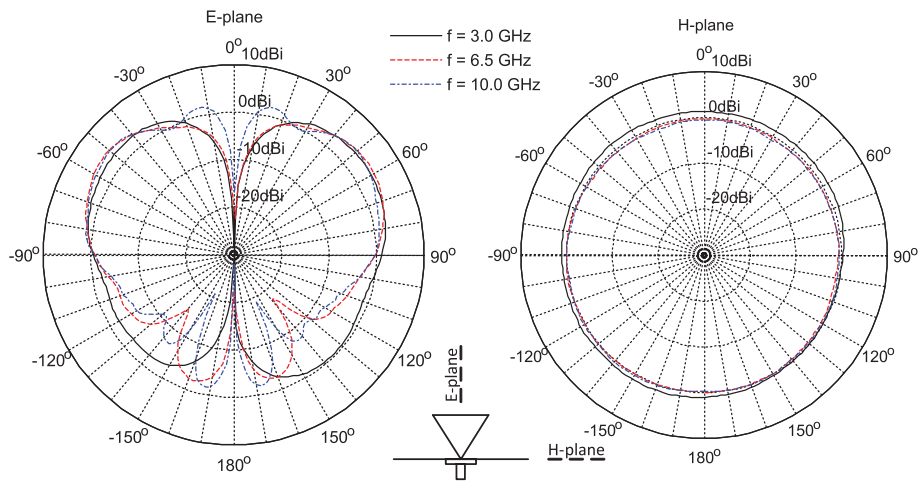
Figure 4 Measured gain pattern of the conical monopole antenna [20].

The number of measured frequency points $N = 801$ for the entire UWB or $N = 159$ for the first band group. Since the in-vehicle channel is assumed to be time invariant, we performed one repetition of the scattering parameter measurement.

The relationship between discrete time delay n and continuous time delay τ is given by:

$$\tau_n = n\frac{1}{B}, \tag{2}$$

where $1/B$ stands for the time resolution (see Equation 7).

For a statistical characterization of the UWB channel, we use the MDP which is defined as the magnitude of complex CIR:

$$A(\tau) = |h(\tau)|. \tag{3}$$

3.1 Statistical description of the received signal
3.1.1 Independent identically distributed (IID) phase
In this chapter, the phase statistics of the measured CIRs are presented. As visible in Figure 5 [right], according to the ecdf evaluated for each measured CIR, the phase $\Phi^\alpha(\tau)$ is uniformly distributed.

Moreover, utilizing the Pearson correlation coefficient $\rho_{\alpha,\beta}$, we evaluate the mutual dependence between phases for all measured positions denoted as α and β. The Pearson correlation coefficient is given as:

$$\rho_{\alpha,\beta} = \frac{\mathrm{E}\left[\left(\Phi^\alpha(\tau) - \xi^\alpha\right)\left(\Phi^\beta(\tau) - \xi^\beta\right)\right]}{\wp^\alpha \wp^\beta}, \tag{4}$$

where $\wp^\alpha$ denotes the standard deviation and ξ^α the mean of $\Phi^\alpha(\tau)$. The evaluation of the Pearson correlation coefficient is visible in Figure 5 [left] showing uncorrelated behavior of $\Phi^\alpha(\tau)$. The operator $\mathrm{E}[\cdot]$ denotes the expected value.
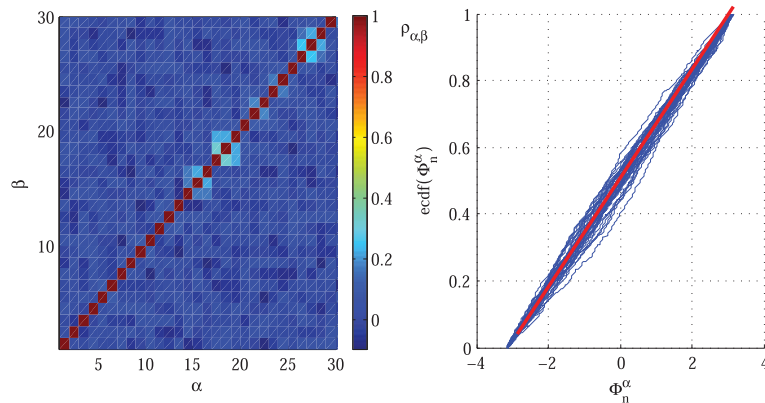
Figure 5 Pearson correlation coefficient and ecdf curves. [left] The Pearson correlation coefficient $\rho_{\alpha,\beta}$ evaluation of the measured $\Phi^\alpha(\tau)$. [right] The ecdf curves of Φ_n^α. The closer the blue ecdf curve to the red line, the closer the probability distribution of $\Phi^\alpha(\tau)$ to the uniform distribution.

Blumenstein *et al. EURASIP Journal on Wireless Communications and Networking* (2015) 2015:104

Page 5 of 10

According to the results presented in Figure 5, we conclude that $\Phi^{\alpha}(\tau)$ is iid uniformly distributed with respect to the measurement number α.

3.1.2 Statistics of the received signal magnitudes and GEV

Utilizing MLEs [21], we have found a statistical model of received signal magnitudes. As seen in Figures 6 and 7, the received signal magnitudes can be approximated using the GEV distribution [22] with the PDF given by:

$$f(x \mid 0, \mu, \sigma) = \frac{1}{\sigma}\exp\{-z - \exp(-z)\}, \text{ where } z = \frac{x - \mu}{\sigma},$$

(5)

with μ being the location parameter and σ the distribution scale parameter. Equation 5 represents the GEV type I distribution, also known as log-Weibull distribution, where the shape parameter defined in the regular GEV is set to zero. This approach is justified in Section 3.1.3.

In order to capture the statistical nature of the environment, we have performed 90 measurements permuting both the TX and RX antenna placements as well as the in-car seat occupancy. In Figure 6, we can see the CDF curves for all permutations of the antenna placement and occupancy, while each curve is fitted by a GEV type I random process obtained by the MLE fitting.

3.1.3 GEV parameters as a random process

According to the observations of resulting GEV parameters, we approximate the corresponding μ, k, and σ parameters with the statistical model obtained by MLE. Figures 8, 9, and 10 compare the CDFs of the measured μ, k, and σ parameters with random processes of corresponding distributions.
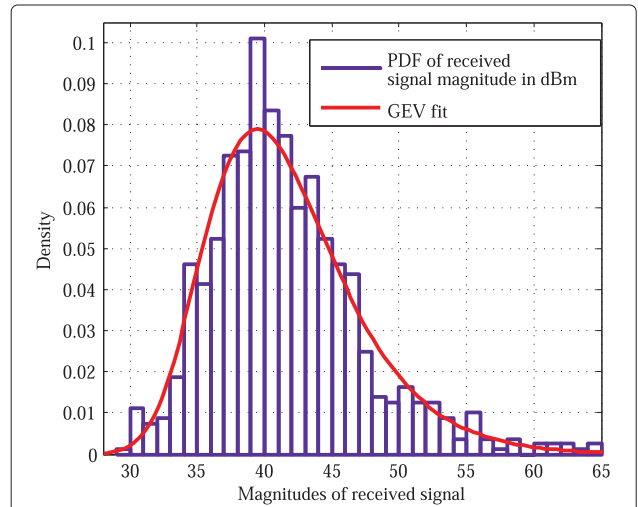
Figure 7 PDF of the received signal magnitudes in dBm for one measurement setup. The measured PDF is fitted with the GEV type I procedure.

The location parameter μ follows the lognormal distribution given as:

$$f(x \mid \eta, \nu) = \frac{1}{x\eta\sqrt{2\pi}}\exp\left(\frac{-(\ln x - \nu)^2}{2\eta^2}\right),$$

(6)

where ν is the mean and η represents the standard deviation. The extracted shape parameter k is of significantly low values; therefore, our choice of the GEV type I (also known as log-Weibull) characterized by $k = 0$ is appropriate (see Equation 5). The scale parameter σ is normally distributed.
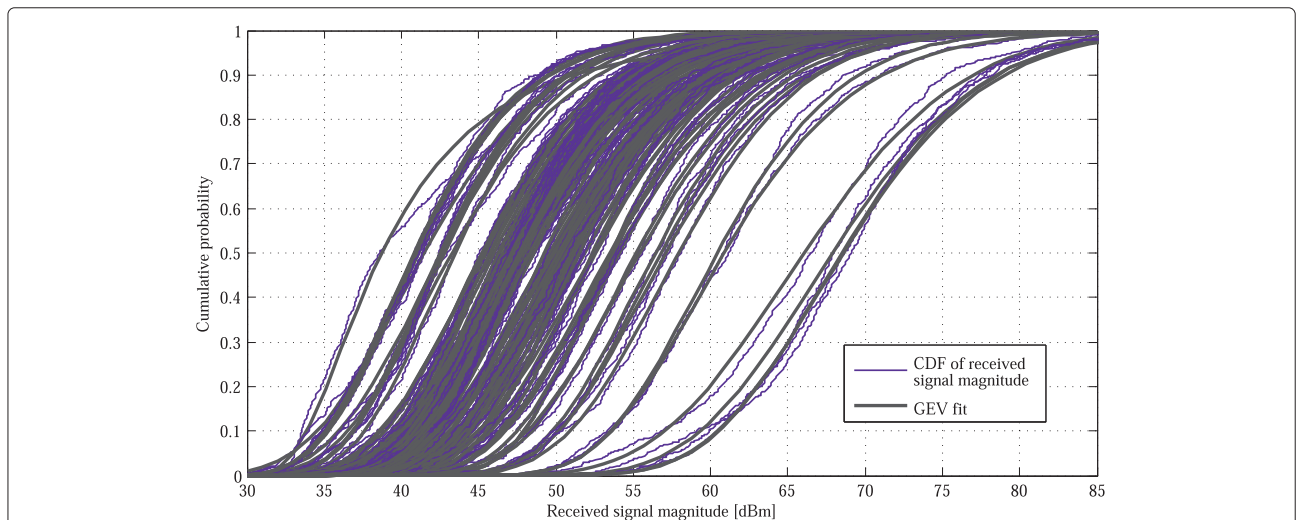
Figure 6 The CDF of received signal magnitude in dBm for all permutations of antenna placement and occupancy. Measured curves are fitted with the GEV type I procedure.

Blumenstein *et al. EURASIP Journal on Wireless Communications and Networking* (2015) 2015:104

Page 6 of 10

Figure 8 The CDF plot of location parameter μ fitted with lognormal distribution (with 95% confidence interval).

Figure 10 The CDF plot of scale parameter σ fitted with a normal distribution (with 95% confidence interval).
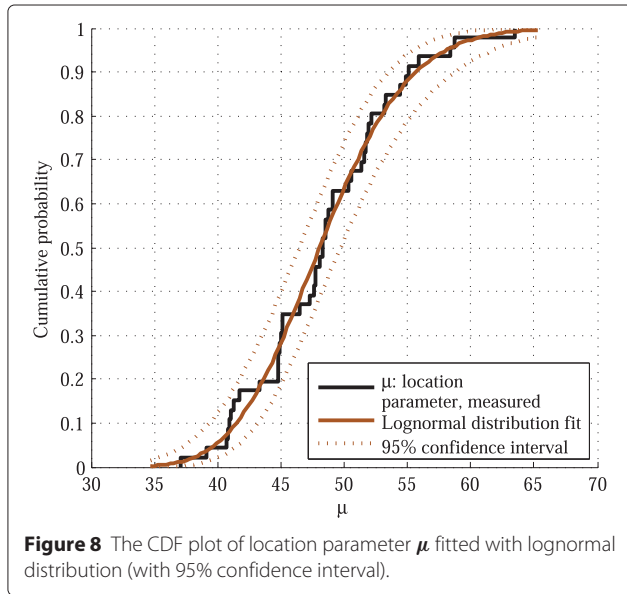
A summarized overview, including the specific values of μ and η, is given in Table 1. Thanks to a high number of performed measurements, the tabulated values represent typical data for an in-vehicle channel which also applies to vehicles of similar size, seat configurations, and materials utilized for its manufacture.

A correlation between the derived parameters μ and η ($k = 0$) exhibits a very weak positive correlation value of 0.35 with a p value below 6×10^{-4}. Thus, to recreate the received signal magnitudes, one can arbitrarily choose the parameters μ and η according to Table 1.

Figure 9 The CDF plot of shape parameter k fitted with a logistic distribution (with 95% confidence interval). Since the values of the k parameter are very small, in the following we set $k = 0$; thus, the GEV becomes a GEV type I (or log-Weibull) distribution.
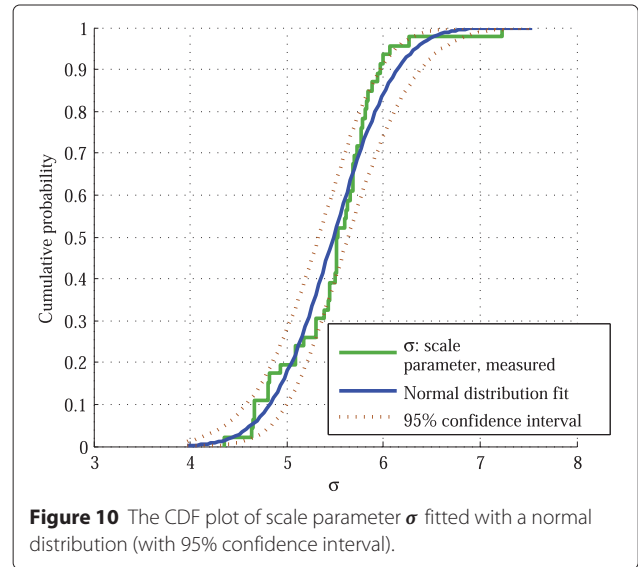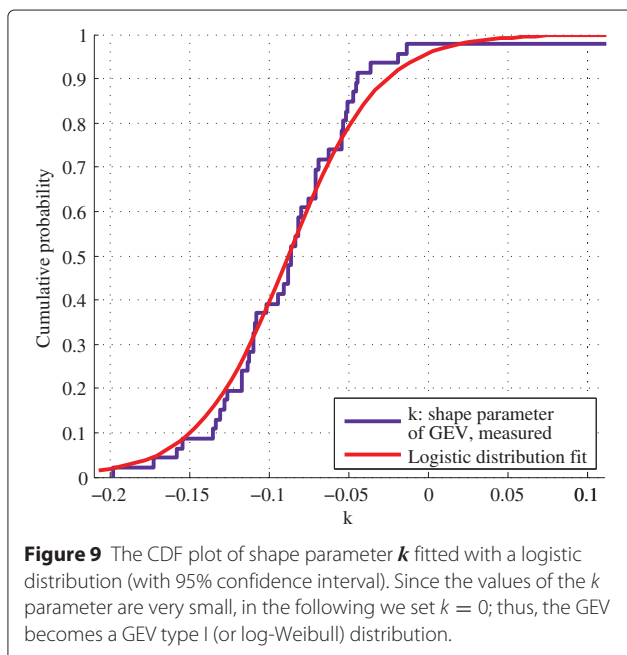
Due to a high flexibility of the GEV fit, which is given by three input parameters as opposed to usual two parameters, the MLE metric recommends the GEV distribution. On other hand, authors in [23] claim that there is no theoretical explanation for encountering this distribution type. We may, however, add that the GEV contains the accepted log-Weibull distribution as a special case for $k = 0$.

4 Localization

One of the often discussed UWB applications is precise ranging and localization especially when the TOA technique is used. As mentioned above, this is because the large UWB bandwidth allows excellent time resolution (see Equation 7) and MPC separation. Because we had measured the channel transfer function for many different antenna positions, we wanted to get some insight into attainable ranging accuracy. Our estimation of the distance results from the CIR calculated from the complex transfer function. This approach gives some limitations compared to a direct channel sounding in the time domain where some advanced techniques such as the matched filtering of the known Gaussian pulses or a well-correlated binary sequences can be used [24].

We calculated the antenna distance using the TOA technique based on the detection of the first ray transmitted

Table 1 Summarization of GEV type I parameters characterizing in-vehicle environment for 90 permutations of antenna placement and car seat occupancy

	μ	σ	k
Distribution type	Lognormal	Normal	Logistic
Mean ν	48.37	5.48	−0.08
Variance η	31.05	0.26	0.002

Blumenstein *et al. EURASIP Journal on Wireless Communications and Networking* (2015) 2015:104

Page 7 of 10

from a particular antenna. The proposed threshold-based search algorithm compares individual signal samples of the CIR with a certain threshold in order to identify the amplitude peak corresponding to the first MPC. This approach allows to calculate distance also in the NLOS scenario because the first ray may not be the strongest ray. However, penetration of the obstacles can cause some measurement accuracy degradation (see below). The aim of this chapter is to give a basic idea about accessible average error and standard deviation of the measured distances for the entire UWB band and for the first band group and also for the empty and occupied car. For more information about the measurements and the distance calculation, see [25]. Because all the particular measurements were done for three TX antennas and one RX antenna, we also calculated RX antenna position using the 2D localization technique in order to assess whether it corresponds at least roughly to reality, i.e., whether it is possible for example to reliably detect a device on a particular seat. Note that most of the above mentioned application does not need an accurate localization but only rough estimation of the device position.

4.1 Basic system parameter calculation

The frequency band B determines the time resolution of measurement by [24]:

$$T_r = \frac{1}{B} = \frac{1}{F_U - F_L}, \qquad (7)$$

where F_U is the upper frequency and F_L is the lower frequency of the band. The propagation distance resolution is then

$$D_r = T_r c, \qquad (8)$$

where $c = 2.998 \times 10^8$ m/s is the speed of the light. The maximum measurable propagation distance depends on the number of measured frequency values N_M inside the frequency band, i.e., on the frequency step f_s according to

$$D_{\max} = \frac{c}{B} N_M = \frac{c}{f_s}. \qquad (9)$$

It is obvious from the equations above that narrowing the bandwidth decreases the distance resolution and the reduction in the measured frequency points shortens the measurable propagation distance.

4.2 Ranging and localization of the receiving antenna

As mentioned above, the main aim of this section is calculation of the average error and standard deviation of the ranging and verification of the RX antenna position (Table 2). The processing of the measured data consists in the following steps:

- Calculation of the CIR
- Detection of the first incident ray
- Calculation of the RX - TX1 to TX3 distances and ranging errors
- RX antenna localization

The CIR was calculated using the IFFT in combination with a Blackman window (see Figure 11) applied to all 801 frequency response points. Before error statistics calculation, we tested a few windows (rectangular, Hann, Hamming, flattop, Blackman, and Kaiser-Bessel). Although some windows (e.g., rectangular) are generally recommended for the applications where good component separation is required, these windows could be inapplicable in our case as they may produce large side lobes that cross the threshold and cause incorrect first ray detection. Experimentally, we found that the best results giving the distances closest to reality are given by the Blackman window. The second best results can be then obtained using the Hann window.

The threshold for the first ray detection is generally determined by the noise floor. Its value is equal to the level of the peaks of noise, i.e., to the maximum amplitude of the CIR where the multipath component amplitudes are below noise level. It is obvious that the proposed algorithm works reliably in both LOS and NLOS scenarios, but it fails in some NLOS cases when the first (direct) ray is strongly attenuated and drowned in noise.

The distance of RX and TX antennas is given by the formula $D_A = cT_D$, where T_D is the first detected ray arrival time. The error statistics were calculated separately for the empty and occupied car. It was experimentally discovered that the two or three passengers sitting in the car compartment cause very similar results, and therefore, these cases were joined into one set of results. For the RX antenna localization, the trilateration technique [24] was applied. Using the three calculated distances, this technique allows 2D localization.

Calculation of the average error and standard deviation of the measured distances is summarized in Table 3 (for

Table 2 The parameters used for the ranging

	Bandwidth [GHz]	Freq. step [MHz]	Time resolution [ns]	Distance resolution [cm]	Max. propag. distance [m]	Max. measurement time [ns]
UWB	8	10	0.125	3.750	30	100
First band group	1.58		0.633	18.987		

Blumenstein *et al. EURASIP Journal on Wireless Communications and Networking* (2015) 2015:104

Page 8 of 10
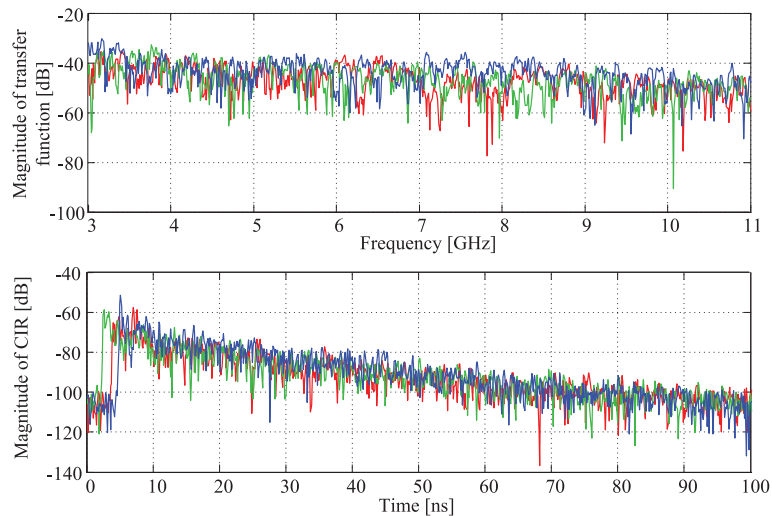
Figure 11 Magnitudes of channel transfer functions and channel impulse responses (RX antenna was placed on right rear seat).

the entire UWB) and Table 4 (for the first band group). The time intervals used for the noise peak detection were 0 to 1.25 ns (before receiving of the first MPC) and 80 to 100 ns (where the MPC can be neglected). These time intervals correspond to the following distances: 0 to 37.5 cm (minimum distance of RX-TX antennas in all scenarios is 50 cm) and 24 to 30 m. The reference antenna distances were measured by a ruler. We compared 15×3 distances without passengers and 15×3 distances with two or three passenger sitting on the seats surrounding the RX antenna. An example of peak detection for the empty car is shown in Figure 12 (upper part for the entire UWB and lower part for the first band group), while Figure 13 depicts the 2D localization result also for the UWB and first band group.

4.3 Positioning results and sources of error

It is obvious that the rough distance resolution in the case of the first band group measurement causes markedly higher average error and standard deviation compared to the measurement of the entire UWB band. The calculated distances exhibit noticeable positive bias caused by a few phenomena:

- *Existence of difference between the calibration plane and phase center of the antenna.* The coaxial interfaces of the antennas (line between the connector and phase center of the antenna) were not included when the VNA was calibrated. They were applied only during channel measurement and increased the total antenna distance.
- *Inaccurate reference measurement.* Distance measured between the antennas by the ruler was performed between the centers of the top of cones which are not identical to the phase centers of antennas. In many cases, the measured distance were slightly shorter (when the TX antenna was upside down with regard to RX antenna) .
- *Time lag in the first ray detection.* The first ray (peak) detection above the threshold exhibits random delay in the interval 0 to D_r due to the discrete nature of the CIR time axis. Received ray cannot be generally detected in advance.

Table 3 Average error and standard deviation of the measured distances for the first band group

	TX1	TX2	TX3	Total
Average error without passengers [cm]	6.76	6.30	5.75	6.27
Average error with two or three passengers [cm]	11.83	10.37	7.62	9.94
Standard deviation without passengers [cm]	7.49	6.86	2.10	5.87
Standard deviation with two or three passengers [cm]	11.13	9.28	8.95	9.80

Table 4 Average error and standard deviation of the measured distances for the first band group

	TX1	TX2	TX3	Total
Average error without passengers [cm]	25.85	21.04	14.3	20.39
Average error with two or three passengers [cm]	34.73	23.50	10.82	23.02
Standard deviation without passengers [cm]	20.76	13.88	8.74	15.67
Standard deviation with two or three passengers [cm]	20.13	12.63	7.88	17.26

Blumenstein *et al. EURASIP Journal on Wireless Communications and Networking* (2015) 2015:104

Page 9 of 10
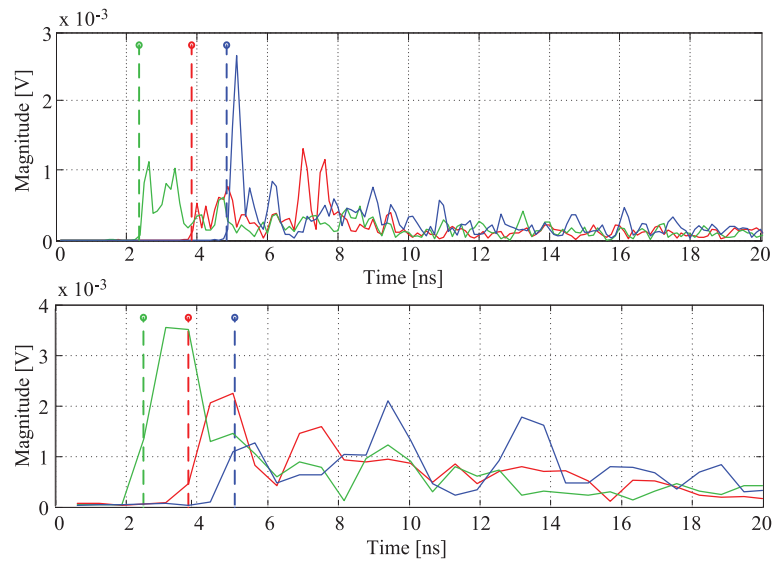
Figure 12 First peak detection of CIRs (for entire UWB) [upper] for empty and [lower] occupied vehicle.

- *Incorrect MPC component detection.* Large attenuation of some obstacles in the car may avoid correct detection of the direct ray. In this case, the other reflected MPC which travels on a longer path is regarded as the first ray.
- *Lower wave propagation velocity in media.* The velocity of an electromagnetic wave penetrating an obstacle is less than that in free space, and it depends on the obstacle material constants.

The first phenomenon is systematic and can be subtracted (it is about 2 cm together for two antennas). The two last phenomena occur only in the NLOS scenario. In

the last case, the velocity in some material can be calculated according the formula $v_p = c/\sqrt{\varepsilon_r \mu_r}$, where v_p is the velocity of propagation in m/s, μ_r is the material relative permeability, and ε_r is the relative permittivity. It is easy to find that when, for example, the wave passes the 10-cm-thick plastic obstacle (ε_r = 2 to 3, μ_r = 1 [26]), the propagation time delays are in the interval 0.138 to 0.244 ns which results in the distance bias from 4.1 to 7.3 cm.

5 Conclusions

We performed an extensive UWB measurement campaign for the vehicular passenger compartment. The measured
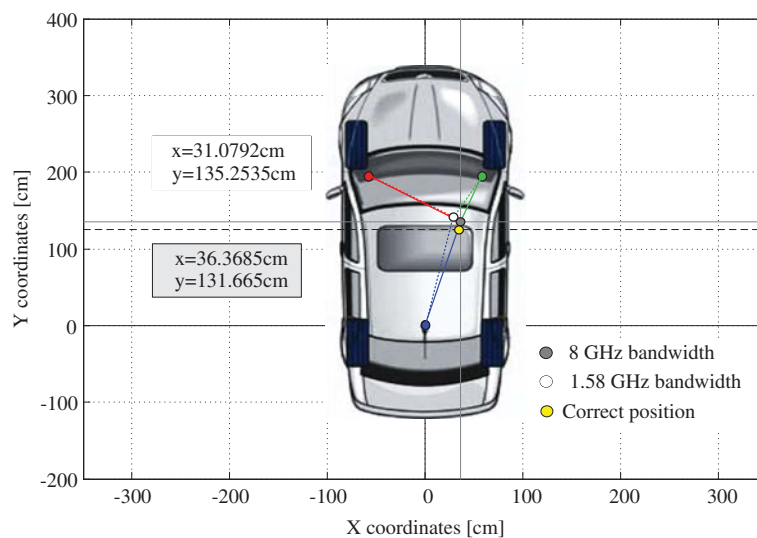
Figure 13 Localization of the RX antenna using TOA (RX antenna was placed on front passenger seat).

channel impulse responses are modeled using the GEV distribution; its parameters are estimated using a MLE. As a result, our statistical description of the received amplitude and phase distribution in the in-vehicle environment fits almost perfectly to the empirical measurement results. We showed that the measured phase is uniformly distributed with iid behavior.

Based on the measurement data, a feasibility study on the use of UWB-based positioning inside the vehicle was conducted. We could show that the accuracy of the transmitter location could be obtained with a standard deviation smaller than 10 cm for the full UWB bandwidth. The standard deviation was smaller than 16 cm for the first UWB band group only. The influence of the antenna position on the localization accuracy was lower than the effect of the occupancy level of the car.

Author details
[1] Department of Radio Electronics, Brno University of Technology, Technicka 12, 612 00, Brno, Czech Republic. [2] AIT Austrian Institute of Technology GmbH, Donau-City-Straße 1, 1220 Vienna, Austria. [3] Institute of Telecommunications, Vienna University of Technology, Gußhausstraße 25/E 389, 1040 Vienna, Austria.

References
1. G Leen, D Heffernan, Expanding automotive electronic systems. Computer. **35**(1), 88–93 (2002)
2. M Win, R Scholtz, Characterization of ultra-wide bandwidth wireless indoor channels: a communication-theoretic view. Selected Areas Commun. IEEE J. **20**(9), 1613–1627 (2002)
3. R-M Cramer, R Scholtz, M Win, Evaluation of an ultra-wide-band propagation channel. Antennas Propag. IEEE Trans. **50**(5), 561–570 (2002)
4. M Schack, J Jemai, R Piesiewicz, R Geise, I Schmidt, T Kurner, in *IEEE Vehicular Technology Conference, 2008*. Measurements and analysis of an in-car UWB channel (VTC Spring 2008 Singapore, 11–14 May 2008), pp. 459–463
5. T Kobayashi, in *2006 IEEE Ninth International Symposium on Spread Spectrum Techniques and Applications, Manaus-Amazon*. Measurements and characterization of ultra wideband propagation channels in a passenger-car compartment, (28–31 Aug 2006), pp. 228–232
6. T Tsuboi, J Yamada, N Yamauchi, in *7th International Conference on ITS Telecommunications, 2007. ITST '07*. UWB radio propagation inside vehicle environments (Sophia Antipolis, 6–8 June 2007), pp. 1–5
7. M Schack, R Geise, I Schmidt, R Piesiewiczk, T Kurner, in *3rd European Conference on Antennas and Propagation, 2009. EuCAP 2009*. UWB channel measurements inside different car types (Berlin, 23–27 March 2009), pp. 640–644
8. A Moghimi, H-M Tsai, C Saraydar, O Tonguz, Characterizing intra-car wireless channels. Vehic. Technol. IEEE Trans. **58**(9), 5299–5305 (2009)
9. J Blumenstein, T Mikulasek, R Marsalek, A Prokes, T Zemen, C Mecklenbrauker, in *2014 IEEE 80th Vehicular Technology Conference (VTC Fall)*. In-vehicle mm-wave channel model and measurement (Vancouver, BC, 14–17 Sept 2014), pp. 1–5
10. PC Richardson, W Xiang, W Stark, Modeling of ultra-wideband channels within vehicles. Selected Areas Commun. IEEE J. **24**(4), 906–912 (2006)
11. L Liu, Y Wang, N Zhang, Y Zhang, in *2010 12th IEEE International Conference on Communication Technology (ICCT)*. UWB channel measurement and modeling for the intra-vehicle environments (Nanjing, 11–14 Nov 2010), pp. 381–384
12. B Li, Z Zhou, D Li, S Zhai, Efficient cluster identification for measured ultra-wideband channel impulse response in vehicle cabin. Prog. Electromagnetics Res. **117**, 121–147 (2011)
13. J Li, T Talty, in *Military Communications Conference, 2006. MILCOM 2006*. Channel characterization for ultra-wideband intra-vehicle sensor networks (Washington, DC, 23–25 Oct 2006), pp. 1–5
14. R Thoma, O Hirsch, J Sachs, R Zetik, in *The Second European Conference on Antennas and Propagation, 2007. EuCAP 2007*. UWB sensor networks for position location and imaging of objects and environments (Edinburgh, 11–16 Nov 2007), pp. 1–9
15. J Blumenstein, R Marsalek, A Prokes, C Mecklenbrauker, in *Multiple Access Communcations*. Impulse noise mitigation for OFDM by time-frequency spreading, vol. 8310 (ser. Lecture Notes in Computer Science. Springer International Publishing Vilnius, Lithuania, 16–17 Dec 2013), pp. 8–20
16. J Blumenstein, T Mikulasek, R Marsalek, A Chandra, A Prokes, T Zemen, C Mecklenbrauker, in *IEEE Vehicular Networking Conference (VNC)*. In-vehicle UWB channel measurement, model and spatial stationarity (Paderborn, 3–5 Dec 2014), pp. 77–80
17. R Fontana, E Richley, J Barney, in *2003 IEEE Conference on Ultra Wideband Systems and Technologies*. Commercialization of an ultra wideband precision asset location system (Reston, VA, USA, 16–19 Nov 2003), pp. 369–373
18. R-R Lao, J-H Tarng, C Hsiao, in *The 57th IEEE Semiannual Vehicular Technology Conference, 2003. VTC 2003-Spring*. Transmission coefficients measurement of building materials for UWB systems in 3-10 GHz, vol. 1 (Jeju, Korea, 22–25 April 2003), pp. 11–14
19. Q Liang, A Audu, H Khani, H Nie, W Xiang, Z Chen, in *2013 IEEE Radio and Wireless Symposium (RWS)*. Measurement and analysis of intra-vehicle UWB channels (Austin, TX, USA, 20–23 Jan 2013), pp. 166–168
20. JD Kraus, *McGraw-Hill Education*, (New York, 1988)
21. RA Fisher, in *Mathematical Proceedings of the Cambridge Philosophical Society*. Theory of Statistical Estimation, (1925), pp. 700–725
22. S Kotz, S Nadarajah, *Extreme Value Distributions*, (World Scientific, Washington, D.C, 2000)
23. H Hashemi, The indoor radio propagation channel. Vehicular Technology, IEEE Transactions on. **81**(7), 594–606 (2002)
24. Z Sahinoglu, S Gezici, I Guvenc, vol. 2. (Cambridge University Press, Cambridge, 2008)
25. J Vychodil, J Blumenstein, T Mikulasek, A Prokes, V Derbek, in *International Conference on Connected Vehicles & Expo 2014 ICCVE 3rd*. Measurement of in-vehicle channel feasibility of ranging in UWB and MMW band (Vienna, 3–7 Nov 2014)
26. DR Lide, *CRC Handbook of Chemistry and Physics*. (CRC Press, 2001)

Serial Subtractive Deconvolution Algorithms for Time-Domain Ultra Wide Band In-Vehicle Channel Sounding

Aniruddha Chandra, **Jiri Blumenstein** , Tomáš Mikulášek, Josef Vychodil, Roman Maršálek, Aleš Prokeš, Thomas Zemen, Christoph F Mecklenbrauker

IF=1.387

Serial subtractive deconvolution algorithms for time-domain ultra wide band in-vehicle channel sounding

Aniruddha Chandra[1] ✉, Jiří Blumenstein[1], Tomáš Mikulášek[1], Josef Vychodil[1], Roman Maršálek[1], Aleš Prokeš[1], Thomas Zemen[2,3], Christoph F. Mecklenbräuker[4]

[1]Department of Radio Electronics, Brno University of Technology, 61600 Brno, Czech Republic
[2]AIT Austrian Institute of Technology GmbH, 1220 Vienna, Austria
[3]Telecommunications Research Center Vienna (FTW), 1220 Vienna, Austria
[4]Institute of Telecommunications, Vienna University of Technology, 1040 Vienna, Austria
✉ E-mail: aniruddha.chandra@ieee.org

Abstract: Ultra-wide band (UWB) communication is expected to play a key role in next generation broadband intra vehicle wireless applications. The car compartment differs significantly from other well studied indoor or outdoor environments. Hence, channel sounding experiments are crucial for gaining a thorough knowledge of the UWB signal propagation characteristics in such a medium. Time domain channel sounding campaigns often employ some sort of deconvolution during measurement post processing as the measured signal in these experiments is the convolution of the channel response and the probing pulse which violates the Nyquist criterion. In this study, a comparison of two variants of time-domain serial subtractive deconvolution algorithm, popularly known as CLEAN, is presented. Appropriate statistical metrics for assessing the relative merit of a deconvolution technique are identified in the context of intra vehicle UWB transmission, and the better algorithm is selected based on its performance over a standard IEEE channel simulation testbed. The chosen method is then applied to extract power delay profile and delay parameters from an empirical time domain sounding experiment performed inside a passenger car. The effects of passenger occupancy, transmitter receiver separation and absence of direct transmission path are studied.

1 Introduction

1.1 Motivation

Intra-vehicular communication, in the conventional sense, refers to transmission of signals between electronic control units and sensors/actuators over a wired common control area network bus [1–3]. The degree of sophistication for automotive vehicles regarding safety, driver assistance and passenger comfort has escalated multifold over the years increasing the overall 'wiring harness' of the in-vehicle electrical network. With the enhanced penetration of Internet and satellite networks in all spheres of modern life, demand for yet another kind of intra-vehicular communication is in rise. According to a survey by Juniper Research, 20% cars in the US and Western Europe will be able to access Internet apps by 2017. Thus, navigational and recreational infotainment networks including live audio/video streaming facilities are expected to be an integral part of every car in near future [4]. As far as the wiring harness is considered, this will surely add up to the already existing cable bundle of several kilometres [5] that run inside a car posing severe design and manufacturing challenges to the automobile industry.

Replacing intra-vehicular wired cables and connectors with wireless links seems to be a promising alternative and offers the following advantages. First, reducing the vehicle weight by 40 kg, typical wiring harness for present day mid-sized cars [6], would increase fuel efficiency by 2%. The value is not very small by automotive engineering standards. On the other hand, the ecological impact gained through reduction of greenhouse gas emission is invaluable. Second, eliminating the cables will reduce cost and labour in design, manufacturing and installation processes. Third, maintenance becomes less likely and much easier without the long running cables cramped in a closed space [7].

However, one should not forget the inherent limitations of wireless communication, especially the random nature of the channel which makes the wireless links unsuitable for safety-critical communications. Moreover, wireless power transfer is still in its infancy and current endeavours are directed towards replacement of data cables only. Power cables are going to stay, and might even increase as every new wireless in-vehicle device requires connection to the electrical power source [1]. Nevertheless, the incentives of wireless harness are attracting huge research fundings, and the quest for replacing cable bundles has already been extended to aircrafts [8] and spacecrafts [9], where both the rewards and stakes are definitely much higher.

Initial candidates for providing wireless access in intra-car applications included narrowband standards such as radio frequency identification, Bluetooth, wireless 1394 [10] and IEEE 802.11 (WiFi) among others. A recent ruling by the European Commission now allows implementation of short range wideband wireless standards inside cars and trains [11], and gradually the focus of intra-car wireless research is now being shifted to tests and measurements in the ultra-wide band (UWB) [12–16] and in millimetre wave (mmW) bands [17–20].

UWB promises very high-data-rate communication, in the order of several hundred Mbps, across distances up to a couple of meters. UWB also provides a reliable means of communication even in environments traditionally considered very hostile to radio by mitigating large-scale (shadowing) as well as small-scale (multipath) fading effects. Furthermore, the low power spectral density of UWB signals ensures minimum interference to nearby cars or fixed wireless infrastructures. UWB propagation characteristics has been already well studied [21] in the context of various indoor and outdoor environments. However, a passenger car compartment with metal body and plastic/foam interiors, is a different environment altogether. 'Confined structures' and 'human

presence' affects UWB propagation [22] significantly necessitating channel sounding experiments for gaining a thorough knowledge of the propagation characteristics.

In general, there are two possible methods for wideband channel sounding [23, 24]. The first is sounding in 'frequency-domain' with a vector network analyser, where the channel is swept at different frequencies. The transfer function parameter (s) provides an estimate of the channel transfer function, $\hat{H}(f)$, which may be used to obtain the impulse response estimate, $\hat{h}(t) = \mathcal{F}^{-1}\hat{H}(f)$, through inverse fast Fourier transform. The second method, 'time-domain' sounding, is more direct where short pulses are sent over the channel and the channel's impulse response convolved with the pulse shape is recorded by an oscilloscope. A desired feature of any wideband time domain sounding is its *super-resolution* capability [25], that is, having the potential to distinguish between multi-path components (MPCs) that are separated by a time duration lesser than the channel sounding pulse width. The goal can be attained by time-domain subtractive deconvolution algorithms (e.g. CLEAN).

1.2   Literature survey

Different versions of CLEAN had been successfully implemented in geotechnical seismic analysis, spectroscopy in radio astronomy and biomedical image processing for last few decades [26]. Multi-template case specific CLEAN algorithms for UWB were also reported in [27, 28]. However, intra-vehicular measurement literature is not particularly rich in this regard as most of the channel sounding were performed in frequency domain [29–31].

Time domain experimental papers often lacked detailed discussion on the implementation of algorithm. The only exception is [16], where a sub-optimal version of CLEAN is presented. In this paper we show that the modified version of the algorithm can perform much better in intra-vehicular environments. Part of these results was published in a conference paper [32]. The experimental domain of the current paper is also entirely different from [16]. While the authors in [16] characterised wireless channels in the engine compartment and under the chassis, with an objective of possible sensor network implementation in vehicles, we carried our measurements in the passenger compartment, and the target application is localisation of people and devices inside the car. Another important goal of this paper is to study the effect of passenger occupancy on the channel parameters.

It may be noted here that a frequency domain successive subtraction algorithm for UWB was presented in [33]. This algorithm has reduced complexity compared with expectation-maximisation (EM) [34] or space-alternating generalised EM (SAGE) [35] algorithms.

1.3   Contributions of the paper

Although we provide an exhaustive description of the UWB measurement campaign which is a part of our GACR project [36] aimed at intra-vehicular channel modelling in UWB, mmW and infra-red (IR) domains, our main contribution lies in the choice of deconvolution and its validation. The selection of a proper deconvolution algorithm is an important step in any time-domain channel sounding experiment. This is particularly important for UWB channel sounding where pulse shape at the transmitter and receiver cannot be chosen according to the Nyquist theorem. Usual channel sounders use a root raised cosine pulse such that the total impulse response gives a Nyquist pulse.

Moreover, study of CLEAN is beneficial in another sense because the algorithm provides discrete impulse response in time domain and helps in locating the first peak resulting from the direct path (or most dominant multipath) which is crucial in localisation applications, the ultimate goal of the GACR project.

Specifically, our contributions are

• We present discrete-time versions of CLEAN algorithms that are readily executable through software packages.

• We identify appropriate statistical metrics for comparing deconvolution methods and validate our choice through standard UWB testbed simulation.

• We obtain channel impulse response (CIR) for various transmitter receiver positions in the passenger compartment of a car through deconvolution operation.

• We calculate power delay profile (PDP), mean excess delay and RMS delay spread from the CIRs.

• We study the effects of passenger occupancy, transmitter receiver separation and obstruction of line of sight path on intra-vehicle wireless channel parameters.

1.4   Organisation of the paper

The structure of this paper is as follows. Section 2 describes the overall measurement campaign in detail. In particular, the choice of the sounding pulse, the measurement environment, the antenna placement and the measurement setup are discussed. Section 3 provides two working versions of the CLEAN algorithm and explains the intricacies of comparison between them. The section also includes the post-processing of the measured data. The calculation of PDP and multipath delay parameters that can be extracted from the measured data as well as the effects of distance, passenger occupancy and line-of-sight (LoS) condition are presented in Section 4. Finally, Section 5 concludes the paper.

2   Measurement campaign

2.1   Sounding pulse

Owing to the availability of cheap and uncomplicated hardware, the UWB systems that were designed and implemented so far are mostly of the type impulse radio (IR-UWB) transmitting some form of Gaussian pulses. A basic Gaussian pulse, popularly known as 'Gaussian monocycle', is defined as

$$p(t) = \sqrt{\frac{1}{t_d}\sqrt{\frac{2}{\pi}}} \exp\left[-\left(\frac{t}{t_d}\right)^2\right] \tag{1}$$

having unit energy and an effective pulse duration of $2t_d$.

The basic pulse, however, possesses a non-zero DC-offset and cannot be efficiently radiated through antennas of realisable dimensions. The widely adopted version is a 'Gaussian doublet', the second derivative ($p_2(t) = \partial^2 p(t)/\partial^2 t$) of the Gaussian pulse

$$p_2(t) = -2\sqrt{\frac{1}{3t_d}\sqrt{\frac{2}{\pi}}}\left(1 - \frac{2t^2}{t_d^2}\right)\exp\left[-\left(\frac{t}{t_d}\right)^2\right] \tag{2}$$

which is obtained at the output of the transmitting antenna if the antenna is fed with a current pulse proportional to the first derivative, $p_1(t) = \partial p(t)/\partial t$, owing to the derivative nature of the antenna [21]. Noting that the Fourier transform (FT) of the basic pulse is

$$\begin{aligned} P(f) &= \mathcal{F}\{p(t)\} \\ &= \sqrt{t_d\sqrt{2\pi}}\exp\left[-(\pi t_d f)^2\right] \end{aligned} \tag{3}$$

and utilising the derivative property of the FT, it is easy to obtain the amplitude spectra of a Gaussian doublet from (3)

$$P_2(f) = -2\sqrt{(t_d/3)\sqrt{2\pi}}(j2\pi f)^2\exp\left[-(\pi t_d f)^2\right] \tag{4}$$

where $j = \sqrt{-1}$ denotes the complex square root of unity. When plotted (see Fig. 1, right-hand side-top, black curve), the spectra shows significant low frequency (<3 GHz) components in spite of
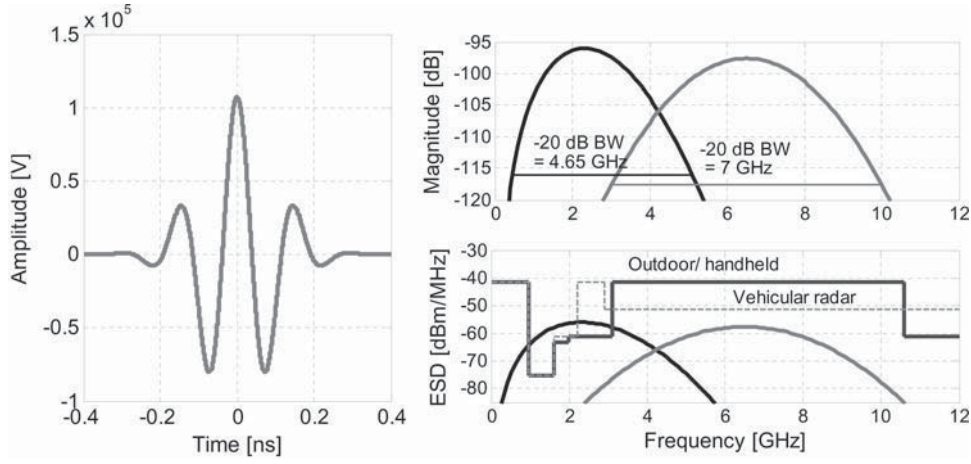
Fig. 1 *Input pulse x(t) (left-hand side), it's amplitude spectra $X(f)_+$ (right-hand side-top) and compliance with FCC UWB emission masks (right-hand side-bottom)*

Black curves depict the frequency-domain characteristics for the Gaussian second derivative with equivalent parameters (unit energy and same t_d)

having a zero DC-offset. The implications can be better understood through a comparison of the energy spectral density with the effective isotropic radiated power (EIRP) emission mask standardised by Federal Communications Commission (FCC) [37], as shown in Fig. 1 [right-hand side-bottom]. The figure clearly reveals that for the given pulse parameters, the Gaussian doublet (black curve) violates the regulations, and to keep the EIRP in limit, the signal strength needs to be reduced causing a drop in the SNR of about 20 dB. The problem is not typical for Gaussian shaped pulses, and exists for other baseband pulses too, say, for example, a raised cosine pulse that obeys Nyquist criterion.

The frequency spectra may be shifted away further from the origin through a 'pseudo-carrier modulation' with the help of a carrier having frequency not much higher than the bandwidth of the Gaussian pulse [38]. This fact prompted us to use a 'sinusoidally modulated Gaussian' pulse for our intra vehicular UWB channel sounding campaign. The unit energy sounding pulse (Fig. 1, left-hand side) used for the field measurements is given by

$$x(t) = \sqrt{\frac{2}{t_d}\sqrt{\frac{2}{\pi}}}\exp\left[-\left(\frac{t}{t_d}\right)^2\right]\cos(2\pi f_c t + \phi) \qquad (5)$$

having an initial phase of $\phi = 0.6\pi$ and a time scaling factor of $2t_d = 0.276$ ns. The carrier frequency, $f_c = 6.5$ GHz, was set at the middle of the FCC approved band, that is, from 3 to 10 GHz. Applying the frequency shifting property of the FT, the corresponding spectra for positive frequencies (red curve) may be derived from (3)

$$X(f)_+ = \sqrt{\frac{2t_d}{\pi}}\exp\left[-\left\{\pi t_d(f - f_c)\right\}^2\right] \qquad (6)$$

which is plotted alongside (4), the spectra of the Gaussian doublet (black curve), in Fig. 1 (right-hand side). It is evident that the sounding pulse has a better compliance with the outdoor/ handheld and vehicular radar emission masks and holds stronger potential to be employed in future in-vehicle UWB communication systems. Further, when the −20 dB bandwidths of the two pulse shapes are compared, we find that while the Gaussian doublet has a bandwidth of 4.65 GHz, the Gaussian sine pulse offers a −20 dB bandwidth of 7 GHz (bandwidth is almost 1.5 times) which results in a much flatter spectrum as desired by FCC and other regulating bodies.

2.2 Description of the environment

The vehicle under study is a right-hand side drive, regular four-door sedan Škoda Octavia III (model 1.8 TSI Combi) with dimensions 4.659 m (length) × 1.814 m (width) × 1.462 m (height), which was parked six storeys beneath ground level in the multi-floored underground garage of the Faculty of Electrical Engineering, Brno University of Technology (VUT). Reinforced concrete walls and floors of the garage provided us with an environment that was free from any 'narrowband interference' (e.g. WiFi, Cellular). Moreover, there were no other cars parked in close vicinity.

Fig. 2 depicts the underground garage and the position of the vehicle in the parking lot. While recording the data, all the test equipments except the transmitter and receiver antennas were kept outside the car compartment. Further, all the doors and windows of the vehicle were closed except a small opening in the driver window allowing to pass the cables which connect antennas with measurement devices.
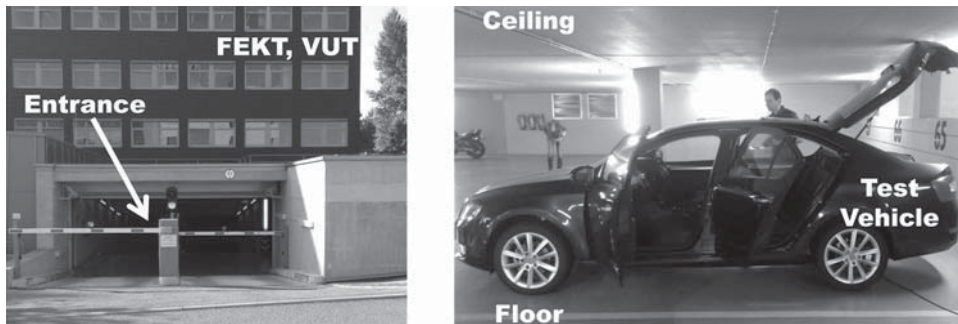
Fig. 2 *(Left-hand side) Underground garage where the measurements were conducted. (Right-hand side) Test vehicle and its surroundings*

2.3 Antenna placement

As shown in Fig. 3 (left-hand side), a total of 52 different transmitter (Tx) and receiver (Rx) antenna positions were tested with Tx-Rx separations ranging from 0.56 to 1.9 m. Distances between antennas were recorded for each setting with a flexible measuring tape. In addition, we also examined the effect of passenger occupancy by keeping some of these Tx-Rx setting fixed, and varying the number of passengers from zero to three. It may be noted that although the car can accommodate four persons, we could vary the passenger count (including the driver) only up to three, as one of the places was always occupied by the receiver antenna and its attachments.

The 'receiver' antenna had been placed on the driver's seat (D) and on the seat behind the driver (RPR, P_3) to imitate a hand-held mobile wireless device that belongs to either the driver or to a passenger. A plastic photographic tripod (JOBY GorillaPod) was used to maintain proper height (hand to lap separation) of the Rx antenna as well as to keep the inverted cone base of the antenna in horizontal position, while placing it on the seat cushion.

A wider variety of locations were set for the 'transmitter' antenna spanning all over the car, including the left- and right-hand side of the dashboard (L_1, R_1) and windshield (L_2, R_2), the rear part of the ceiling ($P_{1,2}$), the luggage space (P_4) and the engine compartment

(P_5). Determination of the Tx antenna positions were governed by two parallel objectives. First, the positions should resemble possible installation site for future in-vehicle wireless systems. For example, in modern cars position $P_{1,2}$ may serve as a wireless docking station because this place usually contains some wiring and antenna for audio system or global positioning system. The second goal is to realise both LoS and 'non-line-of-sight' (nLoS) scenarios. When the receiver was placed at driver's (D) seat, the measurement sets such as R_2-D, L_2-D etc. represented LoS wireless links. On the other hand, putting the receiver antenna in rear passenger seat on the right-hand side (RPR) resulted in nLoS transmission (R_2-RPR, L_2-RPR), because of the blocking by the backrest of the seats [39].

A pair of vertically polarised wideband monopole conical antennas (photos in Fig. 3) were used for both transmission and reception. The monopole conical antennas are omnidirectional, has a low radar cross-section and provide a low voltage standing wave ratio [40]. Fig. 4 describes the simulated radiation pattern of the designed UWB antennas. It can be observed that the azimuth plane pattern is circular and omnidirectional which is invariant within the desired frequency band (3–10 GHz).

Fig. 3 *(Left-hand side) Side-view and top-view schematic of antenna positions, Circle: Tx antennas, Star: Rx antennas. (right-hand side) Real world antenna placement close-ups: on right-hand side windshield (top) and on tripod (bottom). (legends) D: driver, RPR: rear passenger on right-hand side, L/R: left- and right-hand side windshield (subscripts 1 and 2 denote bottom and top), P_1-P_5: position 1 to position 5 of the Tx/Rx antenna*

2.4 Measurement setup

The schematic diagram of the setup for UWB time domain channel sounding and an actual photograph of the field measurement device assembly are shown in Fig. 5.

The channel sounding pulse mentioned in (5) was generated at a sampling rate of $f_s = 50$ Gs/s through the Tektronix AWG70002A arbitrary waveform generator (AWG); after importing the corresponding waveform file from MATLAB. Next, the signal was amplified through a high-power amplifier (HPA) before feeding the signal to the transmitter antenna. We used Wenteq broadband power amplifier ABP1200-01-1825 which provided a gain of around 19 dB.

The receiving portion of the measurement system consisted of an identical receiving antenna, a low-noise amplifier (LNA) and a digital sampling oscilloscope (DSO). For LNA, Wenteq ABL1200-08-3220 was used that had a small signal gain of 32 dB and a noise figure of 2 dB. Finally, the received waveform was stored with the help of the mixed signal oscilloscope Tektronix DPO72004C.

Interconnections among devices and synchronisation between AWG and DSO were realised through flexible coaxial cables. The total cable loss was about 5 dB in total. A programmable DC power supply Voltcraft PPS-11360 powered the HPA and the LNA.

Fig. 4 *Simulated gain pattern of the conical monopole UWB antennas in E-plane (left-hand side) and H-plane (right-hand side)*
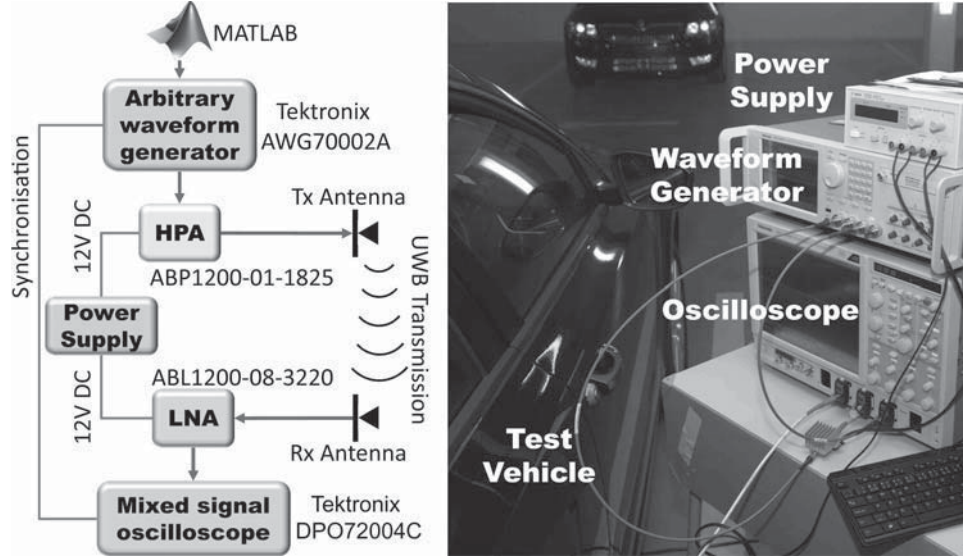
Fig. 5 *(Left-hand side) Block diagram of the measurement setup. (Right-hand side) Photograph of the apparatus assembly*

3 Deconvolution

3.1 Ill-posedness

For a causal time-limited input-output waveform set, $\{x(t), y(t)\}$, where $y(t) = x(t)*h(t) + n(t)$, with $*$ denoting the convolution operator and $n(t)$ being the ambient noise, deconvolution of the CIR, $h(t)$, is, in general, an ill-posed problem [41]. The ill-posedness in the deconvolution problem has two aspects, first, there is no unique solution and second, the solution procedure is often unstable. The instability is reflected in the attempt of a direct frequency-domain inversion $H(\omega) = Y(\omega)/X(\omega)$ which leads to erroneous computation of $h(t)$ as the noise component in $Y(\omega)$ may not be small when $X(\omega) \simeq 0$ [42].

The lack of a direct inverse operation gave rise to multiple deconvolution methods. However, only few of them are having super-resolution capability. The non-iterative algorithms are mostly maximum likelihood estimator based, and they suffer heavily from the noise induced instability problems. This makes the iterative CLEAN algorithms a natural choice for deconvolution in noisy environments.

Algorithm 1

1: **compute** cross-corrlation: $\mathcal{R}^{xy} = x[n] \tilde{*} y[n]$
2: **initialise** dirty map: $d_0 \leftarrow y$,
        clean map: $c_0 \leftarrow 0$,
        threshold: $\mathcal{T} \leftarrow \max |\mathcal{R}^{xy}|/10$,
        loop gain: $\gamma \leftarrow 0.02$,
        stopping criterion: $\mathcal{R}_0^* \leftarrow \mathcal{T} + \epsilon$,
        $N \leftarrow \text{length}\{y\}$
3: **while** $|\mathcal{R}_k^*| > \mathcal{T}$ **do**
4:     **compute** cross-corrlation: $\mathcal{R}_k^{xd} = x[n] \tilde{*} d_k[n]$
5:     **find** $n_k^* = \arg\max_n |\mathcal{R}_k^{xd}[n]|$, $\mathcal{R}_k^* \leftarrow \mathcal{R}_k^{xd}[n_k^*]$
6:     **shift** input $x^s[n] = x[n - n_k^s]$; $n_k^s = N - n_k^*$
7:     **clean** dirty map: $d_k \leftarrow d_{k-1} - \gamma \mathcal{R}_k^* x^s$
8:     **if** $(0 < n_k^s < N)$
        update clean map: $c_k[n_k^s] \leftarrow c_{k-1}[n_k^s] + \gamma \mathcal{R}_k^*$
9:     **end if**
10: **end while**
11: **return** $\hat{h} \leftarrow c$

Fig. 6 *Basic CLEAN*

3.2 Variants of CLEAN

In this section, we present two versions of the CLEAN algorithm (see Figs. 6 and 7). The basic CLEAN algorithm assumes a linear time-invariant tapped delay line model for the channel, and through successive iterations, extracts the CIR, termed as 'clean map', by subtracting shifted input signal replicas from the output or 'dirty map' [43]. For the modified CLEAN algorithm, subtraction takes place in the convolution domain [44]. Both the algorithms are readily implementable in popular software packages (e.g. MATLAB) as they work on the discrete version of the time-domain input-output waveforms, $x[n]; n \in \mathbb{Z}_{\leq N_1}^*$ and $y[n]; n \in \mathbb{Z}_{\leq N_2}^*$. The discrete time index (n) is related to the absolute time (t) through the relation, $t = n/f_s$, where f_s is the sampling rate mentioned in Section 2.4. Before feeding the sequences, appropriate zero-padding is required to make the length of the sequences equal to N, where $N = \max\{N_1, N_2\}$. Further, the discrete cross-correlation operator, $\tilde{*}$, is defined as

$$\mathcal{R}^{xy}[n] = x[n] \tilde{*} y[n] = \hat{R}^{xy}[n - N] \tag{7}$$

where

$$\hat{R}^{xy}[n] = \begin{cases} \sum_{k=0}^{N-n-1} x[n+k]y[k] & \text{for} \quad n \geq 0 \\ \hat{R}^{yx}[-n] & \text{for} \quad n < 0 \end{cases} \tag{8}$$

The stopping criterion for successive cleaning may be chosen to attain a target 'energy capture ratio'

$$\text{ECR} = \left[1 - \left(\frac{||y - \hat{y}||}{||y||} \right)^2 \right] \times 100\% \tag{9}$$

where $\hat{y}(t) = x(t) * \hat{h}(t)$ denotes the reconstructed output generated using the estimated response $\hat{h}(t)$, or to maintain a *dynamic range*

$$\text{DR} = 20\log_{10} \left[\frac{\max_n (\hat{h}[n])}{\min_n (\hat{h}[n])} \right] \tag{10}$$

considering only non-zero elements of $\hat{h}$. In this paper, we considered a threshold, $\mathcal{T}$, equal to 10% of the peak cross-correlation value. A higher value caused missing of

Algorithm 2

1: **compute** cross-corrlation: $\mathcal{R}^{xy} = x[n]\tilde{*}y[n]$
2: **compute** auto-corrlation: $\mathcal{R}^{xx} = x[n]\tilde{*}x[n]$
3: **initialise** dirty map: $d_0 \leftarrow \mathcal{R}^{xy}$,
      clean map: $c_0 \leftarrow 0$,
      threshold: $\mathcal{T} \leftarrow \max |\mathcal{R}^{xy}|/10$,
      stopping criterion: $d_0^* \leftarrow \mathcal{T} + \epsilon$,
      $N \leftarrow \text{length}\{y\}$
4: **while** $|d_k^*| > \mathcal{T}$ **do**
5:     **find** $n_k^* = \arg\max_n |d_k[n]|$, $d_k^* \leftarrow d_k[n_k^*]$
6:     **shift** auto-correlation $\mathcal{R}^{xx,s}[n] = \mathcal{R}^{xx}[n + n_k^s]$;
      $n_k^s = N - n_k^*$
7:     **clean** dirty map: $d_k \leftarrow d_{k-1} - d_k^* \mathcal{R}^{xx,s}$
8:     **if** $(0 < n_k^s)$
      update clean map: $c_k[n_k^s] \leftarrow d_k^*$
9:     **end if**
10: **end while**
11: **return** $\hat{h} \leftarrow c$

Fig. 7 *Modified CLEAN*

significant MPCs, while a lower threshold generated too many paths picking up background noise.

The leverages of the modified algorithm over the basic one are threefold. First, one may note the presence of 'loop gain' (γ) in the basic algorithm (step 7), the choice of which is often empirical and case-dependent. Second, the modified algorithm is 'faster' and computationally less intensive as it avoids the calculation of the correlation at each iteration. Third, there is an absolute assignment of a MPC in step 8, which was not possible for the basic CLEAN algorithm. In Fig. 6, a former value of the index (n_k^s) might repeat (quite frequently if the choice of γ is not optimal) after some iterations, that is, the residues in the dirty map may result in an update of the clean map.

3.3 Comparison

For comparison, we have convolved the input signal given in (5) with some energy normalised ($\sum_n h^2[n] = 1$) synthetic impulse response, added Gaussian noise and applied the algorithms described in Section 3.2 to estimate the CIRs. Although the common strategy is to match the reconstructed signal $\hat{y}(t)$ against the original received signal $y(t)$, we compared $\hat{h}(t)$ directly with h

(t) to see which method provides a better representation of the multipath nature of the channel.

The test is first performed for a simple 3 tap channel with tap gains separated by a distance less than the pulse width, to test the super-resolution potential of CLEAN. A casual inspection of the reconstruction results (Fig. 8, left-hand side) reveals that the modified method results in less spurious components, and the ratio between multipath tap gains are better maintained.

Next we simulated the discrete version of the standard UWB IEEE 802.15.3 channel based on modified Saleh–Valenzuela (SV) model [45]. The model specifies that channel delay taps can be grouped into clusters and the power falls off exponentially from cluster to cluster. Moreover, within each cluster, the power falls off exponentially from tap to tap. For the sake of simplicity, we have assumed non-overlapping clusters of rays. Further, out of the four specified channel models (CMs), the simulation parameters for only CM1 and CM2 (0–4 m, LoS/ nLoS) were implemented to resemble the intra-vehicular environment, and significant paths within 10 dB of the peak have been retained.

Comparison of the estimated CIR profiles (Fig. 8, right-hand side) is no longer possible through visual inspection. In fact, assessing relative merits of two solutions for an ill-posed problem is subjective to the metric used. As an indicative example, measuring the number of significant MPCs is not very meaningful; the multipath profile depends not only on the number of taps, but also on their respective delays. Another crude method is to compare the mean square error (MSE), $\sum_{n=1}^{N} (\hat{h}[n] - h[n])^2/N$. However, the results averaged over 1000 channel samples indicated a marginal improvement (3–4%) of the MSE when the modified algorithm is used.

A better conclusion may be reached by resorting to a statistical comparisons. We begin with computing the Pearson product-moment 'correlation coefficient' between the CIRs estimated via the two different methods and the original CIR profile

$$\rho = \frac{\sum_{n=1}^{N} (h[n] - \mu_h)(\hat{h}[n] - \mu_{\hat{h}})}{\sqrt{\sum_{n=1}^{N} (h[n] - \mu_h)^2}\sqrt{\sum_{n=1}^{N} (\hat{h}[n] - \mu_{\hat{h}})^2}} \qquad (11)$$

where μ_h and $\mu_{\hat{h}}$ denote the expectations of the original and estimated CIR arrays, respectively, and plot a histogram of their difference. The positive skewness (Fig. 9, left-hand side) tells, how often, on average, the CIRs constructed with the modified algorithm matches better than that obtained through the basic algorithm. Note that the suffixes, BC and MC, are used to signify the basic CLEAN and modified CLEAN algorithms.
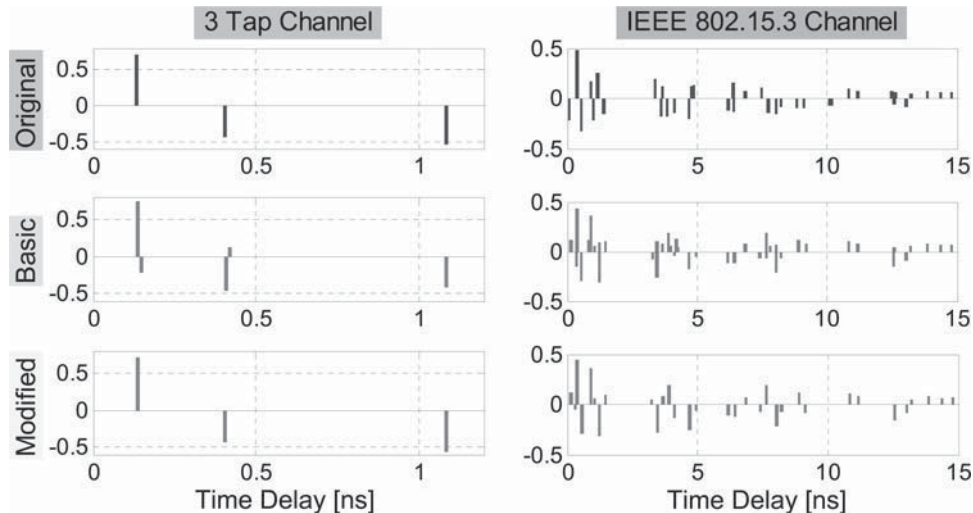
Fig. 8 *Comparison of the estimated CIRs with the original CIR, SNR = 10 dB*
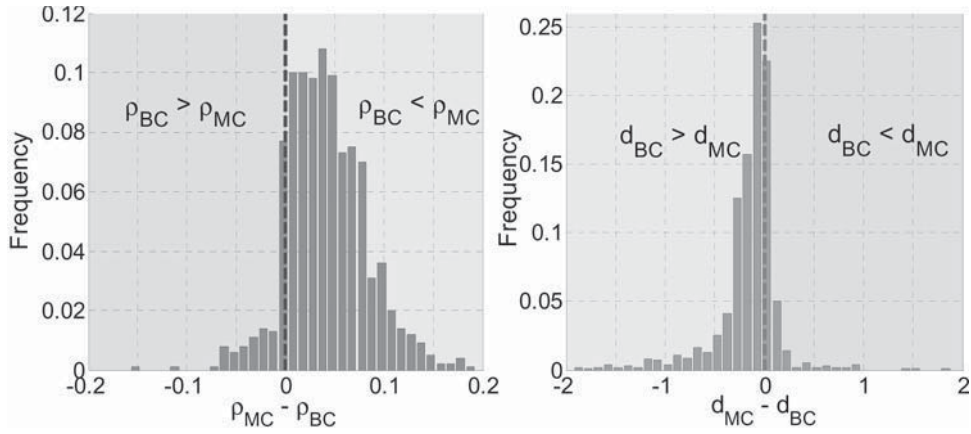
Fig. 9 *Histogram of difference of correlation coefficient (left-hand side) and K–L distance (right-hand side)*

Another such measure is the Kullback–Leibler (K–L) divergence [46]

$$d = \sum_{n=1}^{N} h[n]\log_2\left(\frac{h[n]}{\hat{h}[n]}\right) \qquad (12)$$

which measures the distance between common non-zero elements of the CIR vector. A negative skewness of the histogram (Fig. 9, right-hand side) of the difference of the distances also vouch for the superiority of the modified algorithm.

Finally, a two-sample Kolmogorov–Smirnov (K–S) test is performed. The test is different from the earlier two tests in the sense that it does not judge the one-to-one correlation, rather it focuses on the similarity of the inherent random distribution of CIR tap gains.

The K–S test statistic is defined by [47]

$$D = \max_n \left| F_{\hat{h}}[n] - F_h[n] \right| \qquad (13)$$

where $F[n]$ denotes the empirical cumulative distribution function (CDF). The null hypothesis ($\mathcal{H}_0$) that both $F_{\hat{h}}[n]$ and $F_h[n]$ belong to the same family of distribution, is rejected if $D > D_\alpha$, where the critical value D_α is calculated from the table of Kolmogorov distribution at a given significance level α

$$\Pr\{D \leq D_\alpha\} = 1 - \alpha \qquad (14)$$

If F_D denote the CDF of D, the corresponding p-value is given by, $p = 1 - F_D(D_\alpha)$.

The Kaplan-Meier estimate of the CDF of the p-values, measured against a 5% significance level ($\alpha = 0.05$), are shown in Fig. 10. Irrespective of the loop-gain parameter (γ) value, the CDF for the basic algorithm exceeds the modified one, implying that the probability of obtaining smaller p-values for the basic case is higher. The sensitivity of the basic algorithm to parameter setting is also quite self-explanatory. When γ changes slightly from 0.02 to 0.03, the gap between the CDFs widens drastically.

3.4 Post processing

For a particular measurement, the received signal, $y(t)$, depends not only on the channel response but also on the measurement system effects, and can be represented as [48]

$$y(t) = h_{Rx,Ant} * h(t) * h_{Tx,Ant} * x(t) \qquad (15)$$

where $h_{Tx,Ant}$ and $h_{Rx,Ant}$ are the impulse responses of the transmitter and receiver antennas along with effects of other attached instruments. For proper calibration, a reference input 'template'

$$x_{ref}(t) = h_{Rx,Ant} * h_{Tx,Ant} * x(t) \qquad (16)$$

was obtained by measuring the response of the input $x(t)$ in an anechoic chamber free from reflections and diffractions (Fig. 11, left-hand side). The measurement involved the same set of measurement devices as described in Section 2.4 and the reference distance between Tx and Rx antennas was 1 m. For assessing the need of calibration against temporal variations, some

Fig. 10 *Comparison of CDF p-values obtained from K–S test for γ = 0.02 (left-hand side) and γ = 0.03 (right-hand side)*
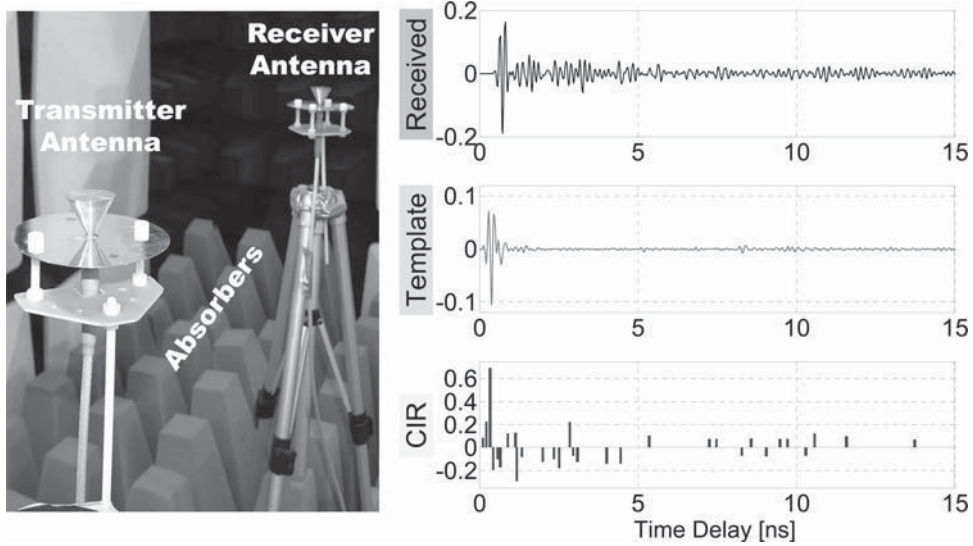
Fig. 11 *Anechoic chamber configuration (left-hand side) and a sample of post-processing of the measured data (right-hand side)*

measurements were repeated but the variation of delay parameters were found to be negligible.

Next, multipath intensity profiles are obtained by deconvolving the received signals with the input template using the modified CLEAN algorithm. A sample of the post processing of data is shown in Fig. 11 [right-hand side]. The entire data set and the post-processing software will be made available at our project documentation webpage [36].

For most of the recorded data sets an energy capture ratio, as denoted in (9), of 60% to 75% is obtained. An interesting fact in this connection is that the ECR does not improve when the threshold ($\mathcal{T}$) is lowered, as one would expect. The dynamic range given by (10), however, increses linearly with the threshold. For the parameter values mentioned in Section 3.2, a dynamic range of about 20 dB is achieved.

4 Results

4.1 Power delay profile

The CIR profiles ($\hat{h}[n]$) obtained after the post-processing via CLEAN can be utilised to construct the PDP which is a squared-magnitude version of the impulse response. The

normalised PDP is calculated from the following relation

$$P(\tau) = \frac{|\hat{h}[n]|^2}{\sum_n |\hat{h}[n]|^2} \qquad (17)$$

In Fig. 12, a typical intra car PDP under LoS condition is depicted. The first arriving multipath component is the strongest one which represents the direct LoS transmission. The time scale is adjusted so that this path has zero excess delay ($\tau_0 = 0$). The PDP decays fast and has a maximum excess delay of 13.55 ns for a 20 dB threshold. The mean excess delay and the RMS delay spread (defined in the next section) values are also comparatively small.

Fig. 13 shows PDPs when the direct path is obstructed by the seats. We have performed three consecutive measurements keeping the Tx and Rx antenna positions fixed. All the three measurements exhibit peaks at same delay instants. This is somewhat expected because when the car is parked (static condition), the relative positions of reflectors and scatterers do not change much, and the wireless channel in the passenger compartment appears 'stationary' with respect to time. When compared with Fig. 12, one can find that for nLoS condition, the first arriving path is no longer the strongest path and the PDP decays at a lower rate.

From both Figs. 12 and 13, dominant multipaths can be identified easily. The amplitudes of the dominant paths decay exponentially
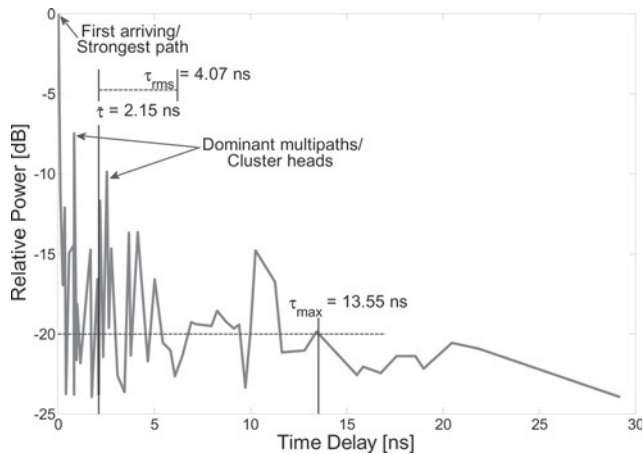
Fig. 12 *PDP for in-vehicle wireless channel under LoS condition (Tx antenna position: L_2, Rx antenna position: D and Tx-Rx distance is 0.97 m)*
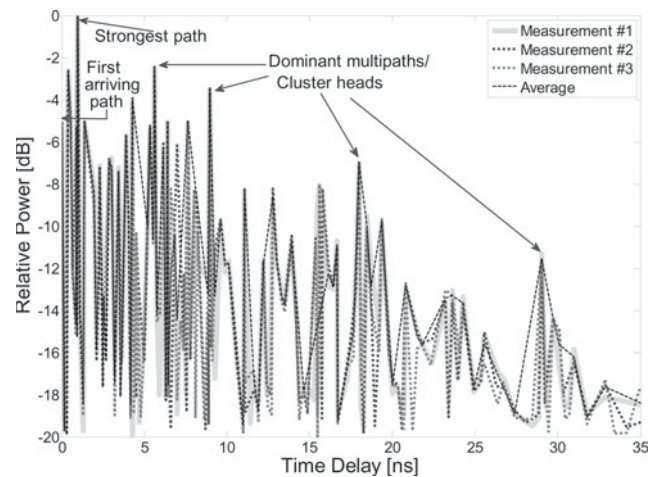
Fig. 13 *PDP for in-vehicle wireless channel under nLoS condition (Tx antenna position: L_1, Rx antenna position: P_3 and Tx-Rx distance is 1.68 m)*
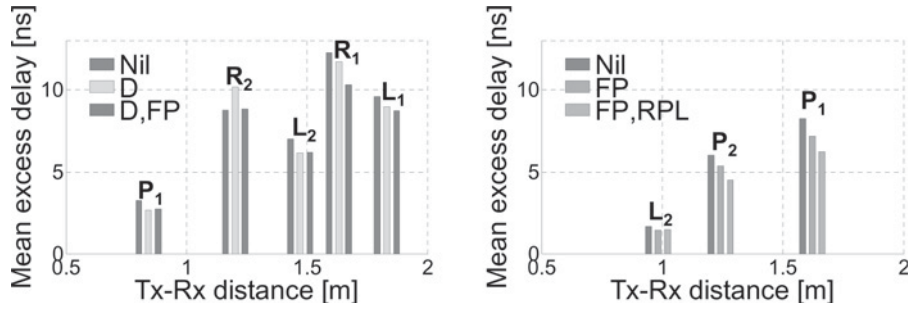
Fig. 14 *Mean excess delay with varying passenger occupancy when Rx antenna is positioned at RPR (left-hand side) and D (right-hand side)*

Bar group top markings denote Tx antenna position
Passenger occupancy legends – D: driver, FP: front passenger, RPL: rear passenger on left-hand side

along the delay axis and multiple other paths exist between two successive dominant peaks. Considering these dominant paths as cluster heads (first path of a multipath cluster) and considering the paths in-between as rays within a cluster, the channel can be characterised following a S–V model. Different parameters for the S-V model such as cluster amplitude, path amplitude, inter-cluster delay, inter-path delay etc. have been derived extensively in [16] and are not repeated here. The observation is, however, very important as it validates our choice of simulation testbed which is also constructed using a S-V model.

The PDP may be exploited to gain other useful information as well. For example, it is possible to extract a tap-delay model (table of tap gains at different tap delays) by sampling the PDP. Next, utilising the table, one may simulate the bit error rate as demonstrated in [49]. It must be noted here that only large scale decaying trend of the PDP is generally considered for such calculations. In another work [50], we have shown that the large scale variation of the PDP for intra-vehicle UWB propagation follows a two-part exponentially decaying function representing the dominant paths and the reverberant diffuse tail. It was also demonstrated that the generalised extreme value distribution serves as a good fit for modelling the small-scale variations.

4.2 Time delay parameters

Analysis of PDP is interesting when one compares LoS and nLoS links but we failed to gain much insight from PDPs regarding the effect of passenger occupancy. This lead us to concentrate on the two most common time dispersive quantities that characterise a wideband multipath channel [51], the 'mean excess delay' ($\bar{\tau}$) and the root mean square (RMS) 'delay spread' (τ_{rms}), which are defined as follows

$$\bar{\tau} = \frac{\sum_n \tau_n |\hat{h}[n]|^2}{\sum_n |\hat{h}[n]|^2} \tag{18}$$

and

$$\tau_{rms} = \sqrt{\frac{\sum_n \tau_n^2 |\hat{h}[n]|^2}{\sum_n |\hat{h}[n]|^2} - \left[\frac{\sum_n \tau_n |\hat{h}[n]|^2}{\sum_n |\hat{h}[n]|^2}\right]^2}$$
$$= \sqrt{\mathbb{E}\{(\tau_n - \bar{\tau})^2\}} \tag{19}$$

where τ_n and $\hat{h}[n]$ are the excess delay and gain associated with the nth path of the estimated CIR, respectively, and $\mathbb{E}\{\cdot\}$ is the expectation operator. The mean excess delay and the RMS delay spread can be derived from the first moment and second central moment of the average PDP. Sometimes, the RMS delay spread measure is considered to be more fundamental as it is not much susceptible to apparatus settings and synchronisation. Moreover, it helps in calculating the maximum data rate attainable without inter-symbol interference (ISI). As a rule of thumb, serious ISI is likely to occur at the receiver (without equaliser) when the symbol duration is less than ten times of the RMS delay spread [16].

Figs. 14 and 15 plots the mean excess delay and RMS delay spread, respectively, against the Tx-Rx 'distance'. Both figures display a weak correlation between distance and delay values, and it is difficult to reach to a clear conclusion. Viewed from another angle, it may be said that the delay parameters do not necessarily increase with distance and the most remote wireless user (with respect to the access point) will not necessarily have the worst quality of service.

More importantly, the figures (Figs. 14 and 15) also exhibit the effect of 'passenger occupancy'. Considering the bar groups, we find that the decrease in mean delay and delay spread values with increased passenger occupancy is consistent. The reduction reflects that fewer MPCs are available because of obstruction and absorption of several MPCs by the human body. The lower values of τ_{rms} with more passengers on-board is very promising for design engineers, because the data rate demand will increase with the number of passengers, and the channel characteristics display
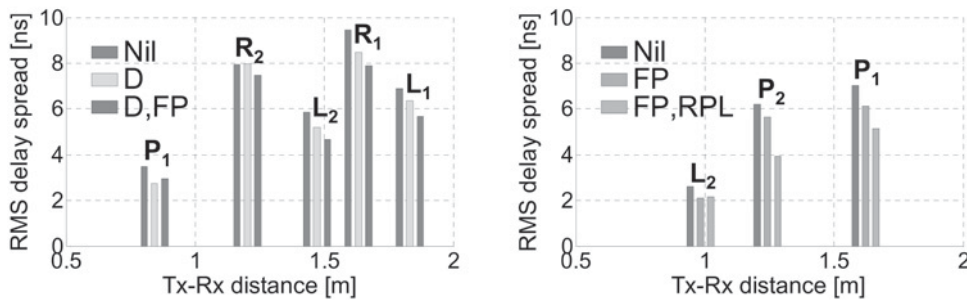
Fig. 15 *RMS delay spread with varying passenger occupancy when Rx antenna is positioned at RPR (left-hand side) and D (right-hand side)*

Bar group top markings denote Tx antenna position
Passenger occupancy legends – D: driver, FP: front passenger, RPL: rear passenger on left-hand side

that this demand can be met, at least theoretically, by employing adaptive modulation and/or coding.

Finally, we studied how the presence of a direct LoS path affects these two delay parameters. When we compare the data set for the following Tx-Rx pair namely, L_1-D (LoS, 1.18 m) and R_2-RPR (nLoS, 1.19 m), we find that the delay parameters (mean and RMS spread) for the nLoS situations are notably 'larger' than that of the LoS scenarios at an equivalent Tx-Rx distance. The reason behind this is the increased number of reflections, as well as signal attenuation, that is incurred in the nLoS case.

5 Conclusions and future work

In this paper, we compared two versions of the CLEAN algorithm for time domain deconvolution. The efficacy of the modified CLEAN algorithm over the basic version is established through statistical measures. Next, the modified algorithm was used to estimate the CIR in an intra-vehicular UWB channel sounding experiment.

The presence of clusters in the PDPs, obtained after post-processing of channel measurement data, validates the S–V assumptions. PDPs also indicated that the passenger compartment wireless channel is time-stationary, when the vehicle is parked.

The time delay parameters obtained from the experimental data were utilised to study the effects of passenger occupancy, Tx-Rx distance and obstruction of LoS path on intra-vehicle wireless channel parameters. The results show that while the mean excess delay and the RMS delay spread are weakly dependent on the antenna separation, they decrease linearly with passenger occupancy. Further, delay parameter values are considerably smaller when a direct LoS path is present.

The observations in the present text are solely based on the data obtained for the static condition. Currently we are collecting data for a variety of alternate conditions, namely when the engine is turned on, or when the vehicle is moving. It will be interesting to find whether similar trends for delay parameters also exist under all these conditions. Further, a pulse compression based time domain channel sounding system has been recently developed at VUT which provides a higher dynamic range because of the inherent correlation gain. We would like to study the suitability of the modified CLEAN algorithm for the new setup.

6 Acknowledgment

7 References

1 Tuohy, S., Glavin, M., Hughes, C., Jones, E., Trivedi, M., Kilmartin, L.: 'Intra-vehicle networks: a review', *IEEE Trans. Intell. Trans. Syst.*, 2014, pp. 1–12, doi: 101109/TITS20142320605

2 Held, G.: 'Inter- and intra-vehicle communications' (Auerbach, Boca Raton, NY, USA, 2008)

3 Nobuhiro, F., Masayoshi, M., Atsuo, I., Masami, G.: 'Intra-and inter-vehicle communication network using low-cost POF links', *IEICE Trans. Inf. Syst. Tech.*, 2002, **E85-D**, (11), pp. 1839–1850

4 Kim, J.Y., Choi, H.K.: 'An enhanced security protocol for VANET-based entertainment services', *IEICE Trans. Commun.*, 2012, **E95-B**, (7), pp. 2245–2256

5 Ahmed, M., Saraydar, C.U., ElBatt, T., Jijun, Y., Talty, T., Ames, M.: 'Intra-vehicular wireless networks'. Proc. IEEE GLOBECOM, Washington DC, USA, 2007, pp. 1–9

6 Hatamoto, H., Ano, S., Kikuchi, N., Shimizu, S.: 'An evaluation of transmission performance for wireless harness systems using propagation models in an automobile engine compartment'. Proc. IEEE PIMRC, London, UK, 2013, pp. 117–121

7 Ohira, M., Umaba, T., Kitazawa, S., Ban, H., Ueba, M.: 'Experimental characterization of microwave radio propagation in ICT equipment for wireless harness communications', *IEEE Trans. Antennas Propag.*, 2011, **59**, (12), pp. 4757–4765

8 Saghir, H., Nerguizian, C., Laurin, J.J., Moupfouma, F.: 'In-cabin wideband channel characterization for WAIC systems', *IEEE Trans. Aerosp. Electron Syst.*, 2014, **50**, (1), pp. 516–529

9 Hamada, S., Tomiki, A., Toda, T., Kobayashi, T.: 'Wireless connections within spacecrafts to replace wired interface buses'. Proc. IEEE AERO, Big Sky, Montana, USA, 2013, pp. 1–9

10 Takahashi, K., Udagawa, T., Zhang, H., Arita, T., Nakagawa, M.: 'Intra-vehicle wireless 1394 system', *IEICE Trans. Commun.*, 2002, **E85-B**, (5), pp. 938–945

11 Sipal, V., Gelabert, J., Allen, B., Stevens, C., Edwards, D.: 'Frequency-selective fading of ultrawideband wireless channels in confined environments', *IET Microw. Antennas Propag.*, 2011, **5**, (11), pp. 1328–1335

12 Demir, U., Bas, C.U., Ergen, S.C.: 'Engine compartment UWB channel model for intravehicular wireless sensor networks', *IEEE Trans. Veh. Tech.*, 2014, **63**, (6), pp. 2497–2505

13 Li, B., Zhao, C., Zhang, H., Sun, X., Zhou, Z.: 'Characterization on clustered propagations of UWB sensors in vehicle cabin: measurement, modeling and evaluation', *IEEE Sensors J.*, 2013, **13**, (4), pp. 1288–1300

14 Bas, C.U., Ergen, S.C.: 'Ultra-wideband channel model for intra-vehicular wireless sensor networks beneath the chassis: from statistical model to simulations', *IEEE Trans. Veh. Tech.*, 2013, **62**, (1), pp. 14–25

15 Bellens, F., Quitin, F., Dricot, J.M., Horlin, F., Benlarbi-Delaï, A., Doncker, P.D.: 'A wideband channel model for intravehicular nomadic systems', *Int. J. Antennas Propag.*, 2011, **2011**, (468072), pp. 1–9

16 Niu, W., Li, J., Talty, T.: 'Ultra-wideband channel modeling for intravehicle environment', *EURASIP J Wirel. Commun. Net.*, 2009, **2009**, (806209), pp. 1–12

17 Nakamura, R., Kajiwara, A.: 'Empirical study on 60 GHz in-vehicle radio channel'. In: Proc. IEEE RWS, Santa Clara, CA, USA, 2012, pp. 327–330

18 Sawada, H., Tomatsu, T., Ozaki, G., *et al.*: 'A sixty GHz intra-car multi-media communications system'. Proc. IEEE VTC, Barcelona, Spain, 2009, pp. 1–5

19 Blumenstein, J., Mikulasek, T., Marsalek, R., Prokes, A., Zemen, T., *et al.*: 'In-vehicle mm-wave channel model and measurement'. Proc. IEEE VTC, Vancouver, Canada, 2014, pp. 1–6

20 Kato, A., Sato, K., Fujise, M., Kawakami, S.: 'Propagation characteristics of 60-GHz millimeter waves for ITS inter-vehicle communications', *IEICE Trans. Commun.*, 2001, **E84-B**, (9), pp. 2530–2539

21 Di Benedetto, M.G., Giancola, G.: 'Understanding ultra wide band radio fundamentals' (Prentice Hall, New Jersey, NY, USA, 2004)

22 Suzuki, Y., Kobayashi, T.: 'Ultra wideband signal propagation in desktop environments', *IEICE Trans. Fundam.*, 2005, **E88-A**, (9), pp. 2272–2278

23 Dezfooliyan, A., Weiner, A.M.: 'Evaluation of time domain propagation measurements of UWB systems using spread spectrum channel sounding', *IEEE Trans Antennas Propag.*, 2012, **60**, (10), pp. 4855–4865

24 Molisch, A.F.: 'Wireless communications' (John Wiley & Sons, West Sussex, England, 2011, 2nd edn.)

25 Candés, E.J., Fernandez-Granda, C.: 'Towards a mathematical theory of super-resolution', *Commun. Pure Appl. Math.*, 2014, **67**, (6), pp. 906–956

26 Clark, B.G.: 'An efficient implementation of the algorithm 'CLEAN'', *Astron. Astrophys.*, 1980, **89**, (3), pp. 377–378

27 Yang, W., Zhang, N.: 'A new multi-template CLEAN algorithm for UWB channel impulse response characterization'. Proc. IEEE ICCT, Guilin, China, 2006, pp. 1–4

28 Muqaibel, A., Safaai-Jazi, A., Woerner, B., Riad, S.: 'UWB channel impulse response characterization using deconvolution techniques'. Proc. IEEE MWSCAS, Tulsa, OK, USA, 2002, vol. 3, pp. 605–608

29 Kobayashi, T.: 'Measurements and characterization of ultra wideband propagation channels in a passenger-car compartment', *IEICE Trans. Fundam.*, 2006, **E89-A**, (11), pp. 3089–3094

30 Kobayashi, T.: 'Measurements and characterization of ultra wideband propagation channels in a passenger-car compartment'. Proc. IEEE ISSSTA, Manaus, Amazon, Brazil, 2006, pp. 228–232

31 Katayama, Y., Tearsaka, K., Higashikatsuragi, K., Matsunami, I., Kajiwara, A.: 'Experimental evaluation of in-vehicle UWB radio propagation characteristics', *IEICE Trans. Fundam.*, 2006, **J89-B**, (9), pp. 1815–1819

32 Chandra, A., Blumenstein, J., Mikulasek, T., *et al.*: 'CLEAN algorithms for intra-vehicular time-domain UWB channel sounding'. Proc. PECCS, Angers, France, 2015, pp. 224–229

33 Santos, T., Karedal, J., Almers, P., Tufvesson, F., Molisch, A.F.: 'Scatterer detection by successive cancellation for UWB – method and experimental verification'. Proc. IEEE VTC, Singapore, 2008, pp. 445–449

34 Feder, M., Weinstein, E.: 'Parameter estimation of superimposed signals using the EM algorithm', *IEEE Trans. Acoust. Speech Signal Process.*, 1988, **36**, (4), pp. 477–489

35 Fleury, B.H., Tschudin, M., Heddergott, R., Dahlhaus, D., Pedersen, K.I.: 'Channel parameter estimation in mobile radio environments using the SAGE algorithm', *IEEE J. Sel. Areas Commun.*, 1999, **17**, (3), pp. 434–450

36 Department of Radio Electronics, Faculty of Electrical Engineering and Communication, Brno University of Technology. Research into wireless channels for intra-vehicle communication and positioning, GACR-13-38735S:

Project documentation page. URL: http://www.radio.feec.vutbr.cz/GACR-13-38735S/

37 Federal Communications Commission. Revision of Part 15 of the Commission's Rules Regarding Ultra-Wideband Transmission Systems: First report and order; 2002. FCC 02-48. URL: www.fcc.gov/Bureaus/Engineering Technology/Orders/2002/fcc02048.pdf

38 Ghavami, M., Michael, L.B., Kohno, R.: 'Ultra wideband signals and systems in communication engineering' (John Wiley & Sons, West Sussex, England, 2007, 2nd edn.)

39 Blumenstein, J., Prokeš, A., Mikulášek, T., Maršálek, R., Zemen, T., Mecklenbräuker, C.: 'Measurements of ultra wide band in-vehicle channel – statistical description and TOA positioning feasibility study', *EURASIP J Wirel. Commun. Net.*, 2015, **2015**, (104), pp. 1–15

40 Taniguchi, T., Maeda, A., Kobayashi, T.: 'Development of an omnidirectional and low-VSWR ultra wideband antenna', *Int J Wirel. Opt. Commun.*, 2006, **3**, (2), pp. 145–157

41 Sarkar, T.K., Tseng, F.I., Rao, S.M., Dianat, S.A., Hollmann, B.Z.: 'Deconvolution of impulse response from time-limited input and output: Theory and experiment', *IEEE Trans. Instrum. Meas.*, 1985, **IM-34**, (4), pp. 541–546

42 Yang, L.: 'The applicability of the tap-delay line channel model to ultra wideband'. MS Thesis, Virginia Polytechnic Institute and State University, Blacksburg, VA, USA, 2004

43 Vaughan, R.G., Scott, N.L.: 'Super-resolution of pulsed multipath channels for delay spread characterization', *IEEE Trans Commun.*, 1999, **47**, (3), pp. 343–347

44 Liu, T.C.K., Kim, D.I., Vaughan, R.G.: 'A high-resolution, multi-template deconvolution algorithm for time-domain UWB channel characterization', *Can. J. Electr. Comput. Eng.*, 2007, **32**, (4), pp. 207–213

45 Molisch, A.F., Je_rey, R.F., Marcus, P.: 'Channel models for ultrawideband personal area networks', *IEEE Wirel. Commun.*, 2003, **10**, (6), pp. 14–21

46 Kulhandjian, H., Melodia, T.: 'Modeling underwater acoustic channels in short-range shallow water environments'. In: ACM WUWNet, Rome, Italy, 2014, pp. 1–5

47 Simard, R., L'Ecuyer, P.: 'Computing the two-sided Kolmogorov-Smirnov distribution', *J. Stat. Softw.*, 2011, **39**, (11), pp. 1–18

48 Liu, L., Wang, Y., Zhang, Y.: 'Ultrawideband channel measurement and modeling for the future intravehicle communications', *Microw. Opt. Tech. Lett.*, 2012, **54**, (2), pp. 322–326

49 Kukolev, P., Chandra, A., Mikulasek, T., Prokes, A., Zemen, T., Mecklenbrauker, C.: 'In-vehicle channel sounding in the 5.8 GHz band', *EURASIP J. Wirel. Commun. Net*, 2015, **2015**, (57), pp. 1–9

50 Blumenstein, J., Mikulasek, T., Marsalek, R., *et al.*: 'In-vehicle UWB channel measurement, model and spatial stationarity'. In: IEEE VNC, Paderborn, Germany, 2014, pp. 77–80

51 Maas, D., Firooz, M.H., Zhang, J., Patwari, N., Kasera, S.K.: 'Channel sounding for the masses: Low complexity GNU 802.11b channel impulse response estimation', *IEEE Trans. Wirel. Commun.*, 2012, **11**, (1), pp. 1–8

Effects of vehicle vibrations on mm-wave channel: Doppler spread and correlative channel sounding

Jiri Blumenstein, Josef Vychodil, Martin Pospisil, Tomas Mikulasek, Ales Prokes

Effects of Vehicle Vibrations on mm-Wave Channel: Doppler Spread and Correlative Channel Sounding

Jiri Blumenstein, Josef Vychodil, Martin Pospisil, Tomas Mikulasek, Ales Prokes,
The Faculty of Electrical Engineering and Communication
Brno University of Technology, Czech Republic
email: blumenstein@feec.vutbr.cz, web: http://www.radio.feec.vutbr.cz/GACR-13-38735S/

Abstract—This paper deals with evaluating the effect of vehicle vibrations on the mm-wave intra-vehicular channel. As some of the vehicles' vibration amplitude may reach the order of millimeters, i.e., the amplitude is comparable with the mm-wave wavelength ($\approx$5 mm), it can produce severe Doppler spreads.

This paper evaluates Doppler spreads utilizing a mm-wave time-domain correlative channel sounder built into a vehicle which has been driven at different speeds on a variety of roads with a broad spectrum of surface quality.

I. INTRODUCTION

The aging population, densification of current traffic and the fundamental demand for safe and reliable transportation has prepared an interesting market opportunity for automated vehicles [1], [2]. It has, however, been recently recognized that the attempts of bringing at least some of the desired functionalities of the smart/automated driving in the form of vehicle-to-vehicle (V2V) communication based on IEEE 802.11p are not quite satisfactory, namely due to the bandwidth and physical layer constraints [3].

The authors in [4] state that the only viable solution for high bandwidth connected vehicles is the millimetric (mm-wave) band. The mm-wave band is usually understood to occupy the frequency range from 55 GHz to 65 GHz. This band provides around 10 GHz of unlicensed bandwidth (depending on the local spectrum management authorities), but it also suffers from high path-loss due to atmospheric absorption. On the other hand, the mm-band enables the usage of high-gain steerable antennas in a small physical form allowing for beamforming, beamsteering or spatial multiplexing [5], [6].

In the field of intra-vehicular channel characterization, there is a number of publications dealing with comparing different frequency bands [7], providing mm-wave channel models and spatial maps [8], [9] or channel stationarity [10]. Not only the passenger compartment is measured, but also for example the engine bay [11]. Also, the frequency domain channel sounding, which has been used in all mentioned publications, is discussed in detail in [12].

One of the rarely addressed issues of the vehicular high bandwidth communication in the mm-wave band is the effect of vibrations. Vibrations are caused by many reasons, for example, bad road conditions with potholes can cause car body relative movements and twisting. Also, the engine produces a variety of vibrations depending on many variables such as its revolutions per minute, temperature et cetera. On top of that,

the vehicle's sound system is also recognized as a source of vibrations.

Now, the typical wavelength of the mm-wave band is around 5 mm and since the amplitude of the vibrations could be in millimeters [13], the Doppler spread caused by this movement could significantly impair any communication system operating in the said conditions.

This paper deals with the characterization of the intra-vehicular radio propagation (i.e., channel characterization) in the frequency range of 55-65 GHz.

A. Contribution of the paper

- The main objective is to evaluate the Doppler spread caused by the vibrations of the vehicle when in operation. The operating conditions are characterized by the vehicle velocity and a subjective index of the road condition.
- The channel impulse response (CIR) characterization in terms of delay spread and exponentially decaying model parametrization.
- We present a mm-wave correlative time-domain channel sounder built from off-the-shelf parts and measurement devices.

II. CORRELATIVE CHANNEL SOUNDING

This section is divided into three subsections. First, we briefly state the time-variant channel parameters, then the theoretical principle of the correlative time-domain channel sounding and finally we provide a specific measurement setup description including a block scheme of the in-house built channel sounder (Fig. 1).

A. Time-variant channel parameters

The impulse response of a linear time-variant channel with P propagation paths is written as [14]:

$$h(t,\tau) = \sum_{p=1}^{P(t)} \alpha_p(t) e^{j2\pi f_{D,p} t} \delta\left(\tau - \tau_p(t)\right), \qquad (1)$$

where $f_{D,p}$ is the Doppler shift, $\alpha_p(t)$ is the complex attenuation and $\tau_p(t)$ is the time delay associated with the p-th path. Next, in order to characterize the time-frequency dispersion of the channel, authors in [15] defined a useful metric, namely the *delay-Doppler spreading function*, written as:
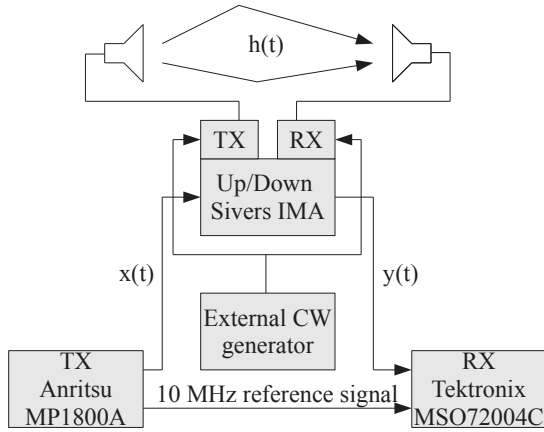
Fig. 1: Block scheme of the time-domain correlative channel sounder based on a m-sequence generator, a matched receiver, an up/down converter and a stable external RF source.

$$S(\tau, f_{\mathrm{D}}) = \int_{-\infty}^{\infty} h(t, \tau) e^{-j2\pi f_{\mathrm{D}} t} dt. \tag{2}$$

While sacrificing the possibility of observing the Doppler effects development in the delay domain, by averaging the delay-Doppler spreading function over the delays, we significantly improve the signal to noise ratio (SNR). Thus, the vibration effect becomes more evident. The averaging is done according to:

$$\bar{S}(f_{\mathrm{D}}) = \frac{1}{\tau_{\mathrm{m}}} \sum_{\tau}^{\tau_{\mathrm{m}}} S(\tau, f_{\mathrm{D}}), \tag{3}$$

where τ_{m} is the maximal excess delay. We denote $\bar{S}(f_{\mathrm{D}})$ as the Doppler spectrum.

The delay-Doppler spreading function allows us to observe the Doppler spread which is caused not only by the vibrations of the vehicle, but also by other moving objects inside the car. Let us point out that the attenuation of the car body and windows is in the order of tens of decibels and the dynamic range of the channel sounder is rather limited, so we do not consider reflectors or scattered objects outside the car to introduce any resolvable effects in the obtained data.

B. Theoretical principle of the correlative channel sounder

Apart from other possible solutions of the time-domain channel sounding (e.g., listed in [14]), we employ a method which utilizes an m-sequence [16] which relates to the family of pseudo-noise sequences. The autocorrelation of the m-sequence designated as R_{xx} is in fact a sharp triangle function, however, for our purpose we can write $R_{xx} \approx \delta(\tau)$.

Now, let us consider a simple input-output relation:

$$y(t) = h(t) \otimes x(t), \tag{4}$$

where $y(t)$ is the signal captured by the channel sounder, $h(t)$ is the CIR, $x(t)$ stands for the transmitted m-sequence and finally $\otimes$ represents the convolution.

Applying the fact that the index of the transmitted m-sequence is known to the receiver, the receiver is able to estimate the CIR from the cross-correlation of the transmitted and received signals $x(t)$ and $y(t)$ respectively because it holds that:

$$R_{xy}(\tau) = \mathbb{E}\left[x^*(t)y(t)\right] = h(t) \otimes R_{xx}(\tau) \approx$$
$$\approx h(t) \otimes \delta(\tau) = h(t). \tag{5}$$

In order to avoid systematic measurement errors and to be able to accept the approximate relation (5), the channel sounder as well as the sounding environment shall fulfill the conditions listed in [17].

C. Measurement setup

1) Measurement site description: During the measurement campaign, we have utilized a typical European passenger vehicle, Skoda Octavia 2, equipped with a two-liter diesel engine. The photographs from the measurement campaign are in Figure 3.

The presented measurement campaign consists of numerous channel measurements performed inside the car, while the car was in motion. For each channel snapshot, we have recorded the actual speed. Moreover, utilizing a subjective three-step metric, the quality of the road was assessed by the driver of the vehicle (i.e., for each channel measurement, we have an index evaluating the "bumpiness" of the actual road).

2) Antennas: The WR15 open-ended waveguide antennas were used at both the RX and TX side with radiation patterns depicted in Figure 2. While the TX antenna and the power amplifier (PA) were mounted on the side-window next to the rear passenger on the right hand side (see Fig. 3b), the RX antenna, the up/down converter and the low-noise amplifier (LNA) were mounted approximately in the middle of the dashboard (see Fig. 3c). The antennas were fastened utilizing suction caps.
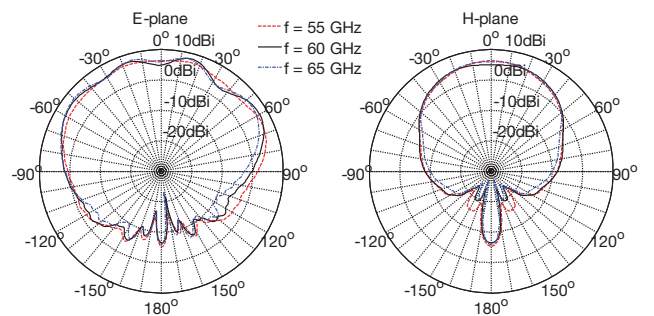
Fig. 2: Measured gain pattern of the open-ended waveguide in the E–plane and the H–plane for 55-65 GHz.

3) Measurement devices: The block scheme of the in-house built channel sounder composed of the off-the-shelf components is visible in Figure 1.

The measurement setup consisted of the Anritsu Signal Quality Analyzer MP1800A for generating the m-sequences with data rate 12.5 Gbit/s and 13 dBm output power. The
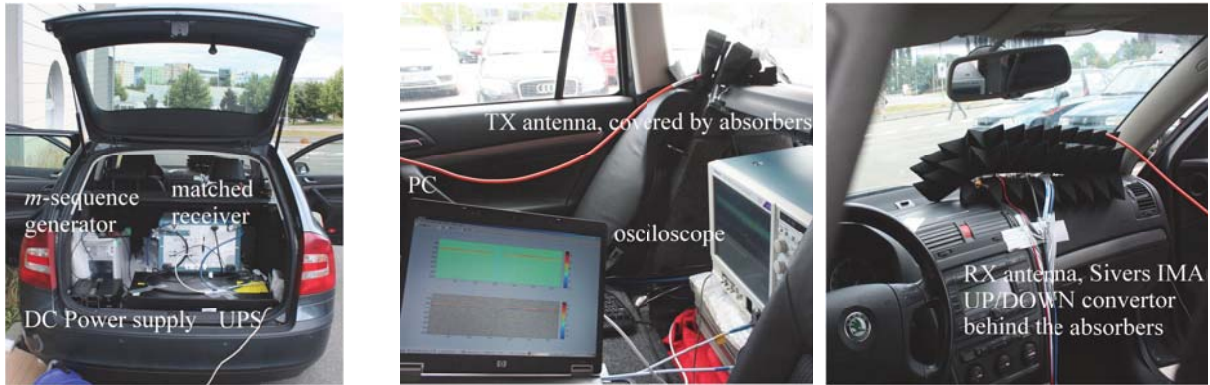
(a) The trunk of the vehicle used for the measurement campaign with UPS ensuring circa 1 hour of operation and DC power supply for LNA and PA.

(b) View from the back seat. The TX antenna is mounted using a suction cap on the side window. The PA and the TX antenna are covered by absorbers.

(c) The view from the drivers seat. Behind the absorbers on the dashboard is the RX part with both the up/down converter and the LNA.

Fig. 3: Photographs taken during the measurement campaign.

oscilloscope Tektronix MSO72004C was used as the matched receiver with 16 GHz bandwidth and 50 GS/s sampling frequency. The dynamic range was extended with the low-noise and power amplifiers QuinStar QLW-50754530-I2 and QPW-50662330 respectively. We also utilized the Sivers IMA FC1003V/01 up and down converter to shift the signal to the band of interest 55 - 65 GHz.

4) Real-time data processing: The length of the m-sequences was determined by the relation $N = 2^k - 1$, where N is the m-sequence length and k is the order of the m-sequence. Through this work, we chose $k = 11$, thus $N = 2047$.

Now, considering that the internal memory of the oscilloscope is 31.25 MS and employing 50 GS/s sampling frequency, we were able to capture 0.625 ms of the transmitted signal into the fast internal memory of the oscilloscope (this represents more than 3000 CIRs snapshot for one measurement). Between each channel snapshot, there is a 1 ms pause. Then, data was uploaded to a PC for post-processing and further measurements could be performed.

III. RESULTS

This sections provides the post-processing results of the measured data from the obtained CIRs as well as the evaluated Doppler spreads.

A. Doppler spread

As depicted in the cutout in Figure 4, the Doppler spread was determined as the spread of the main peak of the Doppler spectra $\bar{S}(f_D)$ exactly 1 dB above the noise floor. The noise floor has been determined as the mean value of $\bar{S}(f_D)$ while not taking into account the vicinity of $\bar{S}(0)$.

An important thing to point out is that we have also performed calibration measurements in a laboratory without the presence of any known vibrations. The result of this measurement is depicted in Fig. 4 in red color. This was done mainly in order to identify possible impairments of the
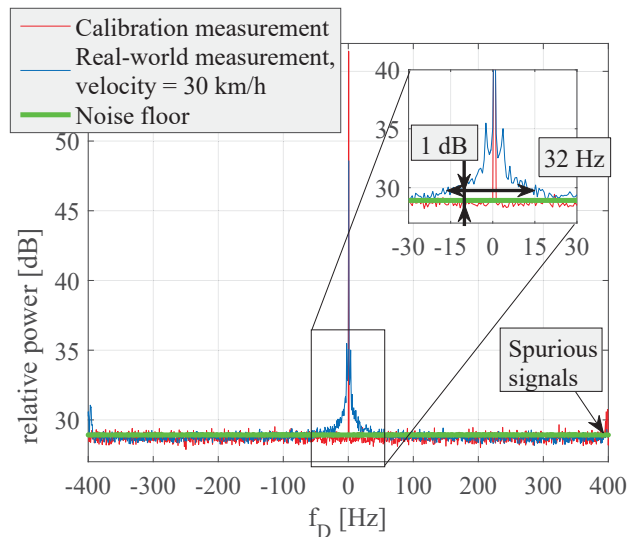
Fig. 4: Comparison of two Doppler spectra. One is estimated while the vehicle was in motion (30 km/h) and the second is from the calibration measurement performed in a laboratory (without vibrations). The cutout on the upper right corner demonstrates how we evaluated the Doppler spread (in this case 32 Hz).

channel sounder. It is visible, that spurious signals are 30 dB weaker compared to the main peak around $\bar{S}(0)$. Moreover, all datasets have been visually inspected such that no spurious signals could affect the results.

In Figure 5 we plot the estimated Doppler spread as the function of the vehicle speed. We also distinguish between the road quality, which has been evaluated via a subjective three-step index (a smooth road, a semi-smooth road and a bumpy road). The road quality was assessed by the driver of the vehicle.

As is seen in Figure 5, on the roads with the worst quality, we have reached only limited speeds between 15-50 km/h. The estimated Doppler spread on the worst roads exhibits a mean value of 37 Hz.

On the semi-smooth roads, with speeds from 80 km/h to 160 km/h, we have recorded a mean Doppler spread of 38.6 Hz and on the smooth roads with the same speeds, the mean Doppler spread is 37.7 Hz. Please note, that in Figure 5, there is plotted a mean Doppler spread for all speeds and road quality indexes together with its standard deviation 12 dB.
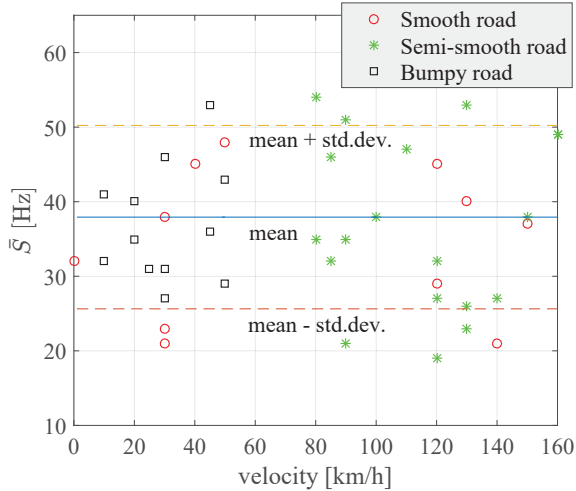
Fig. 5: Comparison of the Doppler spread for various road conditions and velocities. The mean and the standard deviation of the Doppler spread are depicted.

B. Delay domain

As an example, in Figure 6 we plot 100 CIRs recorded during a ride at 30 km/h on a bumpy road. The maximal excess delay across all the captured CIRs is around 1 ns. In literature (e.g., [8]), there are higher values reported, but this is due to the limited dynamic range of the time-domain sounder. Frequency domain channel sounders usually provide notably higher dynamic range, but they can not capture fast channel variations. The measured CIRs are parametrized by the exponentially decaying model as:

$$h(\tau) = \exp\left(\frac{-\tau}{0.37 \text{ ns}}\right) \qquad (6)$$

In Figure 1 we also plot a mean CIR (black curve) calculated as the average of the 100 CIRs plotted in gray. In the mean CIR, one can observe several (four or five) multi-path component (MPC) clusters.

IV. CONCLUSION

Although the vibrations caused by this specific vehicle or its engine may differ from other vehicles on the market, we believe that this evaluation provides reasonable insight on the values of the achieved Doppler spreads occurring in a
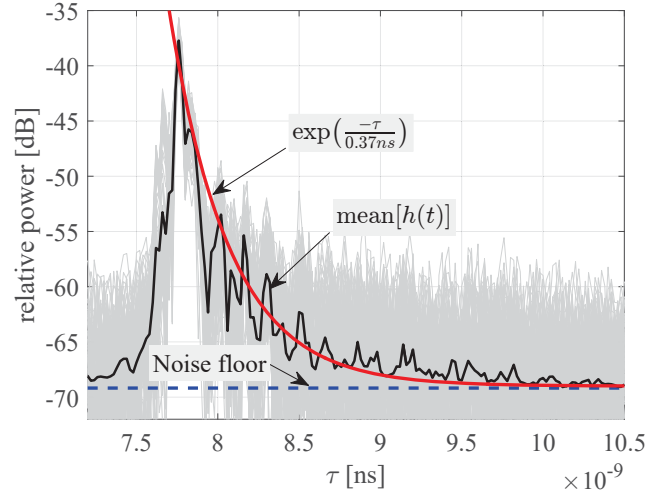
Fig. 6: Example of the measured data. There are 100 measured CIRs depicted in gray. This measurement was performed at 30 km/h on a bumpy road. The decay of the resolvable MPCs clusters is modeled by an exponentially decaying process.

typical in-vehicle environment. We have captured around 30 recordings of the CIRs in a variety of road conditions and speeds (each consisting of more than 3000 individual CIR snapshots).

We compare the vibration-free calibration measurement with the measurement of the vehicle in operation. The estimated mean Doppler spread reaches up to 38 Hz. On the other hand, it is evident that neither the vehicle speed nor conditions of the road has a significant effect on the Doppler spread of the mm-wave in-vehicle channel.

In the delay domain, we have characterized the obtained CIRs by the exponential decay process. Although the dynamic range of the correlative channel sounders is rather limited (compared to the frequency domain method), we see approximately four resolvable clusters of the MPCs.

To enhance the reproducibility of our research, we provide representative datasets from our measurement for free on our web pages: http://www.radio.feec.vutbr.cz/GACR-13-38735S/

REFERENCES

[1] C. Sommer and F. Dressler, *Vehicular Networking*. Cambridge University Press, 2014.

[2] N. Lu, N. Cheng, N. Zhang, X. Shen, and J. Mark, "Connected vehicles: Solutions and challenges," *IEEE Journal Internet of Things*, vol. 1, no. 4, pp. 289–299, Aug 2014.

[3] Z. Xu, L. Bernad, M. Gan, M. Hofer, T. Abbas, V. Shivaldova, K. Mahler, D. Smely, and T. Zemen, "Relaying for IEEE 802.11p at road intersection using a vehicular non-stationary channel model," in *2014 IEEE 6th International Symposium on Wireless Vehicular Communications*, 2014.

[4] J. Choi, N. G. Prelcic, R. C. Daniels, C. R. Bhat, and R. W. Heath, "Millimeter wave vehicular communication to support massive automotive sensing," 2016. [Online]. Available: http://arxiv.org/abs/1602.06456

[5] E. Ben-Dor, T. Rappaport, Y. Qiao, and S. Lauffenburger, "Millimeter-wave 60 GHz outdoor and vehicle AOA propagation measurements using a broadband channel sounder," in *IEEE Global Telecommunications Conference*, Dec 2011.

[6] T. Rappaport, J. Murdock, and F. Gutierrez, "State of the art in 60-GHz integrated circuits and systems for wireless communications," *Proceedings of the IEEE*, vol. 99, no. 8, pp. 1390–1436, Aug 2011.

[7] M. Schack, M. Jacob, and T. Kurner, "Comparison of in-car UWB and 60 GHz channel measurements," in *2010 Proceedings of the Fourth European Conference on Antennas and Propagation*. IEEE, 2010.

[8] J. Blumenstein, T. Mikulasek, R. Marsalek, A. Prokes, T. Zemen, and C. Mecklenbrauker, "In-vehicle mm-wave channel model and measurement," in *Vehicular Technology Conference (VTC Fall), 2014 IEEE 80th*. IEEE, 2014, pp. 1–5.

[9] J. Blumenstein, T. Mikulasek, R. Marsalek, A. Prokes, T. Zemen, and C. Mecklenbruker, "Measurements of ultra wide band in-vehicle channel - statistical description and TOA positioning feasibility study," *EURASIP Journal on Wireless Communications and Networking*, p. 15, 2015.

[10] J. Blumenstein, T. Mikulasek, R. Marsalek, A. Chandra, A. Prokes, T. Zemen, and C. Mecklenbrauker, "In-vehicle UWB channel measurement, model and spatial stationarity," in *Vehicular Networking Conference (VNC), 2014 IEEE*. IEEE, 2014, pp. 77–80.

[11] U. Demir, C. Bas, and S. Ergen, "Engine compartment UWB channel model for intravehicular wireless sensor networks," *IEEE Transactions on Vehicular Technology*, vol. 63, no. 6, pp. 2497–2505, July 2014.

[12] A. Chandra, A. Prokes, T. Mikulasek, J. Blumenstein, P. Kukolev, T. Zemen, and C. F. Mecklenbrauker, "Frequency-domain in-vehicle UWB channel modeling," *IEEE Transactions on Vehicular Technology*, vol. PP, no. 99, 2016.

[13] S. Lakušić, D. Brčić, and V. Tkalčević Lakušić, "Analysis of vehicle vibrations–new approach to rating pavement condition of urban roads," *PROMET-Traffic & Transportation*, vol. 23, no. 6, pp. 485–494, 2011.

[14] F. Hlawatsch and G. Matz, *Wireless communications over rapidly time-varying channels*. Academic Press, 2011.

[15] P. Bello, "Characterization of randomly time-variant linear channels," *IEEE Transactions on Communications Systems*, vol. 11, no. 4, pp. 360–393, 1963.

[16] S. W. Golomb *et al.*, *Shift register sequences*. Aegean Park Press, 1982.

[17] G. Matz, A. F. Molisch, F. Hlawatsch, M. Steinbauer, and I. Gaspard, "On the systematic measurement errors of correlative mobile radio channel sounders," *IEEE Transactions on Communications*, vol. 50, no. 5, pp. 808–821, 2002.

Time-varying K factor of the mm-Wave vehicular channel: Velocity, vibrations and the road quality influence

Jiri Blumenstein, Ales Prokes, Josef Vychodil, Martin Pospisil, Tomas Mikulasek

Time-varying K factor of the mm-Wave Vehicular Channel: Velocity, Vibrations and the Road Quality Influence

Jiri Blumenstein, Ales Prokes, Josef Vychodil, Martin Pospisil and Tomas Mikulasek
The Faculty of Electrical Engineering and Communication, Brno Univ. of Technology, Czech Rep.
email: blumenstein@vutbr.cz

Abstract—**This paper evaluates real-world intra-vehicle millimeter-wave (mmWave) channel measurements performed in a vehicular environment. Utilizing a correlative time-domain channel sounder, we demonstrate the dependency of the time-varying Rician K factor on the road quality and instantaneous velocity of the measured vehicle. Vibrations caused by the movement of the vehicle together with mechanical properties of the vehicle's chassis leads to a mutual movement of the transmitting (TX) and the receiving (RX) antennas mounted on the front windshield and on the rear quarter window respectively. The channel sounding is performed in a frequency bandwidth from 59.1 GHz to 64 GHz with 50 GS/s sampling frequency.**

I. Introduction

To support a further evolution of wireless communication systems, considering that the demand for higher data rates still increases, the utilization of formerly unconventional and to some extent unused frequency bands is a precondition [1]. Recognized and promising is the millimeter-wave (mmWave) band. Orthodoxly perceived, the mmWave band spans from 30 GHz to 300 GHz. In this contribution we are however limited by our channels sounder to the frequency band from 59.1 GHz to 64 GHz. As determined by spectrum managing authorities, the mmWave band overlaps the unlicensed industrial scientific and medical (ISM) bands and thus it is remarkably attractive for both research and the industry.

Moreover, as seen by many researchers, vehicle-to-vehicle (V2V), vehicle-to-infrastructure (V2I) and in-vehicle communications may be one of the decisive features of the future cooperative self-driving vehicles [2]. Therefore, the V2V channel characterization and modeling is performed in [3], with a bandwidth of 240 MHz and 5.6 GHz carrier frequency, or with a bandwidth of 20 MHz at 2.4 GHz and 5.9 GHz carrier frequencies in [4].

In the field of in-vehicular mmWave channel characterization, there is a number of publications describing a mmWave channel stationarity [5], [6] or providing channel models and spatial maps [7]–[9]. Not only the passenger compartment is characterized, but also for example the engine bay characterization is the contribution of [10].

Now, the vehicles are often a subject of vibrations, especially while in operation. The amplitude of the vibrations could be in the order of millimeters [11] and it is therefore comparable with the aptly called mmWave wavelength. The effect of antenna vibrations is studied in [12], [13], where number of possible vibration sources is listed. Mainly, the vibrations are caused by an uneven road surface, engine speed (in revolutions per minute) or sound system of the vehicle. In [12], [13], the vibrations are related to a Doppler spread of the sounding signal.

In this contribution, we utilize the datasets introduced in [12] and we evaluate the in-vehicle line-of-sight (LOS) link vibrations influence via the variations of the K factor.

Please note that the representative datasets, more detailed information about the mmWave time-domain channel sounder is available here: http://www.radio.feec.vutbr.cz/GACR-13-38735S/

II. Measurement

In this section we provide a description of the measurement location and the in-house build (from off-the-shelf components) channel sounder together with the theoretical fundamentals of the time-domain channel sounding with correlative real-time processing.

A. Principle of the correlative channel sounder

The utilized correlative channel sounder measures the transmission channel in the time domain. Other possibility to perform the channel sounding is to utilize the frequency domain channel sounders, where the sounder usually needs some time to sweep the band of interest. Subsequently, sounder stores the channel transfer functions [14]. In the time domain channel sounding, a broadband pulse or sequence is transmitted and the need for the channel sweep time is reduced. Therefore, the time domain channel sounding is suitable for time-variant channels, which is the case of our measured scenario.

(a) The dashboard of the measurement vehicle. Behind the absorbers is the RX with both the up/down Sivers IMA converters and the LNA.

(b) The trunk of the vehicle with the UPS power supply (good for around 1 hour of operation) and DC power supply for LNA and PA.

(c) The back seat. The TX antenna is fastened on the rear quarter window using a suction cap. The PA and the is covered by absorbers.

Fig. 1: Measurement setup pictures.

The time-variant channel is described by the channel impulse response (CIR) and is written as [15]:

$$h_m(t, \tau) = \sum_{n=1}^{N(t)} \alpha_n(t) e^{j2\pi f t} \delta\left(\tau - \tau_n(t)\right), \quad (1)$$

where m is a measurement index and N is the number of propagation paths. The meaning of the measurement index is clarified in section II-B. Note that in this measurement campaign, due to the antenna installation, we ensured that the LOS components $h_{m\text{LOS}}(t, \tau)$ are always present. The summation with the multipath components (MPCs) $h_{m\text{MPC}}(t, \tau)$, i.e.:

$$h_m(t, \tau) = h_{m\text{LOS}}(t, \tau) + h_{m\text{MPC}}(t, \tau), \quad (2)$$

creates alternative formula to (1).

The correlative channel sounding usually utilizes a properties of pseudo-noise sequences. In this paper, we employ m-sequences [16] with autocorrelation R_{xx} which is, in fact, a sharp triangle function. For our purpose, however, we can simplify to $R_{xx} \approx \delta(\tau)$. Thus, it is possible to write:

$$y(t) = h(t) \otimes x(t), \quad (3)$$

where $y(t)$ is the received signal, $x(t)$ represents the transmitted m-sequence and finally $\otimes$ stands for a convolution.

Since the index of the transmitted m-sequence is known to the receiver, it is possible to estimate the CIR from the cross-correlation of the transmitted and received signals $x(t)$ and $y(t)$ respectively due to:

$$R_{xy}(\tau) = \text{E}\{x^*(t)y(t)\} = h(t) \otimes R_{xx}(\tau) \approx$$
$$\approx h(t) \otimes \delta(\tau) = h(t), \quad (4)$$

where E{} stands for the expected value operator. The approximate relation (4) is acceptable if conditions listed in [17] are met.

B. Measurement environment

We have utilized a typical European passenger vehicle, the second gen. Skoda Octavia, with a two-liter diesel engine. The pictures from the measurement campaign are shown in Figure 1.

The measurement campaign itself is consisted from number of channel measurements performed solely inside the car, while the car was in motion. For each channel recording, we have registered the instantaneous velocity. Furthermore, using a subjective three-step metric, the quality of the road was assessed by the driver (i.e., for each channel measurement, we have an index evaluating the "bumpiness" of the actual road). Thus, we have three groups of measurements designated as *smooth road*, *semi-bumpy* and *big potholes*.

Since the measurement setup mimics an intra-vehicle communication link with fixed antenna positions and the presence of the LOS is guaranteed by the installation, we are able to isolate the effect of the vehicle vibrations on the K factor.

1) Measurement devices: The block scheme of the in-house built channel sounder composed from the off-the-shelf components and measurement devices is visible in Figure 2.

The measurement setup consists of the oscilloscope Tektronix MSO72004C (acting as the RX) which was used as the matched receiver with 50 GS/s sampling frequency and 16 GHz bandwidth. The Anritsu Signal Quality Analyzer MP1800A (used as the TX) generates the m-sequences with 13 dBm output power and data rate 12.5 Gbit/s. To improve the dynamic range, the low-noise and power amplifiers QuinStar QLW-50754530-I2 and QPW-50662330 were used. We also utilized

the Sivers IMA FC1003V/01 up and down converter to move the signal to the band of interest.

2) Real-time data processing: The length of the m-sequences is given by the relation $L = 2^k - 1$, where L is the m-sequence length and k is the order of the m-sequence. In this work, we use $k = 11$, thus $L = 2047$.

Now, taking into account that we employ 50 GS/s sampling frequency and that the internal memory of the oscilloscope is 31.25 MS, we are able to capture $T = 3.246$ s of the transmitted signal into the fast internal memory of the oscilloscope (this represents more than 3000 CIRs snapshot for one measurement). Between each channel snapshot, there is a 1 ms pause required. Data are then uploaded to a PC and post-processed. After that, next measurements could be performed.

3) Note on the measurement index m: Each m index denotes a group of over 3000 CIRs recordings. Each group has the total duration of $T = 3.246$ s. In total, we captured $m \in \{1, ..., 50\}$ CIRs groups.
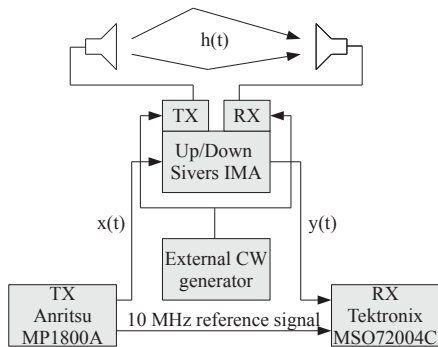
Fig. 2: Time-domain correlative channel sounder utilizing a m-sequence a stable external RF source and a matched receiver.

4) Antennas: The open-ended WR15 waveguide antennas were used at both the RX and TX ends. The radiation patterns are shown in Figure 3.

The TX antenna together with the power amplifier (PA) were mounted on the rear quarter window next to the rear passenger on the right hand side (Fig. 1c). The RX antenna, the low-noise amplifier (LNA) and the up/down converter were fitted approximately in the middle of the dashboard (Fig. 1a). The antennas were attached to the windows with suction caps.

III. DATA ACQUISITION AND PROCESSING

A. Rician K factor estimation

The Rician K factor represents the ratio of the specular part r^2 and the variance of the multipath $2\sigma^2$ and is defined in [18] according to

$$K = 10\log_{10}(r^2/2\sigma^2) \ [\text{dB}]. \qquad (5)$$

Since the utilized channel sounder is capable to capture the bandwidth of 4.9 GHz, we are not able to adopt the widely applied (e.g. [19], [20]) narrowband
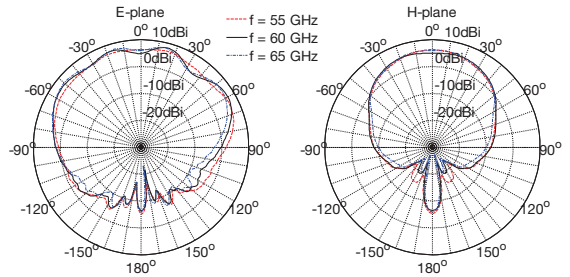
Fig. 3: Measured gain pattern of the open-ended WR15 waveguide in the E–plane and the H–plane for the 55-65 GHz frequency range.

method of moments [21]. We rely on the traditional method for estimation of the K factor from measured power versus time where the LOS component is determined by a peakfinder. Seeing that we measure a fixed link with a single-input single-output (SISO) configuration, the LOS components are always approximately at the same delay bin of the CIR. Therefore, the parametrization of the threshold based method for the estimation of the K factor is straightforward. Then, utilizing (5) and substituting $r(t) = \sum_\tau |h_{\text{LOS}}(t, \tau)|$ and $\sigma(t) = \sum_\tau |h_{\text{MPC}}(t, \tau)|$, we obtain the K factor as a function of time $K_m(t)$.

More detailed information about the channel sounder and how the CIR is obtained from the measured data is available in [13].

1) Decomposition of $K(t)$ into the fast and slow varying components: Based on a visual inspection of the measured data, we operate with a hypothesis that the K factor is composed from two elements according to:

$$K_m^*(t) = K_m(t) + K_m'(t), \qquad (6)$$

where $K_m^*(t)$ is the measured K factor, $K_m'(t)$ represents the superimposed fast varying component (noise component) and $K_m(t)$ is the slowly varying component. This is depicted in Figure 4. The decomposition into the slow and fast varying components is done via a discrete wavelet denoising method introduced in [22].
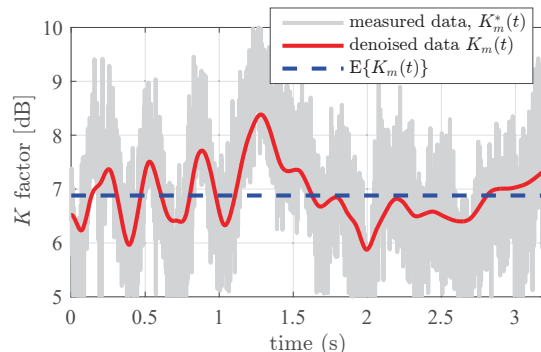
Fig. 4: Example of the K factor evolution in time. The spectrum of the slowly varying signal $K_m(t)$ is further analyzed.

2) Evaluation of the mean K factors: The mean value of the K factor is written as:

$$\text{E}\{K_m(t)\} = \frac{1}{T} \sum_t K_m(t). \tag{7}$$

An example of the mean K factor for one specific measurement index m is depicted in Figure 4. To provide an overview of the mean K factor behavior while driving at variety of speeds and on variety of roads, please see Figure 5. Together with the mean values of the K factor for all measurements m, in Figure 5 we depict a linear fit (written as: $y = kx + c$) obtained by a maximum likelihood estimation (MLE). The values of the parameters k and c are listed in Table I. The interpretation of the results is as follows:

- The higher the speed is, the lower the K factor. It holds namely for the good roads from the group of *smooth surface*.
- If the road quality gets worse (to the level of *semi-bumpy*), the K factor again decreases with increasing speed, however it decreases significantly slower compared to the case of the *smooth surface* group of roads. The reason for this are probably the pronounced vibrations from the road. Interesting is that the *smooth surface* and *semi-bumpy* groups have approximately the same mean K factor for the highest speeds.
- The mean K factors obtained on the worst roads are on similar level as the *semi bumpy*, but we were not able to test all the speeds because the road quality was so poor that we risk damages on the vehicle.
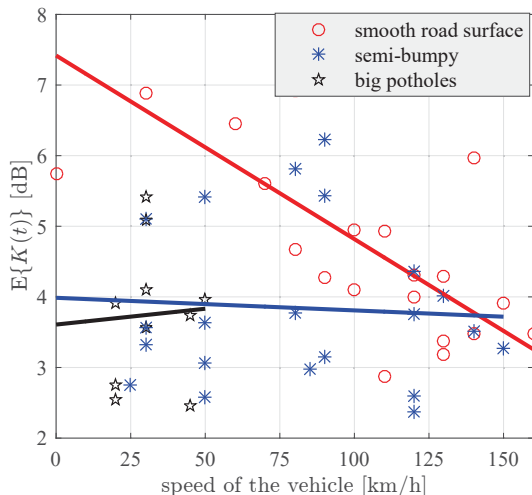
Fig. 5: Mean K factor (over the measurement time T) for all measured datasets $m \in \{1, ...50\}$. Linear fit parameters are listed in Tab. I

3) Analysis of the K factor variations: As demonstrated in Figure 4, the K factor $K_m(t)$ varies with time. Our hypothesis is, that the variations of the K factor are caused by the mechanical vibrations and mutual

movement of the RX and TX antennas in general. The mechanical vibrations are related mainly to the road surface quality and vehicle speed. Therefore, utilizing the fast Fourier transform (FFT), we calculate the spectra of all available measurements m according to

$$K_m(f) = \text{FFT}\{K_m(t)\}. \tag{8}$$

The results are plotted in Figure 6, where we also plot the mean spectral values of the representative road quality groups. It is visible, that as the road quality gets worse, the spectrum of the K factor $K_m(f)$ is broadened. In order to evaluate this broadening effect, we introduce a K factor frequency spread metric. The metric is given as a frequency spread, which is observed at the 40 dB decrease of the K factor spectrum $K_m(f)$ from its maximal value.

Now, the results of the K factor frequency spread are plotted in Figure 7 and we conclude that:

- The best road quality produces the lowest spread of the $K_m(f)$ values and the worst road quality produces the highest spread of the $K_m(f)$ values.
- K factor frequency spread increases with the speed.
- $K_m(f)$ spread increases faster as the road quality worsens.

Intuitively, the effect of the increasing speed and worsening of the road quality leads to a vibration increase. The K factor, influenced by a mutual antenna movement and variations of the of the antenna alignment, is shown as indirectly proportional to the vehicle vibrations.
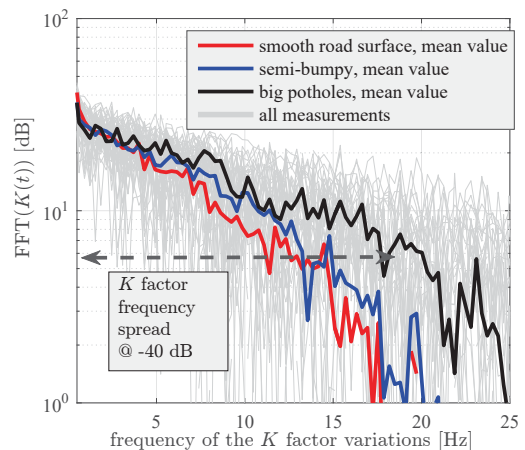
Fig. 6: Spectra of denoised $K(t)$ for all measurements (gray) and spectra of the mean values of the *smooth road*, *semi-bumpy* and *big potholes* groups.

IV. CONCLUSION

We present the K factor evaluation for variety of road conditions and the velocities of the measured vehicle. Since the measurement setup mimics an intra-vehicle communication link with fixed antenna positions and the
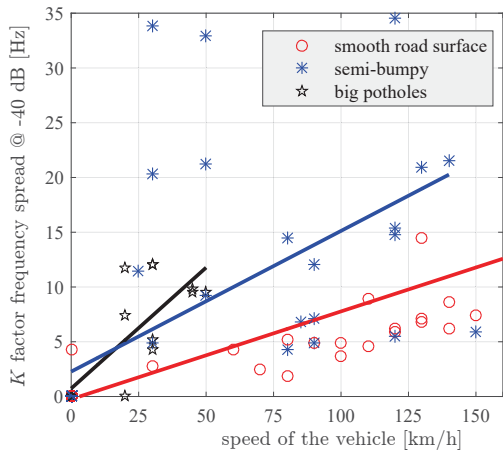
Fig. 7: The frequency spread of the denoised $K(f)$ for all measurements associated to the representative road quality groups.

TABLE I: Linear fit parameters of the of $E\{K_m(t)\}$ and $FFT\{K_m(t)\}\forall m$.

fit params. of $y = kx + c$ approx.	mean K factor		K factor spread	
	k	c	k	c
smooth road	-0.0260	7.418	0.0801	-0.248
semi-bumpy	-0.0017	3.987	0.1285	2.273
big potholes	0.0044	3.608	0.2208	0.732

presence of the LOS is guaranteed by the installation, we are able to isolate the effect of the vehicle vibrations. The baseline hypothesis is confirmed, the higher the speed of the vehicle, the lower the mean K factor. Also, the higher the speed, the higher variations of the K factor in the time domain.

The influence of the subjective index of the road quality on the K factor is also evaluated. The results show that as the road worsens, the mean K factor decreases while the frequency of the K factor variations is increased. In the absolute values, the presented results hold for one specific vehicle, one specific channel sounder and on top of that, for one specific test drive. However, the authors reckon that the shown trends will hold also for other (yet similar) vehicles.

REFERENCES

[1] T. S. Rappaport, S. Sun, R. Mayzus, H. Zhao, Y. Azar, K. Wang, G. N. Wong, J. K. Schulz, M. Samimi, and F. Gutierrez, "Millimeter wave mobile communications for 5G cellular: It will work!" *IEEE access*, vol. 1, pp. 335–349, 2013.

[2] C. Sommer and F. Dressler, *Vehicular Networking*. Cambridge University Press, 2014.

[3] T. Abbas, J. Nuckelt, T. Krner, T. Zemen, C. F. Mecklenbruker, and F. Tufvesson, "Simulation and measurement-based vehicle-to-vehicle channel characterization: Accuracy and constraint analysis," *IEEE Transactions on Antennas and Propagation*, vol. 63, no. 7, pp. 3208–3218, July 2015.

[4] M. Boban, T. T. V. Vinhoza, M. Ferreira, J. Barros, and O. K. Tonguz, "Impact of vehicles as obstacles in vehicular ad hoc networks," *IEEE Journal on Selected Areas in Communications*, vol. 29, no. 1, pp. 15–28, January 2011.

[5] J. Blumenstein, A. Prokes, A. Chandra, T. Mikulasek, R. Marsalek, T. Zemen, and C. Mecklenbruker, "In-vehicle channel measurement, characterization, and spatial consistency comparison of 3-11 GHz and 55-65 GHz frequency bands," *IEEE Trans. Veh. Technol.*, vol. 66, no. 5, pp. 3526–3537, May 2017.

[6] J. Blumenstein, T. Mikulasek, R. Marsalek, A. Chandra, A. Prokes, T. Zemen, and C. Mecklenbrauker, "In-vehicle UWB channel measurement, model and spatial stationarity," in *Vehicular Networking Conference (VNC), 2014 IEEE*. IEEE, 2014, pp. 77–80.

[7] J. Blumenstein, T. Mikulasek, R. Marsalek, A. Prokes, T. Zemen, and C. Mecklenbrauker, "In-vehicle mm-wave channel model and measurement," in *Vehicular Technology Conference (VTC Fall), 2014 IEEE 80th*. IEEE, 2014, pp. 1–5.

[8] M. Schack, J. Jemai, R. Piesiewicz, R. Geise, I. Schmidt, and T. Kurner, "Measurements and analysis of an in-car UWB channel," in *Vehicular Technology Conference, 2008. VTC Spring 2008. IEEE*, 2008, pp. 459–463.

[9] J. Blumenstein, T. Mikulasek, R. Marsalek, A. Prokes, T. Zemen, and C. Mecklenbrauker, "Measurements of ultra wide band in-vehicle channel - statistical description and TOA positioning feasibility study," *EURASIP Journal on Wireless Communications and Networking*, p. 15, 2015.

[10] U. Demir, C. Bas, and S. Ergen, "Engine compartment UWB channel model for intravehicular wireless sensor networks," *IEEE Transactions on Vehicular Technology*, vol. 63, no. 6, pp. 2497–2505, July 2014.

[11] S. Lakušić, D. Brčić, and V. Tkalčević Lakušić, "Analysis of vehicle vibrations–new approach to rating pavement condition of urban roads," *PROMET-Traffic & Transportation*, vol. 23, no. 6, pp. 485–494, 2011.

[12] J. Blumenstein, J. Vychodil, M. Pospisil, T. Mikulasek, and A. Prokes, "Effects of vehicle vibrations on mm-wave channel: Doppler spread and correlative channel sounding," in *2016 IEEE 27th Annual International Symposium on Personal, Indoor, and Mobile Radio Communications (PIMRC)*, Sept 2016, pp. 1–5.

[13] A. Prokes, J. Vychodil, M. Pospisil, J. Blumenstein, T. Mikulasek, and A. Chandra, "Time-domain nonstationary intra-car channel measurement in 60 GHz band," in *2016 International Conference on Advanced Technologies for Communications (ATC)*, Oct 2016, pp. 1–6.

[14] A. Chandra, A. Prokes, T. Mikulek, J. Blumenstein, P. Kukolev, T. Zemen, and C. F. Mecklenbruker, "Frequency-domain in-vehicle UWB channel modeling," *IEEE Trans. Veh. Technol.*, vol. 65, no. 6, pp. 3929–3940, June 2016.

[15] F. Hlawatsch and G. Matz, *Wireless communications over rapidly time-varying channels*. Academic Press, 2011.

[16] S. W. Golomb *et al.*, *Shift register sequences*. Aegean Park Press, 1982.

[17] G. Matz, A. F. Molisch, F. Hlawatsch, M. Steinbauer, and I. Gaspard, "On the systematic measurement errors of correlative mobile radio channel sounders," *IEEE Transactions on Communications*, vol. 50, no. 5, pp. 808–821, 2002.

[18] S. O. Rice, "Statistical properties of a sine wave plus random noise," *The Bell System Technical Journal*, vol. 27, no. 1, pp. 109–157, Jan 1948.

[19] A. Bottcher, P. Vary, C. Schneider, M. Narandzic, and R. S. Thoma, "Estimation of the radio channel parameters from a circular array with directional antennas," in *2011 IEEE 73rd Vehicular Technology Conference (VTC Spring)*, May 2011.

[20] L. Bernado, T. Zemen, F. Tufvesson, A. F. Molisch, and C. F. Mecklenbrauker, "Time- and frequency-varying K-factor of nonstationary vehicular channels for safety-relevant scenarios," *IEEE Transactions on Intelligent Transportation Systems*, vol. 16, no. 2, pp. 1007–1017, April 2015.

[21] L. J. Greenstein, D. G. Michelson, and V. Erceg, "Moment-method estimation of the ricean K-factor," *IEEE Communications Letters*, vol. 3, no. 6, pp. 175–176, June 1999.

[22] D. L. Donoho, "De-noising by soft-thresholding," *IEEE Transactions on Information Theory*, vol. 41, no. 3, pp. 613–627, 1995.

Measured High-Resolution Power-Delay Profiles of Nonstationary Vehicular Millimeter Wave Channels

Jiri Blumenstein, Ales Prokes, Josef Vychodil, Tomas Mikulasek, Jiri Milos, Erich Zochmann, Herbert Groll, Christoph F. Mecklenbrauker, Markus Hofer , David Loschenbrand , Laura Bernado, Thomas Zemen, Seun Sangodoyin, Andreas Molisch

Measured High-Resolution Power-Delay Profiles of Nonstationary Vehicular Millimeter Wave Channels

Jiri Blumenstein*, Ales Prokes*, Josef Vychodil*, Tomas Mikulasek*, Jiri Milos*,
Erich Zöchmann[†‡], Herbert Groll[‡], Christoph F. Mecklenbräuker[‡],
Markus Hofer[x], David Löschenbrand[x], Laura Bernadó[x],
Thomas Zemen[x], Seun Sangodoyin[††], Andreas Molisch[††]

* Department of Radio Electronics, Brno University of Technology, Czech Republic, *blumenstein@vutbr.cz*
† Christian Doppler Laboratory for Dependable Wireless Connectivity for the Society in Motion
‡ Institute of Telecommunications, TU Wien, Austria
x Safety and Security Department, Austrian Institute of Technology, Austria
†† Wireless Devices and Systems Group, University of Southern California, USA

Abstract—This paper reports on a power-delay profile measurement campaign emulating a mobile vehicle-to-infrastructure urban-highway environment. The measured location is in the city of Brno, Czech Republic. Utilizing a correlative 50 GS/s time-domain channel sounder with a center frequency of 59.6 GHz and 8 GHz bandwidth and with open-ended WR15 waveguide antennas, we characterize the representative millimeter wave radio channels in terms of the RMS delay spread and its variability caused by mobile scatterers (i.e., vehicles). The RMS delay spread exhibits notable heteroscedasticity as its standard deviation can decrease by 40 %. The measured high resolution power-delay profiles exhibit clustering behavior, where a typical number of reflected multipath components is four to five.

I. Introduction

Considering vehicle-to-infrastructure (V2I) communications, the license-free millimeter-wave (mmwave) band with 60 GHz center frequency offers several GHz of bandwidth, which is unrivaled to the traditional V2I bands (around 760 MHz or 5.9 GHz [1]). In addition, due to advances in millimeter wave sampling hardware, broadband vehicular millimeter wave communications has recently regained significant attention [2]. The research of mmwave radio propagation intended for vehicular communication has been going on for several decades; however, mostly as narrowband systems. Meinel and Plattner [3] were analyzing a narrowband millimeter wave communication system for a infrastructure to train scenario already in 1983. Akihito et al. [4] were investigating (also narrowband) car-to-car communications in 2001. Either work focused on

path-loss results and demonstrated a two-ray fading behavior [5], [6]. Additional effects of road surfaces have been investigated in [7]–[9].

Broadband vehicle-to-vehicle measurements (with 500 MHz bandwidth) are described in [10], where measured delay and Doppler profiles of overtaking vehicles in the 60 GHz band are presented; however, the time-varying power-delay profile behavior is not discussed and the antenna placement does not match the intended V2I scenario. In [11], delay and Doppler spreads of non-stationary vehicular 4×4 multiple-input multiple-output (MIMO) channels are researched; however the frequency band is 5480-5520 MHz. The effect of vibrations caused by the road surface quality or by the engine operation is evaluated via delay-Doppler spreading functions with several GHz of bandwidth in [12].

The analysis of static millimeter-wave channels is already well researched, see e.g. [13]–[15], where a K-factor and root mean square (RMS) delay spread are evaluated for indoor channels or [16], where a MIMO intra-vehicular channels with a 10 GHz bandwidth are studied. Contrarily, channel sounding concepts for dynamic scenarios have only recently been proposed [17], [18]. With this background, the contributions of this paper are following:

- We provide exemplary power-delay profiles for a typical V2I scenario considering a vehicular broadband mmwave channel.

- Moreover, we provide analysis of the RMS delay spread, which is affected by the passing

vehicles and thus exhibiting heteroscedasticity, i.e. a notable RMS delay spread standard deviation variations over the measured time period.

- We also present a time-domain channel sounder, which consists from off-the-shelf parts and laboratory devices such as oscilloscope or bit sequence generator.

II. SCENARIO DESCRIPTION

The measured V2I site is located in the city of Brno, Czech Republic. The campaign was conducted in a urban-highway environment, where we have emulated the mmwave communication with an overhead (roadside) infrastructure. Obviously, the higher the infrastructure access point is mounted, the higher possibility to experience a line-of-sight propagation towards the passing vehicles. In our case, the TX is placed at our emulated toll-gate, where its height above the road is around 5 m. The RX is placed at the ground level with the antenna height of 1.6 m. The photographs of the scene are depicted in Figure 2a.

Both the RX and TX are static; however, the traffic passing through the measured scene, effectively creating a moving scatterers, could represent an overtaking maneuver of a vehicle imitated by the RX. We assume that reflections with the receiver car are below the receiver noise floor. Therefore, the receiver car is omitted and replaced by a simpler tripod mounting. The blue car (in Figure 2a only the rear part is visible) serves as a carrier of the RX hardware and is not part of the measured scenario.

III. CHANNEL SOUNDER

In this section we provide a description of the in-house built (from off-the-shelf components and laboratory devices) channel sounder including a basic theoretical background of the time-domain channel sounding. A similar setup has been utilized in our contributions [9], [12], [19]; however, the channel sounder utilized in this paper is different as it consists from separate TX and RX sides. The 10 MHz synchronization is done via a coaxial cable or we can utilize two external rubidium oscillators.

A. Principle of the channel sounder operations

The correlative channel sounder captures the transmission channel in the time domain. Another possibility is to perform the channel sounding in the frequency domain, where the sounder usually requires notable amount of time to sweep the measured band [20]. On the other hand, the time domain channel sounding usually transmits a broadband pulse or sequence and the need for the channel sweep time is mitigated.

As a result, the time domain sounding is much more suitable for time-variant channels, which is the case of the measured V2I scenario.

The time-variant channel is characterized by the channel impulse response (CIR) and is written as [21]:

$$h(t, \tau) = \sum_{n=1}^{N(t)} \alpha_n(t) e^{j2\pi f t} \delta\left(\tau - \tau_n(t)\right), \quad (1)$$

where N is the number of propagation paths. Note that in this measurement campaign, due to the antenna installation, the line-of-sight (LOS) components $h_{\mathrm{LOS}}(t, \tau)$ are always present. The summation with the multipath components (MPCs) $h_{\mathrm{MPC}}(t, \tau)$, i.e.:

$$h(t, \tau) = h_{\mathrm{LOS}}(t, \tau) + h_{\mathrm{MPC}}(t, \tau), \quad (2)$$

creates an alternative formula to (1). Correlative channel sounders often exploit properties of pseudo-noise sequences. In this paper, we employ Golay sequences [22] with autocorrelation R_{xx} forming a distinct triangular function. For the purpose of our measurement; however, we simplify to $R_{xx} \approx \delta(\tau)$. Thus, it is possible to write:

$$y(t) = h(t) \otimes x(t), \quad (3)$$

where $y(t)$ is the received signal, $x(t)$ represents the transmitted Goaly sequence and finally $\otimes$ denotes the linear convolution.

Since the transmitted Golay sequence is known to the RX, it is possible to estimate the CIR from the cross-correlation of the transmitted and received signals $x(t)$ and $y(t)$ due to:

$$R_{xy}(\tau) = \mathrm{E}\{x^*(t)y(t)\} = h(t) \otimes R_{xx}(\tau) \approx$$
$$\approx h(t) \otimes \delta(\tau) = h(t), \quad (4)$$

where $\mathrm{E}\{\}$ denotes for the expected value operator.

B. Measurement devices

The block scheme of the time-domain channel sounder is depicted in Figure 1. Note that the channel sounder is composed from off-the-shelf parts and laboratory devices. As a sampling device, we use a oscilloscope Tektronix MSO72004C performing as a matched receiver with 50 GS/s sampling frequency and 16 GHz bandwidth. This signal is filtered in the baseband with a microstrip low-pass filter with 8 GHz bandwidth.

As for the TX, the Anritsu Signal Quality Analyzer MP1800A generates Golay sequences with 13 dBm output power and data rate 12.5 Gbit/s. To improve the dynamic range, the low-noise and power
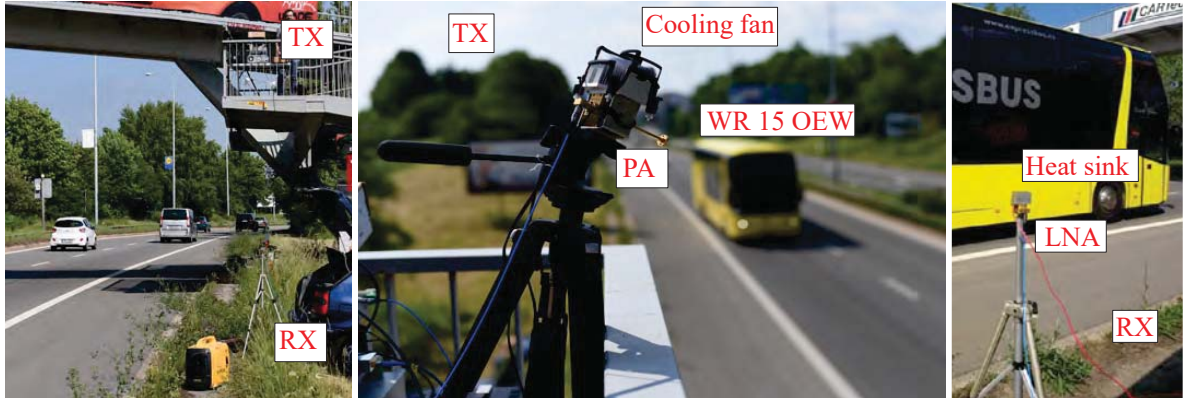
Fig. 1: Photographs of the measurement site. TX side is elevated 5 m above the four-lane highway (counting both directions, equipped with a metallic central barrier), emulating overhead roadside infrastructure installation, while RX is located on the side of the road (antenna height is 1.6 m). The vehicles driving by the RX apparatus emulate the overtaking maneuver.

(a) Time-domain correlative channel sounder utilizing Golay sequences, stable external RF source and a matched receiver.

(b) Measured gain pattern of the open-ended WR15 waveguide in the E–plane and the H–plane for the 55-65 GHz frequency range.
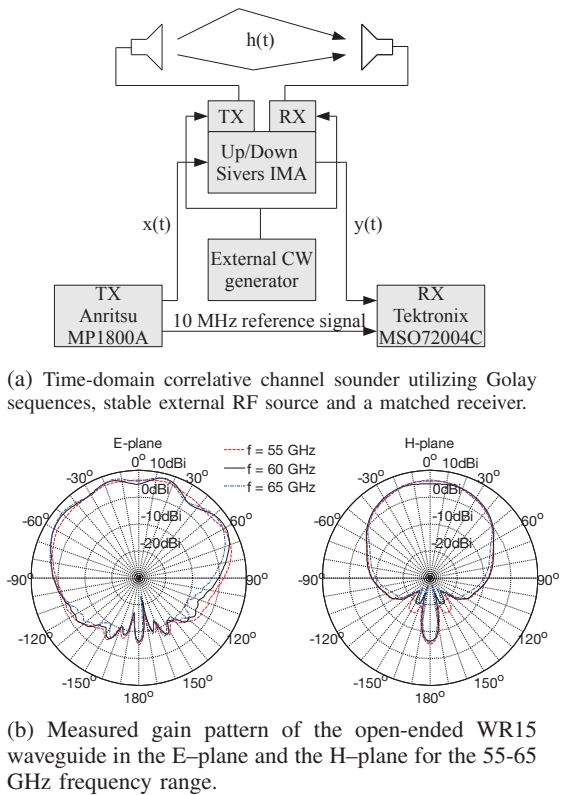
Fig. 2: Channel sounder and utilized WR 15 OEW antennas.

amplifiers QuinStar QLW-50754530-I2 and QPW-50662330 were used. We also utilized the Sivers IMA

FC1003V/01 up and down converter to move the signal to the band of interest.

C. Real-time data processing

The transmitted Golay sequence consists of two complementary sequences a and b. In our case, the length of both sequences is L = 2048. Now, the Golay pair is transmitted twice (forming a cyclic prefix-like pattern), meaning that the total length of the pair is 4L. The utilization of Golay pairs leads to reduced side-lobes in the correlation domain. Moreover, a method utilizing a second Golay pair with inverted polarity is used in order to further mitigate even-order spurious interferences. The transmitted signal obeys the following pattern: $[a, a, b, b, -a, -a, -b, -b]$. Hence, the total length of the transmitted sequence is 8L symbols. This signal is then up-sampled with a factor of four, leading to $4 \times 8L = 65536$ samples. More information about this method and the channel sounder is in [23].

Taking into account that we employ 50 GS/s sampling frequency and that the internal memory of the oscilloscope is 31.25 MS, we are able to capture 492 channel snapshots into the fast internal memory of the oscilloscope. The 492 channel snapshots form a power-delay profile (PDP) recording. Between each channel recording, there is a pause required for data download.

IV. MEASUREMENT RESULT

The measurement results are represented by a set of time-varying PDP recordings, where each recoding captures approx. 0.5 s with a sampling frequency of $1/820\,\mu$s in the time domain (in the delay domain, the sampling is $1/20$ ps). Due to a relatively short duration of the recording, we took a photograph of the scene
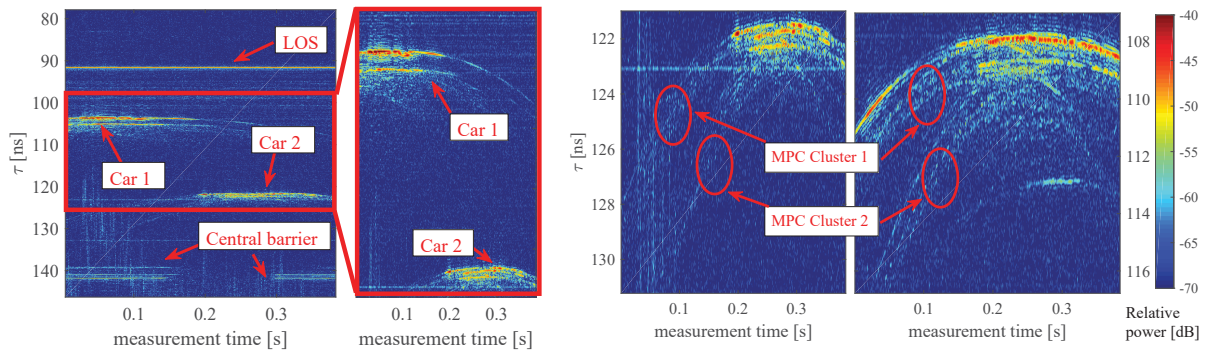
(a) The moving vehicles induce a shadowing effect. Therefore, between $t = 0.15\,\text{s}$ and $t = 0.30\,\text{s}$, the reflection from the central barrier vanishes, consequently the RMS delay spread exhibits heteroscedasticity.

(b) Multiple reflections originating from a single vehicle and forming a clusters 1 and 2 of the multipath components with similar delay domain characteristics.

Fig. 3: Representative example of time-varying power-delay profiles.

both from the RX and TX positions. Thus, we obtain information about the vehicle's configuration on the road and their individual type and size.

A. U-shaped reflections

The exemplary PDPs are depicted in Figure 3. In Figure 3a, the LOS component is visible together with the reflection from a metallic central barrier, effectively forming a clutter (as known from the radar signal processing). The moving vehicles are distinctly visible as the U-shaped MPC clusters. The U-shape is determined by the vehicle speed and its radar cross-section. In the majority of cases, the dead center (where the MPC delay is minimized) of the U-shaped MPC cluster is the most powerful part of the vehicle's reflection. The dead center of the U-shaped MPCs cluster exhibits the smallest accumulated distance (TX-reflection-RX) among other reflections originating from a single vehicle. Therefore, we deduce that the strongest reflections come from the side of the passing vehicle, as this configurations forms a isosceles triangle (from TX to the reflection and finally to the RX). This implies that the simplistic geometrical optics and the Snell's law is to a certain extend relevant also in the mmwave propagation description. In the case of long vehicles, e.g. buses, the middle part of the U-shaped reflections are straightened and forms a line in the PDP.

B. Heteroscedasticity of the RMS delay spread

The sudden presence of a strong reflector or even a number of strong reflectors has its implications to the normalized second-order central moment of the PDP, i.e. to the RMS delay spread.

In Figure 4, we compare 8 superimposed PDP recordings, where the mean RMS delay spread is around $3.5\,\text{ns}$ and was determined considering a static measured scene, i.e. without vehicles. Please note, that here we do not consider e.g. the effects of wind and other minor sources of variability. The presence of a strong reflecting object can alter the RMS delay spread notably. In our case, the presence of vehicles reduce the RMS delay spread from the $3.5\,\text{ns}$ by $1.5\,\text{ns}$, meaning that the reduction is around 40%. Therefore, the RMS delay spread exhibits heteroscedasticity. The presence of cars induce the strong MPC clusters at short delays, the energy is hence more concentrated close to the LOS delay.

C. Shadowing and MPC Clustering

In Figure 3a, we can see a shadowing effect, where the presence of car 1 and car 2 causes the central barrier reflection to disappear. In Figure 3b, several reflections originating from a single vehicle are visible. Moreover, some reflections are parallel, showing similar delay-domain characteristics and thus forming a MPC cluster. Typical number of distinct reflections from a single vehicle are 4 to 5 reflections.

V. CONCLUSION

We have conducted first broadband (with $8\,\text{GHz}$ bandwidth) V2I mmwave channel measurements demonstrating the power-delay profiles of the vehicles passing through the measurement scene. We have considered a V2I scenario with an overhead access point installation. The measured data shows notable heteroscedasticity of the RMS delay spread caused by a stochastic appearance of strongly reflecting objects (cars passing through the measurement location).
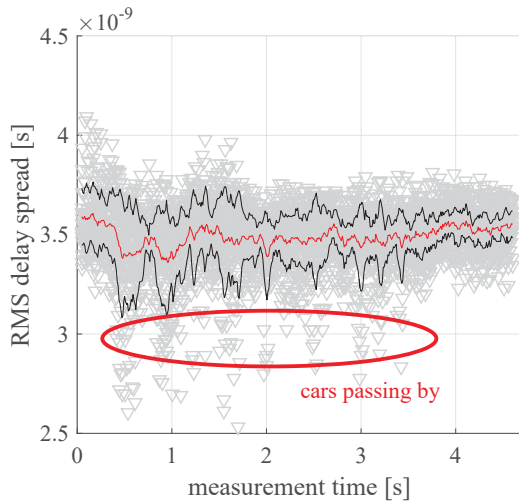
Fig. 4: The measured RMS delay spread variations of 8 superimposed PDP recordings, each capturing one or two cars in the measured scene. The mean value of the RMS delay spread is depicted as the red curve with $\pm$ of its standard deviation (black curves). Vehicles passing by the emulated communication link cause a RMS delay spread heteroscedasticity.

Moreover, we show that a passenger car usually reflects a number of MPCs with similar characteristics, thus showing distinct clustering behavior.

REFERENCES

[1] J. Harding, G. Powell, R. Yoon, J. Fikentscher, C. Doyle, D. Sade, M. Lukuc, J. Simons, and J. Wang, "Vehicle-to-vehicle communications: Readiness of V2V technology for application," Tech. Rep., 2014.

[2] V. Va, T. Shimizu, G. Bansal, and R. W. Heath Jr, "Millimeter wave vehicular communications: A survey," *Foundations and Trends® in Networking*, vol. 10, no. 1, pp. 1–113, 2016.

[3] H. Meinel and A. Plattner, "Millimetre-wave propagation along railway lines," *IEE Proceedings F (Communications, Radar and Signal Processing)*, vol. 130, no. 7, pp. 688–694, 1983.

[4] K. Akihito, S. Katsuyoshi, M. Fujise, and S. Kawakami, "Propagation characteristics of 60-GHz millimeter waves for ITS inter-vehicle communications," *IEICE Transactions on Communications*, vol. 84, no. 9, pp. 2530–2539, 2001.

[5] S. Takahashi, A. Kato, K. Sato, and M. Fujise, "Distance dependence of path loss for millimeter wave inter-vehicle communications," *Radioengineering*, vol. 13, no. 4, p. 9, 2004.

[6] A. Yamamoto, K. Ogawa, T. Horimatsu, A. Kato, and M. Fujise, "Path-loss prediction models for intervehicle communication at 60 GHz," *IEEE Transactions on Vehicular Technology*, vol. 57, no. 1, pp. 65–78, 2008.

[7] K. Sarabandi, E. S. Li, and A. Nashashibi, "Modeling and measurements of scattering from road surfaces at millimeter-wave frequencies," *IEEE Transactions on Antennas and Propagation*, vol. 45, no. 11, pp. 1679–1688, 1997.

[8] A. Yamamoto, K. Ogawa, T. Horimatsu, K. Sato, and M. Fujise, "Effect of road undulation on the propagation characteristics of inter-vehicle communications in the 60 GHz band," in *Proc. of IEEE/ACES International Conference on Wireless Communications and Applied Computational Electromagnetics*, 2005, pp. 841–844.

[9] J. Blumenstein, A. Prokes, J. Vychodil, M. Pospisil, and T. Mikulasek, "Time-varying K factor of the mm-Wave vehicular channel: Velocity, vibrations and the road quality influence," in *2017 IEEE 28th Annual International Symposium on Personal, Indoor, and Mobile Radio Communications (PIMRC)*, Oct 2017, pp. 1–5.

[10] E. Zöchmann, C. F. Mecklenbräuker, M. Lerch, S. Pratschner, M. Hofer, D. Löschenbrand, J. Blumenstein, S. Sangodoyin, G. Artner, S. Caban *et al.*, "Measured delay and Doppler profiles of overtaking vehicles at 60 GHz," in *Proc. of the 12th European Conference on Antennas and Propagation (EuCAP)*, pp. 1–5.

[11] L. Bernadò, T. Zemen, F. Tufvesson, A. F. Molisch, and C. F. Mecklenbräuker, "Delay and Doppler spreads of nonstationary vehicular channels for safety-relevant scenarios," *IEEE Transactions on Vehicular Technology*, vol. 63, no. 1, pp. 82–93, Jan 2014.

[12] A. Prokes, J. Vychodil, M. Pospisil, J. Blumenstein, T. Mikulasek, and A. Chandra, "Time-domain nonstationary intra-car channel measurement in 60 GHz band," in *2016 International Conference on Advanced Technologies for Communications (ATC)*, Oct 2016, pp. 1–6.

[13] E. Zöchmann, M. Lerch, S. Caban, R. Langwieser, C. F. Mecklenbräuker, and M. Rupp, "Directional evaluation of receive power, Rician K-factor and RMS delay spread obtained from power measurements of 60 GHz indoor channels," in *Proc. of IEEE-APS Topical Conference on Antennas and Propagation in Wireless Communications (APWC)*, 2016.

[14] J. Vehmas, J. Jarvelainen, S. L. H. Nguyen, R. Naderpour, and K. Haneda, "Millimeter-wave channel characterization at Helsinki airport in the 15, 28, and 60 GHz bands," in *Proc. of IEEE Vehicular Technology Conference (VTC-Fall)*, 2016.

[15] F. Fuschini, S. Häfner, M. Zoli, R. Müller, E. M. Vitucci, D. Dupleich, M. Barbiroli, J. Luo, E. Schulz, V. Degli-Esposti, and R. S. Thomä, "Analysis of in-room mm-Wave propagation: Directional channel measurements and ray tracing simulations," *Journal of Infrared, Millimeter, and Terahertz Waves*, vol. 38, no. 6, pp. 727–744, 2017.

[16] J. Blumenstein, A. Prokes, A. Chandra, T. Mikulasek, R. Marsalek, T. Zemen, and C. Mecklenbräuker, "In-vehicle channel measurement, characterization, and spatial consistency comparison of 30–11 GHz and 55–65 GHz frequency bands," *IEEE Transactions on Vehicular Technology*, vol. 66, no. 5, pp. 3526–3537, May 2017.

[17] P. B. Papazian, C. Gentile, K. A. Remley, J. Senic, and N. Golmie, "A radio channel sounder for mobile millimeter-wave communications: System implementation and measurement assessment," *IEEE Transactions on Microwave Theory and Techniques*, vol. 64, no. 9, pp. 2924–2932, 2016.

[18] E. Zöchmann, S. Caban, M. Lerch, and M. Rupp, "Resolving the angular profile of 60 GHz wireless channels by delay-Doppler measurements," in *Proc. of IEEE Sensor Array and*

Multichannel Signal Processing Workshop (SAM), 2016, pp. 1–5.

[19] J. Blumenstein, J. Vychodil, M. Pospisil, T. Mikulasek, and A. Prokes, "Effects of vehicle vibrations on mm-wave channel: Doppler spread and correlative channel sounding," in *2016 IEEE 27th Annual International Symposium on Personal, Indoor, and Mobile Radio Communications (PIMRC)*, Sept 2016, pp. 1–5.

[20] A. Chandra, A. Prokes, T. Mikulek, J. Blumenstein, P. Kukolev, T. Zemen, and C. F. Mecklenbräuker, "Frequency-domain in-vehicle UWB channel modeling," vol. 65, no. 6, pp. 3929–3940, June 2016.

[21] F. Hlawatsch and G. Matz, *Wireless communications over rapidly time-varying channels*. Academic Press, 2011.

[22] M. Golay, "Complementary series," *IRE Transactions on Information Theory*, vol. 7, no. 2, pp. 82–87, April 1961.

[23] J. Vychodil, M. Pospisil, A. Prokes, and J. Blumenstein, "Millimeter wave band time domain channel sounder," *IET Communications-submitted*, 2018.

Measured Delay and Doppler Profiles of Overtaking Vehicles at 60 GHz.

Erich Zöchmann, Christoph F Mecklenbräuker, Martin Lerch, Stefan Pratschner, Markus Hofer, David Löschenbrand, **Jiri Blumenstein**, Seun Sangodoyin, Gerald Artner, Sebastian Caban, Thomas Zemen, Aleš Prokeš, Markus Rupp, Andreas F Molisch

Measured Delay and Doppler Profiles of Overtaking Vehicles at 60 GHz

Erich Zöchmann[1,2], Christoph F. Mecklenbräuker[2,3], Martin Lerch[1,2], Stefan Pratschner[1,2], Markus Hofer[4], David Löschenbrand[4], Jiri Blumenstein[3], Seun Sangodoyin[6], Gerald Artner[2], Sebastian Caban[1,2], Thomas Zemen[4], Aleš Prokeš[3], Markus Rupp[2,3], Andreas F. Molisch[6]

[1] Christian Doppler Laboratory for Dependable Wireless Connectivity for the Society in Motion,
[2] Institute of Telecommunications, TU Wien, Austria *ezoechma@nt.tuwien.ac.at*
[3] Department of Radio Electronics, TU Brno, Czech Republic
[4] Center for Digital Safety & Security, AIT Austrian Institute of Technology, Austria
[6] Wireless Devices and Systems Group, University of Southern California, USA

Abstract—We report results from real-world millimetre wave vehicle-to-vehicle channel measurements carried out in an urban street environment, down-town Vienna, Austria. Channel measurements have been acquired with a time-domain channel sounder in the frequency band 59.75–60.25 GHz with a frequency resolution of approximately 5 MHz. We estimate the local scattering function for sequential stationarity regions in time. A multitaper estimator is used to precisely define Doppler and delay resolutions. Estimates for delay and Doppler profiles are evaluated from the local scattering function for several overtaking vehicles at a variety of speeds and for different types of vehicles. The results show that passenger cars are associated with a single Doppler trajectory, whereas larger vehicles, such as trucks, show up in the data with multiple Doppler trajectories.

Index Terms—mmWave, vehicular, propagation, measurement

I. INTRODUCTION

The idea of assisted-driving or even self-driving cars is a game-changer of how people commute and therefore represents a tremendous attraction to both, industry and the research community. More then ten years ago, a first forward collision warning system based on a millimetre wave (mmWave) automotive radar was commercialized [1]. Nowadays, reliable mmWave communication systems, supporting the vehicle-to-vehicle information exchange, are supposed to be the next key enablers for the above mentioned assisted- or self-driving vehicles. Research of narrowband mmWave communication systems intended for vehicular application has been conducted for several decades. Meinel and Plattner [2] analyse a mmWave communication system for an infrastructure to train scenario already in 1983. Akihito et al. [3] investigate 60 GHz based car-to-car communications in 2001. Both works focus on path loss results and show two-ray fading [4], [5].

Due to recent advances in the technology of integrated circuits, broadband vehicular mmWave communications has gained interest [6]. The analysis of static mmWave channels is already well advanced, see for example [7]–[11]. For static environments frequency-domain channel sounding methods based on vector network analysers can be used [12]. However, for dynamic time-variant scenarios a time-domain channel sounding set-up is required, which was treated so far only by few research papers [13], [14]. In 2016, the authors of [15] evaluate the effect of vehicles' vibrations while in operation

via delay-Doppler spreading functions with several GHz of bandwidth. A year later in [16], signal-to-noise ratio (SNR) fluctuations for 60 GHz transmissions with 5 MHz bandwidth in a vehicle-to-infrastructure scenario are investigated.

With this paper, we contribute to the dynamic mmWave vehicle-to-vehicle channel research in terms of: Firstly, introduction of a time-domain channel sounder design. Secondly, presentation of a wideband (500 MHz) time-domain mmWave channel measurement campaign performed in a real-world street environment. Thirdly, evaluation of delay and Doppler profiles for overtaking vehicles at a variety of speeds and for different vehicle types.

II. SCENARIO DESCRIPTION

Our receiver is fixed to the left rear car window, while our transmitter is mounted on a tripod approximately 15 m behind. We are observing the effect off passing/overtaking cars with excess speeds of up to 10 m/s. Although we do not move our receiver and transmitter at all, it is still an accurate model of an overtaking process, since the Doppler relevant velocity is only given by the relative speed between the slower vehicles and a fast vehicle. Our case corresponds to a moving frame of reference. The transmitter (TX) and receiver (RX) placement is shown in Fig. 1. Double reflections at the transmitter car are below the receiver sensitivity. Hence, the transmitter car is omitted and replaced by a simpler tripod mounting. For our set-up the 60 GHz free space path loss calculates to 91.5 dB. At the transmit side a 20 dBi horn antenna is used and aligned to cover both the receiving car and the street, within the 3 dB opening angle. Surrounding buildings are filtered by the directive horn antenna. At the receive side, a less directional antenna such as an omni-directional $\lambda/4$ monopole antenna or an open-ended waveguide (OEW) antenna is used. Thereby, the reflected components of the overtaking car are not spatially filtered. The antenna gain including the cable losses is approximately -4 dBi for the monopole antenna and 2 dBi for the OEW.

III. MEASUREMENT SET-UP

The hardware set-up is illustrated in Fig. 2. Our transmitter consists of an arbitrary waveform generator (AWG), continuously repeating a baseband sounding sequence, once triggered.

light barriers

10 MHz,
trigger
and marker

≈ 15 m

(static) RX

(static) TX
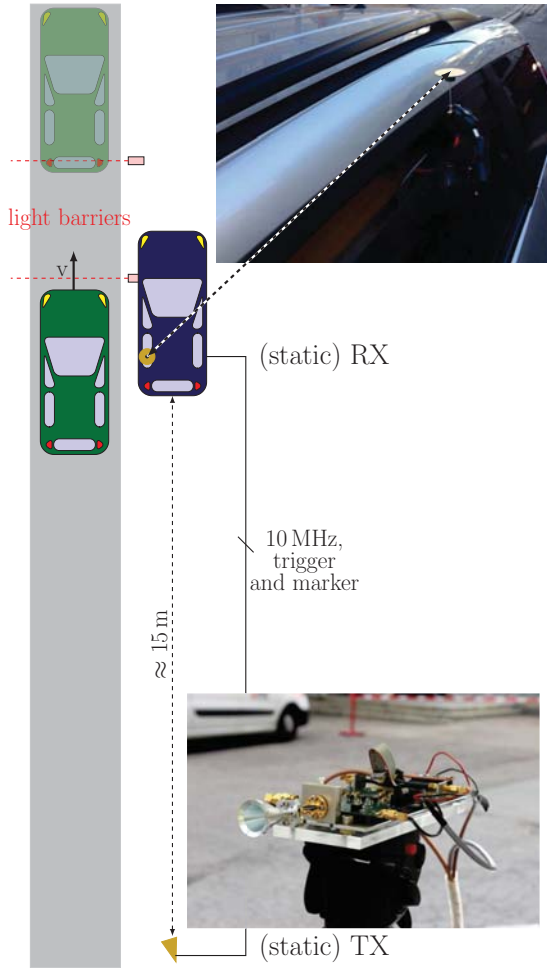
Fig. 1. Measurement scenario sketch.

Fig. 2. Instruments sketch and their interplay.

This baseband sequence described in Sec. III-A is up-converted by an external mixer module. The external mixer module employs a synthesizer phase-locked loop (PLL) for generating the internal local oscillator (LO). The synthesizer PLL is fed by a 285.714 MHz reference, and uses a counter (divider) value of 210 to generate the center frequency of $f_0 = 59.99994$ GHz. Our receiver is a Rohde and Schwarz signal analyser (SA) R&S FSW67. Its sensitivity is $P_{SA,min} = -150$ dBm/Hz at 60 GHz. All radio frequency (RF) devices are synchronized with a 10 MHz reference. A measurement is started when a vehicle passes through a first light barrier, triggering the AWG. The AWG itself plays out the baseband sequence and a sample synchronous marker. This marker signal triggers the recording of the receive samples. We directly access the IQ samples, sampled at a rate of 600 MSamples/s. A second light barrier, 3 m after the first one, is used to estimate the speed of passing vehicles.

A. Excitation Signal

The excitation signal generated by the AWG is a multi-tone waveform. The use of a multi-tone waveform affords us several advantages such as i) ideally, flat frequency spectrum, ii) design flexibility, iii) controllable crest factor, and iv) high SNR through processing gain. These advantages are important for channel transfer function extraction. Using an approach similar to a procedure implemented in [17], the excitation signal is given by $x(n) = \mathrm{Re}\big(\sum_{k=1}^{K/2} \mathrm{e}^{\mathrm{j}\pi \frac{k^2}{K}} \mathrm{e}^{-\mathrm{j}2\pi k \frac{n}{Q}} \big)$, where $n = 0, \ldots, Q-1$ is the time index and k the sub-carrier index. To minimize the crest factor of the signal, the tone phases are chosen quadratic. The crest factor is reduced in order to maximize the average transmitted power while ensuring that all RF components encountered by the excitation signals operate in their linear regions.

For the geometry of our scenario, the length difference between the LOS and the overtaking car should always be smaller than 15 m. Ignoring multiple reflections between the parking RX car and the overtaking car, we can safely assume that the path length difference will not be larger than 30 m and thus 100 ns is our maximum excess delay. To make the symbols shorter and less susceptible to inter-carrier interference caused by phase noise and Doppler, we choose the sub-carrier spacing Δf as large as possible. To still obey the sampling theorem in the frequency domain, we need to fulfil $\Delta f \leq 1/2\tau_{max} = 5$ MHz, where τ_{max} is the maximum excess delay. Our multi-tone waveform has $Q = 121$ maximum available sub-carriers with a sub-carrier spacing $\Delta f = 600\,\mathrm{MHz}/121 = 4.96$ MHz. Due to the sharp (anti-aliasing) filter of the SA, from the $Q = 121$ sub-carriers we effectively utilize only $K = 102$ sub-carriers and a linearly interpolated zero DC sub-carrier, which is equal to a measurement bandwidth $B \approx 510.74$ MHz . With these parameters the delay resolution of the channel sounder is $\tau_{min} = 1/B \approx 1.96$ ns. The receiver sensitivity can be approximated to $P_{RX,min} = P_{SA,min} + 10\log_{10}(\Delta f) + 10\log_{10} K = -63$ dBm.

B. Link budget and other limitations

For the LOS component, the propagation losses including antenna gains and 3 dB alignment margin sum up to $L = 78.5$ dB. For the design of our set-up, we assume that reflected paths are $R = 10$ dB weaker than the LOS

Parameter	Value
sub-carrier spacing	$\Delta f = 4.96\,\text{MHz}$
number of sub-carriers	$K = 102$
center frequency	$f_0 = 59.99994\,\text{GHz}$
maximum alias free delay	$\tau_{\text{max}} = 100.83\,\text{ns}$
transmit antenna	20 dBi conical horn
transmit power	$P_{\text{TX}} = 7\,\text{dBm}$
receiver sensitivity	$P_{\text{RX,min}} = -63\,\text{dBm}$
receive antenna	$\lambda/4$ monopole or OEW
snapshot rate	$T_{\text{snap}} = 129.1\,\mu\text{s}$
delay resolution	1.96 ns
maximum car speed	$v_{\text{car}} = 9.75\,\text{m/s}$
recording time	$T_{\text{rec}} = 720\,\text{ms}$

component. Next, we require an SNR at each sub-carrier of the reflected component of $\text{SNR}_{\text{refl}} = 10\,\text{dB}$. These requirements directly translate to the necessary transmit power $P_{\text{TX,min}} = P_{\text{RX,min}} + L + R + \text{SNR}_{\text{refl}} = 35.5\,\text{dBm}$. The maximum power for our transmit module is $7\,\text{dBm}$. Thus, the transmit power is $28.5\,\text{dB}$ too low. The missing transmit power is realized by coherently averaging over $N = 640$ multi-tone symbols. Averaging over several symbols in time reduces the snapshot rate and limits the channel traceability. Remember, our multi-tone system has a sub-carrier spacing of $\Delta f = 4.96\,\text{MHz}$ and a sounding sequence length of $\tau_{\text{sym}} = 1/\Delta f = 202\,\text{ns}$. The overall pulse length including 640 repetitions, sums up to $T_{\text{snap}} = 129.1\,\mu\text{s}$. Applying the sampling theorem for the Doppler support, we obtain a maximum alias-free Doppler frequency of $\nu_{\text{max}} = \frac{1}{2T_{\text{snap}}} = 3.9\,\text{kHz}$, which limits the speed of overtaking cars to $v_{\text{car}} = \lambda \nu_{\text{max}}/2 = 9.75\,\text{m/s} = 35.1\,\text{km/h}$ [1]. This value is sufficient for our measurements, as the street, were the measurements took place, has a speed limit of $30\,\text{km/h}$. Our receiver is limited to a memory depth of approximately $420\,\text{MSamples}$ or equivalently with a sampling rate of $600\,\text{MSamples/s}$ we can record $T_{\text{rec}} = 720\,\text{ms}$ of the channel evolution. At $9.75\,\text{m/s}$ this equals a driving distance of $7\,\text{m}$. An overview of the channel sounder parameters is given in Table I.

IV. MEASUREMENT EVALUATION

From the IQ samples we calculate the time-variant channel transfer function $H'[m', q]$ by a discrete Fourier transform of length $Q = 121$. Here m' denotes the symbol time index and q the frequency index. After averaging, we divide the resulting channel transfer function by the calibration function, obtained from back-to-back measurements, to equalize the frequency characteristics of the AWG to SA. The resulting function is denoted as $H[m, q]$, with $m = 0, \ldots, S - 1$ denoting the resulting time index after averaging. For the measurement, we record $T_{\text{rec}} = 720\,\text{ms}$ which is equal to $S = 5579$ averaged snapshots.

We characterize the channel by the local scattering function (LSF) explained in [18]–[20]. We assume that the fading

[1]Remember, departing vehicles cause Doppler shifts twice as large.

process is locally stationary within a region of M samples in time and $K + 1$ (including a linearly interpolated zero sub-carrier at DC) samples in frequency domain. For a first evaluation we assume that there is only one stationarity region in the frequency direction. We estimate the LSF for consecutive stationarity regions in time. We use a multitaper based estimator in order to obtain multiple independent spectral estimates from the same measurement and being able to average them. The estimate of the LSF is defined as [18]

$$\hat{\mathcal{C}}[k_t; n, p] = \frac{1}{IJ} \sum_{w=0}^{IJ-1} \left| \mathcal{H}^{(G_w)}[k_t; n, p] \right|^2. \quad (1)$$

We denote by $n \in \{0, \ldots, M-1\}$ the delay index and by $p \in \{-K/2, \ldots, K/2\}$ the Doppler index. The delay and Doppler shift resolutions are given by $\tau_s = 1/((K+1)\Delta f)$ and $\nu_s = 1/(MT_{\text{snap}})$. The time index of each stationarity region is $k_t \in \{0, \ldots, \lfloor S/M - 1 \rfloor\}$ and corresponds to the center of the stationarity regions. The windowed frequency response $\mathcal{H}^{(G_w)}$ is calculated by $\mathcal{H}^{(G_w)}[k_t; n, p] = \sum_{m=-M/2}^{M/2-1} \sum_{q=-K/2}^{K/2} H[m + M(k_t + 0.5), q] G_w[m, q] e^{-j2\pi(pm-nq)}$, where the tapers $G_w[m, q]$ are the discrete prolate spheroidal (DPS) sequences [21]. The number of tapers in time domain is $I = 3$ and in frequency domain $J = 3$.

For a first evaluation of the LSF we set $M = 117$ and $K + 1 = 103$ which corresponds to a stationarity region of $T_{\text{stat}} \approx 15.1\,\text{ms}$ in time and $B_{\text{stat}} \approx 510.74\,\text{MHz}$ in frequency. A more detailed investigation on the stationarity region length similar to [22] is ongoing. The power delay profile (PDP) and the Doppler spectral density (DSD) are calculated as a summation of the LSF over the Doppler or delay domain [18],

$$\hat{\mathcal{P}}_\tau[k_t; n] = E_p\left\{ \hat{\mathcal{C}}[k_t; n, p] \right\} = \frac{1}{M} \sum_{p=-M/2}^{M/2-1} \hat{\mathcal{C}}[k_t; n, p], \quad (2)$$

$$\hat{\mathcal{P}}_\nu[k_t; p] = E_n\left\{ \hat{\mathcal{C}}[k_t; n, p] \right\} = \frac{1}{K} \sum_{n=0}^{K-1} \hat{\mathcal{C}}[k_t; n, p], \quad (3)$$

where $E_i\{\cdot\}$ denotes the expectation with respect to i. In the measurement results we show the DSD and the PDP over time. For the evaluation a rectangular window is considered.

V. RESULTS

As a first example, we provide the DSD and the PDP of a single car. The car is shown in the upper part of Fig. 3. The transmitter height is $h_t = 1.1\,\text{m}$. As receiver, an omni-directional monopole antenna is used. In the middle part of Fig. 3, the PDP shows a strong static LOS component with $50\,\text{ns}$ delay, corresponding to the $15\,\text{m}$ distance, and a second delayed path which comes from the overtaking car. This second path produces the Doppler shift shown in the bottom part of Fig. 3. The second example is an overtaking convoy of two cars. All settings are equal to the first example. Both cars are visible as individual Doppler trajectories in Fig. 4. The last demonstrative example is an overtaking truck. The transmitter
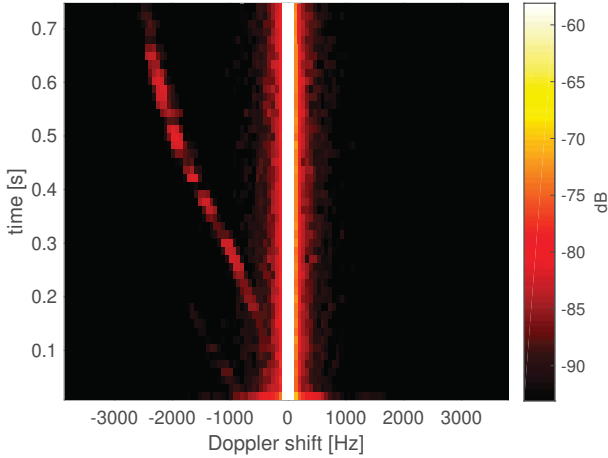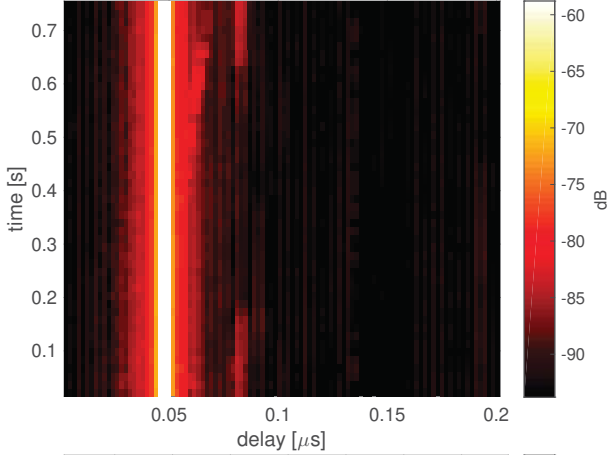
Fig. 3. One car scenario, $v = 7.3\,\mathrm{m/s}$. Top: Webcam snapshot. Middle: PDP. Bottom: DSD.

Fig. 4. Two cars scenario, $v = 5.9\,\mathrm{m/s}$. Top: Webcam snapshot. Middle: PDP. Bottom: DSD.

is now mounted at $h_t = 0.7\,\mathrm{m}$ and the receive antenna is changed to an OEW pointing towards the departing vehicles. Thereby, reflected components of departing cars are increased by the antenna gain. Due to the low transmitter mounting, a ground reflection is visible as second, strong and static component in the delay profile, shown in Fig. 5. The static ground reflection is an artefact due to the static TX and RX. Furthermore, cars parking in front of the RX are now also visible as distant reflection objects, vanishing once the truck drives by. Remarkably, the DSD looks very different from the previous examples. Besides the static Doppler component at $-3\,\mathrm{kHz}$ stemming from a distant car, the truck creates several Doppler traces, clearly demonstrating its spatial extend.

VI. Conclusion

We report empirical PDPs and DSDs from vehicular mmWave channel measurements in the 60 GHz band during September 2017. The channel measurements are characterized by estimates for the local scattering function and its marginal distributions. Different vehicles are distinguishable via their PDPs and DSDs. A passenger car results in a single multipath component, whereas a large vehicle such as a truck produces several multipath components.

Acknowledgment
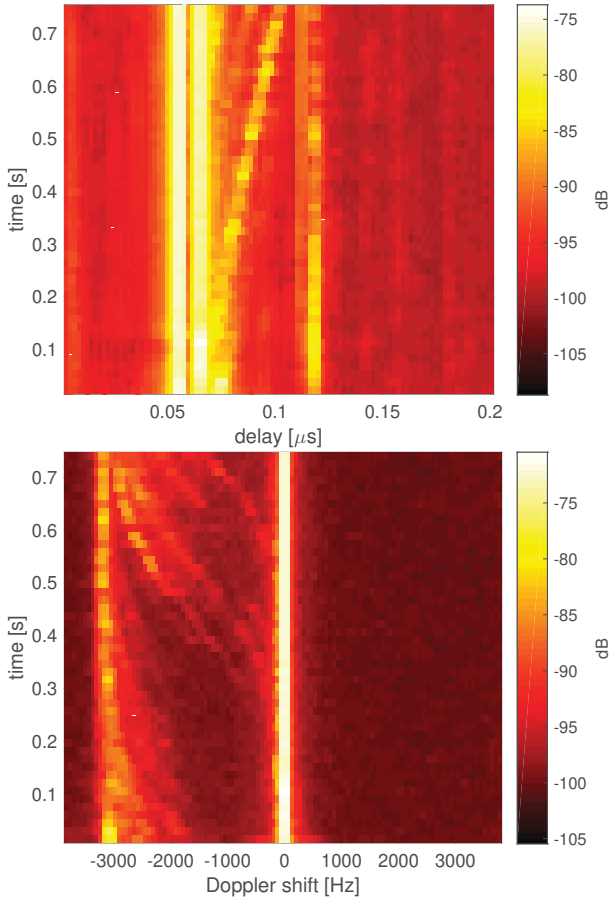
Fig. 5. Truck scenario, $v = 8 \, \mathrm{m/s}$. Top: Webcam snapshot. Middle: PDP. Bottom: DSD.

REFERENCES

[1] T. Tokumitsu, M. Kubota, K. Sakai, and T. Kawai, "Application of GaAs device technology to millimeter-waves," *SEI Technical Review*, no. 79, pp. 57–65, 2014.

[2] H. Meinel and A. Plattner, "Millimetre-wave propagation along railway lines," *IEE Proceedings F (Communications, Radar and Signal Processing)*, vol. 130, no. 7, pp. 688–694, 1983.

[3] K. Akihito, S. Katsuyoshi, M. Fujise, and S. Kawakami, "Propagation characteristics of 60-GHz millimeter waves for ITS inter-vehicle communications," *IEICE Transactions on Communications*, vol. 84, no. 9, pp. 2530–2539, 2001.

[4] S. Takahashi, A. Kato, K. Sato, and M. Fujise, "Distance dependence of path loss for millimeter wave inter-vehicle communications," *Radioengineering*, vol. 13, no. 4, p. 9, 2004.

[5] A. Yamamoto, K. Ogawa, T. Horimatsu, A. Kato, and M. Fujise, "Path-loss prediction models for intervehicle communication at 60 GHz," *IEEE Transactions on Vehicular Technology*, vol. 57, no. 1, pp. 65–78, 2008.

[6] V. Va, T. Shimizu, G. Bansal, and R. W. Heath Jr, "Millimeter wave vehicular communications: A survey," *Foundations and Trends® in Networking*, vol. 10, no. 1, pp. 1–113, 2016.

[7] E. Zöchmann, M. Lerch, S. Caban, R. Langwieser, C. F. Mecklenbräuker, and M. Rupp, "Directional evaluation of receive power, Rician K-factor and RMS delay spread obtained from power measurements of 60 GHz indoor channels," in *Proc. of IEEE-APS Topical Conference on Antennas and Propagation in Wireless Communications (APWC)*, 2016.

[8] J. Vehmas, J. Jarvelainen, S. L. H. Nguyen, R. Naderpour, and K. Haneda, "Millimeter-wave channel characterization at Helsinki airport in the 15, 28, and 60 GHz bands," in *Proc. of IEEE Vehicular Technology Conference (VTC-Fall)*, 2016.

[9] F. Fuschini, S. Häfner, M. Zoli, R. Müller, E. M. Vitucci, D. Dupleich, M. Barbiroli, J. Luo, E. Schulz, V. Degli-Esposti, and R. S. Thomä, "Analysis of in-room mm-Wave propagation: Directional channel measurements and ray tracing simulations," *Journal of Infrared, Millimeter, and Terahertz Waves*, vol. 38, no. 6, pp. 727–744, 2017.

[10] E. Zöchmann, M. Lerch, S. Pratschner, R. Nissel, S. Caban, and M. Rupp, "Associating spatial information to directional millimeter wave channel measurements," in *Proc. of IEEE Vehicular Technology Conference (VTC2017-Fall)*, 2017, pp. 1–5.

[11] J. Blumenstein, A. Prokeš, A. Chandra, T. Mikulasek, R. Marsalek, T. Zemen, and C. Mecklenbräuker, "In-vehicle channel measurement, characterization, and spatial consistency comparison of 30–11 GHz and 55–65 GHz frequency bands," *IEEE Transactions on Vehicular Technology*, vol. 66, no. 5, pp. 3526–3537, May 2017.

[12] A. Chandra, A. Prokeš, T. Mikulasek, J. Blumenstein, P. Kukolev, T. Zemen, and C. F. Mecklenbräuker, "Frequency-domain in-vehicle UWB channel modeling," *IEEE Transactions on Vehicular Technology*, vol. 65, no. 6, pp. 3929–3940, June 2016.

[13] P. B. Papazian, C. Gentile, K. A. Remley, J. Senic, and N. Golmie, "A radio channel sounder for mobile millimeter-wave communications: System implementation and measurement assessment," *IEEE Transactions on Microwave Theory and Techniques*, vol. 64, no. 9, pp. 2924–2932, 2016.

[14] E. Zöchmann, S. Caban, M. Lerch, and M. Rupp, "Resolving the angular profile of 60 GHz wireless channels by delay-Doppler measurements," in *Proc. of IEEE Sensor Array and Multichannel Signal Processing Workshop (SAM)*, 2016, pp. 1–5.

[15] J. Blumenstein, J. Vychodil, M. Pospisil, T. Mikulasek, and A. Prokeš, "Effects of vehicle vibrations on mm-wave channel: Doppler spread and correlative channel sounding," in *Proc. of IEEE International Symposium on Personal, Indoor, and Mobile Radio Communications (PIMRC)*, Sept 2016, pp. 1–5.

[16] A. Loch, A. Asadi, G. H. Sim, J. Widmer, and M. Hollick, "mm-wave on wheels: Practical 60 GHz vehicular communication without beam training," *Proc. of COMSNETS 2017*, pp. 1–5, 2017.

[17] S. Sangodoyin, J. Salmi, S. Niranjayan, and A. F. Molisch, "Real-time ultrawideband MIMO channel sounding," in *Proc. of Antennas and Propagation Conference (EUCAP)*, 2012.

[18] L. Bernadó, T. Zemen, F. Tufvesson, A. F. Molisch, and C. F. Mecklenbräuker, "Delay and Doppler Spreads of Nonstationary Vehicular Channels for Safety-Relevant Scenarios," *IEEE Transactions on Vehicular Technology*, vol. 63, no. 1, pp. 82–93, Jan. 2014.

[19] L. Bernadó, T. Zemen, F. Tufvesson, A. F. Molisch, and C. F. Mecklenbräuker, "Time- and Frequency-Varying K -Factor of Non-Stationary Vehicular Channels for Safety-Relevant Scenarios," *IEEE Transactions on Intelligent Transportation Systems*, vol. 16, no. 2, pp. 1007–1017, 2015.

[20] D. J. Thomson, "Spectrum estimation and harmonic analysis," *Proceedings of the IEEE*, vol. 70, no. 9, pp. 1055–1096, 1982.

[21] D. Slepian, "Prolate Spheroidal Wave Functions, Fourier Analysis, and Uncertainty-V: The Discrete Case," *Bell System Technical Journal*, vol. 57, no. 5, pp. 1371–1430, May 1978.

[22] L. Bernadó, T. Zemen, F. Tufvesson, A. F. Molisch, and C. F. Mecklenbräuker, "The (in-) validity of the WSSUS assumption in vehicular radio channels," in *Proc. of IEEE International Symposium on Personal, Indoor and Mobile Radio Communications (PIMRC)*, Sept 2012, pp. 1757–1762.

In-vehicle mm-Wave Channel Model and Measurement

Jiri Blumenstein, Tomas Mikulasek, Roman Marsalek, Ales Prokes, Thomas Zemen, Christoph Mecklenbräuker

In-vehicle mm-Wave Channel Model and Measurement

Jiri Blumenstein, Tomas Mikulasek,
Roman Marsalek, Ales Prokes
The Faculty of Electrical Engineering and Communication
Brno University of Technology
Brno, Czech Republic
Email: blumenstein@feec.vutbr.cz

Thomas Zemen
FTW Forschungszentrum
Telekommunikation Wien,
Vienna, Austria

Christoph Mecklenbräuker
Institute of Telecommunications,
Vienna University of Technology,
Vienna, Austria

Abstract—This contribution documents and discusses recent wideband radio channel measurements carried out in the intra–vehicle environment. Channels in the millimeter-wave (MMW) frequency band have been measured in 55–65 GHz using open-ended rectangular waveguides.

We present a channel modeling approach based on a decomposition of spatially specific Channel Impulse Responses (CIRs) into the large and small scale fading. The decomposition is done by a Hodrick-Prescott filter. We parametrize the small scale fading utilizing Maximum-likelihood estimates for the parameters of a generalized extreme value (GEV) distribution. The large scale fading is described by a two dimensional polynomial curve. We also compare simulated results with our measurement exploiting two-sample Kolmogorov-Smirnov test.

I. INTRODUCTION

The ever increasing vehicle efficiency goes hand in hand with weight savings. One recognized, yet not fully utilized way to achieve vehicle weight reduction is to replace relatively heavy and costly cable bundles with wireless links. Current upswing of electrically-propelled vehicles struggling with operating range, stress this issue even further. Modern vehicle contains up to several kilometers of wires weighting easily up to 50 kg [1], while the vehicle manufacturers appreciate weight savings in tens of grams. Other significant benefit of wireless communication in the in-vehicle ambiance is represented by the fact that wireless links are universal, thus the necessity to design model-specific cable bundles is to some extent eliminated. Also, the wireless link installation should be easier.

While providing around 10 GHz of unlicensed bandwidth, MMW short range communication systems could beneficially replace the safety non-critical cable bundles e.g. for rear seat entertainment systems or HD video streaming. The MMW systems enable the usage of high-gain steerable antennas [2] which seems to be beneficial for the in-vehicle communication links. On the other hand, the 60 GHz band suffers from high penetration loss and insignificant diffraction contribution [3].

Authors of [2], [4] dealt with comparison of the UWB and 60 GHz in-vehicle channels. Their results include Rician K-factor, RMS delay spread or path-loss but they omit any statistical description. Channel model of in-vehicle ambiance is also not present in the mentioned publications. Moreover, their measurement campaign was performed in slightly dif-

ferent bands (67–70.5 GHz) whereas our measurement was performed in 55–65 GHz.

As discussed in [5], [6], the detailed knowledge of radio channel behavior is of course needed for the physical layer design.

A. Contribution of the paper

- Results of an in-vehicle channel measurement campaign performed in 55-65 GHz frequency band for different antennas placement and occupancy patterns.
- Channel model describing both the large and small scale fading.
- Validation of the simulated Channel Impulse Responses (CIRs) using two-sample Kolmogorov-Smirnov test [7].

The rest of the paper is organized as follows: Firstly we provide measurement setup description, then we present our channel modeling approach and its results. Conclusion rounds up the paper.
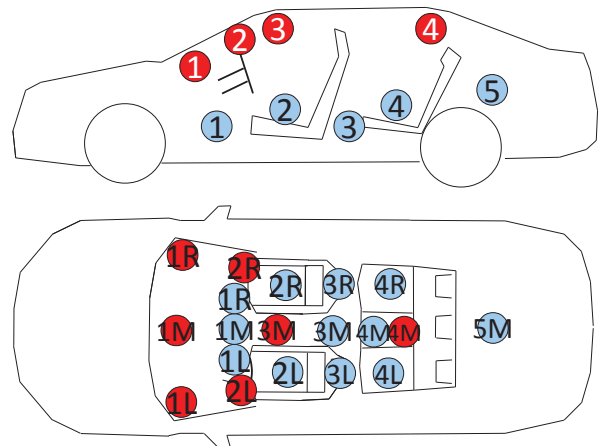
Fig. 1. Antenna placement, RED-receiving antennas, BLUE-transmitting antennas. Measured links between depicted antennas are specified in Table I.

II. MEASUREMENT SETUP

Measurements have been performed using the mid-sized passenger car Skoda Octavia III with transmit and receive
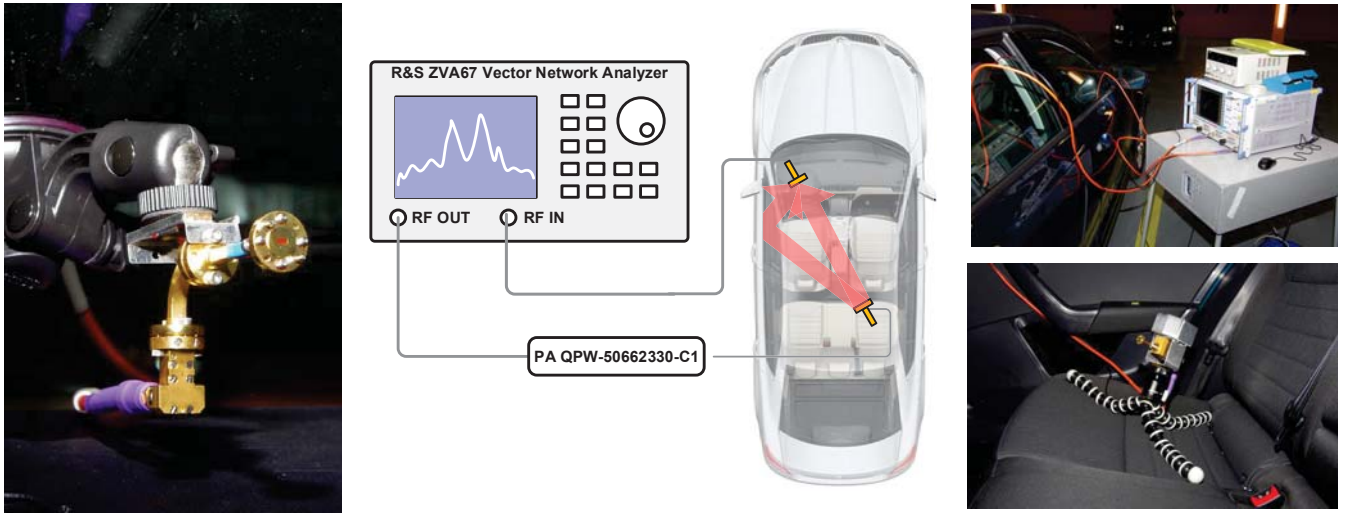
Fig. 2. From left to right: Open waveguide antenna mounted on the front windshield using a sucking cap; The diagram of the mm-wave measurement setting with the vector network analyzer, the low noise and power amplifiers type designation; From above: The vector network analyzer next to the measured vehicle; The receiving waveguide antenna mounted on a tripod on a back seat.

antennas marked with red and blue colors in Figure 1 respectively. The receiving (RX) antenna has been placed at different spatial points inside the car compartment (on all seats, trunk or in front of the seats). The transmitting (TX) antennas have been placed on the left and right side of the dash-board and at the rear part of the ceiling according to Figure 1.

The 4-port vector network analyzer R&S ZVA67 (VNA) was used for measuring the transmission coefficient between two antennas in the frequency band 55–65 GHz. The dynamic range of the measurement setup was extended utilizing the broadband power amplifier (QPW-50662330) on the transmitting side. The open waveguide WR15 having the radiation pattern depicted in Figure 3 was used as a transmitting and receiving antenna. The measurement setup was calibrated for zero transmission while the waveguides were connected to each other. The diagram describing the measurement setup for frequency band 55–65 GHz is depicted in Figure 2.
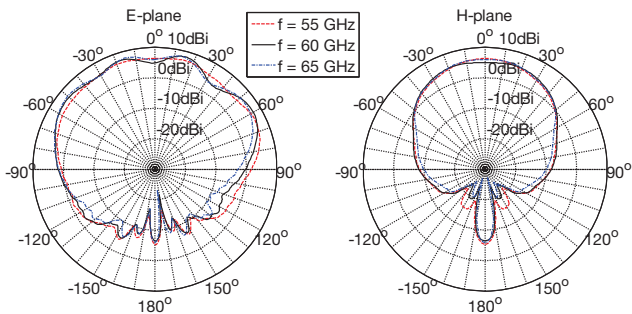
Fig. 3. Simulated gain pattern of the open waveguide in E–plane and H–plane.

TABLE I
TABLE OF ANTENNA POSITIONS α WITH DISTANCES BETWEEN ANTENNAS AND OCCUPANCY.

α	RX ant. pos.	TX ant. pos.	Dist. [cm]	Passangers
1	Outside	4M (Blue)	352	No
2	1R (Red)	4M (Blue)	208	FULL
3	Outside	4M (Blue)	352	No
4	1R (Red)	4M (Blue)	208	D FP RPR RPL
5	1R (Red)	4M (Blue)	208	D
6	1R (Red)	4M (Blue)	208	No
7	1L (Red)	4R (Blue)	170	No
8	4M (Red)	2R (Blue)	165	D
9	2L (Red)	4R (Blue)	148	D
10	1R (Red)	4R (Blue)	149	D
11	2L (Red)	4R (Blue)	148	No
12	1R (Red)	4R (Blue)	149	No
13	1M (Red)	4R (Blue)	162	No
14	1R (Red)	4R (Blue)	149	No
15	1R (Red)	4R (Blue)	149	No
16	1R (Red)	4R (Blue)	149	D
17	1M (Red)	4R (Blue)	162	D
18	4M (Red)	2R (Blue)	165	No
19	4M (Red)	4R (Blue)	88	D
20	1R (Red)	2R (Blue)	72	FP
21	1R (Red)	2R (Blue)	72	No
22	1L (Red)	2R (Blue)	112	FP
23	2R (Red)	4R (Blue)	119	D
24	1L (Red)	2R (Blue)	112	No
25	2R (Red)	4R (Blue)	119	No
26	4M (Red)	4R (Blue)	88	No

Legend: **D**-driver, **FP**-front passenger, **RPR**-rear passenger right, **RPL**-rear passenger left, **FULL**-all passengers, **No**-empty car, **Outside**-outside of the car (not depicted in Figure 1).

III. CHANNEL DESCRIPTION

Since the measurements were performed in the frequency domain with 10 MHz step, we utilize the inverse Fourier transform with rectangular window to obtain the channel impulse response. Then we employ a peak detector in order
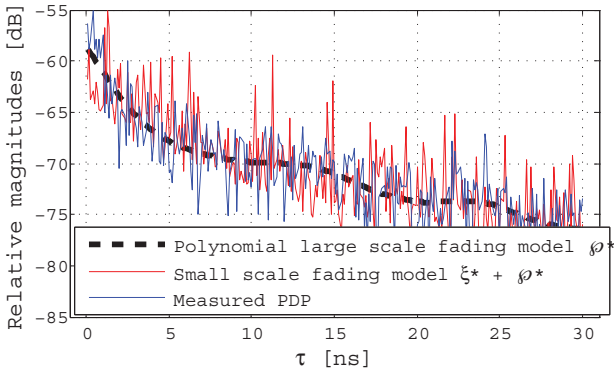
Fig. 4. Comparison of 3-3 order 2D polynomial large scale fading model $\wp^*$, sum of $\wp$ and log-Weibull-distributed small scale fading model ξ^* and measured CIR.

to recognize the first arrival multipath component of examined CIR.

A. Channel Impulse Response (CIR)

The intra vehicle environment is considered as time invariant, therefore the multipath wireless channels are described by the impulse response according:

$$h'_\alpha(\tau) = \sum_{n=0}^{N-1} \rho_n e^{j\Phi_n} \delta(\tau - \tau_n), \qquad (1)$$

where τ_n and $\rho_n e^{j\Phi_n}$ are the propagation delay and complex gain coefficient of the n-th multipath component. The index α denotes the measurement number according to Table I. The $h_\alpha(\tau)$ is a complex number with phase uniformly distributed in the interval $[0, 2\pi)$. In the following text, we use absolute value of CIR, $h_\alpha(\tau) = | h'_\alpha(\tau) |$.

Our hypothesis assumes that CIR is composed of large scale fading and superimposed small scale fading process. To decompose these components, the exploitation of Hodrick-Prescott detrending filter [8] which operates with so called cyclical and trend components is straightforward. When compared with a moving average filter, the Hodrick-Prescott do not cause data loss, thus seems beneficial. In general however, other approaches are certainly possible.

In the following, we derive the channel model of in-vehicle environment for 55–65 GHz considering variety of antenna positions and occupancy configurations (according to Figure 1). This idea is illustrated in Figure 4 taking into account one specific measurement number α. The channel model consists of:

- *large scale fading model* represented by two dimensional polynomial curve $\wp^*_\alpha(\tau)$ where τ is time in delay domain. Let us note that we use * superscript to mark models of measured variables (written without the * superscript).
- *small scale fading model* represented by Generalized Extreme Value (GEV) random process $\xi^*(k, \sigma, \mu)$, where k is the shape parameter, σ is the distribution scale parameter and μ is the location parameter [9]. It will

be shown, that GEV can be simplified into log-Weibull-distributed process $\xi^*(0, \sigma, \mu)$. Therefore we write:

$$h_\alpha(\tau) = \wp_\alpha(\tau) + \xi_\alpha(\tau). \qquad (2)$$

B. Large scale fading

First, by filtering the measured $h_\alpha(\tau)$ by the Hodrick-Prescott de-trending filter according to Equation 3, the cyclical component $\xi_\alpha(\tau)$ is obtained.

$$\xi_\alpha(\tau) = \min_\wp \left(\sum_{\tau=1}^{T} (h_\alpha(\tau) - \wp_\alpha(\tau))^2 + \right. \qquad (3)$$

$$\left. +\lambda \sum_{\tau=2}^{T-1} \left[(\wp_\alpha(\tau+1) - \wp_\alpha(\tau)) - (\wp_\alpha(\tau) - \wp_\alpha(\tau-1)) \right]^2 \right),$$

where $\wp$ represents a trend component and $\tau = 1, \ldots, T$ is the time in delay domain. Let us note that according to the terminology utilized in [8] we consider the cyclical component to represent the small scale variations while the large scale fading is described by the trend component.

The heuristically chosen positive multiplier λ adjusts the filters capability to filter out the short-term fluctuations. This paper utilizes $\lambda = 5e6$, however the range of exploitable values is from $\lambda = 500$ up to $\lambda = 5e6$, while the lower the λ, the faster the $\wp$ changes. We have chosen the λ in the upper range of usable values in order to provide the polynomial fit of the lowest possible order while still maintaining the two-sample Kolmogorov-Smirnov p-values in the > 0.1 region ensuring "very significant match" according to the ingrained interpretation of two-sample Kolmogorov-Smirnov test results. More information regarding the adjustment of Hodrick-Prescott filter is elaborated in [10].

Next, with accordance to Equation 2, the cyclical component ξ is subtracted from measured $h_\alpha(\tau)$ pursuant to:

$$\wp_\alpha(\tau) = h_\alpha(\tau) - \xi_\alpha(\tau), \qquad (4)$$

thus obtaining the large scale fading component $\wp_\alpha(\tau)$. The measured $\wp_\alpha(\tau)$ quantity is visible in Figure 5, where the data are aligned by the first arrival multipath component detected by the peak detector and sorted according to the mean power such that the large scale fading map is described by the polynomial fit of the lowest possible order.

To model the measured large scale fading phenomena, we parametrize the $\wp_\alpha(\tau)$ utilizing two dimensional polynomial fit of order 3 in both domains, namely in the delay domain and the spatial domain represented by variable index α. The 2D polynomial fit is given as:

$$\wp^*_\alpha(\tau) = p_{00} + p_{10}\alpha + p_{01}\tau + p_{20}\alpha^2 + p_{11}\alpha\tau + p_{02}\tau^2 + \quad (5)$$

$$+p_{30}\alpha^3 + p_{21}\alpha^2\tau + p_{12}\alpha\tau^2 + p_{03}\tau^3,$$

with values of the parameters p_{uw} listed in Table II. The modeled $\wp^*_\alpha(\tau)$ is depicted in Figure 6. Let us note that the measurement index α is here treated as variable. Otherwise, if we would provide 1D polynomial fit, we would obtain

specific polynomial parameters for each α. Therefore the 2D fit significantly reduces the number of parameters required to describe all measured CIRs.

p_{00} = -48.14	p_{02} = 0.0002746
p_{10} = 1.335	p_{30} = 0.0007026
p_{01} = -0.1622	p_{21} = 9.416e-05
p_{20} = -0.05851	p_{12} = -1.254e-05
p_{11} = 0.001221	p_{03} = -4.571e-08

C. Small scale fading

Utilizing the Maximum Likelihood Estimation (MLE), we found out that the best fit to the superimposed small scale fading signal ξ is achieved by the Generalized Extreme Value (GEV) distribution [9]. The fitted parameters of the signal ξ as well as the measured data are visible in Figure 7. The Probability Density Function (PDF) of the GEV is given by:

$$f(x \mid k, \mu, \sigma) = \frac{1}{\sigma} \exp\left[-\beta^{-\frac{1}{k}} \right] \beta^{-1-\frac{1}{k}}, \qquad (6)$$

for

$$\beta = 1 + k \frac{x - \mu}{\sigma}, \qquad (7)$$

where μ is the location parameter, k is the shape parameter and σ the distribution scale parameter.

55-65 GHz	Dist. type	Mean ν	Variance η
shape parameter k	GEV	-0.0902	0.0031
scale parameter σ	GEV	4.81	0.1004
location parameter μ	GEV	-2.317	0.0308

As will be documented by the Kolmogorov-Smirnov test results, the small scale fading model ξ^* can be approximated by a log-Weibull (also called as Gumbel) distribution [11]. For specific choice of parameters the log-Weibull reduces to Weibull distribution. The Weibull distribution of path fading is presented in [12], [13].

In [14] the author claim that there is no theoretical explanation for encountering this distribution type. On the other hand, it contains the well accepted Rayleigh distribution as a special case. The best MLE fit is produced by the log-Weibull distribution probably due to the fact that this distribution exploits three parameters which enhances the flexibility to match the empirical data.

IV. VALIDATION AND UTILIZATION OF PRESENTED CHANNEL MODEL

The presented channel model consists of:
- The map of large scale fading $\wp^*_\alpha(\tau)$ presented in Figure 6. This map models measured large scale fading component $\wp_\alpha(\tau)$ extracted from $h_\alpha(\tau)$ utilizing the Hodrick-Prescott detrending filter. In Figure 5, the order of link
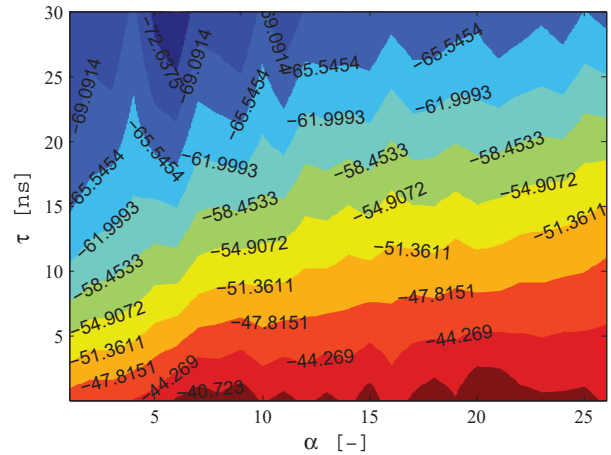
Fig. 5. Measured large scale fading component $\wp_\alpha(\tau)$ representing $h_\alpha(\tau)$ filtered by the Hodrick-Prescott filter using λ=5e6. The data are aligned by the first arrival multipath component detected by peak detector and sorted according to the mean power thus the large scale fading map is described by the polynomial fit $\wp^*$ of the lowest possible order. Values α denotes spatially specific wireless link indexes according to Table I and Figure 1. Values attached to the contours are in dB.
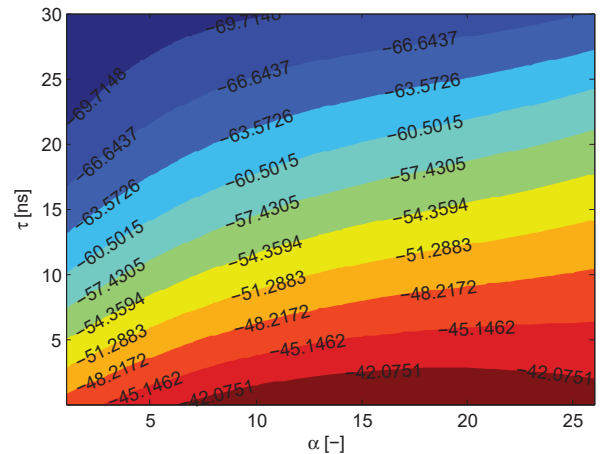
Fig. 6. Large scale fading map $\wp^*_\alpha(\tau)$ representing the polynomial 3-3 order model of $h_\alpha(\tau)$ filtered by the Hodrick-Prescott filter. Values attached to the contours are in dB.

index α in $\wp_\alpha(\tau)$ is sorted such that the mean power is increasing with increasing α. Thus, the polynomial fit is of the lowest possible order while still maintaining the p-values of Kolmogorov-Smirnov test higher than 0.1.
- The log-Weibull-distributed random process ξ^* with parameters according to Table III which is superimposed to the large scale fading $\wp^*_\alpha(\tau)$.

A. Utilization of the channel model

Let us assume, that we are concerned about recreating the CIR for the wireless link between the RX 4M and TX 2R antennas according to Figure 1. The maximal delay spread is for example $\tau_{\max}$ =30 ns. Our maximal time resolution T_r is given by the 10 GHz bandwidth as $T_r = 1/10e9$. From Table
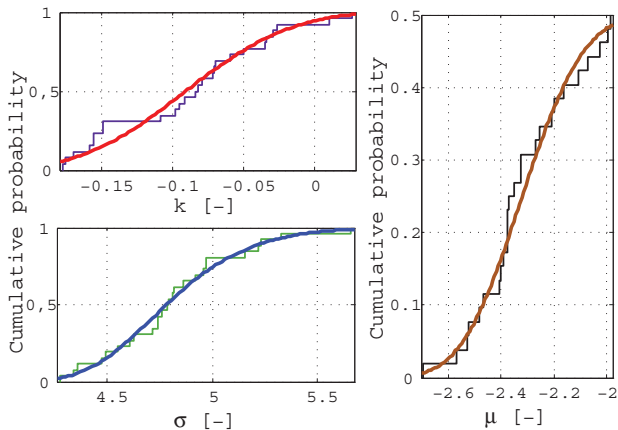
Fig. 7. Cumulative probability of ξ representing small scale fading superimposed to $\wp^*$ model. The small scale fading signal ξ is fitted with Generalized extreme value distribution according to Table III which can be further simplified to log-Weibull-distributed signal ($k = 0$).

1 it is seen, that this configuration is marked as $\alpha = 8$. Next, $\alpha = 8$ is substituted to Equation 5, while τ linearly increase from $T_{\rm r}$ up to the product of $\tau_{\max}$ and $T_{\rm r}$. The result of the Equation 5 is the large scale fading model $\wp_8^*$. The small scale fading ξ^* is obtained using the GEV generator with setting according to Table III. The modeled CIR is then written as: $h_8'(\tau) = [\wp_8^*(\tau) + \xi_8^*(\tau)]e^{j\phi}$, where the phase ϕ is uniformly distributed in the interval $[0, 2\pi)$.

B. Validation of the channel model

In order to validate our in-vehicle channel model, in Figure 8 we provide results of two-sample Kolmogorov-Smirnov test representing a commonly used metric for goodness of fit. The Figure 8 shows resulting p-values where only two cases fall into sub 0.1 region, however all other are cases are in > 0.1 area.
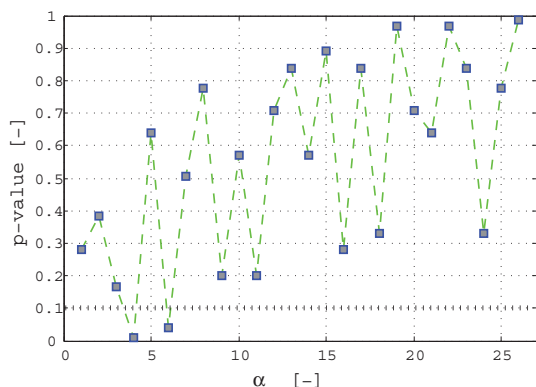
Fig. 8. p-value of Kolmogorov-Smirnov test comparing measured CIR and polynomial CIR model $\wp^*$ of large scale fading with input parameters according to Table II with superimposed log-Weibull-distributed small scale fading model $\xi^*(0, 4.394, -2)$.

V. CONCLUSION

This paper deals with the in-vehicle channel measurement campaign carried out in 55-65 GHz band and provides corresponding channel model including simple application example. The channel model operates with baseline hypothesis of the decomposition of the CIR into the large scale and small scale fading. The decomposition is performed with the Hodrick-Prescott filter. The large scale fading is then simulated with two dimensional polynomial curve while the small scale fading is modeled with the log-Weibull-distributed random process. Finally, we present resulting p-values of the two-sample Kolmogorov-Smirnov test showing no presumption against our hypothesis.

REFERENCES

[1] G. Leen and D. Heffernan, "Expanding automotive electronic systems," *Computer*, vol. 35, no. 1, pp. 88–93, 2002.

[2] E. Ben-Dor, T. Rappaport, Y. Qiao, and S. Lauffenburger, "Millimeter-wave 60 GHz outdoor and vehicle AOA propagation measurements using a broadband channel sounder," in *Global Telecommunications Conference (GLOBECOM 2011), 2011 IEEE*, Dec 2011, pp. 1–6.

[3] C. Gustafson, K. Haneda, S. Wyne, and F. Tufvesson, "On mm-wave multi-path clustering and channel modeling," 2014.

[4] M. Schack, M. Jacob, and T. Kurner, "Comparison of in-car UWB and 60 GHz channel measurements," in *Antennas and Propagation (EuCAP), 2010 Proceedings of the Fourth European Conference on*. IEEE, 2010, pp. 1–5.

[5] S. Krone, F. Guderian, G. Fettweis, M. Petri, M. Piz, M. Marinkovic, M. Peter, R. Felbecker, and W. Keusgen, "Physical layer design, link budget analysis, and digital baseband implementation for 60 GHz short-range applications," *International Journal of Microwave and Wireless Technologies*, vol. 3, no. 02, pp. 189–200, 2011.

[6] J. Blumenstein, R. Marsalek, A. Prokes, and C. Mecklenbrauker, "Impulse noise mitigation for OFDM by time-frequency spreading," in *Multiple Access Communcations*, 2013.

[7] F. J. Massey Jr, "The Kolmogorov-Smirnov test for goodness of fit," *Journal of the American statistical Association*, vol. 46, no. 253, pp. 68–78, 1951.

[8] R. J. Hodrick and E. C. Prescott, "Postwar US business cycles: an empirical investigation," *Journal of Money, credit, and Banking*, pp. 1–16, 1997.

[9] S. Kotz and S. Nadarajah, *Extreme value distributions*. World Scientific, 2000.

[10] M. O. Ravn and H. Uhlig, "On adjusting the Hodrick-Prescott filter for the frequency of observations," *Review of economics and statistics*, vol. 84, no. 2, pp. 371–376, 2002.

[11] E. Gumbel, "Les valeurs extrêmes des distributions statistiques," in *Annales de l'institut Henri Poincaré*, vol. 5, no. 2. Presses universitaires de France, 1935, pp. 115–158.

[12] N. Shepherd, "Radio wave loss deviation and shadow loss at 900 MHz," *Vehicular Technology, IEEE Transactions on*, vol. 26, no. 4, pp. 309–313, Nov 1977.

[13] S. Howard and K. Pahlavan, "Fading results from narrowband measurements of the indoor radio channel," in *Personal, Indoor and Mobile Radio Communications., IEEE International Symposium on*, Sep 1991, pp. 92–97.

[14] H. Hashemi, "The indoor radio propagation channel," *Proceedings of the IEEE*, vol. 81, no. 7, pp. 943–968, 1993.

Intra-vehicular path loss comparison of UWB channel for 3-11 GHz and 55-65 GHz

Jiri Blumenstein, Tomas Mikulasek, Ales Prokes, Thomas Zemen, Christoph Mecklenbrauker

Intra-Vehicular Path Loss Comparison of UWB Channel for 3–11 GHz and 55–65 GHz

Jiri Blumenstein, Tomas Mikulasek, Ales Prokes
The Faculty of Electrical Engineering and Communication
Brno University of Technology
Brno, Czech Republic
Email: blumenstein@feec.vutbr.cz

Thomas Zemen
AIT Austrian Institute
of Technology GmbH,
Vienna, Austria

Christoph Mecklenbräuker
Institute of Telecommunications,
Vienna University of Technology,
Vienna, Austria

Abstract—This paper provides a comparison of a real-world intra-vehicular radio channel measurements of the ultra-wide frequency bands, namely the 3–11 GHz and the 55–65 GHz. The measurement campaign was performed utilizing a vector network analyzer (VNA) and a frequency domain method ensuring a high dynamic range of 70 dB and a frequency resolution of 10 MHz. An inverse Fourier transform is exploited for a transition of the measured data into the time domain and to obtain a channel impulse response (CIR). A delay spread and a path loss are derived and compared. Measured data is freely available online: http://www.radio.feec.vutbr.cz/GACR-13-38735S/

I. Introduction

The inter- and intra-vehicular communication is one of the building blocks of a future smart city infrastructure [1]. Since the amount of wiring inside each vehicle reaches up to several kilometers and weights several tens of kilograms [2], there is a significant effort to replace some of the wire harness with a wireless communication [3]–[6]. This will reduce the weight and consequently also a fuel consumption of vehicles with an internal combustion engine and extend the limited range of electrified vehicles.

A placement of various sensors on the vehicles body and connection of moving parts such as seats, wheels and steering wheel [7] is easier when done wireless. The benefit of wireless connection is also substantiation considering that the wire harnesses of current vehicles is usually platform specific. This feature makes the design and installation of the wire harness a rather demanding process.

As the amount of bandwidth is limited, the potential of high gigahertz bands is growing even despite the unfavorable atmospheric absorption. Therefore, this paper deals with the channel measurement and characterization of the specific in-vehicle environment for the frequency bands of the 3–11 GHz and the 55–65 GHz. Both examined bands offers around 10 GHz of unlicensed bandwidth. However, as we will show in this paper, the radio channel characteristics exhibits notable differences in path loss or delay spread. On one hand, the millimeter wave band suffers from higher atmospheric loss and higher penetration loss compared to the 3–11 GHz band [8], [9]. However, it could benefit from high-gain steerable antennas with small physical dimensions [10]. On the other hand, the 3–11 GHz band provides higher diversity and requires lower transmit power [11].

A. Contribution of the paper

In very similar conditions we compare the 3–11 GHz and the 55-65 GHz frequency bands in terms of:

- The delay spread and root mean square (RMS) delay spread versus antenna separation for the in-vehicle compartment.

- The measured path loss including a comparison with a log-distance path loss model.

- The path loss exponent extraction by means of a maximum likelihood estimate (MLE).

- The measured CIRs for all selected antenna positions.
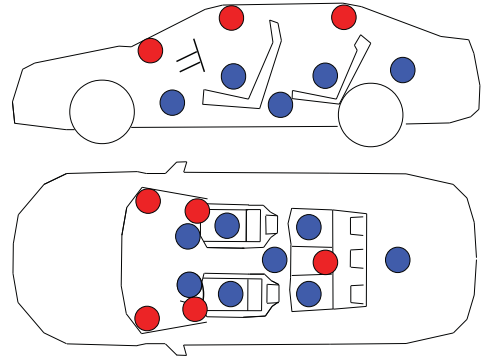
Fig. 1: Antenna placement layout for both 3–11 GHz and 55–65 GHz frequency band. Receiving antennas are depicted in red, transmitting antennas in blue. The VNA is placed outside the vehicle under test. There was no occupancy inside the vehicle during the measurement. The mean antenna separation is 1.28 m while the variance is 0.28 m.

II. Measurement apparatus

The measurements were performed in the mid-sized passenger car Skoda Octavia III. The transmit and receive antennas are marked with red and blue colors in Figure 1 respectively. The receiving (RX) antenna was placed at different spatial points inside the car compartment. The transmitting (TX) antennas were placed on the left and right side of the dash-board and at the rear part of the ceiling according to Figure 1. Please note that the mean antenna separation is 1.28 m while the variance is 0.28 m.

A. 3-11 GHz instrumentation

For each spatial point the s_{41}, s_{42}, and s_{43} scattering parameters corresponding to the channel transfer function (CTF) were measured in the frequency domain utilizing a calibrated four port VNA Agilent Technologies E5071C. The measured radiation patterns of the utilized monoconical antennas are depicted in Figure 2a. The transmitting power was set to 1 dBm.

B. 55-65 GHz instrumentation

The 4-port vector network analyzer R&S ZVA67 was exploited for measuring the transmission coefficient between two antennas in the frequency band 55–65 GHz. The dynamic range of the measurement setup was extended utilizing the broadband power amplifier (QPW-50662330) on the transmitting side. An open waveguide WR15 having the radiation pattern depicted in Figure 2b was utilized as a transmitting and receiving antenna. Here, the transmitting power was set to 13 dBm.
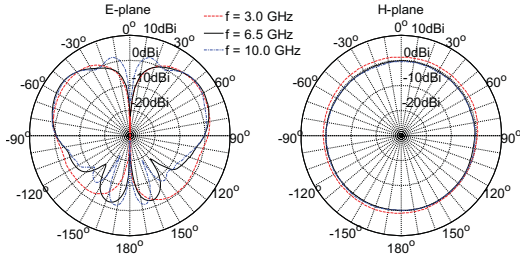
(a) Measured gain pattern of the conical monopole antennas for frequency range 3–11 GHz.
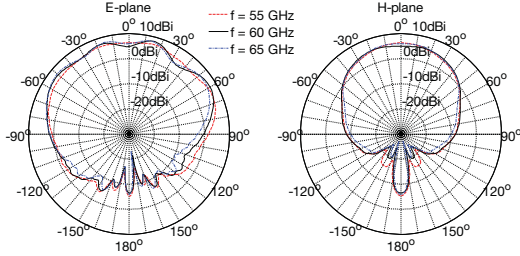
(b) Measured gain pattern of the open ended waveguide in E–plane and H–plane for open ended waveguide antenna at 55–65 GHz.

Fig. 2: Measured radiation patterns of utilized antennas.

III. CHANNEL PARAMETERS

The measurement utilizes swept-frequency channel-sounding method. Thus the CTF is given as:

$$H^{\alpha}(f) = s_{21}^{\alpha}(f), \qquad (1)$$

where f represents a measurement index identifiable with certain frequency and where α denotes the position of the receiving antenna within the measured vehicle as depicted in Figure 1. Utilizing an inverse Fourier transform we transform the CTF into a CIR according to:

$$h^{\alpha}(n) = \sum_{f=0}^{N-1} w(f) H^{\alpha}(f) e^{jfn2\pi/N}, \qquad (2)$$

where n stands for a discrete time in the delay domain and $w(f)$ represents a Blackman window [12]. Next, we write the definition of the PDP as it will be exploited later in this paper. The power-delay profile (PDP) is given as spatial average of squared CIRs:

$$Q(n) = \mathrm{E}_{\alpha}\{|h^{\alpha}(n)|^2\}. \qquad (3)$$

It holds that the time in the delay τ domain is given as $\tau = n/B$, where $1/B$ is the time resolution.
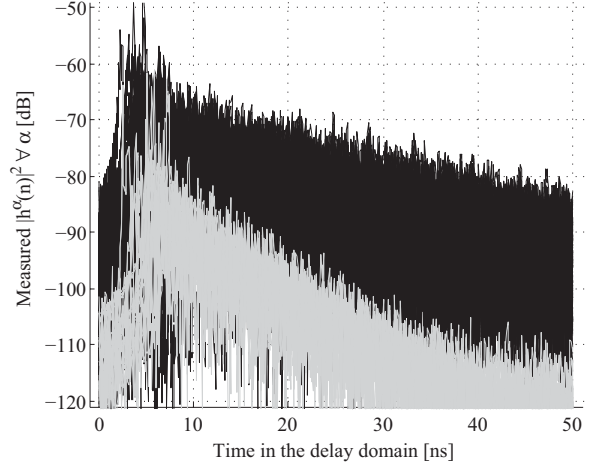
Fig. 4: Overlap of all squared channel impulse responses. The 3–11 GHz are plotted in black, the 55–65 GHz are in gray.

A. Path loss and log-distance path loss model

The path loss or the path attenuation is defined as a difference between transmitted and received power. In free space, this is described by a Friss transmission equation [13]. For the non-free space, the path loss is modeled by the log-distance path loss model. As the path attenuation is specific for each environment and frequency band, the path loss exponent is utilized to determine the particular attenuation. The log-distance path loss model is given as [14]:

$$PL(d) = P_{\mathrm{ref}}(d_0) - 10\gamma\log\frac{d}{d_0} + S, \forall d \in \{0.6, ..., 4\}\mathrm{m}, \quad (4)$$

where γ is the path loss exponent, d is an antenna separation and S stands for a random process describing a signal fading. Please note that we consider the reference distance $d_0 = 1$ m.

Now, the received power in dBm is calculated from the CIR according to [15]:

$$Pr = 10\log\frac{\sum_{n=0}^{N-1}|h^{\alpha}(n)|^2}{0.001\ R}, \qquad (5)$$

where $R = 50\ \Omega$ is the electric resistance of the system. The resulting path loss evaluation is depicted in Figure 5. The respective path loss exponent γ is obtained via MLE fitting. The log-distance path loss model is plotted in a form of solid line together with the measured data. Please note that the x axis is in logarithmic scale. Now, Table I sums the statistical data of the path loss examination.

(a) 3–11 GHz monoconical antenna mounted on front windshield next to the rear-view mirror.

(b) 3–11 GHz monoconical antenna in the middle of the rear seat using a tripod.

(c) The seat behind the front passenger with transmitting open ended waveguide antenna for 55–65 GHz. Please note the heat sink for the power amplifier cooling.
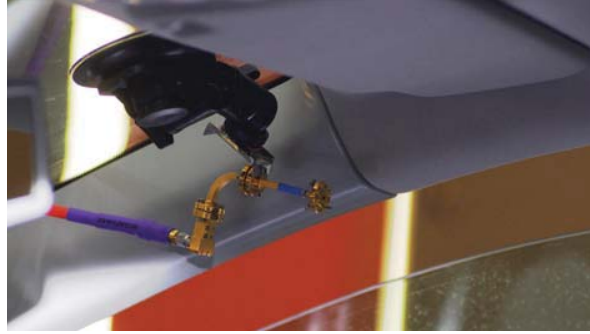
(d) 55–65 GHz open ended waveguide receiving antenna fastened using a suction cap.

Fig. 3: Photographs taken during the measurement campaign.

	$P_{\text{ref}}(d_0)$ [dB]	PL variance [dB]	γ
3-11 GHz	37.39	24.13	0.01
55-65 GHz	65.60	21.40	0.22

TABLE I: Mean and variance of the measured path loss. We derive the path loss exponent γ by means of MLE.

	delay spread		RMS delay spread	
	mean [ns]	variance [ns]	mean [ns]	variance [ns]
3-11 GHz	31.21	10.29	13.18	0.28
55-65 GHz	24.13	4.76	10.05	0.01

TABLE II: Measured delay spread and RMS delay spread values

B. Moments of the PDP

The wireless channel is frequently evaluated via the first and the second central moment of the PDP. The first moment is the mean delay given as [16]:

$$D = \frac{\sum_{n=0}^{N-1} nQ(n)}{\sum_{n=0}^{N-1} Q(n)}, \qquad (6)$$

while the second moment of the PDP, the RMS delay spread is defined according to:

$$S_n = \sqrt{\frac{\sum_{n=0}^{N-1} n^2 Q(n)}{\sum_{n=0}^{N-1} Q(n)} - D^2}. \qquad (7)$$
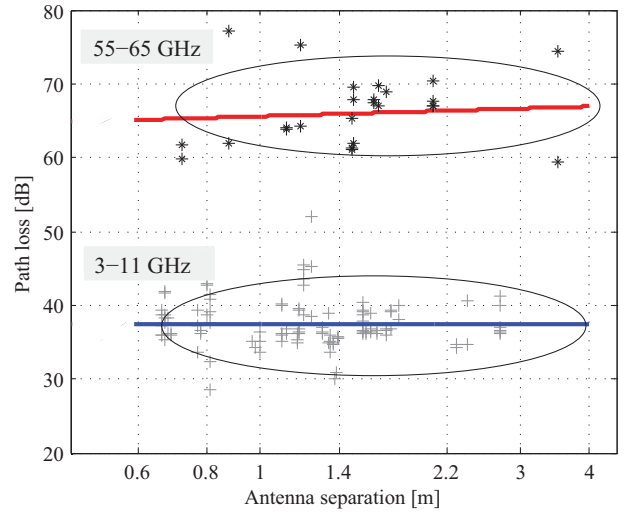
Fig. 5: Path loss evaluation of the 3–11 GHz and the 55–65 GHz band for all antenna positions as depicted in Figure 1 including comparison with the log-distance path loss model (solid lines).

The measured data is plotted in Figure 6 showing around 10 ns higher delay spread in the case of the 3–11 GHz. Detailed statistics are available in Table II.
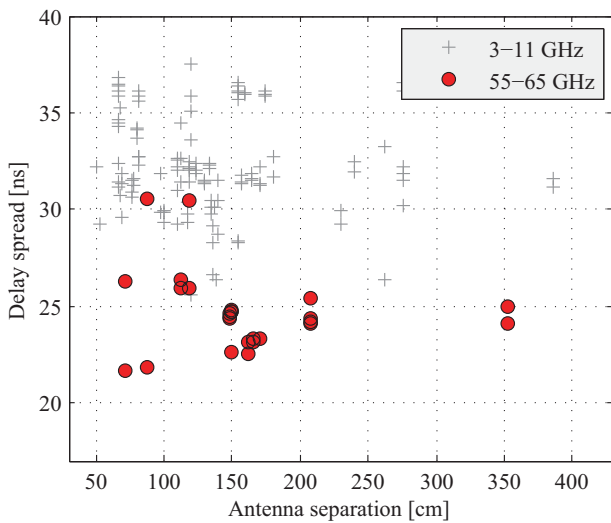
Fig. 6: Delay spread versus antenna separation for the 3–11 GHz band and the 55–65 GHz band.

IV. CONCLUSION

This paper provides a comparison of the radio channel measurement for the 3–11 GHz and the 55–65 GHz frequency bands inside the passenger vehicle. The channel characteristics are evaluated via the path loss, delay spread, RMS delay spread and CIRs. We also present a parametrization of the path loss utilizing the log-distance path loss model where the path loss exponent is extracted by means of MLE. The mean value of the path loss is 36 dB for the 3–11 GHz band and 52 dB for the 55-65 GHz frequency band. The mean antenna separation is 1.2 m. This measurement takes into account a situation, when the antennas for the 55-65 GHz frequency band are directed to each other while the antennas for the 3–11 GHz band exhibits omnidirectional radiation pattern.

It is worth to note that the variance of the path loss is very similar (approx. 20 dB) for both examined frequency bands. It is also interesting to point out that the log-distance path loss exponent reaches values around around 0.01 and 0.22 for the 3-11 GHz and the 55-65 GHz band respectively. It is given by the random placement of the TX-RX antennas inside the vehicle while most of the measured links are non-line of sight (NLOS). Considering the variety of the possible use case scenarios, where the communicating antennas may not be perfectly facing to each other, or in the case of NLOS, the path loss variance is large. Therefore, the validity of the log-distance path loss model for this short-range scenarios is rather poor and the mean path loss with the path loss variance provides more useful information.

The delay spread and the RMS delay spread values for the 3–11 GHz band are 31 ns and 13 ns respectively. For the case of the 55–65 GHz frequency band the delay spread and the RMS delay spread is 24 ns and 10 ns respectively. Also, the variance of the delay spread for the 55–65 GHz band is notably lower, approx. 5 ns compared to 10 ns of the 3–11 GHz band.

To promote a reproducibility of this research, our measured data are freely available online: http://www.radio.feec.vutbr.cz/

REFERENCES

[1] C. Sommer and F. Dressler, *Vehicular Networking*.

[2] G. Leen and D. Heffernan, "Expanding automotive electronic systems," *Computer*, vol. 35, no. 1, pp. 88–93, 2002.

[3] E. Ben-Dor, T. Rappaport, Y. Qiao, and S. Lauffenburger, "Millimeter-wave 60 GHz outdoor and vehicle AOA propagation measurements using a broadband channel sounder," in *Global Telecommunications Conference (GLOBECOM 2011), 2011 IEEE*, Dec 2011, pp. 1–6.

[4] M. Schack, M. Jacob, and T. Kurner, "Comparison of in-car UWB and 60 GHz channel measurements," in *Antennas and Propagation (EuCAP), 2010 Proceedings of the Fourth European Conference on*. IEEE, 2010, pp. 1–5.

[5] Y. Katayama, K. Terasaka, K. Higashikaturagi, I. Matunami, and A. Kajiwara, "Ultra-wideband impulse-radio propagation for in-vehicle wireless link," in *Vehicular Technology Conference, 2006. VTC-2006 Fall. 2006 IEEE 64th*, 2006, pp. 1–5.

[6] J. Blumenstein, T. Mikulasek, R. Marsalek, A. Prokes, T. Zemen, and C. Mecklenbrauker, "In-vehicle mm-wave channel model and measurement," in *Vehicular Technology Conference (VTC Fall), 2014 IEEE 80th*. IEEE, 2014, pp. 1–5.

[7] G. Lasser and C. Mecklenbrauker, "Channel model for tyre pressure monitoring systems (TPMS)," in *Antennas and Propagation (EuCAP), 2010 Proceedings of the Fourth European Conference on*. IEEE, 2010.

[8] C. Gustafson, K. Haneda, S. Wyne, and F. Tufvesson, "On mm-wave multipath clustering and channel modeling," *Antennas and Propagation, IEEE Transactions on*, vol. 62, no. 3, pp. 1445–1455, March 2014.

[9] J. Blumenstein, A. Prokes, T. Mikulasek, R. Marsalek, T. Zemen, and C. Mecklenbrauker, "In-vehicle channel measurement, characterization and spatial consistency comparison of 3-11 GHz and 55-65 GHz frequency bands." *IEEE Journal of Selected Topics in Signal Processing - submitted*.

[10] T. Rappaport, J. Murdock, and F. Gutierrez, "State of the art in 60-GHz integrated circuits and systems for wireless communications," *Proceedings of the IEEE*, vol. 99, no. 8, pp. 1390–1436, Aug 2011.

[11] J. Blumenstein, T. Mikulasek, R. Marsalek, A. Chandra, A. Prokes, T. Zemen, and C. Mecklenbrauker, "In-vehicle UWB channel measurement, model and spatial stationarity," in *Vehicular Networking Conference (VNC), 2014 IEEE*. IEEE, 2014, pp. 77–80.

[12] J. Blumenstein, T. Mikulasek, R. Marsalek, A. Prokes, T. Zemen, and C. Mecklenbruker, "Measurements of ultra wide band in-vehicle channel - statistical description and TOA positioning feasibility study," *EURASIP Journal on Wireless Communications and Networking*, 2015.

[13] H. T. Friis, "A note on a simple transmission formula," *proc. IRE*, vol. 34, no. 5, pp. 254–256, 1946.

[14] A. Molisch, D. Cassioli, C.-C. Chong, S. Emami, A. Fort, B. Kannan, J. Karedal, J. Kunisch, H. Schantz, K. Siwiak, and M. Win, "A comprehensive standardized model for ultrawideband propagation channels," *Antennas and Propagation, IEEE Transactions on*, vol. 54, no. 11, pp. 3151–3166, Nov 2006.

[15] T. Gigl, T. Buchgraber, B. Geiger, A. Adalan, J. Preishuber-Pfluegl, and K. Witrisal, "Pathloss and delay-spread analysis of multipath intensive environments using IEEE 802.15.4a UWB Signals," in *COST 2100 Management Committee Meeting*, Sep 2009. [Online]. Available: www.cost2100.org

[16] A. F. Molisch, *Wireless communications*. John Wiley & Sons, 2010, vol. 15.

On mutual information of measured 60 GHz wideband indoor MIMO channels: Time domain singular values

Jiri Blumenstein, Roman Marsalek, Tomas Gotthans, Ronald Nissel, Markus Rupp

On Mutual Information of Measured 60 GHz Wideband Indoor MIMO Channels: Time Domain Singular Values

Jiri Blumenstein[†], Roman Marsalek[†], Tomas Gotthans[†], Ronald Nissel[‡] and Markus Rupp[‡]

[†]The Faculty of Electrical Engineering and Communication, Brno Univ. of Technology, Czech Rep.

[‡]Christian Doppler Lab. for Dependable Wireless Connectivity for the Society in Motion, TU Wien, Austria

Email: {blumenstein, marsaler, gotthans}@vutbr.cz, {rnissel, mrupp}@nt.tuwien.ac.at

Abstract—This paper presents a report on mutual information based on measured indoor millimeter-wave (mmWave) channels with multiple antennas at input and output (MIMO). We show that for fixed indoor communication systems, an optimal antenna element spacing can be found such that the measured mutual information almost reaches the capacity of a perfectly orthogonal (theoretical) MIMO channel (with the same number of receiver (RX) and transmitter (TX) antennas). Secondly, we present, that even though the measured channel transfer functions (CTFs) exhibit large fluctuations (i.e., temporal dispersion), the mutual information is mainly determined by the mean singular value of the line-of-sight (LOS) components. Due to their strong variations over frequency mmWave channels are tedious when describing them with classical methods in the frequency domain. An approximation by numerous flat subbands leads to an error in mutual information (MI) by 2 bit/s/Hz (for 80% probability). In comparison, our proposed method in the time domain, however, offers a notably smaller error (1 bit/s/Hz for 80% probability).

I. INTRODUCTION

With the lasting upswing of required data rates of almost all communication systems, the utilization of new and unused frequency bands is a must [1]. Recognized and promising is the millimeter-wave (mmWave) band which we consider to span from 55 to 65 GHz. As defined by many spectrum managing authorities, the mmWave band to some extent overlaps the un-licensed industrial scientific and medical (ISM) bands and therefore it is especially attractive for both industry and the research community. On the other hand, mmWave hardware based on gallium arsenide technology comes with a notably higher price than the widespread silicon based technology [2]. One of the proposed solution to lower the price of the mmWave multiple-input multiple-output (MIMO) transceivers is to utilize the spatial modulation (SM), while supporting MIMO, it requires only one radio-frequency (RF) chain [3]. Thus, mmWave SM could represent a cost effective solution for some areas of the wireless communication.

The efficient implementation of mmWave SM MIMO system requires non-mobile line-of-sight (LOS) propagation conditions together with optimal antenna elements spacing. The antenna element spacing is proportional to propagation distance as well as wavelength according to [4]

$$\zeta \approx \sqrt{\frac{D\lambda}{N}}, \qquad (1)$$

where ζ is the antenna element spacing, D is the RX-TX distance, N is the number of antenna elements and λ is the wavelength. Please note that relation (1) represents a simplified solution where perfectly parallel uniform linear arrays (ULAs) with the same number of elements N are used.

This paper deals with the channel characterization of mmWave MIMO channels while the details regarding system design using SM scheme can be found in [4], [5]. In the field of the mmWave channel sounding, an extensive research has been done in the last two decades, e.g. [6]–[8], but for SM, the utilized measurement setups are not optimal mainly in terms of the critical antenna element spacing.

Also, as recently published in [9], where research questions regarding the fundamental mmWave channel capacities have been opened. However, while no real-world measurement aiming at the specifics of the SM scheme has been performed, the contribution of this paper is following:

- We present a channel sounding campaign capturing in total 11 measurement scenarios while over 200 channel transfer functions (CTFs) were recorded for 4×4 and 6×6 MIMO configurations.
- We analyzed the measured mutual information (MI) dependency on 1) bandwidth, 2) antenna element separation and 3) multipath richness of the 60 GHz indoor channel with 10 GHz bandwidth.
- We demonstrate a relation between the overall MI of the channel and the mean singular value of the LOS components.

(a) Measurement site I   (b) Measurement site II
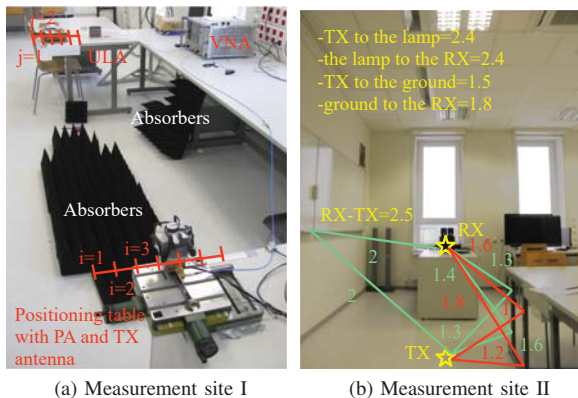
Fig. 1: Photographs of two out of three measurement locations. Measurement site III is similar to the site II, but the xy tables (emulating the ULAs as in [8]) are placed on top of the desk with $12\,\mathrm{cm}$ antenna height from the surface. All dimensions are in meters.

II. MEASUREMENT

A. Measurement locations

The measurement campaign was carried out in the laboratory environment at Brno University of Technology. We have measured mmWave channels in three different sites, where site I and site II are depicted in Figure 1. The difference between the measurement sites is mainly in the multipath richness of the recorded CTFs. Site I features the lowest amount of multipath components (MPCs) due to the absorbing materials covering major reflective surfaces. Site II is without absorbing materials while the ULAs are positioned such that in their near proximity, metallic constructions of the tables are present. This causes a notable increase of the MPCs. Measurement site III was located in the same office as the site II, with the main difference that the ULAs were placed on the top of the tables visible on the right hand side of Figure 1b.

We utilized a $4{\times}4$ MIMO setup configured with an element separation $\boldsymbol{\zeta} \in [\zeta, \frac{\zeta}{\sqrt{2}}, \frac{\zeta}{2}]$. For detailed information about the MIMO configurations and element separations, please see Table I, where all separations are determined with a center frequency $f = 60\,\mathrm{GHz}$.

TABLE I: List of antenna element separations used for selected MIMO configuration and measurement sites. Calculated using Eq. 1

ζ	Site I, II for $D = 3$m		Site III for $D = 2.5$m
	$4{\times}4$	$6{\times}6$	$4{\times}4$
ζ	61.24 mm	3,32 mm	35.3 mm
$\frac{\zeta}{\sqrt{2}}$	43.30 mm	-	25.0 mm
$\frac{\zeta}{2}$	30.61 mm	-	17.6 mm

B. 55–65 GHz Channel sounder

The channel sounder consists of a vector network analyzer (VNA) and the transmitter (TX) and receiver (RX) antenna. As the channel is time invariant, we are allowed to emulate the MIMO setup by changing the positions of the TX and RX antennas utilizing the precise xy-tables on both RX and TX sides. The channel sounder operates on the frequency domain principle described in [7], [8] (The time-domain mmWave sounder is demonstrated in [10]). In this frequency-domain method, a narrow-band continuous wave signal is transmitted via the channel and the signal is swept from 55 to 65 GHz with a step size of 10 MHz.

III. DATA ACQUISITION AND PROCESSING

A. Channel transfer functions

Unlike with correlative channel sounding, the frequency domain channel data acquisition is straightforward according to

$$\tilde{h}_{ji}(f) = s^{21}_{ji}(f), \tag{2}$$

where f is an index to the discrete measurement frequencies, i, j are, respectively, the indices of the antenna elements of the virtual ULAs, and s^{21} is the S-parameter, representing the transmission from the TX antenna to the RX antenna. Utilizing the inverse Fourier transform (IFT), we transform the CTF matrix

$$\mathbf{H}(f) = \begin{pmatrix} \tilde{h}_{11}(f) & \tilde{h}_{12}(f) \\ \tilde{h}_{21}(f) & \tilde{h}_{22}(f) \end{pmatrix} \tag{3}$$

into the channel impulse response (CIR) as

$$h_{ji}(\tau) = \sum_{f=0}^{L-1} \tilde{h}_{ji}(f) \exp\left(j\frac{2\pi f \tau}{N}\right), \tag{4}$$

where $h_{ji}(\tau)$ is the ji-th element of the multipath channel matrix $\mathbf{H}(\tau)$ constructed in a same manner as shown in Equation (3) for $\mathbf{H}(f)$ and τ is an index to the corresponding time instances.

B. Frequency flat subbands of the CTFs

In order to determine the MI of the frequency selective channel, we partition the measured bandwidth $\mathcal{W}$ into n frequency flat subbands according to

$$B_{n\,\mathrm{flat}}(f_1, f_2, r) = \left\{ \Delta f \,\middle|\, \left(|\tilde{h}_{ji}(f_2)| > |\tilde{h}_{ji}(f_1)| - \frac{r}{2}, \right.\right.$$

$$\left.\left. |\tilde{h}_{ji}(f_2)| < |\tilde{h}_{ji}(f_1)| + \frac{r}{2} \right) \right\} \tag{5}$$

such that $B_{n\,\mathrm{flat}}(f_1, f_2, r)$ forms a continuously sampled spectral space, $\Delta f = f_2 - f_1$ and $f_1 < f_2$ where both are limited to the measured frequencies. The tolerance threshold r defines the flatness of the subband. In the following, we utilize $r \in [1.4, 3, 5]\,\mathrm{dB}$. As a result, all
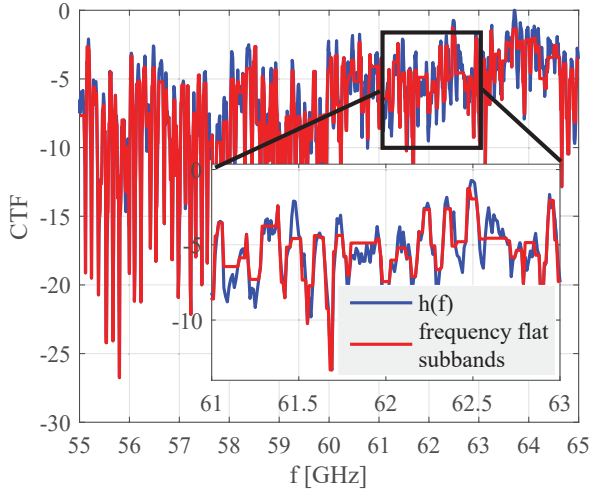
Fig. 2: Typical CTF. The red piecewise linear curve represents the frequency flat subbands.

frequency components within the flat fading subband experience the same magnitude of fading with the maximal difference of r. Then, the measured bandwidth $\mathcal{W}$ is composed of n the subbands by

$$\mathbf{B}_{\text{flat}}(f,r) = [B_{1\,\text{flat}}(f_1, f_2, r), B_{2\,\text{flat}}(f_2, f_3, r), ...]^T. \quad (6)$$

Now, the MIMO channel matrix $\mathbf{H}(f)$ is approximated with

$$\mathbf{H}''(f,r) = \mathbf{H}(\mathbf{B}_{\text{flat}}(f,r)). \quad (7)$$

A graphical representation of the resulting piecewise linear (frequency flat) subband curve is plotted in Figure 2.

C. Frequency domain mutual information determination

As outlined in [11], [12], utilizing the CTF matrix $\mathbf{H}(f)$, the MI of the frequency selective MIMO channel is given by

$$I_\gamma = \frac{1}{\mathcal{W}} \sum_f \log_2 \det(\mathbf{I} + \frac{\gamma}{N} \mathbf{H}(f)\mathbf{H}(f)^H), \quad (8)$$

where $\mathbf{I}$ is an identity matrix and γ is the signal-to-noise ratio (SNR).

In Figure 3, the effect of the antenna separation for $\zeta \in [\zeta, \frac{\zeta}{\sqrt{2}}, \frac{\zeta}{2}]$ is plotted. For the sake of comparison, we also plot the MI function of a perfectly orthogonal LOS (simulated via identity matrix, representing an upper bound of a theoretical channel) and Rayleigh fading.

1) Impact on the antenna element separation: From Figure 3 we read that for γ=20 dB, I_γ=30.60 bit/s/Hz for the orthogonal LOS channel (identity channel), while for the measured channel with the optimal antenna separation I_γ=27.82 bit/s/Hz, so to the upper limit of a theoretical channel, there remains 2.78 bit/s/Hz ($\approx$8.9% decrease). The smaller the element separation, the lower the MI I_γ=23.40 bit/s/Hz ($\approx$23.5% decrease) and finally
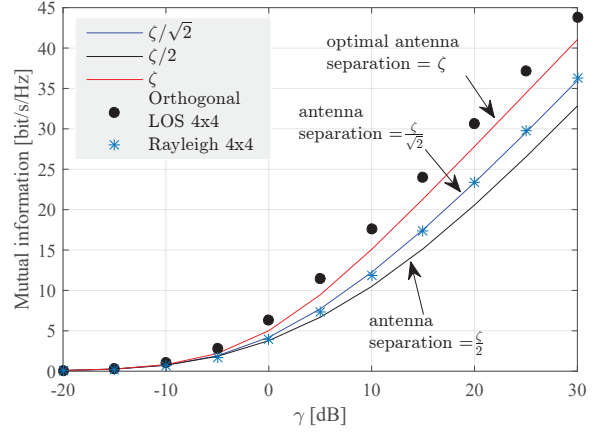
Fig. 3: Variations of the antenna element separation and the effect on the MI. Measurement site I, 4×4.

I_γ=20.57 bit/s/Hz ($\approx$ 32.7% decrease) for the smallest element separation.

2) Impact on the bandwidth: We measure the channel with a bandwidth of 10 GHz while the orthogonality condition Eq. (1) holds only for the center frequency 60 GHz. Therefore, the orthogonality is impaired, the wider the measured bandwidth. This is visible in Figure 4. For γ=20 dB, and a bandwidth of 1 GHz, I_γ=27.82 bit/s/Hz, i.e., 2.83 bit/s/Hz higher then for the case with 10 GHz bandwidth. All the so far mentioned values are for Measurement site I, which has the lowest amount of MPCs.

3) Impact of the Measurement site: In Figure 4 we can also observe the MI function for Measurement site III. It is seen, thanks to the stronger reflections, thus impaired orthogonality, the MI is lower by 1 bit/s/Hz @ BW=1 GHz. For BW=10 GHz, the difference is 3 bit/s/Hz.
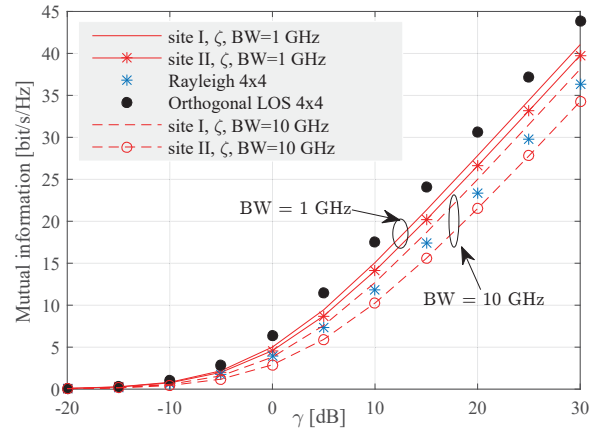
Fig. 4: Influence of the bandwidth BW = $[1, 10]$ GHz. The center frequency $f_c = 60$ GHz.
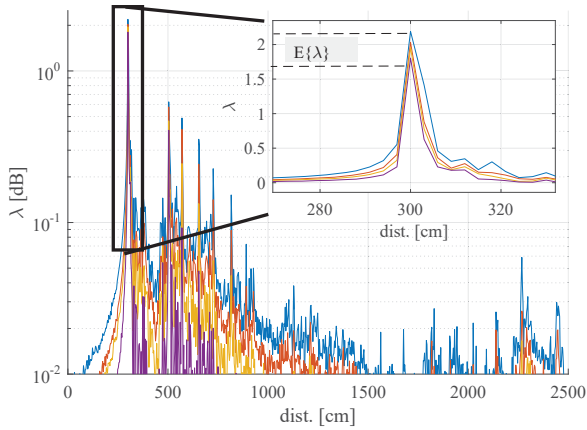
Fig. 5: The time evolution of the singular values of selected data set (4×4, site I, ζ). The x-axis is scaled to the distance and is easy remapped to the delay via $\tau = c/\text{dist.}$, $c = 3 \times 10^8$ m/s.

D. Time domain mutual information determination

Unlike the traditional application of the singular value decomposition (SVD), which is performed in the frequency domain, we define the channel singular values in the delay domain as:

$$\text{SVD}(\mathbf{H}(\tau)) \rightarrow \boldsymbol{\lambda}(\tau), \qquad (9)$$

where

$$\boldsymbol{\lambda}(\tau) = [\lambda_{1,1}(\tau), \lambda_{2,2}(\tau), ..., \lambda_{N,N}(\tau)]. \qquad (10)$$

Now, given the circumstances of the measurements, the LOS components are obtained as

$$\lambda_{\text{LOS}\,ji} = \max_{\tau} \lambda_{ji}(\tau). \qquad (11)$$

The delay domain evolution of $\lambda_{ji}(\tau)$ is visible in Figure 5 highlighting the LOS components.

Now, utilizing all measured datasets, which amounts in total 11 measurements, we show that the MI is related to the mean singular values of the LOS component, i.e.

$$I''_{\gamma} \propto \mathbb{E}\{\lambda_{\text{LOS}\,ji}\} = \frac{1}{N} \sum_{ji} \lambda_{\text{LOS}\,ji}. \qquad (12)$$

Intuitively, this can be explained by the fact that the main singular value contains most of the energy and thus reflects well the channel behavior in terms of MI.

In Figure 6a we plot the measured $I_{\gamma} = f(\mathbf{H}(f), \gamma)$ for $\gamma = 20$ dB and its exponential fit

$$I''^{\text{D}}_{\gamma} = a(\gamma) \exp\{b(\gamma) \mathbb{E}\{\lambda_{\text{LOS}}\}\} \qquad (13)$$

obtained via a maximum likelihood estimation (MLE). The parameters $a(\gamma), b(\gamma)$ of fit (13) are plotted in Figure 6b. The superscript $^{\text{D}}$ designates the calculation from the delay domain.

(a)

(b)
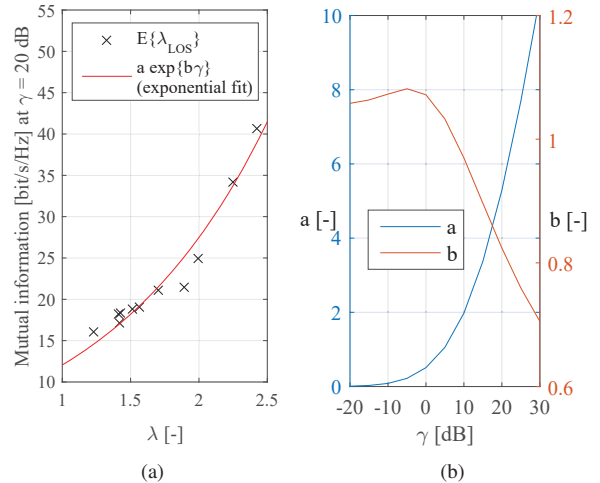
Fig. 6: (a) Dependency of the I_{γ}, the measured mean singular value of the LOS component $\mathbb{E}\{\lambda_{\text{LOS}}\}$ and its exponential fit

(b) Two parameters of the exponential mapping function (13).

IV. VALIDATION

To validate the proposed mapping (13), we define an error magnitude

$$\epsilon = |I_{\gamma} - I''_{\gamma}| \text{ and } \epsilon^{\text{D}} = |I_{\gamma} - I''^{\text{D}}_{\gamma}|, \qquad (14)$$

where $I_{\gamma} = f(\mathbf{H}(f), \gamma)$ and $I''_{\gamma} = f(\mathbf{H}''(f, r), \gamma)$ are evaluated via (8) utilizing the frequency domain data. To evaluate the the mutual information from the temporal domain data, I''^{D}_{γ} is determined by (13).

The cumulative distribution functions (CDFs) of ϵ and ϵ^{D} are depicted in Figure 7. It is visible, that for the threshold $r = 3$ dB and $r = 5$ dB, the precision of the MI evaluation is notably lower compared to the proposed mapping (13). To obtain approximately equal precision, we set $r = 1.4$ dB. This, however, represents several hundreds of $\tilde{h}_{ji}(f)$ coefficients.

V. CONCLUSION

We conclude that:

1) The MI of the measured channels with optimal antenna element separation is close (with 8.9% difference) to the MI of the identity matrix (i.e. the capacity of an ideally decoupled MIMO channel). Thus, for intended application, proper ULA design is of paramount importance.

2) The higher the bandwidth, the lower the MI due to orthogonality disturbance caused by increasing suboptimality antenna element separation.

3) The MI can be estimated from the mean singular value of the LOS component with good precision. In fact, when the MI is calculated as the sum of its individual contributions from the number of frequency
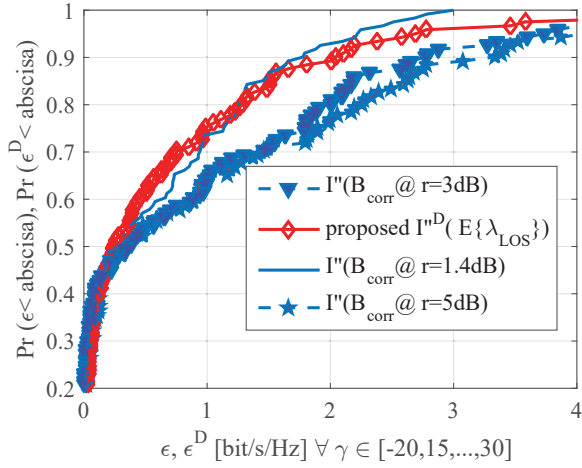
Fig. 7: CDF of the MI estimate error for the proposed technique and three traditional techniques based on the frequency flat subbands with the threshold $r \in \{1.4, 3, 5\}$ dB.

flat subbands, the channel gain variation inside of each subband has to be as low as 1.4 dB, in order to obtain approximately the same MI accuracy as through the proposed method.

ACKNOWLEDGMENT

REFERENCES

[1] T. S. Rappaport, S. Sun, R. Mayzus, H. Zhao, Y. Azar, K. Wang, G. N. Wong, J. K. Schulz, M. Samimi, and F. Gutierrez, "Millimeter wave mobile communications for 5G cellular: It will work!" *IEEE access*, vol. 1, pp. 335–349, 2013.

[2] B. Adelseck, J. Schroth, U. Meiners, and P. Quentin, "Effects of MMIC-design and GaAs technology on mm-Wave module production yield," in *2000 30th European Microwave Conference*, Oct 2000, pp. 1–4.

[3] M. Di Renzo, H. Haas, A. Ghrayeb, S. Sugiura, and L. Hanzo, "Spatial modulation for generalized MIMO: Challenges, opportunities, and implementation," *Proc. IEEE*, vol. 102, no. 1, pp. 56–103, Jan. 2014.

[4] P. Liu, M. Di Renzo, and A. Springer, "Line-of-sight spatial modulation for indoor mmWave communication at 60 GHz," *IEEE Trans. Wireless Commun.*, vol. 15, no. 11, pp. 7373–7389, Nov. 2016.

[5] ——, "Variable-N_u generalized spatial modulation for indoor LOS mmWave communication: Performance optimization and novel switching structure," *IEEE Trans. on Commun.*, vol. PP, no. 99, pp. 1–16, 2017.

[6] A. Maltsev, R. Maslennikov, A. Sevastyanov, A. Khoryaev, and A. Lomayev, "Experimental investigations of 60 GHz WLAN systems in office environment," *IEEE J. Sel. Areas Commun.*, vol. 27, no. 8, pp. 1488–1499, Oct. 2009.

[7] A. Chandra, A. Proke, T. Mikulek, J. Blumenstein, P. Kukolev, T. Zemen, and C. F. Mecklenbruker, "Frequency-domain in-vehicle UWB channel modeling," *IEEE Trans. Veh. Technol.*, vol. 65, no. 6, pp. 3929–3940, June 2016.

[8] J. Blumenstein, A. Prokes, A. Chandra, T. Mikulasek, R. Marsalek, T. Zemen, and C. Mecklenbruker, "In-vehicle channel measurement, characterization, and spatial consistency comparison of 3-11 GHz and 55-65 GHz frequency bands," *IEEE Trans. Veh. Technol.*, vol. 66, no. 5, pp. 3526–3537, May 2017.

[9] G. C. Ferrante, T. Q. Quek, and M. Win, "Revisiting the capacity of noncoherent fading channels in mmWave system," *IEEE Trans. Commun.*, 2017.

[10] J. Blumenstein, J. Vychodil, M. Pospisil, T. Mikulasek, and A. Prokes, "Effects of vehicle vibrations on mm-wave channel: Doppler spread and correlative channel sounding," in *IEEE 27th Annual Int. Symp. on Personal, Indoor, and Mobile Radio Commu. (PIMRC)*, Sep. 2016, pp. 432–437.

[11] G. J. Foschini and M. J. Gans, "On limits of wireless communications in a fading environment when using multiple antennas," *Wireless personal communications*, vol. 6, no. 3, pp. 311–335, 1998.

[12] M. Rupp, J. A. Garcia-Naya, C. Mehlfuhrer, S. Caban, and L. Castedo, "On mutual information and capacity in frequency selective wireless channels," in *2010 IEEE International Conference on Communications (ICC)*, May 2010, pp. 1–5.

7. Physical layer algorithms, full reprints

Performance of Generalized Spatial Modulation MIMO Over Measured 60 GHz Indoor Channels

Peng Liu, **Jiri Blumenstein**, Nemanja Stefan Perović, Marco Di Renzo, Andreas Springer

Performance of Generalized Spatial Modulation MIMO over Measured 60 GHz Indoor Channels

Peng Liu, *Member, IEEE,* Jiri Blumenstein, *Member, IEEE,* Nemanja Stefan Perović, *Student Member, IEEE,*
Marco Di Renzo, *Senior Member, IEEE,* and Andreas Springer, *Member, IEEE*

Abstract—In this paper, we study the capacity and symbol error probability (SEP) of generalized spatial modulation (GSM) multiple-input multiple-output (MIMO) using measured channels that are obtained by channel sounding in an indoor office environment at 60 GHz. Spatial modulation (SM) and GSM are emerging low-complexity MIMO schemes that have been extensively researched for low-GHz (below 6 GHz) communications. Recently, they have been considered and shown to be promising also for millimeter-wave (mmWave) communications. In the simplest possible case, they require only one RF chain both at the transmitter (TX) and receiver (RX), and thus are especially attractive for mmWave communications in which the number of RF chains needs to be as low as possible. Despite of some early works on the theoretical analysis of SM/GSM for mmWave communications, there have been no investigations using real-world channel data. We focus on the office line-of-sight (LOS) scenario and investigate three problems: 1) the performance of GSM using the extracted LOS component of measured channels, 2) the impact of non-LOS (NLOS) components on the performance of GSM, and 3) possible simple modulation and reception algorithms for GSM that rely only on the LOS component of the channel. The results being reported in this paper not only validate the main claims of previous studies based on ideal pure LOS channels but also lead to novel findings. One major conclusion is that NLOS components are harmful to the SEP of GSM and should be avoided. As another important outcome, our results strongly motivate the use of precoding in GSM systems to simultaneously improve the channel capacity and reduce the physical size of MIMO arrays (thus eliminating one major issue of LOS GSM).

Index Terms—Channel sounding, generalized spatial modulation (GSM), indoor, line-of-sight (LOS), multiple-input multiple-output (MIMO), millimeter-wave (mmWave), 60 GHz.

Fig. 1. Conceptual architecture for SM/GSM MIMO.

I. INTRODUCTION

SPATIAL modulation (SM) and generalized spatial modulation (GSM) are emerging low-complexity multiple-input multiple-output (MIMO) schemes for wireless communications [1]. The operating principle of SM/GSM MIMO systems [2]–[5] is radically different from that of conventional spatial multiplexing (SMX) MIMO systems, e.g., D-BLAST (Diagonal-Bell Laboratories Layered Space-Time) [6] and V-BLAST (Vertical BLAST) [7]. In SMX MIMO, the SMX gain is achieved by simultaneous transmission of multiple in-phase and quadrature (IQ) streams at the same frequency. Typically, the same number of transmitter (TX) chains (from baseband to RF) as the number of data streams are needed in SMX MIMO thus introducing significant hardware and data processing complexities. However, in SM/GSM MIMO (see Fig. 1), data streams are transmitted not only in the conventional IQ domain but also in a so-called spatial domain. SM was originally proposed to activate only a single TX antenna and transmit a single stream in the IQ domain, but was later generalized to GSM which supports multiple antenna activation and even multiple IQ stream transmission [8]–[10]. In this paper, for the sake of practical relevance to millimeter-wave (mmWave) communications, we consider the case of GSM with only a single IQ stream. The spatial domain transmission is achieved by selecting a sub-group of TX antennas for transmission of the IQ stream and modulating the spatial stream in the antenna indicies. Compared to SMX, SM/GSM can not only reduce hardware and signal processing complexities [1], but also show significantly improved TX energy efficiency [11], [12].

Extensive research has been conducted on SM/GSM [1]. However, almost all papers are concerned with SM/GSM at low-GHz (below 6 GHz) frequencies. Some early mmWave SM/GSM papers are [13]–[17], which are all concerned with the line-of-sight (LOS) scenario. A major difference between

indoor LOS mmWave SM/GSM and low-GHz SM/GSM lies in the different propagation characteristics. At mmWave frequencies, e.g., 60 GHz, the practical indoor operation range is likely to be limited by penetration loss and therefore mostly confined to a single room [14] and the indoor channel is dominated by the LOS path (if not blocked). The non-LOS (NLOS) paths, which typically suffer from 10 dB loss per reflection and additional path loss due to larger path lengths as compared to the LOS path [18], have only minor contribution to the received power. The LOS component is deterministic and determined by the relative geometries of the antennas, and this, as in LOS SMX [19], [20], gives us opportunities to optimize the performance of SM/GSM in LOS [13], [14]. In the literature and also in this paper, LOS MIMO (SMX/SM/GSM) means a MIMO communication system that is optimized based on the pure LOS component of the channel. More specifically, optimization of the symbol error probability (SEP) and channel capacity of LOS MIMO relies on proper separation of the TX and receiver (RX) antennas (by an amount that is in general much larger than half wavelength). At low-GHz frequencies, in contrast, the channels are usually rich-scattered and exhibit fading and low-coupling characteristics. Excess separation of the antennas at low-GHz is generally not necessary. Antenna separations down to half wavelength usually can lead to sufficiently low channel correlations [21, p.151] and allow exploitation of diversity and multiplexing gains [6].

So far, the work on SM/GSM, regardless of frequency, has been mainly limited to theoretical studies. Although numerical simulation and theoretical analysis serve as important and often reliable tests of the performance of novel technologies, only practical experience can yield definitive answers to their performance in real-world [4]. The only few practical works on SM/GSM are [2]–[5], all at low-GHz frequencies. In [2], a channel measurement campaign considering a 2 GHz urban channel was carried out in the city of Bristol, United Kingdom. The average bit error probability (BEP) of SM was evaluated over the measured Rayleigh fading channel. In [3], a 2×2 MIMO testbed was constructed for SM and SMX at 2.3 GHz carrier frequency. The experiment was carried out in an indoor office environment and the SM principle was validated for the first time in real-time. In [4], the indoor channel inside a teaching building was measured at 6 GHz. Both LOS (corridor-to-corridor) and NLOS (corridor-to-classroom) scenarios were measured. It was concluded that neither an independent and identically distributed (i.i.d.) nor a spatially correlated Rayleigh fading channel model, which were commonly used in theoretical works, were able to predict the behavior of SM in practical (indoor) environments. It was also concluded that owing to the higher de-correlation among antennas, the SM system performs better under NLOS scenarios than LOS scenarios. In [5], a testbed was constructed for communication using GSM with a variable number of activated TX antennas (a.k.a. VGSM) at 2.4 and 5 GHz. The experiment was carried out in an office environment and the concept of GSM was validated. These practical works proved that SM/GSM is a viable technology. But, it was also shown that the performance of SM/GSM cannot always be predicted accurately. This is because theoretical channel models are usually too simplistic and may not capture enough details of the real-world environment.

In this paper, we study the performance of GSM that has a fixed number of activated TX antennas (a.k.a. FGSM) over measured 60 GHz (multipath) indoor channels[1]. The channel measurement was carried out in an office environment at Brno University of Technology, Czech Republic. This is the first time that SM/GSM is studied using real-world mmWave channels. GSM has been studied for application to 60 GHz indoor communications in [14], [15]. The study, however, is of theoretical nature and accounts only for the LOS component of the channel. However, practical channels may not necessarily be the same as those used for ideal pure LOS optimization. For example, NLOS paths may not be so negligible or, because of the hardware components used, the LOS paths may have different characteristics than those used in typical (theoretical) models that are used for optimizing the MIMO performance. Validation of the sensitivity or vulnerability of the optimized system to practical channels, which is the main goal of this paper, is therefore a necessary step before any real implementations. Against this background, the novel contributions of this paper are as follows:

1) We performed 60 GHz channel sounding in an indoor office environment and measured 132 channel impulse responses (CIRs). The measurement was focused on scenarios with LOS (as opposed to LOS blockage), which is the most favorable case for mmWave MIMO communications[2]. A major difference of this paper, as compared to the low-GHz indoor SM/GSM works [3]–[5], lies in the fact that GSM is optimized based on the LOS component of the channel thus making the findings provided in Section IV and Section V novel and unique.

2) We study the channel capacity of GSM using measured channels and compare it with previous theoretical results of [14] that were obtained with ideal pure LOS channels. Simulation results with the LOS component of measured channels show good agreement with the results of [14]. Further simulated results show that the NLOS components of the measured channels tend to improve the GSM capacity only when the MIMO antennas are not properly separated.

3) We study the SEP of GSM using measured channels and compare it with previous theoretical results of [14] that were obtained with ideal pure LOS channels. Simulation results with the LOS component of the measured channel show good agreement with the results of [14]. However, the measured NLOS components, though 10 dB weaker than the LOS component, show a strong disruptive effect on the SEP of GSM when practical TX and RX are

---

[1]We investigated VGSM [15] as well and found that the major claims of this paper generally also apply to VGSM.

[2]This statement is opposite to that for low-GHz MIMO, in which common belief is that NLOS and rich scattering are beneficial. For low-GHz MIMO, a rich scattering environment helps to achieve low channel correlation and a high rank channel matrix, thus facilitating simultaneous transmission of multiple data streams. At mmWave frequencies, owing to high reflection and penetration losses, the LOS component is dominant in the indoor MIMO channel. SM/GSM [13], [14], [16] and SMX [19], [20] MIMO schemes have been optimized to rely on LOS rather than NLOS propagation.

used. With the considered TX and RX schemes, this leads to the recommendation to avoid the reflected paths and exploit only the LOS paths for communication. This finding, of course, depends on the considered TX and RX schemes. Further details are provided in Section V.

4) As compared to ideal deterministic pure LOS channels, the randomness introduced by hardware nonidealities, close reflections (the NLOS components that actually merge into the LOS component due to negligible time dispersion), and more importantly precoding are found to be able to simultaneously improve the GSM capacity and reduce the physical size of MIMO arrays. This finding is a necessary supplement to the SEP optimization of [14] and capacity optimization of [15].

The rest of the paper is organized as follows. In Section II, we introduce the channel and system models, and the principle of LOS GSM. In Section III, we give details about the channel measurement, including the description of the channel sounder setup, the measurement environment and the post-processing of the measured data. In Section IV, we evaluate and analyze the capacity of GSM over the measured channels. In Section V, we evaluate and analyze the SEP of GSM over the measured channels. Finally, Section VI concludes the paper.

II. PRELIMINARIES

A. Channel Model

As shown in Fig. 2, we consider an $N_t \times N_r$ LOS MIMO system that consists of two arbitrarily placed uniform linear arrays (ULAs), where N_t and N_r are the numbers of TX and RX antennas, respectively. The antenna separations in the TX and RX ULAs are s_t and s_r, respectively, and the TX-RX distance is D, which is measured between the center points of the TX and RX ULAs. Geometrically, each ULA has two degrees of freedom, namely the azimuth angle φ and the tilt angle β (or equivalently the elevation angle $\theta = \pi/2 - \beta$). Since we are only interested in their relative geometric relations, only three angles are used — the tilt angles β_t and β_r at the TX and RX, respectively, and the azimuth angle φ_r at the RX. We limit β_t and β_r to $[0, \pi/2]$ yet still being able to cover all cases. The broadsides of the TX and RX arrays are assumed to face each other (but not necessarily parallel to each other) and the main lobes of the antennas of one array are oriented towards the other array such that LOS paths can be established between all pairs of TX and RX antennas. Otherwise, there are no further requirements on the radiation patterns of the array antennas.

For SM/GSM to operate in mmWave indoor environments, antennas with moderate gains of a few dBi are typically necessary [14]. This suggests the use of directional antennas. Motivated by this, in the channel measurement we use open-ended waveguides with a moderate gain of about 5 dBi as directional antennas (see Fig. 3). In this paper, we are interested in the performance of GSM achieved with the communication channel that includes the antennas. The antenna gain pattern, which is naturally included in the measured channel responses, is kept as it is (rather than de-embedded or deconvoluted). Due to the directivity of the antennas, the
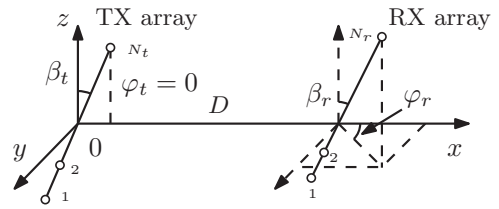
Fig. 2. LOS MIMO using arbitrarily placed ULAs. The coordinate system is chosen such that the center of the TX ULA locates at the origin and the center of the RX ULA lies on the x-axis. Furthermore, the TX ULA lies in the xz-plane, i.e., $\varphi_t = 0$.

number of propagation paths is reduced as compared to the case of using omni-directional antennas.

The impulse response of the indoor MIMO channel is commonly described as [16], [18]–[20]

$$\mathbf{H}(\tau) = \mathbf{H}_{\mathrm{LOS}}(\tau) + \mathbf{H}_{\mathrm{NLOS}}(\tau), \tag{1}$$

where $\mathbf{H}_{\mathrm{LOS}}$ and $\mathbf{H}_{\mathrm{NLOS}}$ are $N_r \times N_t$ matrices respectively representing the LOS and NLOS components of the channel, and τ is the time in the delay domain. The LOS component is assumed to be always present. The j, i-th element of the channel matrix $\mathbf{H}$, which represents the sub-channel between the i-th TX antenna and the j-th RX antenna, is given by [18], [20]

$$
\begin{aligned}
h_{ji}(\tau) = \sum_{k=1}^{K} & G_{\mathrm{TX}}\left(\varphi_{\mathrm{TX}}^{(k)}, \theta_{\mathrm{TX}}^{(k)}\right) G_{\mathrm{RX}}\left(\varphi_{\mathrm{RX}}^{(k)}, \theta_{\mathrm{RX}}^{(k)}\right) \\
& \times \alpha_{ji}^{(k)} \delta(\tau - \tau_{ji}^{(k)}),
\end{aligned}
\tag{2}
$$

where K is the number of paths, $\varphi_{\mathrm{TX}}^{(k)}$, $\theta_{\mathrm{TX}}^{(k)}$, $\varphi_{\mathrm{RX}}^{(k)}$ and $\theta_{\mathrm{RX}}^{(k)}$ are, respectively, the TX azimuth, TX elevation, RX azimuth and RX elevation angles of the k-th path, G_{TX} and G_{RX} are, respectively, the TX and RX gains in the direction of the path, $\alpha_{ji}^{(k)}$ is the amplitude of the path, $\delta(\cdot)$ is the Dirac delta function, and $\tau_{ji}^{(k)}$ is the propagation delay of the path. The path delay is related to the path length $d_{ji}^{(k)}$ by the speed of light c as $\tau_{ji}^{(k)} = d_{ji}^{(k)}/c$. For each sub-channel h_{ji}, there is a single LOS path which is contained in $\mathbf{H}_{\mathrm{LOS}}$. The other $K-1$ paths are NLOS and are contained in $\mathbf{H}_{\mathrm{NLOS}}$. As for the LOS paths, the α in (2) is given according to the Friis's transmission equation [22] by

$$\alpha_{ji}^{(1)} = \frac{\lambda}{4\pi d_{ji}^{(1)}}, \tag{3}$$

where λ is the wavelength of the center frequency, and $d_{ji}^{(1)}$ is the length of the LOS path between the i-th TX antenna and the j-th RX antenna. As for the NLOS paths, the α in (2) includes, in addition to the path loss, also the reflection coefficient(s) [20], and is given by

$$\alpha_{ji}^{(k)} = \frac{\lambda}{4\pi d_{ji}^{(k)}} \prod_{r=1}^{R} \Gamma_r^{(k)}, \quad k = 2, 3, \ldots, K \tag{4}$$

where $d_{ji}^{(k)}$ is the length of the k-th (NLOS) path between the i-th TX antenna and the j-th RX antenna, $\Gamma_r^{(r)}$ is the reflection

coefficient of the r-th reflection of the k-th (NLOS) path that is determined by the material of the surface [23], and R is the number of reflections of the path.

The channel model above provides us with the necessary information for understanding the behavior of the channel. It is worth mentioning, however, that the objective of this paper is to quantify the system performance via measured channels, rather than extracting the above mentioned channel parameters from the measurements. Therefore, the latter issue is left to future analysis.

B. Principle of GSM

In this subsection, we introduce the basic principle of LOS GSM. For ease of presentation, we consider only the (dominant) LOS component of the channel. The impact of NLOS components on the performance of LOS GSM will be considered later in the capacity and SEP analyses in Section IV and Section V.

Since only the LOS component is considered, it is more convenient to use an equivalent form to the $\mathbf{H}_{\mathrm{LOS}}$ modeled in Section II-A, in which the j, i-th element is alternatively given by

$$\underline{h}_{ji} = \frac{\lambda}{4\pi \underline{d}_{ji}} \exp(-\mathrm{j}k\underline{d}_{ji}), \quad (5)$$

where $k = 2\pi/\lambda$ is the wave number, and j is the imaginary unit. The received signal vector $\mathbf{y} \in \mathbb{C}^{N_r \times 1}$ is given by

$$\mathbf{y} = \mathbf{H}_{\mathrm{LOS}} \underbrace{q_m \mathbf{e}_i}_{\triangleq \mathbf{x} \in \mathbb{S}} + \mathbf{n} = q_m \sum_{k \in \mathcal{I}_i} \mathbf{h}_k + \mathbf{n}, \quad (6)$$

where

q_m is an IQ (e.g., M-QAM or M-PSK) symbol, and $m = 1, \ldots, M$ is the IQ symbol index;

$\mathbf{e}_i$ is a spatial symbol which is an $N_t \times 1$ vector containing N_u ones (representing the activated TX antennas) and $N_t - N_u$ zeros (representing the inactivated TX antennas), and $i = 1, \ldots, \binom{N_t}{N_u}$ is the spatial symbol index;

$\mathbb{S}$ $\triangleq \{q_m \mathbf{e}_i \mid i = 1, \ldots, \binom{N_t}{N_u}$ and $m = 1, \ldots, M\}$ is the GSM modulation alphabet;

$\mathbf{x}$ $\in \mathbb{S}$ is a transmitted GSM symbol;

$\mathcal{I}_i$ $\triangleq \{k \mid k \in \{1, \ldots, N_t\}$ and $\mathbf{e}_i(k) = 1\}$ is the set of indices of the activated TX antennas corresponding to the i-th spatial symbol;

$\mathbf{h}_k$ $\triangleq [\underline{h}_{1k}, \underline{h}_{2k}, \ldots, \underline{h}_{N_r k}]^T$ is the k-th column of $\mathbf{H}_{\mathrm{LOS}}$;

$\mathbf{n}$ $\in \mathbb{C}^{N_r \times 1}$ is the i.i.d. additive white Gaussian noise (AWGN) vector which has a covariance matrix $N_0 \mathbf{I}_{N_r}$ ($\mathbf{I}_{N_r}$ is the $N_r \times N_r$ identity matrix).

Due to transmission of only a single IQ stream and TX antenna switching, the received signal vector at the RX contains a combination of N_u columns of the channel matrix which are multiplied by the same IQ symbol q_m. This is different from the SMX, in which the received signal typically contains a combination of multiple columns of the channel matrix which are multiplied by different IQ symbols.

In GSM, there are $\binom{N_t}{N_u}$ activation patterns of the TX antennas thus achieving a spatial data rate of $\log_2 \binom{N_t}{N_u}$ bpcu
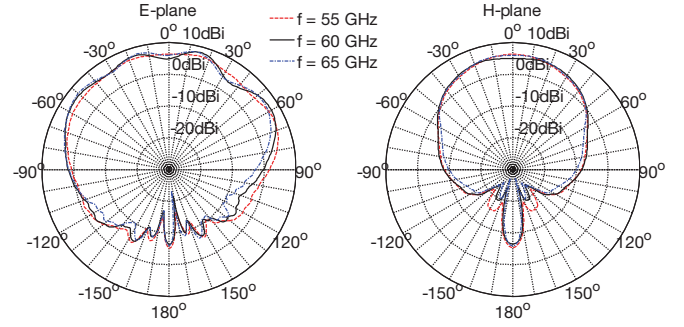
Fig. 3. Measured gain pattern of the open-ended waveguide antennas in the E- and H-planes.

and a total data rate of $\log_2 \binom{N_t}{N_u} + \log_2 M$ bpcu. The maximum rate is achieved when $N_u = \lfloor N_t/2 \rfloor$. This is due to the fact that for a given N_t, $\binom{N_t}{N_u}$ is a symmetric concave function of N_u that is centered around $N_t/2$. In contrast, single-antenna activation SM achieves a spatial rate of $\log_2 N_t$ bpcu and a total rate of $\log_2 N_t + \log_2 M$ bpcu.

C. Optimal Detection

Under the assumption of a pure LOS MIMO channel, the optimal detector for GSM that is based on the maximum likelihood (ML) principle is well-known to be given by [24]

$$\begin{aligned} (\hat{i}, \hat{m}) &= \arg\max_{i, m} p_{\mathbf{y}} \left(\mathbf{y} \mid s_{i,m}, \mathbf{H}_{\mathrm{LOS}} \right) \\ &= \arg\min_{i, m} \|\mathbf{y} - \mathbf{H}_{\mathrm{LOS}} q_m \mathbf{e}_i\|, \end{aligned} \quad (7)$$

where $p_{\mathbf{y}}(\cdot)$ denotes the probability density function (PDF) of $\mathbf{y}$, and $\|\cdot\|$ denotes the Euclidean distance.

D. Optimized Channel Conditions

The deterministic nature of the LOS component of the channel gives us the opportunity of optimizing the performance of GSM. Optimization of the capacity and SEP for GSM based on the LOS component $\mathbf{H}_{\mathrm{LOS}}$ is found in [14], [15]. The relevant findings are as follows.

To minimize the SEP of GSM, $\mathbf{H}_{\mathrm{LOS}}$ has to be column-orthogonal, which in turn requires the TX and RX antennas to be properly separated. The minimum antenna separation product (ASP) is given by [14]

$$s_t s_r \approx D\lambda\zeta/N_r, \quad (8)$$

where $\zeta \triangleq 1/(\cos\beta_t \cos\beta_r)$ is the so-called tilt factor which measures the degree of tilt of the ULAs. In addition, we need $N_r \geq N_t \geq 2$, where $N_r \geq N_t$ is necessary in order to have N_t orthogonal channel columns and $N_t = 2$ is the minimum number of TX antennas needed for SM/GSM to operate. Perfect orthogonality is lost if the actual ASP differs from the optimal value. To measure this, we use an ASP deviation factor η which was previously defined in [25] as

$$\eta = \frac{\text{Minimum ASP for orthogonality}}{\text{Actual ASP}} = \frac{D\lambda\zeta/N_r}{s_t s_r}, \quad (9)$$

where the minimum ASP for orthogonality is given in (8). Note that the term $s_t s_r$ in the denominator of (9) denotes the actual

ASP and should not be confused with the optimal ASP (to achieve channel orthogonality) given in (8). If the actual ASP is larger than the optimal ASP, we have $\eta < 1$; if the actual ASP is smaller than the optimal ASP, we have $\eta > 1$. In what follows, we use η as an (inverted) normalized ASP.

The orthogonality condition (8) usually means excess antenna separations and array lengths. In practice it is very likely that the antennas are under-separated, i.e., $\eta > 1$. Therefore, in this paper we restrict the study to $\eta \geq 1$.

Actually, to maximize the capacity of LOS GSM, $\eta = 1$ tends only to be needed at a moderate signal-to-noise ratio (SNR). At low SNR, beamforming gain is more important and the optimal η tends to be infinity, i.e., the intra-array antenna separations of the TX and RX ULAs should be as small as possible. At high SNR, the optimal η tends to increase with increasing SNR. For example, for a 6×6 ($N_t \times N_r$) system, the optimal η increases from 1 to 6 when the SNR increases from 5 to 30 dB [15, Fig. 7].

III. CHANNEL MEASUREMENTS

A. Measurement Environment and Scenarios

As far as LOS MIMO communications is concerned, it is especially true that the system performance is primarily determined by the installation of TX and RX antennas and the surrounding environment. The channel sounding campaign was performed in a laboratory/office environment at the Brno University of Technology (see Fig. 4), and the measurement captures two typical use cases of LOS GSM, which we denote as measurement Scenario I and measurement Scenario II. The difference between the two scenarios lies mainly in the measurement site geometry (medium-size laboratory vs. small-size laboratory) and the fact that in Scenario I many reflective surfaces were covered by absorbers.

1) Scenario I: Scenario I accounts for a medium-size laboratory ($15\,\text{m} \times 6\,\text{m} \times 2.8\,\text{m}$) that is shown in Fig. 4(a). Absorbers were used to suppress reflections from the floor and metallic table legs. The purpose of using absorbers is two-fold: 1) to make the measured LOS component as much closer to ideal propagation conditions as possible — free of close reflections, i.e., NLOS components that actually merge into the LOS component due to negligible time dispersion — but still allowing reflections from the ceiling and walls, and 2) to better highlight the differences with Scenario II, where no absorbers are used. The TX-RX distance is $3\,\text{m}$ and the height of the TX and RX antennas above the ground is $1.2\,\text{m}$.

Both the TX and RX antennas are placed on xy-tables with a sub-millimeter shifting step. As indicated in Fig. 4(a) with red lines, with proper alignment of the TX and RX xy-tables (which, according to Fig. 2, means azimuth angles $\phi_t = \phi_r = 0$, tilt angles $\beta_t = \beta_r = \pi/2$, and $\eta = 1$), virtual TX and RX ULAs can be emulated using a single pair of antennas. In this scenario, four sets of data were measured corresponding to a 4×4 MIMO system with $\eta = 1, 2, 4$ and a 6×6 MIMO system with $\eta = 1$.

2) Scenario II: Scenario II accounts for a smaller-size laboratory ($6\,\text{m} \times 6\,\text{m} \times 2.8\,\text{m}$) (see Fig. 4(b)). In this scenario, the TX-RX distance is reduced to $2.5\,\text{m}$. The TX-RX link is

(a) Scenario I   (b) Scenario II
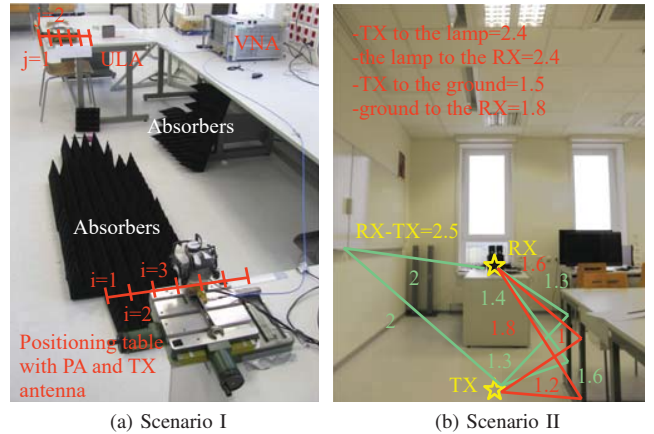
Fig. 4. The measurement site. All dimensions in (b) are in meters.

close to a wall on the left side and no absorbers are used to shield the ground and metallic table legs. As a result, a richer scattering environment is created. The antenna hight, tilt angles and measurement procedure are, on the other hand, the same as those of Scenario I. Three sets of data were measured corresponding to a 4×4 MIMO system with $\eta = 1, 2, 4$ in this scenario.

Despite the use of absorbers, Scenario I can be considered to be a representative example of the channel conditions that are typically encountered in the STA-AP sub-scenario of IEEE 802.11 WLAN [18], where the AP (access point) is installed on the ceiling and the STA (station, or communication device) is placed on a table in the same room. In this regard, Scenario II can be viewed as an emulation of the STA-STA (device to device) sub-scenario of WLAN. In total, we obtained 7 virtual MIMO realizations and 132 CIRs for the two scenarios.

B. 55–65 GHz Channel Sounder

The channel sounder is composed of a vector network analyzer (VNA) and a pair of TX and RX antennas. The MIMO channel is measured by changing the positions of the TX and RX antennas on xy-tables. The channel sounder operates based on the frequency domain measurement principle illustrated in [26], [27] (as opposed to the time-domain principle presented for the mmWave band in [28]). In the frequency-domain method, a narrow-band continuous wave signal is used to sound the channel and the signal is swept from 55 to 65 GHz with a step size of 10 MHz.

The R&S ZVA67 four-port VNA is utilized to measure the transmission coefficient between TX and RX antennas. Perfect synchronization between the TX and RX is achieved because of the use of a VNA. The system dynamic range of the measurement setup is extended utilizing a broadband power amplifier (QuinStar QPW-50662330), which has a measured gain of 35 dB in the band of interest, on the TX side. Similar to [29], we use two WR15 open waveguides, which have the radiation pattern as shown in Fig. 3, as the TX and RX antennas. Phase-stable coaxial cables are used in order to avoid the degradation of the measured phase accuracy due to the

movements of the TX and RX antennas. A VNA output power of 5 dBm and IF bandwidth of 100 Hz are used. The system's dynamic range of this channel sounder is approximately 50 dB.

Before channel sounding, a full 4-port calibration process was performed including the power amplifier (PA) with WR15 output. Therefore, as we utilize the open-ended waveguide as both the RX and TX antenna, the antenna gains are included in the calibration process.

C. Data Acquisition and Post Processing

As the measurement environment has no moving objects, the measured radio channel is considered to be time invariant. The measured frequency domain channel transfer function (CTF) is given by

$$\tilde{h}_{ji}(g) = s_{ji}^{21}(g), \tag{10}$$

where g is any of the measurement frequencies, i, j are, respectively, the indices of the elements of the virtual TX and RX ULAs, and s^{21} is the S-parameter representing the transmission from the feed of the TX antenna to the output of the RX antenna. By invserse Fourier transform (IFT), we convert the CTF into the CIR as

$$h_{ji}(n) = \sum_{g=0}^{L-1} \tilde{h}_{ji}(g) \exp\left(\mathtt{j}\frac{2\pi gn}{N}\right), \tag{11}$$

where $h_{ji}(n)$ is the measured discrete version of the ji-th element of the multipath channel $\mathbf{H}$ given in (1).

D. Validation of the Measured Data

In short range indoor LOS communications, the channel usually contains a long diffused tail because of reflections [30]. In our experiments, we consider a setup where the first few Fresnel zones are free of obstacles, but there are a sufficient number of reflections outside them. As an example, the measured CIRs for a 4×4 MIMO system with $\eta = 4$ for the two scenarios described in Section III-A are plotted in Fig. 5. We see that the measured LOS component is located at the correct positions for both scenarios — at $D = 3\,\mathrm{m}$ for Scenario I and at $D = 2.5\,\mathrm{m}$ for Scenario II. The reason of the presence of the NLOS clusters are discussed in the sub-figures themselves. By comparing Fig. 5 (a) and (b), it is evident that the reflections from the metallic table legs and the ground are effectively suppressed in Scenario I due to the use of absorbers. It is apparent, in addition, that Scenario II represents a richer scattering environment as compared to Scenario I.

As an example, the LOS component of the measured 4×4 MIMO with $\eta = 1$ is plotted in Fig. 6 for the two scenarios. At 60 GHz, the free space path loss (FSPL) for $D = 3\,\mathrm{m}$ excluding the TX and RX antenna gains of 5 dBi is 77.6 dB. Taking into account possibly 2×1 dB cable and connector losses at the TX and RX, the average measured path loss including the antenna gains should be around 69.6 dB. This is confirmed by direct inspection of Fig. 6(a). It can be similarly verified that the measured mean path loss in Fig. 6(b) is reasonable as well. However, in the sub-figures, we can observe some variations around the expected (theoretical) means, i.e., 0.42 dB and 0.33 dB in Fig. 6 (a) and (b), respectively. These variations

are not shown in the corresponding curves for ideal pure LOS channels. We attribute these variations to hardware nonidealities and disturbance from close reflections.

IV. CAPACITY ANALYSIS

In this section, we present simulation results on the capacity of GSM over measured channels. More specifically, we study the performance of the measured LOS component and the impact of the NLOS components of the measured multipath channels on the capacity of GSM. Three case studies are analyzed: 1) the capacity is evaluated with ideal pure LOS channels; 2) the capacity is evaluated with the LOS component extracted from the measured multipath channels; and 3) the frequency-average capacity is evaluated with the measured multipath channels. In addition, the capacity achieved by ideal pure LOS channels is used as a benchmark.

Although the measurement covers a bandwidth of 10 GHz centered at 60 GHz, both the capacity in this section and the SEP in the next section are evaluated by considering a more practical bandwidth of 1 GHz. This bandwidth is still centered around 60 GHz. This is obtained by discarding the CTF that lies outside the band of interest before converting it to the time-domain CIR (see Section III-C).

A. Capacity Evaluation

The LOS component of the measured MIMO channels is not time-dispersive, which means that the relative time delays between the LOS paths are much smaller than the symbol duration. Otherwise, the channel is time-dispersive. The capacity of GSM over non-time-dispersive channels can be evaluated by using (12) given in Appendix A-1. However, the complete measured channels as shown in Fig. 5 are time-dispersive and therefore are frequency-selective in the sense that the channel coefficients vary over frequency. Based on the same consideration as given in [15, Section III-B], the capacity of GSM over the measured channels is evaluated on a narrow band (frequency-flat) basis by using (12) and is averaged over frequency. Further details are available in Appendix A-2.

B. Simulation Results

We first concentrate on Scenario I, and the simulation results on the capacity of GSM are shown in Fig. 7. Each sub-figure corresponds to one set of the measured channel data, and the FSPL due to the TX-to-RX distance D is not counted in the SNR that is shown on the abscissa.

1) Capacity of the Measured LOS Component: As far as the orthogonal setups are concerned, i.e., 4×4 and 6×6 MIMO both with $\eta = 1$ as shown in Fig. 7(a)–(b), the LOS component of the measured channels shows identical performance as the ideal pure LOS channels. The effect of the variations in the power of the LOS paths in Fig. 6 is not visible in this case.

As far as the non-orthogonal setups are concerned, i.e., 4×4 MIMO with $\eta = 2, 4$ as shown in Fig. 7(c)–(d), the capacity of GSM using the LOS component of the measured channels does not perfectly match the curves of the ideal pure LOS channels.

(a) Scenario I

(b) Scenario II
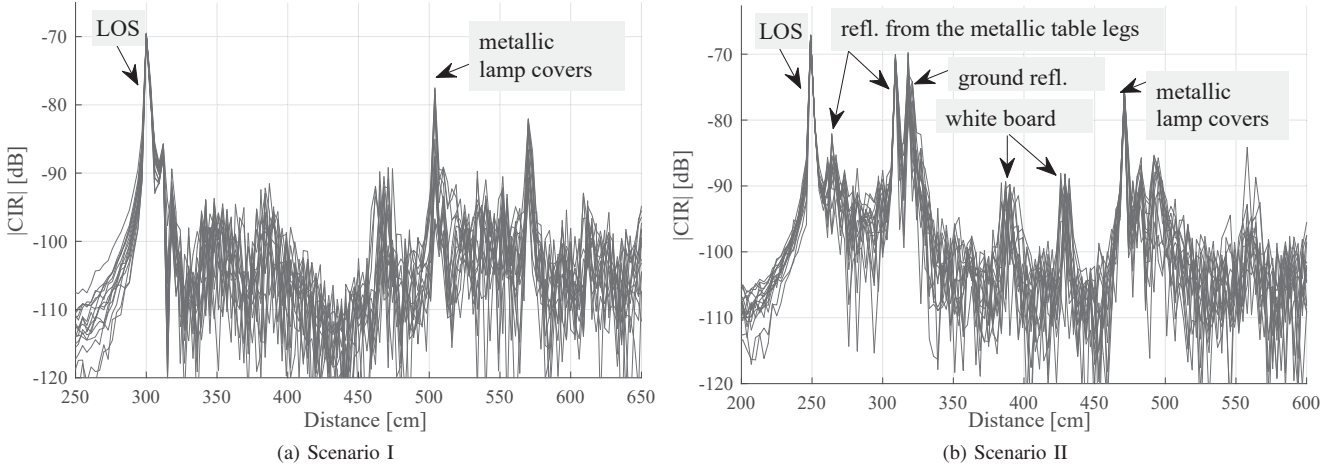
Fig. 5. Measured CIRs for 4×4 MIMO with $\eta = 4$. All 16 CIRs are plotted in each sub-figure.

(a) Scenario I, 4×4 MIMO with $\eta = 1$

(b) Scenario II, 6×6 MIMO with $\eta = 1$
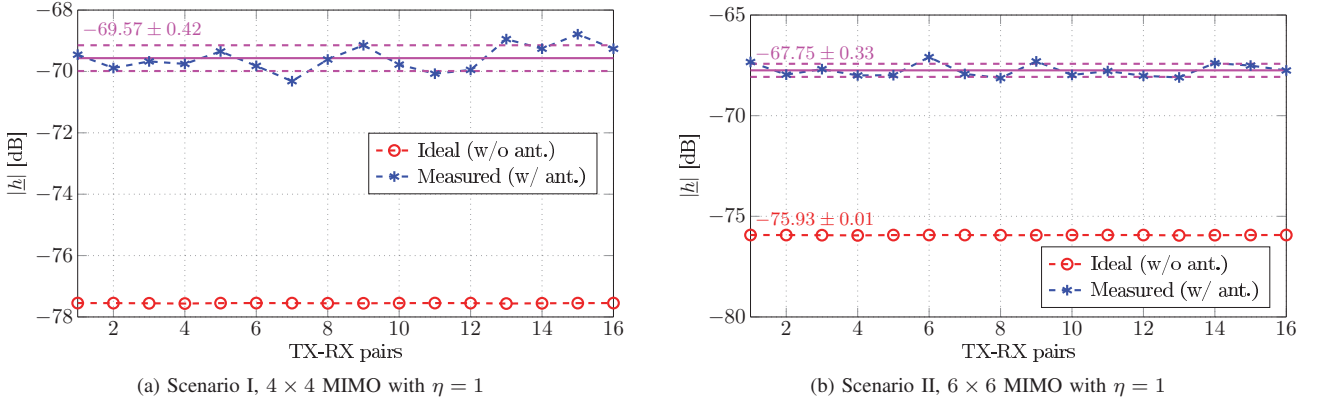
Fig. 6. Magnitudes of measured LOS paths (including TX and RX antennas) vs. the magnitudes of simulated LOS paths (excluding TX and RX antennas). The mean and standard deviation of the measured magnitudes are evaluated in dB scale and indicated with magenta lines.

Comparing Fig. 7(a), (c) and (d), all for 4×4 MIMO but with $\eta = 1$, 2 and 4 respectively, we note that, with increasing η, the capacity of GSM using the LOS component of the measured channels is increasingly worse compared to that of ideal pure LOS channels. By direct inspection of Fig. 7, we find that:

- The IQ capacity C_1 of the measured LOS component is worse than that of ideal pure LOS channels with increasing η. Actually, C_1 of the measured LOS component itself is not noticeably worsened for increasing η, but rather it does not show the increment that is shown by ideal pure LOS channels.
- The spatial capacity C_2 of the measured LOS component, however, seems to be better than that of ideal pure LOS channels with increasing η. Actually, C_2 of the measured LOS component does not seem to be improved due to increased η, but rather it does not show the deficiency that is shown by ideal pure LOS channels.

To further investigate the impact of hardware nonidealities and randomization of the channel on the GSM capacity, we performed capacity simulations by adding artificial randomness on top of deterministic ideal LOS channels. The randomness may represent the contribution from hardware imperfections,

close reflections[3] and precoding. More specifically, we are interested in the case of under-separated MIMO setups (i.e., $\eta > 1$), which means shrunk physical size of the MIMO arrays. As a result, the following findings were obtained. If the MIMO setup is under-separated (i.e., $\eta > 1$), the GSM capacity can indeed be improved by adding sufficient randomness to the channel matrix. We experimented by adding AWGN on top of deterministic LOS channel components, and found that the GSM capacity of 4×4 MIMO with $\eta = 10$ can be maximized by adding AWGN with a power of at least -3 dB in relation to the average LOS path strength (see Fig. 8). For fairness of comparison, the channel matrices (with/without added randomness) are normalized such that the average strengths of the LOS paths are unitary. Taking a close look at the two sets of curves (with/without channel randomization) for $\eta = 10$ in the figure, we see that, at moderate SNR (0–20 dB), the artificial channel randomness added brings clear improvement to the spatial

[3]It has to be noted that along with the channel randomization effect, close reflections may have a cancellation effect. For example, table reflections can be out of phase [18] and the dominant effect may be performance degradation rather than enhancement due to cancellation.
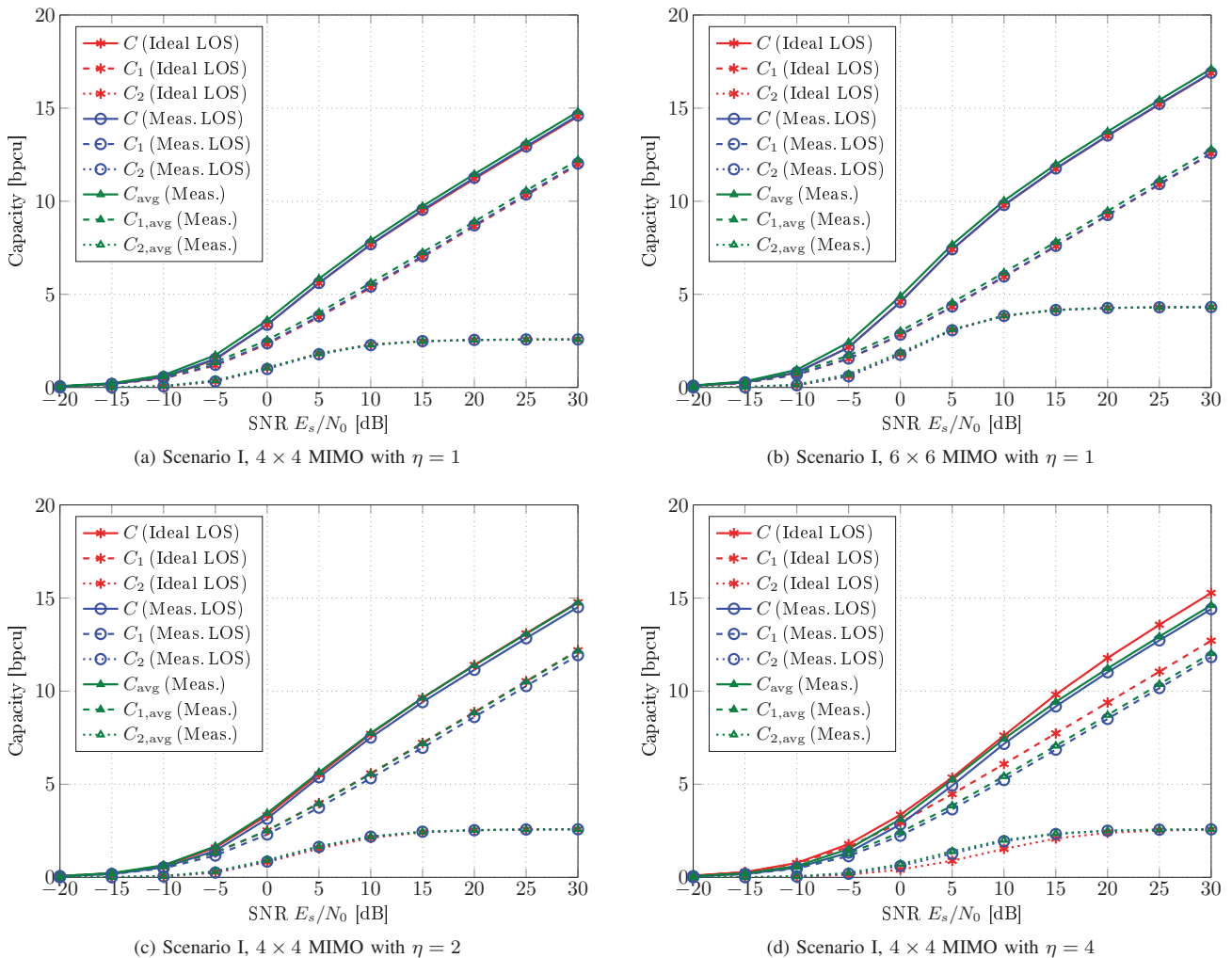
Fig. 7. Simulation results on the capacity of GSM (Scenario I). Legend: "Ideal LOS" — ideal pure LOS channels; "Meas. LOS" — LOS component extracted from measured multipath channels; "Meas." — measured multipath channels including both LOS and NLOS components.

capacity[4], while at the expense of marginal degradation in IQ capacity[5]. As a result, the total GSM capacity is improved as compared to the same setup ($\eta = 10$) but with ideal LOS paths. Moreover, we see that with the randomness added, the setup with $\eta = 10$ achieves superior total GSM capacity than the case with ideal LOS paths and $\eta = 1$[6].

---

[4]This is because the spatial capacity (C_2 in (12)) is limited by small Euclidean distances between certain pairs of the RX-side spatial symbols, which arose from the under-separation of the MIMO setup, and the randomness added increased the small Euclidean distances statistically such that the spatial symbols became less ambiguous.

[5]This is because, due to the randomness added, the average array gain for IQ domain transmission is reduced. To further elaborate, we know from the maximal ratio combining (MRC) principle that, when the noise level is equal over different branches, the optimum strategy is to have equal gains. In our system, the noise level is indeed assumed to be equal over different RX branches, thus the variations in the LOS path strength introduced by artificial randomness degrades array gain and reduces the IQ capacity.

[6]A side comment is that, as compared to the case with orthogonal MIMO setup ($\eta = 1$), higher IQ capacities are shown in the two cases with under-separated MIMO setup ($\eta = 10$). This is because there is no TX array gain in the orthogonal setup. While in the under-separated setup, certain amount of TX array gain is exhibited due to reduced antenna separations.

To sum up, the above results allow us to conclude the following:

- The capacity of GSM as predicted by ideal pure LOS channels in [14] can indeed be achieved in practice with orthogonal MIMO setups.
- As for under-separated MIMO setups (i.e., $\eta > 1$), channel randomization that may be introduced by hardware imperfections, close reflections and precoding shows the capability to simultaneously improve the GSM capacity and reduce the MIMO array size.
- The results in Fig. 8 strongly motivate us to use precoding [31], [32] with GSM. We thus gain maximized GSM capacity and, more notably, significantly shrunk physical size of the MIMO arrays.

2) Impact of Non-LOS Components on Capacity: The frequency-average capacity is evaluated at the measured frequency points and averaged over a 1-GHz bandwidth that is centered at about 60 GHz. The simulation results are presented in Fig. 7. We notice that the NLOS components of the measured channels show a marginal improvement of the IQ capacity C_1
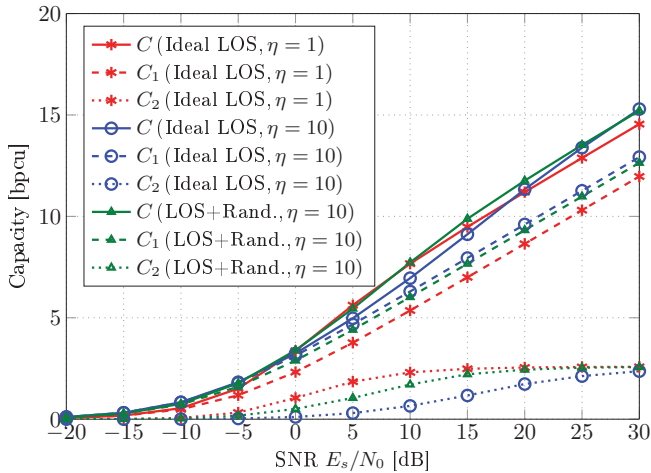
Fig. 8. Effect of channel randomization on the capacity of GSM. The MIMO size is 4×4, and "LOS+Rand." refers to that AWGN with $-3\,\text{dB}$ power in relation to the average LOS path strength is added on top of the deterministic LOS channel component. For fairness of comparison, the channel elements are all normalized to unit average power.
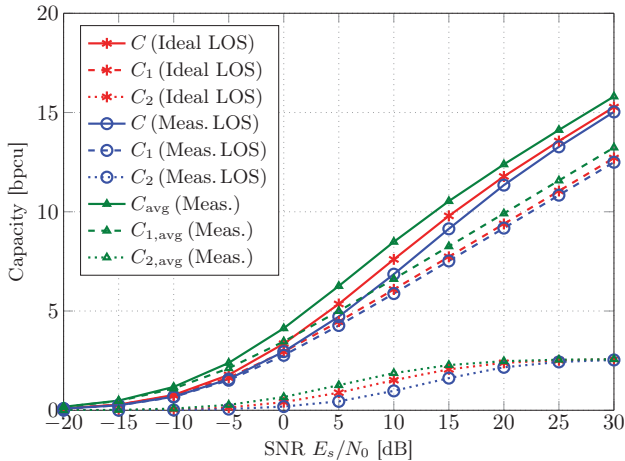
Fig. 9. Simulation results on the capacity of GSM (Scenario II, 4×4 MIMO with $\eta = 4$). The legend terms are the same as in Fig. 7.

but no improvement of the spatial capacity C_2. In summary, the NLOS components of the measured channels provide only marginal improvement on the total capacity C of GSM.

3) Impact of Richer Scattering and Close Reflections: As far as this case study is concerned, we consider Scenario II, which, in contrast to Scenario I, is characterized by richer scattering and close reflections. After performing capacity evaluations with the measured data of Scenario II and comparing it with the results of Scenario I in Fig. 7 (a), (c) and (d), we have the following findings. Due to space limitation, we show only one figure, i.e., Fig. 9, which corresponds to the case study of 4×4 MIMO with $\eta = 4$.

- In Scenario II, both the GSM capacity of the LOS component of the measured channels and the frequency-average GSM capacity of the measured multipath channels are in agreement with those predicted by using ideal pure LOS channels.

- The frequency-average GSM capacity is improved as compared to the GSM capacity of ideal LOS channels in all cases, i.e., $\eta = 1, 2, 4$ (see Fig. 9 for the case of $\eta = 4$). By contrast, there was no such improvement in Scenario I in Fig. 7.

V. SEP ANALYSIS

In this section, we study the SEP of GSM over the measured channels. More specifically, we investigate the following case studies: 1) the SEP of GSM over the LOS component of the measured channels, 2) the impact of the NLOS components of the measured multipath channels on the SEP of GSM, 3) the impact of the NLOS components on the SEP of reduced-complexity (for the sake of practicability) GSM systems, and 4) the impact of richer scattering and close reflections on the SEP of GSM. The SEP of GSM over ideal pure LOS channels is used as a benchmark.

A. Simulation Algorithms

As shown in Fig. 5, the measured channels exhibit a time dispersion time of the order of tens of nanoseconds, which causes an intersymbol interference (ISI) of the order of tens of symbols if we transmit at a symbol rate of the order of $1\,\text{GHz}$. To handle the ISI, we use a receiver that is based on single carrier (SC)-frequency domain equalization (FDE) (see Appendix B-2 for details). Another solution to handle the ISI issue could be to use orthogonal frequency-division multiplexing (OFDM) and apply GSM on a sub-carrier basis. However, per sub-carrier GSM makes it impossible to implement the switching at RF. Instead, baseband switching, which requires N_t full TX chains (from baseband to RF), is needed. Accordingly, baseband detection, which requires N_r full RX chains (from RF to baseband), is needed. We refer to such a system as having a full-complexity TX and RX. In such a solution, one big motivation for SM/GSM — single-RF TX (and simple detection) — is lost. Since hardware and computational complexity is a major concern at millimeter frequencies, the per-subcarrier GSM option is not studied in the present paper. The interested reader may find further details in [33]. In SC-FDE GSM, on the other hand, a simple TX based on RF switching can still be used. We refer to such a system as having a simple TX but full-complexity RX.

Despite of a simple TX, SC-FDE GSM still requires a full-complexity RX, which implies N_r full RX chains from RF to baseband. This may be acceptable in practice if N_r is a small number. In current implementations of mmWave MIMO systems, however, it may not always be practical to dedicate a separate RF chain to each available antenna [34], [35]. Motivated by these implementation constraints, we study the SEP performance of a low-complexity reception scheme which does not necessitate N_r RF chains and is based on a detection algorithm without equalization (see Appendix B-3 for details). In this proposed algorithm, the NLOS components of the channel are ignored and only the LOS component is used for detection. This scheme, besides avoiding both full TX and full RX complexities, leads to a simple RX that can be implemented based on RF phase shifters and a single IQ

down-conversion and sampling chain [14]. We refer to such a system as having full simplicity.

B. Simulation Results

Similar to the capacity analysis in Section IV, we first concentrate on Scenario I and subsequently study Scenario II and compare it with the former case study.

1) SEP over Pure LOS Channels: To study the SEP of GSM over the extracted LOS component of the measured multipath channels, the direct ML detection algorithm without FDE given in (7) is used and the simulation results are presented in Fig. 10. The findings are as follows.

We observe that the SEP of GSM over ideal LOS channels is better if $\eta = 1$ (in Fig. 10 (a) and (b)) as compared to that for $\eta > 1$ (in Fig. 10 (c) and (d)). This agrees with the prediction of [14] that the SEP of GSM in the pure LOS scenario can be minimized by making the channel orthogonal (i.e., $\eta = 1$).

If the MIMO setup is non-orthogonal (i.e., $\eta \neq 1$), on the other hand, the nonidealities — the fluctuations of the measured magnitudes as shown in Fig. 6 — in the measured LOS component can play an important role. As shown in Fig. 10 (c) and (d), if the MIMO setup is non-orthogonal but with reduced ASP, i.e., $\eta > 1$, both the SEP over ideal LOS channels and the SEP over the LOS component of the measured channels deteriorate and are worse for larger η. In this latter case, however, we notice that the SEP over the LOS component of the measured channels is much better than that over ideal pure LOS channels. This is mostly visible in Fig. 10(d), where the SEP over the measured LOS component is better than that over the corresponding ideal pure LOS channel by 5 dB at an error probability equal to 10^{-3}.

Based on this experimental study, we conclude that the simulation results agree with the prediction of [14] that the SEP of GSM in the pure LOS scenario can be minimized by making the MIMO channel orthogonal. Nonidealities in the measured LOS component, however, are likely to play an important role and greatly improve the SEP of GSM if the MIMO antennas are under-separated.

To further investigate the role played by the aforementioed nonidealities, we apply the precoding method of [31] to the set of channel data that is used in Fig. 10(d). The simulation results are plotted in Fig. 11. It is shown that pure precoding and precoding on top of the nonidealities show similar error performance which is about 6 dB improvement with respect to the ideal LOS channel at high SNR. In the example, roughly 5 dB gain is attained by the nonidealities even without precoding. On top of that, precoding has another 2 dB gain, but at the expense of extra hardware (see [31] for details of the precoding structure).

2) Multipath Channel with SC-FDE Reception: Here we study the SEP of GSM over the measured multipath channels by considering the SC-FDE reception scheme that is given in Appendix B-2. As for orthogonal MIMO setups (i.e., $\eta = 1$), Fig. 10 (a) and (b) show that the SEP of GSM over measured multipath channels with FDE reception is slightly worse (within 2 dB in terms of SNR) than that over the extracted LOS component of the measured multipath channels. As for MIMO setups with reduced ASP (i.e., $\eta > 1$), on the other hand, Fig. 10 (c) and (d) show that the SEP over measured multipath channels with SC-FDE reception is significantly worse (e.g., 10 dB in SNR at an SEP level equal to 10^{-3}) than that of the extracted LOS component of the measured multipath channels.

These findings lead to the conclusion that, as far as the SC-FDE reception scheme is concerned, the NLOS components are harmful to the error performance of GSM if the LOS component is present (i.e., not blocked). From the SEP perspective, as a result, the NLOS components deteriorate the achievable performance of GSM. From the implementation perspective, despite of a simple TX, a full-complexity RX is still needed to handle the ISI introduced by multipath propagation. Moreover, the signal processing associated with FDE, which includes fast Fourier transform (FFT), inverse fast Fourier transform (IFFT), and matrix inversion, can lead to a power hungry RX for giga-symbols-per-second systems. From the capacity perspective, on the other hand, Fig. 7 shows that the impact of the NLOS components is marginal and cannot notably improve the capacity of LOS GSM (see Section IV). These findings strongly motivate us to consider eliminating the NLOS components in the LOS scenario. Thanks to the specular nature of indoor propagation, the NLOS components can be avoided by using antennas with sufficient directivity or phased sub-arrays as shown in [20] for LOS SMX. This in turn helps to increase the antenna gain and improve the received SNR.

3) Multipath Channel with Un-Equalized Reception: In the previous paragraph, we have concluded that the NLOS components of the channel in the LOS scenario should be avoided. If the NLOS components are eliminated, ideally the channel becomes pure LOS and the received signal could be detected without the need of equalization. Motivated by this consideration, we study the potential of suppressing the NLOS components by discarding the measured CIR beyond a given maximum path length $dp_{\max}$ and study the SEP of GSM over the truncated measured channels. As mentioned, equalization is not needed in this case and, thus, we consider the low-complexity detection algorithm described in Appendix B-3. The simulation results are presented in Fig. 12. The SEP of GSM over the extracted LOS component of the measured channels is used as a benchmark.

Based on Fig. 5(a), we evaluate two case studies: $dp_{\max} = 4$ m and $dp_{\max} = 6$ m. As for $dp_{\max} = 6$ m, the SEP of GSM over the the truncated measured channels is significantly worse than that over the measured LOS component at moderate SNR (about 5 dB worse at an SEP level 10^{-2}). At high SNR, the SEP is limited by an error floor. The poor SEP performance is attributed to the reflected paths with path lengths in the range of $4.5 - 6$ m in Fig. 5(a). If we reduce $dp_{\max}$ to 4 m, which, in the considered setup, implies that all the major NLOS paths are eliminated, the SEP becomes reasonably good — within 2 dB in SNR as compared to that of the measured LOS component.

In conclusion, our experimental study shows that a simple RX without equalization may be a suitable low-complexity solution for LOS GSM communications, provided that the NLOS components are eliminated.
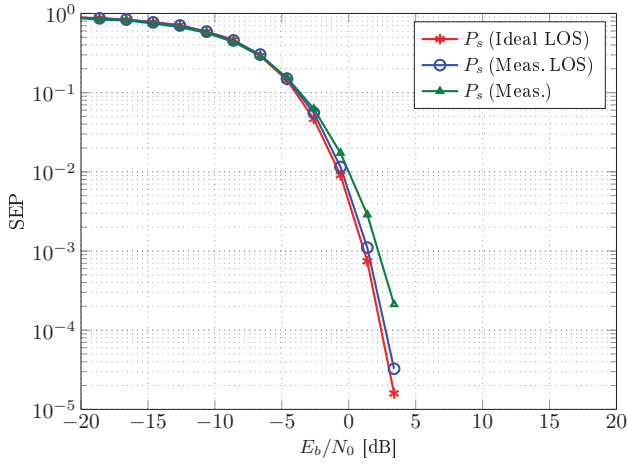
(a) Scenario I, 4×4 MIMO with $\eta = 1$
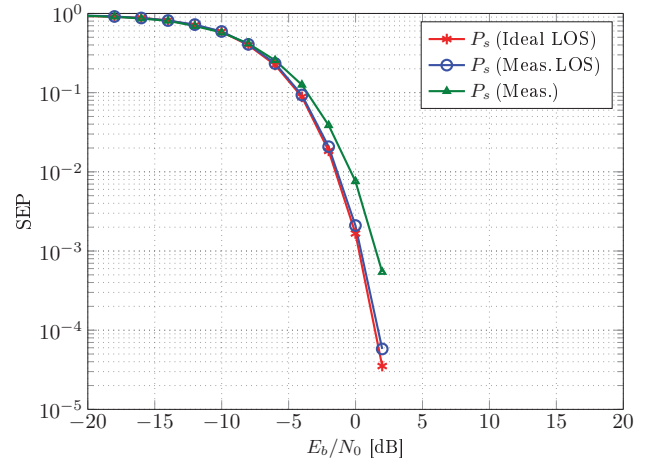
(b) Scenario I, 6×6 MIMO with $\eta = 1$
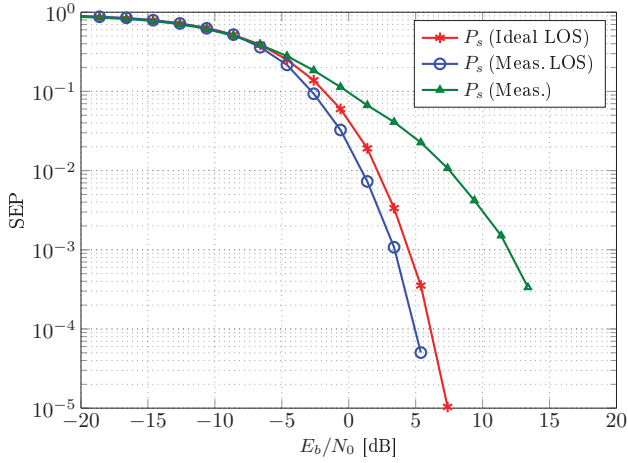
(c) Scenario I, 4×4 MIMO with $\eta = 2$
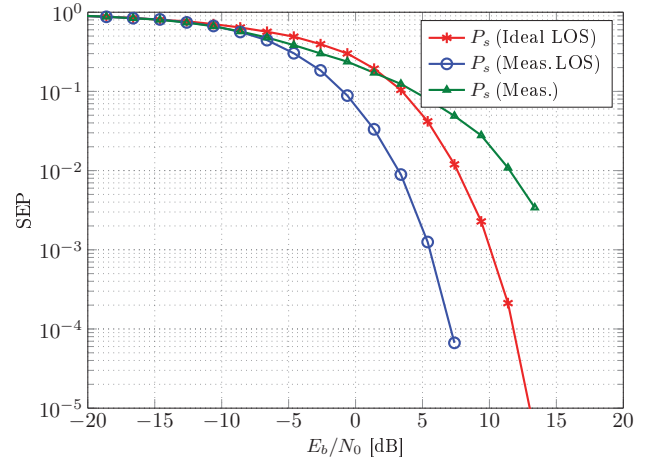
(d) Scenario I, 4×4 MIMO with $\eta = 4$

Fig. 10. Simulation results on the SEP of GSM over the measured channels (Scenario I). Legend: "Ideal LOS" — ideal pure LOS channels and using the ML detection algorithm as given in (7); "Meas. LOS" — LOS component extracted from the measured multipath channels and using (7); "Meas." — measured multipath channels including both LOS and NLOS components and using the SC-FDE algorithm as given in Appendix B-2.
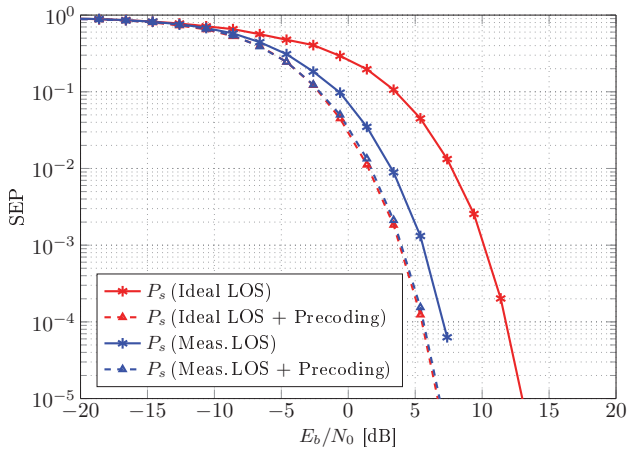
Fig. 11. Effect of precoding on the SEP of GSM. The setup and channel data are the same as Fig. 10(d). Legend: "Ideal LOS" — ideal pure LOS channels and using the ML detection algorithm as given in (7); "Meas. LOS" — LOS component extracted from the measured multipath channels and using (7); "Meas. LOS + Precoding" — Precoding is used on top of "Meas. LOS".

4) Impact of Richer Scattering and Close Reflections: As in Section IV-B3, we consider Scenario II and run the same set of simulations as the one used to generate Fig. 10 (a), (c) and (d). The representative results are illustrated in Fig. 13. The findings are as follows.

- As shown by the "Meas. LOS" curves in Fig. 13, close reflections destroy to some extent the channel orthogonality in the case of $\eta = 1$ thus degrading the GSM SEP (see Fig. 13 (a)). However, if the MIMO setup is largely under-separated, i.e., $\eta >> 1$, the GSM SEP can be improved by the randomness introduced by close reflections (see Fig. 13 (b) for the case of $\eta = 4$).

- As shown by the "Meas." curves in Fig. 13, the NLOS components of the channel in the richer scattered environment produce results that lead to the same conclusions as those made for Scenario I in Section V-B2, i.e., NLOS components are generally harmful to the error performance of GSM because equalization would then be needed while the SEP can be even worse than the extracted LOS
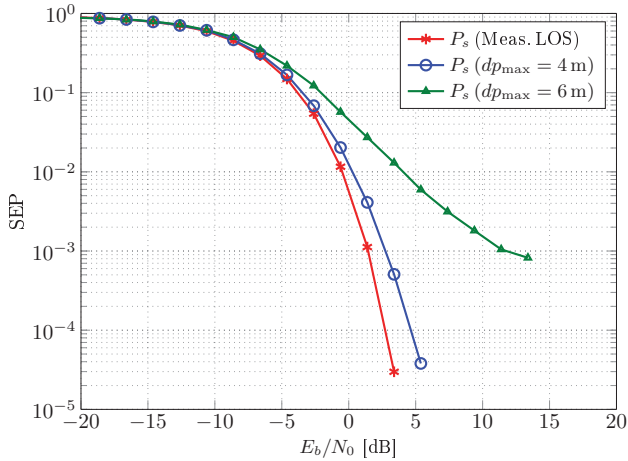
(a) Scenario I, 4×4, $\eta = 1$
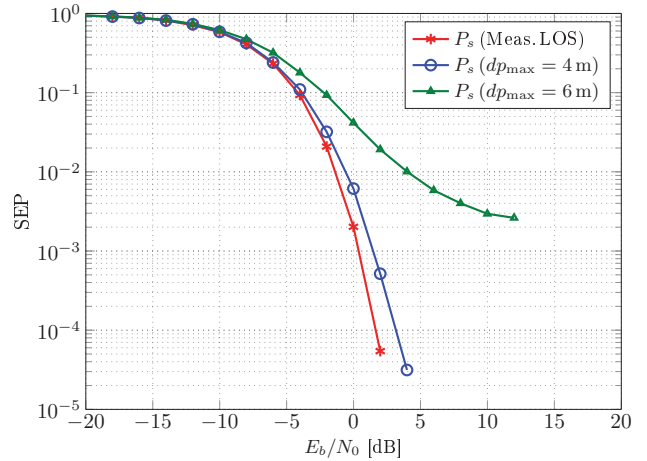
(b) Scenario I, 6×6, $\eta = 1$

Fig. 12. Simulation results on the SEP of GSM over the measured channels (Scenario I). Legend: "Meas. LOS" — LOS component extracted from the measured multipath channels and using (7); $dp_{\max}$ — measured multipath channels and using the algorithm given in Appendix B-3, but the MIMO CIRs are truncated to include only paths with a path length not exceeding $dp_{\max}$.
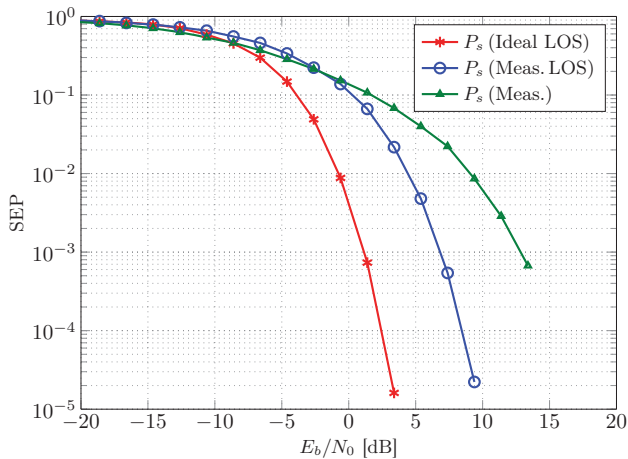
(a) Scenario II, 4×4 MIMO with $\eta = 1$
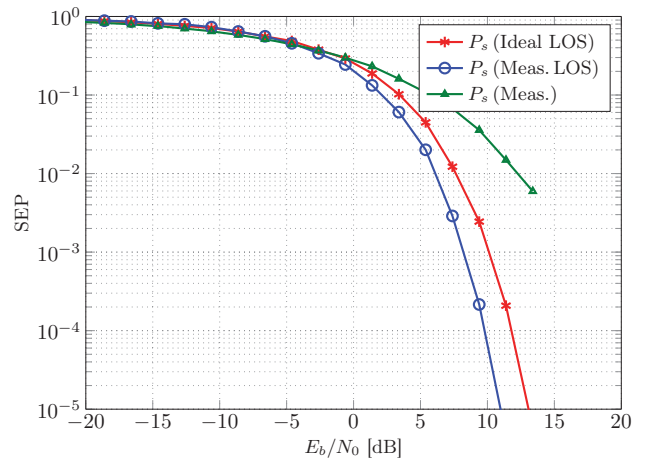
(b) Scenario II, 4×4 MIMO with $\eta = 4$

Fig. 13. Simulation results on the SEP of GSM (Scenario II). The legend terms are the same as in Fig. 10.

component.

VI. CONCLUSIONS

In this work, we performed channel sounding at 60 GHz in an indoor office environment and studied the capacity and SEP of GSM based on measured channel data. The major findings are as follows:

1) The capacity and SEP of GSM given in [14] based on ideal pure LOS analysis can indeed be achieved with the LOS component of the measured channels. The SEP of GSM in the LOS scenario can be minimized by properly separating the TX and RX antennas and making the MIMO channel orthogonal. Thus previous theoretical work in [14] is validated.

2) For capacity optimization, our results strongly suggest that precoding should be used with LOS GSM to simultaneously achive GSM capacity maximization and

MIMO array size reduction. This finding is a necessary supplement to the SEP optimization of [14] and capacity optimization of [15].

3) The NLOS components of the measured channels, although can marginally improve the frequency-average capacity of GSM, are actually harmful for GSM in the presence of the LOS component. In communications with a symbol rate of the order of 1 GHz, the ISI introduced by the NLOS components spans tens of symbols. SC-FDE can handle this ISI but at the expenses of an increased hardware and signal processing complexity and a worse SEP as compared to the measured LOS component.

4) Despite of the cost and complexity introduced by the implementation of the equalizer, the SEP of SC-FDE GSM over multipath channels is worse than that over the measured LOS component and with direct detection. It is thus suggested to avoid the NLOS components in the

LOS scenario and design GSM communication systems that solely rely on LOS paths. As a result, a system with full simplicity (i.e., with both a simple TX and RX) can be used to achieve GSM communication, provided that the reflected paths are eliminated.

5) When the MIMO setup does not fulfill the orthogonality condition, i.e., $\eta \neq 1$, the SEP of GSM deteriorates over both the LOS component of the measured channels and the ideal pure LOS channels. However, the nonidealities in the measured LOS component showed potential to improve the SEP as compared to the ideal pure LOS channels. This suggests that channel randomness introduced by hardware nonidealities, close reflections and precoding can improve the SEP of GSM when the array antennas are largely not sufficiently separated (in regard to the orthogonal setup).

It has to be noted that the conclusion that the NLOS components are harmful and should be avoided is made based on using practical detectors. However, the capacity analysis shows that this may not be true if a capacity-achieving detector is used. This highlights that more complicated/optimal receivers may be needed in order to take advantage of the NLOS channels — even though the gain is expected not to be very significant. This research issue is left for further work.

APPENDIX A
CAPACITY EVALUATION ALGORITHMS

1) Frequency-Flat Channels: For capacity calculation, the system model given in (6) for LOS channels and discrete IQ symbols is extended into a more general form for any frequency-flat channels and a continuous-envelope IQ signal as

$$\mathbf{y} = \mathbf{H}\mathbf{e}_i s + \mathbf{n} = s \sum_{k \in \mathcal{I}_i} \mathbf{h}_k + \mathbf{n}, \qquad (13)$$

where $\mathbf{H}$ is an $N_r \times N_t$ matrix of frequency-flat channel coefficients, $\mathbf{h}_k$ is the k-th column of $\mathbf{H}$, s is the (complex) IQ signal, and $\mathbf{e}_i$ and $\mathbf{n}$ are as defined in (6). According to [14, Theorem 1], the capacity achieved by GSM, using zero-mean complex Gaussian (ZMCG) signaling in the IQ domain and uniform signaling in the spatial domain, is given by (12) on page 14, where C_1 and C_2 are the IQ and spatial capacities respectively, $E_s \triangleq \mathbb{E}[|s|^2]$ is the average energy of the IQ symbol, $\mathbb{E}_{\mathbf{y}|i}[\cdot]$ is the expectation over the conditional random vector $\mathbf{y}$ (conditioned on i), $p(i)$ is the probability mass function (PMF) of i, $p(\mathbf{y}|i)$ is the conditional PDF of $\mathbf{y}$ given by

$$p(\mathbf{y}|i) = \frac{1}{|\pi\mathbf{\Gamma}_i|} \exp\left[-\mathbf{y}^H \mathbf{\Gamma}_i^{-1} \mathbf{y}\right], \qquad (14)$$

where $\mathbf{\Gamma}_i \in \mathbb{C}^{N_r \times N_r}$ is the co-variance matrix of $\mathbf{y}$ given by

$$\mathbf{\Gamma}_i = \frac{E_s}{N_u} \cdot \left[\sum_{k \in \mathcal{I}_i} \mathbf{h}_k\right] \left[\sum_{k \in \mathcal{I}_i} \mathbf{h}_k^H\right] + N_0\mathbf{I}, \qquad (15)$$

where $\mathbf{H}$ and $\mathbf{h}_k$ are defined in (13), and $\gamma \triangleq E_s/N_0$ is the SNR. Note that we refer to the conceptual TX model shown in Fig. 1 and do not consider the power loss introduced by the switch. As a result, E_s can be viewed as the average transmit power and γ can be interpreted as the average transmit power to noise power ratio.

2) Frequency-Selective Channels: In frequency-selective channels, the channel coefficients vary over frequencies. We calculate a frequency-average capacity of GSM as

$$C_{\text{avg}} = \underbrace{\sum_{k=0}^{K} C_1\left(\mathbf{H}_f(k), \gamma\right)}_{C_{1,\text{avg}}} + \underbrace{\sum_{k=0}^{K} C_2\left(\mathbf{H}_f(k), \gamma\right)}_{C_{2,\text{avg}}}, \qquad (16)$$

where $C_{1,\text{avg}}$ and $C_{2,\text{avg}}$ are the frequency-average IQ and spatial capacities respectively, $\mathbf{H}_f(k)$ given in (10) is the channel coefficients at the k-th frequency position. The above frequency-average capacity can be realized using an OFDM-style waveform, i.e., each sub-carrier is treated as an individual GSM channel with its own IQ stream and spatial modulation.

APPENDIX B
LINK-LEVEL SIMULATION

1) Transmission: For unified presentation of both algorithms, the link level transmission is assumed to be on a block basis: each K subsequent GSM symbols are regarded as a block, and a cyclic prefix (CP) of length at least $L - 1$, where L is the maximum number of channel taps, is added to each block at the TX. At the RX, the CP is first removed (before equalization or detection), thus the inter-block interference is avoided. The block of K GSM symbols, after being mapped to the TX antennas, can be expressed as

$$\mathbf{X} = \begin{bmatrix} x_1(1) & \cdots & x_1(K) \\ \vdots & \ddots & \vdots \\ x_{N_t}(1) & \cdots & x_{N_t}(K) \end{bmatrix} \in \mathbb{C}^{K \times N_t}, \qquad (17)$$

where $x_i(k)$ denotes the transmitted signal on the i-th TX antenna within the k-th time slot. The block representation of the noise signal $\mathbf{N}$ and received signal $\mathbf{Y}$ are defined likewise. The transmission for one block, without explicitly showing the CP insertion and removal, can be expressed as

$$\underbrace{\begin{bmatrix} y_1(1) \\ \vdots \\ y_1(K) \\ \vdots \\ y_{N_r}(1) \\ \vdots \\ y_{N_r}(K) \end{bmatrix}}_{\triangleq \bar{\mathbf{y}}} = \underbrace{\begin{bmatrix} \mathbb{H}_{11} & \cdots & \mathbb{H}_{1N_t} \\ \vdots & \ddots & \vdots \\ \mathbb{H}_{N_r 1} & \cdots & \mathbb{H}_{N_r N_t} \end{bmatrix}}_{\mathbb{H}} \underbrace{\begin{bmatrix} x_1(1) \\ \vdots \\ x_1(K) \\ \vdots \\ x_{N_t}(1) \\ \vdots \\ x_{N_t}(K) \end{bmatrix}}_{\triangleq \bar{\mathbf{x}}} + \underbrace{\begin{bmatrix} n_1(1) \\ \vdots \\ n_1(K) \\ \vdots \\ n_{N_r}(1) \\ \vdots \\ n_{N_r}(K) \end{bmatrix}}_{\triangleq \bar{\mathbf{n}}} \qquad (18)$$

where $\bar{\mathbf{x}}$, $\bar{\mathbf{n}}$, and $\bar{\mathbf{y}}$ are the transposed and stacked versions of the vectors $\mathbf{X}$, $\mathbf{N}$ and $\mathbf{Y}$ respectively, and $y_j(k)$ is the received signal on the j-th RX antenna within the k-th time slot. According to the noise definition in (6), we have $\mathbf{n} \sim C\mathcal{N}(\mathbf{0}, N_0\mathbf{I}_{N_r K})$. The j, i-th sub-matrix of $\mathbb{H}$ is a circulant

$$C(\mathbf{H}, \gamma) = \underbrace{\sum_i p(i) \left[\log_2 \left(1 + \frac{E_s}{N_u N_0} \left\| \sum_{k \in \mathcal{I}_i} \mathbf{h}_k \right\|^2 \right) \right]}_{C_1} + \underbrace{\log_2 \binom{N_t}{N_u} - \frac{1}{\binom{N_t}{N_u}} \sum_i \mathbb{E}_{\mathbf{y}|i} \left[\log_2 \frac{\sum_{i'} p(\mathbf{y}|i')}{p(\mathbf{y}|i)} \right]}_{C_2}, \qquad (12)$$

matrix composed of the sampled version of the CIR $h_{ji}(\tau)$ in (2) (sampled at symbol rate) and is given by

$$\mathbb{H}_{ji} = \begin{bmatrix} h_{ji}(0) & h_{ji}(L-1) & \cdots & h_{ji}(1) \\ h_{ji}(1) & h_{ji}(0) & \cdots & h_{ji}(2) \\ \vdots & \vdots & \ddots & \vdots \\ h_{ji}(L-1) & h_{ji}(L-2) & \cdots & h_{ji}(0) \end{bmatrix}, \qquad (19)$$

where $h_{ji}(k)$ is the k-th sample of $h_{ji}(\tau)$.

2) FDE Reception: The time-domain block transmission model given in (18) can be converted into the frequency domain using the discrete Fourier transform (DFT) as [36]

$$\underbrace{(\mathbf{I}_{N_r} \otimes \mathbf{U}) \cdot \bar{\bar{\mathbf{y}}}}_{\triangleq \bar{\mathbf{y}}^f} = \mathbf{\Lambda} \cdot \underbrace{(\mathbf{I}_{N_r} \otimes \mathbf{U}) \cdot \bar{\bar{\mathbf{x}}}}_{\triangleq \bar{\mathbf{x}}^f} + \underbrace{(\mathbf{I}_{N_r} \otimes \mathbf{U}) \cdot \bar{\bar{\mathbf{n}}}}_{\triangleq \bar{\mathbf{n}}^f}, \quad (20)$$

where $\mathbf{U} = \mathbf{F}/\sqrt{K}$, with $\mathbf{F} = [\exp(-\mathrm{j}2\pi kl)]$ for $k,l = 0, 1, \ldots, K-1$, is the unitary DFT matrix, $\otimes$ is the Kronecker product operator, and

$$\mathbf{\Lambda} = \begin{bmatrix} \mathbf{\Lambda}_{11} & \cdots & \mathbf{\Lambda}_{1N_t} \\ \vdots & \ddots & \vdots \\ \mathbf{\Lambda}_{N_r 1} & \cdots & \mathbf{\Lambda}_{N_r N_t} \end{bmatrix} \qquad (21)$$

with $\mathbf{\Lambda}_{ji}$ being a diagonal matrix of the frequency domain channel response between the i-th TX antenna and the j-th RX antenna given by

$$\mathbf{\Lambda}_{ji} = \mathrm{diag}\left(\mathbf{U}\mathbf{h}_{ji}\right). \qquad (22)$$

It is important to note that, $\bar{\mathbf{x}}^f$, $\bar{\mathbf{n}}^f$, and $\bar{\mathbf{y}}^f$ are the equivalent frequency-domain versions of $\bar{\bar{\mathbf{x}}}$, $\bar{\bar{\mathbf{n}}}$ respectively, and $\bar{\bar{\mathbf{y}}}$ and (20) is the equivalent frequency-domain model of the time-domain block-wise transmission system in (18). As a result, $\bar{\mathbf{x}}^f$ can be recovered by frequency domain equalization as

$$\bar{\mathbf{x}}_f^\dagger = \mathbf{W}\bar{\mathbf{y}}_f \qquad (23)$$

where $\mathbf{W}$ is the frequency-domain equalizer, and $\bar{\mathbf{x}}_f^\dagger$ is the equalized frequency domain signal. For the considered SC-FDE receiver, the equalizer can be designed according to the zero forcing (ZF) or minimum mean square error (MMSE) criterion. It is well-known that the latter has superior performance, since it takes into account the noise power and eliminates the noise amplification issue. Furthermore, MMSE equalization has been commonly used in other SC-FDE systems for 60 GHz communications [37]–[39]. Hence, we also use MMSE equalization, which is given by [36]

$$\mathbf{W}_{\mathrm{MMSE}} = \frac{\mathbf{\Lambda}^{\mathrm{H}}}{N_t} \left(\frac{\mathbf{\Lambda}\mathbf{\Lambda}^{\mathrm{H}}}{N_t} + N_0 \mathbf{I}_{N_r K} \right)^{-1} \qquad (24a)$$

$$= \left(\frac{\mathbf{\Lambda}^{\mathrm{H}}\mathbf{\Lambda}}{N_t} + N_0 \mathbf{I}_{N_t K} \right)^{-1} \frac{\mathbf{\Lambda}^{\mathrm{H}}}{N_t}, \qquad (24b)$$

where (24b) is known as the alternative form of the MMSE equalizer which is obtained by applying the matrix inversion lemma [40, (9)] to (24a). The alternative form is more computationally efficient than the original form for $N_r > N_t$.

Once the received signal is equalized, it is converted back into the time domain as

$$\bar{\mathbf{x}}^\dagger = \left(\mathbf{I}_{N_t} \otimes \mathbf{U}^{\mathrm{H}} \right) \bar{\mathbf{x}}_f^\dagger. \qquad (25)$$

Finally, we use ML detection to recover the GSM symbols as

$$\hat{\mathbf{x}}(k) = \arg\min_{\mathbf{x} \in \mathbb{S}} \left\| \mathbf{x}^\dagger(k) - \mathbf{x} \right\|^2 \quad \forall k = 1, 2, \ldots, K, \quad (26)$$

where $\mathbf{x}^\dagger(k) \triangleq \left[x_1^\dagger(k), x_2^\dagger(k), \ldots, x_{N_t}^\dagger(k) \right]^T$ is the un-stacked version of $\bar{\mathbf{x}}^\dagger$, the mapping of $x_i^\dagger(k)$ in $\bar{\mathbf{x}}^\dagger$ is similar to the mapping of $x_i(k)$ in $\bar{\mathbf{x}}$ in (18). For the whole block, we have $\widehat{\mathbf{X}} = [\hat{\mathbf{x}}(1), \hat{\mathbf{x}}(2), \ldots, \hat{\mathbf{x}}(K)]$. If no error occurs, we have $\widehat{\mathbf{X}} = \mathbf{X}$. The simulated SEP is calculated as the ratio of the number of wrongly detected GSM symbols to the total number of GSM symbols sent.

3) Un-Equalized Reception: In the non-equalized reception, following (18), the received signal is directly detected without conversion into the frequency domain. The ML detection in this case is written as

$$\hat{\mathbf{x}}(k) = \arg\min_{\mathbf{x} \in \mathbb{S}} \left\| \mathbf{y}(k) - \mathbf{H}_{\mathrm{LOS}}\mathbf{x} \right\|^2 \quad \forall k = 1, 2, \ldots, K, \quad (27)$$

where $\mathbf{H}_{\mathrm{LOS}}$ is the LOS component of the measured channel, $\mathbf{y}(k) = [y_1(k), y_2(k), \ldots, y_{N_r}(k)]^{\mathrm{T}}$ is the received signal given in (18). The simulated SEP is calculated similarly as above in the previous case.

References

[1] M. Di Renzo, H. Haas, A. Ghrayeb, S. Sugiura, and L. Hanzo, "Spatial modulation for generalized MIMO: Challenges, opportunities, and implementation," *Proc. IEEE*, vol. 102, no. 1, pp. 56–103, Jan. 2014.

[2] A. Younis, W. Thompson, M. Di Renzo, C.-X. Wang, M. Beach, H. Haas, and P. Grant, "Performance of spatial modulation using measured real-world channels," in *2013 IEEE 78th Veh. Technol. Conf. (VTC Fall)*, Sep. 2013, pp. 1–5.

[3] N. Serafimovski, A. Younis, R. Mesleh, P. Chambers, M. Di Renzo, C.-X. Wang, P. Grant, M. Beach, and H. Haas, "Practical implementation of spatial modulation," *IEEE Trans. Veh. Technol.*, vol. 62, no. 9, pp. 4511–4523, Nov. 2013.

[4] J. Zhang, Y. Wang, L. Ding, and N. Zhang, "Bit error probability of spatial modulation over measured indoor channels," *IEEE Trans. Wireless Commun.*, vol. 13, no. 3, pp. 1380–1387, Mar. 2014.

[5] K. M. Humadi, A. I. Sulyman, and A. Alsanie, "Experimental results for generalized spatial modulation scheme with variable active transmit antennas," in *Cognitive Radio Oriented Wireless Networks*, ser. Lecture Notes of the Inst. for Comput. Sci., Social Informatics and Telecommun. Eng. Springer Int. Publishing, Apr. 2015, no. 156, pp. 260–270.

[6] G. J. Foschini, "Layered space-time architecture for wireless communication in a fading environment when using multi-element antennas," *Bell Labs Tech. J.*, vol. 1, no. 2, pp. 41–59, 1996.

[7] P. Wolniansky, G. Foschini, G. Golden, and R. Valenzuela, "V-BLAST: An architecture for realizing very high data rates over the rich-scattering wireless channel," in *URSI Int. Symp. on Signals, Systems, and Electronics*, Sep. 1998, pp. 295–300.

[8] J. Wang, S. Jia, and J. Song, "Generalised spatial modulation system with multiple active transmit antennas and low complexity detection scheme," *IEEE Trans. Wireless Commun.*, vol. 11, no. 4, pp. 1605–1615, Apr. 2012.

[9] A. Younis, "Spatial modulation: Theory to practice," Ph.D. dissertation, University of Edinburgh, 2014. [Online]. Available: http://hdl.handle.net/1842/8990

[10] O. Osman, "Variable active antenna spatial modulation," *IET Microwaves, Antennas & Propagation*, vol. 9, no. 15, pp. 1816–1824, dec 2015.

[11] A. Stavridis, S. Sinanovic, M. Di Renzo, and H. Haas, "Energy evaluation of spatial modulation at a multi-antenna base station," in *IEEE 78th Veh. Technol. Conf. (VTC Fall)*, Sep. 2013, pp. 1–5.

[12] P. Patcharamaneepakorn, S. Wu, C. X. Wang, e. H. M. Aggoune, M. M. Alwakeel, X. Ge, and M. D. Renzo, "Spectral, energy, and economic efficiency of 5G multicell massive MIMO systems with generalized spatial modulation," *IEEE Trans. Veh. Technol.*, vol. 65, no. 12, pp. 9715–9731, Dec. 2016.

[13] P. Liu and A. Springer, "Space shift keying for LOS communication at mmWave frequencies," *IEEE Wireless Commun. Lett.*, vol. 4, no. 2, pp. 121–124, Apr. 2015.

[14] P. Liu, M. Renzo, and A. Springer, "Line-of-sight spatial modulation for indoor mmWave communication at 60 GHz," *IEEE Trans. Wireless Commun.*, vol. 15, no. 11, pp. 7373–7389, Nov. 2016.

[15] P. Liu, M. Di Renzo, and A. Springer, "Variable-N_u generalized spatial modulation for indoor LOS mmwave communication: Performance optimization and novel switching structure," *IEEE Trans. on Commun.*, vol. PP, no. 99, pp. 1–16, 2017.

[16] N. Ishikawa, R. Rajashekar, S. Sugiura, and L. Hanzo, "Generalized spatial modulation based reduced-RF-chain millimeter-wave communications," *IEEE Trans. Veh. Technol.*, vol. PP, no. 99, pp. 1–1, 2016.

[17] N. S. Perović, P. Liu, M. D. Renzo, and A. Springer, "Receive spatial modulation for LOS mmWave communications based on TX beamforming," *IEEE Commun. Lett.*, vol. 21, no. 4, pp. 921–924, Apr. 2017.

[18] A. Maltsev, V. Erceg, E. Perahia, C. Hansen, R. Maslennikov, A. Lomayev, A. Sevastyanov, A. Khoryaev, G. Morozov, M. Jacob, S. Priebe, T. Kürner, S. Kato, H. Sawada, K. Sato, and H. Harada, "Channel models for 60 GHz WLAN systems," Tech. Rep. IEEE 802.11-09/0334r8, May 2010. [Online]. Available: https://mentor.ieee.org/802.11/dcn/09/11-09-0334-08-00ad-channel-models-for-60-ghz-wlan-systems.doc

[19] F. Bohagen, P. Orten, and G. Oien, "Design of optimal high-rank line-of-sight MIMO channels," *IEEE Trans. Wireless Commun.*, vol. 6, no. 4, pp. 1420–1425, Apr. 2007.

[20] E. Torkildson, U. Madhow, and M. Rodwell, "Indoor millimeter wave MIMO: Feasibility and performance," *IEEE Trans. Wireless Commun.*, vol. 10, no. 12, pp. 4150–4160, Dec. 2011.

[21] William C. Jakes, "Multipath interference," in *Microwave Mobile Communications*. IEEE Press, 1974.

[22] H. Friis, "A note on a simple transmission formula," *Proc. IRE*, vol. 34, no. 5, pp. 254–256, May 1946.

[23] K. Sato, H. Kozima, H. Masuzawa, T. Manabe, T. Ihara, Y. Kasashima, and K. Yamaki, "Measurements of reflection characteristics and refractive indices of interior construction materials in millimeter-wave bands," in *IEEE 45th Veh. Tech. Conf.*, vol. 1, Jul. 1995, pp. 449–453 vol.1.

[24] J. Jeganathan, A. Ghrayeb, and L. Szczecinski, "Spatial modulation: Optimal detection and performance analysis," *IEEE Commun. Lett.*, vol. 12, no. 8, pp. 545–547, Aug. 2008.

[25] F. Bohagen, P. Orten, and G. E. Oien, "Construction and capacity analysis of high-rank line-of-sight MIMO channels," in *IEEE Wireless Commun. and Networking Conf.*, vol. 1, 2005, pp. 432–437.

[26] A. Chandra, A. Prokeš, T. Mikulášek, J. Blumenstein, P. Kukolev, T. Zemen, and C. F. Mecklenbräuker, "Frequency-domain in-vehicle UWB channel modeling," *IEEE Trans. Veh. Technol.*, vol. 65, no. 6, pp. 3929–3940, JUNE 2016.

[27] J. Blumenstein, A. Prokes, A. Chandra, T. Mikulasek, R. Marsalek, T. Zemen, and C. Mecklenbräuker, "In-vehicle channel measurement, characterization and spatial consistency comparison of 3-11 GHz and 55-65 GHz frequency bands," *IEEE Trans. Veh. Technol.*, vol. PP, no. 99, 2016.

[28] J. Blumenstein, J. Vychodil, M. Pospisil, T. Mikulasek, and A. Prokes, "Effects of vehicle vibrations on mm-wave channel: Doppler spread and correlative channel sounding," in *IEEE 27th Annual Int. Symp. on Personal, Indoor, and Mobile Radio Commu. (PIMRC)*, Sep. 2016, pp. 432–437.

[29] H. Xu, V. Kukshya, and T. Rappaport, "Spatial and temporal characteristics of 60-GHz indoor channels," *IEEE J. Sel. Areas Commun.*, vol. 20, no. 3, pp. 620–630, Apr. 2002.

[30] T. Pedersen, G. Steinbock, and B. Fleury, "Modeling of reverberant radio channels using propagation graphs," *IEEE Trans. Antennas Propag.*, vol. 60, no. 12, pp. 5978–5988, Dec 2012.

[31] N. S. Perović, P. Liu, and A. Springer, "Design of a simple phase precoder for generalized spatial modulation in los millimeter wave channels," in *11th int. ITG conf. on systems communications and coding (SCC17)*, 2017.

[32] C. Masouros and L. Hanzo, "Constellation randomization achieves transmit diversity for single-RF spatial modulation," *IEEE Trans. Veh. Technol.*, vol. 65, no. 10, pp. 8101–8111, Oct. 2016.

[33] P. Yang, Y. Xiao, Y. L. Guan, K. V. S. Hari, A. Chockalingam, S. Sugiura, H. Haas, M. Di Renzo, C. Masouros, Z. Liu, L. Xiao, S. Li, and L. Hanzo, "Single-carrier SM-MIMO: A promising design for broadband large-scale antenna systems," *IEEE Commun. Surveys Tuts.*, vol. 18, no. 3, pp. 1687–1716, 2016.

[34] R. W. Heath, "Millimeter wave MIMO: A signal processing perspective," Apr. 2015. [Online]. Available: http://users.ece.utexas.edu/rheath/presentations/2015/MmWaveMIMOaSPPerspectiveICASSP2015Heath.pdf

[35] O. E. Ayach, S. Rajagopal, S. Abu-Surra, Z. Pi, and R. W. Heath, "Spatially sparse precoding in millimeter wave MIMO systems," *IEEE Trans. Wireless Commun.*, vol. 13, no. 3, pp. 1499–1513, Mar. 2014.

[36] S. Sugiura and L. Hanzo, "Single-RF spatial modulation requires single-carrier transmission: Frequency-domain turbo equalization for dispersive channels," *IEEE Trans. Veh. Technol.*, vol. PP, no. 99, pp. 1–1, 2014.

[37] C. Park and T. S. Rappaport, "Short-range wireless communications for next-generation networks: UWB, 60 GHz millimeter-wave WPAN, and ZigBee," *IEEE Wireless Commun.*, vol. 14, no. 4, pp. 70–78, 2007.

[38] M. Lei, I. Lakkis, H. Harada, and S. Kato, "MMSE-FDE based on estimated SNR for single-carrier block transmission (SCBT) in multi-Gbps WPAN (IEEE 802.15.3c)," in *IEEE Int. Conf. on Commu. Workshops*, May 2008, pp. 52–56.

[39] F. Hsiao, A. Tang, D. Yang, M. Pham, and M.-C. F. Chang, "A 7Gb/s SC-FDE/OFDM MMSE equalizer for 60GHz wireless communications," in *IEEE Asian Solid State Circuits Conf.*, 2011, pp. 293–296.

[40] L. Szczecinski and D. Massicotte, "Low complexity adaptation of MIMO MMSE receivers, implementation aspects," in *IEEE Global Telecommun. Conf. (GLOBECOM)*, vol. 4, Dec. 2005, pp. 2327–2332.

Optimization of the Cut-Off Rate of Generalized Spatial Modulation with Transmit Precoding

Nemanja Stefan Perović, Peng Liu, **Jiri Blumenstein**, Marco Di Renzo, Andreas Springer

IEEE Transactions on Communications

IF=4.671

Optimization of the Cut-Off Rate of Generalized Spatial Modulation with Transmit Precoding

Nemanja Stefan Perović, Peng Liu, *Member, IEEE,*

Jiri Blumenstein, *Member, IEEE,* Marco Di Renzo, *Senior Member, IEEE,*

and Andreas Springer, *Member, IEEE*

Abstract

Spatial modulation (SM) and generalized spatial modulation (GSM) are emerging multiple input multiple output (MIMO) schemes that use the transmitter (TX) antenna switching for data transmission. Their operating principle makes the optimization of the channel capacity and the mutual information generally more difficult than in conventional MIMO schemes that are not based on antenna switching. Therefore, we propose the use of the channel cut-off rate as a relevant and more tractable metric for optimizing the performance of SM/GSM systems, as it constitutes a practical lower-bound of the channel capacity. In particular, we propose four TX precoding schemes for increasing the cut-off rate of SM/GSM systems. We show that the TX precoding schemes that are designed for increasing the array gain provide the largest improvement of the cut-off rate at a low signal-to-noise ratio (SNR). On the other hand, the TX precoding schemes that are designed for increasing the minimum Euclidean distance between different GSM symbols are more suitable for application at a medium-high SNR in correlated channels. The proposed precoding schemes are shown to enhance the mutual information, and the gain is shown to be of the same order of magnitude as the gain of the corresponding channel cut-off rate.

Index Terms

Channel cut-off rate, generalized spatial modulation (GSM), optimization, TX precoding, channel capacity, mutual information.

I. Introduction

Among the many multiple input multiple output (MIMO) schemes that exist in the literature, spatial modulation (SM) and generalized spatial modulation (GSM) have attracted a lot of

research interest during the last decade [1], [2]. In the last years, in particular, many schemes that enhance and optimize the performance of SM/GSM systems have been proposed. Most of them are focused on optimizing the error performance, while only a few of them are concerned with the optimization the channel capacity and mutual information. This is due to the inherent complexity of formulating the channel capacity of SM/GSM systems in a mathematically tractable manner that is suitable for system optimization [3]. This is, on the other hand, relatively simpler to do for the error probability. To overcome this issue, we propose to use the channel cut-off rate, as a practical surrogate of the channel capacity, for optimizing the capacity and the mutual information of SM/GSM systems [4].

The channel cut-off rate constitutes an upper-bound of the codeword error probability of a communication system over the ensemble of random binary channel codes, and, thus, it is independent of the specific code being used. The main motivation for proposing it as a substitute of the channel capacity for optimizing the performance of SM/GSM systems originates from James Massey, who suggested that, as a rule of thumb, the channel cut-off rate is the *practical* upper-limit on the code rate for reliable communications whereas the channel capacity is the *theoretical* upper-limit [4]. Therefore, the channel cut-off rate is a widely accepted and sensible performance indicator for comparing channels for which a coding scheme with finite complexity is used [5]. In the context of optimizing the design of SM/GSM systems, relying on the channel cut-off rate instead of the channel capacity has two main advantages: i) the optimization of the modulator is independent of the specific channel code that is used [6]; and ii) there is no need to deal with the intractable mathematical expression of the channel capacity of SM/GSM [3].

In mathematical terms, the relation between the channel cut-off rate, R_0, and the codeword error probability, P_e, can be formulated as $P_e \leq e^{-n(R_0 - R)}$, where n is the number of times that the channel is used for transmitting a codeword (i.e., the codeword's length), and R is the information rate in bits per channel use (i.e., the binary code rate) [7], [8]. For very long code sequences $n \to \infty$, P_e approaches zero, i.e., it becomes arbitrarily small, if $R < R_0$. Hence, the channel cut-off rate can be interpreted as a practical lower-bound of the channel capacity [9].

In SM-MIMO systems, two data streams are transmitted — one in the conventional in-phase and quadrature (IQ) domain by employing, e.g., M-PSK or M-QAM modulation, and the other one in the so-called spatial domain, i.e., by selecting and activating one out of N_t antennas that are available at the transmitter (TX) [1], [2]. A generalization of SM consists either of activating more than one TX antenna per time slot while still transmitting a single IQ stream [10], or

of activating multiple TX antennas and transmitting more than one IQ stream [11], [12]. This generalized scheme is referred to as GSM and it provides higher data rates than SM, at the cost of an increased complexity. In this paper, due to its promising tradeoff between achievable rate and implementation complexity, we focus our attention on the GSM scheme where a fixed number of $0 < N_a < N_t$ TX antennas is activated and a single IQ stream is transmitted from all of them. Compared with conventional spatial multiplexing (SMX) systems [13], [14], which typically need the same number of full TX chains (from baseband to RF) as the number of transmitted IQ streams, GSM offers three main advantages [2], [15]: 1) reduced signal processing complexity and hardware cost due to the fact that it needs a single RF chain at the TX; 2) improved energy efficiency at the TX [16], since a single power amplifier is needed; and 3) avoidance of the inter-channel interference at the receiver (RX), which significantly reduces the complexity of the maximum likelihood (ML) demodulator [17].

Due to the encoding of information data into the IQ and spatial domains, it is not an easy task to derive a tractable and closed-form expression of the channel capacity of SM/GSM systems. The approaches available in the literature for computing the channel capacity of SM/GSM systems are, in fact, not so many. In [18], the channel capacity of SM for multiple input single output (MISO) systems is formulated as a sum of the channel capacities of IQ and spatial domains. The computation of the channel capacity of the spatial domain requires numerical integrations. Thus, no closed-form expression is provided. The approach proposed in [18] is generalized in [10], [19] for computing the channel capacity of SM/GSM MIMO systems. However, numerical integration is still needed. In [20], [21], the authors propose a lower-bound for the mutual information of SM/GSM systems that assume Gaussian signaling for the IQ symbols. A closed-form approximation for the mutual information of SM-MISO systems is introduced in [3]. In [22], unlike the previous papers that assume Gaussian signaling for the IQ symbols, a lower-bound for the mutual information of SM-MISO systems that employ a discrete IQ modulation alphabet is derived. This analysis is generalized for application to GSM systems in [23].

Due to the difficulty of formulating the channel capacity of SM/GSM systems in a tractable closed-form expression, only in a limited number of research works the authors have attempted to design improved schemes based on the maximization of the channel capacity. In [24], the authors propose an antenna selection algorithm based on maximizing the channel capacity, that is applicable only to SM systems. In [25], an algorithm that optimizes the antenna selection probability for application to SM-MISO systems is studied. In [26], power allocation algorithms

that increase the mutual information of SM-MISO systems are introduced. An iterative algorithm for optimizing the precoder of GSM systems based on the mutual information is studied in [23].

To circumvent the direct calculation of the channel capacity of SM/GSM systems, we propose to employ the channel (or simply) cut-off rate for optimizing the performance of SM/GSM systems. To the best of our knowledge, this is the first time that the cut-off rate is utilized for optimizing the performance of SM/GSM systems. Indeed, just a few research works available in the literature are focused on optimizing the cut-off rate of conventional MIMO systems. In [9], the authors consider SMX-MIMO systems and propose a phase precoder design that increases the cut-off rate averaged with respect to the channel statistics. The impact of channel state information at TX (CSIT) on the optimization of the cut-off rate of MIMO systems is studied in [7]. Precoding schemes that optimize the cut-off rate of MIMO systems, under imperfect channel estimation, are proposed in [27], [28]. In [29], [30], the authors propose new designs for the IQ modulation that optimize the cut-off rate of MIMO systems.

Against this background, the contributions made by this paper are the following:

1) We propose to utilize the cut-off rate as a performance metric for optimizing the mutual information (i.e., channel capacity) of SM/GSM systems that employ a discrete IQ modulation alphabet. We show that the cut-off rate of SM/GSM systems can be formulated in a closed-form expression, which makes it easier to compute and to optimize compared with the actual channel capacity. Thus, the cut-off rate is proved to be a convenient surrogate of the channel capacity for system optimization and design.

2) We propose four different precoding schemes for increasing the cut-off rate of SM/GSM systems. The proposed precoding schemes employ different strategies for system optimization, which include grouping the TX antennas, applying singular value decomposition (SVD) or SVD-discrete Fourier transform (DFT) pre-processing and selecting a subset of inputs, and employing DFT precoding. We prove that the precoding scheme based on SVD-DFT pre-processing usually outperforms its counterpart based on SVD pre-processing.

3) We evaluate the performance of the proposed precoding schemes with the aid of numerical simulations. All the schemes with the exception of DFT precoding provide gains in the low-medium signal-to-noise ratio (SNR) regime. The latter precoding scheme, on the other hand, is shown to outperform the other schemes in the medium-high SNR regime and especially in highly correlated channels.

4) We show that the improvement of the cut-off rate of SM/GSM systems that is obtained by

using the proposed precoding schemes is comparable with the improvement of the mutual information that is computed numerically. We show that the proposed precoding schemes can be applied for enhancing the cut-off rate of SMX-MIMO systems as well. Compared with SM/GSM systems, the gain is, however, smaller. Finally, we prove that optimizing the symbol error probability (SEP) leads to smaller improvements of the mutual information compared with those obtained by maximizing the cut-off rate.

The rest of the paper is organized as follows. In Section II, we introduce the system model and derive an expression of the cut-off rate of SM/GSM systems. In Section III, we propose four precoding schemes that aim to increase the cut-off rate. In Section IV, we illustrate simulation results of the cut-off rate for the proposed precoding schemes, and discuss the advantages and limitations of each of them. Finally, Section V concludes this paper.

Notation: Lowercase bold symbols denote column vectors; uppercase bold symbols denote matrices; $|\cdot|$ and $\|\cdot\|$ denote absolute value and L_2-norm, respectively; $\exp(\cdot)$, $\log_2(\cdot)$, $\Re\{\cdot\}$ and $\mathbb{E}\{\cdot\}$ denote the exponential function, the base-two logarithm, the real part of a complex number and the mean (expected) value of a random variable, respectively; $\mathbf{j}$ denotes the imaginary unit; $p(\cdot)$, $\mathcal{H}(\cdot)$ and $\mathcal{I}(\cdot)$ denote the probability, the entropy, and the mutual information, respectively; $\mathbf{A}(i,j)$ denoted the j-th element of the i-th row of matrix $\mathbf{A}$; $\mathbf{B}(:,j)$ denotes the j-th column of matrix $\mathbf{B}$; $\mathcal{CN}(\cdot,\cdot)$ denotes a circularly symmetric complex Gaussian random variable.

II. SYSTEM MODEL

The receive signal vector of $N_t \times N_r$ SM/GSM system can be formulated as follows

$$\mathbf{y} = \mathbf{H}\mathbf{e}_i s_m / \sqrt{N_a} + \mathbf{n}, \tag{1}$$

where $\mathbf{H} \in \mathbb{C}^{N_r \times N_t}$ is the channel matrix and s_m ($m = 1, \cdots, M$) is an IQ (e.g., *M*-QAM) symbol. The number of the active TX antennas during each symbol interval is N_a. Hence, $N_c = \binom{N_t}{N_a}$ TX antenna activation patterns are used[1], where each TX antenna activation pattern consists of N_a active TX antennas. Spatial symbol $\mathbf{e}_i$ is a $N_t \times 1$ vector with N_a ones (representing the active TX antennas) and $N_t - N_a$ zeros (representing the inactive TX antennas), and $i = 1, \cdots, N_c$ is the spatial symbol index. Each spatial symbols specifies a unique TX antenna activation pattern.

---

[1]We do not restrict N_c to be a power of 2. We assume to use all the TX antenna activation patterns, which can be realized by using the so-called fractional bit modulation method in [31] or by using the approach in [32].

The indices of the active TX antennas for the i-th TX antenna activation pattern are denoted by the set Ω_i. Finally, $\mathbf{n} \in \mathbb{C}^{N_r \times 1}$ is the noise vector whose distribution is $\mathcal{CN}(\mathbf{0}, N_0\mathbf{I})$, where N_0 denotes the noise variance and $\mathbf{I}$ is the identity matrix.

Since the data bits are encoded in both the IQ and spatial domains, the total number of GSM symbols is equal to $N_{\mathrm{GSM}} = N_c M$. As result, $\log_2 N_{\mathrm{GSM}} = \log_2(N_c M)$ bpcu are transmitted.

A. Cut-off Rate

Based on the definition in [4], the cut-off rate of GSM systems can be formulated, by assuming equiprobable GSM symbols, as follows:

$$R_0 = -\log_2 \left[(1/N_{\mathrm{GSM}}^2) \int_{\mathbf{y}} \sum_{i,j,m,n} \sqrt{p(\mathbf{y}|s_m, \mathbf{e}_i) p(\mathbf{y}|s_n, \mathbf{e}_j)} \mathrm{d}\mathbf{y} \right] \tag{2}$$

for $i, j = 1, \cdots, N_c$ and $m, n = 1, \cdots, M$, and the conditional probability density function of the received data can be written as follows:

$$p(\mathbf{y}|s_m, \mathbf{e}_i) = (\pi N_0)^{-N_r} \exp \left(-\left\| \mathbf{y} - \mathbf{H}\mathbf{e}_i s_m / \sqrt{N_a} \right\|^2 / N_0 \right). \tag{3}$$

By inserting (3) in (2) and with the aid of some algebraic manipulations, the cut-off rate can be written as follows:

$$R_0 = -\log_2 \left[(1/N_{\mathrm{GSM}}^2) \sum_{i,j,m,n} \exp \left(-\Phi_{m,n,i,j}/(4N_0) \right) \right], \tag{4}$$

where the Euclidean distance between two GSM symbols at the RX is equal to:

$$\Phi_{m,n,i,j} = \left\| \mathbf{H} \left(\mathbf{e}_i s_m - \mathbf{e}_j s_n \right) \right\|^2 / N_a. \tag{5}$$

It is worth mentioning that the cut-off rate in (2) is computed by assuming that the GSM symbols are equally probable. This assumption is made because this is the typical operating scenario of communication systems. Since the definition of cut-off rate in (4) requires CSIT, the performance may be further improved by optimizing the probability of emitting GSM symbols as a function of the CSIT [4]. This is an interesting generalization of the study reported in the presented paper. Due to space limitations, however, it is postponed to future research. In the present paper, we are interested in focusing our attention to the sole impact of TX precoding.

III. Proposed Precoding Schemes

In this section, we introduce different precoding schemes that are capable of improving the cut-off rate of GSM systems. The first precoding scheme is based on grouping TX antennas that have the smallest Euclidean distance between them. The grouped TX antennas are activated simultaneously for data transmission. The second and third precoding schemes first apply SVD and SVD-DFT pre-processing, respectively, and then select a sub-set of active inputs. The fourth and last precoding scheme is based on minimizing, for each TX antenna activation pattern, the Euclidean distance between GSM symbols at the RX.

A. TX Antenna Grouping Precoding

From the direct inspection of (4), we note that the cut-off rate depends on the Euclidean distances (5). More specifically, the smallest Euclidean distances constitute the dominant terms. Accordingly, the first precoding scheme is based on optimizing the cut-off rate by grouping the TX antennas whose channel impulse responses have the smallest Euclidean distance. The grouped TX antennas are activated simultaneously, and, thus, they can be viewed as a virtual TX antenna whose impulse response is the normalized sum of the channel impulse responses of the physical TX antennas, i.e., $\mathbf{H}$. Accordingly, the RX signal after applying the proposed TX antenna grouping algorithm can be formulated as follows:

$$\mathbf{y} = \mathbf{H}_g \hat{\mathbf{e}}_i s_m / \sqrt{N_a} + \mathbf{n}, \tag{6}$$

where $\mathbf{H}_g \in \mathbb{C}^{N_r \times N_{va}}$ is the equivalent channel matrix after the TX antenna grouping and N_{vt} is the number of virtual TX antennas with $N_{vt} \leq N_t$. Spatial symbol $\hat{\mathbf{e}}_i$ is a $N_{vt} \times 1$ vector with N_a ones (representing the active virtual TX antennas) and $N_{vt} - N_a$ zeros (representing the inactive virtual TX antennas), and $i = 1, \cdots, \binom{N_{vt}}{N_a}$ is the index of the active spatial symbol.

In general, a virtual TX antenna is made of the scaled summation of one or more physical TX antennas. An example of TX antenna grouping is provided as follows.

Example 1. Let us consider a GSM system with $N_t = 8$ physical TX antennas and let the grouping set be $\omega = \{\{1,3\}, 2, \{4,5,7\}, \{6,8\}\}$. Thus, the matrix $\mathbf{H}_g$ consists of $N_{vt} = 4$ columns as follows: $\mathbf{h}_{g1} = (\mathbf{h}_1 + \mathbf{h}_3)/\sqrt{2}$, $\mathbf{h}_{g2} = \mathbf{h}_2$, $\mathbf{h}_{g3} = (\mathbf{h}_4 + \mathbf{h}_5 + \mathbf{h}_7)/\sqrt{3}$ and $\mathbf{h}_{g4} = (\mathbf{h}_6 + \mathbf{h}_8)/\sqrt{2}$. We assume that the transmit power is uniformly distributed among the TX antenna groups and equally allocated within each group.

Algorithm 1 TX Antenna Grouping Precoding

1: $R_{old} = \inf$
2: $R_{new} = \inf$
3: $N_{vt} = N_t$
4: $\omega = 1 : N_t$
5: $\mathbf{H}_g = \mathbf{H}$
6: **while** $(R_{new} <= R_{old})$ & $(N_{vt} >= N_a)$ **do**
7:     $R_{old} = R_{new}$
8:     $R_{new} = \text{cutoffarg}(\mathbf{H}_g)$
9:     **if** $N_{vt} > N_a$ **then**
10:        $(\hat{i}, \hat{j}) = \underset{i,j=1,\ldots,N_{vt}}{\arg\min} \left\| \mathbf{h}_{g,i} - \mathbf{h}_{g,j} \right\|^2$
11:        $[\mathbf{H}_g, \omega] = \text{grouping}(\mathbf{H}, \omega, \hat{i}, \hat{j})$
12:     **end if**
13:     $N_{vt} = N_{vt} - 1$
14: **end while**
15: $R_0 = -\log_2(\min(R_{old}, R_{new}))$

The precoding scheme based on TX antenna grouping is detailed in Algorithm 1. We note that the argument inside the logarithm function of (4) is minimized in order to maximize the cut-off rate R_0. As a starting point, N_{vt} is set equal to N_t and ω is initialized to the N_t physical antennas. In the subsequent steps, the TX antennas are grouped iteratively and the argument of the logarithm function in (4) is obtained. These steps are repeated as long as the logarithm function is decreasing ($R_{new} \leq R_{old}$) and the number of virtual TX antennas N_{vt} is greater than or equal to N_a. In particular, the argument of the logarithm function in (4) for a given channel matrix $\mathbf{H}_g$ is computed as follows (line 8 of Algorithm 1):

$$R_{new} = \left(\binom{N_{vt}}{N_a} M \right)^{-2} \sum_{i,j,m,n} \exp\left[-\left\| \mathbf{H}_g \left(\hat{\mathbf{e}}_i s_m - \hat{\mathbf{e}}_j s_n \right) \right\|^2 / (4N_0 N_a) \right],$$

where $i, j = 1, \ldots, \binom{N_{vt}}{N_a}$ and $m, n = 1, \ldots, M$. Then, we identify the indices of the virtual TX antennas that have the smallest Euclidean distance between their impulse responses and group them together. These steps are reported in lines 10 and 11 of Algorithm 1, which are executed only if $N_{vt} > N_a$ in order to avoid antenna groupings with $N_{vt} < N_a$. At each iteration, the number of virtual TX antennas N_{vt} is decreased by one. Finally, the cut-off rate is computed[2].

---

[2]It should be noticed that R_{new} determines the cut-off rate R_0 only when $R_{new} < R_{old}$ and R_{new} is computed in the case $N_{vt} = N_a$. In all other situations R_{old} determines R_0.

B. SVD-Based Precoding With Input Selection

The second precoding scheme is based on SVD pre-processing at the TX. SVD precoding is often used in multi-stream SMX-MIMO systems, and, therefore, it constitutes an attractive solution for communication devices that incorporate SMX and GSM operation modes and that use them based on the required rate and performance.

By applying SVD decomposition to the channel matrix $\mathbf{H}$, we obtain $\mathbf{H} = \mathbf{U}\mathbf{\Lambda}\mathbf{V}^{\mathrm{H}}$, where $\mathbf{U}$ and $\mathbf{V}$ are unitary matrices and $\mathbf{\Lambda}$ is a diagonal matrix whose singular values are, assuming $N_t \leq N_r$, $\lambda_1, \ldots, \lambda_{N_t}$. By using the matrix $\mathbf{V}$ as the precoding matrix, the RX signal vector can be written as follows:

$$\mathbf{y} = \mathbf{H}\mathbf{V}\mathbf{e}_i s_m / \sqrt{N_a} + \mathbf{n} = \mathbf{U}\mathbf{\Lambda}\mathbf{e}_i s_m / \sqrt{N_a} + \mathbf{n} = \mathbf{G}\mathbf{e}_i s_m / \sqrt{N_a} + \mathbf{n}. \qquad (7)$$

The equivalent channel matrix (i.e., the product of channel and precoding matrices) is denoted by $\mathbf{G}$ and it is a column orthogonal matrix. More precisely, the transmission system in (7) consists of N_t orthogonal sub-channels that correspond to the inputs of $\mathbf{G}$. If $N_a = 1$, in particular, the Euclidean distance between two GSM symbols is as follows:

$$\Phi_{m,i,i,j} = \left\| \mathbf{G}(\mathbf{e}_i s_m - \mathbf{e}_j s_n) \right\|^2 = \left\| \mathbf{g}_i s_m - \mathbf{g}_j s_n \right\|^2 = \lambda_i^2 \left| s_m \right|^2 + \lambda_j^2 \left| s_n \right|^2, \qquad (8)$$

where $\mathbf{g}_i$ and $\mathbf{g}_j$ are the i-th and j-th column of $\mathbf{G}$. Equation (8) is useful for understanding why the grouping strategy employed in Section III-A is not effective in this case. Assume, e.g., that two arbitrary columns, N_1 and N_2 with $1 \leq N_1 < N_2 \leq N_t$, of $\mathbf{G}$ are grouped together. The resulting impulse response would be equal to $(\mathbf{g}_{N_1} + \mathbf{g}_{N_2})/\sqrt{2}$ and the following would hold:

$$\left\| \mathbf{g}_{N_1} + \mathbf{g}_{N_2} \right\|^2 / 2 = \left(\lambda_{N_1}^2 + \lambda_{N_2}^2 \right) / 2 \leq \lambda_{N_1}^2 = \left\| \mathbf{g}_{N_1} \right\|^2. \qquad (9)$$

In other words, the power gain without grouping is larger than the power gain with grouping. From the direct inspection of (8) and (9), we note, in addition, that by grouping the columns of $\mathbf{G}$ we obtain an Euclidean distance between two GSM symbols that is smaller than that corresponding to the larger singular value of $\mathbf{G}$. Based on this example, we evince that antenna grouping is not a suitable approach based on (7). A better strategy is, in fact, to select only a subset of active columns of $\mathbf{G}$ rather than grouping them. The column orthogonality property of $\mathbf{G}$ facilitates this task. Based on (9), in fact, the columns with the largest norm can be selected to optimize the cut-off rate. This implies that the cut-off rate can be maximized by selecting the

Algorithm 2 SVD Precoding With Input Selection

1: $R_{old} = \inf$
2: $R_{new} = \inf$
3: $N_e = N_a$
4: $\mathbf{G} = \mathbf{HV}$
5: **while** $(R_{new} <= R_{old})$ & $(N_e <= N_t)$ **do**
6:     $R_{old} = R_{new}$
7:     $\mathbf{G}_e = \mathbf{G}(:, 1 : N_e)$
8:     $R_{new} = \text{cutoffarg}(\mathbf{G}_e)$
9:     $N_e = N_e + 1$
10: **end while**
11: $R_0 = -\log_2(\min(R_{old}, R_{new}))$
---

largest singular values of the channel matrix $\mathbf{H}$. By assuming, without loss of generality, that the singular values are sorted in descending order, the first N_e ($N_a \leq N_e \leq N_t$) columns of $\mathbf{G}$ need to be selected. Under these assumptions, the RX signal vector in (7) can be re-written as:

$$\mathbf{y} = \mathbf{G}_e \bar{\mathbf{e}}_i s_m / \sqrt{N_a} + \mathbf{n}, \tag{10}$$

where $\mathbf{G}_e \in \mathbb{C}^{N_r \times N_e}$ consists of the first N_e columns of $\mathbf{G}$ and $\bar{\mathbf{e}}_i$ is a spatial symbol, i.e., a $N_e \times 1$ vector with N_a ones (representing the active columns of $\mathbf{G}_e$) and $N_e - N_a$ zeros (representing the inactive column of $\mathbf{G}_e$), where $i = 1, \ldots, \binom{N_e}{N_a}$ is the index of the active spatial symbol.

The details of the proposed precoding scheme are reported in Algorithm 2. Similar to Algorithm 1, we aim to minimize the argument of the logarithm function of the cut-off rate. The difference between Algorithm 2 and Algorithm 1 is that, at each iteration, the subset of active columns of $\mathbf{G}$ is increased rather than decreased. The initialization of Algorithm 2 is similar to that of Algorithm 1. In particular, N_e is set equal to N_a because we have to activate at least N_a columns of $\mathbf{G}$. In the next few steps, we iteratively increase the set of active columns of $\mathbf{G}$ until the argument of the logarithm function of the cut-off rate decreases. The argument of the logarithm function of the cut-off rate is calculated in line 8 of Algorithm 2 as follows:

$$R_{new} = \left(\binom{N_e}{N_a}M\right)^{-2} \sum_{i,j,m,n} \exp\left[-\left\|\mathbf{G}_e\left(\bar{\mathbf{e}}_i s_m - \bar{\mathbf{e}}_j s_n\right)\right\|^2 / (4N_0 N_a)\right],$$

where $i, j = 1, \ldots, \binom{N_e}{N_a}$ and $m, n = 1, \ldots, M$. It is worth nothing that the computational complexity of this step can be significantly reduced. At each iteration, in fact, we need to

calculate only the Euclidean distances that are determined by the N_e-th column of $\mathbf{G}$ because all the other Euclidean distances have been pre-computed at the previous iterations

C. SVD-DFT Precoding With Input Selection

Based on the previous section, we evince that SVD precoding applied to GSM systems, similar to SMX systems [14], transforms the channel matrix into a set of orthogonal sub-channels. From [14], [33], it is known that SMX systems that employ SVD precoding achieve the largest channel capacity if the water-filling power allocation strategy is utilized, i.e., the highest power is allocated to the sub-channels that correspond to the largest singular values of the channel matrix. In [34], the authors have proposed a precoding scheme aiming to improve the error performance of SMX systems, which transforms a SMX system that consists of orthogonal sub-channels with unequal allocated power into a SMX system that consists of non-orthogonal sub-channels with equal power allocation. This is obtained by applying a DFT precoding matrix. In this paper, we are not interested in power allocation, as this is left to future research work. We, however, introduce and optimize, from the cut-off rate point of view, a precoding scheme that takes inspiration from the SVD-DFT precoding introduced in [34]. The proposed precoding scheme is depicted in Fig. 1. The main difference between the SVD-DFT precoding scheme in Fig. 1 and the precoding scheme in [34] is the size of DFT precoding matrix. In [34], the authors have used a DFT precoding matrix with fixed size equal to $N_t \times N_t$. In Fig. 1, on the other hand, we use a DFT precoding matrix whose size is variable and is equal to $N_e \times N_e$, where N_e is the number of active inputs that is not is fixed but changes similar to the SVD precoding matrix of the previous section. Another difference compared with [34] lies in considering a GSM system and, thus, transmitting a single IQ stream but encoding some information bits into the columns of the TX matrix. In the following text, first we introduce the SVD-DFT precoding scheme for application to GSM systems and then we compare the minimum Euclidean distance of SVD and SVD-DFT precoding schemes.

1) SVD-DFT Precoding: Based on Fig. 1, the RX signal of a GSM system with SVD-DFT precoding can be formulated as follows:

$$\mathbf{y} = \mathbf{G}_e \mathbf{W}_{N_e} \bar{\mathbf{e}}_i s_m / \sqrt{N_a} + \mathbf{n} = \mathbf{F}\bar{\mathbf{e}}_i s_m / \sqrt{N_a} + \mathbf{n}. \tag{11}$$
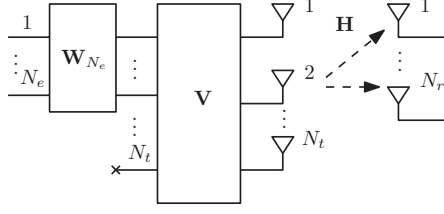
Fig. 1. Block diagram of GSM with SVD-DFT precoding with the DFT matrix $\mathbf{W}_{N_e}$ and the matrix $\mathbf{V}$ from the SVD of the channel matrix $\mathbf{H}$. By removing the precoding matrix $\mathbf{W}_{N_e}$ we get a block diagram of GSM with SVD precoding.

which is obtained from (7) by multiplying the precoding matrix $\mathbf{V}$ by the DFT matrix whose elements are $\mathbf{W}_{N_e}(i,j) = (1/\sqrt{N_e}) \exp\left(-\mathbf{j}2\pi(i-1)(j-1)/N_e\right)$ and the matrix $\mathbf{F}$ is given as:

$$\mathbf{F} = \mathbf{G}_e \mathbf{W}_{N_e} = \mathbf{G}(:, 1:N_e)\mathbf{W}_{N_e}. \tag{12}$$

The scaling factor $1/\sqrt{N_e}$ ensures that the average signal power remains constant, i.e., $\mathrm{Tr}(\mathbf{W}_{N_e}\mathbf{W}_{N_e}^{\mathrm{H}}) = N_e$. The algorithm for maximizing the cut-off rate is the same as Algorithm 2. The only difference is that, at each iteration of the algorithm, the matrix $\mathbf{G}_e$ is replaced by the matrix $\mathbf{F}$.

2) Performance Comparison of SVD Precoding and SVD-DFT Precoding: In order to get insight into the achievable cut-off rate of SVD and SVD-DFT precoding schemes, we study and compare the minimum Euclidean distance of the GSM symbols at the RX when the two precoding schemes are used. Since in GSM systems the data is encoded into both the IQ and spatial domains, the computation of the minimum Euclidean distance is more challenging than for SMX systems [34]. To make the mathematical development tractable, therefore, we restrict our analysis to SM systems, i.e., we assume $N_a = 1$. The main result is reported in Theorem 2. However, we first introduce some intermediate results that are useful for the proof of the main theorem. Also, with the exception of Lemma 2 that is similar to [34, Lemma 2], all the other results are new and, to the best of our knowledge, have never been published.

Theorem 1. *For SM system with SVD precoding and M-QAM modulation ($M \geq 4$), the minimum Euclidean distance between two SM symbols at the RX is:*

$$\Phi_{\mathrm{min}} = 2\lambda_{N_e}^2 \mathrm{r}_{\mathrm{min}}^2, \tag{13}$$

where $\mathrm{r}_{\mathrm{min}} = \min_m |s_m|$.

Proof: If two SM symbols differ by the transmitted IQ symbol but activate the same TX

antenna ($m \neq n, i = j$), the Euclidean distance between them is:

$$\Phi_{m,n,i,j} = \left\| \mathbf{G}_e(:, i)\, (s_m - s_n) \right\|^2 = \left\| \mathbf{G}_e(:, i) \right\|^2 |s_m - s_n|^2 \geq \lambda_{N_e}^2 \mathrm{d}_{\min}^2 \tag{14}$$

where $\mathrm{d}_{\min} = \min_{m,n(m \neq n)} |s_m - s_n|$. If two SM symbols differ by the active TX antenna ($i \neq j$), the Euclidean distance between them is:

$$\Phi_{m,n,i,j} = \left\| \mathbf{G}_e(:, i)s_m - \mathbf{G}_e(:, j)s_n \right\|^2 = \left\| \mathbf{G}_e(:, i)s_m \right\|^2 + \left\| \mathbf{G}_e(:, j)s_n \right\|^2 \geq \left(\lambda_{N_e-1}^2 + \lambda_{N_e}^2 \right) \mathrm{r}_{\min}^2. \tag{15}$$

where the last inequality holds for $m \neq n$ and $m = n$, provided that $|s_m| = |s_n| = \mathrm{r}_{\min}$. Since $\mathrm{d}_{\min}^2 = 2\mathrm{r}_{\min}^2$ for M-QAM constellations if $M \geq 4$ and the inequality $\lambda_{N_e-1}^2 + \lambda_{N_e}^2 \geq 2\lambda_{N_e}^2$, the minimum Euclidean distance between two different SM symbols at the RX is given by (13). ■

Lemma 1. *The inner-product of the columns of the matrix* $\mathbf{F}$ *is given by:*

$$\langle \mathbf{f}_i, \mathbf{f}_j \rangle = (1/N_e) \sum_{m=1}^{N_e} \lambda_m^2 \exp \left(\mathbf{j} 2\pi (m-1)(i-j)/N_e \right). \tag{16}$$

Proof: The i-th column of $\mathbf{F}$ is $\mathbf{f}_i = \mathbf{G}_e \mathbf{W}_{N_e}(:, i)$. So, we obtain:

$$\langle \mathbf{f}_i, \mathbf{f}_j \rangle = \frac{\mathbf{W}_{N_e}^{\mathrm{H}}(:, i) \mathbf{G}_e^{\mathrm{H}} \mathbf{G}_e \mathbf{W}_{N_e}(:, j)}{N_e} = \frac{1}{N_e} \sum_{m=1}^{N_e} \lambda_m^2 e^{\mathbf{j}\frac{2\pi(m-1)(i-1)}{N_e}} e^{-\mathbf{j}\frac{2\pi(m-1)(j-1)}{N_e}} = \frac{1}{N_e} \sum_{m=1}^{N_e} \lambda_m^2 e^{\mathbf{j}\frac{2\pi(m-1)(i-j)}{N_e}}$$

from which the proof follows. ■

Lemma 2. *All the columns of matrix* $\mathbf{F}$ *have the same norm, which is equal to:*

$$\|\mathbf{f}_i\|^2 = \frac{1}{N_e} \sum_{m=1}^{N_e} \lambda_m^2, \quad i = 1, \ldots, N_e. \tag{17}$$

Proof: If follows directly from Lemma 1. ■

Lemma 3. *Let* $N > 1$ *be a positive integer number and* $k \in \{\pm 1, \pm 2, \ldots, \pm(N-1)\}$. *The following equation holds true:*

$$\sum_{m=1}^{N} \cos \left(2\pi(m-1)k/N \right) = 0. \tag{18}$$

Proof: It is known that, except for the first row and column, the sum of the elements of

each row and column of a DFT matrix is equal to zero. Therefore, we have:

$$\sum_{m=1}^{N} \exp\left(\mathbf{j}2\pi(m-1)k/N\right) = 0, \tag{19}$$

where k takes any value in the set $\{-1, -2, \cdots, -(N-1)\}$. Accordingly, the real part of (19) must be equal to zero and (18) holds true for $k < 0$. Since the cosine is an even function, (18) is valid for $k > 0$ as well. ∎

Theorem 2. *For SVD-DFT precoding assisted SM system that employs M-QAM modulation in the IQ domain, and has parameters $M \geq 4$ and $N_e > 1$, the minimum Euclidean distance is greater than the $\Phi_{\min}$ given in (13).*

Proof: To simplify the writing, we define $\mathrm{d}_{\min} = \min_{m,n(m\neq n)} |s_m - s_n|$ and $\mathrm{r}_{\min} = \min_m |s_m|$, similar to Theorem 1. Three cases are analyzed separately.

Case 1. Assume that two SM symbols have different IQ constellation points but the activated antenna is the same. The minimum Euclidean distance between the corresponding two SM symbols at the RX is the following:

$$\Phi_{m,n,i,j} = \left\| \mathbf{f}_i \left(s_m - s_n\right) \right\|^2 = \|\mathbf{f}_i\|^2 |s_m - s_n|^2 \geq \sum_{k=1}^{N_e} \lambda_k^2 \mathrm{d}_{\min}^2 / N_e = 2 \sum_{k=1}^{N_e} \lambda_k^2 \mathrm{r}_{\min}^2 / N_e. \tag{20}$$

From (13) and taking into account that:

$$2 \sum_{k=1}^{N_e} \lambda_k^2 \mathrm{r}_{\min}^2 / N_e \geq 2\lambda_{N_e}^2 \mathrm{r}_{\min}^2, \tag{21}$$

we conclude that the minimum Euclidean distance of a SM system with SVD-DFT precoding is greater than its counterpart with SVD precoding.

Case 2. Assume that two SM symbols activate different TX antenna, but transmit the same IQ constellation point. The minimum Euclidean distance between the corresponding two SM symbols at the RX is the following:

$$\Phi_{m,n,i,j} = \left\| (\mathbf{f}_i - \mathbf{f}_j)s_n \right\|^2 = \left[\|\mathbf{f}_i\|^2 + \|\mathbf{f}_j\|^2 - 2\Re\left\{\mathbf{f}_i^{\mathrm{H}}\mathbf{f}_j\right\} \right] |s_n|^2 =$$
$$\geq 2\frac{\mathrm{r}_{\min}^2}{N_e} \sum_{k=1}^{N_e} \lambda_k^2 \left[1 - \cos\left(2\pi(k-1)(i-j)/N_e\right) \right]. \tag{22}$$

In (22), $i - j$ can take all possible values lying in the interval $[-N_e + 1, N_e - 1]$ except the zero value. In general, it is not easy to determine the value of $i - j$ that yields the minimum

of (22). Therefore, we need to prove that (22) is greater than the minimum Euclidean distance from (13), i.e., $2\lambda_{N_e}^2 r_{\min}^2$, for all possible values of $i - j$. In other words, we need to prove the following inequality:

$$\frac{1}{N_e} \sum_{k=1}^{N_e} \lambda_k^2 \left[1 - \cos \left(2\pi(k-1)(i-j)/N_e \right) \right] \geq \lambda_{N_e}^2. \tag{23}$$

With the aid of Lemma 3, we obtain:

$$N_e \lambda_{N_e}^2 = \sum_{k=1}^{N_e} \lambda_{N_e}^2 \left[1 - \cos \left(2\pi(k-1)(i-j)/N_e \right) \right]. \tag{24}$$

By plugging (24) in (23), we obtain:

$$2 \sum_{k=1}^{N_e} \left(\lambda_k^2 - \lambda_{N_e}^2 \right) \sin^2 \left(\pi(k-1)(i-j)/N_e \right) \geq 0. \tag{25}$$

The inequality in (25) implies that SVD-DFT precoding provides a larger minimum Euclidean distance than SVD precoding.

Case 3. Assume that two SM symbols have different IQ constellation points and that the activated TX antennas are different as well. The minimum Euclidean distance between the corresponding two SM symbols at the RX is the following:

$$\Phi_{m,n,i,j} = \left\| \mathbf{f}_i s_m - \mathbf{f}_j s_n \right\|^2 = \|\mathbf{f}_i\|^2 |s_m|^2 + \left\| \mathbf{f}_j \right\|^2 |s_n|^2 - 2\Re \left\{ \mathbf{f}_i^{\mathrm{H}} \mathbf{f}_j s_m^* s_n \right\} =$$

$$= \frac{1}{N_e} \sum_{k=1}^{N_e} \lambda_k^2 \left[r_m^2 + r_n^2 - 2 r_m r_n \cos \left(\varphi_{mn} + 2\pi(k-1)(i-j)/N_e \right) \right] \tag{26}$$

where $r_m = |s_m|$, $r_n = |s_n|$ and $s_m^* s_n = r_m r_n \exp(\mathbf{j}\varphi_{mn})$. In this case, the comparison of the minimum Euclidean distances is intractable. Thus, we restrict the analysis to the case study $r_m = r_n = r_{\min}$, which ensures to consider the minimum of the first two terms in (26). By applying a procedure similar to that utilized for computing (22)–(24), we obtain:

$$2 \sum_{k=1}^{N_e} \left(\lambda_k^2 - \lambda_{N_e}^2 \right) \sin^2 \left(\varphi_{mn}/2 + \pi(k-1)(i-j)/N_e \right) \geq 0 \tag{27}$$

which implies that, at least for $r_m = r_n = r_{\min}$, SVD-DFT precoding is capable of increasing the minimum Euclidean distance compared with SVD precoding. ∎

By comparing (21), (25) with (27), we evince that SVD-DFT precoding is not capable of increasing the minimum Euclidean distance if $\lambda_1 = \lambda_2 = \ldots = \lambda_{N_e}$ holds true. This scenario, however, is unlikely to occur. In the worst case that it occurs, the precoding schemes would offer

the same minimum Euclidean distance. Therefore, we conclude that SM systems with SVD-DFT precoding are expected to have a larger minimum Euclidean distance between different RX symbols, which, in turns, results into a better cut-off rate compacted with SM systems that employ SVD precoding. The numerical results in Section V confirm this finding.

D. DFT Precoding

In this section, we consider a precoding scheme that aims to improve the cut-off rate of SM/GSM systems by selecting, for each possible TX antenna pattern, the precoding vector that provides the largest minimum Euclidean distance between the SM/GSM symbols at the RX [35]. The precoding vector is selected among a given set of candidate precoding vectors. Identifying this set is, however, a difficult and open issue. In the present paper, the set of candidate precoding vectors is obtained from the columns of the DFT matrix introduced in the previous section. For this reason, the scheme proposed in this section is referred to as DFT precoding. The GSM signal vector at the RX can be formulated as follows:

$$\mathbf{y} = \mathbf{H}\tilde{\mathbf{P}}\tilde{\mathbf{e}}_i s_m / \sqrt{N_a} + \mathbf{n}, \tag{28}$$

where $\tilde{\mathbf{P}} \in \mathbb{C}^{N_t \times N_c}$ is the precoding matrix and each column of $\tilde{\mathbf{P}}$ contains N_a non-zero elements and $N_t - N_a$ zero elements. The positions of the non-zero elements correspond to the indices of the active TX antennas of the i-th TX antenna activation pattern. $\tilde{\mathbf{e}}_i$ is a spatial symbol, i.e., a $N_c \times 1$ vector with a single one and $N_c - 1$ zero elements, and $i = 1, \ldots, N_c$ is the spatial symbol index that specifies the activated TX antenna pattern.

The details of the proposed DFT precoding scheme for GSM systems are reported in Algorithm 3. First, we generate a $N_t \times N_t$ DFT matrix $\mathbf{W}$ whose elements are: $\mathbf{W}(i,j) = \exp\left(-\mathbf{j}2\pi(i-1)(j-1)/N_t\right)$. Then, from $\mathbf{W}$, we construct the precoding candidate matrix $\mathbf{T} \in \mathbb{C}^{N_t \times N_t}$, which contains the set of candidate precoding vectors for a single TX antenna pattern. As far as the i-th ($i = 1, \ldots, N_c$) TX antenna activation pattern is concerned, the matrix $\mathbf{T}$ is constructed by taking the rows of $\mathbf{W}$ whose indices are determined by the elements of Ω_i, i.e., the indices of the active TX antennas (see Section II). All the other rows of $\mathbf{T}$, whose indices are different from the elements of Ω_i, contain only zero values. Therefore, each column $\mathbf{t}_k$ ($k = 1, \ldots, N_t$) of $\mathbf{T}$ provides the candidate precoding vectors and has N_a non-zero elements at the positions that correspond to the indices of the active TX antennas of the i-th TX antenna pattern. Subsequently, we construct N_t $\tilde{\mathbf{P}}_k$ matrices ($k = 1, \ldots, N_t$). Each $\tilde{\mathbf{P}}_k$ matrix is

---

Algorithm 3 DFT Precoding

1: $\mathbf{W} = N_t \times N_t$ DFT matrix
2: $\tilde{\mathbf{P}} = [\ ]$
3: **for** $i = 1 \to N_c$ **do**
4:     $\mathbf{T} = \mathbf{W}.*\mathrm{repmat}(\mathbf{e}_i, 1, N_t)$
5:     **for** $k = 1 \to N_t$ **do**
6:         $\tilde{\mathbf{P}}_k = [\tilde{\mathbf{P}}; \mathbf{t}_k]$
7:     **end for**
8:     $\hat{k} = \underset{k=1,\ldots,N_t}{\arg\max} \ \underset{\substack{(m,l)\neq(n,i) \\ m,n=1,\ldots,M \\ l=1,\ldots,i}}{\min} \ \tilde{\Phi}'(n,l,m,k)$
9:     $\tilde{\mathbf{P}} = \tilde{\mathbf{P}}_{\hat{k}}$
10: **end for**
11: $R_0 = \mathrm{cutoff}(\mathbf{H}, \tilde{\mathbf{P}})$

---

obtained by adding the k-th column ($k = 1, \ldots, N_t$) of $\mathbf{T}$ to the matrix $\tilde{\mathbf{P}}$ that is obtained at the previous iteration. Finally, we select, among all the $\tilde{\mathbf{P}}_k$ matrices, the matrix with the largest minimum Euclidean distance. Due to the constant increase of the number of columns of $\tilde{\mathbf{P}}$, the Euclidean distances are calculated as follows: $\tilde{\Phi}'(n,l,m,k) = \left\| \mathbf{H}\left(\tilde{\mathbf{P}}_k(:,i)s_n - \tilde{\mathbf{P}}_k(:,l)s_m \right) \right\|^2$. Thus, at each iteration we need to calculate only the Euclidean distances that are affected by the candidate precoding vector $\mathbf{t}_k$. This procedure is repeated for each TX antenna activation pattern. After determining the precoding matrix $\tilde{\mathbf{P}}$, the cut-off rate is calculated as follows:

$$R_0 = 2\log_2(MN_c) - \log_2\left[\sum_{i,j,m,n} \exp\left(-\left\| \mathbf{H}\tilde{\mathbf{P}}\left(\tilde{\mathbf{e}}_i s_m - \tilde{\mathbf{e}}_j s_n \right) \right\|^2 / (4N_0 N_a) \right) \right], \quad (29)$$

where $i,j = 1, \cdots, N_c$ and $m,n = 1, \cdots, M$. In contrast to the other proposed precoding schemes, DFT precoding keeps the same number of GSM symbols and data rate as the original GSM system without precoding. Algorithm 3 provides the appropriate precoding vector for each TX antenna activation pattern and, therefore, it does not reduce the number of GSM symbols as the other precoding schemes. The consequences of this property are analyzed in Section IV.

IV. SIMULATION RESULTS

In this section, we evaluate the cut-off rate of the proposed precoding schemes with the aid of Monte Carlo simulations. The study is conducted for a typical indoor propagation channel. As a benchmark to quantify the gains of the proposed precoding schemes, a GSM system without precoding is considered [10], [12]. Besides the cut-off rate, we study the impact of the

precoding schemes on the mutual information of GSM systems, and show that to an improvement of the cut-off rate corresponds an improvement of the mutual information. Finally, we study the suitability of the proposed precoding schemes for application to SMX systems and demonstrate that optimizing the SEP, instead of the cut-off rate, usually results into a smaller improvement of the mutual information.

A. Cut-off Rate of SM/GSM

At low-GHz frequencies (i.e., below $6\,\mathrm{GHz}$), an indoor channel is usually modeled by using the Rician distribution [36] and the channel matrix can be written as $\mathbf{H} = \sqrt{K/(K+1)}\mathbf{H}_{\mathrm{LOS}} + \sqrt{1/(K+1)}\mathbf{H}_{\mathrm{NLOS}}$, where $\mathbf{H}_{\mathrm{LOS}}$ and $\mathbf{H}_{\mathrm{NLOS}}$ are the line-of-sight (LOS) and non-LOS (NLOS) channel matrices, respectively. The element of $\mathbf{H}_{\mathrm{LOS}}$ that corresponds to the normalized channel coefficient between the j-th TX antenna and the i-th RX antenna is given by the Friis formula:

$$\mathbf{H}_{\mathrm{LOS}}(i,j) \approx (D/d_{ij}) \exp\left(-\mathbf{j}2\pi d_{ij}/\lambda\right), \tag{30}$$

here λ is the wavelength, d_{ij} is the length of the LOS path between the antennas and D is the distance between the mid-points of the TX and RX uniform linear array (ULA). The inter-antenna separations of the TX and RX ULAs are assumed to be $\lambda/2$, so that the inter-antenna interference can be assumed to be negligible. The elements of $\mathbf{H}_{\mathrm{NLOS}}$ are distributed according to $\mathcal{CN}(0,1)$. The Rician factor K can take two values in our simulations: 0 and $+\infty$, which implies that either pure LOS channels or pure independent and identically distributed (i.i.d.) Rayleigh fading channels are considered. We use these two extreme channel models to shed light on the impact of LOS and NLOS channel components on the proposed precoding schemes.

A MIMO system with 8 TX and 8 RX antennas is considered. The operating frequency is $f = 5\,\mathrm{GHz}$, i.e. $\lambda = 6\,\mathrm{cm}$, and the inter-antenna separations of TX and RX ULAs, d_t and d_r, are both $3\,\mathrm{cm}$. The distance between the TX and RX ULA is $D = 10\,\mathrm{m}$. For a fair comparison among all the considered systems, we select the parameters N_a and M such that the same data rate of $8\,\mathrm{bpcu}$ is achieved.

1) Cut-Off Rate in i.i.d. Rayleigh Fading Channels: The cut-off rate of the different precoding schemes and of the benchmark GSM system are compared against each other in Fig. 2 by assuming an i.i.d. Rayleigh fading channel model. We observe that the SVD-DFT precoding scheme provides the best cut-off rate at a low-medium SNR. The SVD precoding scheme provides a slightly lower cut-off rate in the same SNR regime. In Fig. 2(b), for example, the SVD-DFT

(a) $N_a = 1$ and $M = 32$.

(b) $N_a = 2$ and $M = 8$.

(c) $N_a = 3$ and $M = 4$.
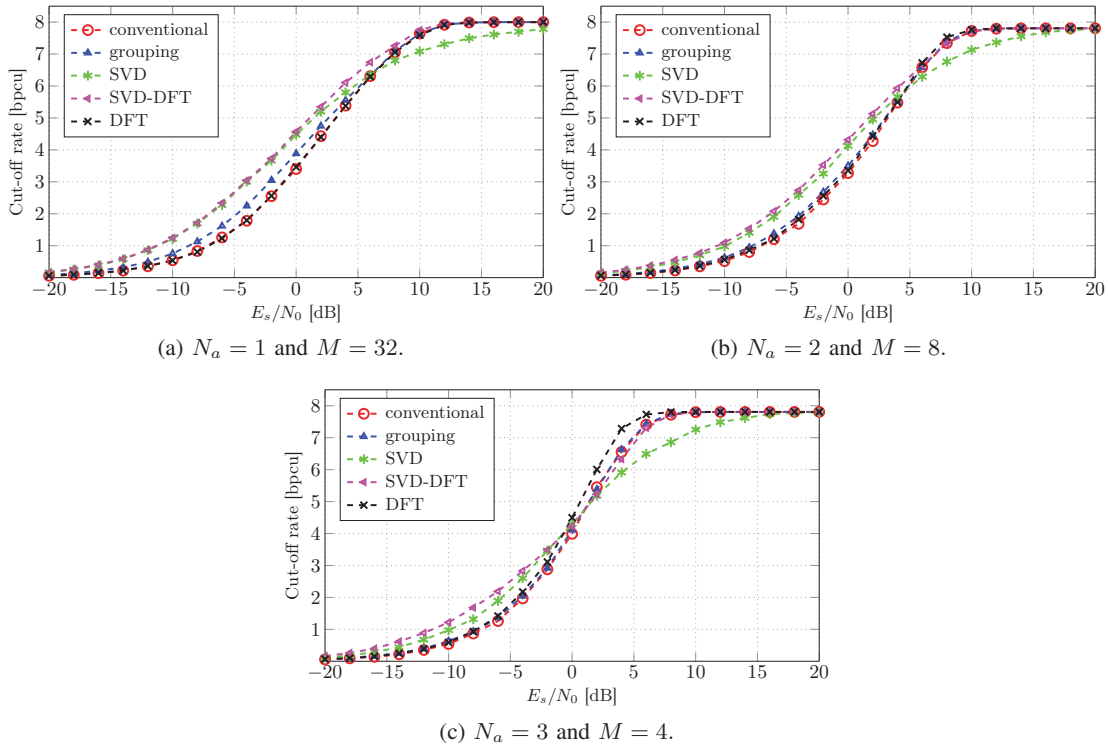
Fig. 2. Cut-off rate of conventional GSM and GSM with the proposed precoding schemes in an i.i.d. Rayleigh fading channel.

and SVD precoding schemes provide an improvement of the cut-off rate of about $1\,\mathrm{bpcu}$ for $\mathrm{SNR} = -4\,\mathrm{dB}$ compared with the benchmark without precoding. On the other hand, SVD precoding does not offer good performance in the medium SNR regime. The reason of this performance trend originates from the fact that the SVD precoding scheme does not activate the columns of the precoding matrix that provide the smallest Euclidean distance among the GSM symbols at the RX. More precisely, the total number of GSM symbols with SVD precoding is smaller than its counterpart that adopt other precoding schemes. As a result, GSM systems with SVD precoding provides worse performance than the benchmark and the other precoding schemes. In contrast to SVD and SVD-DFT precoding, the precoding scheme based on TX antenna grouping offers only a negligible cut-off rate improvement in the low-to-medium SNR regime. This performance trend is justified in Appendix A.

In general, TX antenna grouping, SVD and SVD-DFT precoding schemes transmit the TX signal from more than N_a physical antennas per symbol interval, with the aim of improving the cut-off rate by realizing a large array gain, which is especially important in the low SNR regime [10], [19]. Hence, in the very low SNR regime it may occur that SVD and SVD-DFT precoding schemes select only N_a active inputs, and that the TX antenna grouping scheme
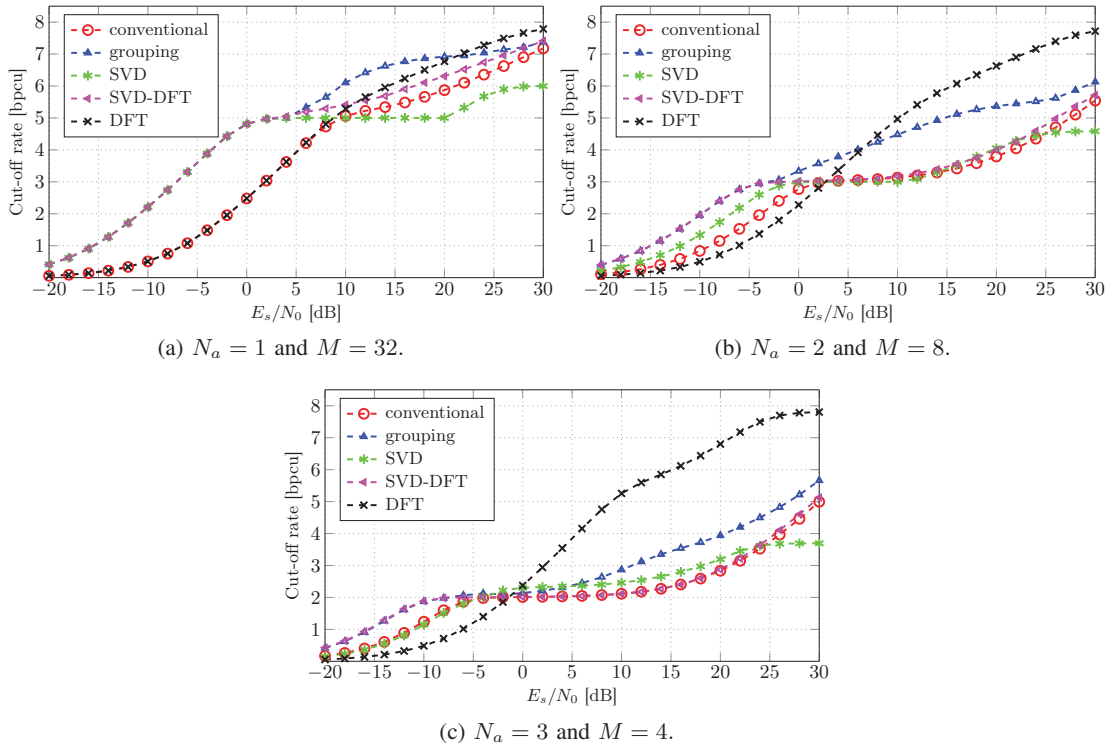
Fig. 3. Cut-off rate of conventional GSM and GSM with the proposed precoding schemes in a pure LOS channel.

has only N_a virtual TX antennas. This setup ensures, in fact, that the largest array gain is obtained but at the cost of having no signal transmission in the spatial domain. DFT precoding, on the other hand, is based on a fundamentally different operating principle. Its performance is predominately determined by the order of the IQ constellation, i.e., M. By using DFT precoding, the largest improvement of the cut-off rate is obtained by decreasing M. If high-order IQ modulation alphabets are used, in particular, the minimum Euclidean distance between different GSM symbols is determined by the minimum Euclidean distance of the IQ constellation. So, a large gain of the cut-off rate is usually not expected. If low-order modulation alphabets are utilized, on the other hand, the DFT precoding scheme is expected to provide a larger gain because it aims to maximize the minimum Euclidean distance between GSM symbols with different TX antenna activation patterns disregarding the array gain. Thus, it can not improve the cut-off rate at a low SNR and it is more suitable for environments with correlated channels. So, it can provide only a limited cut-off rate improvement in i.i.d. Rayleigh fading channels.

2) Cut-Off Rate in Pure LOS Channels: In Fig. 3, the cut-off rate of conventional GSM systems and of the proposed precoding schemes over a pure LOS channel is illustrated. In the low SNR regime, we observe that the cut-off rate of conventional GSM increases by increasing
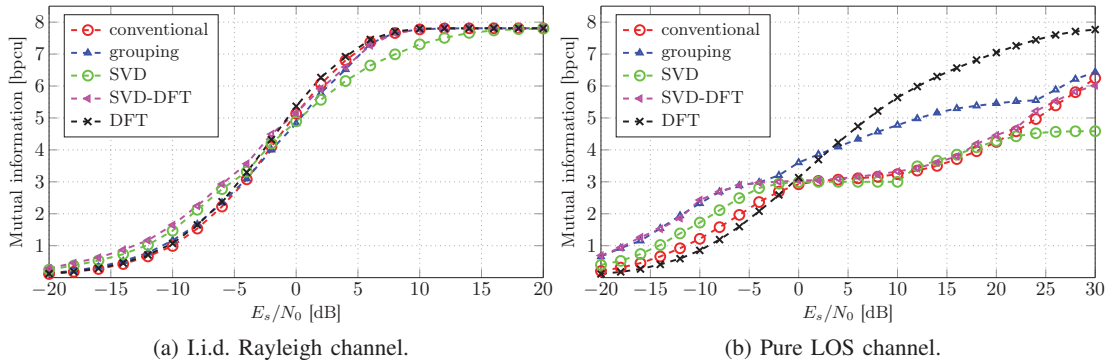
Fig. 4. Mutual information of conventional GSM systems and GSM systems with the proposed precoding schemes in an i.i.d. Rayleigh channel and a pure LOS channel. The setup of parameters is: $N_t = N_r = 8$, $N_a = 2$ and $M = 8$.

N_a. This is due to the fact that in correlated fading channels, e.g., in pure LOS channels, the activation of several TX antennas that emit the same IQ symbol increases the array gain, which in turn increases the cut-off rate. In the medium-high SNR regime, on the other hand, channel models with high spatial correlation cause a reduction of the cut-off rate of conventional GSM systems as a function of N_a. As far as the proposed precoding schemes are concerned, the following conclusions can be drawn. The precoding scheme based on TX antenna grouping offers a linear increase of the cut-off rate in the low SNR regime. In the same SNR regime, SVD and SVD-DFT precoding schemes operate with N_a active inputs and the TX antenna grouping precoding scheme has N_a virtual antennas. Therefore, no bits are encoded into the spatial domain in order to achieve the highest array gain. In the medium-high SNR regime, on the other hand, the TX antenna grouping precoding offers a larger cut-off rate increase than SVD and SVD-DFT precoding. It is worth noting that in the high SNR regime ($> 20\,\mathrm{dB}$), the SVD precoding scheme provides a cut-off rate that is even worse than the cut-off rate of conventional GSM systems. This is because most of the singular values of a pure LOS channel are either zero or are close to zero, which results in a limited number of active precoding matrix inputs. The DFT precoding scheme, on the other hand, provides the largest improvement of the cut-off rate in the medium-high SNR regime. This is obtained thanks to its capability of increasing the minimum Euclidean distance between GSM symbols with different TX antenna activation patterns. The resulting improvement is inversely proportional to M and it is greater than $3\,\mathrm{bpcu}$ if $M = 4$. Similar to the i.i.d. Rayleigh fading case, on the other hand, DFT precoding is unable to provide a good cut-off rate in the low SNR regime because it is not conceived for achieving a large array gain.

B. Comparison to Mutual Information of SM/GSM

As discussed in Section I, the cut-off rate constitutes a lower-bound of the channel capacity. Therefore, it is important to analyze to what extend improving the cut-off rate results into a corresponding improvement of the mutual information. The mutual information of GSM system, based on the system model given in (1), can be calculated by using the analytical framework in [22], [23], as follows:

$$\mathcal{I}(s_m, \mathbf{e}_i; \mathbf{y}) = \log_2 N_{\mathrm{GSM}} - \frac{1}{N_{\mathrm{GSM}}} \sum_{m,i} \mathbb{E}_\mathbf{n} \left\{ \log_2 \left[\sum_{n,j} \exp\left(-\left(\left\| \mathbf{d}_{m,i}^{n,j} + \mathbf{n} \right\|^2 - \left\| \mathbf{n} \right\|^2 \right) / N_0 \right) \right] \right\}$$

(31)

where $m, n = 1, \ldots, M$ and $i, j = 1, \ldots, N_c$. The difference vector of two GSM symbols at the RX is equal to $\mathbf{d}_{m,i}^{n,j} = \mathbf{H}(s_m \mathbf{e}_i - s_n \mathbf{e}_j)/\sqrt{N_a}$. It is worth mentioning that the mutual information in (31) corresponds to the channel capacity of GSM systems over a discrete-input continuous-output memoryless channel (DCMC) with uniformly distributed GSM symbols [37]. Hence, (31) can be used to calculate and compare the mutual information of conventional GSM systems and GSM systems with the proposed precoding schemes

The mutual information is illustrated in Fig. 4. Similar to the previous case study, i.i.d. Rayleigh fading and pure LOS channel models are studied by keeping the same simulation setup. In the low SNR regime, SVD and SVD-DFT precoding schemes outperform, for both channel models, conventional GSM systems. The TX antenna grouping precoding scheme offers a substantial improvement of the mutual information in pure LOS channels and almost no gain in i.i.d. Rayleigh fading channels. The DFT precoding scheme improves the mutual information in the medium-high SNR regime, especially for LOS channels. In addition, we observe that the mutual information and the cut-off rate provide similar performance trends. Quantitatively, the gains are similar as well, but the gains observed for the mutual information are slightly smaller than those observed for the cut-off rate. This similarity can be justified with the aid of the lower-bound expression of the mutual information of GSM systems that is derived in Appendix B. The final result is as follows [38]:

$$\mathcal{I}_{\mathrm{LB}} = N_r(1 - \log_2 e) + R_0(N_0/2),$$

(32)

where $R_0(N_0/2)$ corresponds to the cut-off rate in (4) by reducing the noise power by half (i.e., by doubling the SNR). Of course, the expression of the mutual information in (32) is well defined

(a) I.i.d. Rayleigh channel.   (b) Pure LOS channel.
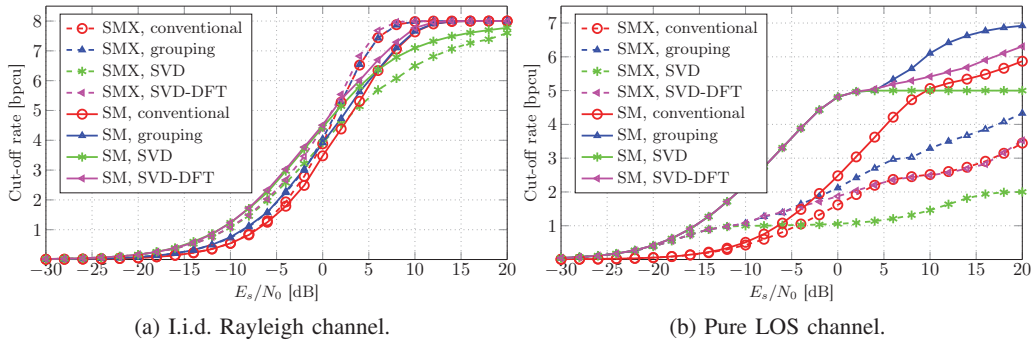
Fig. 5. Cut-off rate comparison between SMX and SM systems (both systems employ the proposed precoding schemes).

for values of the SNR for which it is positive. Equation (32), even though may be considered a very crude approximation for the mutual information, distinctly and explicitly highlights the dependency between the cut-off rate and the mutual information. In particular, it shows that an increase of the cut-off rate results in an increase of the mutual information as well. In summary, (32) and the numerical illustrations in Fig. 4 justify the choice of the cut-off rate as a meaningful metric for optimizing the mutual information of GSM systems with precoding.

C. Comparison with Spatial Multiplexing (SMX)

In this section, we focus our attention on comparing the cut-off rate of GSM systems with and without the proposed precoding schemes against its counterpart for SMX systems. To make the comparison fair and meaningful, the same precoding schemes used for GSM systems are applied to conventional SMX systems as well. More precisely, the RX signal vector of a $N_t \times N_r$ conventional SMX system can be written as follows:

$$\mathbf{y} = \mathbf{H}\mathbf{s}_m/\sqrt{N_t} + \mathbf{n}, \tag{33}$$

where the SMX symbol $\mathbf{s}_m = [s_1 \cdots s_{N_t}]^{\mathrm{T}}$ is a column vector consisting of N_t IQ symbols that are chosen from a symbol alphabet of M elements. We assume a normalized symbol alphabet, i.e., $\mathbb{E}\{|s_i|^2\} = 1$. By using the same line of thought as for GSM systems, the cut-off rate of a SMX system with equiprobable IQ symbols can be formulated as follows:

$$R_0 = -\log_2 \left[M^{-2N_t} \sum_{m,n} \exp\left(-\left\| \mathbf{H}\left(\mathbf{s}_m - \mathbf{s}_n\right) \right\|^2 / (4N_0 N_t) \right) \right], \tag{34}$$

where $m, n = 1, \ldots, M^{N_t}$. The cut-off rate of SMX systems employing the precoding schemes introduced in Section III can be obtained in a similar manner as for GSM systems. Due to space
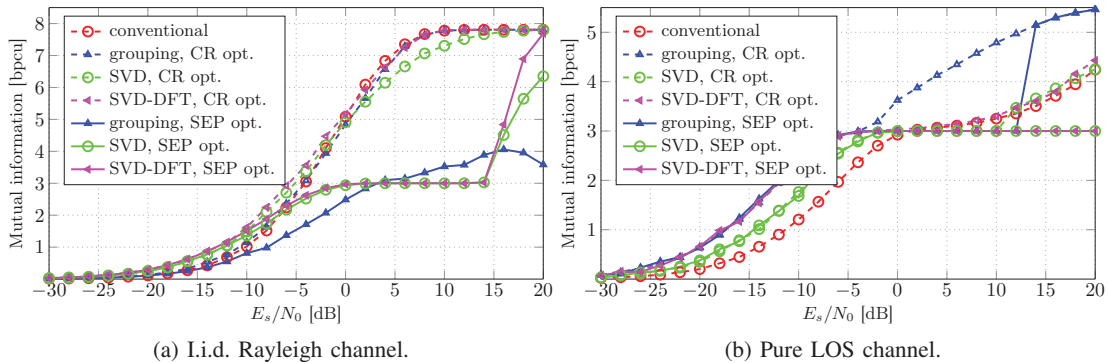
Fig. 6. Mutual information of GSM with the proposed precoding schemes based on cut-off rate (CR) and the SEP optimization.

limitations, the details are omitted for brevity. The only exception is DFT precoding, which cannot be used for SMX systems. This is due to the fact that it is not possible to change the TX antennas that are activated for different SMX symbols.

We consider a 8×8 SMX-MIMO system. In order to obtain the same bpcu as for GSM systems, i.e., 8 bpcu, $M = 2$ is considered. The numerical results in Fig. 5 show that conventional SMX outperforms conventional SM in i.i.d. Rayleigh fading channels, because different IQ steams can be easily resolved at the RX. This confirms early results on the performance of SMX systems about the suitability of this modulation scheme for uncorrelated fading channels. In highly correlated channels, i.e., pure LOS channels, the situation is opposite and conventional SM shows an advantage. In addition, we observe that the proposed precoding schemes enable the cut-off rate increase which is, in general, larger for SM, especially in pure LOS channels. A reason for this performance trend lies in a larger reduction of the number of TX symbols for SMX systems as opposed to SM systems. For example, the largest reduction of the number of TX symbols occurs when SVD and SVD-DFT precoding schemes have only one active column in the precoding matrix, and just one virtual antenna is used for the TX antenna grouping precoding scheme. Then, the number of SM symbols is 16 times larger than the number of SMX symbols.

D. Cut-off rate vs. SEP Optimization

By direct inspection of (2), we note that the analytical expression of the cut-off rate resembles the upper-bound of the SEP of GSM systems, which can be formulated as follows:

$$\text{SEP} \leq (1/N_{\text{GSM}}) \sum_{\substack{m,n,i,j \\ (m,i) \neq (n,J)}} \exp\left(-\left\|\mathbf{H}\left(\mathbf{e}_i s_m - \mathbf{e}_j s_n\right)\right\|^2 / (4N_0 N_a)\right) \tag{35}$$

where $m, n = 1, \cdots, M$ and $i, j = 1, \cdots, N_c$. This similarity motivates us to study the effectiveness of maximizing the cut-off rate for increasing the mutual information of GSM systems as opposed to minimizing the SEP. To this end, we optimize the proposed precoding schemes based on the minimization of the SEP rather then on the maximization of the cut-off rate. In other words, Algorithms 1, and 2 still apply and the only modification consists of replacing the argument of the logarithm function of the cut-off rate with (35). The only scheme that is not considered is DFT precoding, since in this case maximizing the cut-off rate and minimizing the SEP are equivalent. This is not the case, on the other hand, for the other precoding schemes.

The results are illustrated in Fig. 6. We observe that, in the medium-high SNR regime, optimizing the cut-off rate results in a larger mutual information compared with the optimization of the SEP. The reason of this performance trends lies in the larger number of GSM symbols that results from optimizing the cut-off rate as opposed to optimizing the SEP. The details of this finding are reported in Appendix C. In a nutshell, the following approximation holds true in the high SNR regime $\left\| \mathbf{d}_{m,i}^{n,j} + \mathbf{n} \right\|^2 - \left\| \mathbf{n} \right\|^2 \approx \left\| \mathbf{d}_{m,i}^{n,j} \right\|^2$ and the mutual information in (31) can be re-written as follows:

$$\mathcal{I}(s_m, \mathbf{e}_i; \mathbf{y}) \approx \log_2 N_{\text{GSM}} - \frac{1}{N_{\text{GSM}}} \sum_{m,i} \log_2 \left[\sum_{n,j} \exp \left(- \left\| \mathbf{d}_{m,i}^{n,j} \right\|^2 / N_0 \right) \right]. \tag{36}$$

In (36), in the high SNR regime, the exponential terms that satisfy the condition $(m, i) \neq (n, j)$ approach 0. This implies that the minimum Euclidean distance between different GSM symbols is a less important factor for maximizing the mutual information as opposed to the number of GSM symbols available. Since optimizing the systems based on the cut-off rate usually provides more GSM symbols, a better mutual information is expected as well.

This performance trend becomes evident in i.i.d. Rayleigh fading channels at medium-high SNR, where the optimization of the SEP results in a very small number of TX antenna activation patterns. The figure shows that optimizing the SEP may lead to a mutual information that is worse than the benchmark that does not use precoding. In a pure LOS channel, the proposed precoding schemes based on either the cut-of rate or the SEP as a utility function for optimization use only a subset of all the available TX antenna activation patterns (except in the very high SNR regime). This is due to the larger channel correlation between the columns of the channel matrix. As a result, the differences in the mutual information are smaller. In the low SNR regime, there is almost no difference between optimizing the SEP and the cut-off rate because they both

result in maximizing the array gain. Hence, a small (usually minimum) number of TX antenna activation patterns is used.

V. Conclusion

In this paper, we proposed the use of the cut-off rate as a simple and meaningful utility function for optimizing the channel capacity and the mutual information of SM/GSM systems. Also, we proposed four precoding schemes whose precoding matrices are obtained by maximizing the cut-off rate. Numerical results confirmed that they provide a better mutual information than the conventional SM/GSM systems. More precisely, we showed that the precoding schemes that aim to maximize the array gain are more suitable for application in the low-medium SNR regime. On the other hand, the precoding schemes that aim to maximize the minimum Euclidean distance between different SM/GSM symbols are more suitable for application in the medium-high SNR regime. In summary, our study confirmed that the cut-off rate is a suitable metric for optimizing the channel capacity of SM/GSM systems and that the proposed precoding schemes are capable of enhancing the mutual information. Depending on the operating SNR regime, different precoding schemes need to be used in order to achieve the best channel capacity and mutual information.

Appendix A
Cut–off Rate of TX Antenna Grouping Precoding

In this appendix, we analyze the improvement of the cut-off rate that the TX antenna grouping precoding is capable of providing in a i.i.d. Rayleigh fading channel and in a pure LOS channel. For ease of description, only groups of two antennas as considered. Similar findings and trends hold for a large number of antenna in each group. Let $\mathbf{h}_i$ and $\mathbf{h}_j$ ($i, j \in \{1, \ldots, N_t\}$, $i \neq j$) be the impulse responses of two physical TX antennas. Let us denote by $\mathbf{h}_g$ the virtual TX antenna after grouping them. The following holds:

$$\mathbb{E}\left\{\left\|\mathbf{h}_g\right\|^2\right\} = \mathbb{E}\left\{\|\mathbf{h}_i\|^2 + \left\|\mathbf{h}_j\right\|^2 + 2\Re\left\{\mathbf{h}_i^{\mathrm{H}}\mathbf{h}_j\right\}\right\}/2. \tag{37}$$

In an i.i.d. Rayleigh fading channel, the mean value of the inner product of two different columns of $\mathbf{H}$ is equal to 0, i.e., $\mathbb{E}\{\Re\{\mathbf{h}_i^{\mathrm{H}}\mathbf{h}_j\}\} = 0$. In addition, we have $\mathbb{E}\{\|\mathbf{h}_i\|^2\} = N_r$ for $\forall i \in \{1, \ldots, N_t\}$. Hence, (37) simplifies as $\mathbb{E}\left\{\left\|\mathbf{h}_g\right\|^2\right\} = N_r$, and the average power gain is the same as without grouping the physical antennas.

In a pure LOS channel, on the other hand, we have $d_t, d_r \ll D$, i.e., the columns of $\mathbf{H}$ are highly correlated. This implies $\mathbb{E}\{\Re\{\mathbf{h}_i^{\mathrm{H}}\mathbf{h}_j\}\} > 0$. In this regime, the approximation $||\mathbf{h}_i||^2 \approx N_r$ for $\forall i \in \{1, \ldots, N_t\}$ holds true (cf. (30)) and (37) simplifies as $\mathbb{E}\left\{\left\|\mathbf{h}_g\right\|^2\right\} > N_r$.

In a pure LOS channel, therefore, the TX antenna grouping precoding scheme increases the average power gain and, as a result, it is expected to provide a large improvement of the cut-off rate as opposed to the i.i.d. Rayleigh fading case.

APPENDIX B
LOWER-BOUND OF MUTUAL INFORMATION

In this appendix, we derive a lower-bound of the mutual information of GSM systems. The mutual information of a GSM system is defined as follows:

$$\mathcal{I}(s_m, \mathbf{e}_i; \mathbf{y}) = \mathcal{H}(\mathbf{y}) - \mathcal{H}(\mathbf{y}|s_m, \mathbf{e}_i) = \mathcal{H}(\mathbf{y}) - \mathcal{H}(\mathbf{n}). \tag{38}$$

By using the Jensen's inequality, we obtain:

$$\mathcal{H}(\mathbf{y}) = \mathbb{E}_{\mathbf{y}}\left\{-\log_2\left(p(\mathbf{y})\right)\right\} \geq -\log_2\left(\int_{\mathbf{y}} p(\mathbf{y})^2 \mathrm{d}\mathbf{y}\right). \tag{39}$$

In addition, we have:

$$p(\mathbf{y}) = \sum_{m,i} p(s_m, \mathbf{e}_i)p(\mathbf{y}|s_m, \mathbf{e}_i) = (1/N_{\mathrm{GSM}})\sum_{m,i} p(\mathbf{y}|s_m, \mathbf{e}_i), \tag{40}$$

where $p(\mathbf{y}|s_m, \mathbf{e}_i)$ is available in (3) and the GSM symbols are uniformly distributed. By plugging (40) in (39) and applying some algebraic manipulations similar to the computation of the cut-off rate, we obtain the following:

$$\mathcal{H}(\mathbf{y}) \geq N_r \log_2\left(2\pi N_0\right) - \log_2\left(\frac{1}{N_{\mathrm{GSM}}^2} \sum_{m,n,i,j} e^{-\left\|\mathbf{H}\left(\mathbf{e}_i s_m - \mathbf{e}_j s_n\right)\right\|^2/(2N_0 N_a)}\right) = N_r \log_2\left(2\pi N_0\right) + R_0(N_0/2) \tag{41}$$

for $m, n = 1, \cdots, M$ and $i, j = 1, \cdots, N_c$. From [14], we have $\mathcal{H}(\mathbf{n}) = N_r \log_2\left(e\pi N_0\right)$ and eventually obtain the lower-bound reported in (32).

In this appendix, we discuss the reason why the precoding schemes that maximize the cut-off rate instead of the SEP result in a larger number of TX antenna activation patterns. First of all, we note that maximizing the cut-off rate is equivalent to minimizing the argument of the logarithm function of the cut-off rate, which is denoted as AG and related to the SEP as follows:

$$\mathrm{AG} = \left(1 + \mathrm{SEP}\right)/N_{\mathrm{GSM}}. \tag{42}$$

Let us consider the TX antenna grouping precoding. Let us assume that the number of TX antenna activation patterns decreases from N_{GSM} to $N_{\mathrm{GSM}} - \triangle N$ at an iteration of the algorithm and that the reduction of the SEP is $\triangle \mathrm{SEP} > 0$. Under these assumptions, the argument of the logarithm function of the cut-off rate after optimizing the SEP is given as $\mathrm{AG}_1 = \left(1 + \mathrm{SEP} - \triangle \mathrm{SEP}\right)/\left(N_{\mathrm{GSM}} - \triangle N\right)$, while before optimizing the SEP, we have AG_0 in (42). If optimizing the SEP does not reduce the argument of the logarithm function of the cut-off rate, we obtain: $\triangle \mathrm{SEP} < \left(\triangle N/N_{\mathrm{GSM}}\right)\left(1 + \mathrm{SEP}\right)$. By taking into account that the number of virtual TX antennas at an iteration reduces by 1, i.e., from N_{vt} to $N_{vt} - 1$, we have:

$$\triangle \mathrm{SEP} < \left(N_a/N_{vt}\right)\left(1 + \mathrm{SEP}\right). \tag{43}$$

If (43) holds true, the number of TX antenna activation patterns obtained by optimizing the cut-off rate is larger than the number of TX antenna activation patterns that is obtained by optimizing the SEP. Otherwise, they result in the same number of TX antenna activation patterns. What is left to prove is to show that optimizing the SEP cannot provide a larger number of TX antenna activation patterns compared to its counterpart that is obtained by maximizing the cut-off rate. Let us assume that at an iteration of the TX antenna grouping algorithm the SEP increases by $\triangle \mathrm{SEP} > 0$. Then, we have $\mathrm{AG}_1 = \left(1 + \mathrm{SEP} + \triangle \mathrm{SEP}\right)/\left(N_{\mathrm{GSM}} - \triangle N\right) > \mathrm{AG}_0$ and the argument of the logarithm function of the cut-off rate increases, too. Hence, the number of GSM symbols provided by the SEP optimization can not be larger than the the number of GSM symbols provided by the cut-off rate optimization.

As far as SVD and SVD-DFT precoding schemes are concerned, the result can be proved based on the following argument. At each iteration of both algorithms, the SEP is reduced by

adding an additional column to the precoding matrix. This operation inherently decreases the argument of the logarithm function in (42) and, thus, increases the cut-of-rate. The opposite, on the other hand, is not always true. Therefore, optimizing the cut-off rate of GSM systems by using SVD and SVD-DFT precoding provides a larger (or the same in the worst case) number of TX antenna activation patterns than minimizing the SEP.

REFERENCES

[1] R. Mesleh *et al.*, "Spatial modulation — A new low complexity spectral efficiency enhancing technique," in *1st Int. Conf. on Communications and Networking in China*, vol. 1, Oct. 2006, pp. 1–5.

[2] M. Di Renzo *et al.*, "Spatial modulation for generalized MIMO: Challenges, opportunities, and implementation," *Proc. IEEE*, vol. 102, no. 1, pp. 56–103, Jan. 2014.

[3] E. Faregh *et al.*, "A closed-form mutual information approximation for multiple-antenna systems with spatial modulation," *IEEE Commun. Lett.*, vol. 5, no. 6, pp. 636–639, Dec. 2016.

[4] J. L. Massey, "Coding and modulation in digital communications," in *Proc. of Int. Zurich Seminar*, 1974, pp. E2.1–E2.4.

[5] G. Caire *et al.*, "Bit-interleaved coded modulation," *IEEE Trans. Inf. Theory*, vol. 44, no. 3, pp. 927–946, May 1998.

[6] F. Rey *et al.*, "Linear precoder design through cut-off rate maximization in MIMO-OFDM coded systems with imperfect CSIT," *IEEE Trans. Signal Process.*, vol. 58, no. 3, pp. 1741–1755, Mar. 2010.

[7] M. T. Ivrlac *et al.*, "Fading correlations in wireless MIMO communication systems," *IEEE J. Sel. Areas Commun.*, vol. 21, no. 5, pp. 819–828, Jun. 2003.

[8] J. Proakis and M. Salehi, *Digital Communications*, 5th ed.   Boston: McGraw-Hill Science/Engineering/Math, 2007.

[9] R. U. Nabar *et al.*, "Cut-off rate based transmit optimization for spatial multiplexing on general MIMO channels," in *2003 IEEE Int. Conf. on Acoustics, Speech, and Signal Processing, (ICASSP '03)*, vol. 5, Apr. 2003, pp. 61–64.

[10] P. Liu *et al.*, "Line-of-sight spatial modulation for indoor mmWave communication at 60GHz," *IEEE Trans. Wireless Commun.*, vol. 15, no. 11, pp. 7373–7389, Nov. 2016.

[11] J. Wang *et al.*, "Generalised spatial modulation system with multiple active transmit antennas and low complexity detection scheme," *IEEE Trans. Wireless Commun.*, vol. 11, no. 4, pp. 1605–1615, Apr. 2012.

[12] A. Younis *et al.*, "Generalised spatial modulation," in *2010 Conf. Rec. of the 44th Asilomar Conf. on Signals, Systems and Computers (ASILOMAR)*.   IEEE, 2010, pp. 1498–1502.

[13] G. J. Foschini, "Layered space-time architecture for wireless communication in a fading environment when using multi-element antennas," *Bell Labs Tech. J.*, vol. 1, no. 2, pp. 41–59, 1996.

[14] E. Telatar, "Capacity of multi-antenna gaussian channels," *Eur. Trans. Telecommun.*, vol. 10, no. 6, pp. 585–595, Nov. 1999.

[15] C.-X. Wang *et al.*, "Cellular architecture and key technologies for 5G wireless communication networks," *IEEE Commun. Mag.*, vol. 52, no. 2, pp. 122–130, Feb. 2014.

[16] A. Stavridis *et al.*, "Energy evaluation of spatial modulation at a multi-antenna base station," in *Vehicular Tech. Conf. (VTC Fall)*, Sep. 2013, pp. 1–5.

[17] R. Rajashekar *et al.*, "Reduced-complexity ML detection and capacity-optimized training for spatial modulation systems," *IEEE Trans. Commun.*, vol. 62, no. 1, pp. 112–125, Jan. 2014.

[18] Y. Yang and B. Jiao, "Information-guided channel-hopping for high data rate wireless communication," *IEEE Commun. Lett.*, vol. 12, no. 4, pp. 225–227, Apr. 2008.

[19] P. Liu *et al.*, "Variable-N_u generalized spatial modulation for indoor LOS mmwave communication: Performance optimization and novel switching structure," *IEEE Trans. Commun.*, vol. 65, no. 6, pp. 2625–2640, Jun. 2017.

[20] Z. An *et al.*, "Mutual information analysis on spatial modulation multiple antenna system," *IEEE Trans. Commun.*, vol. 63, no. 3, pp. 826–843, Mar. 2015.

[21] ——, "Mutual information and error probability analysis on generalized spatial modulation system," *IEEE Trans. Commun.*, vol. 65, no. 3, pp. 1044–1060, Mar. 2017.

[22] X. Guan *et al.*, "On the mutual information and precoding for spatial modulation with finite alphabet," *IEEE Commun. Lett.*, vol. 2, no. 4, pp. 383–386, Aug. 2013.

[23] S. R. Jin *et al.*, "Linear precoding design for mutual information maximization in generalized spatial modulation with finite alphabet inputs," *IEEE Commun. Lett.*, vol. 19, no. 8, pp. 1323–1326, Aug. 2015.

[24] R. Rajashekar *et al.*, "Antenna selection in spatial modulation systems," *IEEE Commun. Lett.*, vol. 17, no. 3, pp. 521–524, Mar. 2013.

[25] C. Liu *et al.*, "Optimal spatial-domain design for spatial modulation capacity maximization," *IEEE Commun. Lett.*, vol. 20, no. 6, pp. 1092–1095, Jun. 2016.

[26] Y. Shi *et al.*, "Optimal power allocation in spatial modulation systems," *IEEE Trans. Wireless Commun.*, vol. 16, no. 3, pp. 1646–1655, Mar. 2017.

[27] A. Yadav *et al.*, "Linear precoder design for correlated partially coherent channels with discrete inputs," in *ISWCS 2013; The Tenth Int. Symp. on Wireless Communication Systems*, Aug. 2013, pp. 1–5.

[28] ——, "Linear precoder design for doubly correlated partially coherent fading MIMO channels," *IEEE Trans. Wireless Commun.*, vol. 13, no. 7, pp. 3621–3635, Jul. 2014.

[29] S. G. Srinivasan and M. K. Varanasi, "Constellation design for the noncoherent MIMO rayleigh-fading channel at general SNR," *IEEE Trans. Inf. Theory*, vol. 53, no. 4, pp. 1572–1584, Apr. 2007.

[30] A. Yadav *et al.*, "Partially coherent constellation design and bit-mapping with coding for correlated fading channels," *IEEE Trans. Commun.*, vol. 61, no. 10, pp. 4243–4255, Oct. 2013.

[31] N. Serafimovski *et al.*, "Fractional bit encoded spatial modulation (FBE-SM)," *IEEE Commun. Lett.*, vol. 14, no. 5, pp. 429–431, May 2010.

[32] Y. Yang and S. Aissa, "Information guided channel hopping with an arbitrary number of transmit antennas," *IEEE Commun. Lett.*, vol. 16, no. 10, pp. 1552–1555, Oct. 2012.

[33] D. Tse and P. Viswanath, *Fundamentals of Wireless Communication*. Cambridge, UK: Cambridge University Press, 2005.

[34] Q.-T. Ngo *et al.*, "General minimum euclidean distance-based precoder for MIMO wireless systems," *EURASIP J. Adv. Signal Process.*, vol. 2013, no. 1, pp. 1–12, 2013.

[35] N. S. Perović *et al.*, "Design of a simple phase precoder for generalized spatial modulation in LOS millimeter wave channels," in *11th Int. ITG Conf. on Systems, Communications and Coding (SCC 2017)*, 2017.

[36] N. Serafimovski *et al.*, "Practical implementation of spatial modulation," *IEEE Trans. Veh. Technol.*, vol. 62, no. 9, pp. 4511–4523, Nov. 2013.

[37] R. Zhang *et al.*, "Error probability and capacity analysis of generalised pre-coding aided spatial modulation," *IEEE Trans. Wireless Commun.*, vol. 14, no. 1, pp. 364–375, Jan. 2015.

[38] S. Guo *et al.*, "On the mutual information and constellation design criterion of spatial modulation MIMO systems," in *2014 IEEE Int. Conf. on Communication Systems (ICCS)*. IEEE, 2014, pp. 487–491.

Two dimensional signal spreading in UMTS LTE: Exploiting time-frequency diversity to increase throughput

Jiri Blumenstein, Michal Šimko, Roman Marsalek, Zbynek Fedra, Jan Prokopec, Markus Rupp

Two dimensional signal spreading in UMTS LTE: exploiting time-frequency diversity to increase throughput

J. Blumenstein, M. Šimko, R. Marsalek,
Z. Fedra, J. Prokopec, M. Rupp

Abstract This paper proposes a two-dimensional spreading method in UMTS Long Term Evolution (LTE). Such method brings additional time-frequency diversity which is beneficial in terms of the ability to decode transmitted data at the receiver side under multipath fading. Additional diversity is caused by the fact that chips of transmitted signals are spread with a Walsh-Hadamard spreading sequence over several subcarriers as well as over several time-slots simultaneously.

A comparison with state-of-the-art LTE downlink transmission is provided. To enable reproducibility and to increase credibility of our results, open source Vienna LTE simulator is utilized.

LTE transmissions with the proposed 2D spreading are tested on a several channel models. Simulations show that apart from an Additive White Gaussian Noise (AWGN) channel model, the 2D spreading based method outperforms the throughput performance of standard LTE. At high Signal to Noise Ratio (SNR), the throughput increase in most channel models is higher than 10%.

Keywords LTE · 2D spreading · Throughput maximization · VSF-OFCDM · Vienna LTE Simulator

1 Introduction

It is without any doubt that one of the main concerns of any communication system is to have the highest possible data throughput independent of the

J. Blumenstein · R. Marsalek · Z. Fedra · J. Prokopec
Department of Radio Electronics Brno University of Technology Purkyňova 118, 612 00, Brno, Czech Republic, E-mail: xblume00@phd.feec.vutbr.cz

M. Šimko · M. Rupp
Institute of Telecommunications, Vienna University of Technology Gusshausstrasse 25/389, A-1040 Vienna, Austria, E-mail: msimko@nt.tuwien.ac.at, mrupp@nt.tuwien.ac.at

channel conditions. To maximize the throughput, we exploited time and frequency diversity. Apart from utilization of expensive techniques such as using extra bandwidth, adding more antennas or simply increasing the transmitting power, our method can be interpreted as a coding technique with code rate one. This method only increases the demand for computational power.

The idea behind this paper is to reveal the efficiency of a 2D spreading method when it is incorporated in the most relevant wireless standard which is currently available. Therefore we chose an open source LTE simulator [1–3] to find out whether LTE can be enhanced by our proposed 2D signal spreading and show that is indeed outperforms a standard LTE downlink in terms of throughput.

An example of implementation of 2D signal spreading and thus a time-frequency diversity utilization can be found in Variable Spreading Factor Orthogonal Frequency Code Division Multiplex (VSF-OFCDM) systems [4–7]. The authors claim that the 2D spreading based VSF-OFCDM system exhibits a better performance than Orthogonal Frequency Division Multiplexing (OFDM) wireless transmission methods.

A three-cell frequency reuse OFDM system and one-cell reuse VSF-OFCDM system was compared. Due to the fact that VSF-OFCDM systems could benefit from the utilization of the code domain and the cells have been distinguished by a spreading code the VSF-OFCDM system reached significantly better throughput in a multi cell environment [8]. The reason of this is that there has been enabled a possibility to use the entire system bandwidth in a VSF-OFCDM system when compared by a third of the bandwidth in case of pure OFDM.

LTE however uses a one-cell frequency reuse [9] and could benefit only from exploitation of the time-frequency diversity. To keep the comparison of 2D LTE and LTE fair, the bandwidth has to be the same as in the case of LTE.

When presenting our novel method, the need for comparing with a-state-the-art system is very important. Hence, the system model is based on the Vienna LTE simulator [1, 2] as a reference model. This simulator is released under a free non-commercial, academic use license. Such a release model enables algorithms to be tested and being compared using a common, known, and verifiable environment. We are certain this transparency not only improves the quality of the published results but also their credibility.

As results, we present throughput comparisons based on power-delay profile (PDP) channel models of the followed types: Pedestrian channel model of type A (PedA), Pedestrian channel model of type B (PedB), Vehicular channel model of type A (VehA), Additive White Gaussian Noise (AWGN), Typical urban channel model (TU), Extended typical urban channel model (ETU), Rural area channel model (RA) and Hilly terrain channel model (HT) [10,11].

The remainder of this paper is organized as follows: In Section System Model, the implementation of the 2D signal spreading into the LTE signal processing chain is described. In Section Spreading Factor we explain its selection and in Section Experiment and Results the comparison of the standard
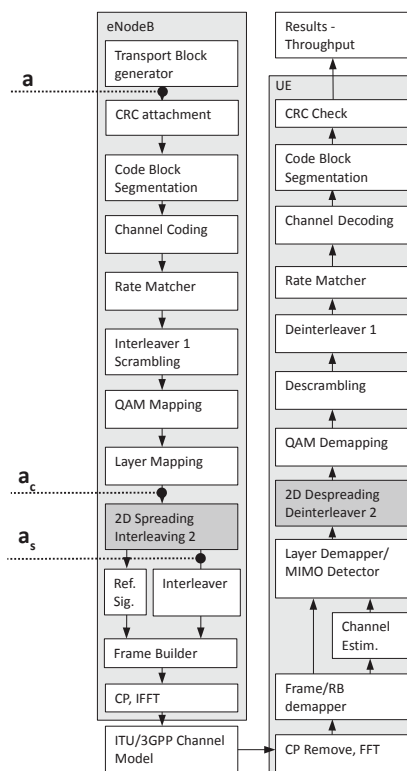
Fig. 1 The LTE signal processing chain. The dark gray blocks represents the additional blocks for 2D spreading and despreading. Other parts remain the same in both versions, 2D spreading based LTE and standard LTE. White blocks are according to [13–15].

LTE downlink and the 2D spreading based LTE transmission is provided. At the end of the paper, Section Conclusion rounds up the paper.

2 System Model

The 2D spreading, as it is presented in [12], is rather repeating symbols which are multiplied by some spreading sequence. Resulting chips are repeated in time, frequency or code domain. The presented algorithm exploits one dimensional Walsh-Hadamard sequences. Nevertheless, due to interleaving of spread data among multiple carrier frequencies and multiple OFDM symbols, two dimensions are utilized. Therefore, we refer to this scheme as two-dimensional spreading.

Figure 1 represents the LTE signal processing chain. The dark gray blocks indicate additional blocks for 2D spreading and despreading. Other parts remain the same in both versions, 2D spreading based LTE and standard LTE downlink. White blocks are according to the 3GPP standards [13–15].

Vector $\mathbf{a_c}$ from Equation (1) denotes the Cyclic Redundancy Check (CRC) secured, segmented, scrambled, turbo-coded, rate matched, QAM and layer mapped data vector $\mathbf{a}$.

$$\mathbf{a_c} = (a_{c1}, a_{c2}, \ldots, a_{ce}), \tag{1}$$

where the index e is the number of elements in the vector $\mathbf{a_c}$. We consider the output of the layer mapping block, vector $\mathbf{a_c}$, as the input of a 2D spreading block. In the 2D spreading block, vector $\mathbf{a_c}$ is chopped to SF parts, where SF stands for Spreading Factor - as explained below. This operation is illustrated by (2), where $\mathrm{SP}\{\mathbf{a_c}\}|_{\mathrm{SF}}$ denotes a Serial-to-parallel (SP) transformation of vector $\mathbf{a_c}$.

$$\mathrm{SP}\{\mathbf{a_c}\}|_{\mathrm{SF}} := \underbrace{\begin{pmatrix} a_{c\,1} & a_{c\,2} & \cdots & a_{c\,\frac{e}{SF}} \\ a_{c\left(\frac{e}{SF}+1\right)} & a_{c\left(\frac{e}{SF}+2\right)} & \ddots & \vdots \\ \vdots & \ddots & a_{c\,(e-SF-2)} & a_{c\,(e-SF-1)} \\ a_{c\,(e-SF)} & \cdots & \cdots & a_{ce} \end{pmatrix}}_{\mathbf{A_c}}. \tag{2}$$

Each row of matrix $\mathbf{A_c}$ is then multiplied with one Walsh-Hadamard sequence, i.e., one column of matrix Ξ specified by (4). This is described by Equation (3) and depicted in Figure 2.

$$\mathbf{A_s} = \mathbf{A_{c}}_{(i,*)} \otimes \Xi_{(*,i)} =$$

$$= \begin{pmatrix} a_{c\,1}\xi_{1,1} & a_{c\left(\frac{e}{SF}+1\right)}\xi_{1,2} & \cdots & a_{c\,(e-SF)}\xi_{1,SF} \\ a_{c\,1}\xi_{2,1} & a_{c\left(\frac{e}{SF}+1\right)}\xi_{2,2} & \vdots & \vdots \\ \vdots & \vdots & & \\ a_{c\,1}\xi_{SF,1} & a_{c\,2}\xi_{1,1} & \vdots & \vdots \\ a_{c\,2}\xi_{1,1} & a_{c\left(\frac{e}{SF}+2\right)}\xi_{1,2} & & \\ \vdots & \vdots & a_{c\,(e-SF-2)}\xi_{SF-1,SF-1} & \vdots \\ a_{c\,\frac{e}{SF}}\xi_{SF,1} & \vdots & a_{c\,(e-SF-1)}\xi_{SF,SF-1} & a_{ce}\xi_{SF,SF} \end{pmatrix}^T,$$

$$\forall i \in \{1, \ldots, SF\} \tag{3}$$

where

$$\Xi = \begin{pmatrix} \xi_{1,1} & \cdots & \xi_{1,SF} \\ \vdots & & \vdots \\ \xi_{SF,1} & \cdots & \xi_{SF,SF} \end{pmatrix}. \tag{4}$$

Matrix Ξ then represents the Walsh-Hadamard matrix utilized as a bank of spreading sequences, $\mathbf{A_{c}}_{(i,*)}$ denotes the i-th row of matrix $\mathbf{A_c}$ and $\Xi_{(*,i)}$

selects the i-th column of matrix $\mathbf{\Xi}$. The symbol $\otimes$ denotes the Kronecker product and $(.)^T$ denotes a matrix transposition.

Consequently, all the rows of the resulting matrix $\mathbf{A_s}$ are summed together according to Equation (5), thus we obtain a vector of spread data $\mathbf{a_s}$ of length SF. Each row of matrix $\mathbf{A_c}$ forms the code sheet, as shown in Figure 2.

$$\mathbf{a_s} = \sum_{j=1}^{SF} \mathbf{A_{s}}_{(j,*)} =$$

$$= \begin{bmatrix} a_{c\,1}\xi_{1,1} + a_{c\,1}\xi_{2,1}+ & \dots & +a_{c\,\frac{e}{SF}}\xi_{SF,1} \\ a_{c\left(\frac{e}{SF}+1\right)}\xi_{1,2} + a_{c\left(\frac{e}{SF}+1\right)}\xi_{2,2}+ & \dots & +a_{c\left(\frac{e}{SF}+1\right)}\xi_{SF,2} + a_{c\left(\frac{e}{SF}+2\right)}\xi_{1,2} \\ & & \vdots \\ \vdots & \dots & +a_{c\,(e-SF-1)}\xi_{SF,SF-1} \\ a_{c\,(e-SF)}\xi_{1,SF}+ & \dots & +a_{ce}\xi_{SF,SF} \end{bmatrix}^T$$

(5)

In order to spread the chips (the elements of vector $\mathbf{a_s}$) over the entire bandwidth and over all time slots (OFDM symbols), all positions of the chips are randomly interleaved.

Vector $\mathbf{a_s}$, containing all the spread data is of the same length as the output of the layer mapping block, i.e., $\|\mathbf{a_s}\| = \|\mathbf{a_c}\|$.

Due to the fact that Walsh-Hadamard sequences are orthogonal, we are able to separate them at the receiver site. This principle is well-known from the Code Division Multiple Access (CDMA) systems [12].

When spreading a signal, we have an SF times higher amount of data to transmit due to the spreading process, however we also obtain SF times more space in the code domain which we can utilize. The increase in terms of data is in this case the same as the increase of the space dedicated to the transmission. As a result, after the summation of all the code sheets as presented in Figure 2, the amount of data is kept the same as in the case of standard LTE and thus no extra bandwidth is required.

However, the transmitted data occupies an SF-times higher amount of the time-frequency space, thus we gain on time-frequency diversity. At the receiver site, we will have SF realizations of one bit. Due to the interleaving of these chips all over the transmission channel, the influence of deep fades of a transfer function [16] will be reduced.

However the data share their space with other $SF - 1$ data elements and thus, as will be shown in the next section, their performance on AWGN channels will not be improved.

3 Spreading Factor

For a better understanding of our proposed algorithm, a brief description of the LTE time-frequency signal grid according to [14] is stated in the following
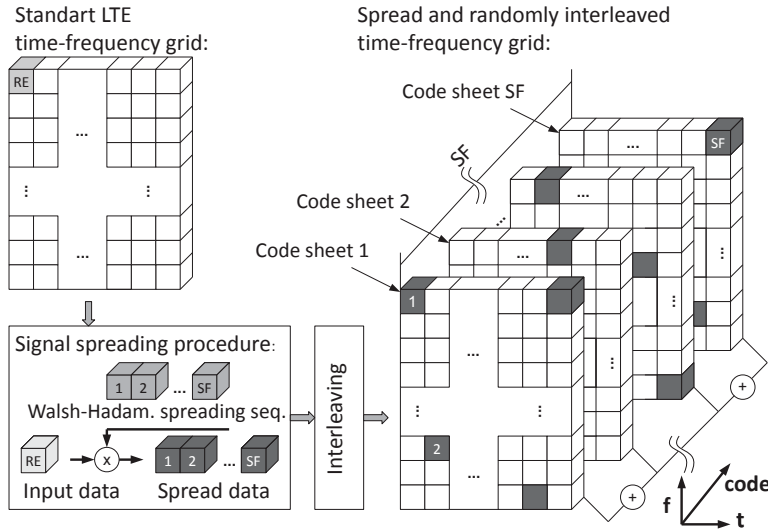
Fig. 2 The two-dimensional signal spreading process. We are spreading the signal right after the layer mapping block. The signal from the layer mapper is multiplied with all Walsh-Hadamard sequences of order SF. As a result we receive SF vectors, which represents the code-sheets. These are then summed together and we obtain a vector which serves as a frame builder input.

section. Using a 'normal' cyclic prefix, seven symbols with 12 subcarriers each form one resource block. One element of such a grid is called resource element (RE).

The maximal number of resource blocks transmitted in LTE is given by a total system bandwidth BW, where BW$\in \{1.4, 3, 5, 10, 15, 20\}$MHz. This corresponds to the number of resource block $N_{rb} \in \{6, 15, 25, 50, 75, 100\}$, which can be exploited for data transmission.

The spreading factor SF has to be chosen carefully, the length of the vector $\mathbf{a_c}$ representing the amount of transmitted data has to be divisible by SF. This is due to the fact that the 2D spreading block cuts its input vector $\mathbf{a_c}$ into SF parts in order to allow the spreading. For a more detailed explanation, the chopped data are multiplied by the spreading sequence and then their length will be SF-times larger. The length of the spread data will then be exactly the same as the length of the 2D spreading block input vector $\mathbf{a_c}$. This is a necessary property. The frame builder then can remain intact as well as the generation of pilot signals used for channel estimation. As a result, only minimal changes in the LTE standard are needed. Additionally, the comparison of such a system is more relevant.

In the configuration presented below, where BW=1.4MHz, the number of user equipments nUE=1, N_{rb}=6, a vector from the layer mapping block is of

Table 1 LTE system parameters of the presented simulations

System bandwidth	1.4 MHz
Subcarrier spacing	15 kHz
Subframe duration	1 ms
Number of User Equipments (UEs)	1
Number of eNodeBs	1
Transmission Scheme	SISO
Number od subframes	10 000
Channel Quality Information (CQI)	15
SNR	30dB
SF	48
CP length	'normal' [13]
Channel estimation method	MMSE
Channel model	PedA, PedB, VehA, AWGN, TU, ETU, RA, HT [10, 11]
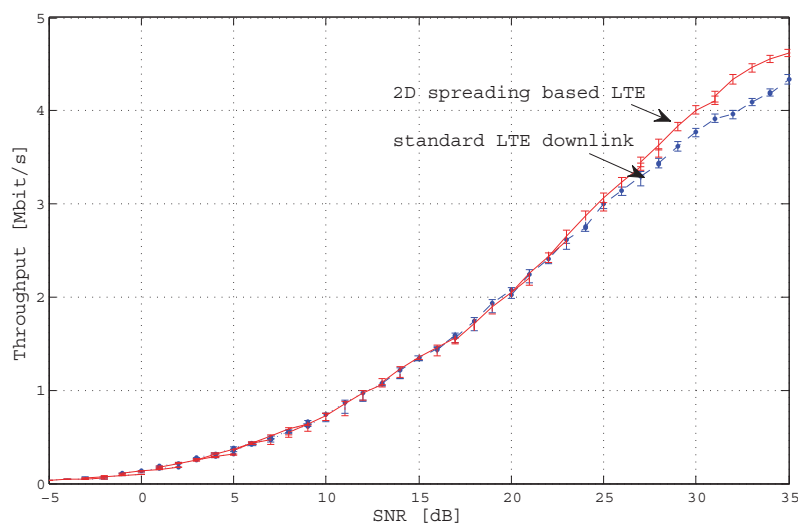
Fig. 3 The throughput curves for PedB channel model, 1.4MHz, single-user, 5000 subframes, CQIs from 1 to 15, SF=48 The 2D spreading based LTE is ploted in red, the standart LTE is dashed and blue. The 99% confidence intervals are also depicted, indicating a high confidence of the plotted results.

length 816 for the first subframe and 960 for the second subframe, respectively. Due to this, the maximal spreading factor is SF=48. The reason is that 48 is the highest common divisor of 816 and 960 for which we also found a Walsh-Hadamard matrix.

4 Experiment and results

This section describes the simulation setup as well as the results of the 2D spreading based LTE model.

Figure 3 depicts the comparison of a standard compliant LTE downlink transmission with a non standard compliant 2D LTE downlink. Adaptive CQI mapping's, for which the CQI is adapted in order to provide the highest possible data throughput at given SNR, are utilized. The setup of the simulation presented in Figure 3 is as follows: PedB channel model, 1.4MHz, single-user, 5000 subframes, CQIs from 1 to 15, SF=48. The 2D spreading based LTE transmission is ploted in red, the standart LTE transmission is dashed and blue. The 99% confidence intervals are also depicted in order to provide a statistical perspective on the accuracy of the presented data.

As can be observed, the 2D spreading enhanced LTE copes better in the multi-path environment when compared to the standard LTE downlink. A considerable throughput improvement comes however only at rather high SNR around 25dB and more, depending on the channel model. A significant improvement is achieved at SNR=30dB according to Figure 3. In that case the 2D spreading enables a possibility to exploit higher CQI at given SNR level in comparison with the standard form of LTE.

Table 2 gives an insight on important parameters of the next simulation, where we examined the 2D spreading influence applying a cornucopia of channel models, namely PedA, PedB, VehA, AWGN, TU, ETU, RA and HT [10,11] which are available in the LTE simulator [1,3]. Results are presented in Figure 4 where we can observe the throughput increase in percent. The 2D LTE achieves higher throughput and the increase is from 9% to more then 25% in five out of eight channel models. In one channel model the increase is about 2-3 percent. Only in 2 channel models, there is no increase at all.

5 Conclusion

This paper describes a new 2D spreading mapping suitable for LTE transmissions. We implemented this algorithm into the state-of-the art simulation system developed at Vienna University of Technology. For a comparison of the proposed 2D spreading enhanced LTE and standard LTE downlink, several channel models have been applied.

The proposed spreading requires only minor modifications of LTE standards while it brings considerable improvement in the throughput performance of such systems. We showed that in most channel models, the utilization of the 2D spreading is beneficial in terms of throughput increase. This increase ranges from 5 percent to more than 25 percent (99% confidence interval). It should be also noted, that the exploitation of the 2D spreading does not require extra bandwidth.
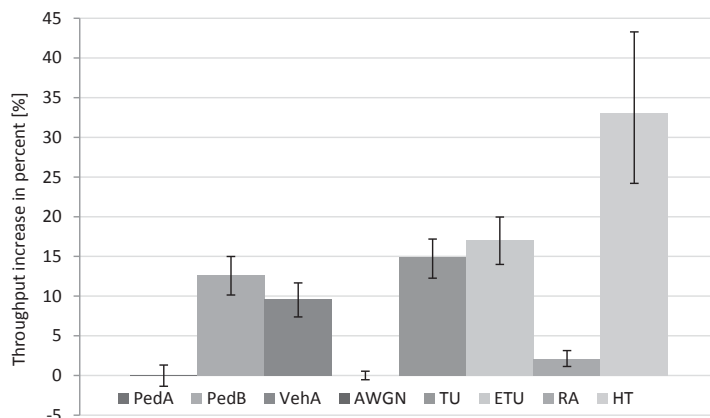
Fig. 4 The throughput increase for various channel models and for SNR=30dB. Simulation settings are listed in Table 1. The error bars represents 99% confidence intervals.

References

1. LTE simulator homepage. [Online]. Available: http://www.nt.tuwien.ac.at/ltesimulator/
2. C. Mehlführer, M. Wrulich, J. C. Ikuno, D. Bosanska, and M. Rupp, "Simulating the Long Term Evolution physical layer," in *European Signal Processing Conference (EU-SIPCO)*, Glasgow, Scotland, August 2009.
3. C. Mehlführer, J. Colom Ikuno, M. Simko, S. Schwarz, M. Wrulich, and M. Rupp, "The Vienna LTE simulators - enabling reproducibility in wireless communications research," *EURASIP Journal on Advances in Signal Processing*, vol. 2011, no. 1, p. 29, 2011. [Online]. Available: http://asp.eurasipjournals.com/content/2011/1/29
4. N. Maeda, Y. Kishiyama, H. Atarashi, and M. Sawahashi, "Variable spreading factor-ofcdm with two dimensional spreading that prioritizes time domain spreading for forward link broadband wireless access," in *Vehicular Technology Conference, 2003. VTC 2003-Spring. The 57th IEEE Semiannual*, vol. 1, april 2003, pp. 127 – 132 vol.1.
5. H. Atarashi, N. Maeda, S. Abeta, and M. Sawahashi, "Broadband packet wireless access based on VSF-OFCDM and MC/DS-CDMA," in *Personal, Indoor and Mobile Radio Communications, 2002. The 13th IEEE International Symposium on*, vol. 3, sept. 2002, pp. 992 – 997 vol.3.

6. N. Maeda, H. Atarashi, S. Abeta, and M. Sawahashi, "Throughput comparison between VSF-OFCDM and OFDM considering effect of sectorization in forward link broadband packet wireless access," in *Vehicular Technology Conference, 2002. Proceedings. VTC 2002-Fall. 2002 IEEE 56th*, vol. 1, 2002, pp. 47 – 51 vol.1.

7. J. Blumenstein, Z. Fedra, and V. Sebesta, "Performance of pilot aided channel estimation technique in 2D spreading based systems," *Radioengineering*, vol. 19, pp. 507–510, 2010.

8. C.-C. Chong, F. Watanabe, H. Inamura, D. Wang, H. Minn, and N. Al-Dhahir, "On the performance comparison of VSF-OFCDM and OFDM," in *Personal, Indoor and Mobile Radio Communications, 2008. PIMRC 2008. IEEE 19th International Symposium on*, sept. 2008, pp. 1 –6.

9. S. Sesia, I. Toufik, and M. Baker, *LTE, The UMTS Long Term Evolution: From Theory to Practice.* John Wiley & Sons, 2009.

10. "Recommendation ITU-R m.1225: Guidelines for evaluation of radio transmission technologies for IMT-2000," Tech. Rep., Tech. Rep., 1997.

11. 3GPP, "Technical specification group radio access network; deployment aspects (release 7)," 3GPP, Tech. Rep. 25.943 V7.0.0, Jan 2007.

12. K. Fazel and S. Kaiser, *Multi-carrier and spread spectrum systems: from OFDM and MC-CDMA to LTE and WiMAX.* Wiley, 2008. [Online]. Available: http://books.google.com/books?id=RzUJsPqe-dgC

13. 3GPP Technical Specification Group RAN, "E-UTRA; physical channels and modulation," 3GPP, Tech. Rep. TS 36.211 Version 8.7.0, May 2009.

14. ——, "E-UTRA; multiplexing and channel coding," 3GPP, Tech. Rep. TS 36.212, March 2009.

15. ——, "E-UTRA; physical layer procedures," 3GPP, Tech. Rep. TS 36.213, March 2009.

16. L. Hanzo, *OFDM and MC-CDMA for broadband multi-user communications, WLANs, and broadcasting.* J. Wiley, 2003. [Online]. Available: http://books.google.com/books?id=hQ6bl3RG04sC

Channel estimation method for OFDM in low SNR based on two-dimensional spreading

Jiri Blumenstein, Roman Maršálek, Zbynek Fedra, Aleš Prokeš, Christoph Mecklenbräuker

Channel estimation method for OFDM in low SNR based on two-dimensional spreading

J. Blumenstein, R. Maršálek, Z. Fedra,
A. Prokeš, Ch. Mecklenbräuker

Abstract In this paper, we present a channel estimation method based on two-dimensional signal spreading applicable to Orthogonal Frequency Multiple Access (OFDM) multicarrier systems. Our method exploits a spreading of a transmitted data signal as well as a pilot signal over the assigned frequency range and time period. As a spreading sequence we exploited orthogonal Walsh-Hadamard sequences.

When compared with traditional pilot symbol based channel estimation, our method is beneficial in low Signal to Noise Ratio (SNR).

For a comparison of our method with state-of-the-art channel estimation method, we utilized an open source LTE downlink simulator developed at TU Vienna. This enables a reproducibility of our results. Considering the LTE system, our method outperforms the traditional approach in typical range of SNR from -5 dB to 10 dB. For a comparison of a throughput performance, a number of channel models has been employed.

Keywords Channel estimation · LTE · 2D signal spreading · OFDM

1 Introduction

Precise yet robust channel estimation is one of the key enablers of the vast data throughput increases we had experienced in last two decades. Considering a state-of-the-art example of multicarrier communication system, the Channel State Information (CSI) is usually obtained by comparison of the received

J. Blumenstein, R. Maršálek, Z. Fedra, A. Prokeš
Department of Radio Electronics Brno University of Technology Purkyňova 118, 612 00, Brno, Czech Republic, E-mail: xblume00@phd.feec.vutbr.cz

Ch. Mecklenbräuker
Institute of Telecommunications, Vienna University of Technology Gusshausstrasse 25/389, A-1040 Vienna, Austria, E-mail: christoph.mecklenbraeuker@tuwien.ac.at

training sequences with the transmitted ones which are known at the receiver side [1].

This training sequence has to be two-dimensional in order to tackle the channel transfer function fluctuations in both the time and frequency domains [2]. Therefore, the training sequence, or more commonly the pilot symbols, occupies certain time and frequency resources which are then unable to carry any data payload. Between those time-frequency resources occupied by the pilot symbols, the CSI stays unknown and can only be estimated by interpolation [3].

Obviously, the more pilot symbols and the denser the time-frequency estimation grid we apply, the more reliable CSI. However, the higher overhead and the lower data throughput. Nowadays, the effort is focused mainly to determine the most effective way of processing the channel state information samples. High effort is also given into a research of a pilot density [4], or optimal pilot power allocation [5]. Moreover, second order statistic data about the noise distribution are exploited in order to improve the CSI reliability [6], thus throughput performance.

The idea of two-dimensional signal spreading in systems employing the Orthogonal Frequency Division Multiplex (OFDM) is presented in [7,8], where the authors exploit a possibility of one-cell frequency reuse which led to significant throughput increase compared with three-cell frequency reuse. This had been possible due to the utilization of an orthogonal signal spreading, thus profiting by a code domain as well known from Code Division Multiple Access (CDMA) systems.

However, one-cell reuse is supposed for LTE [9], so we could not benefit from obtaining any additional frequency bands. Conversely, to keep the comparison of newly presented method with the state-of-the-art fair, the bandwidth widening is not acceptable.

The method proposed in this paper incorporates the two-dimensional signal spreading as we presented in [10]. However, in mentioned paper, the spreading is done only over the signal, which carries useful data. Thus, the pilot structure remains LTE standard compliant. As such, the method in [10] outperforms the standard LTE in rather high SNRs taking advantage of increased time-frequency diversity.

Our novel method for channel estimation proposes to spread the pilot signal as well as the useful data signal all over the assigned time and frequency space. As a result, each pilot symbol will be a composite of several spread parts (chips), each influenced by a noise individually. Thus the resulting CSI will be more robust to noise influence. This is nevertheless a trade off between a noise robustness and detailed resolution of the CSI. Compared with one traditional pilot symbol, several pilot chips consumes more time-frequency resources.

To provide a fair comparison, our system model is based on the open source Vienna LTE simulator [11–13]. We believe that this approach enables a repeatability and also improves the credibility of our results.

The remainder of this paper is organized as follows: In Section System Model, the principle of the method and the implementation of the 2D sig-

nal spreading into the LTE signal processing chain is described including the method for pilot symbol spreading. In Section Experiment and Results the comparison of the standard LTE downlink and the 2D spreading based estimation enriched LTE transmission is provided. We used number of channel models as VehA, VehB, ETU, RA, PedA, PedB or HT [14, 15]. Section Conclusion rounds up the paper.

2 System model

In order to illustrate the principle of the method, we consider the implementation to the LTE physical layer system model. The aim of this section is to describe the LTE features related to the proposed method. The LTE utilizes a frequency bandwidth BW, where BW $\in (1.4, 3, 5, 10, 15, 20)$ MHz. This corresponds to the number of resource block $N_{rb} \in (6, 15, 25, 50, 75, 100)$, where so called resource block is a grouping of 12 subcarriers with 15 kHz spacing.

In time domain, as visible in Figure 1, the resources are described as frames, which lasts for 10 ms, those are divided into two slots and further, the slots consists of ten equal subframes with duration of 0.5 ms. One subframe then consists of 14 OFDM symbols. An intersection of one OFDM symbol and one subcarrier forms a resource element.

As depicted in Figure 2, LTE time-frequency grid contains pilot symbols that occupy certain resource elements. The placing of those pilot-symbols is standardized [16], nevertheless LTE does not mandate any specific channel estimation technique so there is a complete freedom in implementation assuming that the performance requirements are met and the complexity is affordable [9].

Since we benefit from utilization of the LTE downlink simulator [11,12], an implementation of our novel method is straightforward. The signal processing chain of the LTE simulator is visible in Figure 3 with white-marked blocks according to standard [16–18]. The dark gray blocks represent the additional non-LTE standard compliant blocks for 2D spreading, despreading, modified frame builder and channel estimation.
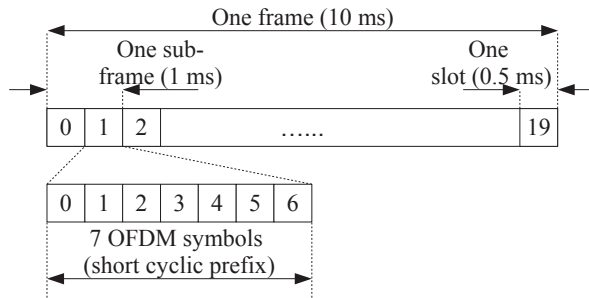
Fig. 1 The description of LTE resources in time domain. In case of 'normal' cyclic prefix we utilize 7 OFDM symbols in one subframe.
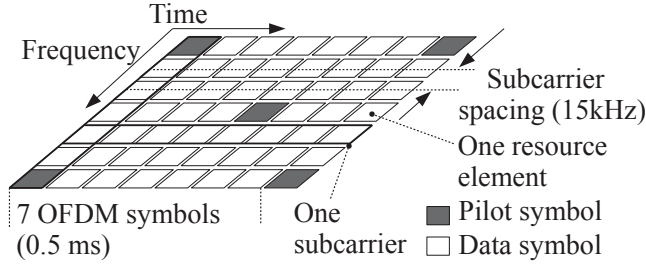
Fig. 2 The pilot symbols (gray) are placed in a 3GPP standard compliant time-frequency pattern. The CSI between the pilot symbols should be estimated via interpolation.

The received signal vector $\mathbf{y} \in \mathbb{C}^{1 \times n}$ is written as:

$$\mathbf{y} = \mathbf{Z}\mathbf{h} + \mathbf{v}, \tag{1}$$

so that the $\mathbf{h} \in \mathbb{C}^{1 \times n}$ is a vector of channel coefficients, n is a number of transmitted symbols and corresponds to the bandwidth BW. The $\mathbf{v} \in \mathbb{C}^{1 \times n}$ is an additive white Gaussian noise vector. One element of $\mathbf{v}$ is defined according to:

$$v = \sqrt{\frac{N_{\text{fft}}}{N_{\text{tot}}}} 10^{-\frac{SNR}{20}} \left(N(0,1) + jN(0,1) \right), \tag{2}$$

where $N(0,1)$ denotes zero-mean, normally distributed pseudo-random number with variance one. The j stands for basic imaginary unit. Other symbols are described in Table 1. The fraction $\sqrt{\frac{N_{\text{fft}}}{N_{\text{tot}}}}$ compensates the fact that LTE utilizes so-called zero subcarriers and is given in Table 2.

2.1 Least Squares estimation

The $\mathbf{Z} \in \mathbb{C}^{n \times n}$ from Equation 1 is a diagonal matrix written as:

$$\mathbf{Z} = \text{diag}(\mathbf{z}), \tag{3}$$

Table 1 LTE system parameters of the presented simulations

$\mathbb{N}, \mathbb{R}, \mathbb{C}$, and $\mathbb{N}_{0 \leq 1}$	Natural, Real, Complex and Natural non-negative number system respectively.
$N(0,1)$	zero-mean, normally distributed pseudorandom number with variance one.
j	basic imaginary unit
$\otimes$	Kronecker product
$\odot$	Hadamard product
$\mathbf{Z}^{\text{H}}$	Hermitian transpose of $\mathbf{Z}$
$\mathbf{X}_{\mathbf{d}(i,*)}$	i-th row of the matrix $\mathbf{X}_\mathbf{d}$
Ξ	Orthogonal Walsh-Hadamard matrix

Fig. 3 The LTE signal processing chain. The dark gray blocks represents the additional non-LTE standard compliant blocks for 2D spreading, despreading and channel estimation. Other parts remain the same in both versions, 2D spreading based LTE and standard LTE. White blocks are according to [16–18].

where the $\mathbf{z}$ is a permuted data and pilot composite vector $\tilde{\mathbf{z}} = [\mathbf{z_p}^\mathrm{T}, \mathbf{z_d}^\mathrm{T}]^\mathrm{T}$, permuted according $\mathbf{z} = \mathbf{P}\tilde{\mathbf{z}}$ where the matrix $\mathbf{P} \in \mathbb{N}_{0 \leq 1}^{n \times n}$ is a standardized permutation matrix given by [16]. The LS estimation is then performed according:

$$\hat{\mathbf{h}}_\mathrm{p}^\mathrm{LS} = \mathbf{Z}_\mathrm{p}^\mathrm{H} \mathbf{y}_\mathrm{p}. \tag{4}$$

The vector $\mathbf{y}_\mathrm{p} \in \mathbb{C}^{1 \times p}$ represents the received pilot signal of length p and the $\mathbf{Z}_\mathrm{p}^\mathrm{H}$ is the Hermitian transpose of the transmitted signal matrix $\mathbf{Z}$ at specific pilot positions. The channel coefficients between the pilot symbols have to be obtained by interpolation. In the experiments, we apply linear interpolation.

2.2 LMMSE estimation

The Linear Minimum Mean Square Error (LMMSE) estimation requires knowledge of the second-order statistic of the noise and radio channel. It is visible in [19] that the LMMSE estimator represents the filtered Least Squares (LS):

$$\hat{\mathbf{h}}_{\text{LMMSE}} = \mathbf{A}_{\text{LMMSE}}\hat{\mathbf{h}}_{\text{p}}^{\text{LS}}, \tag{5}$$

by minimizing MSE, we obtain the filtering matrix $\mathbf{A}_{\text{LMMSE}}$:

$$\mathbf{A}_{\text{LMMSE}} = \mathbf{R}_{\mathbf{h},\mathbf{h_p}} \left(\mathbf{R}_{\mathbf{h_p},\mathbf{h_p}} + \sigma^2 \mathbf{I} \right)^{-1}, \tag{6}$$

where $\mathbf{R}_{\mathbf{h},\mathbf{h_p}}$ is the channel cross-covariance matrix and $\mathbf{R}_{\mathbf{h_p},\mathbf{h_p}}$ is the channel covariance matrix. $\mathbf{I}$ is the identity matrix and σ^2 is the noise variance. Those variables are assumed to be either exactly known, which represents ideal case, or they needs to be estimated using training sequence. Both those cases are evaluated it the section Experiment and results .

2.3 2D spreading channel estimation method

2.3.1 Transmitter

In this subsection, the system model of the modified 2D spreading based LTE downlink will be described in detail. The signal from the Layer Mapping block represented by vector $\mathbf{x} \in \mathbb{C}^{1 \times n}$, as seen in Figure 3, is written as:

$$\mathbf{x} = [\mathbf{x_d}^{\text{T}}, \mathbf{x_p}^{\text{T}}]^{\text{T}}, \tag{7}$$

The vector $\mathbf{x_d}^{\text{T}} \in \mathbb{C}^{1 \times (n-p)}$ is a vector of data symbols and $\mathbf{x_p}^{\text{T}} \in \mathbb{C}^{1 \times p}$ is a vector of pilot symbols (here we assume vector of ones). Again, the n corresponds with the system bandwidth and p is number of subcarriers. The received signal $\mathbf{y}$ is then, similarly as in the LS case, given by:

$$\mathbf{y} = \mathbf{X_s}\mathbf{h} + \mathbf{v}, \tag{8}$$

where the $\mathbf{h}$ and the $\mathbf{v}$ vectors represent the same variables as in Equation 1. The $\mathbf{X_s} \in \mathbb{C}^{n \times n}$ is also a diagonal matrix describing the spreading operation of the pilots and data. The matrix $\mathbf{X_s}$ is composed as:

$$\mathbf{X_s} = \text{diag} \left(\underbrace{w_{SF} \left(\mathbf{x_p} \otimes \mathbf{\Xi}_{(SF,*)} \right)}_{\text{pilot sequence}} + \underbrace{\sum_{i=1}^{SF-1} w_i \left(\mathbf{X}_{\mathbf{d}(i,*)} \otimes \mathbf{\Xi}_{(i,*)} \right)}_{\text{data}} \right), \tag{9}$$

where

$$\mathbf{X_d} = \begin{bmatrix} x_1 & \cdots & x_{n/SF} \\ x_{n/SF+1} & \ddots & \vdots \\ \vdots & \cdots & x_n \end{bmatrix}, \tag{10}$$

and

$$\mathbf{\Xi} = \begin{bmatrix} \xi_{1,1} & \cdots & \xi_{1,SF} \\ \vdots & \ddots & \vdots \\ \xi_{SF,1} & \cdots & \xi_{SF,SF} \end{bmatrix}. \tag{11}$$

The SF is the spreading factor, the $\mathbf{\Xi} \in \mathbb{N}_{0 \leq 1}^{SF \times SF}$ is the SF-th order Hadamard matrix, the $\otimes$ represents the Kronecker product [20] and the $\mathbf{X}_{\mathbf{d}(i,*)}$ denote i-th row of the matrices $\mathbf{X_d}$. For simplicity, the $\mathbf{x_p} = \mathbf{1}_{1,n/SF}$, i.e. vector of ones of the length $\frac{n}{SF}$. The $\mathbf{x_p}$ is known at the transmitter as well as the receiver side so this is the pilot sequence, later referred to as a pilot layer.

The w_i is an element of a vector $\mathbf{w} \in \mathbb{R}_{>0}^{1 \times SF}$ representing a constant weight factors for adjusting the per-layer SNR. Here we assume the weights 1.5 for the whole pilot layer and 0.99 for all data layers. At the transmitter side, we ensure the same signal power level as in the case of standard LTE downlink signal exploiting RMS power normalization as shown in Figure 4.

Fig. 4 In order to keep the same transmit power levels for both, the standard compliant LTE and the novel 2D spreading method, the RMS based power normalization is employed.

Our novel method for channel estimation results in simplification of the frame builder block so that the spread data symbols will be stacked one after another. Since the data symbols are spread with spreading factor SF, the amount of transmitted chips (spread data symbols) is SF times the number of symbols, it equals to eSF. The chips are summed in a code domain as depicted in Figure 5. In the receiver side, thanks to the orthogonality of Hadamard sequences, code layers can be separated. Due to the addition of the spread signal in the code domain, the resulting signal is of length n, i.e. the same length as in a case of standard LTE, thus the bandwidth of the spread signal remains the same as in the case of standard LTE downlink.

As seen in Figure 5, the first $SF-1$ code layers are devoted to data transmission, whereas the SF-th code layer carries the pilot signal - in Equation 9 noted as the variable $\mathbf{x_p}$.

Table 2 LTE system parameters of the presented simulations:

System bandwidth BW	1.4 MHz
Carrier frequency	2.1 GHz
Number of symbols contained in one subframe	$n \in (816, 960)$
Subcarrier spacing	15 kHz
Subframe duration	1 ms
N_{fft}	128
N_{tot}	72
Number of UE	1
Number of eNodeBs	1
Transmission Scheme	SISO
Number of subframes	1 000
CQI	1-5
SF	48
CP length	'normal' [16]
Channel estimation method	LS and 2D spreading based estimation
Channel model	VehA, VehB, ETU, RA, PedA, PedB, HT [14, 15]
User Terminal (UE) velocity	10km/h

2.3.2 Receiver

The received signal $\mathbf{y} \in \mathbb{C}^{1 \times n}$ can be written as:

$$\mathbf{y} = (y_1, y_2, \ldots, y_n). \tag{12}$$

Similarly to a conventional CDMA receiver, the signal is despread by correlating with the spreading matrix $\mathbf{\Theta} \in \mathbb{N}_{0 \leq 1}^{SF \times n}$. First step is the Hadamard multiplication with the despreading matrix:

$$\mathbf{Y} = \begin{pmatrix} \mathbf{y}_1 \\ \mathbf{y}_2 \\ \vdots \\ \mathbf{y}_{SF} \end{pmatrix}, \text{where } \mathbf{y}_{\text{v}} = \frac{1}{\text{SF}} \left(\mathbf{y} \odot \mathbf{\Theta}_{(\text{v},*)} \right), \tag{13}$$
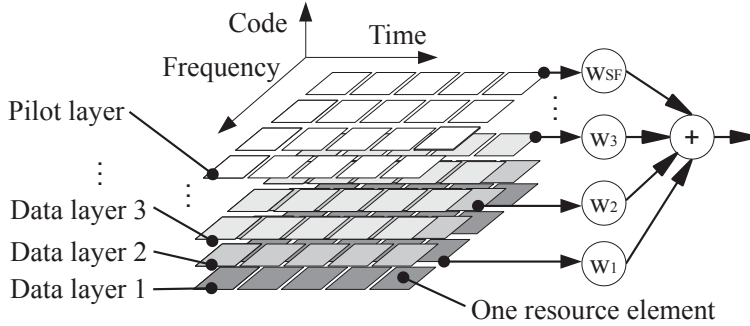
Fig. 5 Proposed novel 2D spreading based time-frequency-code grid. The first $SF-1$ code layers are devoted to data transmission, whereas the SF-th code layer carries the pilot signal. The $\mathbf{w}$ is a vector of constant weight factors for adjusting the per-layer SNR.

where the $\odot$ represents the Hadamard product [20] and the despreading matrix $\boldsymbol{\Theta}$ is the $\frac{n}{SF}$ times replicated $\boldsymbol{\Xi}$ matrix. This is written as:

$$\boldsymbol{\Theta} = \left[\boldsymbol{\Xi}_1, \boldsymbol{\Xi}_2, \ldots, \boldsymbol{\Xi}_{\frac{n}{SF}}\right] \text{ such that } \boldsymbol{\Xi}_{\mathrm{m}} = \boldsymbol{\Xi}, \forall \mathrm{m} \in \left(1, 2, \ldots, \frac{\mathrm{n}}{\mathrm{SF}}\right). \quad (14)$$

The resulting matrix $\mathbf{Y_d} \in \mathbb{C}^{\frac{n}{SF} \times SF}$ is constructed by partial summation of elements y from the matrix $\mathbf{Y} \in \mathbb{C}^{n \times SF}$ defined in Equation 13:

$$\mathbf{Y_d} = \begin{pmatrix} \mathbf{y_{d1}} \\ \mathbf{y_{d2}} \\ \vdots \\ \mathbf{y_{d \frac{n}{SF}}} \end{pmatrix}, \text{where } \mathbf{y_{d_i}} = \left(\sum_{k=1}^{SF}\{y_{(k,SF(i-1)+1)}\}, \right.$$

$$\left. \sum_{k=1}^{SF}\{y_{(k,SF(i-1)+2)}\}, \ldots, \sum_{k=1}^{SF}\{y_{(k,iSF)}\} \right), \forall i = (1, 2, \ldots, \frac{n}{SF}). \quad (15)$$

Considering the pilot vector as vector of ones, the channel estimate is expressed as SF-th code layer of the $\mathbf{Y_d}$ matrix. Since the pilot layer is transmitted in the spread form, it needs to be spread again in order to achieve complete CSI estimate over all assigned time-frequency recourses. Therefore, no interpolation is needed. Therefore it is straightforward to write:

$$\hat{\mathbf{h}}^{\mathrm{2D}} = \mathbf{y_{d \frac{n}{SF}}} \otimes \boldsymbol{\Xi}_{(SF,*)}. \quad (16)$$

The computational complexity is approximately the same as in the case of the LS method. There is also no need for any kind of a priori information.

3 Experiment and results

The simulations were performed in the modified Vienna LTE downlink simulator with the setting summarized in Table 2 for various channel models (VehA, VehB, ETU, RA, PedA, PedB, HT [14, 15]).

Common metric for comparing channel estimators is a Mean Square Error (MSE) of the channel estimate when compared with a perfect channel knowledge. We test the following estimators:

- LMMSE estimator with ideal covariance matrix
- LMMSE estimator with covariance matrix estimated from a training sequence
- LS estimation
- 2D spreading estimation method

In Figure 6 we can observe MSE performance of all these estimators. The LMMSE estimator with ideal covariance matrix produces the lowest MSEs, however the method exploits a perfect knowledge of the second order statistic of the radio channel, namely the Channel Covariance Information (CCI) [21].

The CCI is not always available, thus it needs to be estimated from the training sequence. Performance of the LMMSE estimator with estimated channel covariance matrix is notably worse and it is close to the LS estimator which does not need the CCI. Our novel method exploits an averaging principle when estimating the CSI, thus it provides superior performance in low SNRs, however at higher SNRs the channel estimate is not as detailed as in the case of LMMSE and LS estimators. This phenomenon is represented by the MSE floor of the 2D spreading based estimation method shown in Figure 6.
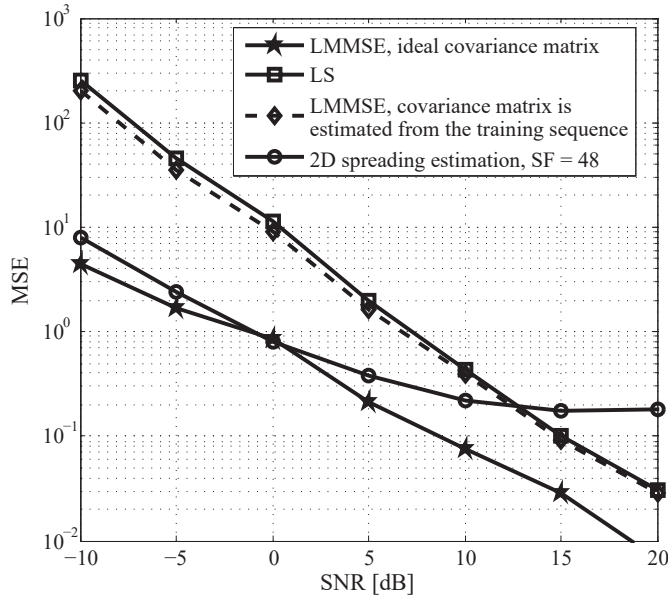
Fig. 6 The dependency of MSE on SNR. Results are plotted for PedA channel model while the channel state is assumed to change during one symbol interval.

In terms of data throughput, which is calculated by counting the acknowledgment bits of correctly received and decoded data, our novel method outperforms the LS method significantly as we can see in Figure 7. Here the left hand side shows the resulting throughput curves for the PedA and the right hand side shows the PedB channel model. Figure 7 compares LS and 2D spreading method only, since the LMMSE with estimated covariance matrix provides almost the same performance as the LS, yet is roughly 4 times computationally more demanding. We do not include the LMMSE with ideal covariance matrix, since in real scenarios the ideal covariance matrix is usually not available.

As seen in Figure 6, our novel method is beneficial mainly under low SNR conditions. For enhanced lucidity, we therefore plotted the throughput curves in Figure 7 only for the CQI 1-5. For higher CQIs our method loses its superiority over the LS and LMMSE and these become the more beneficial methods.

This phenomena is visible in the right part of Figure 7, where above SNR 8 dB the LS method overcomes the 2D spreading based method. Moreover, this correlates with the result presented in Figure 6 leading us to propose a hybrid design, where for low SNRs the 2D spreading based method will be considered, whereas for higher SNRs, the traditional pilot based method will be utilized. The data are provided with the 95% confidence intervals.
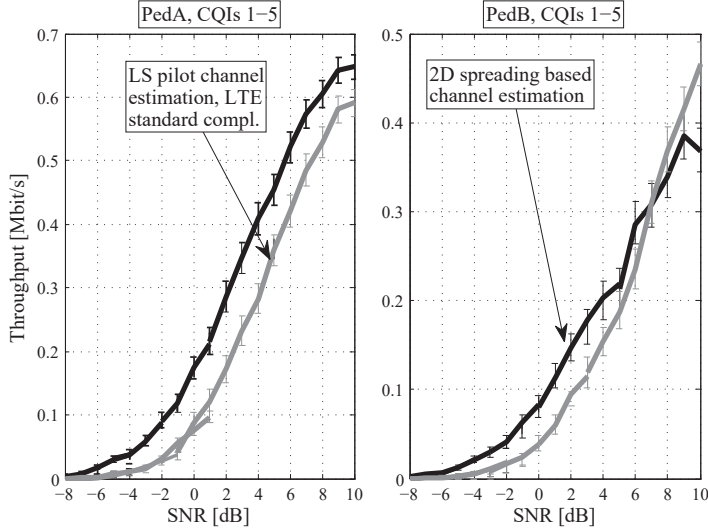
Fig. 7 The Throughputs for PedA and PedB channel models (with 95% confidence intervals). We plotted a maximal throughput curve for CQIs 1-5. Black: 2D spreading based channel estimation, gray: LS pilot based channel estimation.

Considering very low SNR pilot signal at the LS based channel estimation input, its output is obviously highly unreliable. Thus often wrong in a way that the forward error correction mechanism is not able to correctly cope with such distortion which leads to lowering the data throughput.

Our novel method calculates the channel estimate across SF resource elements and then, thanks to the averaging principle, determines the channel estimate. This is of course a trade off between the averaging of the noise and the ability of the estimator to precisely describe the time-frequency variations of the radio channel. It means on the other hand, when considering high SNRs, the pilot-symbol based signal according to the 3GPP is capable to describe the channel state more precisely than the presented spreading based method. Therefore we experience higher throughput at high SNRs for the LS and LMMSE channel estimator. For the high SNRs, however, it may be beneficial to employ the two dimensional signal spreading only over the data signal and keep the channel estimation 3GPP standard compliant. This approach is shown in [10].

We have also researched an influence of the increase of the User Terminal (UE) velocity. As seen in Figure 8, we plotted the data throughput as a function of the UE velocity. This has been done for RA channel model, speeds from 0km/h up to 400km/h and CQI 3. As we can see, the throughput curve naturally decreases with increasing speed, still the 2D spreading based estimation method holds its higher performance over the LS method.

In addition, we compared several other channel models which are available in the Vienna LTE simulator. Table 3 rounds up the results. As an illustrative example, we picked up throughput numbers for CQI 1, SNR = 0dB and UE velocity 10 km/h. Other major parameters are according to Table 2. As we can see from Table 3, in this very favorable conditions for our novel channel estimation method, the throughput increase is perceptible. The throughput increase is from 10% up to more then 50%. It needs to be however said, that for higher SNRs, the throughput increase will be negative.

4 Conclusion

This paper describes a new 2D mapping of spread pilot symbols suitable for multicarrier communication systems suffering by adverse noise conditions. For the credible reference on the performance results, we implemented this method into the state-of-the art simulation system developed at Vienna University of Technology. For a comparison of the proposed channel estimation method enhanced LTE with the standard LTE downlink, we applied various channel models.

The proposed channel estimation method requires only minor modifications of LTE physical layer standard while it brings significant throughput increase in case of low SNR.
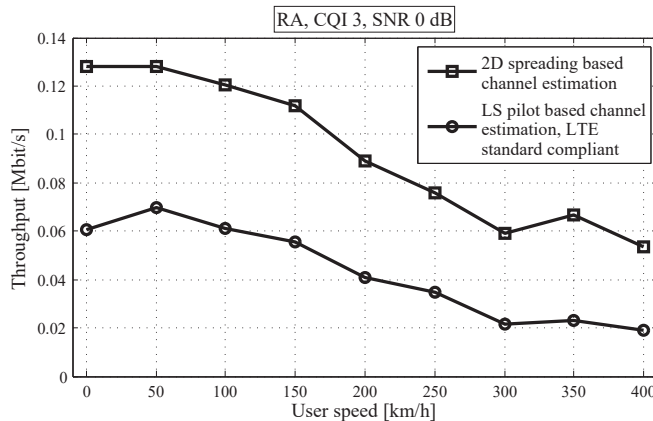
Fig. 8 The Doppler effect influences the throughput performance. The simulation is for CQI = 3, SNR = 0dB and RA channel model.

Table 3 Throughput comparison of the novel 2D spreading based estimation method with LS method

CQI 1, SNR = 0dB	VehA	VehB	ETU	RA	PedA	PedB	HT
Throughout [kbit/s] 2D estim.	43	26	52	65	68	50	34
Throughout [kbit/s] LS estim.	36	24	38	40	45	34	28
Throughout increase [%]	19.44	8.33	36.84	62.5	51.11	47.05	21.43

We showed that in most channel models, the utilization of the 2D spreading based estimation method is beneficial in terms of throughput increase. This increase ranges from 8% up to more than 50%. It should be however noted, that this increase is achieved in low SNR conditions from -10dB to 10dB. Considering higher SNR values, the standard pilot based approach will overcome the 2D spreading based estimation.

The exploitation of the 2D spreading does not require extra bandwidth, there is no need for any a priori information regarding the noise. The computational demands are commensurate to the LS method.

References

1. Y. Li, "Pilot-symbol-aided channel estimation for OFDM in wireless systems," *Vehicular Technology, IEEE Transactions on*, vol. 49, no. 4, pp. 1207–1215, 2000.
2. P. Hoeher, S. Kaiser, and P. Robertson, "Pilot-symbol-aided channel estimation in time and frequency," in *Multi-carrier spread-spectrum*. Springer, 1997, pp. 169–178.
3. X. Dong, W.-S. Lu, and A. Soong, "Linear interpolation in pilot symbol assisted channel estimation for OFDM," *Wireless Communications, IEEE Transactions on*, vol. 6, no. 5, pp. 1910–1920, 2007.
4. S. Lee, K. Kwak, J. Kim, and D. Hong, "Channel estimation approach with variable pilot density to mitigate interference over time-selective cellular OFDM systems," *Wireless Communications, IEEE Transactions on*, vol. 7, no. 7, pp. 2694–2704, 2008.
5. M. Simko, S. Pendl, S. Schwarz, Q. Wang, J. C. Ikuno, and M. Rupp, "Optimal pilot symbol power allocation in LTE," in *Vehicular Technology Conference (VTC Fall), 2011 IEEE*. IEEE, 2011, pp. 1–5.
6. O. Edfors, M. Sandell, J.-J. Van de Beek, S. K. Wilson, and P. O. Borjesson, "OFDM channel estimation by singular value decomposition," *Communications, IEEE Transactions on*, vol. 46, no. 7, pp. 931–939, 1998.
7. H. Atarashi, S. Abeta, and M. Sawahashi, "Variable spreading factor-orthogonal frequency and code division multiplexing VSF-OFCDM for broadband packet wireless access," *IEICE transactions on communications*, vol. 86, no. 1, pp. 291–299, 2003.

8. K. Fazel and S. Kaiser, *Multi-carrier and spread spectrum systems: from OFDM and MC-CDMA to LTE and WiMAX*. Wiley, 2008. [Online]. Available: http://books.google.com/books?id=RzUJsPqe-dgC

9. S. Sesia, I. Toufik, and M. Baker, "LTE-the UMTS long term evolution: From theory to practice, 2009 john wiley & sons, ltd."

10. J. Blumenstein, M. Simko, R. Marsalek, Z. Fedra, J. Prokopec, and M. Rupp, "Two dimensional signal spreading in umts lte: Exploiting time-frequency diversity to increase throughput," *Wireless Personal Communications*, pp. 1–11, 2012. [Online]. Available: http://dx.doi.org/10.1007/s11277-012-0864-3

11. C. Mehlführer, J. C. Ikuno, M. Šimko, S. Schwarz, M. Wrulich, and M. Rupp, "The Vienna LTE simulators - enabling reproducibility in wireless communications research," *EURASIP Journal on Advances in Signal Processing*, vol. Vol. 2011, pp. 1–13, 2011.

12. C. Mehlführer, M. Wrulich, J. C. Ikuno, D. Bosanska, and M. Rupp, "Simulating the long term evolution physical layer," in *Proc. of the 17th European Signal Processing Conference (EUSIPCO 2009)*, Glasgow, Scotland, Aug. 2009. [Online]. Available: http://publik.tuwien.ac.at/files/PubDat_175708.pdf

13. J. Blumenstein, J. C. Ikuno, J. Prokopec, and M. Rupp, "Simulating the long term evolution uplink physical layer," in *ELMAR, 2011 Proceedings*. IEEE, 2011, pp. 141–144.

14. "Recommendation ITU-R M.1225: Guidelines for evaluation of radio transmission technologies for imt-2000," Tech. Rep., Tech. Rep., 1997.

15. 3GPP, "Technical specification group radio access network; deployment aspects (release 7)," 3GPP, Tech. Rep. 25.943 V7.0.0, Jan 2007.

16. 3GPP Technical Specification Group RAN, "E-UTRA; physical channels and modulation," 3GPP, Tech. Rep. TS 36.211 Version 8.7.0, May 2009.

17. ——, "E-UTRA; multiplexing and channel coding," 3GPP, Tech. Rep. TS 36.212, March 2009.

18. ——, "E-UTRA; physical layer procedures," 3GPP, Tech. Rep. TS 36.213, March 2009.

19. S. Omar, A. Ancora, and D. T. M. Slock, "Performance analysis of general pilot-aided linear channel estimation in LTE OFDMA systems with application to simplified MMSE schemes," in *Personal, Indoor and Mobile Radio Communications, 2008. PIMRC 2008. IEEE 19th International Symposium on*, 2008, pp. 1–6.

20. S. Liu and G. Trenkler, "Hadamard, khatri-rao, kronecker and other matrix products," *Int. J. Inform. Syst. Sci*, vol. 4, no. 1, pp. 160–177, 2008.

21. A. Assalini, E. Dall'Anese, and S. Pupolin, "Linear MMSE MIMO channel estimation with imperfect channel covariance information," in *Communications, 2009. ICC '09. IEEE International Conference on*, 2009, pp. 1–5.

Coarse Time Synchronization Utilizing Symmetric Properties of Zadoff–Chu Sequences

Jiri Blumenstein, Marek Bobula

Coarse Time Synchronization Utilizing Symmetric Properties of Zadoff–Chu Sequences

Jiri Blumenstein and Marek Bobula

Abstract— We demonstrate a novel metric for coarse time synchronization suitable for wireless communication. The novel metric benefits from a symmetry of Zadoff–Chu sequences in the time domain. The time-domain symmetry is obtained after a simple manipulation of the sequence polarity. As opposed to the well-known methods, with the utilization of the Zadoff–Chu sequence symmetry property, more correlation terms are possible to be exploited. Thus, the novel metric provides higher correlation gain and notable improvement in the probability of correct time synchronization. The method is evaluated via Monte-Carlo simulations utilizing unique word single-carrier/frequency-domain equalization frames.

Index Terms—Synchronization, UW-SC/FDE, Zadoff-Chu sequences, time-domain symmetry.

I. Introduction

EVEN though being an integral part of wireless communication systems for decades, time synchronization still represents an open research question. For coarse time synchronization, among other sequences, the Zadoff-Chu sequences (ZCs) [1] are especially used due to their favorable autocorrelation properties. Moreover, ZC belongs to the family of constant amplitude zero autocorrelation (CAZAC) waveforms implying a good peak-to-average power ratio (PAPR) and beneficial channel estimating capabilities. On the other hand, the symbols of the ZC sequence are not selected from a common quadrature amplitude modulation (QAM) symbol alphabet, which may be a drawback in certain situations.

In this letter we consider a single carrier system (SC) with frequency domain equalization (FDE) similarly as in the case of Long-Term Evolution (LTE) uplink [2]. As opposed to LTE, where a cyclic prefix (CP) is used, we utilize the concept of unique word (UW), proposed in [3] and [4] and originally intended for orthogonal frequency-division multiplexing (OFDM). The synchronization performance of the UW-SC-FDE approach is compared with other methods in [5]. In CP-OFDM, the cyclic prefix is filled with a random sequence, whereas UW is designed as deterministic. Therefore, UW can be selected optimally for appropriate tasks like synchronization and/or channel estimation [3]. The concept of UW is similar to the approach presented in [6] and [7],

J. Blumenstein is with the Department of Radioeletronics, Brno University of Technology (BUT), 601 90 Brno, Czech Republic (e-mail: blumenstein@vutbr.cz).

M. Bobula is with RACOM s.r.o., 592 31 Nové Město na Moravě, Czech Republic (e-mail: marek.bobula@racom.eu).

where cyclic prefixes together with suffixes and postfixes, respectively, are elaborated.

In this letter, the well-known coarse time synchronization methods by Schmidl *et al.* [8] and derived methods [9]–[11] are further researched while a novel correlative metric is shown. This novel metric utilizes the time-domain symmetry of the ZC sequence and therefore achieves higher correlation gain compared to the state-of-the art methods. Another approach to the coarse synchronization problem, which produces a timing metric without notable sidelobes, is presented in [12]. In essence, it is a differential cross-correlation with ZC weighted by pseudo noise (PN) sequences.

The time-domain symmetry of the ZC sequence is exploited in [13], where symmetric samples are added prior to multiplication with its replica, thus the multiplication complexity is reduced. In [14] a signature format based on symmetric ZC sequences is proposed to deal with the frequency offset being a multiple of subcarrier bandwidth. In this paper, we exploit this symmetry for synchronization purposes. The contribution of the letter is following:

- Demonstration of the novel correlative metric for coarse time synchronization.
- Comparison with well-known methods by *Bhargava et al.* and *Serpedin et al.* showing superior performance in the AWGN channel and partly also in the intersymbol interference (ISI) channel.
- The novel method is not sensitive to a carrier frequency offset (CFO) and provides better in-phase and quadrature sampling resolution, thus improving FDE capabilities.
- We evaluate the influence of the ZC root index influence on the timing accuracy.

II. System Model

A. Synchronization Sequences

Each time instant n of the complex valued ZC sequences $z(n) \in C^{1 \times N_{ZC}}$ is described by:

$$z(n) = \begin{cases} \exp\left(-j\frac{\pi u n(n+1)}{N_{ZC}}\right) & \text{for odd } u, \\ \\ \exp\left(-j\frac{\pi u n^2}{N_{ZC}}\right) & \text{for even } u, \end{cases} \quad (1)$$

where u is the root index and it holds that $0 < u < N_{ZC}$.

B. Synchronization Frame Designs

As a benchmark, we utilize the methods proposed in [9] and [10] which we refer to as *Bhargava et al.* and *Serpedin et al.* The synchronization frame design of the proposed method is different compared to the benchmark methods. The conventional approach is depicted in Fig. 1a.
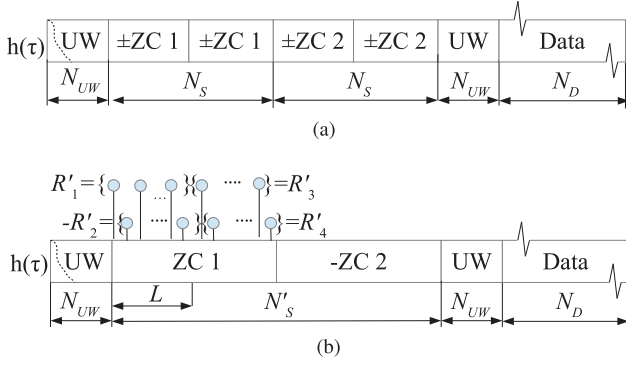
Fig. 1. Schemes of the synchronization frame designs, (a) the methods by *Bhargava et al.* or *Serpedin et al.* (the frames differ in the polarity of the third ZC sequence), (b) The proposed method. The total length of the synchronization frames is equal. The depicted polarity of the $\mathbf{R}'_i$ segments corresponds to the case of odd u.

In particular, the difference to the proposed method is that in Minn *et al.* [9] and Shi and Serpedin [10] use frame schemes [+B+B−B−B] or [+B+B−B+B], respectively, where B stands for the ZC sequence of the length $L = N_S/2$. This means that within one synchronization frame we need to subsequently transmit four ZC replicas with different polarity.

In Fig. 1b, we propose the novel synchronization frame such that the scheme is [+A−A]. Now, A represents a ZC sequence with length $L' = N'_S/2$, i.e., we transmit only two ZCs, however, each sequence is double the length of the sequence used in the conventional schemes $L' = 2L$. Therefore, the in-phase and quadrature sampling is improved and, as ZC sequences of synchronization frames are often used for channel estimation, this capability is potentially enhanced.

C. Unique Word Guard Interval

In order to maintain the possibility to perform cyclical convolution and to transform ZCs into the frequency domain via fast Fourier transform (FFT), we utilize the concept of UW. The common approach with CP could be also used, however, in our case, given that CP would be composed from the partial replica of the synchronization sequence, the correlation metrics may select a timing instant corresponding to CP instead of the intended synchronization sequence. Therefore, in the simulations, we utilize a vector of zeros with a length of twelve samples as the UWs.

D. Timing Metrics

1) State-of-the Art: The received signal, in the case of the benchmark methods, is written as:

$$\mathbf{R}_i = \{r(k+(i-1)L), \ldots, r(k+iL-1)\}, \quad i = [1, 2, 3, 4], \tag{2}$$

where $L = \frac{N_S}{2}$ is the length of the received signal segment $\mathbf{R}_i$, and i indexes signal sections used for the correlation metric according to:

$$\mathbf{M}_B = \frac{|\mathbf{R}_1^H \mathbf{R}_2 + \mathbf{R}_3^H \mathbf{R}_4|}{|\mathbf{R}_2|^2 + |\mathbf{R}_4|^2} \tag{3}$$
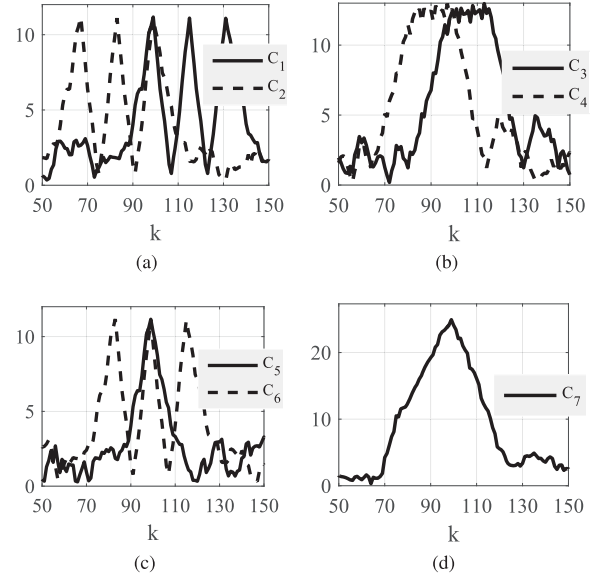
Fig. 2. Individual correlation terms of the proposed metric.

for the *Bhargava et al.* method. Here, $()^H$ is the Hermitian transpose. Please note that four $\mathbf{R}_i$ segments are utilized to determine $\mathbf{M}_B$. Now, the *Serpedin et al.* method utilizes a more complex timing metric written as:

$$\mathbf{M}_S = \frac{|\mathbf{R}_1^H \mathbf{R}_2 + \mathbf{R}_3^H \mathbf{R}_4 - \mathbf{R}_2^H \mathbf{R}_3|}{3(|\mathbf{R}_3|^2 + |\mathbf{R}_4|^2)} + \frac{|\mathbf{R}_1^H \mathbf{R}_3 + \mathbf{R}_2^H \mathbf{R}_4| + |\mathbf{R}_1^H \mathbf{R}_4|}{3(|\mathbf{R}_3|^2 + |\mathbf{R}_4|^2)}, \tag{4}$$

which means that twelve $\mathbf{R}_i$ segments are used. The timing metrics are depicted in Fig. 3b. Please note that we evaluated the methods by *Serpedin et al.* and *Bhargava et al.* not only for the ZC sequences; however, simulations were done also for pseudo-noise sequences and for Legendre sequences resulting in insignificant performance deviations.

2) The Novel Timing Metric: The novel timing metric utilizes different indexing of the received signal. It is written as:

$$\mathbf{R}_{1,2} = \mathbf{R}'_1 || \mathbf{R}'_2 \text{ where}$$
$$\mathbf{R}'_1 = a_1\{r(k), \ldots, r(k+L/2-1)\}$$
$$\mathbf{R}'_2 = a_2\{r(k+1), \ldots, r(k+L/2)\}$$
$$\mathbf{R}_{3,4} = \mathbf{R}'_3 || \mathbf{R}'_4 \text{ where}$$
$$\mathbf{R}'_3 = a_3\{r(k+L/2), \ldots, r(k+L-1)\}$$
$$\mathbf{R}'_4 = a_4\{r(k+L/2+1), \ldots, r(k+L)\}$$
$$\mathbf{R}_{5,6} = \mathbf{R}'_5 || \mathbf{R}'_6 \text{ where}$$
$$\mathbf{R}'_5 = a_5\{r(k+L), \ldots, r(k+2L-1)\}$$
$$\mathbf{R}'_6 = a_6\{r(k+L+1), \ldots, r(k+L+L/2)\}$$
$$\mathbf{R}_{7,8} = \mathbf{R}'_7 || \mathbf{R}'_8 \text{ where}$$
$$\mathbf{R}'_7 = a_7\{r(k+L+L/2), \ldots, r(k+2L-1)\}$$
$$\mathbf{R}'_8 = a_8\{r(k+L+L/2+1), \ldots, r(k+2L)\}, \tag{5}$$

where a_l, $l \in [1, \ldots, 8]$ is an element of vector:

$$\mathbf{a} = \begin{cases} [+1, -1, +1, +1, +1, -1, +1, +1] & \text{for odd } u \\ [+1, -1, +1, -1, -1, +1, -1, +1] & \text{for even } u \end{cases} \tag{6}$$
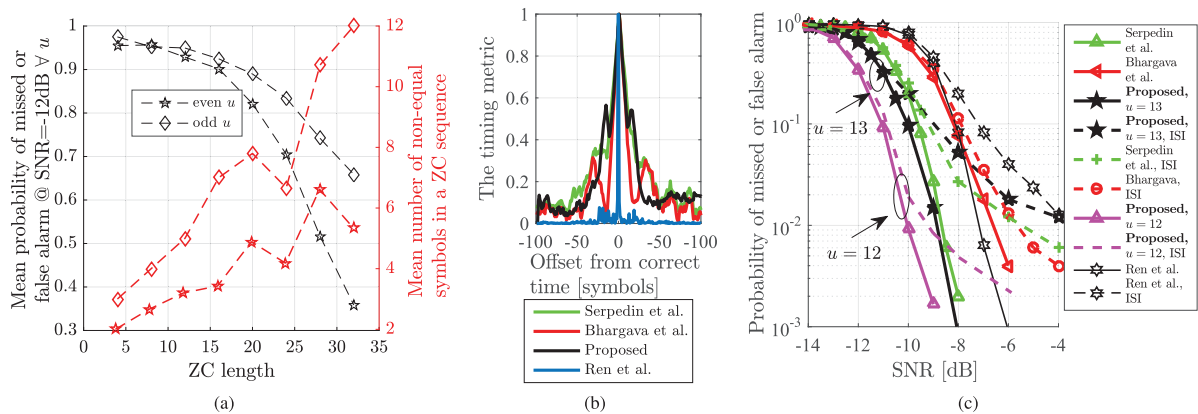
Fig. 3. (a) Influence of the ZC root indexes parity and ZC length. (b) Comparison of normalizer timing metrics (c) The curves of the missed and false alarm probabilities for both AWGN and ISI channels. Utilized root indexes $u = 12$ and $u = 13$.

and where || stands for vector concatenation. Please note that the vector $\mathbf{a}$ controls the polarity of the signal segments $\mathbf{R}'_i$. Then, for one certain time instant, i.e., the intended synchronization moment, it holds that:

$$\mathbf{R}'_i = \pm\mathbf{R}'_{i+2}, \quad i \in [1, 2, 3, 4, 5, 6], \tag{7}$$

which we refer to as the time domain symmetry. It holds for both the real and imaginary parts of $\mathbf{R}'_i$. In fact, Eq. (7) means that every odd and even $\mathbf{R}'_i$ segment are equal. Thus, each concatenated segment $\mathbf{R}_{i,i+1}$, constructed in Eq. (5), contains one $\mathbf{R}'_i$ segment, which is equal to a different $\mathbf{R}'_j$ ($i \neq j$) segment included in a different concatenated $\mathbf{R}_{j,j+1}$ segment. Therefore, we can construct the correlation terms $\mathbf{C}_p$ as:

$$\mathbf{C}_1 = \mathbf{R}_{1,2}^{\mathrm{H}}\mathbf{R}_{3,4}, \quad \mathbf{C}_2 = \mathbf{R}_{5,6}^{\mathrm{H}}\mathbf{R}_{7,8}, \quad \mathbf{C}_3 = \mathbf{R}_{1,2}^{\mathrm{H}}\mathbf{R}_{5,6},$$
$$\mathbf{C}_4 = \mathbf{R}_{3,4}^{\mathrm{H}}\mathbf{R}_{7,8}, \quad \mathbf{C}_5 = \mathbf{R}_{1,2}^{\mathrm{H}}\mathbf{R}_{7,8}, \quad \mathbf{C}_6 = \mathbf{R}_{3,4}^{\mathrm{H}}\mathbf{R}_{5,6},$$
$$\mathbf{C}_7 = (\mathbf{R}_{1,2}||\mathbf{R}_{3,4})^{\mathrm{H}}(\mathbf{R}_{5,6}||\mathbf{R}_{7,8}), \tag{8}$$

where the number of $\mathbf{R}_{i,i+1}, i \in [1, 2, \ldots, 7]$ signal segments used for the correlations is sixteen. It is worth noting that the two ZC sequences utilized in the proposed synchronization frame are divided into four $\mathbf{R}_{i,i+1}$ segments where the length of an individual $\mathbf{R}_{i,i+1}$, segment equals to $L'/2$, i.e., the length L of the ZC sequence utilized in the benchmark schemes. Thus, the total synchronization frame size is equal among the proposed scheme and the schemes proposed by *Bhargava et al.* and *Serpedin et. al*. The individual correlations $\mathbf{C}_p$, $p \in [1, \ldots, 7]$ are depicted in Fig. 2. The correlation terms $\mathbf{C}_1$, $\mathbf{C}_2$ and $\mathbf{C}_5$ create either three equal peaks or a slightly broadened peak in $\mathbf{C}_6$. The correlation terms $\mathbf{C}_3$ and $\mathbf{C}_4$ both exhibit a plateau, similarly as the metric proposed by *Schmidl and Cox*. If the two terms $\mathbf{C}_3$ and $\mathbf{C}_4$ are summed, one distinct peak occurs (as utilized in the method of Wang *et al.* [15]).

In its non-normalized form, the metric is written as:

$$\mathbf{M} = |\mathbf{C}_P| + \sum_{p=1}^{P-1} |\mathbf{C}_p + \mathbf{C}_{p+1}|, \quad \text{where } P = 7. \tag{9}$$

3) Note on the Correlation Gain: The benefit of the proposed timing metric is higher correlation gain compared to the benchmark methods. For example, suppose $N_S = 32$ symbols, i.e. $L = \frac{N_S}{2} = 16$. This means that for calculating

TABLE I

PARAMETER SET OF THE INVESTIGATED
SYNCHRONIZATION FRAME SETUP

Sequences	Zadoff-Chu
N_S / length	32 symbols
N'_S length	64 symbols
Channels	(1) AWGN, (2) ISI (20 samples)
Pulse shaping	RRC (roll-off $= 0.25$)
Samples per symbol	6

$\mathbf{M}_{\mathrm{B}}$ we use $4 \times L = 64$ symbols and for $\mathbf{M}_{\mathrm{S}}$ we utilize $12 \times L = 192$ symbols. For determining the novel metric $\mathbf{M}$ we use $16 \times L'/2 = 256$ symbols. This property clearly enhances the noise tolerance of the novel timing metric.

E. ISI Channel Model and the Carrier Frequency Offset

To emulate multipath propagation, we utilize exponentially decaying normally distributed complex channel taps to convolve with the transmitted signal. The length of such channel impulse response is 20 samples. With 6 samples per symbol, this channel causes ISI over 3.33 symbols. For comparison, we also use the additive white Gaussian noise (AWGN) channel.

Considering a time invariant CFO, the presented method, similarly as the benchmark methods by *Bhargava et al.* and *Serpedin et al.*, is not influenced by the frequency offset and channel phase. This is due to the fact that the CFO influences both ZC 1 and ZC 2 sequences equally. The received signal with the CFO is written as: $r'(k) = r(k)\exp(\mathrm{j}2\pi\epsilon k/N)$, where ϵ is the CFO and the correlation terms form Eq. (8) are written as: $\mathbf{C}_p = \exp(\mathrm{j}2\pi\epsilon k/N)(\mathbf{R}_{i,i+1}^{\mathrm{H}}\mathbf{R}_{j,j+1}), \forall\{p, i, j\}$. Subsequently, as $|\exp(\mathrm{j}2\pi\epsilon k/N)| = 1$, the absolute value operations in Eq. (9) ensures the insensitivity of the metric $\mathbf{M}$ to the CFO.

III. SIMULATION RESULTS

The main simulation results are plotted in Fig. 3c. It shows that the proposed method is superior in the AWGN channel to the methods of *Serpedin et al.*, *Bhargava et al.*, and *Ren et al.*. This is namely due to higher correlation gain. The parameter set of the investigated synchronization setup is in Table I.
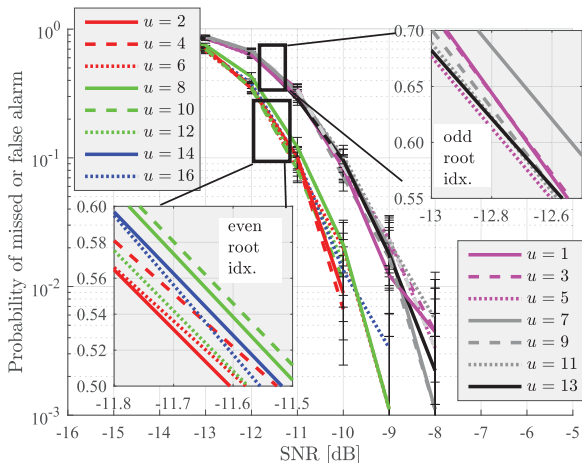
Fig. 4.   Influence of the root index selection and parity on the probability of a missed or false alarm of the proposed method. The curves are equipped with 95% confidence intervals. The ZC length is sixteen symbols.

The method by *Bhargava et al.*, performing worst in solely AWGN, provides better results in ISI from SNR of -6 dB. The method by *Serpedin et al.* performs better in the SNR region from -9.5 dB to -6 dB while the proposed method is superior in the SNR region from -14 dB to -9.5 dB. This holds for the odd u. For the even u, the proposed method outperforms the benchmarks both in AWGN and ISI environment.

1) Root Index Parity: The influence of the root index parity is evaluated via Monte-Carlo simulations and is depicted in Fig. 3a. It is seen that if averaged over all the even or odd root indexes (for the specified ZC length), the even root indexes result to overall better performance. Here it is interesting to point out, that the mean number of non-equal symbols contained in the ZC generated with odd u is significantly higher then the mean number of non-equal symbols generated with even u (see Fig. 3a). This property enables the higher noise resistance of ZCs generated with the even root indexes.

If we compare e.g. the odd root indexes $u = [1, 3, 5, \dots, 15]$, as seen in Fig. 4, we see slightly different results for the individual odd root index realizations. The difference between the best- and the worst-case root index realization is; however, in the order of 0.01 probability of the missed or false alarm at the 9 dB signal-to-noise ratio (SNR) level. While all the depicted 95% confidence intervals include all the simulated odd root indexes, we conclude very weak sensitivity on the root index selection within both root index parity groups.

2) ZC Sequence Length Influence: Another influence on the false or missed alarm probability has the ZC length. Apart from the evident fact, that the longer the ZC, the higher the correlation gain, it is worth mentioning that only the ZC lengths equal to the multiples of four (i.e., $L = [4, 8, 12, \dots]$) provide sharp peak in the proposed metric **M**. The other even ZC lengths (i.e., $L = [2, 6, 10, \dots]$) create a two-symbol wide plateau, thus the resulting synchronization instant is not recognized. Notable cases are the prime ZC lengths which provide equal number of ZC symbols for both the odd and even root indexes. In addition, the prime ZC lengths results to the highest number of non-equal ZC symbols, thus they are not

well suitable for the synchronization (see Fig. 3a). Contrary, for the FDE purposes, the prime ZC lengths are attractive due to higher resolution sampling.

3) Computational Complexity: The relative computational complexity is evaluated with respect to the length of the ZC sequence L and without considering the normalization. Note that we mark the number of multiplications as $(\cdot)$ and the number of additions as $(+)$. For *Bhargava et al.* we have $12L(\cdot)$ and $11L(+)$, for *Serpedin et al.*: $36L(\cdot)$, $39L(+)$ while the proposed method requires $60L(\cdot)$ and $53L(+)$ operations.

IV. Conclusion

The novel timing metric has been proposed and it shows a superior behavior in the AWGN and ISI channel due to higher correlation gain. The novel metric utilizes ZC sequences with twice the length of the benchmark methods; however, the total synchronization frame length is preserved as the number of the required sequence repetitions is halved. The proposed method is invulnerable to the CFO and the phase shift of the channel.

References

[1]   D. Chu, "Polyphase codes with good periodic correlation properties (Corresp.)," *IEEE Trans. Inf. Theory*, vol. 18, no. 4, pp. 531–532, Jul. 1972.

[2]   *Evolved Universal Terrestrial Radio Access (E-UTRA); Physical Layer Procedures*, document TS 36.213, 3GPP Technical Specification Group RAN, Mar. 2009.

[3]   M. Huemer, C. Hofbauer, and J. B. Huber, "Non-systematic complex number RS coded OFDM by unique word prefix," *IEEE Trans. Signal Process.*, vol. 60, no. 1, pp. 285–299, Jan. 2012.

[4]   H. Steendam, "Theoretical performance evaluation and optimization of UW-OFDM," *IEEE Trans. Commun.*, vol. 64, no. 4, pp. 1739–1750, Apr. 2016.

[5]   S. Reinhardt and R. Weigel, "Pilot aided timing synchronization for SC-FDE and OFDM: A comparison," in *Proc. IEEE Int. Symp. Commun. Inf. Technol. (ISCIT)*, vol. 1. Oct. 2004, pp. 628–633.

[6]   M. M. U. Gul, X. Ma, and S. Lee, "Timing and frequency synchronization for OFDM downlink transmissions using Zadoff–Chu sequences," *IEEE Trans. Wireless Commun.*, vol. 14, no. 3, pp. 1716–1729, Mar. 2015.

[7]   C. L. Wang and H. C. Wang, "On joint fine time adjustment and channel estimation for OFDM systems," *IEEE Trans. Wireless Commun.*, vol. 8, no. 10, pp. 4940–4944, Oct. 2009.

[8]   T. M. Schmidl and D. C. Cox, "Robust frequency and timing synchronization for OFDM," *IEEE Trans. Commun.*, vol. 45, no. 12, pp. 1613–1621, Dec. 1997.

[9]   H. Minn, M. Zeng, and V. K. Bhargava, "On timing offset estimation for OFDM systems," *IEEE Commun. Lett.*, vol. 4, no. 7, pp. 242–244, Jul. 2000.

[10]   K. Shi and E. Serpedin, "Coarse frame and carrier synchronization of OFDM systems: A new metric and comparison," *IEEE Trans. Wireless Commun.*, vol. 3, no. 4, pp. 1271–1284, Jul. 2004.

[11]   H. Abdzadeh-Ziabari, W. P. Zhu, and M. N. S. Swamy, "Improved coarse timing estimation in OFDM systems using high-order statistics," *IEEE Trans. Commun.*, vol. 64, no. 12, pp. 5239–5253, Dec. 2016.

[12]   G. Ren, Y. Chang, H. Zhang, and H. Zhang, "Synchronization method based on a new constant envelop preamble for OFDM systems," *IEEE Trans. Broadcast.*, vol. 51, no. 1, pp. 139–143, Mar. 2005.

[13]   B. M. Popovic and F. Berggren, "Primary synchronization signal in E-UTRA," in *Proc. IEEE 10th Int. Symp. Spread Spectr. Techn. Appl.*, Aug. 2008, pp. 426–430.

[14]   G. Cui, Y. He, P. Li, and W. Wang, "Enhanced timing advanced estimation with symmetric Zadoff–Chu sequences for satellite systems," *IEEE Commun. Lett.*, vol. 19, no. 5, pp. 747–750, May 2015.

[15]   K. Wang, M. Faulkner, J. Singh, and I. Tolochko, "Timing synchronization for 802.11 a WLANs under multipath channels," in *Proc. ATNAC*, 2003, pp. 1–5.

Block frequency spreading: A method for low-complexity MIMO in FBMC-OQAM

Ronald Nissel, **Jiri Blumenstein**, Markus Rupp

Block Frequency Spreading: A Method for Low-Complexity MIMO in FBMC-OQAM

Ronald Nissel[†], Jiri Blumenstein[‡], and Markus Rupp[†]

[†]Christian Doppler Laboratory for Dependable Wireless Connectivity for the Society in Motion, TU Wien, Vienna, Austria
[‡]The Faculty of Electrical Engineering and Communication, Brno University of Technology, Brno, Czech Republic
Email: rnissel@nt.tuwien.ac.at, blumenstein@feec.vutbr.cz, mrupp@nt.tuwien.ac.at

Abstract—**Filter Bank Multi-Carrier (FBMC) offers better spectral properties than conventional Orthogonal Frequency Division Multiplexing (OFDM). However, the lack of Multiple-Input and Multiple-Output (MIMO) compatibility is one of its biggest obstacles. By spreading symbols in frequency, we are able to restore complex orthogonality in FBMC, so that all MIMO methods known in OFDM can be straightforwardly applied. The spreading process itself has low computational complexity because it is based on a Fast-Walsh-Hadamard transform, thus completely free of multiplications. Orthogonality only holds if the channel is approximately frequency flat within the spreading length. We thus suggest the usage of frequency blocks which are separated by a guard subcarrier. We also investigate the effect of a doubly selective channel on our block frequency spreading approach. Finally, MIMO simulations validate the applicability.**

Index Terms—**FBMC-OQAM, MIMO, Walsh-Hadamard Coding, Multipath channels, Time-varying channels.**

I. INTRODUCTION

Filter Bank Multi-Carrier (FBMC) with Offset Quadrature Amplitude Modulation (OQAM), in short just FBMC, has better spectral properties compared to Orthogonal Frequency Division Multiplexing (OFDM) and usually does not need a Cyclic Prefix (CP) [1]. All this nice features of FBMC, however, come at a price, namely, an intrinsic imaginary interference. A theoretical explanation for the imaginary interference can be found in the Balian-Low theorem. In many cases, the imaginary interference has either no, or only a minor influence on the performance. However, some important techniques, such as pilot symbol aided channel estimation [2], Alamouti's space-time-block-code [3] or maximum likelihood Multiple-Input and Multiple-Output (MIMO) detection [4] are seriously hampered by the imaginary interference and innovative solutions for those challenges need to be found. While there exist many practical solutions for channel estimation [5], the issue of MIMO transmissions is not fully solved yet. The intrinsic imaginary interference prevents a straightforward implementation of space time block codes such as Alamouti's. However, by considering not only one data symbol, but rather clustered symbols, we can circumvent the Balian-Low theorem and restore complex orthogonality. In [3], a Hadamard spreading approach was proposed to enable Alamouti space-time-block-code. Similar, [4] suggested Fast Fourier Transform (FFT) spreading in time. On the other hand, authors in [6] proposed a block-Alamouti scheme (over time). The same method was recently applied by [7] in the frequency domain.

In this paper, we follow the Hadamard spreading approach suggested in [3]. Compared to the recently introduced method in [7], our approach has the following advantages: Firstly, we restore complex orthogonality. Thus, our method not only works for 2×1 Alamouti (as in [7]), but additionally allows to straightforwardly use all other methods known in OFDM, such as channel estimation, space-time-block codes for a higher number of antennas or low-complexity maximum likelihood symbol detection. Secondly, the peak-to-average power ratio is slightly lower due to the spreading process. Thirdly, compared to [7], the required guard overhead is reduced by a factor of two. The disadvantages, on the other hand, are: Firstly, a slightly higher computational complexity. However, only summations are required; no multiplications are necessary! Additionally, by employing a Fast-Walsh-Hadamard transform, we can further decrease the computational complexity, so that it becomes almost neglectable. Secondly, the spreading length must be a power of two. By comparing the pros and cons of our method with the technique proposed in [7], it is evident that Hadamard spreading provides the overall better package.

The novel contribution of our paper can be summarized as follows:

- Authors in [3] assume a frequency flat channel for the frequency spreading approach. We, on the other hand, allow for a doubly-selective channel, propose a block frequency spreading approach and derive closed-form expressions for the induced signal-to-interference ratio.
- In contrast to our paper in [8], [9], we spread in frequency instead of time. This reduces the latency and improves the robustness in a time-variant channel.

In order to support reproducibility, our MATLAB code can be downloaded at **https://www.nt.tuwien.ac.at/downloads/**.

II. FBMC-OQAM

In FBMC we transmit symbols over a rectangular time-frequency grid. Let us denote the transmit symbol at subcarrier position l and time-position k by $x_{l,k}$. The transmitted signal, consisting of L subcarriers and K time-symbols, can then be expressed as:

$$s(t) = \sum_{k=1}^{K} \sum_{l=1}^{L} g_{l,k}(t)\, x_{l,k}, \qquad (1)$$

with

$$g_{l,k}(t) = p(t - kT)\, \mathrm{e}^{\mathrm{j}2\pi\, lF\,(t - kT)}\, \mathrm{e}^{\mathrm{j}\frac{\pi}{2}(l+k)}. \qquad (2)$$

The basis pulse $g_{l,k}(t)$ is, essentially, a time and frequency shifted versions of the prototype filter $p(t)$. We employ the PHYDYAS prototype filter [10]. The variable T denotes the time-spacing and F the frequency spacing (subcarrier spacing). In FBMC, the prototype filter $p(t)$ is orthogonal for a time-frequency spacing of $TF = 2$. To achieve the same data rate as in OFDM (without CP), we reduce the time-spacing as well as the frequency spacing by a factor of two, leading to $TF = 0.5$. This time-frequency squeezing causes interference, which, however, is shifted to the purely imaginary domain by the phase shift $\mathrm{e}^{\mathrm{j}\frac{\pi}{2}(l+k)}$. Taking the real part removes the imaginary interference and allows low-complexity symbol detection. However, we can only transmit real-valued symbols $x_{l,k} \in \mathbb{R}$ in such a way. The underlying imaginary interference in FBMC is problematic for some MIMO techniques, which justifies the block frequency approach presented in Section III.

To simplify analytical investigations, we consider a discrete-time representation in combination with a vector notation [1]. The sampled transmit signal $\mathbf{s} \in \mathbb{C}^{N \times 1}$, see (1), can then be expressed by:

$$\mathbf{s} = \mathbf{G}\,\mathbf{x}, \qquad (3)$$

with

$$\mathbf{G} = \begin{bmatrix} \mathbf{g}_{1,1} & \mathbf{g}_{2,1} & \cdots & \mathbf{g}_{L,1} & \mathbf{g}_{1,2} & \cdots & \mathbf{g}_{L,K} \end{bmatrix}. \qquad (4)$$

Transmit matrix $\mathbf{G}$ is build-up by the transmit vector $\mathbf{g}_{l,k} \in \mathbb{C}^{N \times 1}$, representing the sampled basis pulse in (2). On the other hand, transmit symbol vector $\mathbf{x} \in \mathbb{C}^{LK \times 1}$ in (3) is defined as:

$$\mathbf{x} = \mathrm{vec}\left\{ \begin{bmatrix} x_{1,1} & \cdots & x_{1,K} \\ \vdots & \ddots & \vdots \\ x_{L,1} & \cdots & x_{L,K} \end{bmatrix} \right\} \qquad (5)$$

$$= \begin{bmatrix} x_{1,1} & x_{2,1} & \cdots & x_{L,1} & x_{1,2} & \cdots & x_{L,K} \end{bmatrix}^{\mathsf{T}}. \qquad (6)$$

In an Additive White Gaussian Noise (AWGN) channel, a matched filter maximizes the Signal-to-Noise Ratio (SNR), so that the receive matrix is chosen as $\mathbf{G}^{\mathsf{H}}$. The whole transmission system can then be expressed by:

$$\mathbf{y} = \mathbf{G}^{\mathsf{H}}\mathbf{G}\,\mathbf{x} + \mathbf{G}^{\mathsf{H}}\mathbf{n}, \qquad (7)$$

where $\mathbf{n}$ represent the Gaussian noise, $\mathbf{n} \sim \mathcal{CN}(\mathbf{0}, P_{\mathrm{n}}\mathbf{I}_N)$. The real orthogonality condition in FBMC implies that the transmission matrix is orthogonal only in the real domain, that is, $\Re\{\mathbf{G}^{\mathsf{H}}\mathbf{G}\} = \mathbf{I}_{LK}$. In the appendix, we provide a simple example for such transmission matrix. As comparison, OFDM has (complex) orthogonality, $\mathbf{G}^{\mathsf{H}}\mathbf{G} = \mathbf{I}_{LK}$. Note that for the same transmission bandwidth FL and the same transmission time KT, both systems have the same bit rate (OFDM without CP), despite the fact that FBMC only transmits real-valued symbols ($\to$ half the information). This is possible because FBMC transmits twice as many symbols within the same time interval.
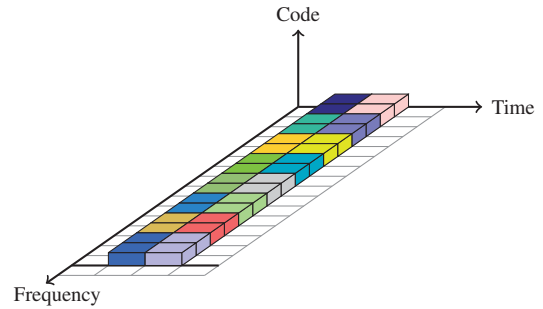
Fig. 1. In conventional FBMC-OQAM, real valued symbols are transmitted over a rectangular time-frequency grid ($TF = 0.5$). Two real valued symbols are required to transmit one complex valued symbol. Thus, the name "offset"-QAM whereas we apply the offset not in time (as often done in literature) but in frequency to be consistent with Fig. 2. Illustration: $L = 16$, $K = 2$.
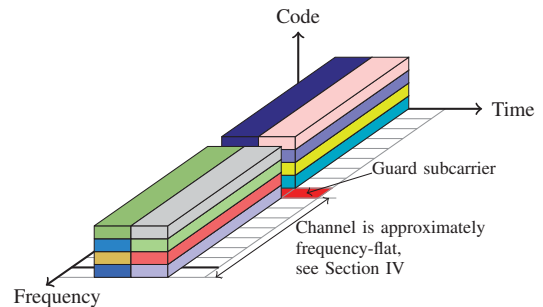
Fig. 2. In coded FBMC-OQAM, complex valued symbols are spread over several subcarriers. The spreading process itself has negligible computational complexity because a Fast-Walsh-Hadamard transform can be used. Different frequency blocks are separated by a guard subcarrier. Fig.: $L = 8$, $K = 2$ and two frequency blocks $\to$ same number of data symbols as in Fig. 1.

III. BLOCK FREQUENCY SPREADING

Fig. 1 illustrates a conventional FBMC transmission. As explained in Section II, we can only transmit real-valued data symbols in FBMC due to the imaginary interference, limiting the applicability of certain techniques such as Alamouti's space time block codes. By spreading symbols in frequency, however, we are able to restore complex orthogonality, so that all transmission techniques known in OFDM, such as Alamouti's space time block codes or multi-user precoding, can be straightforwardly applied in FBMC (on a frequency-block basis instead of per-subcarrier). Our block frequency spreading approach is illustrated in Fig. 2. We assume that the channel is approximately frequency-flat within the spreading interval and approximately time-flat for the duration of one FBMC symbol. This allows the employment of low-complexity equalizers and enables the straightforward usage of MIMO. In Section IV, we will explain in more detail what "approximately" frequency-flat and "approximately" time-invariant means. As indicated in Fig. 2, we add a guard subcarrier between blocks to mitigate interference (orthogonality is only restored within the same block). Because the PHYDYAS prototype filter has very sharp edges in the frequency domain, those frequency blocks are completely separated. This is different to the time-spreading approach we presented in [8], where block interference occurs due to the underlying Hermite prototype filter. A minor

drawback of the guard subcarrier is a reduction in the time-frequency efficiency. We define the time-frequency efficiency loss by

$$\eta = \frac{1}{L+1}. \tag{8}$$

For example, if we spread over $L = 32$ subcarriers, $\eta = 3\%$, implying that the data rate of our approach is 3% lower compared to conventional FBMC. However, a 1.4 MHz Long Term Evolution (LTE) system has an efficiency loss of 28% (72 out of 93.33 subcarriers and a CP length of 4.7μs), so that the efficiency loss of our block frequency spreading approach is relatively low (and to some extend scalable).

Let us now mathematically describe the spreading approach. At the transmitter, we spread the data symbols $\tilde{\mathbf{x}} \in \mathbb{C}^{\frac{LK}{2} \times 1}$ by a precoding (spreading) matrix $\mathbf{C} \in \mathbb{R}^{LK \times \frac{LK}{2}}$, according to

$$\mathbf{x} = \mathbf{C}\,\tilde{\mathbf{x}}. \tag{9}$$

At the receiver, we de-spread the received symbols by $\mathbf{C}^{\mathsf{H}}$, so that the received data symbols $\tilde{\mathbf{y}} \in \mathbb{C}^{\frac{LK}{2} \times 1}$ can be written as:

$$\tilde{\mathbf{y}} = \mathbf{C}^{\mathsf{H}}\,\mathbf{y}. \tag{10}$$

Orthogonality is restored if we are able to find a coding matrix $\mathbf{C}$ which satisfies the following orthogonality condition,

$$\mathbf{C}^{\mathsf{H}}\mathbf{G}^{\mathsf{H}}\mathbf{G}\mathbf{C} = \mathbf{I}_{LK/2}, \tag{11}$$

where $\mathbf{G}^{\mathsf{H}}\mathbf{G}$ represents the FBMC transmission matrix, see (7). By utilizing the underlying structure of our notation (vectorization, see (5) and (6)) and the fact that we spread over frequency only, we are able to rewrite the coding matrix $\mathbf{C}$ by:

$$\mathbf{C} = \mathbf{I}_K \otimes \mathbf{C}_0, \tag{12}$$

where $\mathbf{C}_0 \in \mathbb{R}^{L \times \frac{L}{2}}$ describes the frequency spreading matrix for one time-slot. The Kronecker product $\otimes$ together with the identity matrix then map coding matrix $\mathbf{C}_0$ to the correct time-slot. Finally, we find the coding matrix $\mathbf{C}_0$ by taking every second column out of a sequency ordered [11] Walsh-Hadamard matrix $\mathcal{H} \in \mathbb{R}^{L \times L}$, that is,

$$[\mathbf{C}_0]_{l,m} = [\mathcal{H}]_{l,2m} \quad \text{for} \quad l = 1 \dots L; m = 1 \dots \frac{L}{2}. \tag{13}$$

In the appendix, we provide a simple example of such coding matrix. Note that we could also start from the second column of the Walsh-Hadamard matrix, that is, $[\mathcal{H}]_{l,1+2m}$. In (9) and (10), we describe the spreading process by a coding matrix $\mathbf{C}$. However, we have keep in mind that the internal structure is based on a Walsh-Hadamard matrix, so that a Fast-Walsh-Hadamard transform can be used to reduce the computational complexity. Thus, for each complex valued data symbol, we only need $\log_2(L) - 1$ extra additions/subtractions at the transmitter and $\log_2(L)$ extra additions/subtractions at the receiver. No additional multiplications are required! The only minor drawback of the Walsh-Hadamard approach is that the spreading length has to be a power of two.

IV. DOUBLY-SELECTIVE CHANNELS

Wireless channels are characterized by time-variant multipath propagation, which destroys orthogonality of our system. This results in a certain Signal-to-Interference Ratio (SIR). However, as long as the SIR is approximately 10 dB higher than the SNR, the noise completely dominates the interference which can thus be neglected. Even if the SNR approaches the SIR, we only observe a small performance degeneration equivalent to an SNR shift of approximately 3 dB.

To characterize the influence of a doubly-selective channel, we ignore noise and include a time-variant convolution matrix $\mathbf{H} \in \mathbb{C}^{N \times N}$ in our system, so that (10) together with (7) and (9) transform to:

$$\tilde{\mathbf{y}} = \mathbf{C}^{\mathsf{H}}\mathbf{G}^{\mathsf{H}}\mathbf{H}\mathbf{G}\mathbf{C}\,\mathbf{x}. \tag{14}$$

In a doubly-flat Rayleigh channel, that is, $\mathbf{H} = \bar{h}\,\mathbf{I}_N$ with $\bar{h} \sim \mathcal{CN}(0,1)$, orthogonality still holds. However, in a doubly-selective channel, matrix $\mathbf{H}$ is no longer a scaled identity matrix, leading to off-diagonal elements in $\mathbf{C}^{\mathsf{H}}\mathbf{G}^{\mathsf{H}}\mathbf{H}\mathbf{G}\mathbf{C}$ and thus interference. The diagonal elements, on the other hand, describe the desired signal components and are utilized in a one-tap equalizer. To derive an analytical SIR expression, we consider the received data symbol at code position m and time-position k, so that (14) transforms to:

$$\tilde{y}_{m,k} = \mathbf{c}_{m,k}^{\mathsf{H}}\mathbf{G}^{\mathsf{H}}\mathbf{H}\mathbf{G}\mathbf{C}\,\mathbf{x} \tag{15}$$

$$= \left((\mathbf{G}\mathbf{C}\,\mathbf{x})^{\mathsf{T}} \otimes (\mathbf{c}_{m,k}^{\mathsf{H}}\mathbf{G}^{\mathsf{H}})\right)\text{vec}\{\mathbf{H}\}. \tag{16}$$

Vector $\mathbf{c}_{m,k} \in \mathbb{R}^{N \times 1}$ represents the i-th column of $\mathbf{C}$ with $i = \frac{L}{2}(k-1) + m$. Furthermore, we rewrite (15) by (16) in order to simplify statistical investigations, allowing us to express the SIR by

$$\text{SIR}_{m,k} = \frac{[\boldsymbol{\Gamma}]_{i,i}}{\text{tr}\{\boldsymbol{\Gamma}\} - [\boldsymbol{\Gamma}]_{i,i}}, \tag{17}$$

with $i = \frac{L}{2}(k-1) + m$, and

$$\boldsymbol{\Gamma} = \left((\mathbf{G}\mathbf{C})^{\mathsf{T}} \otimes (\mathbf{c}_{m,k}^{\mathsf{H}}\mathbf{G}^{\mathsf{H}})\right)\mathbf{R}_{\text{vec}\{\mathbf{H}\}}\left((\mathbf{G}\mathbf{C})^{\mathsf{T}} \otimes (\mathbf{c}_{m,k}^{\mathsf{H}}\mathbf{G}^{\mathsf{H}})\right)^{\mathsf{H}}. \tag{18}$$

The j-th diagonal element of $\boldsymbol{\Gamma}$ is denoted by $[\boldsymbol{\Gamma}]_{j,j}$ and represents the contribution of transmit symbol $[\mathbf{x}]_j$ on the received power $\mathbb{E}\{|\tilde{y}_{m,k}|^2\}$. Thus, we can directly calculate the SIR as shown in (17). The statistical properties of the channel are included in the correlation matrix, $\mathbf{R}_{\text{vec}\{\mathbf{H}\}} = \mathbb{E}\{\text{vec}\{\mathbf{H}\}\text{vec}\{\mathbf{H}\}^{\mathsf{H}}\}$, and depend on the power delay profile and the Doppler spectral density.

One of the biggest challenges is to find a meaningful channel model. For example, it has been shown in [12] through real world 3G measurements that in many cases, the Root Mean Square (RMS) delay spread is lower than typically assumed in simulations. We expect that the RMS delay spread will further decrease due to beamforming, higher carrier frequencies and smaller cell sizes. This is particularly important for our frequency spreading approach which only works for a low delay spread. To cover a large range of possible scenarios, we include three different Rayleigh fading
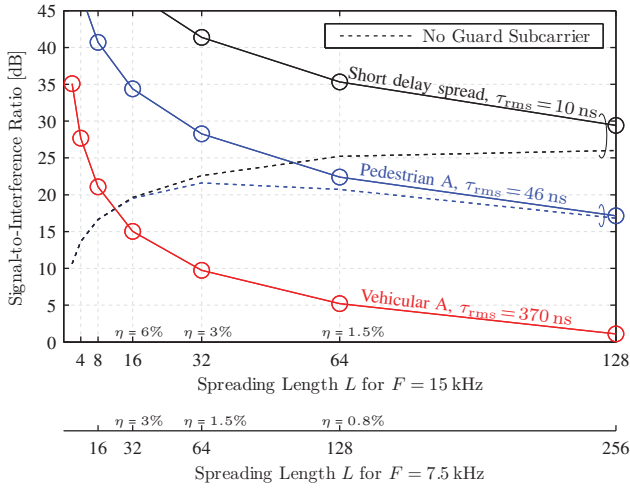
Fig. 3. The interference can be neglected if the SIR is approximately 10 dB higher than the SNR. A guard subcarrier increases the SIR significantly, especially for a short spreading length. The higher the spreading length, the higher the spectral efficiency. However, a high spreading length also leads to high interference caused by the channel.

Fig. 4. A time-variant channel leads to additional interference. For high velocities, FBMC shows approximately the same SIR as OFDM. Thus, OFDM no longer performs better in terms of SIR but has a worse spectral efficiency than FBMC. The SIR for velocity zero can be found in Fig. 3.

channel models in our performance evaluation. Firstly the Vehicular A channel model [13] with a relatively large delay spread of 370 ns. Secondly, the Pedestrian A channel model [13] with a moderate delay spread of 46 ns. Thirdly, a short delay spread of 10 ns for which we assume 3 equally spaced taps. These taps are 100 ns apart and the power of each tap is 20 dB lower then the previous tap. Such short delay spread represents, for example, an indoor scenario.

Fig. 3 shows how the SIR, see (17), depends on the spreading length. In many practical cases, the SNR is below 20 dB. Thus, for a short delay spread (10 ns), we can easily spread over $L = 128$ subcarriers, leading to an almost negligible time-frequency efficiency loss of $\eta = 0.8\%$. For a Pedestrian A channel model we are able to spread over $L = 32$ subcarriers, leading to $\eta = 3\%$. Only for a high delay spread, our method is suboptimal due to the large overhead required for a sufficiently high SIR. Alternatively, we could employ multi-tap equalizers at the cost of increased computational complexity [14]. As a reference, we also include the SIR in case of no guard subcarriers (dotted line). In some cases, especially for low to medium SNR ranges, we do not need a guard subcarrier, leading to a maximum spectral efficiency ($\eta = 0\%$).

Fig. 4 shows how the SIR depends on the velocity. Even high velocities, such as 200 km/h, generate only small additional interference, so that the SIR remains sufficiently high for a short delay spread and a Pedestrian A channel model. Compared to the time-spreading approach we investigated in [8], frequency spreading provides higher robustness in time-variant channels. As a reference, we also include the SIR for conventional CP-OFDM.

V. MIMO SIMULATIONS

So far, we have presented a detailed description of how spreading can be used to restore complex orthogonality. This allows the straightforward usage of all MIMO techniques
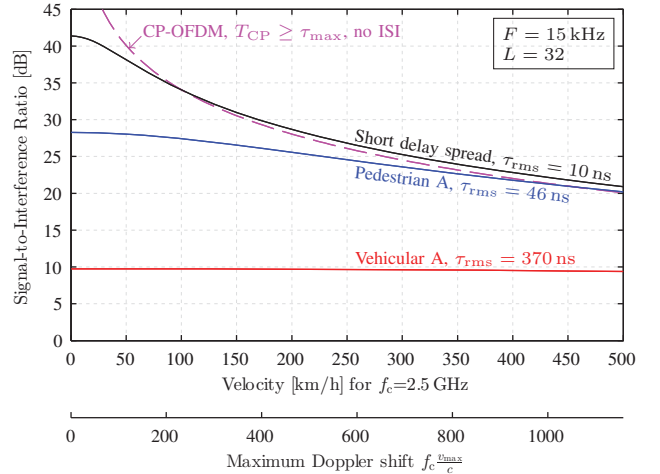
known in OFDM. In this section, we validate the applicability of our block frequency spreading approach by simulations. We assume a Pedestrian A channel model and a Jakes Doppler spectrum (velocity 100 km/h at 2.5 GHz). The subcarrier spacing is set to $F = 15$ kHz and the symbol alphabet is chosen from a 16-Quadrature Amplitude Modulation (QAM) signal constellation. For FBMC we assume a spreading length of $L = 32$ and a total of $N_B = 16$ frequency blocks. This leads to a transmission bandwidth of $F(L + 1)N_B = 7.92$ MHz. OFDM uses the same bandwidth, that is 528 subcarriers. Note, however, that in practice, OFDM requires additional guards band due to its large out-of-band emissions. The transmission time is for both methods the same and given by $KT = 1$ ms. The zero guard subcarrier in FBMC leads to a slightly higher SNR compared to OFDM (but only by $(L + 1)/L = 1.03$ which has almost no influence).

Similar as in [8], we consider 2×1 Alamouti's block coding. Furthermore, we include maximum likelihood symbol detection whereas we ignore any channel induced interference to keep the complexity low. Both of these schemes do not work with conventional FBMC. As a reference, we also include zero forcing equalization.

Fig. 5 shows that FBMC has almost the same Bit Error Ratio (BER) performance as OFDM [15]. FBMC, however, has the additional advantage of much better spectral properties. Only for high SNR values we observe small deviations between OFDM and FBMC. This can be explained by the channel induced interference which leads to an SIR of approximately 27 dB, see Fig. 4. Such interference, however, has no influence for low to medium SNR values. Only for high SNR values, we might have to decrease the spreading length in order to gain robustness.

VI. CONCLUSION

If the channel delay spread is not too high, block frequency spreading becomes an efficient method to restore complex

$$\mathbf{G}^H\mathbf{G} = \begin{bmatrix} 1 & +j0.2181 & 0 & 0 & +j0.5769 & +j0.1912 & 0 & 0 \\ -j0.2181 & 1 & +j0.2181 & 0 & -j0.1912 & -j0.5769 & -j0.1912 & 0 \\ 0 & -j0.2181 & 1 & +j0.2181 & 0 & +j0.1912 & +j0.5769 & +j0.1912 \\ 0 & 0 & -j0.2181 & 1 & 0 & 0 & -j0.1912 & -j0.5769 \\ -j0.5769 & +j0.1912 & 0 & 0 & 1 & +j0.2181 & 0 & 0 \\ -j0.1912 & +j0.5769 & -j0.1912 & 0 & -j0.2181 & 1 & +j0.2181 & 0 \\ 0 & +j0.1912 & -j0.5769 & +j0.1912 & 0 & -j0.2181 & 1 & +j0.2181 \\ 0 & 0 & -j0.1912 & +j0.5769 & 0 & 0 & -j0.2181 & 1 \end{bmatrix} \tag{19}$$
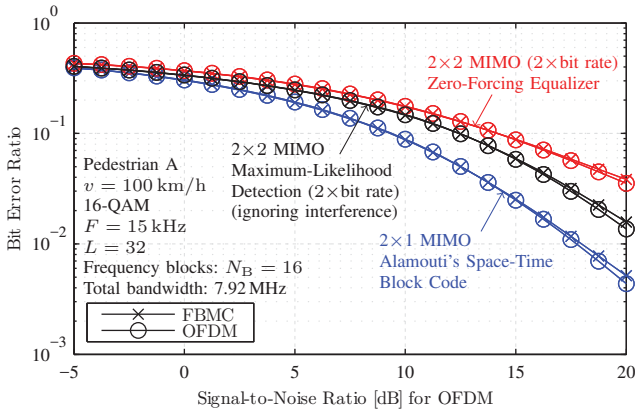
Fig. 5. Simulations validate that FBMC, based on block frequency spreading, has approximately the same BER as OFDM. However, FBMC has the additional advantage of a higher spectral efficiency. Only for high SNR values, we observe small deviations due to channel induced interference, see Fig. 4.

orthogonality in FBMC, allowing us to straightforwardly apply all MIMO methods known in OFDM. To reduce interference between frequency blocks, we might need a guard subcarrier. This reduces the spectral efficiency slightly. The overall spectral efficiency, however, is still much better than in OFDM due to lower out-of-band emissions in FBMC.

APPENDIX

For a better understanding of our notation and the underlying concept, we provide a simple example for $L = 4$ subcarriers and $K = 2$ FBMC symbols. The transmission matrix in (7) can then be calculated as in (19). Note that only real orthogonality holds true, $\Re\{\mathbf{G}^H\mathbf{G}\} = \mathbf{I}_{LK}$. Furthermore, the imaginary interference weight between neighboring subcarriers is given by j0.2181 while between neighboring symbols it is j0.5769. This emphasizes the fact that the PHYDYAS prototype filter has better localization in frequency than in time. By applying the algorithm presented in Section III, see (12) and (13), we find the precoding matrix as:

$$\mathbf{C} = \frac{1}{2}\begin{bmatrix} 1 & 1 & 1 & 1 & 0 & 0 & 0 & 0 \\ 1 & -1 & -1 & 1 & 0 & 0 & 0 & 0 \\ 0 & 0 & 0 & 0 & 1 & 1 & 1 & 1 \\ 0 & 0 & 0 & 0 & 1 & -1 & -1 & 1 \end{bmatrix}^{\mathsf{T}} \tag{20}$$

It can be easily checked that the complex orthogonality condition holds, that is, $\mathbf{C}^H\mathbf{G}^H\mathbf{G}\mathbf{C} = \mathbf{I}_{\frac{LK}{2}}$.

REFERENCES

[1] R. Nissel, S. Schwarz, and M. Rupp, "Filter bank multicarrier modulation schemes for future mobile communications," *IEEE Journal on Selected Areas in Communications*, 2017, to appear.

[2] R. Nissel and M. Rupp, "On pilot-symbol aided channel estimation in FBMC-OQAM," in *IEEE International Conference on Acoustics, Speech and Signal Processing (ICASSP)*, Shanghai, China, March 2016.

[3] C. Lélé, P. Siohan, and R. Legouable, "The Alamouti scheme with CDMA-OFDM/OQAM," *EURASIP Journal on Advances in Signal Processing*, vol. 2010, no. 1, p. 1, 2010.

[4] R. Zakaria and D. Le Ruyet, "A novel filter-bank multicarrier scheme to mitigate the intrinsic interference: application to MIMO systems," *IEEE Trans. Wireless Commun*, vol. 11, no. 3, pp. 1112–1123, 2012.

[5] R. Nissel, S. Caban, and M. Rupp, "Experimental evaluation of FBMC-OQAM channel estimation based on multiple auxiliary symbols," in *IEEE Sensor Array and Multichannel Signal Processing Workshop (SAM)*, Rio de Janeiro, Brazil, July 2016.

[6] M. Renfors, T. Ihalainen, and T. H. Stitz, "A block-Alamouti scheme for filter bank based multicarrier transmission," in *European Wireless Conference (EW)*, 2010.

[7] D. Na and K. Choi, "Intrinsic ICI-free Alamouti coded FBMC," *IEEE Communications Letters*, vol. 20, no. 10, pp. 1971–1974, 2016.

[8] R. Nissel and M. Rupp, "Enabling low-complexity MIMO in FBMC-OQAM," in *IEEE Globecom Workshops (GC Wkshps)*, Washington, USA, Dec 2016.

[9] R. Nissel, E. Zöchmann, M. Lerch, S. Caban, and M. Rupp, "Low-latency MISO FBMC-OQAM: It works for millimeter waves!" in *IEEE International Microwave Symposium*, Honolulu, Hawaii, June 2017.

[10] M. Bellanger, D. Le Ruyet, D. Roviras, M. Terré, J. Nossek, L. Baltar, Q. Bai, D. Waldhauser, M. Renfors, T. Ihalainen *et al.*, "FBMC physical layer: a primer," *PHYDYAS, January*, 2010.

[11] J. Manz, "A sequency-ordered fast Walsh transform," *IEEE Transactions on Audio and Electroacoustics*, vol. 20, no. 3, pp. 204–205, 1972.

[12] H. Asplund, K. Larsson, and P. Okvist, "How typical is the 'typical urban' channel model?" in *IEEE Vehicular Technology Conference (VTC)*, 2008.

[13] "Recommendation ITU-R M.1225: Guidelines for Evaluation of Radio Transmission Technologies for IMT-2000," ITU, Tech. Rep., 1997.

[14] R. Nissel, M. Rupp, and R. Marsalek, "FBMC-OQAM in doubly-selective channels: A new perspective on MMSE equalization," in *IEEE International Workshop on Signal Processing Advances in Wireless Communications (SPAWC)*, Sapporo, Japan, Jul. 2017.

[15] R. Nissel and M. Rupp, "OFDM and FBMC-OQAM in doubly-selective channels: Calculating the bit error probability," *IEEE Communications Letters*, 2017, to appear.

Sensor-based predictive communication for highly dynamic multi-hop vehicular networks

Roman Alieiev, **Jiri Blumenstein** , Roman Maršalek, Thorsten Hehn, Andreas Kwoczek, Thomas Kürner

Sensor-Based Predictive Communication for Highly Dynamic Multi-Hop Vehicular Networks

Roman Alieiev*, Jiri Blumenstein†, Roman Maršalek†, Thorsten Hehn*, Andreas Kwoczek*, Thomas Kürner‡

*Group Research, Volkswagen AG, Wolfsburg, Germany
†The Faculty of Electrical Engineering and Communication, Brno University of Technology, Czech Republic
‡Institut für Nachrichtentechnik, Technische Universität Braunschweig, Braunschweig, Germany
*{roman.alieiev, thorsten.hehn, andreas.kwoczek}@volkswagen.de,
†{blumenstein, marsaler}@feec.vutbr.cz, ‡kuerner@ifn.ing.tu-bs.de

Abstract—**We introduce a sensor-aided predictive algorithm for multi-hop link quality estimation. The proposed concept uses vehicle sensor data to improve a link adaptation and end-to-end path selection for a vehicular multi-hop data transmission. The obtained results show that the proposed concept allows better multi-hop link quality estimation and significantly improves end-to-end transmission characteristics in dynamic vehicular environments.**

I. INTRODUCTION

The process of driving tasks automation and vehicle-to-vehicle (V2V) communications have become key trends in shaping automotive industry of the future. These technological advances combined with various types of mission critical and functional safety applications impose high requirements on the quality of the end-to-end communication between vehicles [1]. However, high dynamics of vehicles, acting as communicating partners, combined with unique properties of vehicular environment such as an impact of Doppler effects, presence of scatterers at both sides of the communication link pose a range of distinct link quality estimation challenges compared to existing cellular-based solutions.

In wireless communications, the optimal transmission scheme is adaptively selected based on the estimated channel state information (CSI). The time required for CSI estimation and dynamics of the channel eventually result in a selection of a suboptimal data transmission scheme and in an overall network performance degradation, also known as CSI aging [2].

The problem of channel estimation and optimal end-to-end path selection in dynamic multi-hop networks is even more challenging. A large number of possible links and hops to be monitored by a decision making node results in an increased mismatch between the estimated and actual CSI at the transmission time.

The importance of minimizing CSI aging is a recognized problem in literature [3]. It has been also shown [4] that technological achievements of modern vehicles lead by developments in automated driving solutions can be beneficially used to improve communication between two vehicles due to a better understanding of the nature of communication link properties. The benefits of sensor-aided prediction for direct link vehicular communications were highlighted in [5]. To the best of our knowledge, existing works do not address the possibility of applying sensor-based vehicular prediction algorithms for a multi-hop link quality forecasting and an end-to-end path selection in highly dynamic vehicular networks.

In current work we extend the concept of sensor-aided predictive communications, originally developed for a direct-link [5], to a multi-hop V2V scenarios. The *key contributions* of this paper are:

- We evaluate the benefit of sensor-based predictive communications in vehicular multi-hop link-quality-estimation tasks,
- We present different ways how the concept of predictive communication can be applied to multi-hop V2V,
- We verify the applicability of the proposed approach via simulation in a select vehicular scenario with realistic sensors and environment properties.

II. THE PROBLEM OF CHANNEL STATE INFORMATION AGING

In this section we highlight the problem of an CSI aging in direct-link and multi-hop vehicular communications.

Let us consider a multi-hop decode-and-forward V2V communication environment. Due to high dynamics of vehicles, surrounded by other objects, the communication link between two partners experiences time-varying large and small scale fading effects. We also assume each relay to employ the single carrier frequency division multiplexing (SC-FDM) with the LTE-A uplink reference symbol structure and a Zero-forcing (ZF) equalization strategy [6].

A. Single-hop CSI aging

Given the aforementioned assumptions, a received symbol vector $\boldsymbol{y}$ at subcarrier k can be expressed as [7]

$$\boldsymbol{y}_k = \boldsymbol{H}_{k,k}\boldsymbol{W}_k\boldsymbol{s}_k + \sum_{k' \neq k} \boldsymbol{H}_{k,k'}\boldsymbol{W}_{k'}\boldsymbol{s}_{k'} + \boldsymbol{n}_k, \qquad (1)$$

where $\boldsymbol{H}_{k,k'} \in \mathbb{C}^{N_r \times N_t}$ is a channel matrix for N_t transmit and the N_r receive antennas between k-th and k'-th subcarrier, $\boldsymbol{W}_k \in \mathbb{C}^{N_t \times N_l}$ is an N_l-layer precoding matrix at k-th subcarrier, and $\boldsymbol{s}_k \in \mathbb{C}^{N_l}$ is a vector of data symbols with σ_s^2 being the average power transmitted on each layer. The component $\sum_{k' \neq k} \boldsymbol{H}_{k,k'}\boldsymbol{W}_{k'}\boldsymbol{s}_{k'}$ represents the impact of the so-called Inter-Carrier Interference (ICI) with the power σ_{ICI}^2,

and $\boldsymbol{n} \in \mathbb{C}^{N_r}$ denotes zero mean additive white Gaussian noise with variance σ_n^2 on antenna n_r.

Since the pilot symbols are separated in time, the time-varying nature of the channel results in an inevitable channel estimation error between the true channel $\boldsymbol{H}$ and the estimated channel $\hat{\boldsymbol{H}}$ at data positions:

$$\boldsymbol{E} = \boldsymbol{H} - \hat{\boldsymbol{H}}, \qquad (2)$$

with σ_e^2 being the mean squared error (MSE) at each element.

Inserting (1) into (2) and denoting $\boldsymbol{e}_{s_k} = \boldsymbol{s}_k - \hat{\boldsymbol{s}}_k$, where $\hat{\boldsymbol{s}}_k$ is the ZF estimate of $\boldsymbol{s}_k$, we compute the layer-dependent symbol estimation MSE covariance matrix [7]:

$$MSE = \mathbb{E}\left\{ \boldsymbol{e}_{s_k} \boldsymbol{e}_{s_k}^{\mathrm{H}} \right\} = (\sigma_n^2 + \sigma_{\mathrm{ICI}}^2 + \sigma_e^2 \sigma_d^2)\hat{\boldsymbol{\Psi}} \qquad (3)$$

where σ_{d} is data symbol power and $\hat{\boldsymbol{\Psi}} \in \mathbb{C}^{N_l \times N_l}$ is the inverse of squared estimated effective channel.

From (3) the following estimated signal-to-interference-plus-noise ratio (SINR) at m-th layer is defined [6]:

$$\hat{\gamma}_m = \frac{\sigma_s^2}{(\sigma_n^2 + \sigma_{\mathrm{ICI}}^2 + \sigma_e^2 \sigma_d^2)\hat{\psi}_m}, \qquad (4)$$

with $\hat{\psi}_m$ being m, m-th element of $\hat{\boldsymbol{\Psi}}$.

Additionally we assume that precoded symbols are transmitted in blocks using a set of M modulation and coding schemes (MCS), $C = \{C_1, C_2, \ldots, C_M\}$, characterized by SINR thresholds S and spectral efficiencies R. The block is assumed to be transmitted efficiently if the estimated SINR $\hat{\gamma}_m$ exceeds the threshold S_j with the selected MCS index j.

Due to channel aging, the actual link quality may deviate from underestimated $\hat{j} < j$ or overestimated $\hat{j} > j$ applied MCS indexes. In the latter case the link will not be able to successfully transmit data and will need an additional time for the failure detection, MCS reconfiguration and data retransmission. As a result, in both cases the the spectral efficiency of the link becomes underutilized.

B. Multi-hop CSI aging

The problem of delayed channel feedback is even more significant in dynamic multi-hop vehicular environments.

To highlight the problem, let us consider a SISO-based multi-hop communication, where the **end-to-end link selection and resource allocation** is done at the node initiating the transmission, denoted as $\mathcal{A}$. Also each node is only capable to signal pilot symbols for channel quality estimation only within its scheduled resource blocks. In this case the *end-to-end multi-hop feedback delay* will have twofold contributions. On one hand, estimation of a reliable CSI-feedback at each link takes time:

$$d_{\mathrm{link}} = k_{\mathrm{avg}} \cdot d_{\mathrm{ps}}, \qquad (5)$$

where d_{ps} is a time interval between two consecutive pilot symbols and k_{avg} is a number of consecutive channel estimations needed to obtain reliable channel feedback.

On the other hand the maximum network-relevant delay $d_{\mathrm{nr,est}}(\mathcal{N})$ between a specific node $\mathcal{N}$ and the decision making node $\mathcal{A}$ is caused by a periodicity of feedback reports d_{pFB}

to the decision making node, time per each hop $i_{\mathcal{N}}$ to deliver $d_{\mathrm{d},i_{\mathcal{N}}}$ and process $d_{\mathrm{pr},i_{\mathcal{N}}}$ the channel relevant information over $I_{\mathcal{N}}$ hops between $\mathcal{A}$ and $\mathcal{N}$:

$$d_{\mathrm{nr,est}}(\mathcal{N}) = d_{\mathrm{pFB}} + \sum_{i_{\mathcal{N}}=1}^{I_{\mathcal{N}}} (d_{\mathrm{d},i_{\mathcal{N}}} + d_{\mathrm{pr},i_{\mathcal{N}}}), \qquad (6)$$

Finally, the vector of maximum feedback delays for the shortest path between the decision making node and each of L nodes of interest will depend on vectors of scheduled feedback periodicities $\boldsymbol{d}_{\mathrm{pFB}}$ and multi-hop feedback delivery times:

$$\boldsymbol{d}_L = k_{\mathrm{avg}} d_{\mathrm{ps}} + \boldsymbol{d}_{\mathrm{pFB}} + \begin{bmatrix} \sum_{i_1=1}^{I_1} (d_{\mathrm{d},i_1} + d_{\mathrm{pr},i_1}) \\ \sum_{i_2=1}^{I_2} (d_{\mathrm{d},i_2} + d_{\mathrm{pr},i_2}) \\ \cdots \\ \sum_{i_L=1}^{I_L} (d_{\mathrm{d},i_L} + d_{\mathrm{pr},i_L}) \end{bmatrix}. \qquad (7)$$

After the required CSI-information has been received by the decision making node, the *path selection* and *resource allocation* process will be affected by feedback delays $\boldsymbol{d}_L$.

In contrast to the path selection and resource allocation, the efficiency of the actual **end-to-end data transmission** at any given link B between node $\mathcal{N}$ and its direct neighbor will be also affected by the maximum delay $d_{\mathrm{nr,est}}(\mathcal{N})$ to deliver and process CSI feedback from $\mathcal{N}$ to $\mathcal{A}$ plus the additional delay to deliver and process data from $\mathcal{A}$ to $\mathcal{N}$ over $I_{\mathcal{N}}$ links:

$$d_{\mathrm{nr,data}}(\mathcal{N}) = d_{\mathrm{nr,est}}(\mathcal{N}) + \sum_{i_{\mathcal{N}}=1}^{I_{\mathcal{N}}} (d_{\mathrm{d},i_{\mathcal{N}}} + d_{\mathrm{pr},i_{\mathcal{N}}}). \qquad (8)$$

Finally, the dynamics of the SINR aging compared to actual SINR $\gamma(B)$ for the fixed path at a given link B will be

$$a_\gamma(B) = \frac{\gamma(B) - \hat{\gamma}(B)}{d_{\mathrm{nr,data}}(\mathcal{N})}. \qquad (9)$$

Based on (4), (7) and (8), the resulting impact of CSI-aging on an end-to-end link efficiency in a multi-hop network will be characterized by the following parameters:

- applied channel estimation techniques
- relation between the dynamics of the link quality change and the feedback delay
- statistical distribution of the feedback delays
- applied method of the feedback delivery
- ability to predict the expected CSI state

III. SENSOR-BASED PREDICTION FOR MULTI-HOP COMMUNICATIONS

The need for channel prediction to compensate a feedback delay is a known problem [3]. Existing approaches collect multiple past channel estimates to predict future channel conditions [8]. Nevertheless, most of them are application- or scenario-limited. For example, the performance of spline interpolation and averaging highly depends on the dynamics of environment, while historical averaging fails completely in dynamic environments with direct link communications [8].
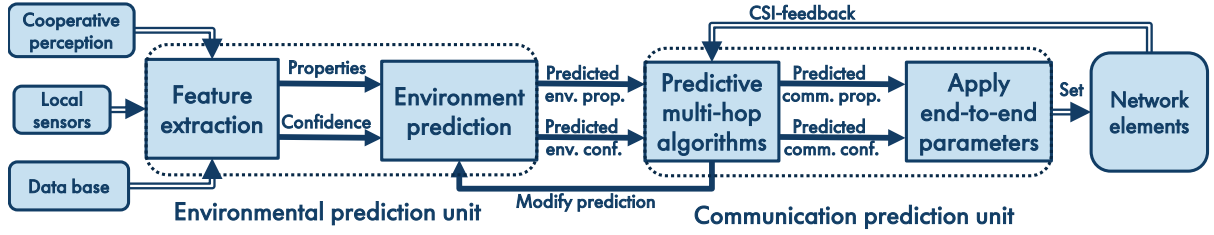
Fig. 1. Block-scheme of the sensor-based multi-hop predictive vehicular communication

A. Sensor-based prediction in V2V communications

Recently it has been shown, that the ability of vehicles to collect surrounding information via on-board sensors brings unique context-aware advantages for direct V2V communications [5]. In this paper we extend the sensor-based prediction scheme to the multi-hop vehicular communication according to Fig. 1 and evaluate corresponding applicability regions.

Let us assume a sensor-equipped vehicle capable to fuse available sensor data, process it and conduct feature extraction. This information can be transferred to the communication system, which will learn about the vehicle's position, dynamics, presence of objects with distinct properties and will enable estimation of expected environmental states. Since the exchange of local information about environment is the inherent property of V2V communications, we assume that each vehicle is capable to obtain dynamic and static properties of the surrounding environment including other vehicles with the precision of the available off-the-shelf sensor equipment.

Let us further assume a V2V network with M vehicles involved in multi-hop communication tasks, as shown in Fig. 2. We further assume that the information about environment is periodically exchanged among the vehicles. Finally at the time instant t the following processed information will be available at the decision making node:

- a vector of M estimated positions and directions $\hat{\boldsymbol{p}}_{\mathrm{vh}}$ combined with absolute velocities of each vehicle $\hat{\boldsymbol{v}}_{\mathrm{dv}}$,
- a matrix of estimated positions $\hat{\boldsymbol{P}}_{\hat{O}}$ and estimated dimensions $\hat{\boldsymbol{D}}_{\hat{O}}$ of $\hat{O}$ detected scattering objects,
- a vector of delayed CSI-feedbacks $\boldsymbol{f}_{\mathrm{CSI}}(\gamma)$ from L scheduled links between M nodes,
- vectors of corresponding feedback delays $\boldsymbol{d}_L$ and data transmission delays $\boldsymbol{d}_{\mathrm{nr,data}}(\mathcal{N})$ defined in (7) and (8),
- a vector of confidence intervals for received feedback parameters, which depend on properties of detected objects.

Based on this information, a range of predictive algorithms can be realized at the decision making node by solving an optimization problem and applying a proper constraint. To mention a few: the minimization of the multi-hop CSI-aging impact, minimization of required feedback over the network, selection of the most efficient or stable end-to-end path, etc.

In the current work we limit our scope on applying the predictive multi-hop communication to minimize the impact of CSI-aging on the end-to-end data transmission efficiency between the decision making node $\mathcal{A}$ and the node $\mathcal{D}$.

Let us define the optimal efficiency at time t of the end-to-end transmission as the spectral efficiency $R_{j,D_{\mathrm{w}}}$ of the weakest link D_{w} between a node $\mathcal{D}_{\mathrm{w}-1}$ and $\mathcal{D}_{\mathrm{w}}$ which has the highest SINR out of all weakest links in all possible paths between $\mathcal{A}$ and $\mathcal{D}$. As it was discussed in Chapter II, the actually selected spectral efficiency for each link deviates from the optimal due to multi-hop CSI-aging. Then, if the end-to-end path was optimally selected and following (8), the *non-predictive* approach according to Section II-B results in the following SINR mismatch:

$$\Delta\gamma_{\mathcal{A}\mathcal{D}}(D_{\mathrm{w}}) = a_\gamma(D_{\mathrm{w}})(d_{\mathrm{pFB}} + 2\sum_{i_{\mathcal{D}_{\mathrm{w}}}=1}^{I_{\mathcal{D}_{\mathrm{w}}}} (d_{\mathrm{d},i_{\mathcal{D}_{\mathrm{w}}}} + d_{\mathrm{pr},i_{\mathcal{D}_{\mathrm{w}}}})).$$

(10)

In contrary, for the *predictive* communication the following algorithm is applied at the decision making node, see Fig. 1:

1) based on available information about environment, such as $\hat{\boldsymbol{p}}_{\mathrm{vh}}$, $\hat{\boldsymbol{v}}_{\mathrm{dv}}$, $\hat{\boldsymbol{P}}_{\hat{O}}$, $\hat{\boldsymbol{D}}_{\mathrm{O}}$, and received delayed CSI-feedbacks from each link of interest, predict the expected CSI-states and confidence intervals for every link d out of L at the time of potential link use,
2) find the optimal end-to-end path from $\mathcal{A}$ to $\mathcal{D}$ given the predicted CSI-states and confidence intervals,
3) start transmission and, if applicable, adjust feedback periodicity requests $d_{\mathrm{pFB,pred}}(\mathcal{D}_{\mathrm{w}}) = d_{\mathrm{pFB}} \cdot d_{\alpha(D_{\mathrm{w}})}$ according to coefficient $d_{\alpha(D_{\mathrm{w}})}$ dependent on prediction deviation parameter $\alpha(D_{\mathrm{w}})$,
4) adjust confidence intervals based on the new feedback.

Now the predictive SINR mismatch at the weakest link D_{w} depends on prediction deviation per unit of time $\alpha(D_{\mathrm{w}})$ and time $d_{\mathrm{pred}}(\mathcal{D}_{\mathrm{w}})$ to reach the link D_{w}, which is similar to the non-predictive $d_{\mathrm{nr,data}}(\mathcal{D})$ case but has variable feedback periodicity parameter $d_{\mathrm{pFB,pred}}(\mathcal{D}_{\mathrm{w}})$ instead of fixed $d_{\mathrm{pFB}}(\mathcal{D})$:

$$\Delta\gamma_{\mathrm{prd}}(D_{\mathrm{w}}) = \alpha(D_{\mathrm{w}})d_{\mathrm{pred}}(\mathcal{D}_{\mathrm{w}}).$$

(11)

Plugging (8) in (11) the expanded form will be:

$$\Delta\gamma_{\mathrm{prd}}(D_{\mathrm{w}}) = \alpha(D_{\mathrm{w}})(d_{\mathrm{pFB}}d_{\alpha(D_{\mathrm{w}})} + 2\sum_{i_{\mathcal{D}_{\mathrm{w}}}=1}^{I_{\mathcal{D}_{\mathrm{w}}}} (d_{\mathrm{d},i_{\mathcal{D}_{\mathrm{w}}}} + d_{\mathrm{pr},i_{\mathcal{D}_{\mathrm{w}}}})).$$

(12)

As can be seen from (12), the sensor-based predictive approach differs by the prediction deviation parameter $\alpha(D_{\mathrm{w}})$ and by the periodicity coefficient $d_{\alpha(D_{\mathrm{w}})}$.
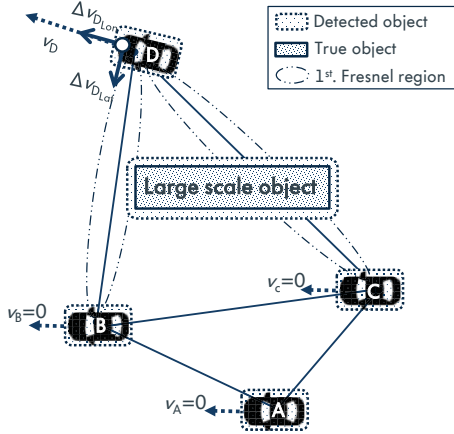
Fig. 2. An illustrative example of multi-hop V2V communication affected by the presence of an obstacle with a static sender node $\mathcal{A}$, two static relay nodes $\mathcal{B}$ and $\mathcal{C}$, and the highly dynamic receiving node $\mathcal{D}$

IV. SIMULATION AND RESULTS

In this chapter we define the scenario of interest, describe the simulation setup and present and discuss obtained results.

A. Scenario definition

In order to conduct simulations we first consider the oversimplified configuration with only four vehicles involved in the communication, denoted as $\mathcal{A}$, $\mathcal{B}$, $\mathcal{C}$, $\mathcal{D}$, as shown in Fig. 2. We assume vehicle $\mathcal{A}$ to be a source, which collects CSI feedback, and vehicle $\mathcal{D}$ a sink of the multi-hop transmission, respectively, while $\mathcal{B}$ and $\mathcal{C}$ are possible relays. Further we assume only vehicle $\mathcal{D}$ to have non-zero velocity of $v_D = 55$ m/s and limit our setup to maximum allowed number of hops being two. We also assume that over the simulation time period the moving vehicle passes next to the obstacle which results in a sharp NLOS-to-LOS transition for the $\mathcal{B}$-$\mathcal{D}$ link.

B. Simulation setup

The simulation was conducted in two phases. First, the link level channel mismatch power levels σ_e^2 discussed in Section II-A were estimated for a typical range of absolute and relative velocities and typical link level channel conditions for the select scenario, namely *Highway: free flow* [9]. The initial simulations were performed in a Matlab-based **V2V link-level simulation environment**, which is developed from the Vienna LTE-A uplink simulator [10]. For this purpose a set of changes was introduced to reflect key properties of direct link V2V environment, for the link-level implementation details and simulation setup, see [5]. For all simulation scenarios we consider a 5.9 GHz carrier frequency, which results in the most challenging Doppler effects among widely used frequencies for V2V communications. Besides these modifications, we estimated the impact of Doppler effects on the SINR based on available sensor information and sensor accuracy [5].

After the link level properties for a select scenario were obtained, the results in terms of estimated mean squared error

(MSE) powers σ_e^2 per Doppler shift, Rician K-factor[1] and sensor-accuracy were plugged into the specifically developed **large scale multi-hop simulation environment**. At this point the evolution of large scale parameters for each object was found. The distance dependent pathloss function for V2V Highway scenario defined in [11] was coupled with the impact of three largest Fresnel zones. Then the correlation properties of slow fading process were coupled with the select scenario properties and with an evolution of each link over space according to [12]. The prediction-relevant properties, such as velocity, positioning and object recognition error parameters are derived from the existing sensor-fusion solutions, available in [13]. Modifications of the simulator and key parameters of both simulation setups are summarized in Table I.

Setup for Simulation and Channel Model	
Antenna configuration	SISO
Tx and Rx ant. heights, [m]	[1.5, 1.5]
Type of a channel Model	Modified SCME [14]
Number of scenario realizations	100
NLOS-LOS transition time, [ms]	80
Carrier Frequency, [GHz]	5.9
Bandwidth, [MHz]	1.4
Access technique	SC-FDMA
Absolute velocity for $\mathcal{A}$, $\mathcal{B}$, $\mathcal{C}$, $\mathcal{D}$, [m/s]	[0, 0, 0, 55]
Slow fading, deviation [dB]	3
Slow fading, 90% correlation distance [m]	1.25
Tx power at each relay, [dBm]	23
Obstacle attenuation, [dB]	[5 : 5 : 20]
Mean position (x, y) error, $\boldsymbol{\mu}^{\Delta p}$	[0, 0]
Position error deviation, $\boldsymbol{\sigma}$	[0.25, 0.5]

TABLE I
SIMULATION SETUP

C. Simulation results

To highlight the benefit of predictive algorithms and to understand the regions of their applicability, in the **first simulation setup** we evaluate the network efficiency loss in terms of SINR mismatch between the actual value and the values available at node $\mathcal{A}$ via delayed CSI feedback of the weakest link over different levels of channel variations a_γ. For this purpose we fix the multi-hop path to be $\mathcal{A}$-$\mathcal{B}$-$\mathcal{D}$ and vary the steepness of the signal attenuation change by changing maximum NLOS attenuation level of the scatterer.

Two different configurations of CSI-feedback updates were considered in this setup: (a) non-predictive periodic CSI-feedback with maximum feedback delays set to $\boldsymbol{d}_{\text{pfb}} = [7, 27]$ ms; (b) predictive periodic CSI-feedback with positioning inaccuracy modeled by Gaussian process with deviation set to $\boldsymbol{\sigma} = [0.25, 0.5]$ m. In the latter case, the prediction and expected steepness of the SINR change for the NLOS-LOS transition of the weakest link is found based on difference between the actual SINR level at NLOS region and expected SINR at the time of LOS. The predicted SINR for the given link as well as the start and end of the NLOS-LOS transition is estimated based on sensor-aided information about environment, available at vehicles, as discussed in Section III-A.

---

[1]The ratio between the power of the specular and diffuse components.
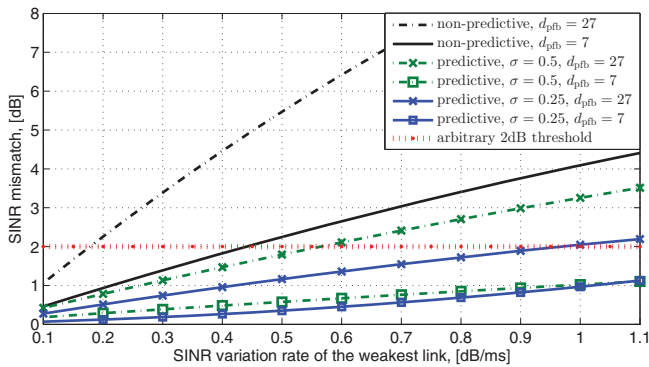
Fig. 3. Impact of the link variation rate on the SINR mismatch, when a multi-hop feedback is delayed. The link variation rate is defined as the SINR variation a rate of the weakest link in the multi-hop setup

Fig. 4. Average number of feedback messages during NLOS-LOS transition. The transition region is defined by the range of attenuation change, which is the difference between maximum and minimum attenuation over the transition process

The results of this simulation setup are shown in Fig. 3. The predictive algorithm shows superior performance compared to the non-predictive algorithms. Additionally, it can be seen that position uncertainty of detected objects (vehicles and obstructing objects) influences the efficiency of predictive approach, while an increase in channel variations deteriorates performance of both algorithms.

In the **second simulation setup** we demonstrate how the predicted information about future CSI at each link reduces the number of feedback messages required to limit the SINR mismatch. For this purpose we consider a non-predictive case with periodic CSI-feedback as in the first simulation setup and predictive approach with the adaptive periodicity of the CSI-feedback generation $d_{pfb,pred}$, as described in Section III-A. First, the SINR mismatch at different levels of SINR variation rates are calculated for various possible feedback intervals, as described in the previous simulation setup. Then certain tolerable threshold is arbitrary selected based on allowed mean SINR mismatch. Finally, the predicted feedback periodicity is obtained from the intersecting point of the arbitrary threshold and one of feedback periodicity curves at position of the expected SINR variation rate. Fig. 3 illustrates the predictive selection of $d_{pfb,pred} = \{7, 27\}$ for the arbitrary threshold of 2 dB (which approximately corresponds to one MCS step). The simulation results presented in Fig. 4 show that predictive algorithms are capable to significantly reduce the number of CSI-feedback over the wide range of transition regions compared to non-predictive periodic CSI-feedback.

V. CONCLUSIONS AND FUTURE WORK

We presented the concept of vehicle sensor-aided predictive link quality estimation for multi-hop V2V communications in dynamic environments. The obtained results show the applicability of the proposed concept in multi-hop V2V networks, where nodes are capable to obtain and exchange information about the surrounding environment. In future work, other road scenarios will be investigated. Besides this, further analysis of the impact of scattering reflections, and number of nodes on sensor-aided prediction in multi-hop transmission will be done.
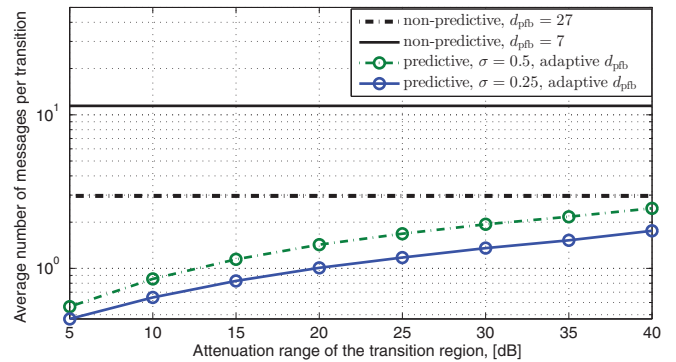
REFERENCES

[1] A. Sherer, J. Rose, and R. Oddone, "Ensuring functional safety compliance for ISO26262," in *2015 52nd ACM/EDAC/IEEE Design Automation Conference (DAC)*, June 2015, pp. 1–3.

[2] R. A. Akl, S. Valentin, G. Wunder, and S. Stanczak, "Compensating for cqi aging by channel prediction: The lte downlink," in *2012 IEEE Global Communications Conference (GLOBECOM)*, Dec 2012, pp. 4821–4827.

[3] A. Duel-Hallen, "Fading channel prediction for mobile radio adaptive transmission systems," *Proceedings of the IEEE*, vol. 95, no. 12, pp. 2299–2313, Dec 2007.

[4] R. C. Daniels and R. W. Heath, "Link adaptation with position/motion information in vehicle-to-vehicle networks," *IEEE Transactions on Wireless Communications*, vol. 11, no. 2, pp. 505–509, February 2012.

[5] R. Alieiev, T. Hehn, A. Kwoczek, and T. Kürner, "Sensor-based communication prediction for dynamic Doppler-shift compensation," in *Proceedings. (ITST 2017). International Conference on ITS Telecommunications*, IEEE, May 2017.

[6] A. Hedayat, A. Nosratinia, and N. Al-Dhahir, "Linear equalizers for flat rayleigh mimo channels," in *Proceedings. (ICASSP '05). IEEE International Conference on Acoustics, Speech, and Signal Processing, 2005.*, vol. 3, March 2005, pp. iii/445–iii/448.

[7] M. Šimko, Q. Wang, and M. Rupp, "Optimal pilot symbol power allocation under time-variant channels," *EURASIP Journal on Wireless Communications and Networking*, vol. 2012, no. 1, p. 225, 2012.

[8] T. Cui, F. Lu, V. Sethuraman, A. Goteti, S. P. Rao, and P. Subrahmanya, "First order adaptive iir filter for cqi prediction in hsdpa," in *2010 IEEE Wireless Communication and Networking Conference*, April 2010.

[9] L. Elefteriadou, "The highway capacity manual 6th edition: A guide for multimodal mobility analysis," *ITE Journal*, vol. 86, no. 4, 2016.

[10] J. Blumenstein, J. C. Ikuno, J. Prokopec, and M. Rupp, "Simulating the long term evolution uplink physical layer," in *ELMAR, 2011 Proceedings*. IEEE, 2011, pp. 141–144.

[11] A. F. Molisch, F. Tufvesson, J. Karedal, and C. F. Mecklenbräuker, "A survey on vehicle-to-vehicle propagation channels," *IEEE Wireless Communications*, vol. 16, no. 6, pp. 12–22, December 2009.

[12] A. Paier, J. Karedal, N. Czink, C. Dumard, T. Zemen, F. Tufvesson, A. F. Molisch, and C. F. Mecklenbräuker, "Characterization of vehicle-to-vehicle radio channels from measurements at 5.2 GHz," *Wireless Personal Communications*, vol. 50, no. 1, pp. 19–32, 2009.

[13] C. Merfels and C. Stachniss, "Pose fusion with chain pose graphs for automated driving," in *Proceedings of the IEEE/RSJ International Conference on Intelligent Robots and Systems (IROS)*, 2016.

[14] D. S. Baum, J. Hansen, and J. Salo, "An interim channel model for beyond-3G systems: extending the 3GPP spatial channel model (SCM)," in *2005 IEEE 61st Vehicular Technology Conference*, vol. 5, May 2005, pp. 3132–3136 Vol. 5.

8. Mitigation of radio frequency hardware imperfections, full reprints

Adaptive-order Polynomial Methods for Power Amplifier Model Estimation

Jiri Dvorak, Roman Marsalek, **Jiri Blumenstein**

2013 23rd International Conference Radioelektronika

Adaptive-order Polynomial Methods for Power Amplifier Model Estimation

Jiri Dvorak, Roman Marsalek and Jiri Blumenstein
Dept. of Radio Electronics
Brno University of Technology
Brno, Czech Republic
xdvora87@stud.feec.vutbr.cz

Abstract—**Linearization techniques are required to reduce the undesirable effects of power amplifier nonlinearities in the wideband power-efficient radio communication systems. The polynomial model and its extension to the memory-polynomial are commonly used to model power amplifier nonlinearities. Determination of the appropriate order of the nonlinearity model is an actual issue to achieve effective methods for subsequent linearization techniques. Having in mind these facts, we compare two adaptive methods employing the determination of the appropriate order of the nonlinearity model. The first algorithm is the adaptive order recursive (ORLS) method, while the proposed solution is based on the recursive least squares method with the sequential updates. In the first stage the models were simulated in MATLAB. Depending on the mean square error estimate we decide on the appropriateness of the nonlinearity order increase. The parameters of the power amplifier models are based on the data experimentally obtained using the Universal Software Radio Peripheral (USRP) device with WBX front-end driven with an OFDM signal. After further performance evaluation, the order adaptation method will be used for efficient digital adaptive predistorter design.**

Keywords—power amplifier; adaptive polynomial model; order recursive least squares; sequential least squares

I. INTRODUCTION

Modern communication systems require strict spectrum management and thus high order and nonconstant envelope modulations. These modulation techniques, such as an orthogonal frequency division multiplex (OFDM) suffer from very high peak-to-average power ratio (PAPR) and frequency selective characteristics.

The most significant distortion in the transmitter is generated by the power amplifier (PA). They often operate close to the saturation to maximize power efficiency. This saturation causes nonlinear effects and signal envelope distortion. The signal with high dynamic reaches the area of nonlinearity much more. Nonlinearities cause undesirable effects to the transmitted signal, such as the intersymbol interferences, spectral regrowth and distortion of constellation diagram [1-3]. A linear PA with minor distortion can be designed however these designs are mostly non-effective due to compromises between efficiency and linearity. Another way how to mitigate or eliminate unwanted effect of PA's nonlinearity is to employ PA linearization techniques. Various methods of linearization have been proposed such as feedforward linearization [4], linear amplification with nonlinear components [5] and predistortion [6].

For design and realization of the predistorter, an appropriate model of the PA must be chosen. We consider the memoryless PA model in this phase but the presented approach can be easily extended to the case with PA memory that, as we are fully aware, can not be ignored for wide band applications.

The paper is organized as follows: in section II, the main PA modeling methods are introduced and polynomial modeling, which we focus on, is presented. Section III describes an order recursive least square algorithm for model adaptation. Section IV focuses on the sequential least squares where signal is processed sample-by-sample. The simulation results are given in section V. Finally, conclusion and comparison of the both approaches are given.

II. PA MODELING

The nonlinear PA is usually modelled as Wiener model [7], its common used extended version is Hammerstein model [8] (and their combination) or we can use Volterra model [9]. Special simplified case of Volterra system is the polynomial model [10].

If we consider that current output depends only on the current input, the PA model can be memoryless. We can use this assumption if we consider narrow-band signals. The memoryless PA model can be described by

$$y(n) = \sum_{k=1}^{K} c_k x(n)|x(n)|^{k-1} \qquad (1)$$

where $y(n)$ is the output signal of the PA at sample n, $x(n)$ is the input and c_k are the k-th order coefficients of the PA model. For wide-band application memory effects must be considered. The PA model must capture the memory nonlinear effects anyway. The memory polynomial model can be described by

$$y(n) = \sum_{k=1}^{K} \sum_{q=1}^{Q} c_{kq} x(n-q)|x(n-q)|^{k-1} \qquad (2)$$
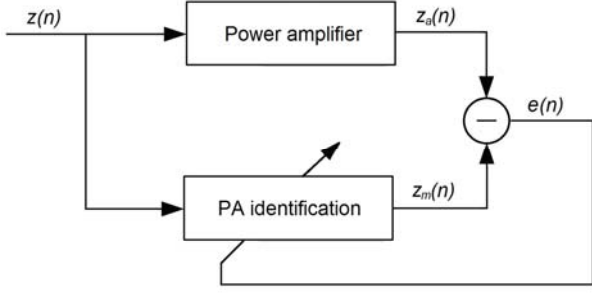
Figure 1. Simulation model.
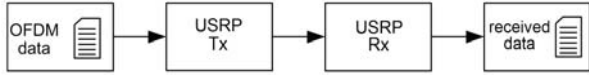
Figure 2. The measured set-up diagram.

$$\mathbf{H} = \begin{bmatrix} 1 & x_1^1 & \dots & x_1^{k-1} \\ 1 & x_2^1 & \dots & x_2^{k-1} \\ \vdots & \vdots & \ddots & \vdots \\ 1 & x_N^1 & \dots & x_N^{k-1} \end{bmatrix},$$

$$\mathbf{c} = [c_1\ c_2\ \dots\ c_k].$$

The first step is computation of coefficient c_1 when order $k=1$ as

$$c_1 = (\mathbf{H_1}^T \mathbf{H_1})^{-1}\ \mathbf{H_1}^T \mathbf{Y} \tag{3}$$

where $\mathbf{H_1} = [1\ 1\ \dots\ 1]^T$.

Then minimum LS error is

$$J_{min} = (\mathbf{Y} - \mathbf{H_1} c_1)^T\ (\mathbf{Y} - \mathbf{H_1} c_1). \tag{4}$$

For increase of the order to $k+1$, the matrix $\mathbf{H}$ is extended by one column. As a new observation matrix we have

$$\mathbf{H}_{k+1} = [\mathbf{H}_k\ \mathbf{h}_{k+1}]$$

with $\mathbf{h}_{k+1} = [x_1^k\ x_2^k\ \dots\ x_N^k]^T$.

We can then compute the coefficients for increased order as

$$\mathbf{c}_{k+1} = \begin{bmatrix} \mathbf{c}_k - \dfrac{(\mathbf{H}_k^T \mathbf{H}_k)^{-1} \mathbf{H}_k^T \mathbf{h}_{k+1} \mathbf{h}_{k+1}^T \mathbf{P}_k \mathbf{Y}}{\mathbf{h}_{k+1}^T \mathbf{P}_k \mathbf{h}_{k+1}} \\ \dfrac{\mathbf{h}_{k+1}^T \mathbf{P}_k \mathbf{Y}}{\mathbf{h}_{k+1}^T \mathbf{P}_k \mathbf{h}_{k+1}} \end{bmatrix} \tag{5}$$

where $\mathbf{P}_k = \mathbf{I} - \mathbf{H}_k (\mathbf{H}_k^T \mathbf{H}_k)^{-1} \mathbf{H}_k^T$.

The inversion of term $(\mathbf{H}_k^T \mathbf{H}_k)$ can be eliminated when we define

$$\mathbf{D}_k = (\mathbf{H}_k^T \mathbf{H}_k)^{-1} \tag{7}$$

We have now

$$\mathbf{D}_{k+1} = \begin{bmatrix} \mathbf{D}_k + \dfrac{\mathbf{D}_k \mathbf{H}_k^T \mathbf{h}_{k+1} \mathbf{h}_{k+1}^T \mathbf{H}_k \mathbf{D}_k}{\mathbf{h}_{k+1}^T \mathbf{P}_k \mathbf{h}_{k+1}} & -\dfrac{\mathbf{D}_k \mathbf{H}_k^T \mathbf{h}_{k+1}}{\mathbf{h}_{k+1}^T \mathbf{P}_k \mathbf{h}_{k+1}} \\ -\dfrac{\mathbf{h}_{k+1}^T \mathbf{H}_k \mathbf{D}_k}{\mathbf{h}_{k+1}^T \mathbf{P}_k \mathbf{h}_{k+1}} & \dfrac{1}{\mathbf{h}_{k+1}^T \mathbf{P}_k \mathbf{h}_{k+1}} \end{bmatrix} \tag{8}$$

where the recursive approach is used and

$$\mathbf{P}_k = \mathbf{I} - \mathbf{H}_k \mathbf{D}_k \mathbf{H}_k^T. \tag{9}$$

Finally we can compute minimum LS error for increased order of polynomial as

$$J_{\min k+1} = J_{\min k} - \dfrac{(\mathbf{h}_{k+1}^T \mathbf{P}_k \mathbf{Y})^2}{\mathbf{h}_{k+1}^T \mathbf{P}_k \mathbf{h}_{k+1}}. \tag{10}$$

where K represents the maximum nonlinearity order and Q represent the maximum memory order. Determination of appropriate nonlinearity and memory order is the main issue not deeply studied in the current literature. It is difficult to find balance between complexity of the model implementation and yet sufficient effect of linearization. For good linearization performance we need larger orders but concurrently it leads to an increasing complexity.

The structure that was used for the PA model identification is shown in Fig. 1. For our research we used the baseband OFDM signal with 512-points FFT size, 256 data subcarriers and 256 null subcarriers. The signal was transmitted and received by the Universal Serial Radio Peripheral device (USRP) with a WBX daughter board centered at carrier-frequency 2 GHz. The output was captured to a data file. The measurement set-up is shown in Fig. 2. A delay of the received signal was corrected. In this way we obtained input and output signals of a real power amplifier. These signals were used for memoryless polynomial model fit.

III.   ORDER RECURSIVE LEAST SQUARES (ORLS)

In the classical least square approach, it is important to determinate least square (LS) error for every increase of polynomial order of model. For a new set of coefficients and value of LSE we do not need to compute all corresponding signal samples with new extended observation matrix [11]. We can reduce many computations by update the LSE with values obtained for the previous order. We can represent (1) as a matrix

$$\mathbf{Y} = \mathbf{H}\mathbf{c} \tag{3}$$

where $\mathbf{Y}$ is output, $\mathbf{H}$ is observation matrix that includes input samples $x(n)$, $\mathbf{c}$ is vector of coefficients.

$$\mathbf{Y} = [y(1)\ y(2)\ \dots y(N)]^T,$$

Figure 3. AM/AM characteristics computed through the ORLS algorithm.
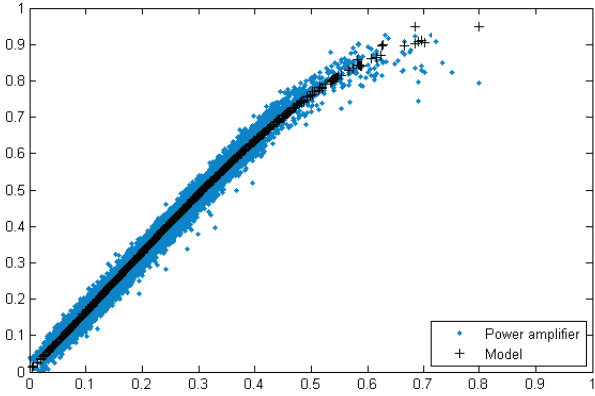
Fig. 4. AM/AM characteristics computed through the sequential LS algorithm.

By comparing $J_{\min k+1}$ and $J_{\min k}$ we can decide if is useful to increase the polynomial order with respect to appropriate compromise between efficiency and computational complexity. Fig. 3 depicts comparison of the AM/AM characteristics of the measured data and the model computed through the ORLS algorithm for $K=4$.

IV. SEQUENTIAL LEAST SQUARES

If the data are processed sample-by-sample, it is appropriate to adapt the model sequentially in time. To adapt the model we use LS error criterion similarly to [12]

$$J(n) = |e(n)|^2 = \sum_{l=1}^{n} (z_a(l) - z_m(l))^2 \tag{11}$$

where $z_a(l)$ is output of the PA and z_m is defined as

$$z_m(n) = \sum_{k=1}^{K} c_k z(n)^{k-1} = c^T Z(n) \tag{12}$$

where

$$c = [c_0 \ c_1 \ ... \ c_K]$$

and

$$Z = [1 \ z(n) \ z^2(n) \ ... \ z^{K-1}(n)]$$

For coefficients we have $c = P^{-1}(n)q(n)$.

These matrices $P^{-1}(n)$ and $q(n)$ are updated sequentially with every new sample. Inversion of $P^{-1}(n)$ can be eliminated by application of the "*Matrix Inversion Lemma*" [13]

$$P_{inv}(n) = \frac{P_{inv}(n-1)}{\lambda} - \frac{\frac{1}{\lambda^2} P_{inv}(n-1)ZZ'P_{inv}(n-1)}{1 + \frac{1}{\lambda}ZZ'P_{inv}(n-1)} \tag{14}$$

$$q(n) = \lambda q(n-1) + z(n)Z \tag{15}$$

where λ is the forgetting factor which decreases weight of old samples and makes the system adaptable to PA variations in time. Finally with these partial updates and after simplification we can sequentially update coefficients as

$$c(n) = c(n-1)P_{inv}(n)Z(z(n)Zc(n-1)) \tag{16}$$

In order to get the appropriate predistorter nonlinearity order the LS error is computed after the coefficient update. Based on the requirements we can decide to increase or not the polynomial order. In this case, the matrices are extended for the next step using formulas:

$$c(n+1) = [c(n) \ 0]$$

$$P_{inv}(n+1) = \begin{bmatrix} P_{inv}(n) & 0 \\ 0 & 1 \end{bmatrix}$$

$$q(n+1) = \begin{bmatrix} q(n) \\ 0 \end{bmatrix}.$$

Fig. 4 shows the AM-AM characteristics of the measured data and the model computed through the sequential LS algorithm for $K=4$.
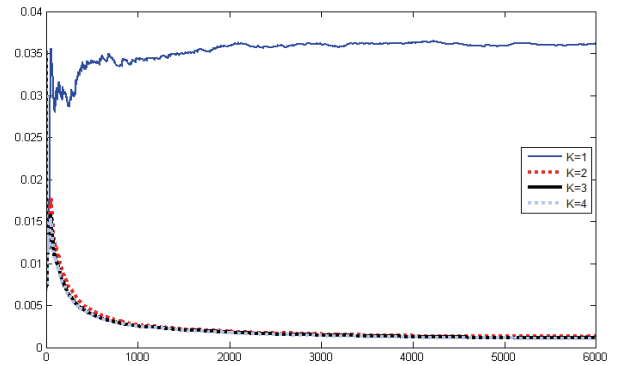
Figure 5. Effects of the increase the order on least squares error.
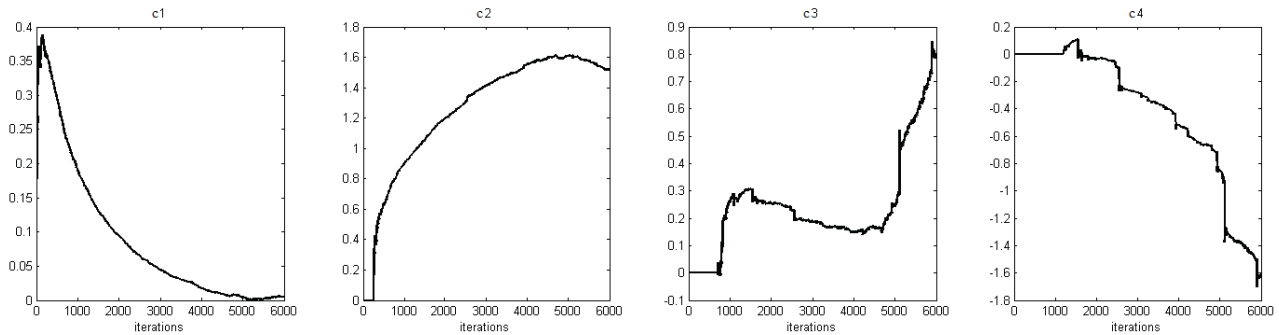
Figure 6. A value of the coefficients depending on the iteration.

V. SIMULATION RESULTS

TABLE I. COMPARSION OF COEFFICENTS

Algorithm	Coefficients for K=4
ORLS	c=[0,0171 1,3013 1,7283 -2,6309]
Seq. LS	c=[0,0235 1,2312 1,8876 -2,7470]

Besides the presented AM/AM curves, the coefficients for model order $K=4$ are presented in Table I. They only slightly differ for the both methods due to adaptable behavior of the sequential LS algorithm. More results for the sequential LS method are shown in Fig. 5 and Fig. 6. The Fig. 5 represents LS error for model order K in range 1-4. The time evolution of model coefficients is shown in Fig. 6. At the beginning, the only coefficient c_1 is used. Subsequently the order is increased to 2,3 and 4 at iteration interval 250, 700 and 1200.

VI. CONCLUSION

In the presented paper we compared two methods of polynomial order adaptation for behavioral modeling of the nonlinear power amplifiers. For the sake of simplicity, the methods were compared on the memoryless nonlinearity and pure AM/AM characteristics. The validation was carried on the experimental data obtained from the commercially available USRP software defined radios. The both investigated methods lead to similar model's coefficients. Nevertheless, the sequential LS algorithm is more flexible to the PA's time variation. Currently we are working on the extension to the case with memory. The results will be used in further research of pre-distortion algorithms for power amplifier linearization.

ACKNOWLEDGMENT

REFERENCES

[1] J. Vuolevi and T. Rahkonen, "Distortion in RF power amplifiers," Artech House, 2003.

[2] D. Taggart, R. Kumar, and S. Raghavan, "Simulation and Modeling of Amplifier Nonlinearities for Multicarrier Wireless Communication Systems," IEEE Vehicular Telemetry Conference, vol. 6, pp. 4195-4202, September 2004.

[3] G. T. Zhou, "Analysis of spectral regrowth of weakly nonlinear power amplifiers," in IEEE Acoustics, Speech, and Signal Processing Conf., vol. 5, Jun. 2000, pp. 2737-2740.

[4] M. Younes, F. M. Ghannouchi, "An accurate predistorter based on a feedforward hammerstein structure," Broadcasting, IEEE Transactions on, vol. 58, pp. 454-461, September 2012.

[5] A. Azirar and I. D. Robertson, "Linear frequency translation and amplification with nonlinear components", Electronics Letters, vol. 40, pp. 322-323, March 2004.

[6] L. Larson et al., "Digital predistortion techniques for linearized power amplifiers," in Proc. Asia–Pacific Microw. Conf., pp. 1048-1051., December 2006.

[7] I. M. Iqbal and N. Aziz, "Comparison of various Wiener model identification approach in modelling nonlinear process," Data Mining and Optimization (DMO), 2011 3rd Conference on, pp.134-140, June 2011.

[8] F. Mkadem and S. Boumaiza, "Extended Hammerstein model for RF power amplifier behavior modeling," Microwave Conference, 2009. EuMC 2009. European, pp.1066-1069, October 2009.

[9] M. Tummla, M. T. Donovan, B. E. Watkins and R. North, "Volterra series based modeling and compensation of nonlinearities in high power amplifiers," Acoustics, Speech, and Signal Processing, 1997. ICASSP-97., 1997 IEEE International Conference on, vol.3, pp. 2417-2420, April 1997.

[10] J. Kim and K. Konstantinou, "Digital predistortion of wideband signals based on power amplifier model with memory," Electronics Letters, vol.37, no.23, pp.1417-1418, November 2001.

[11] S. M. Kay, "Fundamentals of Statistical Signal Processing: Estimation Theory," New Jersey: Prentice Hall, 1993.

[12] R. Marsalek, P. Jardin, and G. Baudoin, "From post-distortion to predistortion for power amplifiers linearization," IEEE Commun. Lett., vol. 7, no. 7, pp. 308–310, 2003.

[13] S. Haykin, "Adaptive filter theory," second edition, Prentice-Hall, 1991.

On the lower I/Q imbalance sensitivity using real-valued feedback of digital predistortion

Tomas Gotthans, Roman Maršálek, Martin Pospíšil, Tomáš Urbanec, Jan Král, **Jiri Blumenstein**

On the Lower I/Q Imbalance Sensitivity Using Real-valued Feedback of Digital Predistortion

Tomáš Gotthans, Roman Maršálek, Martin Pospíšil, Tomáš Urbanec, Jan Král, Jiří Blumenstein
Department of Radio Electronics, Brno University of Technology,
Technicka 3082/12, 616 00 Brno,CZ
Email: gotthans@feec.vutbr.cz

Abstract — The adaptive digital predistortion is currently widely used to compensate for the nonlinearities. Usually the observing (feedback) path of the predistorter is required to be very accurate. That means it is compensated for any radio frequency front-end imperfections.

In this paper we demonstrate that recently proposed (real-valued) digital predistortion algorithm employing only one of the signals in the quadrature pair implies the reduced sensitivity of the predistorter adaptation to the I/Q modulator imbalance in the feedback path. The lower sensitivity is demonstrated using both simulation as well as by an experiment conducted using the mm-Wave setup with integrated direct-conversion transceiver with important imbalances in both transmitting (Tx) as well as in receiving (Rx) path.

Index Terms — Linearization, predistortion, I/Q impairments, real-valued feedback.

I. INTRODUCTION

An efficiency and linearity are two important merits for the radio frequency (RF) power amplifiers (PA's). In order to maximize the efficiency, PA's have to be operated close to saturation, where they exhibit strong nonlinear behavior. One of the widely-employed methods for PA linearization is a digital predistortion (DPD) based on the pre-processing the signal by the inverse characteristics of PA, [1]. In order to track the changes of PA characteristics adaptive baseband DPD system is required, the PA output has to be monitored by the dedicated feedback (observation) path, where the part of the signal is down-converted to the baseband in-phase (I) and quadrature (Q) components. Moreover, as has been widely demonstrated [2], the standard DPD adaptation algorithm is sensitive to RF impairments, such as DC offset or I/Q modulator/demodulator imbalances. Recently, the DPD adaptation algorithm, employing only one of the I and Q signals from the quadrature pair of down-converted PA output has been proposed in [3]. In this paper we demonstrate that such algorithm is not only beneficial due to its lower hardware complexity, but we lower sensitivity on I/Q imperfections as well show. The lower sensitivity is demonstrated using both simulation as well as by an experiment conducted using the mm-Wave setup with

integrated direct-conversion transceiver with important imbalances in both transmitting (Tx) as well as in in receiving (Rx) path.

II. DIGITAL PREDISTORTION

Digital predistortion is one of techniques used for overcoming the non-linear behavior of PA. It is well known, [1] the non-linear regime is related with PA efficiency resulting to several undesirable effects such as spectrum widening in the adjacent channel interferences or memory effects, etc. The most general form of predistorters are based on Volterra series models. Nevertheless, for practical reasons, several less complex models derived from Volterra series have been derived in the past. Overcoming the complexity of the general Volterra series, an effective model pruning method, called dynamic deviation reduction (DDR) of 2nd-order was proposed and used in several recent papers [4], [5], [6] to demonstrate its performance in DPD application. The overall model structure determined by 2 parameters: the non-linearity order K and the memory length M. The number of coefficients b is thus $2MK + (\frac{K+1}{2})M$. Throughout this paper, we use such model to describe the nonlinear function output, i.e., the output of the predistorter $z(t)$ as:

$$
\begin{aligned}
z(t) = & \sum_{k=0}^{\frac{K-1}{2}} \sum_{i=0}^{M} b_{2k+1,1}(i)\ |x(t)|^{2k} x(t-i) \\
& + \sum_{k=1}^{\frac{K-1}{2}} \sum_{i=1}^{M} b_{2k+1,2}(i)\ |x(t)|^{2(k-1)} x^2(t) x^*(t-i) \\
& + \sum_{k=1}^{\frac{K-1}{2}} \sum_{i=1}^{M} b_{2k+1,3}(i)|x(t)|^{2(k-1)}\ x(t)|x(t-i)|^2 \\
& + \sum_{k=1}^{\frac{K-1}{2}} \sum_{i=1}^{M} b_{2k+1,4}(i)|x(t)|^{2(k-1)}\ x^*(t) x^2(t-i),
\end{aligned}
\tag{1}
$$

with $x(t)$ being the nonlinear function, i.e., predistorter input. The model coefficients as well as its instantaneous

input samples can be arranged into vector/matrix using feedback signal $y(t)$. Using the indirect learning architecture [7] of DPD the criteria can be written as:

$$\mathbf{x} = \mathbf{Ub}. \quad (2)$$

III. Real-valued Feedback Signal

By splitting the real and imaginary parts, further denoted as $(.)_r$ and $(.)_i$, of equation 2 we get

$$\mathbf{x}_r + j\mathbf{x}_i = (\mathbf{U}_r + j\mathbf{U}_i)(\mathbf{b}_r + j\mathbf{b}_i), \quad (3)$$

$$\mathbf{x}_r + j\mathbf{x}_i = \mathbf{U}_r\mathbf{b}_r + j\mathbf{U}_i\mathbf{b}_r + j\mathbf{U}_i\mathbf{b}_i - \mathbf{U}_i\mathbf{b}_r. \quad (4)$$

$$\mathbf{x}_r = \mathbf{U}_r\mathbf{b}_r - \mathbf{U}_i\mathbf{b}_i \quad \wedge \quad \mathbf{x}_i = \mathbf{U}_i\mathbf{b}_r - \mathbf{U}_r\mathbf{b}_i \quad (5)$$

$$\mathbf{M}_a = [\mathbf{U}_r \ -\mathbf{U}_i] \quad \wedge \quad \mathbf{M}_b = [\mathbf{U}_i \ \mathbf{U}_r] \quad (6)$$

$$\mathbf{\Theta}_a = [\mathbf{b}_r \ -\mathbf{b}_i] \quad \wedge \quad \mathbf{\Theta}_b = [\mathbf{b}_r \ \mathbf{b}_i] \quad (7)$$

$$\mathbf{\Theta}_a = \left(\mathbf{M}_a^H\mathbf{M}_a\right)^{-1}\mathbf{M}_a^H\mathbf{x}_r \quad \wedge \quad \mathbf{\Theta}_b = \left(\mathbf{M}_b^H\mathbf{M}_b\right)^{-1}\mathbf{M}_b^H\mathbf{x}_i, \quad (8)$$

where $(.)^H$ represents Hermitian transpose. In the equation (9) we may observe, that on the right-hand side of the equation we have $\mathbf{x}_r$ or $\mathbf{x}_i$. But adventitiously using Iterative learning control (ILC) we may interchange $\mathbf{x}$ and $\mathbf{y}$. ILC, [8] is a widely-recognized technique that can help to obtain the inverse of a system. Fundamentally the approach divides the problem into the two steps estimation of a model and predistortion. Thus, instead of focusing on identifying the predistorter parameters, an iterative learning algorithm is used to identify the optimal power amplifier (PA) model. Once the optimal PA model is found (we used DDR2 as well), then the parameters of the predistorter are estimated using standard modeling approach such as least squares.

IV. I/Q Imbalance in Feedback Path

In this paragraph, we would like to show that DPD adaptation based on the real/in-phase (or imaginary/quadrature) part of the demodulated signal is less sensitive to Rx quadrature demodulator imbalances than DPD adaptation methods based on standard LS criteria as eq. (2). Suppose first that we can neglect the noise and thus the received passband signal in the feedback path of DPD is identical to the transmitted signal with the baseband components $y(t) = y_r(t) + jy_i(t)$:

$$y_{RF}(t) = \Re\left\{y(t)e^{j\omega t}\right\} = y_r(t)cos(\omega t) - y_i(t)sin(\omega t), \quad (9)$$

Multiplying the passband signal by the two local oscillator signals and passing through a pair of low-pass filters, one obtains the demodulated baseband signals. After rearrangements we can write the symmetrical model burdened by I/Q imbalance:

$$\begin{aligned} y(t)'_r &= (1+\epsilon)\left[y_r(t)cos(\phi) - y_i(t)sin(\phi)\right] \\ y(t)'_i &= (1-\epsilon)\left[y_i(t)cos(\phi) - y_r(t)sin(\phi)\right] \end{aligned} \quad (10)$$

where ϵ is a gain imbalance and ϕ is a phase imbalance. In order to express the performance of the real-valued DPD adaptation method (using only one of the I or Q components) in contrast to the standard complex-valued adaptation method, we may define the error ratio as:

$$E = 10log_{10}\left(\frac{\sum_{n=1}^{N}(\mathbf{y}(n) - \mathbf{y}'(n))(\mathbf{y}(n) - \mathbf{y}'(n))^*}{\sum_{n=1}^{N}(\Re\{\mathbf{y}(n)\} - \Re\{\mathbf{y}(n)\}')^2}\right), \quad (11)$$

with the analytic solution presented in Appendix of this paper. Where $(.)^*$ is complex conjugation and $\Re(.)$ is real and $\Im(.)$ imaginary part and N is length of a vector $\mathbf{x}$.

A. Typical system

To better illustrate the practical benefits of real-valued method, the dependency of the error ratio E on the gain imbalance ϵ and the phase imbalance ϕ is shown in Fig.1. On an example of the selected practical values of imbalances, e.g. $\epsilon = 0.02$ and $\phi = 0.35$ ° the error ratio is equal to $E = 4.5 \ dB$, that means that the proposed (i.e. real-valued) adaptation method is approximately 6.5 times better in term of insensitivity to I/Q mismatch.
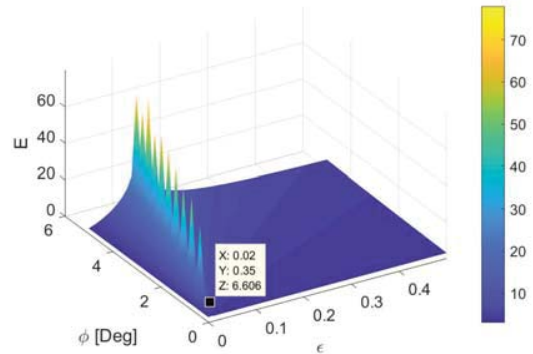
Fig. 1. Error ratio dependency as function of phase ϕ and gain ϵ imbalances.

V. Measurement Setup

The performance of the DPD adaptation based on the real-valued PA feedback has been evaluated using the 60 GHz mm-wave measurement setup, with the block structure and photo shown in Fig. 2. This setup is based

on the Infineon BGT-60 evaluation board, CompuGen 4302, a 4-channel 300 MSa/s arbitrary waveform generator board with 12-bit resolutionand the CompuScope 12400, 2-channel data acquisition card with maximal sampling speed of 400 MSa/s with 12-bit resolution. The sampling speed 250 MSa/s was selected. The output of BGT-60 RF in-built PA is, after attenuation by a Quinstar V-band attenuator visualized on the FSUP spectrum analyzer equipped with FS-Z75 harmonic mixer. A part of the PA output signal is fed back to BGT-60 receiver part through the in-house fabricated directional coupler.
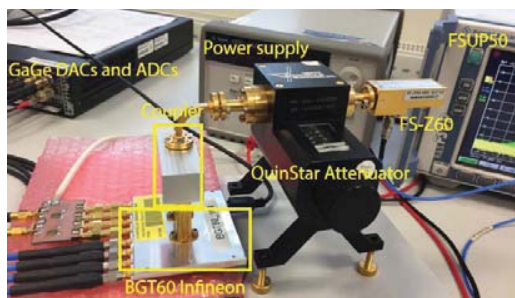
Fig. 2. Photo of experimental setup for mm-Waves used for testing the digital predistortion.

VI. RESULTS

According to the data-sheet of BGT-60 chipset, the present I/Q demodulator exhibits a phase error of $\phi = 2\,°$ and gain mismatch of 0.5 dB. The tests described below have been carried out for the relatively narrow-band (12.5 MHz BW) QAM signals with 16 samples per symbol and root raised cosine shaping with roll-off 0.3. In order to asses the sensitivity of the standard and real-valued feedback DPD adaptation methods, in the first experiment, the I/Q imbalances were left uncompensated. The I/Q imbalance effect on the AM/AM characteristic of the PA are clearly visible in Fig. 3. The standard indirect learning DPD adaptation method failed to estimate DPD characteristics due to the presence of I/Q imbalances, nevertheless the real-valued based DPD adaptation method performed well. With the I/Q imbalances of RF front-end compensated (using approach from [9]) both methods were able to find the stable solution of DPD, as demonstrated in Fig. 3. The superior performance of the real-valued feedback DPD adaptation (denoted as single-channel DPD) is confirmed as well.

VII. CONCLUSION

We have investigated the performance of a standard (i.e. using both real and imaginary parts of feedback signal) least-squares solution of the digital predistorter coefficients calculation in comparison with the recently proposed
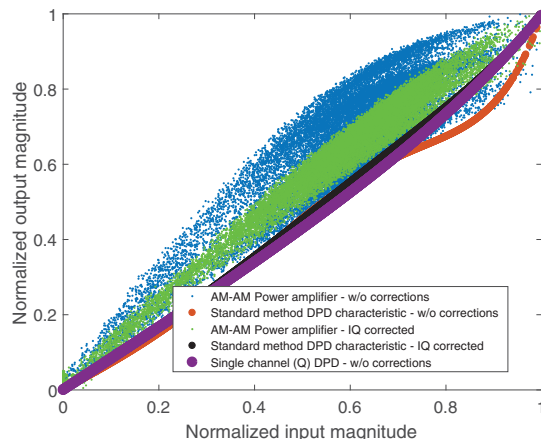
Fig. 3. AM-AM characteristics without applied I/Q corrections and with applied I/Q Tx and Rx corrections.

method, based on using either real or imaginary part of feedback signal separately. We have demonstrated, both analytically as well as through the practical experiment with the direct conversion mm-wave transceiver system, the lower sensitivity of this recent approach to the uncompensated gain and phase imbalances in the predistorter feedback path. The reason of unsuccessful calculation of DPD coefficients in case of I/Q imbalances can be due an inversion of matrix made of observation samples (measurements).

REFERENCES

[1] J. K. Cavers, "Amplifier linearization using a digital predistorter with fast adaptation and low memory rrequirements," *Vehicular Technology, IEEE Transactions on*, vol. 39, no. 4, pp. 374–382, 1990.

[2] T. Gotthans, R. Marsalek, J. Gotthans, and G. Baudoin, "Influence of filter-bank rf transceiver chain imperfections on digital predistortion performance," in *2016 International Symposium on Wireless Communication Systems (ISWCS)*, Sept 2016, pp. 623–627.

[3] J. Chani-Cahuana, M. Ozen, C. Fager, and T. Eriksson, "Digital predistortion parameter identification for rf power amplifiers using real-valued output data," *IEEE Transactions on Circuits and Systems II: Express Briefs*, vol. PP, no. 99, pp. 1–1, 2017.

[4] A. Zhou, J. C. Pedro, and T. J. Brazil, "Dynamic deviation reduction-based volterra behavioral modeling of rf power amplifiers," *Microwave Theory and Techniques, IEEE Transactions on*, vol. 54, no. 12, pp. 4323–4332, 2006.

[5] T. Gotthans, G. Baudoin, and A. Mbaye, "Comparison of modeling techniques for power amplifiers," in *Radioelektronika (RADIOELEKTRONIKA), 2013 23rd International Conference*, 2013, pp. 232–235.

[6] Z. Anding, P. Draxler, J. Yan, T. Brazil, D. Kimball, and P. Asbeck, "Open-loop digital predistorter for rf power amplifiers using dynamic deviation reduction-based volterra series," *Microwave Theory and Techniques, IEEE Transactions on*, vol. 56, no. 7, pp. 1524–1534, 2008.

[7] J. Chani-Cahuana, C. Fager, and T. Eriksson, "A new variant of the indirect learning architecture for the linearization of power amplifiers," in *2015 European Microwave Conference (EuMC)*, Sept 2015, pp. 1295–1298.

[8] J. Chani-Cahuana, P. N. Landin, C. Fager, and T. Eriksson, "Iterative learning control for rf power amplifier linearization," *IEEE Transactions on Microwave Theory and Techniques*, vol. 64, no. 9, pp. 2778–2789, Sept 2016.

[9] I. Held, O. Klein, A. Chen, and V. Ma, "Low complexity digital iq imbalance correction in ofdm wlan receivers," in *59th IEEE Vehicular Technology Conference. VTC 2004-Spring*, vol. 2, May 2004, pp. 1172–1176 Vol.2.

APPENDIX

After some manipulations, the instantaneous error ratio $E(n)$ defined in equation (11) can be analytically expressed by equation (12). For our simulations (visualizations in Fig. 1) we expect that the mean value of transmitted signals is close to zero, as can be expected for both multi-carrier as well as single-carrier QAM signals.

$$E(n) = 10\log\frac{\left[(y(n) - (y(n) + \epsilon y(n)^*)\cos(\phi) - j(\epsilon y(n) - y(n)^*)\sin(\phi)\right]\left[y(n) - (y(n) + \epsilon y(n)^*)\cos(\phi)\right]^* + j(-y(n) + \epsilon y(n)^*)\sin(\phi)}{(1 - \epsilon)\left[\cos(\phi)\Im(y(n)) - \Re(y(n))\sin(\phi)\right] + \Re\left\{y(n) - (1 + \epsilon)\cos(\phi)\Re(y(n)) + (1 + \epsilon)\Im(y(n))\sin(\phi)\right\}^2} \quad (12)$$

Experimental evaluation of digital predistortion with FBMC and OFDM signals

Tomáš Gotthans, Roman Maršálek, **Jiri Blumenstein**, Geneviève Baudoin

2015 IEEE 16th Annual Wireless and Microwave Technology Conference (WAMICON)

Experimental evaluation of digital predistortion with FBMC and OFDM signals

Tomáš Gotthans, Roman Maršálek,
Jiří Blumenstein
Department of Radio Electronics, BUT,
Technicka 3082/12, 616 00 Brno,CZ
e-mail:gotthans@feec.vutbr.cz

Geneviève Baudoin
Université Paris-Est, ESIEE
93162 Noisy Le Grand, France
Email: genevieve.baudoin@esiee.fr

Abstract—**In this paper we would like to point out one open issue related with filtered bank multi-carrier signals (FBMC). The experiment was trying to give an answer whether the FBMC signals would keep their beneficial properties even whilst real non-linear power amplifiers were employed. As one of the merits that have been used were error vector magnitude (EVM) and adjacent channel power (ACP). Due to higher sensitivity to angle rotations the digital predistortion have been employed in order to evaluate the importance of linearization.**

Keywords—*FBMC, OFDM, MCM, linearization, predistortion, power amplifier, non-linear, ACP, EVM.*

I. INTRODUCTION

In the vision of future radio systems where the amount of transfered data rises, the demands for more efficient technologies arises. In today communication systems orthogonal frequency division multiplexing signals (OFDM) with cyclic prefix are widely used [1]. It was proved that using multi-carrier modulations (MCM) is an efficient way of transmission [2] and has better resistance to multi-path channels than single carrier modulations. The key technologies that have been lately discussed for the future 5G networks are: non-orthogonal multiple access, millimeter frequencies, 3D massive MIMO, cognitive spectrum radio sensing, ultra wideband signals, ultra dense networks (UDN) with heterogeneous cells (HetNet), multiple technology carrier aggregation and filtered bank multi-carrier (FBMC) signals [3], [4].

It was demonstrated that FBMC/OQAM signals are more sensitive to phase rotations than OFDM ones [5]. It was also shown in [5] that the intrinsic interference in FBMC/OQAM will increase the error probability. But in the case of perfect phase correction the FBMC signal the performance is similar as OFDM [6]. Therefore the natural step is to try to use digital predistortion techniques for mitigating the non-linearity and memory effects introduced by power amplifiers (PA). Consequently comparison with OFDM adopted in 4G systems is from authors point of view a great interest.

II. BRIEF DESCRIPTION OF FBMC/OQAM

Due to properties of prototype filter in the FBMC systems, offset quadrature amplitude modulation (OQAM) is used. Offset means the in-phase and quadrature components are time staggered by half of symbol period. According to the above definition and as presented in [7] and [8] the baseband model of FBMC/OQAM transmitter can be written

$$x[t] = \sum_{m=-\infty}^{+\infty} \sum_{k=0}^{N-1} (\theta^k \Re\{X_k[m]\} h[t - m\ N] +$$

$$\theta^{k+1} \Im\{X_k[m]\} h[t - m\ N - \frac{N}{2}])\ e^{j\frac{2\pi}{N}k(t-mN)} \tag{1}$$

where X_k is a modulation part of a symbol, θ^{k+1} is real part phase rotation vector for the imaginary part θ^k respectively, $h[.]$ is general prototype filter for each sub-carrier with impulse response length $L = KN$ with K so-called overlapping factor and N number of sub-carriers.

There exists several approaches implementing FBMC modulator/demodulator such as NK-IFFTs operating in parallel, two N-IFFTs and polyphase filtering and with lower complexity single N-FFT and polyphase filtering [7]. The last mentioned method was implemented in this paper. The principle of computing the discrete inverse Fourier transform of two real functions simultaneously is used [7]. Such approach is beneficial because then the concept can be easily reconfigured as OFDM transmitter.

According to [8] the input signal of IFFT can be expressed as $\Re\{X_k[m]\}\theta^k + j\Im\{X_k[m]\}\theta^k$ where multiplication with a vector $\theta^k = e^{j\frac{2\pi}{4}k}$ in frequency domain induce circular shift of $\frac{N}{4}$ in the time domain. The principle is commonly named as folding scheme [1].

III. DIGITAL PREDISTORTION

In order to fulfill the increasing demands of higher data rates, higher energy efficiency of power amplifiers, and better spectral efficiency, the digital predistortion system (DPD) can be used. Unfortunately a drawback of higher efficiency needs is that the PAs are operating in non-linear regime. Non-linearities of PAs usually introduces unwanted signal properties such as compression, memory effects, spectrum regrowth in adjacent channels and intermodulation products.

One of the possible technique for dealing with nonlinearities is usage of digital predistorion (DPD). Usually the predistorter is inserted between power amplifier and transmitter. The digital predistorter monitors output of a PA. The feedback path is usually used for calculation of DPD

coefficients [9].

The predistortion principles have been introduced many times, but so far no general rule for choice of proper DPD have not been yet presented.

Demonstrating the DPD and overcoming the complexity of the general Volterra series, an effective model pruning method, called dynamic deviation reduction (DDR) [10], [11], [12] was used. A simplified version of the model is defined by

$$
\begin{aligned}
z(t) = & \sum_{k=0}^{\frac{K-1}{2}} \sum_{i=0}^{M} g_{2k+1,1}(i) \, |x(t)|^{2k} x(t-i) \\
& + \sum_{k=1}^{\frac{K-1}{2}} \sum_{i=1}^{M} g_{2k+1,2}(i) \, |x(t)|^{2(k-1)} x^2(t) x^*(t-i) \\
& + \sum_{k=1}^{\frac{K-1}{2}} \sum_{i=1}^{M} g_{2k+1,3}(i) |x(t)|^{2(k-1)} \, x(t) |x(t-i)|^2 \\
& + \sum_{k=1}^{\frac{K-1}{2}} \sum_{i=1}^{M} g_{2k+1,4}(i) |x(t)|^{2(k-1)} \, x^*(t) x^2(t-i).
\end{aligned}
$$

$$(2)$$

where $x(n)$ and $z(n)$ are the complex envelopes of the input and output of the PA, respectively, and $g_{2k+1,j}$ is the complex Volterra kernel of the system.

For the calculation, explanation of principles and closer information the readers could be referred to [11].

IV. EXPERIMENTAL EVALUATION

In order to prove the concept, the experimental test-bench was assembled. The signal-processing and additional post-processing has been done with Matlab that was communicating with Rohde&Schwarz generator SMU200A and with real-time spectrum analyzer Rohde&Schwarz FSVR. The generator was synchronized with analyzer using 10 MHz reference signal and the beginning of test sequence was triggering the acquisition with signal marker. Then in PC additional processing have been done (such as integer synchronization based on correlation, fractional synchronization based on Farrow filters, etc.). The generated FBMC signal had 1024 sub-carriers and prototype filter of fourth order was used [13]. The total generated data sequence had 16384 samples. For the OFDM signal, the same initial data with similar setup but rectangular filter was used. The signal had oversampling ratio 4, sampling frequency $f_s = 20\ MHz$, with carrier frequency $f_c = 1\ GHz$, and with inner OQAM modulation level $M = 4$. Therefore the total bandwidth of transmitted signals was $BW = 5\ MHz$. The equipment with high dynamical ranges and low noise figures had to be threated very carefully for taking advantage of FBMC properties.

Keeping higher accuracy of the measurements, each point od results was repeated 10 times and then the mean value was used. Also for credibility of the results three different PAs

have been used. The are denoted as: Tesla 1, Mini Circuits, Tesla 2 with AM/AM and AM/PM characteristics given if Fig.1. We may see that the presented PAs have different non-linear characteristics with different memory effects. For testing the nonlinear order of DPD was chosen as $K = 13$ and memory depth of $M = 1$.

We have been measuring ACP (Fig.2) at the output of PA with offset of 5.1 MHz and bandwidth of (5 MHz). The EVM Fig.3 after demodulation of all sub-carriers (without quantification) is also evaluated. From the results presented in
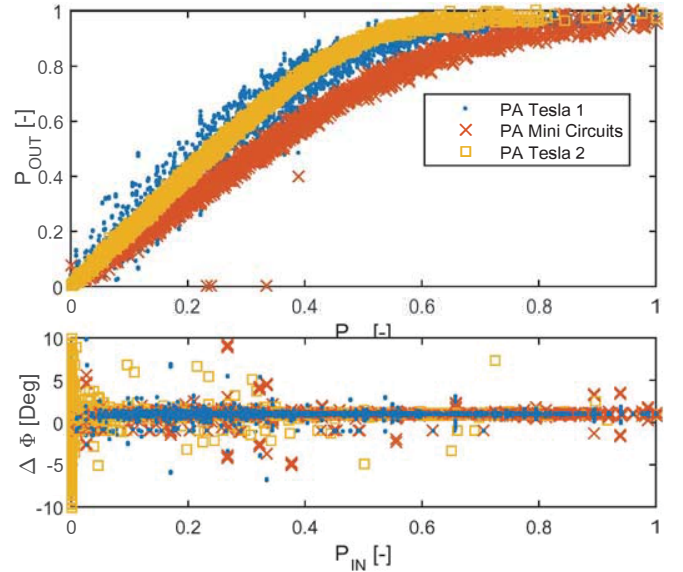
Fig. 1. Normalized AM/AM characteristics (Top) of three different PAs and corresponding AM/PM characteristics (Bottom).
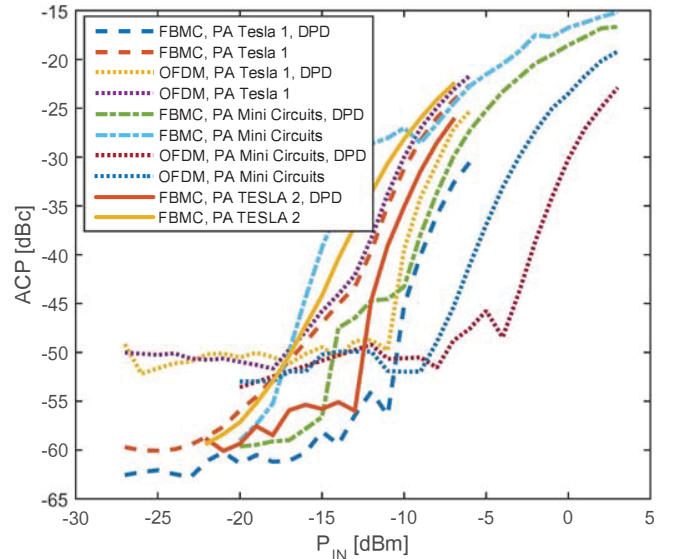
Fig. 2. The experimentally measured ACP of FBMC and OFDM for three different PAs depending on the input power P_{IN}.

Fig.2 and Fig.3 we may observe that the FBMC signals have in
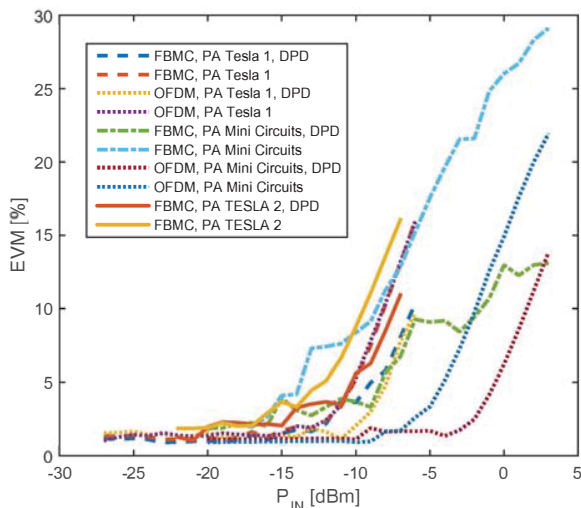
Fig. 3. The experimentally measured EVM before quantification depending on the input power P_{IN}.

general 10 dB lower ACP, but as presented in Fig.3 the FBMC signals tend to be more sensitive to non-linear distortions than OFDM. Further the figures also demonstrates the necessary need for using DPD. The power spectrum densities can be seen in the Fig.4, where the green trace represents FBMC signal without DPD, black signal is FBMC signal with DPD and blue curve is OFDM signal without DPD.
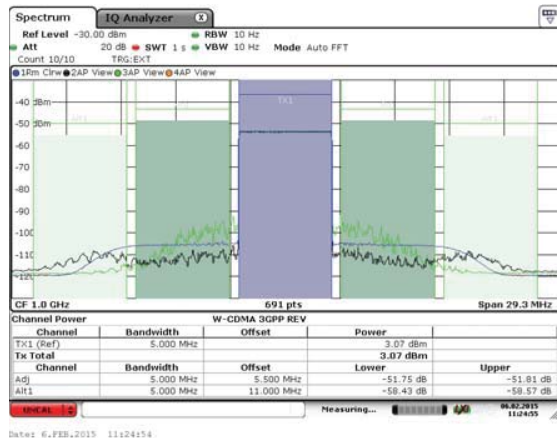
Fig. 4. The power spectrum density where green trace represents FBMC signal without DPD, black signal is FBMC signal with DPD and blue curve is OFDM signal without DPD. The signals were obtained at the output of PA denoted as Mini Circuits with input power $P_{IN} = -14dBm$.

V. CONCLUSION

The FBMC signals are resolutely candidates for future 5G systems. In this brief paper experimental study and comparison of FBMC and OFDM signals distorted by real non-linear power amplifiers have been tested. In order to guarantee higher accuracy of presented results three power amplifiers have been used. In this paper we have experimentally proved that using FBMC signals, lower ACP

can be achieved, however lower resistance than OFDM signals to non-linear distortions must be taken into the account. Using DPD systems the immunity of FBMC can be boosted for the undoubted cost of higher complexity. The results indicates, that FBMC modulation can achieve in general better ACP then OFDM signals. The EVM figures shows, that the DPDs can improve the error rate. We tried to prove that the DPD is even more important for FBMC than for OFDM signals.

REFERENCES

[1] H. Zhang, D. Le Ruyet, and M. Terre, "Spectral efficiency comparison between ofdm-oqam- and ofdm-based cr networks," *Wirel. Commun. Mob. Comput.*, vol. 9, no. 11, pp. 1487–1501, Nov. 2009. [Online]. Available: http://dx.doi.org/10.1002/wcm.v9:11

[2] J.-B. Dore, V. Berg, N. Cassiau, and D. Ktenas, "Fbmc receiver for multi-user asynchronous transmission on fragmented spectrum," *EURASIP Journal on Advances in Signal Processing*, vol. 2014, no. 1, p. 41, 2014. [Online]. Available: http://asp.eurasipjournals.com/content/2014/1/41

[3] H. Lin and P. Siohan, "Multi-carrier modulation analysis and wcp-coqam proposal," *EURASIP Journal on Advances in Signal Processing*, vol. 2014, no. 1, 2014. [Online]. Available: http://dx.doi.org/10.1186/1687-6180-2014-79

[4] J. Nadal, C. Abdel Nour, A. Baghdadi, and H. Lin, "Hardware prototyping of FBMC/OQAM baseband for 5G mobile communication systems," in *RSP 2014 : IEEE International Symposium on Rapid System Prototyping*, 2014, pp. 135 – 141.

[5] H. Bouhadda, H. Shaiek, D. Roviras, R. Zayani, Y. Medjahdi, and R. Bouallegue, "Theoretical analysis of ber performance of nonlinearly amplified fbmc/oqam and ofdm signals," *EURASIP Journal on Advances in Signal Processing*, vol. 2014, no. 1, p. 60, 2014. [Online]. Available: http://asp.eurasipjournals.com/content/2014/1/60

[6] Y. Medjahdi, M. Terre, D. Le Ruyet, D. Roviras, and A. Dziri, "Performance analysis in the downlink of asynchronous ofdm/fbmc based multi-cellular networks," *Wireless Communications, IEEE Transactions on*, vol. 10, no. 8, pp. 2630–2639, August 2011.

[7] L. Varga and Z. Kollar, "Low complexity fbmc transceiver for fpga implementation," in *Radioelektronika (RADIOELEKTRONIKA), 2013 23rd International Conference*, April 2013, pp. 219–223.

[8] Z. Kollr and P. Horvth, "Papr reduction of fbmc by clipping and its iterative compensation," *Journal of Computer Networks and Communications*, vol. 2012, 2012.

[9] J. K. Cavers, "Amplifier linearization using a digital predistorter with fast adaptation and low memory requirements," *Vehicular Technology, IEEE Transactions on*, vol. 39, no. 4, pp. 374–382, 1990.

[10] Z. Anding, J. C. Pedro, and T. J. Brazil, "Dynamic deviation reduction-based volterra behavioral modeling of rf power amplifiers," *Microwave Theory and Techniques, IEEE Transactions on*, vol. 54, no. 12, pp. 4323–4332, 2006.

[11] T. Gotthans, G. Baudoin, and A. Mbaye, "Comparison of modeling techniques for power amplifiers," in *Radioelektronika (RADIOELEKTRONIKA), 2013 23rd International Conference*, 2013, pp. 232–235.

[12] Z. Anding, P. Draxler, J. Yan, T. Brazil, D. Kimball, and P. Asbeck, "Open-loop digital predistorter for rf power amplifiers using dynamic deviation reduction-based volterra series," *Microwave Theory and Techniques, IEEE Transactions on*, vol. 56, no. 7, pp. 1524–1534, 2008.

[13] T. Ihalainen, A. Viholainen, T. Stitz, and M. Renfors, "Generation of filter bank-based multicarrier waveform using partial synthesis and time domain interpolation," *Circuits and Systems I: Regular Papers, IEEE Transactions on*, vol. 57, no. 7, pp. 1767–1778, July 2010.

Measured Capacity of mm-Wave Radio Link Under IQ Imbalance

Roman Marsalek, **Jiri Blumenstein**, Martin Pospisil, Markus Rupp

2018 IEEE 29th Annual International Symposium on Personal, Indoor and Mobile Radio Communications (PIMRC)

Measured Capacity of mm-Wave Radio Link Under IQ Imbalance

Roman Marsalek*, Jiri Blumenstein*, Martin Pospisil*, Markus Rupp*†

*Faculty of Electrical Engineering and Communication, Brno Univ. of Technology, Czech Rep.,
†Institute of Telecommunications, TU Wien, 1040 Vienna, Austria, *email: marsaler@feec.vutbr.cz*

Abstract—**Millimeter waves represent a promising solution to provide a sufficiently wide spectrum to satisfy the future requirements on broadband services. In this paper we evaluate the capacity of a short-range indoor wireless 60 GHz channel affected by quadrature imperfections of a real RF transceiver with orthogonal division multiplex approach. In our investigation, we consider spatially-dependent channel transfer function coefficients obtained from real measurements.**

I. INTRODUCTION

The use of millimeter waves (mm-waves) to provide sufficient bandwidth for enhanced Mobile BroadBand services in the 5-th generation (5G) of mobile services is envisaged. The most promising is the 28 GHz band, but also the 60 GHz band is interesting for the research community. An extensive research has been done in the last decades in the area of mm-wave channel sounding [1] and the capacity of the mm-wave radio channel has also been analyzed recently [2]. Similarly to 4G systems, the orthogonal frequency division multiplex (OFDM) or its filtered successors are considered for 5G [3]. The capacity of the radio link is affected not only by the channel itself, but also by the imperfections of radio frequency (RF) transceivers, such as nonlinear effects of the amplifiers or IQ up/down converters. In [4], the theoretical influence of the IQ imbalances on the ergodic and outage capacity of generic OFDM-based link has been investigated. The aim of this short paper is an attempt to join the results of channel sounding and RF transceiver characterization to estimate the capacity of real mm-wave RF link with impairments.

II. CHANNEL MEASUREMENT

The channel sounder was formed by a vector network analyzer (VNA), a power amplifier and transmitter (TX) and receiver (RX) antennas (open-ended waveguides). A short-range time invariant channel, where we emulate a mutual RX-TX movement by shifting the RX-TX locations (antenna placements) on a precise xy-table (see Fig. 1) was considered. The measurement was performed in frequency domain (discussed in e.g. [5]) in a range of 55-65 GHz, while the RX-TX locations were stationary during the channel transfer function (CTF) recording. Via the spatial shifting of the antennas, we captured 160 CTF snapshots for three different indoor locations,

(a) Measurement site I   (b) Measurement site II
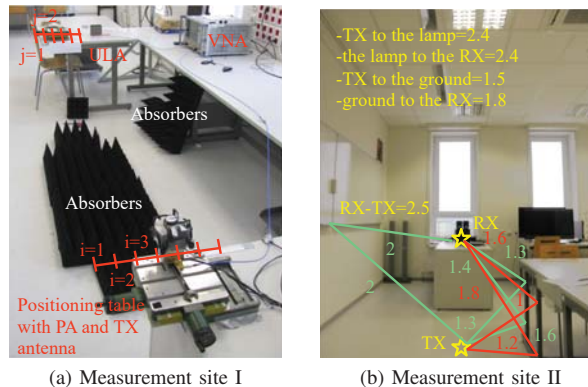
Fig. 1: Two out of three measurement sites. Site III is similar to the site II, but the xy tables are on top of the desk with 12 cm antenna height from the surface. The dimensions are in meters.

as ilustrated in Figure 1. Thus, although our channel is stationary, it exhibits the spatially-related variations due to the RX-TX location change. More information concerning this measurement campaign and the data processing can be found in [6], [7].

III. IQ MISMATCH MEASUREMENTS

Although the measurement of the RF channel was taken in 10 GHz bandwidth (BW), many of the currently available RF transceivers are limited to 1 GHz BW, such as Infineon BGT60 [8] we used as the RF up/down converter. The baseband part of the setup shown in Fig. 2 was created based on high speed A/D and D/A converters with FPGA interface board from Texas Instruments, complemented with an in-house designed front-end module. With this setup, we measured the frequency-dependent amplitude and phase imbalances, shown in Fig. 3. In order to cover the 10 GHz BW to characterize the device completely, the center frequency has been swept. Based on the imbalances, the Image Leakage Ratio (ILR) at OFDM subcarriers n (with corresponding image at carrier $-n$) can be computed [4]. Hereinafter, a frequency spacing of 10MHz has been considered.

IV. CAPACITY ANALYSIS

An expression for capacity at OFDM subcarrier n as a function of ILR_n and instantaneous values of normalized
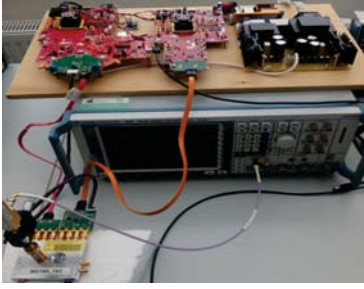
Fig. 2: Setup for IQ imbalances measurements, based on BGT60
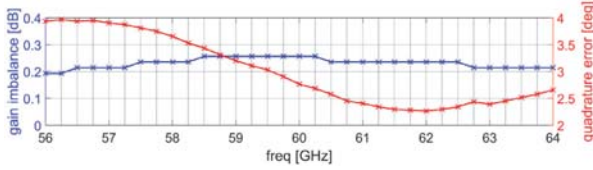
Fig. 3: Measured amplitude and phase imbalances of BGT60

channel amplitude coefficients ψ_n, ψ_{-n} at $n-$th and its mirror subcarrier $-n$ was derived [4]:

$$C_n = \log_2\left(1 + \frac{\psi_n^2 \mathrm{SNR}}{1 + \mathrm{ILR}_n(\psi_{-n}^2 \mathrm{SNR} + 1)}\right), \quad (1)$$

with SNR being the average signal to noise ratio. The ergodic channel capacity can then be obtained by averaging over the joint probability density function (PDF) $p(\psi_n, \psi_{-n})$ of channel amplitude coefficients:

$$\overline{C}_n = \int_0^\infty \int_0^\infty C_n p(\psi_n, \psi_{-n}) d\psi_n d\psi_{-n}. \quad (2)$$

Based on our channel sounding campaign described above, we estimated the sampled version of the joint PDF $p(\psi_n, \psi_{-n})$ as shown in Fig. 4. The PDF was smoothed with a 2D median filter. Note that as the instantaneous bandwidth of BGT60 is limited to 1 GHz, we used hereinafter only the 1 GHz portion of RF spectrum around 60 GHz center frequency to estimate the PDF.
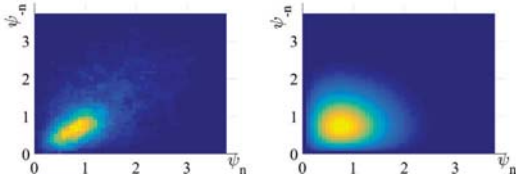
Fig. 4: Estimated $p(\psi_n, \psi_{-n})$ (left), joint Rayleigh pdf [4] (right)

Based on $p(\psi_n, \psi_{-n})$, the ergodic capacity at n-th subcarrier has been estimated as a function of average SNR. We considered several cases of ILRs - the case of perfectly compensated IQ transceiver corresponding to ILR=-50 dB, the case of uncompensated IQ transceiver with nominal value [8] of ILR=-20 dB and the case of measured average ILR=-27 dB. Fig. 5 shows the ergodic

capacity, together with the Shannon limit case and the case of Rayleigh channel expected in [4].
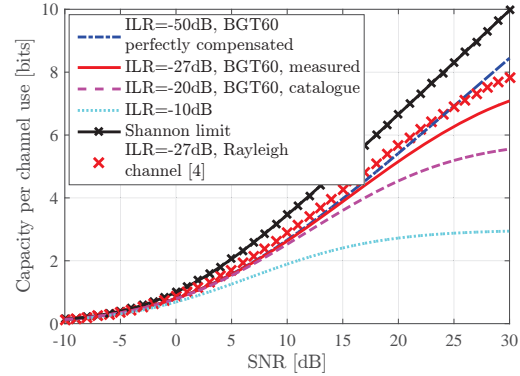
Fig. 5: Capacity of the measured channel under IQ imperfections

V. CONCLUSION

In this short paper, we have demonstrated how the ergodic capacity of a real millimeter-wave channel is affected by the IQ mismatch of real RF transceiver. For the future, we will estimate how the application of frequency-independent and frequency-dependent IQ compensation methods will practically affect the capacity on different center frequencies.

REFERENCES

[1] A. Maltsev, R. Maslennikov, A. Sevastyanov, A. Khoryaev, and A. Lomayev, "Experimental investigations of 60 GHz WLAN systems in office environment," *IEEE J. Sel. Areas Commun.*, vol. 27, no. 8, pp. 1488–1499, Oct. 2009.
[2] G. C. Ferrante, T. Q. Quek, and M. Win, "Revisiting the capacity of noncoherent fading channels in mmWave system," *IEEE Trans. Commun.*, vol. 65, no. 8, pp. 3259–3275, 2017.
[3] R. Nissel and M. Rupp, "Pruned DFT spread FBMC: Low PAPR, low latency, high spectral efficiency," *IEEE Transactions on Communications*, pp. 1–1, 2018 (Early Access).
[4] S. Krone and G. Fettweis, "Capacity analysis for OFDM systems with transceiver I/Q imbalance," in *IEEE GLOBECOM 2008- 2008 IEEE Global Telecommunications Conference*, Nov 2008, pp. 1–6.
[5] J. Blumenstein, A. Prokes, A. Chandra, T. Mikulasek, R. Marsalek, T. Zemen, and C. Mecklenbruker, "In-vehicle channel measurement, characterization, and spatial consistency comparison of 3-11 GHz and 55-65 GHz frequency bands," *IEEE Trans. Veh. Technol.*, vol. 66, no. 5, pp. 3526–3537, May 2017.
[6] J. Blumenstein, R. Marsalek, T. Gotthans, R. Nissel, and M. Rupp, "On mutual information of measured 60 GHz wideband indoor MIMO channels: Time domain singular values," in *IEEE PIMRC 2017*, Oct 2017, pp. 1–5.
[7] P. Liu, J. Blumenstein, N. S. Perovic, M. D. Renzo, and A. Springer, "Performance of generalized spatial modulation MIMO over measured 60 GHz indoor channels," *IEEE Transactions on Communications*, vol. 66, no. 1, pp. 133–148, Jan 2018.
[8] "Single Chip SiGe Transceiver Chipset for V-band Backhaul Applications from 57 to 64 GHz - Application Note AN376," Infineon Technologies AG, Tech. Rep., 06 2014.